Planet Mercury

and the behavior of elements in reduced conditions

Hadrien Pirotte

Ph.D. advisor and co-advisor:

Dr. Bernard Charlier

Dr. Anne Pommier

Ph.D. dissertation submitted in partial fulfilment of the requirements for the degree of Doctor of Sciences from the University of Liège.

2023

Jury:

Prof. Frédéric Hatert	Université de Liège, Belgium	President
Dr. Bernard Charlier	Université de Liège, Belgium	Advisor - Secretary
Dr. Anne Pommier	Carnegie Institution for Science, USA	Co-advisor
Prof. Camille Cartier	Université de Lorraine, France	External examiner
Prof. Olivier Namur	Katholieke Universiteit Leuven, Belgium	External examiner
Prof. Max Collinet	Université de Namur, Belgium	External examiner

A Szaniszló

Remerciements

Je tiens en tout premier lieu à remercier Bernard, qui m'a suivi avec attention depuis maintenant de nombreuses années. Je le remercie pour la grande liberté et la confiance qu'il m'a laissé dans ma recherche, que ce soit sur les sujets que j'ai souhaité développer ou la méthode que je voulais employer pour y arriver. Je remercie Anne pour son invitation et son accueil dans son laboratoire aux Etats-Unis, pour m'avoir impliqué dans des projets annexes, et pour m'avoir apporté son aide et son soutien tout au long de ma thèse. Je vous remercie tous les deux pour le temps que vous m'avez accordé et pour toutes les discussions que nous avons pu avoir. Merci aussi pour tous les bons moments passés en dehors du boulot !

Je remercie Jacqueline Vander Auwera et Olivier Namur, membres de mon comité de thèse, pour leur suivi et leurs conseils. Je remercie en particulier ce dernier pour son aide et les discussions, et pour la rigueur qu'il a apporté à mon travail. Merci également à Camille Cartier.

Je remercie Nicolas pour son aide dans le laboratoire, ainsi que les professeurs et membres scientifiques du département qui ont chacun participé à construire mon esprit scientifique durant ces 10 années d'étude et de doctorat. Merci Joëlle et Mariella pour toute l'aide que vous m'avez fournie, et pour le temps que vous avez passé à régler tous les problèmes qu'on rencontre durant une thèse ! Merci Joëlle pour les magnifiques peluches crochetées. Elles trônent fièrement au-dessus de la cheminée.

Je remercie tous mes collègues du B20 : Merry, Melvin, Michiel, Jarno, Anne-Christine, Damien, Fabrizio, Laurie et les autres. Merci pour votre aide et votre bonne humeur. Je remercie particulièrement les courageux volontaires qui m'ont donné un coup de main pour sortir mes expériences du four ! Merci aussi aux collègues de Leuven, en particulier Sander, pour tous les chouettes souvenirs qu'on a créé au fil du temps.

Je remercie le laboratoire de paléo pour son accueil toujours chaleureux durant ces années de thèse. Merci à Valentin, Antoine, Raphaël, Isaure, Yann, Cyrille et tous les autres pour tous ces temps de midi passés avec vous et les fous rires qui vont avec. Un merci tout particulier à Narimane pour son incroyable disponibilité à faire toutes ces pauses conviviales !

Je remercie également les membres du laboratoire de minéralo pour leur accueil dans leur bibliothèque et pour toutes les discussions enrichissantes qu'on a eu autour d'un verre. Merci Martin et Fabrice pour tous ces bons moments passés ensemble !

Merci à tout le département pour toutes les soirées barbecues, les après-midi pétanque, les journées balades et tous les autres évènements qui animent la vie au bureau.

Je remercie tous mes amis qui m'ont accompagné durant ces années, et m'ont redonné le sourire durant les moments difficiles de la thèse et de la vie. Pensées pour les Liègéos, les scouts, les potes de Namur,

et les autres. Merci Thibault et Jonas pour votre amitié depuis maintenant plus de 15 ans. Merci Manon pour avoir toujours été là malgré la distance. Enfin, merci à tous ceux qui de près ou de loin m'ont soutenu durant cette thèse.

Je veux maintenant remercier mon papa et ma maman, qui m'ont toujours encouragé dans mes choix et qui ont été très présents ces dernières années pour me soutenir et m'écouter. Merci à ma belle-famille pour tous les bons moments et votre soutien. Merci à Quinoa et à Ural, qui arrivent à me remonter le moral sans parler, et ça c'est fort. Merci enfin à Helena, sans qui je ne serais jamais arrivé là. Merci pour tout ton amour et ton soutien.

Abstract

Planet Mercury exhibits exotic characteristics compared to Earth. Its surface shows highly reduced lavas devoid of FeO (<1 wt%) and rich in sulfur (2 - 4 wt%). Its internal structure is also very different, with an enormous iron core and a thin mantle. An FeS layer, at the core mantle boundary, has also been proposed. These features make Mercury unique compared the other terrestrial planets. To understand processes that shaped the surface and the interior of the planet, we need information on the chemical behavior of elements under very reducing conditions. As these peculiar redox conditions are not met on Earth, the use of experimental petrology to constrain the partitioning of elements among the different reservoirs of Mercury is needed.

In this thesis, we performed around a hundred experiments using various experimental apparatuses, spanning a large pressure and temperature range (0.0001 – 6 GPa and 1200 – 1700 °C) on powders whose compositions are representative of Mercury's silicate part and lavas. The quenched products of our experiments show three equilibrated melts (metal, sulfide, and silicate) as well as solid Fe-free sulfides (CaS/MgS) and were used to calculate metal-silicate and sulfides-silicate partition coefficients for over 30 elements.

We use U, Th and K partitioning data to determine the distribution of these heat-producing elements during primordial differentiation and partial melting of the mantle. We show that, based on the Th/U ratios measured on the surface, there cannot be an FeS layer formed in equilibrium with the silicate part. Moreover, we show that surficial K/Th and K/U are several times lower than expected from chondritic compositions. By modelling the distributions of Ti, Cr and Mn and comparing those values to their measured surface contents, we show that the residual mantle of Mercury after partial melting and production of the secondary volcanic crust should host a significant amount of CaS that incorporates Cr and Mn, but not Ti. In particular, Mn should be very compatible in the mantle, requiring the presence of alabandite (MnS). Finally, we show that the value of the difference of partitioning of two different elements in a sample is directly proportional to their difference in electronegativity. Based on a large dataset from the literature, we propose a new equation to predict metal-silicate partition coefficients with relatively high accuracy ($\sigma \sim 1$-2 in natural logarithm) for a large number of elements, provided that the partition coefficient of at least one element in the studied sample is known to serve as a standard.

Résumé

La planète Mercure présente des caractéristiques exotiques comparée à la Terre. Sa surface est faite de laves formées en conditions très réductrices, très pauvre en FeO (<1 wt%) et riche en soufre (2 - 4 wt%). Sa structure interne est aussi très différente, avec un énorme noyau de fer et un fin manteau. L'existence d'une couche de FeS à l'interface noyau-manteau a aussi été suggérée. Ces caractéristiques font de Mercure un astre à part en comparaison des autres planètes telluriques. Afin de comprendre les processus géologiques qui ont mené à ce qu'on observe à sa surface, nous avons besoin d'informations sur le comportement chimique des éléments sous conditions très réductrices. Ces conditions redox uniques ne se rencontrent pas sur Terre, et la pétrologie expérimentale devient nécessaire afin d'étudier le partage des éléments entre les différents réservoirs de Mercure.

Nous avons effectué une centaine d'expériences sur plusieurs appareils expérimentaux, couvrant une large gamme de pressions et de températures (0.0001 – 6 GPa et 1300 – 1700 °C) sur des poudres de compositions représentatives de la partie silicatée de Mercure et de ses laves. Les charges expérimentales produites présentes trois liquides en équilibres (métallique, sulfurée et silicatée) ainsi que des sulfures sans fer (CaS/MgS), et nous avons pu calculer pour une trentaine d'éléments les coefficients de partage entre les différentes phases en présence.

Nous avons utilisé les données de partages de U, Th et K pour déterminer la distribution de ces éléments producteurs de chaleur durant la différenciation primordiale et la fusion partielle du manteau. Nous montrons, en nous basant sur le ratio Th/U mesuré à la surface, qu'une couche FeS formée en équilibre avec la partie silicatée ne peut pas exister. De plus, nos modèles montrent que les ratios K/Th et K/U sont inférieurs à ce qui serait attendu si les ratios initiaux étaient chondritiques. En modélisant la distribution de Ti, Cr et Mn et en comparant ces résultats avec leur concentration mesurée à la surface, nous montrons que le manteau résiduel de Mercure durant sa fusion partielle doit être composé d'une grande fraction de CaS, ce dernier incorporant du Cr et du Mn, mais pas de Ti. En particulier, le Mn devrait adopter un comportement très compatible dans le manteau, ce qui impliquerait la présence d'alabandite (MnS). Enfin, nous montrons que la valeur de la différence des coefficients de partage métal-silicate de deux éléments au sein d'un même échantillon est directement proportionnelle à leur différence en électronégativité. En nous basant sur une large base de données de la littérature, nous proposons une nouvelle équation pour prédire la valeur des coefficients de partage métal-silicate avec une exactitude de 1-2 σ (en logarithme népérien) pour un grand nombre d'éléments, pour autant que le coefficient de partage d'au moins un élément dans l'échantillon étudié est connu pour servir de standard.

Table of content

General introduction

Understanding the distribution of chemical elements between minerals and magmatic melts is fundamental in geology, for economic aspects and for fundamental scientific research. In planets, the elements are distributed among different reservoirs, the two most important in mass being the core and the silicate part. The incorporation of elements in those reservoirs has deep implications for the evolution of the planets as; for example, light elements in planetary cores change its melting temperature, delaying its solidification and thus impact on the thermal budget of the planet. The concept of behavior of elements stems from this distribution amongst the different reservoirs, as observed in meteorites (Goldschmidt, 1937): siderophile for those who concentrate in metals (i.e., the core), chalcophile for those in association with sulfur (i.e., sulfide layers), and lithophile for the elements concentrated in oxides and silicates (i.e., the silicate part).

This work is centered on two main axes: first, we determined the behavior of a large number of elements under the conditions prevalent on Mercury during its formation, differentiation, and geological evolution using experimental petrology. Secondly, we applied these new data, in combination with the literature, to better understand the internal structure of Mercury, its volatile content, and the mineralogy and processes in the mantle.

Mercury is a unique planet compared to its peers. Its very high density reflects its unusually high proportion of metal to silicate, which challenges models of planetary formation. Its volcanic surface, older than 3.5Ga, has not seen any resurfacing as observed on Venus, the Earth and Mars, which offers a unique chance to improve the constrains on early mantle processes and planetary formation. The latest probe to orbit the planet, MESSENGER, revealed key data that led to an improved understanding of the planet, especially its structure and silicate composition. The surface, rich in S (3 wt%) and poor in FeO (<1 wt%), is the product of volcanic processes that occurred under very reducing conditions (~IW-3 to ~IW-7). The abundance of other volatiles, such as K, Na and Cl, also questioned the relevance of planetary formation models for planets formed so close to the Sun.

One of the main unknowns regarding Mercury is the effect of its high sulfur content on mantle processes, and in particular the role of the Fe-free sulfides (CaS/MgS) that should be abundant in its silicate part. Another one is the effect of reducing conditions on the behavior of elements. While numerous studies have showed that elements become more siderophile (metal-loving) and chalcophile (sulfide-loving) with increasingly reducing conditions, there are still some elements whose behavior are poorly constrained, such as U and Th.

The lack of sample from the planet has brought the need for experimental petrology to reproduce these unusual conditions, that are exotic relative to the oxidant Earth. In this work, we thus carried out experiments under low to high pressures (0.0001 – 6GPa), high temperatures (1300 – 1700) and very

reducing conditions (~IW-1 – IW-8) on powders whose compositions are representative of either the silicate part of Mercury or the lavas observed at the surface. The powders were doped in minor and trace elements, different sources of S were added (S, FeS, CaS) and the oxygen fugacity was kept low by varying the ratio of Si_{metal}/Si_{silica} and keeping the same amount of Si_{tot}. Those experiments have been used to tackle a range of subjects, leading to the following chapters:

Chapter **one** introduces several concepts regarding the behavior, partitioning, and abundance of elements in planetary bodies of the solar system.

Chapter **two** aims to give a comprehensive introduction on planet Mercury, discussing the history of its exploration, its internal structure, its surface composition and magmatic features, its magnetosphere and exosphere, as well as the different scenarios proposed to explain the formation of such a unique planetary body.

Chapter **three** describes the methods used in this work to produce the data used in the discussion. Descriptions of the various apparatuses used are given, with an emphasis on the piston-cylinder and the evacuated silica tube. The analytical methods are also explained. An inventory of the samples produced and analyzed can be found at the end of the chapter.

Chapter **four** discusses the work done on the distribution of heat-producing element (U, Th and K) between the core, the silicate part and the hypothetical sulfide layer on Mercury. The work focusses on demonstrating that the measured surface Th/U is incompatible with the existence of an FeS layer formed in equilibrium with the silicate part under reducing conditions. The volatility of Mercury is also discussed based on a comparison between the expected K/Th and K/U if Mercury formed from chondritic material versus what we measured on the surface. We conclude that there was probably a stark loss of K during the history of the planet, either during its accretion or from the action of the solar wind on its surface. This chapter is published in Icarus.

Chapter **five** attempts to model the measured Cr/Ti and Mn/Ti ratios at the surface in order to constrain the mineralogy of the mantle. The abundance of these three elements in chondrites is relatively constant, and their behavior during core-silicate differentiation is easily modeled, so that we have a good idea of the expected concentrations of Ti, Cr and Mn in the silicate part. Thanks to the volcanic nature of the surface, which derives mainly from high partial melting of the mantle, we can constrain the mineralogy of the residual mantle that fits the observed ratios. Based on the Mn/Ti, Mn needs to be strongly compatible, so that Fe-free sulfides are probably abundant in the mantle (CaS and/or MgS), with MnS as an important accessory mineral, as observed in enstatite chondrites. The variation of the Cr/Si ratio measured at the surface with different degrees of partial melting is best explained by the presence of Cr-rich sulfides (CaS and/or MgS) that melts with higher partial melting, releasing more Cr. Finally, we show that CaS should be the dominant Fe-free sulfide of the mantle based on the concentration of Ti, as CaS does not incorporate Ti.

Chapter **six** discusses the link between the electronegativity and the siderophile behavior of an element. Electronegativity, as defined by Pauling (1932), is the capacity of an element to attract and hold on to electron. By using the large number of metal-silicate partition coefficients for around 60 elements available from the literature, we show that their value is directly linked to oxygen fugacity and the electronegativity of the element. Moreover, in a single sample with fixed pressure and temperature conditions, the difference in the partition coefficient values of two different elements is directly proportional to their difference in electronegativities. As such, it is possible to predict the partitioning of many elements by knowing the partition coefficient of only one element. In practice, there are still some deviations observed between the predicted and the observed values for certain element, for which we provide some explanations that keep this theoretical relationship valid.

Finally, there is a general conclusion, a glossary (for words marked with an asterisk *), the references, and the appendixes. Appendix A reports the development of a new experimental setup developed at the APS synchrotron in Chicago in 2019 (Pommier et al., 2021). Appendix B describes the experiments carried out at the University of California San Diego and at the Carnegie Institution for Science in 2019 - 2020 and 2021, respectively, followed by the paper that resulted from the analyzes and interpretations of the samples produced (Pommier et al., 2023). Appendix C presents the paper in revision in Geochimica and Cosmochimica Acta on the work done by Cartier and co-authors on metal-silicate partitioning of Ni-Co (Cartier et al., in rev). Appendix D presents tables on the chemical compositions measured by EPMA and LA-ICPMS of previously unpublished experiments presented here.

Chapter 1: The behavior of elements

1.1 The classification of the elements

As analytical methods developed throughout the twentieth century, it enabled scientists to measure precisely very low concentrations of elements, opening the way for quantifying trace elements in geological settings. They observed that almost all elements were present in natural rocks and minerals and that each one of them has different affinities within these phases. Some elements, such as platinum, were only present as traces in rocks, but were concentrated in native metals and iron meteorites. Based on these observations, Washington (1920) was the first to divide the elements in two classes: the rock elements, called “petrogenetic” and ore elements, named “metallogenetic”. He observed that, in nature, petrogenetic elements, such as Rb, Cs, Sr, Ba or Y, occurs as oxides, silicates, fluorides or chlorides, but almost never as sulfides or native metals. On the other hand, the metallogenetic elements, including Cu, Ag, Zn, Cd or Ga, are rarely found as silicates, oxides, fluorides or chlorides, but as sulfides or as native metals. While Washington (1920) observed some exceptions in his classification, such as the presence of sulfides formed by petrogenetic elements in meteorites, he did not make the link between change in redox conditions and the changes of elements behavior. Acknowledging the work from Washington (1920), Goldschmidt (1937) established his famous classification of elements between 5 groups (Figure 1-1); siderophile (metal-loving), chalcophile (sulfur-loving), lithophile (rock-loving), atmophile (found naturally as gas) and biophile (elements that are the basis of life). His work was based, again, on the refinement of analytical methods, notably spectrographic analysis, optical and X-ray spectra. He explained the classification of the elements by the structure of their electron shells and their potential of ionization. He noted the importance of the geological context on the behavior of elements, such as the temperature and the degree of reduction of a system.

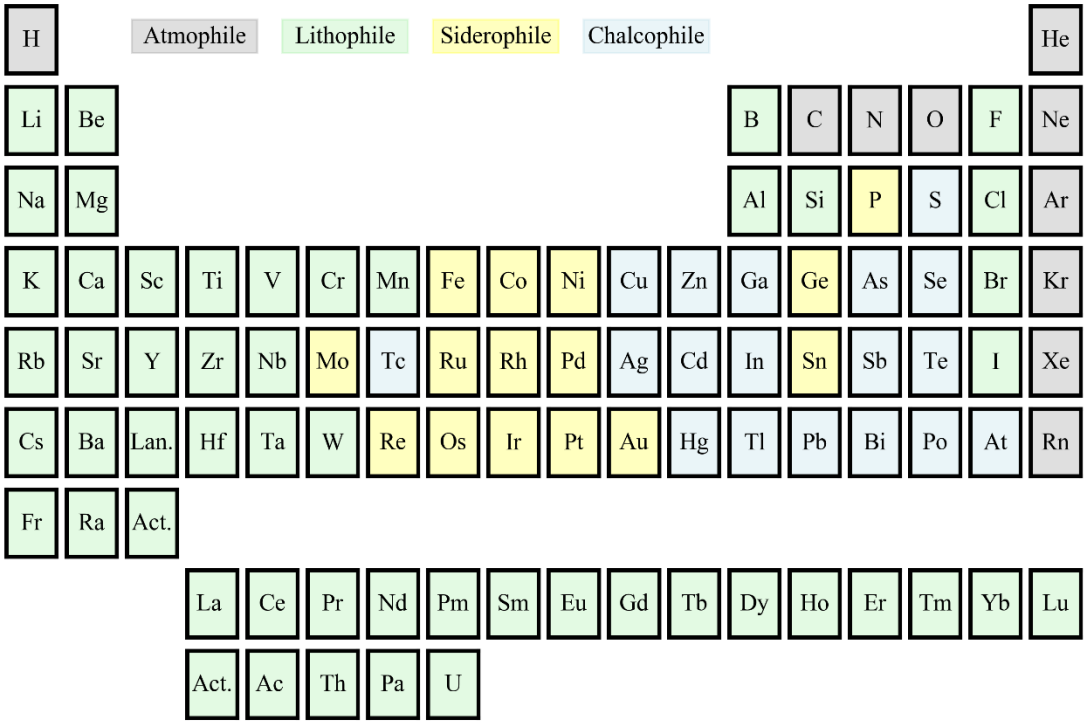

Figure 1-1: Periodic table showing the Goldschmidt classification of elements (data from Albarède, 2009).

As shown by Gibson (1949), the distinction was made between partitioning of element during planetary differentiation, with siderophile elements in the core, lithophile in the silicate part, and chalcophile in an intermediate transition zone between the two, and mineral - melt partitioning during the subsequent crystallization. In the first case, the element's electronic structure was determinant, while in the other one (i.e. in minerals), it was the valence and the ionic radius that were the key. While Goldschmidt established 3 rules to predict the mutual replacement of ions in magmatic minerals, they required modifications to account the rather numerous exceptions encountered in nature (Fyfe, 1951; Ramberg, 1952; Shaw, 1953; Ringwood, 1955).

1.1 The abundance of elements

Much knowledge has been acquired on the abundance of elements since Clarke's (1889) attempts to quantify the elements' relative abundance. Clarke (1911) recognized the limitation of their knowledge in undertaking this endeavor; while the global composition of the oceans could be estimated, it was much more difficult for the crust. Not only was its thickness unknown, but estimating the proportion of igneous rocks, metamorphic rocks, and sedimentary rocks proved to be challenging, not to talk about the accuracy of measurements of the elements themselves. At the time, the presence of a core at the center of the Earth, containing iron and other elements, was not even a certainty. However, Earth being

a mixture of elements in equal proportion by weight could be excluded, as its density was lower than what would be expected in such scenario. Oddo (1914) and Harkins (1917) separately reported that elements with an even atomic number have higher relative abundance than the elements before and after in atomic number, that have odd atomic numbers (Figure 1-2); it was, for a time, considered that the relative abundance of elements should simply decrease with higher atomic number.

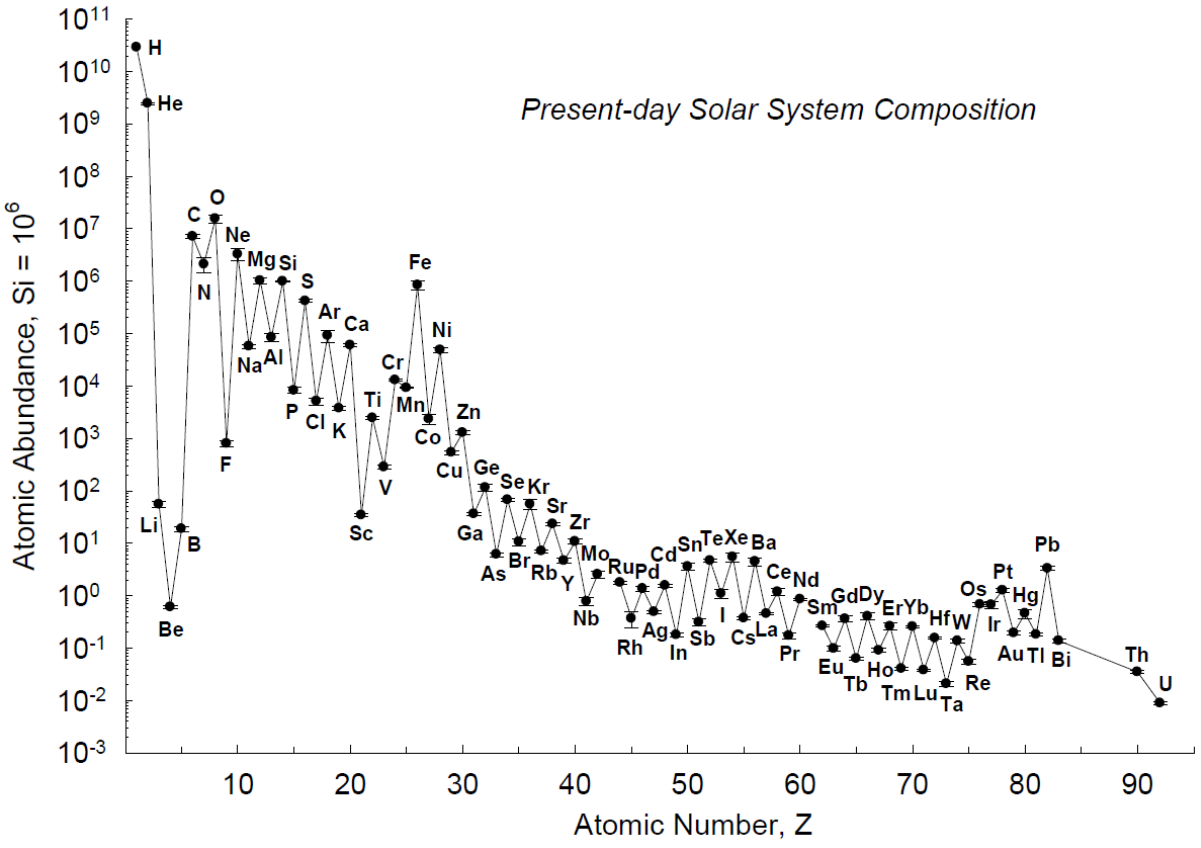

Figure 1-2: Atomic abundances of elements in the solar photosphere as a function of their atomic numbers Z (from Lodders et al. 2009).

The study of meteorites, especially chondrites, drastically improved the quest for the natural abundance of elements. Indeed, undifferentiated bodies dated back to the formation of the solar system are a lot more representative than the rocks on the surface of the Earth, which experienced loss of volatile during its formation, core-mantle differentiation, partial melting, and weathering (Goldschmidt, 1923; Goldschmidt, 1937; Suess and Urey, 1956). Goldschmidt, based on the hypothesis that the planet initially differentiated between a metal melt, a sulfide melt and a silicate melt, proposed that meteorites, which show the same three melts (more precisely three types of phases, namely silicates, sulfides and metals), could be used as a proxy to infer the chemical abundance of the Earth, bypassing the unsolvable problem of probing Earth deep interior.

1.2 Partition coefficients

The partition coefficient of an element between two phases expresses the relative affinity of this element for the two phases. It is a dimensionless value, that vary from 0 (in theory strictly superior to 0) to infinity. It is expressed as the ratio of the concentration of an element E in phase A and B, such as:

$$D_E^{A/B} = [E]_A/[E]_B$$

where $D_E^{A/B}$ is the partition coefficient, [E] is the concentration of element E in phase A and phase B. The most common partition coefficient, called Nernst coefficient, is calculated from the mass concentration of the element, but some calculate it from its molar concentration, which is then called molar coefficient. Partition coefficients are usually used to quantify the compatibility of an element in a mineral in equilibrium with a liquid (if the coefficient is above 1, it is compatible, and below 1 incompatible), but it can also be used between two liquids. In this work, partitioning between silicate melts, sulfide melts and metal melts is frequently used. The compatibility of an element is also widely used in the context of partial melting: when a rock partially melts, an element can either mainly stay in the remaining rock, making it compatible, or it can mainly go into the melt, making it incompatible. In the same way, we can calculate the bulk partition coefficient of an element between the mantle and the melt, by summing the partition coefficient between each phase in the residual mantle and the melt, times their respective fraction. If it is above 1, the element is compatible during partial melting, while it is incompatible if it is below 1.

Partition coefficients are experimentally determined, as their calculations necessitate measuring both the melts (or the glasses) and the mineral in equilibrium, which are rarely found in nature, except for some very rapidly cooled lavas. Moreover, experiments enable a precise control of intensive (temperature, oxygen fugacity) and extensive (pressure, composition) parameters.

Partition coefficient determination is very sensible to extreme value. For example, elements that are highly siderophile, such as Nickel, will have a very high concentration in metal and a very low concentration in silicate melts, so that any slight error on the latter value will have strong effect on the final coefficient value. Concentrations close to the detection limit should be used with caution when calculating partition coefficients.

1.3 Oxygen fugacity

Oxygen fugacity, written fO_2, is defined as the partial pressure of oxygen in a determined setup (typically in rocks in geological studies) corrected for the non-ideal behavior of the gas. The partial pressure of oxygen in rocks is very low, as almost all the oxygen is bound with cations in minerals or in silicate melts, and oxygen fugacity can be interpreted as the amount of free oxygen available in the system.

The concept was introduced by Eugster (1957). He discovered that controlling the partial pressure of oxygen (PO_2) was necessary to experimentally synthetize ferrous biotite (annite), as failing to do so always produced magnetite and sanidine. He realized that the PO_2 of his assemblage was too high, and that annite would only form below a certain PO_2 value, which itself depends on the temperature. In order to do so, he created an assembly where the sample is placed in a Pt capsule, which is enclose in a gold tube filled with an oxygen buffer and water. As Pt is permeable to H_2 but not to O_2 and H_2O, the dissociation of water caused by its equilibration with the buffer led to the migration of H_2 inside the Pt cell, which binds with oxygen to form water, and thus decrease the amount of free oxygen in the sample. The term "oxygen fugacity" was later introduce by Eugster and Wones (1962), as fugacity is the correct thermodynamical word to use when discussing partial pressure of non-ideal gases.

Since then, fO_2 has been used extensively to estimate redox conditions of various systems, and it is an intensive parameter as important as temperature and pressure. While it can be expressed as an absolute value of partial pressure in oxygen, it is commonly compared to the value of a buffer. Buffers are reactions between solids and a fluid phase that induce changes in the oxidation state of an element. As long as all components of the reaction are present, their chemical potentials are constant and so they fix the oxygen potential (Eugster, 1977; Frost, 1991). As the values of buffers depend on temperature and pressure, they need to be calculated as well. Some common buffers include:

Magnetite – hematite (MH): $4Fe_3O_4 + O_2 = 6Fe_2O_3$

Ni – NiO (NiNiO): $2Ni + O_2 = 2NiO$

Fayalite – magnetite – quartz (FMQ): $3Fe_2SiO_4 + O_2 = 2Fe_3O_4 + SiO_2$

Iron – wustite (IW): $2Fe + O_2 = 2FeO$

Iron is widely used to estimate the oxygen fugacity of geological samples because it is a ubiquitous element naturally found in three different oxidation states (0, +2 and +3). This is the reason for its presence in most buffers used in geosciences to describe redox states. On Earth, surface rocks are mainly oxidized, while deeper in the mantle the conditions are more reducing (down to the IW buffer in the deep mantle, McCammon, 2005), and the redox state of most terrestrial rocks are usually expressed relative to FMQ (e.g., Haggerty, 1978). On Mercury, in meteorites and in our experiments, conditions are much more reducing and so it will be compared to the IW buffer.

There is a section for each chapter of discussion in this work to detail how oxygen fugacity was calculated. In any case, it was calculated for all literature data using the same consistent method, based on the work of Prof. Olivier Namur (details can be found in Namur et al., 2016a).

1.4 The elements under reduced conditions

As seen above, Goldschmidt established its classification based on the observed behavior of elements in nature, and he rightfully saw that some elements could belong to different classes. For example, iron is observed in metals, sulfides and in oxides and silicates. In this case, the oxidation state plays a crucial role on the metallic behavior of elements, as their reduction to the state 0 grants their incorporation in metal phases. The availability of free oxygen, measured by oxygen fugacity, is the main driver behind these changes in behavior: while decreasing oxygen fugacity directly decrease the oxidation state of elements, it also impairs the possibility for some cations to bind with oxygen, leading to an increase in chalcophilic behavior if sulfur is available (see Ringwood, 1955). In melts, the affinity of cations for anions is dependent on the difference in electronegativity; the largest the difference, the stronger the ionic bond is, so that the elements are firmly bound together (Ringwood, 1955; Barnes and Maier, 1999). This explains in a large part why the highly electronegative elements, which are highly siderophile, are also very chalcophile: they are the first to be deprived of oxygen, which "prefers" to bind with lower electronegative elements such as alkaline ones. More on this subject in Chapter 6:.

The change in valence of elements with fO_2 has been extensively studied and put in relation with their change in incorporation in silicates, sulfides and metals (e.g., Hillgren, 1991; Borisov et al., 1994; Holzheid et al., 1994; O'Neill et al., 1995; Gessmann et al., 1999; Papike et al., 2005; Cartier et al., 2014a). In highly reduced systems, such as in meteorites, multi-valent elements such as Ti, V and Cr show lower valence in silicates than currently observed on Earth, thus changing their partitioning behavior as a function of the redox conditions (respectively Ti^{3+}, V^{2+} and Cr^{2+}, e.g., Papike et al., 2005; Righter et al., 2011; Sutton et al., 2022). The different valences of Ti (4+, 3+ and 2+), for example, changes the network and the liquidus of melts (Tranell et al., 2002 and references therein).

On Earth, we find a large diversity of redox conditions, from the reduced lower mantle (around the IW buffer) to the very oxidized lamprophyres (~IW+8, Carmichael, 1991 and references therein; McCammon, 2005; Figure 1-3). On the other hand, chondrites, and particularly enstatite chondrites, present the most reduced rocks (Wadhwa, 2008), showing a mineralogy that is exotic to Earth, with abundant sulfides (Keil and Andersen, 1965; Mason, 1966; Keil, 1968; Skinner and Luce, 1971; Okada and Keil, 1982; Wadhwa et al., 1997; Keil, 2007). Estimation for Mercury's oxygen fugacity ranges from IW-3 to IW-7 (McCubbin et al., 2012; Zolotov et al., 2013; Figure 1-3), much lower than rocks on Earth, and so we expect similar exotic mineralogies to be present on the planet.

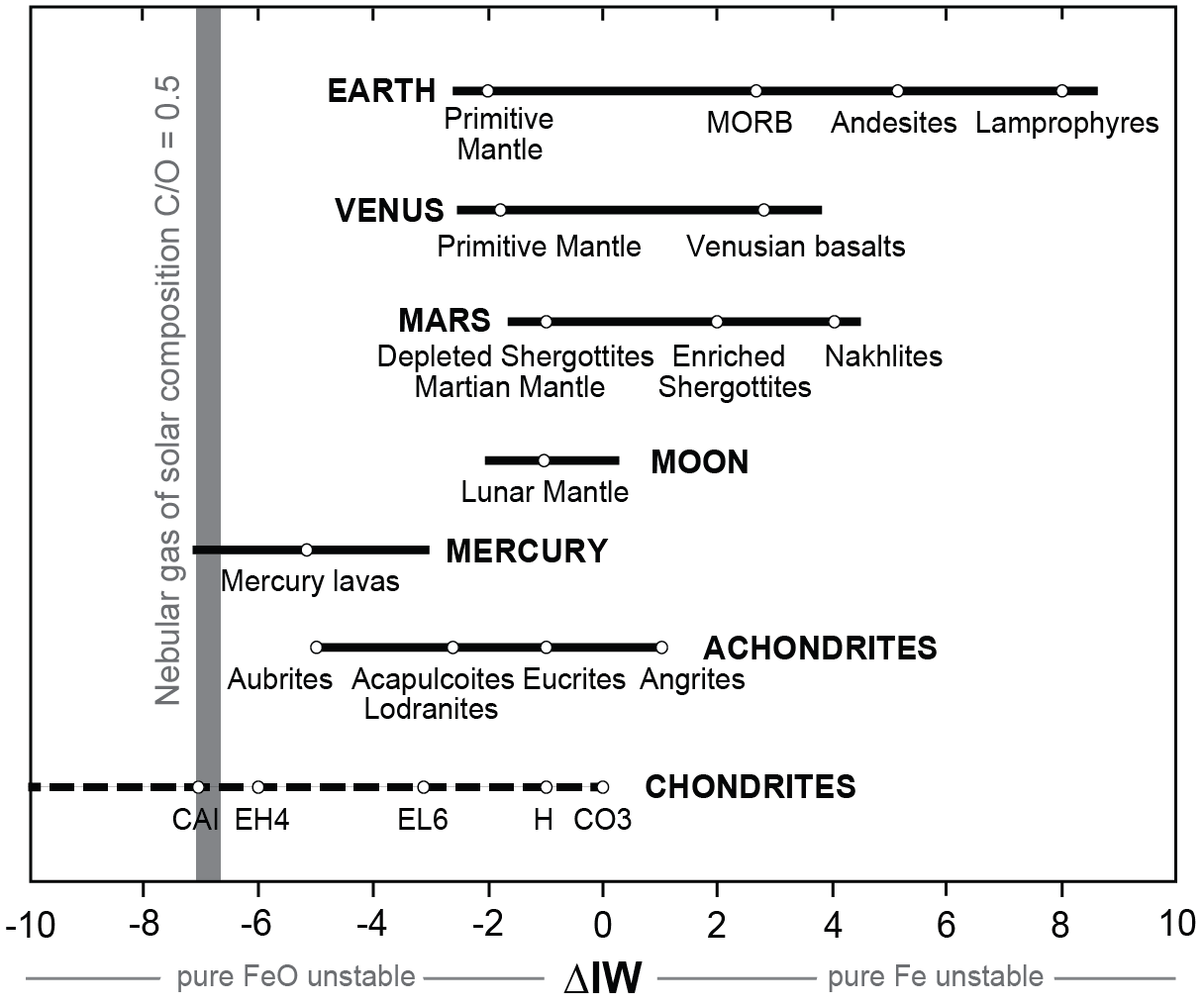

Figure 1-3: Comparison of the redox state on different bodies of the solar system, relative to the iron-wüstite buffer. CAI: calcium-aluminium inclusion; EH4 and EL: enstatite chondrites; H: high metal chondrite; CO3: carbonaceous chondrite (from Cartier and Wood, 2019). Mercury's oxygen fugacity is estimated between ~IW-3 to ~IW-7 (McCubbin et al., 2012).

These very reducing conditions are accompanied by strong changes in elemental behavior, as seen in meteorites. Elements that are lithophile in most Earthly conditions partition into sulfides and metals under reduced conditions (e.g., Mason, 1965; Easton, 1985; Lodders and Fegler, 1993; Gannoun et al., 2011). Experimental petrology was extensively used to understand the incorporation of such elements in these phases and to produce metal/silicate melt and sulfide/silicate melt partition coefficients (e.g., Kilburn and Wood, 1997; McCoy et al., 1999, Wohlers and Wood, 2017; Steenstra et al., 2020a). This enabled authors to better understand chondrites, planetary formation and the incorporation of elements in either the core, the sulfide melts when present, or the silicate part. Understanding the distribution of elements in planets is crucial to understand their structure and history. For example, the distribution of heat-producing elements (U, Th and K) has been used to predict the internal heat budget of Mercury's interior as well as its mantle processes (Wohlers and Wood, 2015,2017; Boukaré et al., 2019; Boujibar et al., 2019; Mouser and Dygert, 2023). Other studies, such as Cartier et al. (2020) and Pirotte et al.

(2023), used respectively the fractionation of Ti/Al and Th/U between the different reservoirs during planetary differentiation to constrain the internal structure of Mercury. In this thesis, the use of experimentally determined partition coefficients is also used to constrain the mineralogy of Mercury's mantle.

Chapter 2: Planet Mercury

2.1 Introduction

Mercury is a scorched planet. The surface is barren, composed of volcanic rocks. No atmosphere exists. Days last an eternity compared to Earth; almost 176 terrestrial days, due to the planet's 3:2 spin-orbit resonance. Its surface offers a mix of different shades of grey, showing diverse morphologies, from lava plains to impact craters, ridges, mountains, highlands… But this world is also a complex puzzle, whose geology and chemistry are still largely unknown, that challenged our planetary formation models. This planet, devoid of the strong scientific and public interest that Mars enjoys, has still managed to gather a large community of researchers, which led to the sending of three probes to study it, despite the very high complexity of these missions. Indeed, reaching Mercury is hard; the planet lies deep inside the Sun's gravity well*, so that the energy required to reach its orbit is tenfold that to reach Mars'. Complex orbital maneuvers are computed and executed to decrease this enormous energy requirement, using gravity assists*, which extend the trips to more than half a decade.

This chapter aims to introduce several important aspects of the planet, and to provide an extensive list of references to delve deeper in the subject. It starts with a review of the exploration of the planet, and then focusses on its internal structure, geology, magnetic field, exosphere and surface composition. After the presentation of the current state of knowledge of the planet, the last section reviews the different proposed scenarios to explain its origin and formation. A comparison on some basic properties of the terrestrial planets in our solar system is shown in Table 2-1.

Table 2-1: Comparison of some basic properties of the terrestrial planets, with "d" for Earth day and "h" for hour. Data from the Jet Propulsion Laboratory Horizons system.

	Mercury	Venus	Earth	Mars
Mean Radius (km)	2440	6052	6371	3390
Mass (in 10^{23} kg)	3.302	48.685	59.72	6.417
Surface Gravity (m/s²)	3.701	8.87	9.82	3.71
Density (g/cm³)	5.427	5.204	5.51	3.933
Sidereal rotational period	58.65 (d)	243.02 (d)	23.94 (h)	24.62 (h)
Sidereal orbital period (d)	87.97	224.7	365.26	686.98
Mean solar day (d)	175.94	116.75	1	1.03
Mean temperature (°C)	167	462	15	-63
Atmospheric pressure (bar)	$5x10^{-15}$	90	1	0.006

2.2 Exploration

2.2.1 Ground-based observations

Mercury has been known since the antiquity. Its rapid apparent motion in the sky was associated with the divinity Mercury (Hermes for the Greeks), the wing-footed messenger of the gods. However, until the mid-20th century, the planet remained almost a mystery. Its observation with telescopes is difficult because of its size and its proximity to the Sun, which makes it only observable at dawn or dusk, when it is close to the horizon. Mapping of the planet from the ground was hard (e.g., Camichel and Dollfus, 1968) and, even though some recent effort gave better results (e.g., Dantowitz et al., 2000), only spacecrafts were able to produce qualitative images of the surface. Nonetheless, radio observation of the planet from Earth gave significant information on its properties, such as its true rotation rate (Pettengill and Dyce, 1965) while ground-based spectrometers enabled the discovery of the main components of Mercury's exosphere (e.g., Potter and Morgan, 1985). Radar altimetry from Earth was also important in understanding the morphology of the surface (e.g., Harmon et al., 1986). However, the great majority of our knowledge comes from the two spacecrafts that visited Mercury, namely Mariner 10 and MESSENGER. Another probe, BepiColombo, is on its way and should arrive in 2025. Future concepts, such as landers, are also being proposed by members of the scientific community, with the aim to reach Mercury's surface in two decades.

2.2.2 Mariner 10

Mariner 10 was launched by NASA on the third of November 1973 from Cape Canaveral. It was the first spacecraft to aim for Mercury, and on the 29th of March 1974, it reached its destination. The use of gravity assists to decrease the energy requirement made it the most difficult mission at the time. Because of the enormous energy requirement to put an object in the planet's orbit, the plan for the probe was to perform a fly-by*, which drastically reduced the need to transport fuel, but it also meant that there was a very short amount of time to collect data. After the launch of Mariner 10, Giuseppe Colombo, who was a mathematician and a mechanical engineer, calculated that Mariner 10 could intercept Mercury again after its first flyby with some minor course corrections. Thanks to its contribution, the probe managed to perform three flybys instead of only one, as planned. Thanks to this, the mission's data output was greatly enhanced.

The objectives of the mission were to study Mercury's atmosphere, surface and physical characteristics. The cameras mapped half of the planet, showing a moon-like surface, with craters, ridges and mares, and a lack of atmosphere. The magnetometers detected a weak, peculiar magnetic field, which was unexpected, and the surface temperature was precisely determined with the radiometer, showing huge differences between nighttime and daytime, due to the aforementioned absence of an atmosphere. In particular, the planet's density was precisely measured, which confirmed that Mercury must host a very large iron core. Finally, no natural satellite was found, which was still an unknown at the time (Murray

et al., 1974a). With these 3 flybys, Mariner 10 was able to give us a glimpse on this mysterious planet (see Strom, 1979 and Cremonese et al., 2007, for details on the mission).

2.2.3 MESSENGER

A long wait of 30 years separates Mariner 10 from MESSENGER, as technological advancements were direly needed to perform an orbital mission on Mercury (Cremonese et al., 2007). This second mission from NASA was highly anticipated, as its objective was to acquire a comprehensive set of data on the planet's surface composition and features, its internal structure, its magnetic field and the interaction between the solar wind and the exosphere. The spacecraft carried a large number of instruments, and was designed to enter a stable orbit for several years (Solomon et al., 2001). The probe launched on the 3rd of August of 2004, but this time, it took more than 6 year to attain Mercury's orbit. This very long trip, compared to Mariner 10, was necessary to reduce the mass of propellant needed; by using gravity assists* from the Earth, Venus and Mercury itself, the spacecraft was able to reach the orbit of Mercury with a minimum of fuel, at the expense of a strong increase in travel time. MESSENGER entered orbit on the 18th of March 2011, and data acquisition started a few days later. It managed to mapped the entire surface in high resolution, revealing new surface features, such as vents and hollows. The X-Ray Spectrometer (XRS) and the Gamma-Ray Spectrometer (GRS) acquired compositional data of the surface, measuring elemental ratio relative to Si for Na, Mg, Al, S, Cl, K, Ca, Ti, Cr, Mn, Fe, Th and U (see Nittler et al., 2018a; Nittler and Weider, 2019). One of the most surprising results were the very low surface FeO and the high content of volatile elements Na, Cl, K and especially S. The high sulfur content coupled with the low amount of FeO of the surface hinted to planetary scenarios of formation under very reducing conditions. However, it was (and still is) difficult to reconcile the high content of volatile on the surface with classic models of planetary formation in the solar system (see Charlier and Namur, 2019). Precise measurement of Mercury's librations, as well as other physical parameters, improved our understanding of its structure. In particular, the size of the solid inner core is now getting constrained, and an FeS layer at the core-mantle interface was proposed (see Hauck and Johnson, 2019). MESSENGER really revolutionized our understanding of Mercury and planetary formation.

2.2.4 BepiColombo

BepiColombo is a joined mission led by ESA and JAXA. ESA and JAXA had respective plans to study Mercury by an orbiter since the nineties. At the start of the 2000s, the two projects were joined together, and the name of the mission was given in honor of Giuseppe Colombo. As such, it carries two modules, the Mercury Planetary Orbiter (MPO), built by ESA, and the Mercury Magnetospheric Orbiter (MMO), built by JAXA. The mission was successfully launched on the 19th of October 2018. The two probes carry almost 3 times the scientific payload of MESSENGER (120kg), and will complement the data produced by the latter. To reach its destination, the probes has to undergo multiple gravity assist, in the same manner as MESSENGER. It will put itself in orbit on the 5th of December 2025. The mission

should last until the 1st of May 2027 for the nominal mission, with a possible extension up to the 1st of May 2028. The two spacecrafts will produce new detailed data to help understanding the formation and evolution of Mercury, but also more generally planetary formation in proximity to the host star. They will acquire data on Mercury's interior, surface, exosphere* and magnetosphere*. In particular, the Mercury Imaging X-ray Spectrometer (MIXS) and the Mercury Gamma ray and Neutron Spectrometer (MGNS) are expected to provide new surface data for Ni and P, and measures the concentration of other elements, such as U, Th and K at higher resolution than MESSENGER (Benkhoff et al., 2010, 2021; Baumjohann et al., 2020; Rothery et al., 2020).

2.2.5 Proposed future missions

Hauck et al. (2010) provided a detailed study on the feasibility of landing a probe on Mercury. They highlighted the difficulty of this endeavor. The main obstacle is the enormous quantity of energy required to land on the planet. Contrary to Mars or Venus, Mercury is devoid of atmosphere, so that any aerobraking* is prohibited. Instead, all the orbital velocity has to be lost by firing rockets, which increase the mass of the spacecraft significantly. Moreover, thermal challenges, already faced by MESSENGER, are increased as the spacecraft reaches the surface; it should land on a site in the sunset, with the night only a few Earth day away, to minimize the impact of heat on the probe. This requirement increases the difficulty to power the spacecraft, as it has to use another source than solar panels.

Vander Kaaden et al. (2019) advocated for a sample return mission from Mercury, emphasizing that there are limits to the quality of data we can obtain from orbit measurements. Indeed, acquiring a sample and bringing back on Earth would enable the scientific community to perform the most extensive analysis on it (notably, isotopic ones), which would be an invaluable source of information for both the formation of Mercury and the solar system. The difficulty however is of an order of magnitude higher than the mission proposed by Hauck et al. (2010). Indeed, not only does the spacecraft need to land successfully and overcome the challenges exposed by Hauck et al. (2010), but it needs to launch back from the surface of Mercury, reach the orbit, depart from it and land on Earth. The energy requirement for such a task is enormous, which massively increase the weight of the lander, and thus the energy to land it on Mercury in the first place.

More recently, Ernst et al., (2022) re-evaluated the proposal from Hauck et al. (2010) in light of the new technological advancements and economical context of today, incorporating the mission as part of the New Frontier program of the NASA. Their proposal includes a departing from Earth in 2035, with a cruising time of 10 years using electrical propulsion and gravity assists, aiming to land in 2045. They planned for an entire mercurial year of surface operation (88 Earth days) with a suite of 11 instruments to study the planet's chemistry, structure, magnetic field and exosphere.

2.3 The peculiar internal structure of Mercury

2.3.1 General background

Early calculation of Mercury's structure was based on erroneous estimate for the planet's mass and diameter, and poor understanding of planetary composition. Before the contested measurements made by Rabe (1950), the density of Mercury was estimated to be low, between 3 and 4 $g.cm^{-3}$ (e.g., Jeffreys, 1937; Whipple, 1941; Smart, 1951). At the time, the core of Mercury was thought to be small or inexistent (Jeffreys, 1937; Birch, 1952), and thus that the planet was mainly made of silicates. During this period, many proposals were made regarding the interior of Mercury, such as Ramsey (1948, 1949, 1950) who proposed that the core was made of a dense metallic phase of olivine, which was disputed by others (e.g., Birch, 1952). The important work of Urey (1952), Urey and Craig (1953) and Suess and Urey (1956), combined with the increased accuracy in measuring Mercury's mass and radius (Rabe, 1950; Dollfus, 1963) allowed for a renewed understanding of the interior of the planet; it appeared that it should be composed of a large core and a small mantle. For example, Plagemann (1965) calculated that the mantle should be 334 km thick. However, before the work of Pettengil and Dyce (1965), Mercury was thought to be tidally locked with Sun (i.e., the period of rotation is equal to the period of revolution), so that one hemisphere always bathes in sunlight while the other is perpetually in the dark, which led to incorrect interpretations for Mercury's internal heat budget and mantle's composition (e.g., Walker, 1960; McDonnald, 1963; Plagemann, 1965). After the discovery of Mercury's true rotation rate, and before Mariner 10, the core radius was estimated to be around 1800 km with a 600 km silicate part (Lyttleton, 1969). The discovery of Mercury's magnetic field by Mariner 10 confirmed that the planet was indeed differentiated, with a mantle estimated to be ~600 km thick (Strom, 1979). Harder and Schubert (2001) calculated that the mantle could be either 660 km thick (for a pure iron core) or absent (for a pure FeS core). The arrival of MESSENGER completely renewed the view of the structure of Mercury's silicate part. Smith et al. (2012), based on radio tracking data from the probe, determined that Mercury has a thin silicate shell 410 ±37 km thick, ~30% lower than previous estimates. Concerning the crust, Padovan et al. (2015) calculated it to be 35 ±18 km, much lower than reported before (100-300km: Nimmo, 2002), but it is still the highest crust to mantle thickness ratio of the terrestrial planets. Finally, based on the new data from MESSENGER, an FeS layer at the core-mantle boundary was proposed (e.g., Malavergne et al., 2010; Smith et al., 2012).

In summary, Mercury, like the 3 other terrestrial planets, is composed of a silicate crust, a silicate mantle, and a metallic core, but the planet has a unique structure. Its crust is very thick compared to the silicate part, its mantle is thin and, in opposition, its core is very large (Figure 2-1).

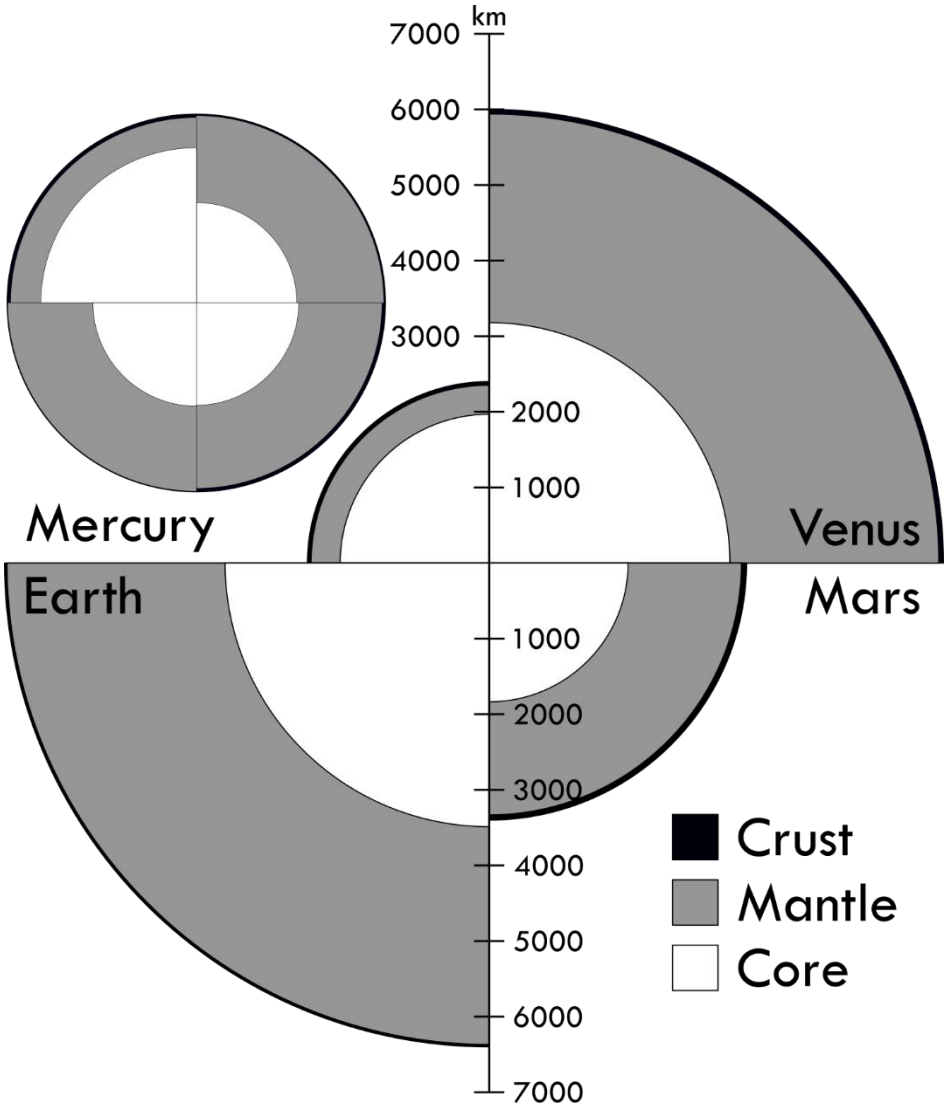

Figure 2-1: Comparison of the internal structure of the terrestrial planets. Upper left: comparison of the structure if all planets had the same radius. Center: comparison of the planets to scale.

2.3.2 The core

One of the most striking features of Mercury is its gigantic core. Early measurements show that the planet's density is similar to Earth (~5.43 vs 5.514 g cm^{-3}) even though it is smaller (~2440 km vs ~6400 km). Because the materials are much more compressed in the center of the Earth than of Mercury (because of the difference in size), it means that Mercury needs a very large core to equal Earth's density. Indeed, if we compare uncompressed densities*, Mercury is the densest planet (~5.3 g cm^{-3} vs ~4.4 g cm^{-3} for the Earth). Rivoldini et al. (2009) showed, based on models with different silicate and core composition, that its radius should be above 1828 km. Thanks to the new data provided by MESSENGER on the planet's gravity field, its radius has been reevaluated to be ~2000 km (Hauck et al., 2013; Rivoldini and Van Hoolst, 2013). In particular, the core makes up 80% of the planet's radius, ~60% in volume, and ~75% in mass. In comparison, Earth's core is 55% of the total radius, ~15% in volume and a third of its mass.

The state of the core (solid or liquid) has been debated; Siegfried and Solomon (1974) argued that, if the core is made up of pure iron, it should have cooled down and solidified by now. Other, such as Fricker et al. (1976), stressed that the core could have retained a liquid outer part. The presence of light elements in the core, as observed on Earth (e.g., Poirier, 1995), could also strongly modify its thermal evolution. In particular, the presence of sulfur in the core, that accumulated during Mercury's probable accretion from volatile-bearing planetesimals, could extend the presence of an outer liquid core up to this day (Schubert et al., 1988). While the detection of a magnetic field could be caused by a liquid core (by a dynamo effect, see section 2.6), it was not a sufficient argument as there were other ways to explain its origin.

One key aspect to determine the structure of the core is to observe the planet's orbital properties. Mercury has a 3:2 spin-orbit resonance; its means that for 3 rotations on itself it revolves 2 times around the Sun. Because of the planet's equatorial ellipticity, reversing gravitational solar torques are applied, causing small deviations from the means rotations rate. These deviations are called forced librations, and they have an orbital period of ~88 days, which corresponds to the orbital period of Mercury (Dumberry, 2011, and references therein). Peale (1976) developed a new method to constrain the structure of the core by observing the dynamics of Mercury's rotation; he found that the amplitude of these librations can be used to determine if there is a decoupling between a solid part (the mantle and the crust) and a liquid one (the core). Margot et al. (2007), using ground-based telescopes and data from Mariner 10, used this method and showed that the amplitude of the forced librations was twice as large as expected if the planet was fully solidified. This does not prevent however the presence of a solid inner core. The librations only hint at a decoupling between a solid mantle and a liquid part below it. Thermal models also support the idea of a (at least) partially solidified core due to planetary cooling (Solomon, 1976; Stevenson et al., 1983). Moreover, surface features, such as lobate scarps, support a global contraction of the planet caused by the gradual solidification of the core (e.g., Strom et al., 1975; Watters et al., 1998, and references therein). There were several estimations of the planet's contraction; between 1 and 2 km for Strom et al. (1975), <1 km for Watters et al. (1998), up to 7 km for Byrne et al. (2014) using MESSENGER data, and, more recently, no more than 1 – 2 km (Watters, 2021).

A solid inner core, in addition to a liquid outer core, would also have its own librations, different from that of the mantle. Indeed, in the absence of a solid core, the amplitude of Mercury's librations results solely from the librations of the mantle. If a solid core is present, its librations would affect the ones of the mantle, and we would see a difference between the observed and the predicted amplitude if the librations were coming only from the mantle. This effect would be negligible if the inner core is small, typically <1000 km (Veasey and Dumberry, 2011; Van Hoolst et al., 2012; Dumberry et al. 2013). The gravitational interaction between the mantle and the inner core would affects long terms librations, observable on a larger timescale (around a decade) (Dumberry, 2011; Veasey and Dumberry, 2011). Dumberry (2011), Van Hoolst et al. (2012) and Dumberry et al. (2013) proposed that a large core (>1000

km) could have effects measurable on the 88 days librations and that the effects would be more visible for long terms librations. Further effort to constrain the size of Mercury's inner core have focused on modeling core cooling of different compositions and comparing the results with the observed physical parameters of Mercury and the observed planetary contraction. As of today, the proposed radius for the inner core ranges from 0 to ~1700 km (Knibbe and Van Westrenen, 2015, 2018; Knibbe et al., 2021; Goossens et al., 2022). The future data produced by BepiColombo are expected to better constrain Mercury's structure, and especially its core (Genova et al., 2019; Steinbrügge et al., 2021).

2.3.3 The FeS layer

As Margot et al. (2007) showed the existence of a probable (partially) liquid core (see above), a pure metallic iron core on Mercury is then not possible, as it should have completely solidified by now because of the high melting point of pure iron (Siegfried and Solomon, 1974). Consequently, the incorporation of light elements, notably sulfur, seems probable (Stevenson et al., 1983; Harder and Schubert, 2001; Chen et al., 2008). Also, the very reduced conditions on Mercury should allow silicon to enter the metallic phase (McCoy et al., 1999; Gessmann et al., 2001; Malavergne et al., 2004; Berthet et al., 2008; Malavergne et al., 2010). However, there is a miscibility gap in the Fe-Si-S system at the pressures of Mercury's core-mantle boundary; S-rich and Si-rich iron liquids coexists, and do not mix (McCoy et al., 1999; Malavergne et al., 2007; Berthet et al., 2008; Morard and Katsura, 2010). Based on these observations, Malavergne et al. (2010) were the first to propose the existence of a compositionally layered core, with an S-rich and a Si-rich iron parts. Because FeS is less dense than Fe-Si, the S-rich liquid should rise and stay at the core mantle boundary, forming an FeS layer. Malavergne et al. (2010) performed mass balance modeling and estimated the thickness of this layer to be ~15 km if the planet formed from Bencubbinite chondrites or ~220 km if it formed from enstatite chondrites, which are richer in sulfur. Smith et al. (2012) showed that the presence of an FeS layer at the base of the mantle is consistent with models of Mercury's gravity field, obtained with data from MESSENGER. Initially, other studies also considered the existence of a (thick) solid FeS layer (Hauck et al., 2013; Chabot et al., 2014). It was also consistent with Mercury's magnetic field measurements (Anderson et al., 2012). Namur et al. (2016) estimated, based on mass balance calculations of sulfur during the differentiation, that the thickness of the FeS layer should be comprised between 0 to 90 km. Cartier et al. (2020) modeled the evolution of the Ti/Al ratio during differentiation. They calculated that Ti, which is slightly chalcophile under Mercury's redox conditions, should partition into the FeS layer and thus decrease the remaining silicate Ti/Al. By comparing the surface Ti/Al with their model, they showed that the existence of an FeS layer formed in equilibrium with the silicate part is improbable. In the same way, Pirotte et al. (2023) showed, based on the Th/U ratio, that the existence of an FeS layer is only possible if the conditions were more oxidizing (>IW - 4) or if the bulk planetary Th/U was sub-chondritic. As the existence of an FeS layer formed in equilibrium with the silicate part requires the planet to be initially saturated in sulfur, it is probable that Mercury was in fact undersaturated. However, all these scenarios

considered the formation of an FeS layer during differentiation, that formed in equilibrium with both the core and the silicate part. It still possible to have an FeS layer formed by exsolution of the liquid Fe-Si-S core during the inner core crystallization. Indeed, as the Fe-Si core crystallize, S is rejected to the outer liquid part, and accumulates. Once it reaches saturation in the Fe-Si-S liquid core (Morard and Katsura, 2010), FeS is exsolved from the core and, by density, forms a layer atop the core and below the now solidified mantle (Charlier and Namur, 2019; Pirotte et al., 2023). In this case, the layer would absorb chalcophile elements from the core; on the reducing conditions of Mercury, this would deplete the core in U and Th which partition more into FeS than metal (Pirotte et al., 2023).

2.3.4 The silicate part

2.3.4.1 The magma ocean

The different possible scenarios for the formation of Mercury are exposed in section 2.8. Here, the goal is to describe the planet's state just after accretion, when the temperature was so hot that the surface was completely molten, forming what is known as a magma ocean. Exposing the proposed scenarios for Mercury's magma ocean is important to understand the composition and structure of the mantle and the crust, which is covered in the section 2.3.4.2.

The concept of magma ocean arose after Apollo 11 brought anorthositic rocks back from the moon. To explain their surprising presence on the Moon, Wood et al. (1970) proposed that a layer of anorthosites floated on a primordial planet-wide magma made of denser gabbro. Subsequent papers investigated the concept (e.g., Wood, 1975; Walker et al., 1975; Solomon and Longhi, 1977; Minear and Fletcher, 1978) and expanded it to other terrestrial bodies (e.g., Anderson, 1981; Nibset and Walker, 1982; Warren, 1985). The partial or complete melting of planets during their formation is caused from the combined effect of radiogenic heating produced by short-lived radioisotope (such as Al^{26}) and the enormous kinetic energy released during accretional impacts. Taylor and Norman (1992) gave a definition for magma oceans: they must behave rheologically as a liquid (<50% crystal) and entirely cover the body over a substantial depth (>10%). It is now accepted that all terrestrial planets and the moon experienced a magma ocean early in their history (e.g., Warren, 1985; Solomatov, 2007; Brown and Elkins-Tanton, 2009).

The crystallization of the magma ocean is a crucial step in planetary evolution, as it controls the initial silicate differentiation (i.e., formation of the mantle and the crust) and the formation of the primary (or primordial) crust. The turbulent convection expected to occur in a magma ocean leads to its cooling and crystallization (e.g., Solomatov, 2007; Maurice et al., 2017). On Mercury, crystallization probably started at the bottom of the magma ocean and upwards ("bottom-up" crystallization, Elkins-Tanton, 2012). The crystallization can be either fractional or at equilibrium. Fractional crystallization means that the crystals are separated from the melt, which makes its composition evolves with further crystallization. Equilibrium crystallization happens when the entrainment of the crystals causes them to

always be in equilibrium with the liquid. The first case leads to a differentiated solid mantle, while the second case leads to a homogeneous one (Elkins-Tanton, 2012; Tosi and Padovan, 2021).

The observed crustal composition on the surface of Mercury does not match with a primordial quench crust, made of solidified (quenched) magmatic material (Charlier et al., 2013). Depending on the concentration of iron in the magma ocean and the melt fraction, crystallizing minerals like plagioclases may rise and float on top of it, forming a primary crust (like on the moon, e.g., Warren, 1985; Figure 2-2). However, the low-FeO content of Mercury tends to show that no rock-forming mineral could be buoyant in respect with the coexisting magma ocean (Riner et al., 2009; Brown and Elkins-Tanton, 2009; Vander Kaaden and McCubbin, 2015). Only graphite could rise and form a primary crust, as hypothesized by Vander Kaaden and McCubbin (2015).

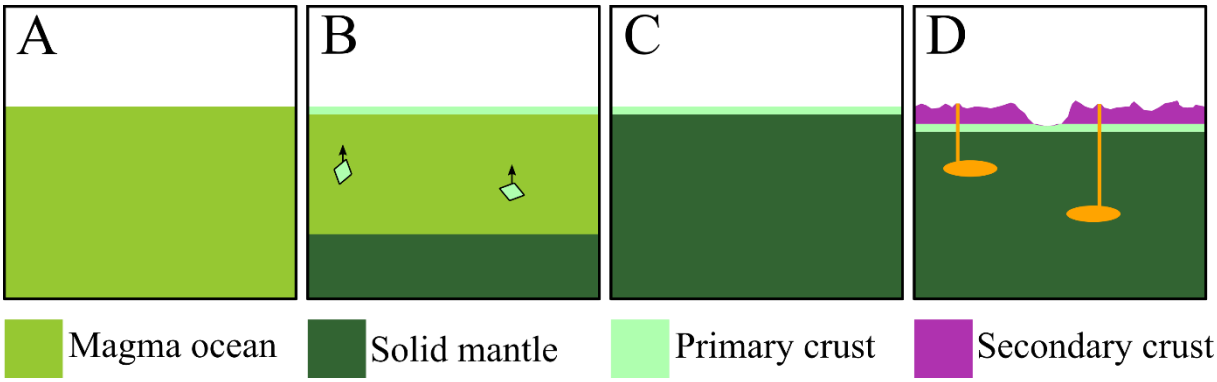

Figure 2-2: Formation of a primary (flotation) crust and a secondary crust. A) Magma ocean, no crust. B) Crystallization of light minerals that rise through a dense magma ocean, and form a primary flotation crust. C) Complete solidification of the mantle. D) Partial melting of the mantle, creating lavas that erupts on the surface and forms the secondary crust. Impacts can reveal the previous, buried primary crust. On Mercury, the primary crust is thought to be made of graphite, which was the only buoyant mineral in the FeO-poor magma ocean (see Vander Kaaden and McCubbin, 2015).

Similarly, depending on the FeO content of the residual magma ocean during its fractional crystallization, an overturn phenomenon could have happened, where shallow dense cumulates, formed from FeO-rich residual melt, are overlying light crystals (Figure 2-3). If there is no convection present, this gravitational instability is resolved by an overturn, where the denser minerals sink, which leads to a stable stratification (Riner et al., 2009; Brown and Elkins-Tanton, 2009; Mouser et al., 2021). However, the FeO-poor nature of the mantle may hinder overturns from FeO-rich cumulates.

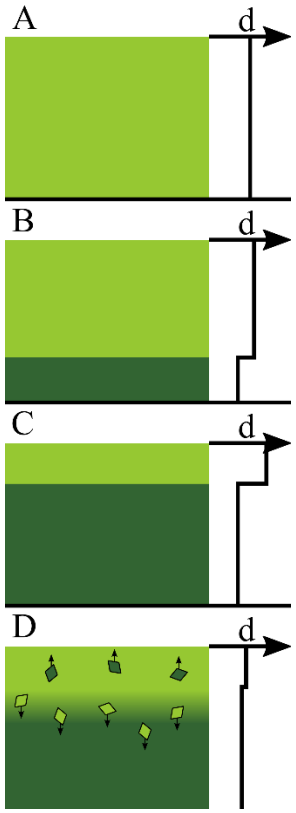

Figure 2-3: Sketches of an overturn. A simplified density profile is also present on the right ("d"). Light green: the crystallizing magma; dark green: mantle cumulates. A: mixed magma ocean. B: FeO-poor minerals cumulates crystalize. C: the density profile reached a tipping point, the FeO-rich magma is no longer stable above the less dense cumulates below. D: the overturn; overlying dense crystals sink while underlying light crystals rise, leading to a mixed mantle.

The cooling-rate of a magma ocean is critical on the future dynamics of the planet's mantle. Fast-cooling would favor overturns, as convection has no time to set in. On the other hand, slow cooling magma ocean would lead to convection and crystallization to happen simultaneously. Several factors can decrease the cooling rate of magma oceans, such as the presence of a primary crust (Elkins-Tanton et al., 2011; Mouser et al., 2021) or the presence of a dense, primitive atmosphere (e.g., Elkins-Tanton, 2008; Zhang et al., 2022). The low thickness of Mercury's silicate part would impair the triggering of convection, and so formation of a primary lid as well as overturn leading to a stratified mantle are favored by Tosi and Padovan (2021). The presence of a stratified mantle has been linked with surface compositional heterogeneities, where different lavas would come from the partial melting of a deep mantle and a shallower one, different in composition (Charlier et al., 2013; Namur et al., 2016b).

On Mercury, sulfides might play a key role in the dynamics of Mercury's silicate part. As the surface lavas are rich in sulfur (up to ~4wt%, Nittler et al., 2011), the mantle should contain between 7 to 11 wt% of S (Namur et al., 2016a). Boukaré et al. (2019) showed that sulfide layers could form in Mercury's magma ocean and, depending on their incorporation of heat-producing elements (HPE), could provide significant amount of heat to melt neighboring rocks. The redox conditions and the bulk sulfur content determine the thickness and the depth of formation of these layers, while the (still poorly unconstrained)

density of the sulfides determine if they would sink (or stay where they formed) or float. They notably discussed the peculiar case of a floating pure-sulfide primary crust, concentrating the HPE near the surface. However, they showed that the underneath S-free mantle could still be convecting if the initial S content of the planet is low (between 0 and 3 wt% depending on the oxygen fugacity), despite the presence of this lid. Moreover, sulfides, depending on their density, could also be responsible for overturns in the magma ocean, if there are dense sulfides emplaced at shallow depths or light sulfides at deeper depth, causing gravitational instabilities (Mouser and Dygert, 2023).

2.3.4.2 The mantle and the crust

Ringwood (1966) hypothesized that Mercury's silicate part should be mainly composed of Ca and Al silicates, while Lewis (1972) proposed that it should be made of Fe-free magnesium silicates, and almost devoid of alkali, sulfur and FeO. There were also doubts on the possibility and the duration of convections on such a thin mantle, which affects the duration of planetary volcanism. Mantle convection needs thermal energy, which can be provided by two sources: the release of heat from the core, and from heat-producing elements (HPE: U, Th and K) in the mantle. Prior to MESSENGER, the concentration of heat-producing elements in the mantle was unknown; depending on the model of formation, Mercury could be lacking K (Weidenschilling, 1978), lacking U and K (Fegley and Cameron, 1987), depleted of U, Th and K (Wänke and Dreibus, 1988) or enriched in them compared to Earth (Lodders and Fegley, 1998). While a very hot Mercury after accretion was probable, leading to convection in the mantle early on, the quantity of heat-flux from the core after this period was difficult to estimate (Redmond and King, 2007; Breuer et al., 2007). Depending on models, convection could still happen to this day (Redmond and King, 2007) or have ceased some time after the Late Heavy Bombardment (Hauck et al., 2004).

Generally, crust on terrestrial bodies are divided into three categories: primary (or primordial), secondary and tertiary. Primary crusts are the result of the solidification of the magma ocean, secondary from the partial melting of the mantle, and tertiary from the remelting of the secondary crust (Taylor and McLennan, 2009). MESSENGER confirmed the volcanic nature of the crust (Head et al., 2008, 2011; Denevi et al., 2009, 2018; Byrne et al., 2018), and so it should be mainly of secondary origin, while darker material and the high carbon content of the surface has been interpreted as remnants of the primary graphite crust proposed by Vander Kaaden and McCubbin (2015), extruded by deep meteoritic impacts (Denevi et al., 2013; Murchie et al., 2015, 2019). Contrary to Earth, there is no crustal recycling on stagnant-lid* body such as Mercury. The crust is representative of the whole magmatic history of the planet. In this light, the determination of the thickness of the crust and the age of surface lavas places powerful constrains on mantle processes. Indeed, the high thickness of the crust compared to the mantle (~10%, compared to ~1% on Earth, Padovan et al., 2015) and the old age of the crust (end of effusive volcanism around 3.5Ga, Byrne et al., 2016) hint toward a rapid and efficient crust emplacement.

There are two way for a planet to release heat: by conduction or convection in the mantle, with conduction being a fairly inefficient process to lose heat compared to convection. A useful way to quantify the convective character of a planet is to use a dimensionless value called the Rayleigh number (Ra), developed by Rayleigh (1916). Convections can happen if Ra is superior to a critical value, called Ra_c. Ra mainly depends on the thickness of the convecting layer (i.e., the thickness of the mantle), the viscosity (i.e., the composition of the mantle) and the difference in temperature between the top and the bottom (i.e., the internal heating). The new compositional data of the surface showed that the surface was rich in volatile, confirmed its Fe-poor nature, and that HPE concentrations was similar to other terrestrial bodies (Nittler et al., 2011; Peplowski et al., 2011; see Section 2.5). Based on the new data, the range of mantle viscosity and the production of heat from HPE was revised, and Michel et al. (2013) proposed that mantle's convections should have lasted for a long time on Mercury, maybe even to present-day. On the other hand, Tosi et al. (2013) advocated for a cessation of convecting activities after 3-4 Gyr. Guerrero et al. (2021) showed that the mantle of Mercury underwent a transition from a convecting to a conductive regime at least a billion years ago, and that it could explain the observed magnetic field and match the constrain on the size of the inner core. One key difference between Mercury and other bodies is the FeO-poor mantle, which has a high thermal diffusivity, which is crucial for the thermal cooling of the core and its subsequent crystallization (Guerrero et al. 2021). Boukaré et al. (2019), while exploring the effect of sulfides on the mantle dynamics (see previous section) proposed that sulfides could inhibit convection if they are concentrated in the shallow mantle, by concentrating the HPE, or enable sulfide-plumes convections if they reside at the core-mantle boundary. Recently, Mouser et al. (2021) demonstrated the effect of sulfur on melt viscosities. It seems that higher S content decreases viscosity, but as higher S content in the silicate melt correlates to lower oxygen fugacity (see Namur et al., 2016a), it is somewhat difficult to clearly distinguish the effect of S and fO_2. They stressed that the presence of a flotation crust has dampening effect on the mixing of the mantle, leading to its heterogeneity. In conclusion, the duration of convection on Mercury is still debated, even though it seems reasonable to assume that the early mantle was convecting. More experimental data are needed to constrain the parameters necessary to calculate the Rayleigh number.

The composition of Mercury's mantle has been inferred from surface lavas' composition. One of the key features of the surface is the presence of different geochemical terranes (e.g., Weider et al., 2015). There were several processes invoked to explain these differences. The melting of a homogeneous mantle at different depth and time was suggested (Weider et al., 2012), but it is not favored anymore because it cannot account for the strong compositional differences of the lavas (Charlier et al., 2013). Charlier et al. (2013) identified two mineralogical groups on the surface of Mercury and proposed a heterogeneous mantle to explain their formation. Indeed, they cannot be related by fractional crystallization of a common mantle. They considered a lherzolitic (ol + opx + cpx) and a harzburgitic (ol+ opx) source, that produced lavas by partial melting from adiabatic decompression. Namur et al.

(2016b) also identified heterogeneous mantle sources as the cause for the diverse composition of the basalts, confirming the conclusions of Charlier et al. (2013). However, they showed that the sources should be of lherzolitic composition only (albeit different), on the basis of new compositional data for Na_2O, so that a strictly harzburgitic component was not necessary. In summary, the history of Mercury's magmatism is linked to its cooling history, with the oldest lavas coming from deep and high temperature partial melting, while the youngest were formed from shallower and cooler sources (Namur and Charlier, 2017). Finally, it is important to note that giant impacts, such as the Caloris basin, probably heated the mantle below, leading to renewed volcanic activity (e.g., Roberts and Barnouin, 2012).

2.4 Surface features

The first observations of Mercury were made by telescope. The planet, due to its proximity to the sun and its size, is difficult to optically observe from Earth. Nonetheless, photographs of the planet have been made during the 20th century and, based on those, cartographic works (Figure 2-4) (e.g., Camichel and Dollfus, 1968; Murray et al., 1972).

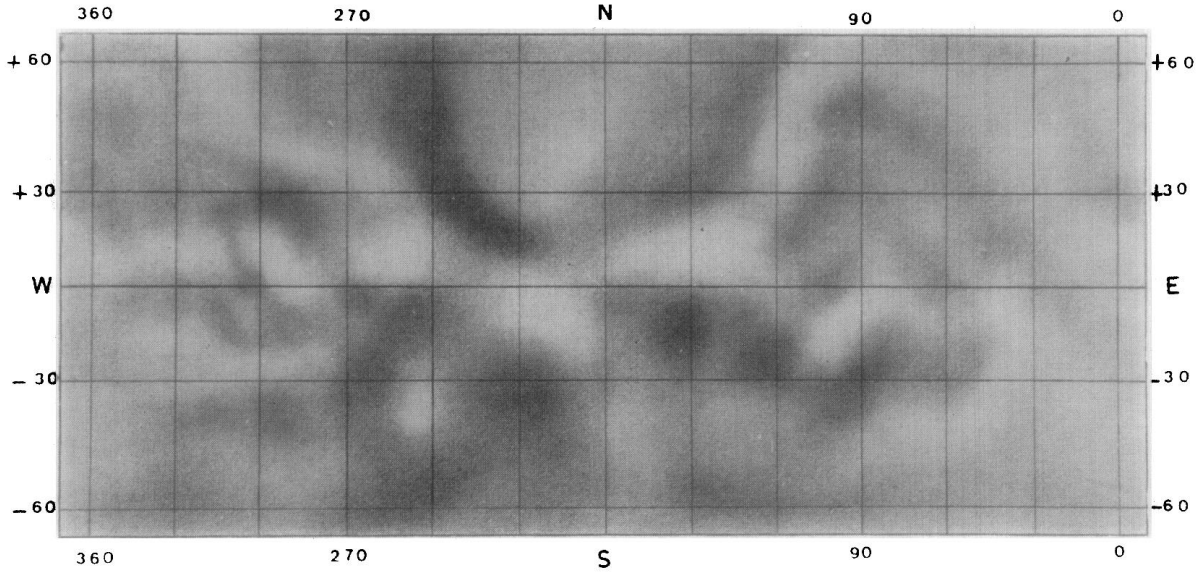

Figure 2-4: Map of Mercury from photographs taken by ground-based telescopes (from Murray et al., 1972).

As seen in Figure 2-4, the quality of the photographs was not good enough to distinguish any significant feature. The flybys of Mariner 10 provided the first qualitative imaging of the surface. The probe was able to image ~45% of the planet (Figure 2-5), which allowed for true cartographic and features characterization works to start. Early reports focused on the apparent similarities between the surface of Mercury and the moon (Murray et al., 1974a, 1974b). They identified craters, impact basins and plains. They also identified irregular (lobate) scarps*, absent in the moon's morphology (Murray et al., 1974a). Main features were recognized, characterized and named, such as the Caloris Basin, the largest structure

observed by Mariner 10 (Murray et al., 1974b; Morrison, 1976), and various geological maps were constructed (e.g., Trask and Guest, 1975).

What particularly distinguishes Mercury from the other terrestrial planets were its tectonic features; there is widespread evidence for contractional tectonics resulting from the diminution of the planet's radius (Strom et al., 1975). It was confirmed that there never was an atmosphere on Mercury (at least not for the last ~4 billon years) as the surface features, such as the craters, present no trace of wind erosion (Murray et al., 1975). The plains were recognized to be probably of volcanic origin (Murray et al., 1975; Robinson and Lucey, 1997), but the data from MESSENGER would be crucial to resolve the issue. Indeed, the plains Apollo 16 landed on were thought to be of volcanic origin, but upon further investigation, it was found that they were the product of impact-related processes (Head, 1974). This led to comparison of plains from the moon and Mercury, and to the interpretation that mercurian plains were formed by similar processes, namely by ballistic erosion and sedimentation (Oberdeck et al., 1977). Further Earth based imaging occurred after Mariner 10 while waiting for the MESSENGER mission, that tried to fill in the gaps of Mariner 10's surface imaging (e.g., Dantowitz et al., 2000; Mendillo et al., 2001). A review of the geology of Mercury before the MESSENGER mission can be found in Head et al. (2007).

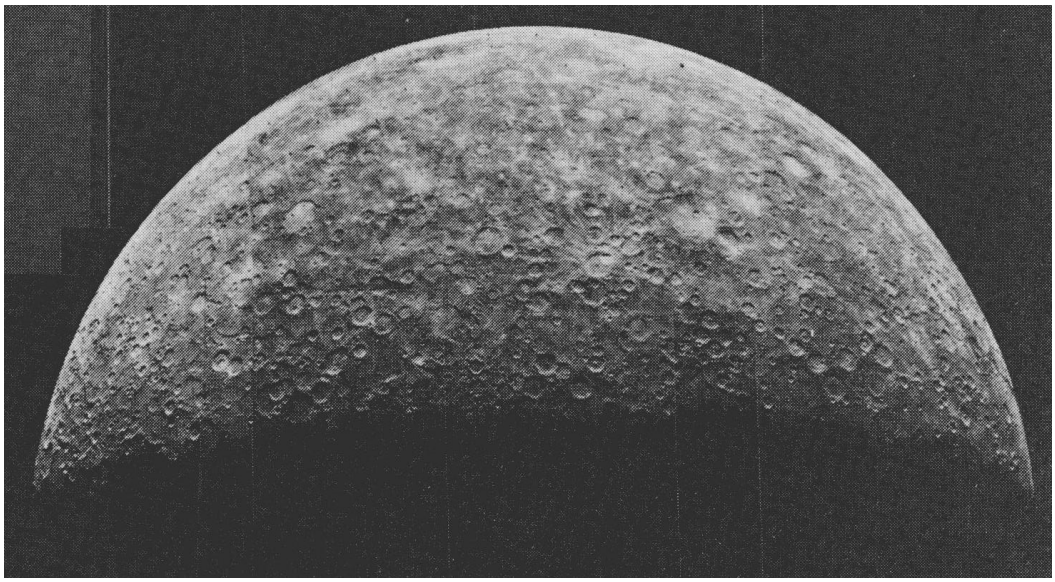

Figure 2-5: One of the first published photographs obtained by Mariner 10. The similarities with the Moon are apparent. Note: the spin-rotation axis is from left to right on this photograph (modified from Murray et al., 1974a).

MESSENGER produced high-resolution images that cover the entirety of the planet (e.g.: Solomon et al., 2008; Head et al., 2008; Denevi et al., 2009). This input of new data widely expanded the knowledge of Mercury acquired by Mariner 10. As of today, the main geomorphological units are defined as follow: the smooth plains, that have a flat surface, and a low crater density; the intercrater plains, filled with small carters (5-15km in diameter), found between large craters and basins; and finally, the impact craters (Prockter et al., 2016; Denevi et al., 2018; Domingue et al., 2019).

The crust appears to be mostly of volcanic origin, ending the debate set by Mariner 10 (Head et al., 2008, 2011; Denevi et al., 2009, 2018; Byrne et al., 2018). The smooth plains, which cover a quarter of the surface, are the result of effusive volcanism (Denevi et al., 2013), and the intercrater plains are also of volcanic origin (Whitten et al., 2014). In fact, evidence suggest that a global resurfacing period of volcanic origin happened during the late heavy bombardment (Marchi et al., 2013). Moreover, proofs of explosive volcanism have been found (Head et al., 2008; Blewett et al., 2009), with identification of pyroclastic deposits, volcanic vents and a shield volcano (Figure 2-6; Head et al., 2009; Kerber et al., 2011; Thomas et al., 2014a; Rothery et al., 2016). However, some doubts still persist on the formation mechanism of these vents, as their rarity is unusual considering the widespread volcanism on Mercury's surface (Wright et al., 2018). The explosive volcanism reflects the composition of mercurian lavas, which appear to be rich in volatile (see section 2.5). In particular, Weider et al. (2016) proposes that S and C depleted deposits could be the result of the oxidation of these elements (and thus the formation of volatile species) during magma ascent, via processes similar to explosive volcanism on Earth.

Widespread effusive volcanism on Mercury probably stopped around 3.5 Ga, as evidenced by crater size-frequency distributions techniques (Byrne et al., 2016). Using recent craters, Banks et al. (2017) estimated that pyroclastic eruptions continued well after 3.5 Ga, up to 280 Ma. The origin of the late-stage volcanism on Mercury has been put in relation with impact processes (Byrne et al., 2016; Jozwiak et al., 2018). Indeed, internal cooling of one-plate planets* leads to compressional tectonics and lithospheric stresses that inhibits surface volcanism (Solomon, 1978). Impacts promotes magma ascent by relaxing compressive stresses, removing overburden, and fracturing the lithosphere (Byrne et al., 2016).

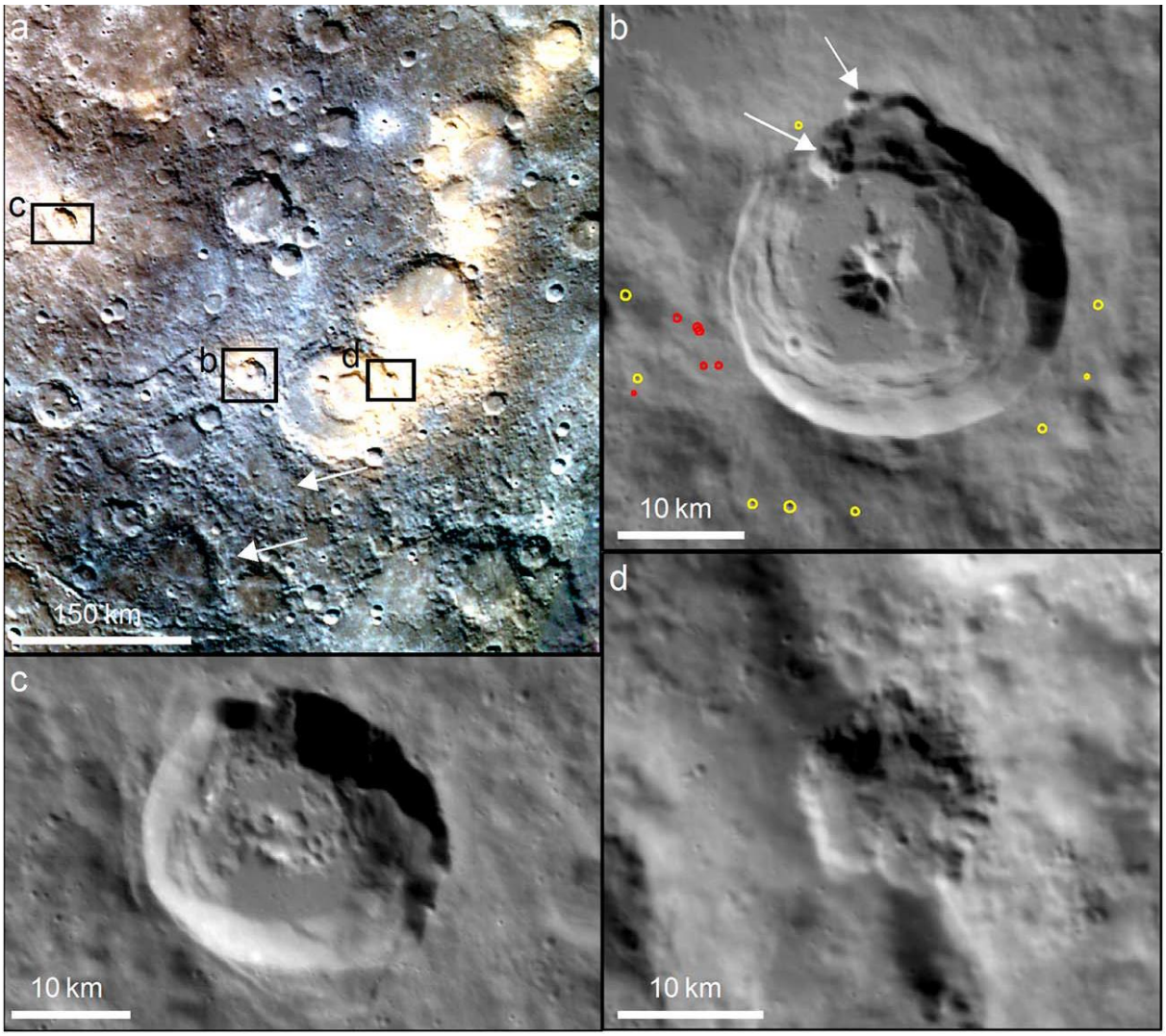

Figure 2-6: Example of explosive volcanism on Mercury. a) emplacement of the three vents seen in b), c) and d). The bright regions visible in panel a) are interpreted as pyroclastic deposits, and are called faculae. In panel b), the green and red circles outline the primary and secondary impact craters, respectively. Figure from Thomas et al. (2014a).

Blewett et al. (2011) were the firsts to describe hollows, which are rimless shallow depressions of irregular shapes, with a flat interior. Their spectral reflectance is high, surrounded with a diffuse bright halo. Their size varies from tens of meters to several kilometers across (Figure 2-7), and they are usually associated with impact structures (Blewett et al., 2011, 2013, 2016). Blewett et al. (2011) hypothesized that they might still be forming to this day because of their fresh appearance. They are thought to be caused by the release of volatile from the ground, leading it to crumble and creating depressions. Several (concomitant) processes have been proposed, such as; sublimation (Blewett et al., 2011, 2013; Thomas et al., 2014b), various space weathering processes (see Section 2.7; Blewett et al., 2011, 2013), pyroclastic volcanism heating the volatiles (Blewett et al., 2013; Thomas et al., 2014b), or destruction of graphite by proton bombardment (Blewett et al., 2016). Lucchetti et al. (2018) recently summarized their formation as being the combination of 1) the volatilization of some materials, which forms a depression 2) the widening of this initial depression, as deepening is no longer possible due to the upper

material consisting now of volatile-poor material. It is in agreement with the work of Blewett et al. (2013, 2016).

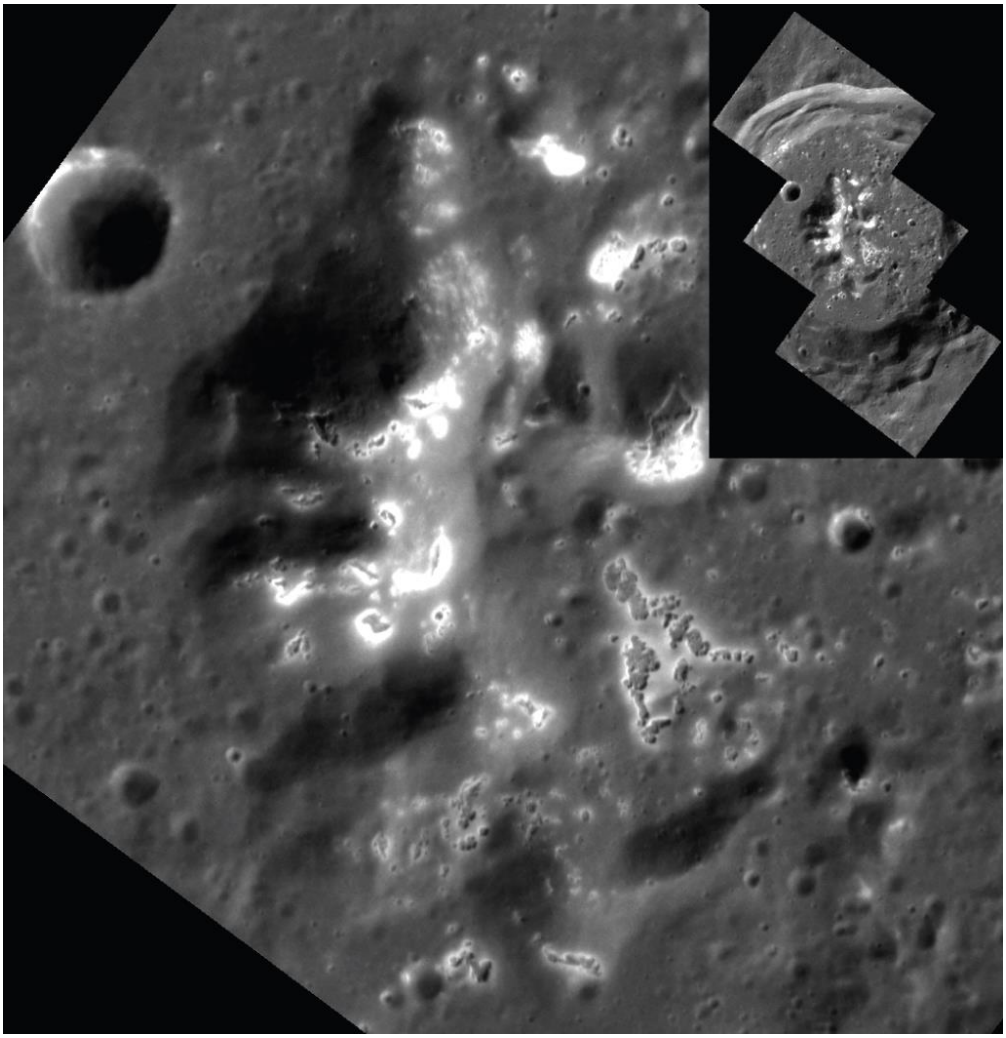

Figure 2-7: Hollows on the surface of Mercury (modified from Blewett et al., 2011).

While hollows may be the best example of Mercury's richness in volatiles, the chaotic terrains at the antipode of the Caloris basin may also be evidence of the abundance of volatiles. This part of the surface is characterized by hilly and lineated terrains, with deep depressions and the disruptions of pre-existing landforms (Schultz and Gault, 1975; Lü et al., 2011). Rodriguez et al. (2020) proposed that the formation of this region is linked to the evacuation of volatiles within the crust by sublimation, caused by the presence of magmas below. The important fracturing of the crust, probably caused by the Caloris impact, promoted the loss of volatile species, which fragilized the terrain and led to its collapse (Figure 2-8).

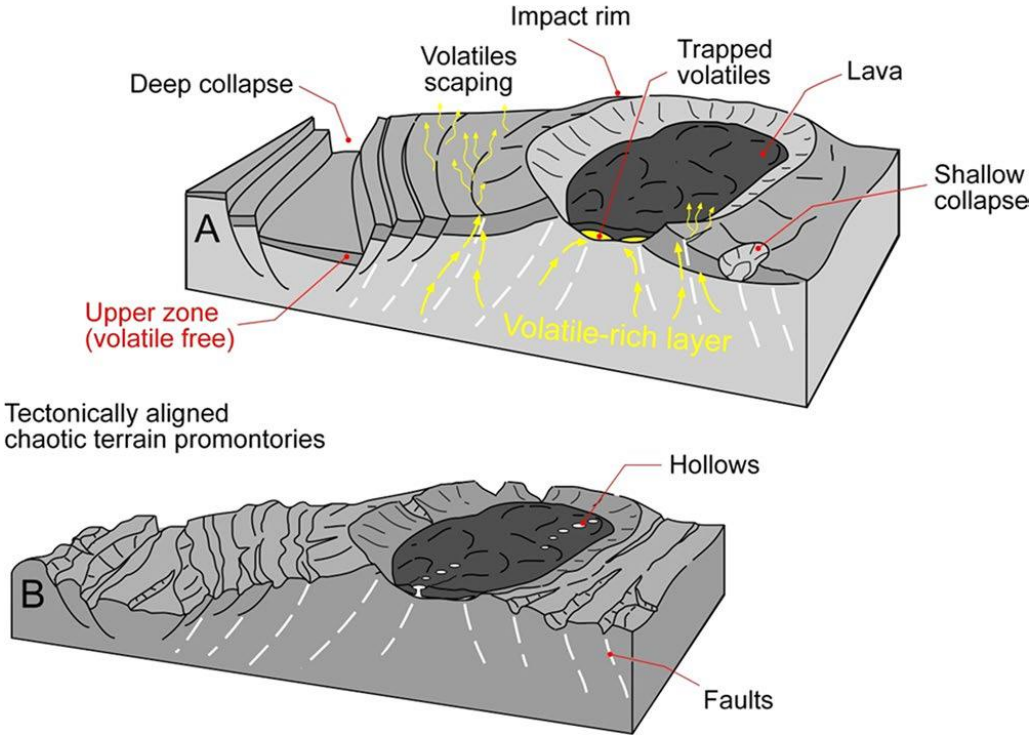

Figure 2-8: Formation of chaotic terrains. The loss of volatile from the basal volatile-rich layer creates instabilities for the terrain above, causing collapses (from Rodriguez et al., 2020).

As discovered by Mariner 10, the dominant tectonic features are of contractional origins; lobate scarps*, wrinkle ridges* and high-relief ridges*. Extensional features were only found in the interior of the Caloris basin, notably grabens* (Watters and Nimmo, 2010, and references therein). MESSENGER considerably extended the inventory of extensional faulting, with the identification of other grabens and graben complexes in numerous basins, such as Caloris, Rachmaninoff and Rembrandt (e.g., Watters et al., 2009; Blair et al., 2013; Ferrari et al., 2015). Moreover, the new images of the surface enabled the study of the distribution of the contractional features. Their origin is still debated, with possibly multiple formation processes involved, notably global contraction, tidal despinning (i.e., slowing of the rotation of the planet), or even mantle convection (Giacomini et al., 2020 and references therein). Indeed, the distribution and orientation cannot be explained by either global contraction or tidal despinning alone (Watters et al., 2015), which makes evaluation of the global contraction difficult. The estimation of Mercury's contraction, caused by the core solidification, has produced very different results (1-2km: Strom et al., 1975; up to 7 km: Byrne et al., 2014; no more than 1 – 2 km: Watters, 2021). It was also found that contraction is still likely happening to this day (Banks et al., 2015), with some features being less than 50 Ma (Watters et al., 2016). In this light, Watters (2021) favors a scenario where Mercury's interior is cooling slowly to explain the low contraction of the planet, either by insulation of the core by an insulating FeS layer (see Pommier et al., 2019) or a tick megaregolith (see Grott et al., 2011; Zhang et al., 2013).

Polar craters of Mercury host a large amount of volatile, as they are permanently shaded regions (PSR)*. While Thomas (1974) suggested that water ice could be present in polar PSR, its first detection at the North pole was obtained by earth-based radar almost 20 years later (Harmon and Slade, 1992; Paige et al., 1992; Slade et al., 1992; Butler et al., 1993). Further radar studies demonstrated the presence of frozen volatiles (including water ice) at both poles (Harmon et al., 2011; Chabot et al., 2018), and MESSENGER confirmed these findings (Paige et al., 2013; Chabot et al., 2014; Chabot et al., 2016; Chabot et al., 2018).

Some more anecdotical features have also been observed. Xiao and Komatsu (2013) identified central pits in craters, which was surprising at first as they were thought to be formed from volatile-rich crust, and it led to comparative study with other bodies and a better understanding of this phenomenon (Barlow et al., 2017). Ejecta flows and landslides in craters were also observed (Figure 2-9) (Xiao and Komatsu, 2013; Brunetti et al., 2015). Finally, Zharkova et al. (2020) provided detailed information regarding the textures of the regolith.

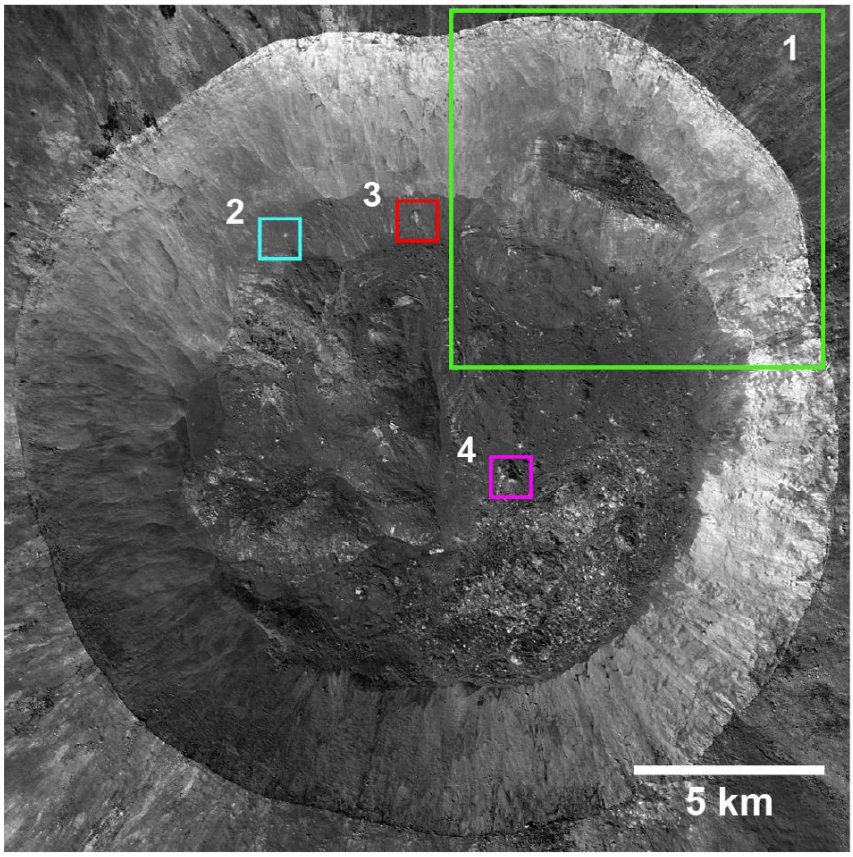

Figure 2-9: Landslide morphologies in Mercury's craters. 1) Large landslide. 2,3,4) smaller rock fall evidence (from Brunetti et al., 2015).

2.5 Composition

The first spacecraft to make direct measurement of Mercury's surface composition was MESSENGER. Mariner 10, the first spacecraft to reach the planet, did not possess any instruments capable of directly measuring the surface composition. Instead, it was only able, using its camera, to image around 45% of the planet's surface, which gave the impression that it was very similar to the Moon (Cremonese et al., 2007). So, before MESSENGER, all surface composition data came from Earth-based observations. The electromagnetic radiations received from Mercury by the Earth comes from the reflected light of its surface and the emitted radiations from the Sun's heating of the surface (Vilas, 1988). The proximity of Mercury to the Sun makes it difficult to observe, as measurements are only possible during daylight or twilights, but observations in ultraviolet, visible and near-infrared lights gave insights on the surface composition. Because of Earth's atmosphere, a lot of data processing is necessary, and it limits the amount of information that it is possible to acquire. For example, the water present in Earth's atmosphere has absorption features that partially cover the absorption spectrum of Fe^{2+} (Vilas, 1988). Ground-based observations showed that the surface is composed of silicate materials, probably plagioclase-rich (anorthite) and poor in FeO (Vilas, 1988; Blewett et al., 1997 and references therein). Other information on the surface's compositions acquired from Earth were obtained from the identification of exospheric species. The exosphere of Mercury contains Na, K, and Ca, which should be derived from the surface (Nittler et al., 2018a, and references therein; Nittler and Weider, 2019; see section 2.7). For more information on Earth-based observations of Mercury, see Murchie et al. (2018, 2019).

MESSENGER was equipped with instruments capable of determining the elemental composition of the surface. Three main instruments were used: the X-Ray Spectrometer (XRS), the Gamma-Ray Spectrometer (GRS), and the Neutron Spectrometer (NS). Solar flares were required to measure heavier elements with the XRS, such as Ca, Ti, Cr, Mn and Fe; normal solar conditions only enabled MESSENGER to measure Mg, Al and Si (Nittler et al., 2011, 2018a; Weider et al., 2012, 2014, 2015). The cartography of elements at the surface was also highly dependent on the orbit of the spacecraft; because it was in an elliptical, polar orbit, it spent a short amount of time over the northern hemisphere at close distance, and a longer time over the southern hemisphere at further distance. This translates in more detailed cartography but incomplete coverage of heavy elements for the northern hemisphere, as the spacecraft spent less time over it, and were able to acquire heavy elements data less often as solar flares are rare. For the southern hemisphere, there are more data but with a worse spatial resolution. The GRS, on the other hand, is not dependent on the solar activity. It measured surface concentration of C, O, Na, Al, Si, K, S, Cl, Ca, Fe, Th and U (Peplowski et al, 2011, 2012, 2014, 2015; Evans et al., 2012,2015). The elemental cartography is however limited to the northern hemisphere, because of the elliptic orbit. Finally, the NS detected water (as ice) in permanently shadowed craters located in the poles, as well as C (Lawrence et al., 2013; Peplowski et al., 2016). Because K, Th and U naturally decay, they were the only elements where absolute abundance could be accurately calculated. The other

elements are usually expressed as ratio of Si, because it is abundant on the surface and measured by both the XRS and the GRS.

There were several surprising results from MESSENGER data. First, the surface was actually rich in volatiles, as shown by its content in Na, Cl, S and K, which discarded the formation scenarios envisioning a volatile-free Mercury (see section 2.8). S, in particular, has an average surface content equivalent to bulk chondrites, at around ~2-4% (Nittler et al., 2011). This concentration is largely above the surface of other terrestrial planets, including Mars, which is volatile rich (Figure 2-10) (Namur et al., 2016a).

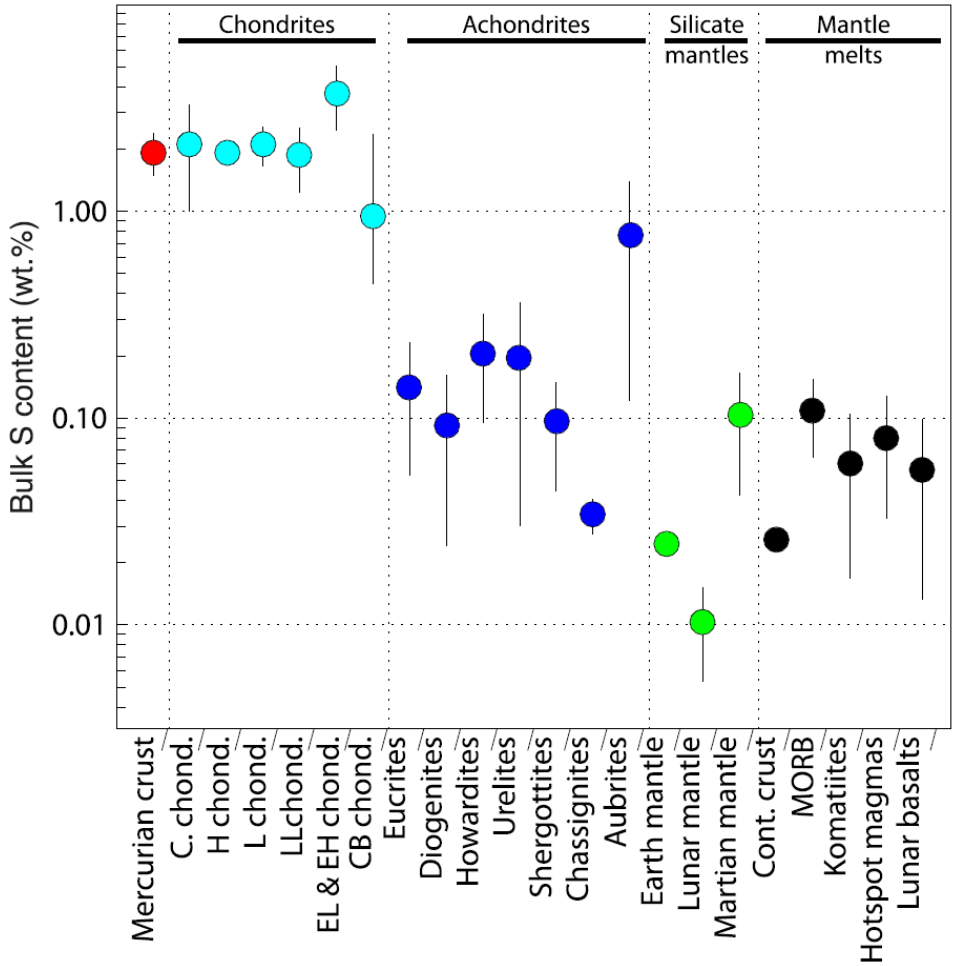

Figure 2-10: Abundances of sulfur in different bodies and settings found in the solar system. The symbols show average concentration, and the vertical line 1σ standard deviations (from Namur et al., 2016).

Secondly, while Mercury has been thought to be similar to the Moon in many ways, its surface composition is actually different; it has a higher Mg/Si and lower Al/Si, and its Fe abundance is very low (<2wt%), with only <1 wt% of FeO, meaning that some amount of Fe must be included in sulfides or as a metal phase (Murchie et al., 2015). The data for minor elements, such as Ti and Cr, have recently been reinvestigated and new, more detailed concentration data were produced (Cartier et al., 2020; Nittler et al., 2023). For Mn, only a few concentration data points were produced, during solar flares

(Nittler et al., 2018a). Finally, carbon could be an important component of Mercury's surface, with an average upper limit of ~4 wt% (Peplowski et al., 2015). Based on these data, the global composition of rocks on the surface can be described as alkali-rich komatiites/boninites, enriched in S and Fe-poor (Vander Kaaden and McCubbin, 2016; Peplowski and Stockstill-Cahill, 2019; Morlok et al., 2023). Komatiites are very refractory rocks, only found on Earth during the Proterozoic and the Archean. They are mainly characterized by a very high MgO (> 18wt%), low SiO_2 (<52 wt%) and low TiO_2 (<1 wt%) contents, while boninites are characterized by MgO and SiO_2 contents of >8 wt% and <52 wt% respectively (Le Bas, 2000).

The composition of the surface is not homogeneous, and several compositional distinct regions were determined (Figure 2-11) (Peplowski et al., 2012, 2015; Weider et al., 2012, 2014, 2015; Vander Kaaden et al., 2017).

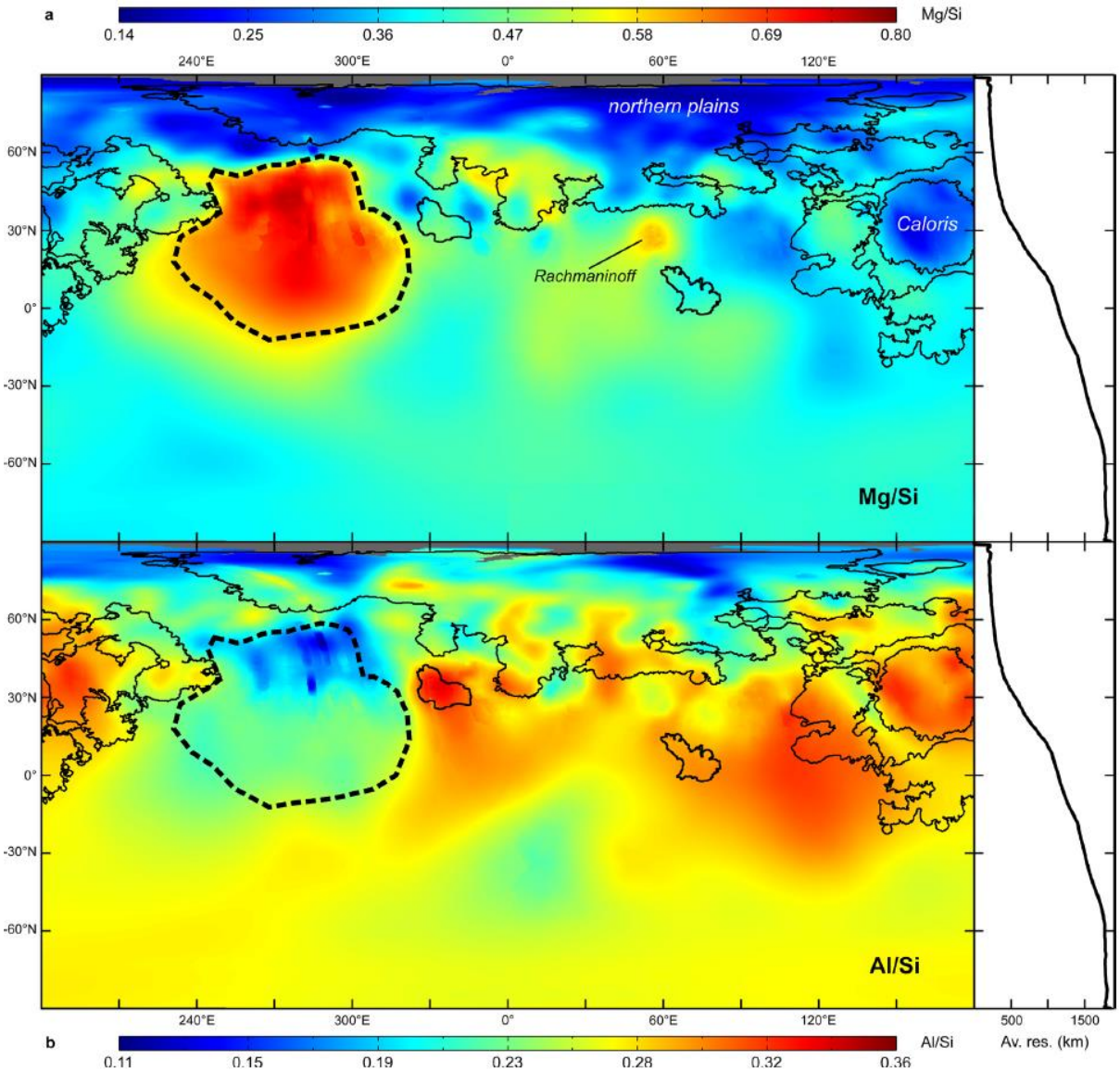

Figure 2-11: Elemental weight ratios maps of Mg/Si (above) and Al/Si (below). Mg/Si varies from 0.14 to 0.80, while Al/Si changes from 0.11 to 0.36, showing clear and distinct geochemical terrains (from Weider et al., 2015).

It is important to note that authors realized the geochemical terranes do not exactly match the geomorphological units (Peplowski and Stockstill-Cahill, 2019; Figure 2-12). While the names and extents of these terranes vary with different authors, the main recognized ones are the Low-Mg Northern Volcanic Plain (Low-Mg NVP), the High-Mg Northern Volcanic Plain (High-Mg NVP), the Smooth Plains, the Inter Crater Plains and Heavily Cratered Terrains (IcP-HCT), and the High-Mg Province (e.g., Weider et al., 2015; Vander Kaaden and McCubbin, 2016; Peplowski and Stockstill-Cahil, 2019)

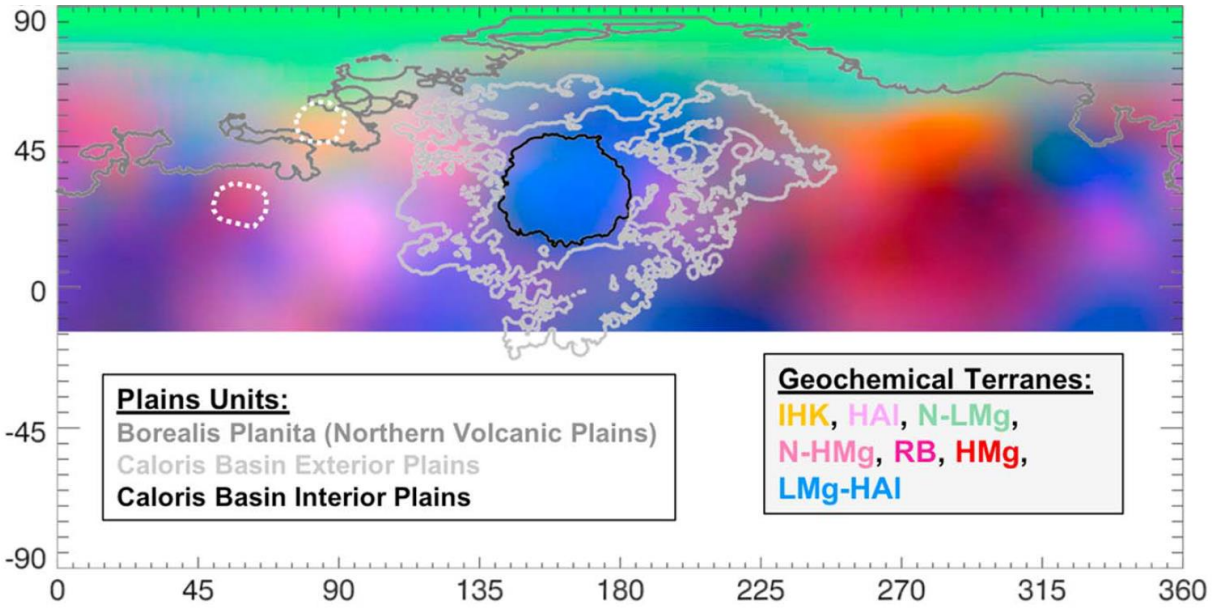

Figure 2-12: Geochemical terranes identified by Peplowski and Stockstill-Cahill (2019), which is consistent with the previous work of Vander Kaaden et al (2017), albeit for two regions. Some geomorphological regions are superposed to the terranes. IHK: intermediate, high-K; HAI: high-Al; N-LMg: low-Mg North ; N-HMg: high-Mg North; RB: Rachmaninioff basin; HMg: high-M terrane; LMg-HAI: low-Mg, high-Al (from Peplowski and Stockshill-Cahill, 2019).

As instruments onboard MESSENGER only gave elemental data, it is difficult to infer the mineralogy of the surface. Moreover, the crystallinity of the rocks (how much of the surface is made of quenched glass or crystal) is unknown. Early work by Stockstill-Cahill et al. (2012) and Charlier et al. (2013) determined that the surface of Mercury should be dominated by high-Mg, low-Ca pyroxene and plagioclase. Namur and Charlier (2017) further investigated the issue, showing heterogeneities in the mineral composition of the surface between different regions; the Borealis Plain (known before as the Northern Volcanic Plains, NVP) and the Smooth Plains are dominated by plagioclase, the High-Mg Province by forsterite, and the Intermediate Plains by forsterite, plagioclase and enstatite. Diopside and quartz are also silicate components of Mercury's mineralogy.

One of the most exotic features of the mineralogical assemblage is the probable presence of sulfides at the surface, which is supported by MESSENGER data (Evans et al., 2012; Vilas et al., 2016; Namur and Charlier, 2017), even though Sprague et al. (1995) hypothesized their presence before. Because of the very reduced conditions on Mercury, the solubility of S in silicate melts increases up to several

percent (Namur et al., 2016a). Lavas could either transport sulfur to the surface as S^{2-} in the melts (Zolotov, 2013; Namur et al., 2016) or as sulfide droplets (Malavergne et al., 2014). The correlation between S and Mg and Ca has been interpreted as the presence of MgS and CaS sulfides on the surface (Evans et al., 2012), and subsequent crystallization of S-rich lavas at the surface could be responsible to the formation of (Ca,Mg)S (Cartier and Wood, 2019). Localized presence of MgS or CaS could be explained by volcanic activity, where sulfides would be brought as slags deposits in hollows (Helbert et al., 2013; Vilas et al., 2016; Varatharajan et al., 2019; Renggli et al., 2022). Regarding chlorine, another volatile, it could be contained in magmatic formed halide (such as halite, sylvite or lawrencite), while apatite, mica and amphibole have been ruled out as host phases (Evans et al., 2015).

Finally, McCubbin et al. (2017) proposed that a significant part of the surface is made up of metallic materials to explain the low O/Si ratio of the surface measured by the GRS. They calculated that there should be 12-20% metallic phases of Si-rich, Fe-Si alloys. The formation of these alloys are most probably the results of space weathering and smelting by carbon. Iacovina et al. (2023) favored the smelting hypothesis during magmatic eruption for the formation of these alloys.

2.6 The magnetic field

Before Mariner 10's flybys, little was known on Mercury's magnetic field*. There was no experimental data to exploit, but some observations hinted toward the absence of a magnetic field. It was thought that the very slow rotation of the planet might hinder the generation of a magnetic field, and the absence of detection for nonthermal radio emission from Mercury was consistent with the non-existence of a magnetic field (Ness and Whang, 1971). However, it was believed that a magnetic field could still be produced by the interaction of the solar wind with a dense atmosphere (Ness and Whang, 1971). Despite it has been shown, by the late sixties, that the atmosphere of Mercury was very thin (e.g., Belton et al., 1967; see the section 2.7), there were still possibilities to form a magnetic field from a rarified atmosphere (Banks et al., 1970). In any case, the view at the time was that Mercury was similar to the Moon in many ways, and so it should also be, as the Moon, devoid of a magnetic field (Ness and Whang, 1971). Mariner 10 produced an unexpected result; it observed a clear bow shock*, the magnetopause* boundaries and part of the magnetotail*, showing that Mercury possesses a weak, dipolar magnetic field, of intrinsic origin (Ness et al., 1974; Ness et al., 1975). Indeed, as opposed to Venus, where a magnetosphere is produced by atmosphere-ionosphere* interactions, the magnetic field on Mercury should come directly from the planet (i.e., intrinsic) (Broadfoot et al., 1974; Howard et al., 1974; Ness et al., 1975). The data from MESSENGER brought new insights into the field's morphology. While it is similar to Earth in many ways, it also has some highly unusual characteristic; it is surprisingly weak (~1% of Earth's strength), its dipole has a northward offset from the geographic equator of ~500km, and it is axisymmetric (the dipole is aligned with Mercury's axis of rotation) (Anderson et al., 2011). Several

factors can contribute to the intrinsic magnetic field: remnant crustal magnetizations (as on Mars), induction currents, and a core dynamo (as on Earth).

Crustal remanence from a past magnetic field has been proposed to explain the weak magnetic field (Stephenson, 1976; Srnka, 1976). Others pointed toward a possible incompatibility of crustal remanence with the hot temperatures on Mercury's surface, as they could be close to the Curie temperature (the temperature where magnetism is lost, Schubert et al., 1988). Aharonson et al. (2004) showed that the present magnetic field could be generated in the crust if it contains rocks capable of sustaining high magnetizations, or if the planet had had a dynamo field more intense than Earth. However, early data from MESSENGER showed that a crustal remanent field was probably not an important contributor to the planet's magnetic field (Solomon et al., 2008). Even though the measured magnetic field is not produced by crustal remanence, weak magnetization of surface rocks was detected, which can give us insights into the early magnetic field of Mercury. As time passed and the altitude of MESSENGER decreased, it gave evidence for weak remanent magnetization in Mercury's crust (Johnson et al., 2015; Hood et al., 2018). The association of magnetic anomalies with craters points toward the magnetization of metallic material brought by impactors during the early history of Mercury, and not by the present magnetic field (Hood et al., 2018; Oliveira et al., 2019). The study of these anomalies permits the modeling of the early magnetic field and its evolution, although higher resolution data from BepiColombo are necessary for it (Heyner et al., 2021).

Induction currents are a form of induced magnetic field, resulting from the penetration into the core of time-varying magnetic field from the magnetosphere. All magnetosphere contains current systems flowing in their magnetopause, called Chapman-Ferraro currents. Because of the small size of Mercury's magnetosphere, the magnetic field generated in the magnetopause contributes to the surface magnetic field and, because of Mercury's thin crust, they penetrate the core, creating an induced magnetic field superposing the internal, dynamo-generated one (Hood and Schubert, 1979; Grosser et al., 2004; Glassmeier et al., 2007a). Glassmeier et al. (2007b) suggested that this phenomenon could create a feedback loop, where the dynamo is influenced by the field generated in the magnetopause, the latter being also dependent on the dynamo. If the feedback is negative (because the induced magnetic lines are in the opposite direction in Mercury's core), this could explain the planet's weak magnetic field (Glassmeier et al., 2007b; Heyner et al., 2011). Another possible phenomenon due to induction currents is the balancing of the effect of the solar wind; if the intensity of solar wind increases, the magnetosphere is compressed, which increases the induction currents themselves, strengthening the magnetosphere, and thus counterbalancing the effect of solar wind (e.g., Slavin et al., 2014; Johnson et al., 2016; Jia et al., 2019). This effect would effectively shield the surface from the bombardment of the solar wind, which has profound implication for the generation of exospheric species (see section 2.7).

Finally, several studies tried to model a core dynamo in Mercury, which depends heavily on the composition and structure of its core (see section 2.3.2), and the presence of an insulating layer atop the core, such as an FeS matte (see section 2.3.3). There are been a very large number of models proposed, whose complexities far exceed the global approach presented here. A good review of these models and their comparison with each other can be found in Heyner et al. (2021). The debate is still open, and the data from BepiColombo are highly awaited.

2.7 The exosphere

As the observation of Mercury from Earth is difficult, there were thoughts that Mercury may had an atmosphere in the sixties (Dollfus, 1961; Field, 1964). Closer examinations hinted toward the possible existence of only a very thin atmosphere based on the absorption spectra of CO_2 (Spinrad et al., 1965). Belton et al. (1967) further decreased the upper pressure limit of a mercurian atmosphere. Banks et al. (1970) considered the problems of maintaining an atmosphere on Mercury, as there should be important loss of atmospheric material through photoionization* and thermal evaporation*. They predicted the presence of an exosphere*, rich in He, Ar and Ne, produced by the solar wind*. Mariner 10 was rigged to measure He, Ne, Ar, H, O, Xe and C, based on the expected atmospheric constituent of Mercury (Broadfoot et al., 1976). However, Mariner 10 only detected H and He, as well as a signal close to the limit of detection for O (Broadfoot et al., 1976). Ground-based observations allowed for the detection of Na and K in the exosphere (Potter and Morgan, 1985; 1986), and later Ca (Bida et al., 2000). Mg was discovered thanks to MESSENGER (McClintock et al., 2009), as well as Al, Fe and Mn (Doressoundiram et al., 2009; Bida and Killen, 2016; Vervack et al., 2016). One of the striking features of Mercury's exosphere is that the distribution of Na is highly variable in time and space, with changes within a day, and variations between different latitudes (Potter and Morgan, 1990; Killen et al., 1990; Leblanc et al., 2009; Mangano et al., 2013). These variations were later observed for other species, such as Ca and Mg (Burger et al., 2012, 2014; Killen and Hahn, 2015; Merkel et al., 2017; Chaufray et al., 2022).

The processes occurring in Mercury's exosphere that leads to its observed composition and variation through time are complex and are dominated by interactions of gas particles with the surface and the magnetospheric plasma. These interactions lead to a constant entry and exit of particles in the exosphere. For H and He, the main source is the solar wind, while the processes supplying the other elements are photon-simulated desorption*, thermal evaporation*, impact vaporization*, ion sputtering* and chemical sputtering* (Figure 2-13, Milillo et al., 2005; Killen et al., 2018; McClintock et al., 2018). However, the existence and the importance of these processes at work on Mercury is still debated, and each process affects differently the exospheric elements. For example, the presence of Na in the exosphere is still puzzling, and it seems to result from multiple processes (Killen et al., 2018 and

references therein), while impact vaporization seems to be the most important contribution to Ca in the atmosphere (Killen and Hahn, 2015), but sputtering could play an important role too (Pfleger et al., 2015). As shown by the very low pressure on Mercury, the lifetime of atoms and molecules in the exosphere is short so that no atmospheric build-up occurs; the particles are lost to radiation pressure*, photoionization* and Jeans escape*, or by sticking to the surface after impacting it (Figure 2-13, Killen et al., 2018; McClintock et al., 2018).

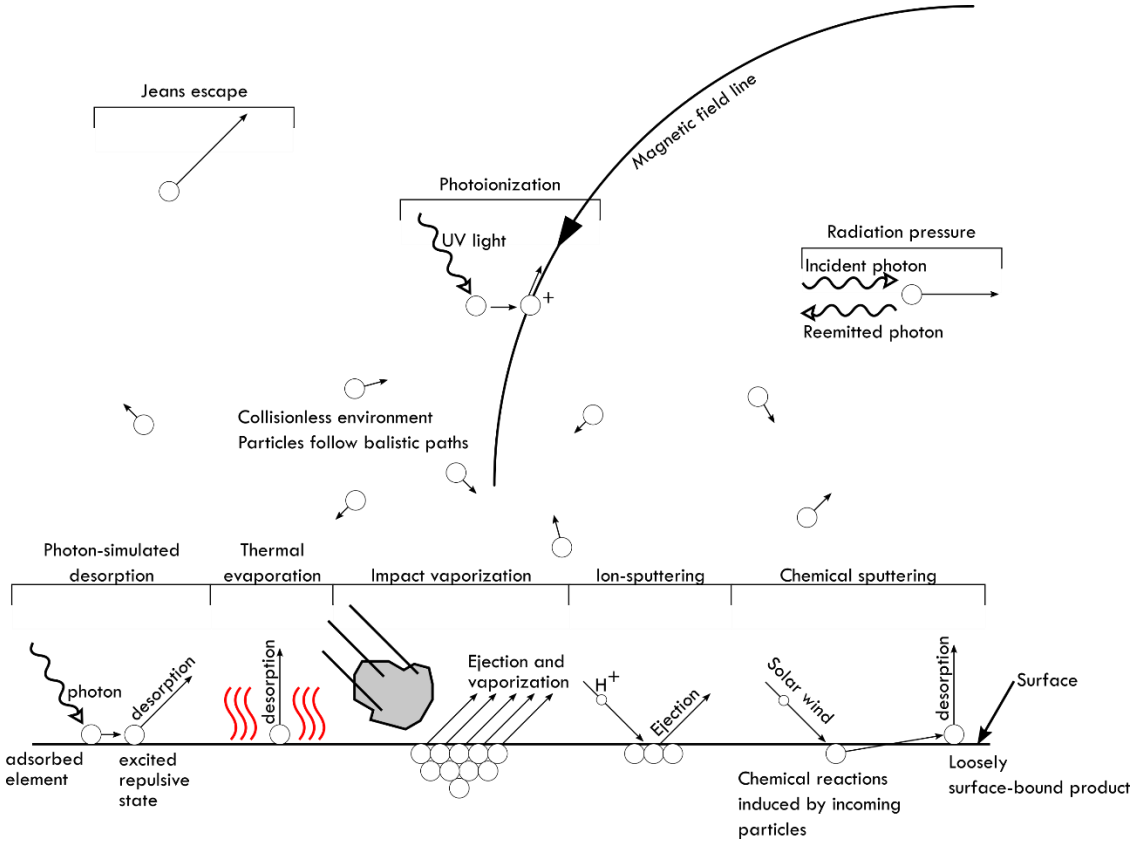

Figure 2-13: Schematic of exospheric processes. The processes on the bottom of the figure are those that replenish the exosphere, while the three on the top are those responsible for its depletion. The thick black line on the bottom represents the surface. Particles above it are adsorbed, while the ones below make up the subsurface.

2.8 The formation of Mercury

The sections above have described a planet very different from the three other terrestrial worlds of our solar system. As shown in the section below, there seems to exist for each formation hypothesis one or more features which are irreconcilable with. However, considerable progress has been made since the seventies, and each formation scenarios can be looked under a new light. They are mainly two classes of scenarios: in the first ones, the present bulk composition of Mercury is similar to its initial bulk composition, just after accretion (with the same high Fe/Si) and in the second ones, the planet formed

from material similar to the other terrestrial planets and some later processes removed a large chunk of its silicate part.

2.8.1 Some general concepts of planetary formation

2.8.1.1 Formation of the solar nebula

The formation of a stellar system starts with the gravitational collapse of a dense molecular cloud, composed primarily of hydrogen and helium (Figure 2-14). A very small fraction of this cloud is made up of dust grains and gaseous molecules that are not hydrogen or helium. This collapse forms a core in the center of the cloud, which starts accreting matter and heating up. Overtime, the cloud flattens due to the effects of rotational motions and magnetic fields. In the center lies a protostar, surrounded by a protostellar disk (Figure 2-14). Matter from the protostellar disk continues to fall in and feed the protostar. The former eventually develop into a protoplanetary disk, where planets will form, which surrounds a protostar (Boss and Ciesla, 2014, and references therein). The origin of this theory of stellar system formation can be traced back to the 18th century, to Swedenborg, Kant and Laplace. It was corrected and expended upon over the years (e.g., Kuiper, 1956a,b,c; Schmidt, 1957; Safronov, 1969).

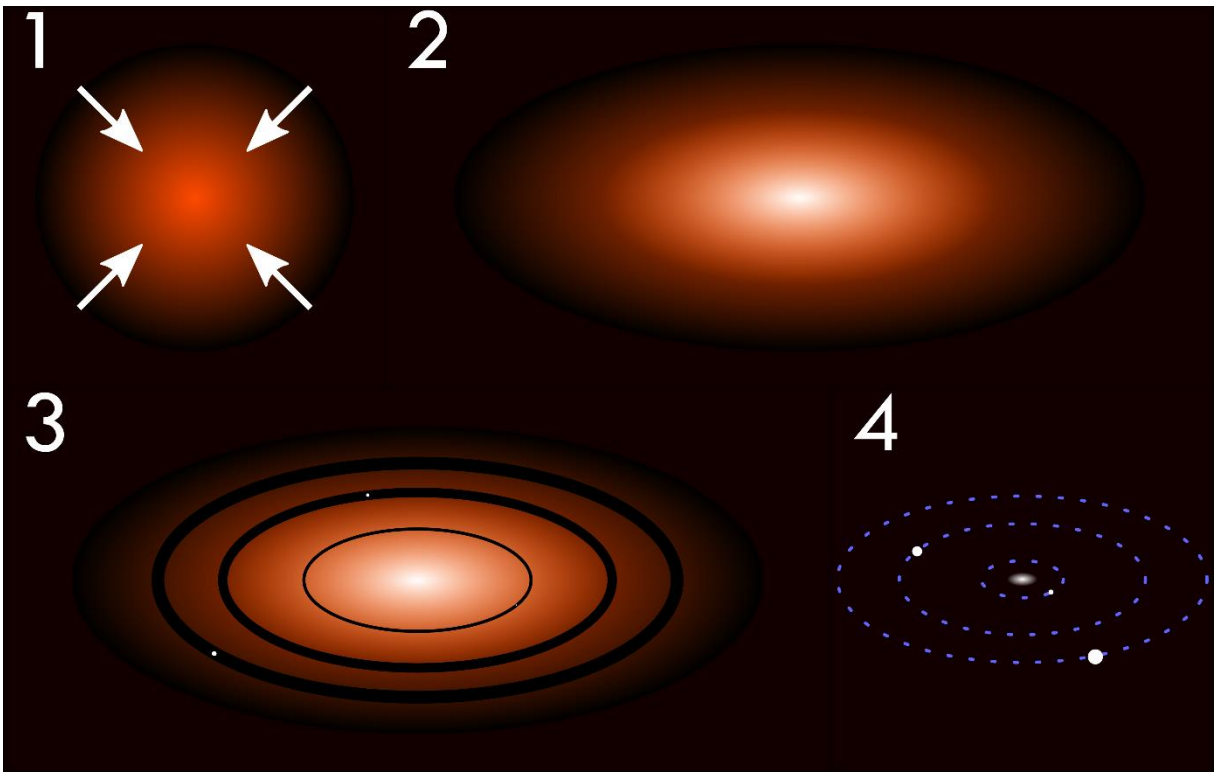

Figure 2-14: Simplified evolution of a solar nebula, from the molecular cloud to the solar system. 1. Gravitational collapse of a dense molecular cloud. 2. Formation of a protostar (white, in the center), surrounded by a protostellar disk made of gas and dust. The disk flattens and rotates around its center. 3. Formation of a protoplanetary disk, where planetesimals accrete the dust and gas in the path of their orbits. Overtime, the planetesimals grow to form protoplanets (white dots). 4. The solar system after accretion of the planets (white dots), which now occupy stable orbits (blue dotted lines). There is no more gas and dust to accrete.

2.8.1.2 Accretion of planets

The protoplanetary disk is composed of gases (~99%) and solids (~1%). These solid dust particles collide, and, depending on the force of the collision, can be bound together by electrostatic forces. However, this process cannot go on to form lager bodies, as it would be expected; indeed, models show that it is not possible to form particles larger than ~1 mm this way because they start to bounce with each other at that size and consequently do not accrete. There have been various different models to overcome this barrier and explain how particles can grow in size and form planetesimals km to hundreds of km large, with the currently most promising one called "streaming instability" (Johansen et al., 2007). In any case, once the accretion of these small pebble resumes, they can grow to km large bodies called planetesimals. These hundreds planetesimals collide with each other in the solar disk, growing in size very rapidly, during a phase called the "runaway growth". After, the larger ones attract and incorporate the smaller ones, so that only a few large bodies remain (the "oligarchic growth"). While this model of planetary accretion correctly describes the building of Mars-size protoplanets, it struggles to explain the formation of large ones (with the mass of the Earth or above), and so another process called "Pebble accretion" has now been invoked to explain the observed planetary masses (see Johansen and Lambrechts, 2017, and references therein). The last processes of planetary formation include gas accretion to form an atmosphere and planetary migration (see Raymond and Morbidelli 2022 and references therein for a thorough review of solar nebula and (proto)planetary formations).

During planetary formation, an enormous amount of energy is released by accretion, large impacts and decay of short-lived radioisotopes (such as Al^{26}), which leads to extensive melting; Fe-rich metals sink to the center of the planet, incorporating siderophile element, leading to core-mantle differentiation (Righter, 2003; Rubie et al., 2015). Later processes include magma ocean formation and crust-mantle differentiation, as discussed in section 2.3.4.1.

2.8.1.3 The building-blocks of planets

As seen in the previous section, the accretion of dust particles, via different processes, led to the formation of planets. These dust particles themselves form by condensation as the temperature of gases in the solar nebula decreases. Because elements have different temperature of condensation (Figure 2-15), the temperature profile of the solar nebula is determinant for the composition of the material that is going to accrete with distance to the Sun. Indeed, the temperature of the nebula decreases with distance to the Sun, with one of the stark boundaries being the snow line, where H_2O condense to form water ice (e.g., Morbidelli et al., 2016). Elements with high condensation temperatures are named refractory, and those that have low condensation temperatures are called volatile.

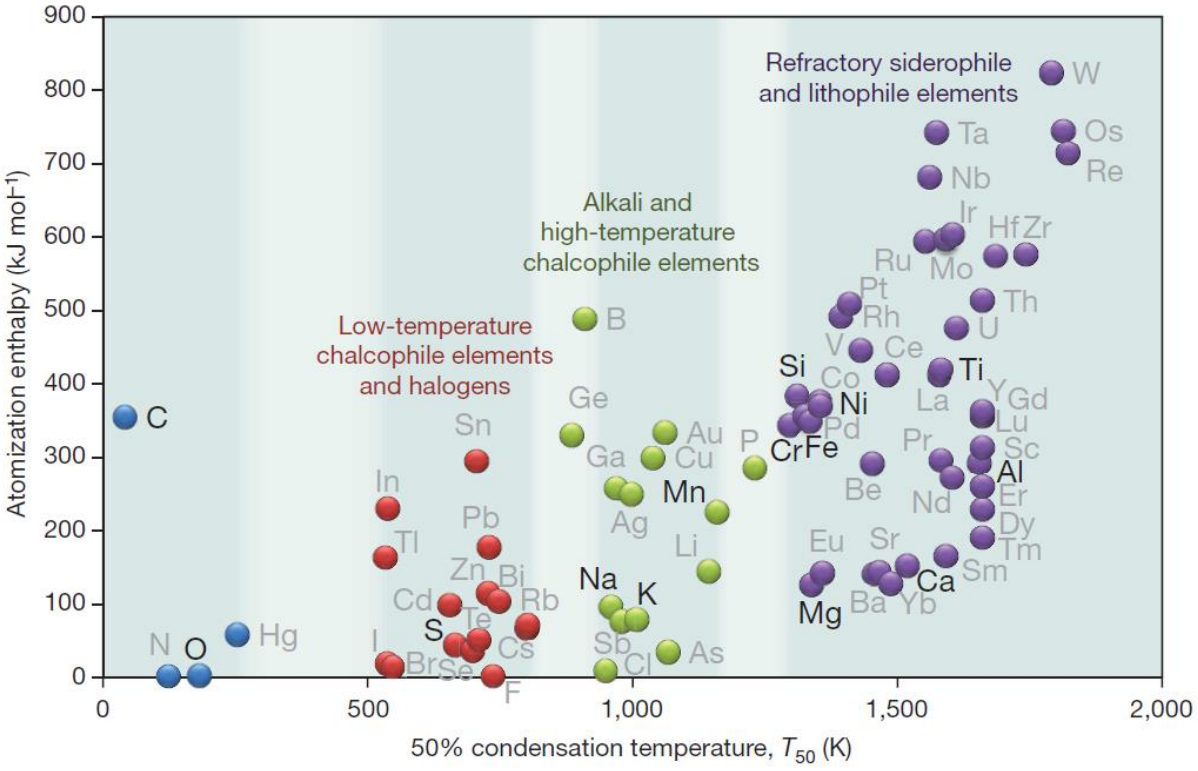

Figure 2-15: The volatility of elements. The two axes show different measures of the volatility of elements; the 50% condensation temperature corresponds to the temperature where 50% of the element would condense in a solar nebula, and the atomization enthalpy is the mean bonding energy per atom in solids. Inner planets (Mercury, Venus, Earth and Mars) are depleted in volatile elements compared to outer planets, as the temperature in the nebula before the snow line was higher than the condensation temperature of these elements (from Albarède, 2009).

This difference in composition with heliocentric distance is thought to be responsible for the difference in the bulk composition of planets, even though planetary migration complexify this simple vision (e.g., Clement et al., 2021). Planets in the external system (Jupiter and beyond) are indeed gas and ice giants, composed of a massive envelope of volatile, while their moons are a mix of rock (and sometimes metal) and ice (Figure 2-16).

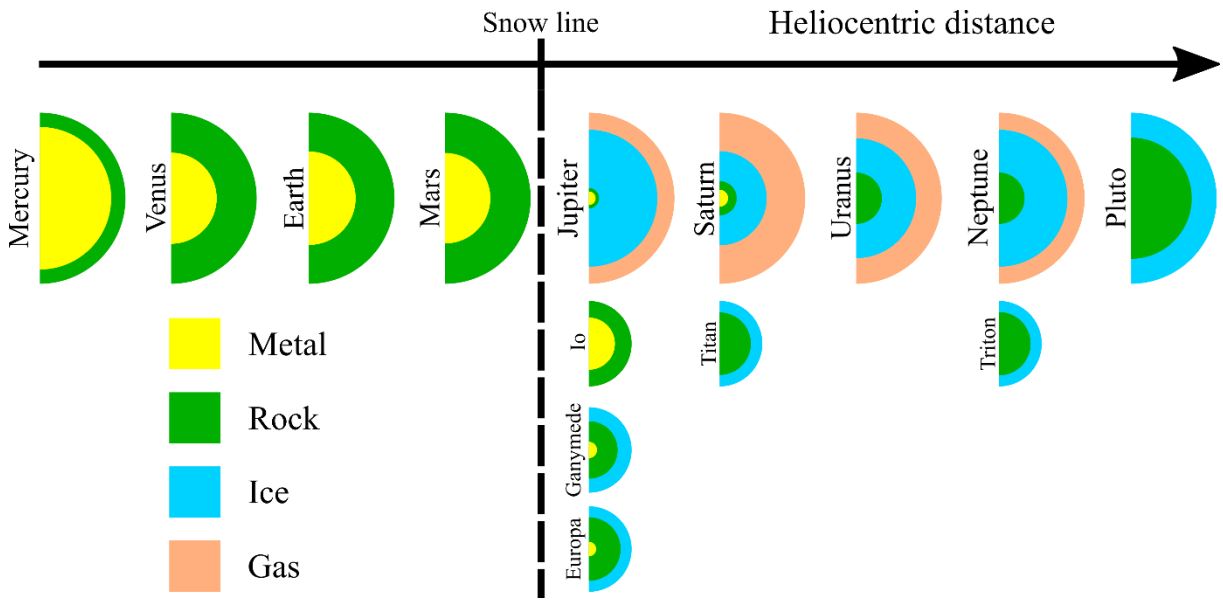

Figure 2-16: Simplified internal composition of planetary bodies in the solar system as a function of heliocentric distance. All the planets and Pluto have the same scale, and the moons are also shown as having the same size, and are place below their respective host planet. Data from Lodders and Fegley, 1998.

On the other hand, the terrestrial planets are "dry", volatile-poor bodies compared to the other ones. Moreover, redox conditions also evolve with distance from the Sun, with conditions becoming more oxidizing with increasing distance from the Sun, as more and more volatiles condense.

Amongst the vast diversity of meteorites that exist, there is a class that is of particular interest to understand the composition of today's planets. These are the chondrites, the most primitive type of meteorites. They are composed of chondrules (5-80 vol%) which are small (mm-size) spheres composed of a mixture of silicates and metal (Alexander et al., 2001). They also exhibit CAIs (calcium-aluminum-rich inclusions), which are the oldest known solar system materials, dating back to 4.56 billion years ago (Amelin et al., 2005). Finally, presolar grains have also been found in some chondrites (see Lodders and Amari, 2005), confirming their very primitive status. They are chemically similar to the composition of the Sun (excluding H, C, N, O and noble gas), but there are variations in their bulk compositions, thought to be caused by their different positions of formation in the solar nebula (Alexander et al., 2001). Because of these variations, they were divided into 3 groups, themselves divided into subgroups: carbonaceous (CI, CM, CO and CV), ordinary (H, L, LL) and enstatite (EH, EL). Amongst them, the CI chondrites are the closest in composition with the photosphere (Alexander et al., 2001; Palme et al., 2014), and so the composition of other chondrites are often compared to them to highlights depletions or enrichment of elements. Because of isotopic relations, it is assumed that chondrites are the parent body of the terrestrial planets. For Earth, enstatite chondrites have been proposed to be the dominant precursor material (e.g., Smith, 1982; Javoy, 1995; Javoy et al., 2010), but more recent studies advocate for a mix of ordinary and enstatite chondrites, even though interpretations are complicated by the presence of late veneers (Dauphas, 2017; Fisher-Gödde and Kleine, 2017). For Mars, it may also be a

mix dominated by enstatite and ordinary chondrites (Sanloup et al., 1999; Brasser et al., 2017). The variety of compositions of the three groups of chondrites points to different location of origin varying in distance from the Sun during planetary formation, with enstatite chondrite being the closest and carbonaceous the farthest (e.g., Fisher-Gödde and Kleine, 2017). This explains the importance of migration models (such as the Grand Tack model, Raymond and Morbidelli, 2014) in predicting their proportions as planet building blocks.

2.8.2 Hypotheses on the formation of Mercury

2.8.2.1 Pre-MESSENGER scenarios

Around the time of the Mariner 10 mission, the proposed models of planetary formations relied on the condensation of a chemically homogeneous cloud of dust and gas. The difference in planets densities were explained by some metal/silicate fractionation processes (Urey, 1951; Bullen, 1952). To avoid the need of these processes and keep a compositionally homogeneous nebula, Ringwood (1966) proposed that the variation of redox condition with distance from the Sun would change the valence of Fe (from Fe^0 to Fe^{3+}), which would impact the density of the planets formed at different place. On the contrary, based on the work of Urey (1951), Lewis (1972) proposed that the observed difference in densities of the terrestrial planets can be solely explained by the variation of temperature and pressure with heliocentric distance. He proposed that the bodies closed to the sun condensed from dense refractory material ($CaTiO_4$, $MgSiO_3$, Fe^0), with condensations of less refractory material as distance with the Sun increased (e.g., FeS, FeO, tremolite or talc) (Figure 2-17).

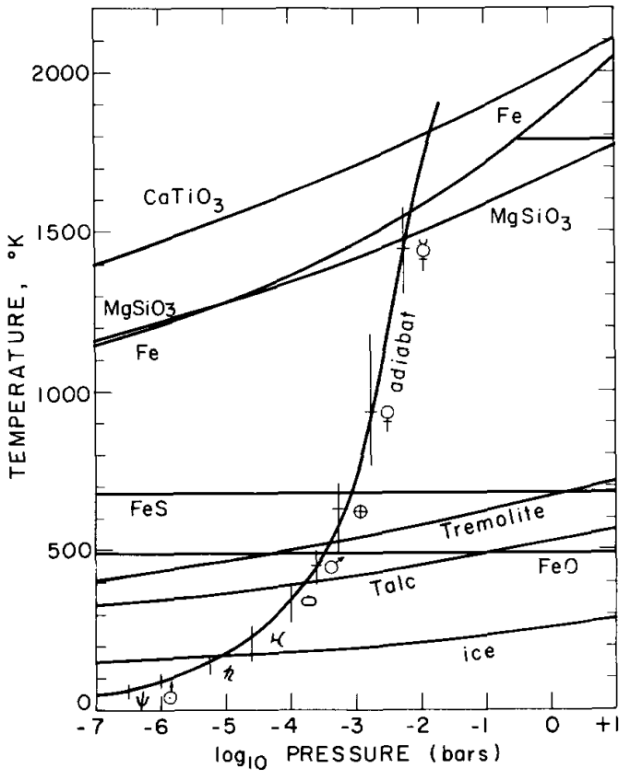

Figure 2-17: Condensation curves of common phases as a function of the temperature and the pressure of the nebula. The symbols the solar system's planets are placed on the adiabat of the nebula (from top to bottom: Mercury, Venus, Earth, Mars, the asteroids, Jupiter, Saturn, Uranus and Neptune; from Lewis, 1972).

Weidenschilling (1978), noticed that the scenario of Lewis (1972) needed very peculiar conditions for a planet with a Mercury-like composition to form. Moreover, the new data of Mariner 10 hinted toward the presence of a molten outer core (due to the detection of the magnetic field), which is incompatible with the equilibrium condensation model which predicts volatile poor Mercury (notably K and S, necessary to produce heat and to decrease the melting temperature of the core, respectively). He proposed that gas-drag on small planetesimals in a solar nebula of lower temperature fractionated silicate and metal, a model which could retain some volatile. Indeed, the drag should be less important on denser planetesimals (i.e., Fe-rich), while the others would be slowed down and drift toward the Sun, leading to a preferential accretion of metal-rich planetesimals.

Cameron (1985) proposed that much of the silicate envelope of Mercury was removed during a very hot phase of the solar nebula. In this scenario, proto-Mercury was more than twice as massive as today, and the heating (2500-3500K) in this part of the nebula vaporized a large part of its enstatite mantle. It also implies that Mercury should be strongly volatile-depleted and refractory-rich (Fegley and Cameron, 1987). However, there were doubts that the nebula could reach these very high temperatures (e.g., Boss, 1996).

As seen in the previous section, chondrites represent the oldest undifferentiated material from the solar system, and they may be the building blocks of planets. Based on this idea, the search for a mercurial

precursor has been concentrated on two types of chondrites; the Bencubbin-like chondrites and the enstatite chondrites (EC). The first group is made of meteorites with the highest amount of Fe^0 (60 wt%, Weisberg et al., 2001), close to the amount expected on Mercury (e.g., Brown and Elkins-Tanton, 2009) and were considered as building-blocks (Taylor and Scott, 2003). Because of the very reduced conditions of Mercury, it was deemed possible that the EC, which are the most reduced known meteorites, were its building blocks. Moreover, Wasson (1988) suggested that they may form in the region close to Mercury orbits. However, their Fe/Si content is lower than Mercury (Taylor and Scott, 2003).

Finally, impacts on a large proto-Mercury that stripped a large amount of its silicate part were proposed by Smith (1979) and Benz et al. (1988). As noted by Taylor and Scott (2003), the characteristics of such an impact would be highly unusual, requiring a very high speed of collision, which is necessary to avoid the ejecta to reaccrete.

2.8.2.2 After MESSENGER

One of the most important discovery from MESSENGER that helped constrain its formation has been the high volatile content at the surface (Nittler et al., 2011). Indeed, most pre-MESSENGER models predicted a volatile-depleted planet (e.g., Lewis, 1972; Cameron, 1985), and models of formation from Bencubbin-like chondrites also pose a problem as they are volatile-depleted. New post-MESSENGER models have been proposed, and a few are listed here.

Ebel and Alexander (2011) proposed a variant of the condensation model, where Mercury formed from reduced, C-rich and water-poor dust, which is represented today by what is called chondritic interplanetary dust particles, which are considered the most pristine example of the early solar system dust, with a C-rich anhydrous chondrite composition (Schramm et al., 1989; Thomas et al., 1993). This model explains well the very reduced state of Mercury (the very low FeO abundance), as well as the presence of volatile on it (which are refractory under low fO_2). However, there are difficulties to explain the high Fe/Si ratio of the planet with this model; their postulated scenario for a high Fe/Si should result in an olivine rich surface, which is in contradiction with MESSENGER data.

Wurm et al. (2013) hypothesized that regions close to the sun form dense planets, enriched in Fe, based on the observation of two dense rocky exoplanets orbiting close to their star. They proposed that photophoresis* could separate metal from silicate, as the former have higher thermal conductivity than the latter.

Finally, Hubbard (2014) showed that the conditions in the outer edge of the inner protoplanetary disk can heavily magnetize iron, leading to high speed collisions which eject the non-magnetized silicates, thus enriching the region in iron.

Regarding impact scenarios, one of the key questions is the fate of volatile and moderately volatile elements during such an event. Indeed, it was assumed that the heat released during this cataclysm would vaporize most of them, leaving a volatile-depleted body behind. However, it seems from recent works that volatiles, such as K and Na, could survive giant impacts (Stewart et al., 2016). Another key problem is to prevent the re-accretion of the ejected materials (see Gladman and Coffey, 2009). To resolve the problem of re-accretion, hit-and-run scenarios have been proposed. In those, proto-Mercury comes in contact with a larger, more massive body. The planets do not collide head-on, but skim pas each other and continue their path after the impact. The less massive body (proto-Mercury) is stripped of a large part of its silicate part, while the other one is only barely scratched. After, the ejected materials are dominantly re-accreted by the massive body, leaving proto-Mercury depleted of a large silicate chunk (Asphaug and Reufer, 2014).

In conclusion, there is a strong lack of constrain to model the formation of Mercury, and it is possible that its formation results from a mix of processes exposed above. In particular, one of the biggest unknown concerns the migration of planets after (or during) accretion. Because there is a high chance that planetary migrations happened (see Grand Tack model, Raymond and Morbidelli, 2014, or Clement et al., 2021, for the terrestrial planets), it may seem difficult to consider that Mercury formed where it now resides (i.e., close to the Sun), and that nebular metal/silicate fractionation processes where the dominant causes for its large metallic core.

Chapter 3: Experimental and analytical methods

3.1 Introduction

The lack of meteorites from Mercury makes experimental petrology the best tool to investigate the hypothesized rocks and minerals that should have formed on the planet. For Earth-related studies, experimental petrology is an indispensable method to understand the processes responsible for the formation of the rocks we observe on the surface, and a great way to probe deep inside the mantle, whose mineralogy is not directly available to us. Its use is a bit different for Mercury, as we cannot readily compare the sample produced in the laboratories to true mercurian ones. We have to use proxies to infer the composition of the lava sources from surface composition, and we estimate the intensive and extensive parameters (such as temperature, oxygen fugacity and pressure) from the data recovered by the spacecrafts. The exotic nature of the planet naturally guides us to experimental petrology, as some processes happening on Mercury are not observed on Earth. During the thesis, I have used various apparatuses to create samples representative of Mercury. Here, I focus on thoroughly describing two devices used for this work, namely the piston-cylinder and the vacuum line from the University of Liège. While I did more than 20 experiments using the multi-anvil apparatuses of different laboratories, the majority of the samples produced were used in works led by Dr. Anne Pommier. Moreover, as opposed to the two other apparatuses, there is no multi anvil in Liège, and so only a short paragraph is written about this method. A brief description of the internally heated pressure vessel from the University of Hanover is given as well. This section also describes the preparation of the various starting compositions, as well as the analytical tools used to qualify and quantify the samples. Finally, I briefly list and describe the different samples we obtained.

3.2 Powder preparation

For this work, two kinds of powders were prepared: some analogues of the silicate part of enstatite chondrites (EC), and compositions similar to the North Volcanic Plains of Mercury (NVP, now called Borealis basin). As seen in the introduction on Mercury, the silicate composition of enstatite chondrites is considered as a good proxy for the silicate part of Mercury; they are highly reduced, they have very low FeO, with a high S content, and are very refractory. Similar powders were used in many studies focusing on the differentiation of the planet (e.g., Namur et al., 2016a). The samples synthetized with these EC powders were used to study the partitioning of minor and trace elements between the silicate, metal and sulfide melts (e.g., Pirotte et al., 2023; Cartier et al., in revision), to carry out preliminary study on the electrical conductivity of S-rich silicate melt at UCSD, and to perform various test on the stability of Fe-free sulfides. On the other hand, NVP powders are less refractory (lower Mg/Si and higher Al/Si, Table 3-1), and so their liquidus temperature is hundreds of °C lower than EC ones. This is the

main reason they were made, as we needed to synthetize silicate glass in the vacuum line, which can be used up to ~1450°C. The silicate glass created in evacuated silica tubes were used to study the electrical conductivity of melts, as well as the melt structure of these S-rich silicate glass (Pommier et al., 2023). Because NVP powders were doped in minor and trace elements, they are also used to study the partitioning of elements between silicate melt and Fe-free sulfides, especially U, Th and K (Lldó et al., in prep). All powders were prepared from pure, commercially available oxides, silicates, and phosphates.

Table 3-1: Compositions of the base powders used for this work. From these initial powders, dozens of different sub-powders were created by adjusting the Si/SiO_2 ratios and the amount of S, Fe, FeS or CaS added.

	EC001/EC002*	EC003	EC004	NVP**
SiO_2	61.26	62.00	51.98	62.64
TiO_2	0.10	0.00	0.21	0.36
Al_2O_3	2.76	3.00	4.24	14.24
Cr_2O_3	0.82	0.00	0.00	0.10
Fe_2O_3	0.00	0.00	0.00	0.00
FeO	0.00	0.00	0.00	0.00
MnO	0.43	0.00	0.00	0.22
MgO	31.37	32.00	37.64	10.09
CaO	1.65	3.00	3.84	5.71
Na_2O	1.55	0.00	1.29	6.18
K_2O	0.19	0.00	0.04	0.17
P_2O_5	0.90	0.00	0.00	0.10
Total	101.03	100.00	99.24	99.81

**EC002 had MgO replaced by MgSO4, and the excess of O was compensated by increasing the Si/SiO_2 ratio.*

***The Ca in NVP was added either as $CaSiO_3$ or CaS, keeping both the Ca and Si content identic.*

They were kept dried in the oven at 120°C before use. Most experiments were performed on powders doped in a large number of minor and trace elements (EC001 and NVP) using premixed standard solutions. Some powders were used as tests, and thus were not doped (notably the EC002 and EC003 compositions).

3.3 The piston-cylinder apparatus

3.3.1 Introduction

The piston cylinder apparatus, invented by Boyd and England (1960), is a device used to apply high temperatures (up to 2000 °C) and high pressures (up to 4 GPa) to a sample, which is contained in a cell.

The apparatus is composed of several concentric cylinders with a hole in the center, and one of them, the pressure vessel, contains the cell in its bosom. The cylinders, which are placed one above another, are put under pressure by a top hydraulic press, which maintains the assembly stable. A smaller piston delivers pressure to the cell from below. The core of the pressure vessel, surrounding the cell, is made of tungsten carbide in order to withstand the applied pressures. The pressure inside the cell is calibrated with the pressure of the lower piston (see Condamine et al., 2022), and temperature can be monitored with thermocouples placed inside the cell, close to the capsule.

3.3.2 The press

The press used in Liege is a MavoPress LPC 250 – 300/50 designed by Voggenreiter (Figure 3-1). The upper (end-load) and lower piston (master ram) are capable of exerting a maximum pressure of 2500 bar each. The pressure for both pistons is controlled manually, and showed on two independent gauges. A third gauge show the pretension of the pressure storage for the return stroke, which is the pressure necessary to lift the upper piston after its pressure is back to zero (after an experiment, for example). The pressure of both pistons can be released by opening the bleeder valve of the manual pumps, or using the fine dosing valves to slowly decrease the pressure in the systems (mostly for the upper piston, which reach higher pressures than the lower piston). A slow decrease in pressure is necessary to extend the lifespan of the apparatus, especially of the pressure vessel. Another valve, inside the apparatus, is used to equilibrate oil level between the three system (upper piston, lower piston and return stroke). Air bleeder screws are present on the oil storages of both piston pumps. The should be kept slightly opened (a quarter turn).

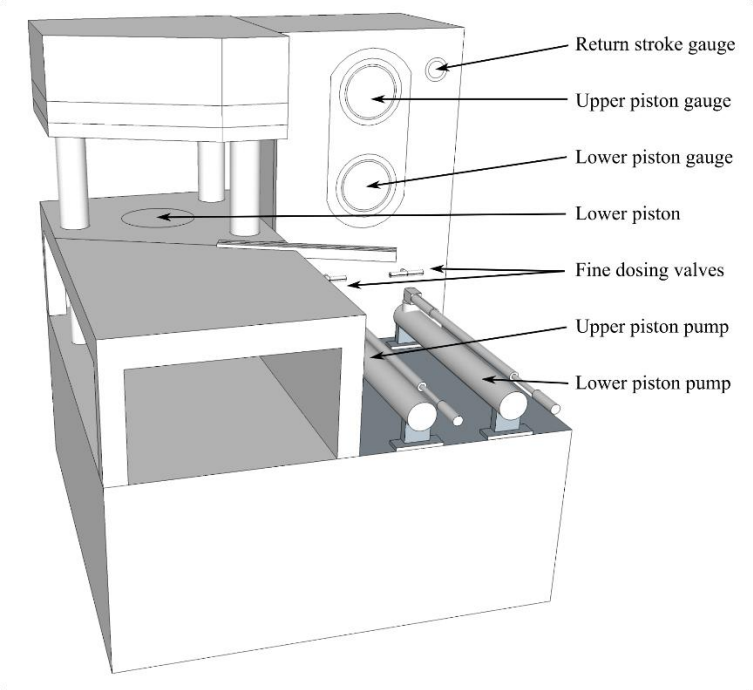

Figure 3-1: 3D schematic of the MavoPress LPC 250 – 300/50 in Liège. The piston cylinder apparatus is placed on the "Lower piston", in its center.

The apparatus is paired with a tool heater cabinet, whose purpose is to control electrical current in the apparatus. Externally, it is composed of a main switch (on/off), a switch to activate and deactivate heating, a control panel, and an ethernet connector. A control lamp lights up if heating is on. The control panel is composed of a screen, showing various parameters of the running experiment (such as temperature, voltage, amperage, pressure, resistance of the sample…) and several buttons, that can be used to control the display, the electrical input, or program an experimental run. The ethernet port allows the user to link the cabinet to a computer, and control an experiment's heating directly from the computer, instead of the control panel, via a computer software created by Voggenreiter. This software allows to program experiments' runs, where temperature, heating rate, dwell time, duration, cooling and quench can be precisely controlled.

Water circulation is crucial to cool piston-cylinder experiments. While some labs use an open cooling system, where tap water circulate from the faucet back to the sink, we use a closed system with a pump which cools the circulating water. We use deionized water, which is changed regularly to avoid accumulation of dirt in the system.

3.3.3 The piston-cylinder

The piston-cylinder apparatus was also designed by Voggenreiter to fit its press. It is composed of four cylindric parts; the base, the pressure vessel, the spacer plate and the top plate (Figure 3-2). Other pieces consist of the small piston, water pipes, and plastic spacers. The base is the heaviest of all the parts, which is placed directly on the lower piston. The base is divided in an outer part, with a conic hole in its

center, and a cone-like inner part which fits directly inside the outer part, so that the latter can move vertically inside the former. The lower piston transmits its vertical movement to the inner part, which move upwards and applies pressure to the sample through the small piston, which sits on top of the base. The base also has two water ports, where two pipes can be plugged for water circulation at the interface between the base and the pressure vessel. The pressure vessel is the most important part of the assembly; the cell with the sample sits in its bosom. It is composed of two different metals. The outer ring is made of stainless steel, while its core, which is in direct contact with the sample, is made of tungsten-carbide. The core has a hole in its center, where the cell fits perfectly. This part is the most subject to wear, as it is subjected to very high pressures because it contains the pressure exerted by the horizontally compressed sample. As such, each experiment and its compression, quench and decompression stages are damaging the core, which cause it to break after extensive use. Typically, a pressure vessel lifespan is around 1000 experiments, but it can vary depending on the pressures applied, the rate of compression and especially of decompression. This makes it a relatively dangerous part, as a sudden break of the tungsten carbide core can result in a violent release of energy (i.e., an “explosion”). This is why absolute care should be brought to this part when using it, and any sign of wear or crack should be looked after. It is advised to send damaged pressure vessel back to the manufacturer for repair. In any case, a damaged pressure vessel should never be used. The pressure vessel also hosts two water pipes, enabling water to flow around the heated tungsten carbide core. The spacer plate is a plain stainless-steel part with a small hole in the middle, designed for the thermocouple. As for the two other parts, it has two water port for water to flow at the interface between the pressure vessel and the space plat. Finally, the top part is a thick cylinder of steel, designed to endure the pressure from the upper piston. There is a cavity in its center at the bottom connected to a groove. The cavity accommodates the top of the thermocouple, and the wires go through the groove to reach the outside of the apparatus. Two water pipes can be plugged to cool the part.

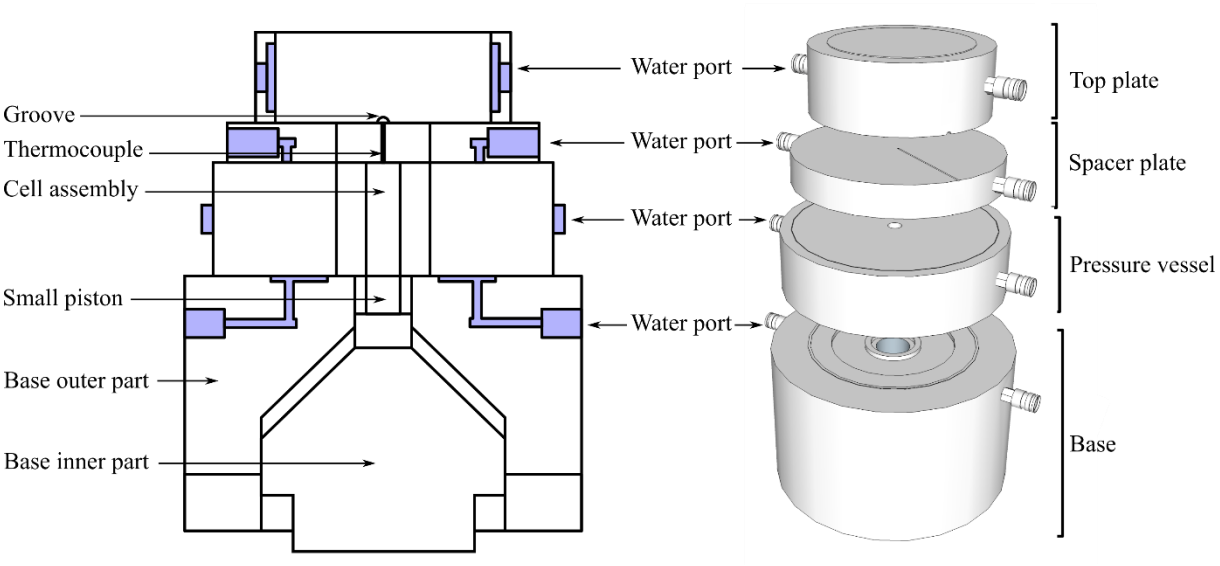

Figure 3-2: 2D (left) and 3D (right) schematics of the piston-cylinder used in Liège.

The small piston is composed of a rod (the piston itself) inserted in a small cylindric part. Because it is responsible of transmitting the pressure from the lower piston to the cell, it is made of tungsten-carbide to resist the pressure. The small piston is placed at the center of the inner part of the base. Because this part is in direct contact with the cell, it accumulates dirt (graphite and barium carbonate dust and MoS_2 lubricant) and needs to be thoroughly cleaned after each experiment. The rod needs to be in good shape to apply the pressure perfectly horizontally on the cell. A damage rod could apply uneven pressure, breaking the cell, or it could even damage the interior of the pressure vessel. The plastic spacers are simple plastic hollow cylinders which are placed between the pressure vessel and the spacer plate, and between the spacer plate and the top plate. They are used to keep the assembly perfectly centered before pressurization. Finally, the water pipes consist in an inflow pipe, 3 short pipes, and an outflow pipe. The water starts to flow from the top plate, circulates in each part and exit out of the base.

3.3.4 The cell assembly

The cell assembly is the finished assembly that is inserted into the pressure vessel. It contains the sample, but also all the other parts that are necessary to the success of piston-cylinder experiments. Assembly designs can vary in shape, size, components, and material. It is generally composed of a cell, a furnace, a capsule, an alumina ring, a wafer, a pedestal placed below the capsule, and an upper part with hole placed above the wafer (Figure 3-3).

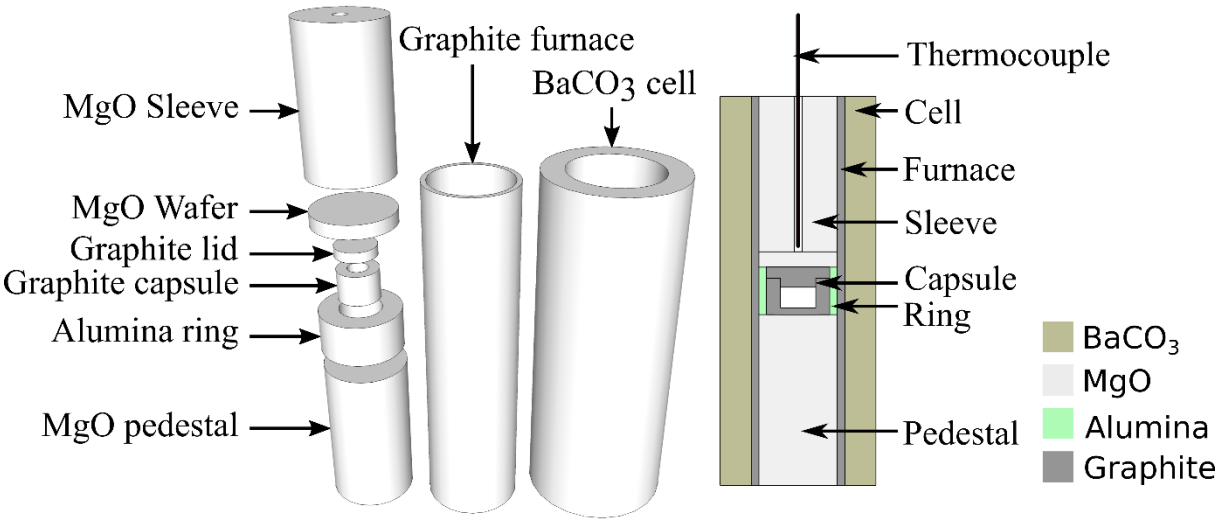

Figure 3-3: Schematic of the cell assembly used at the University of Liège.

The most important part is of course the capsule, which contains the sample. Samples are usually powders. Capsules can be made of gold, palladium-gold or platinum, in which case the capsule is sealed by wielding the top. In other cases, it can be made of graphite or MgO, or even silicates such as olivine. In these cases, they are often paired with a lid made of the same material, to form a closed, albeit not sealed, container. In some experiments, the use of a double capsule (a classic example is an inner capsule of graphite and outer of platinum) is necessary to completely close the system, and avoid volatile loss notably. Because the capsule is situated at the center of the assembly, it receives the most pressure and temperature. The powder inside needs to be compacted as much as possible to avoid gaps which could cause the capsule to break at high pressure.

The alumina ring has the same height as the capsule, and its inner diameter is made for the capsule to fit inside. The part electrically isolates the capsule from the furnace.

The pedestal is a solid cylinder which support the capsule, usually made of MgO. The height of the pedestal is very important, because the capsule vertical position in the pressure vessel depends on it; the capsule needs to sit precisely in the middle. Its purpose is to transmit the deformation caused by the pressure. There is a similar part above the capsule, made in the same material, but with a hole in its center. Its purpose is to transmit deformation too, but also to host the thermocouple. Its height should also be precisely checked to keep the capsule in the center of the pressure vessel.

The wafer is a thin cylinder placed between the capsule and the upper part. It is made of the same material as the pedestal and the upper part, and its role is to separate the thermocouple from the capsule, to avoid any chemical reaction between the two. The wafer should be thin to limit the error on the temperature measure, but thick enough to not break under pressure.

The furnace is a thin tube made of conductive material (graphite) which is as long as the cell. It connects the bottom of the cell to its top and transmit the electrical current. The circulation of the current heats

the graphite furnace, which itself heats the alumina ring and the capsule. The quality of the part is very important, as there is a risk of experimental failure if the electricity cannot flow through.

Finally, the cell is a thick tube that encapsulates all the other components. It can be made of various materials, the most common ones being talc, NaCl or barium carbonate (e.g., McDade et al., 2002).

To minimize friction during compression, which could damage the cell and break the assembly, the cell is rolled into something to help it slide, but a lubricant (like powdered MoS_2) can also be applied directly on the cell. In Liège, we used to roll a lead sheet around the barium carbonate cell, and make sure that it does not touch the top or the bottom of the furnace to avoid the current passing through the lead instead of the furnace. More recently, we moved to using paraffin sheets to improve health safety in the laboratory.

3.3.5 Operating the piston-cylinder

3.3.5.1 Loading the cell assembly

Once the cell assembly is complete, it can be sled into the pressure vessel. The sliding is done horizontally (the pressure vessel sits on its side) after the hole in the pressure vessel has been lubricated (usually with MoS_2). Once the cell assembly is inside, we slide a thin graphite cylinder under the assembly to keep all the parts together and to assure a perfect electrical connectivity between the small piston and the furnace. The pressure vessel is then flipped on its back, and can be placed above the base, onto the small piston (Figure 3-4). Two more pieces need to be inserted into the top of the pressure vessel; the steel plug, surrounded by the pyrophyllite ring. The steel plug is a steel cylinder with a hole in its center to insert the thermocouple. It is surrounded by pyrophyllite to avoid contact between the steel and the tungsten carbide core. The base with the pressure vessel on top can be pushed inside the press, on top of the lower piston and against the metal railing. The base and the lower electrode can be screwed, so that the former is fixated and cannot move anymore.

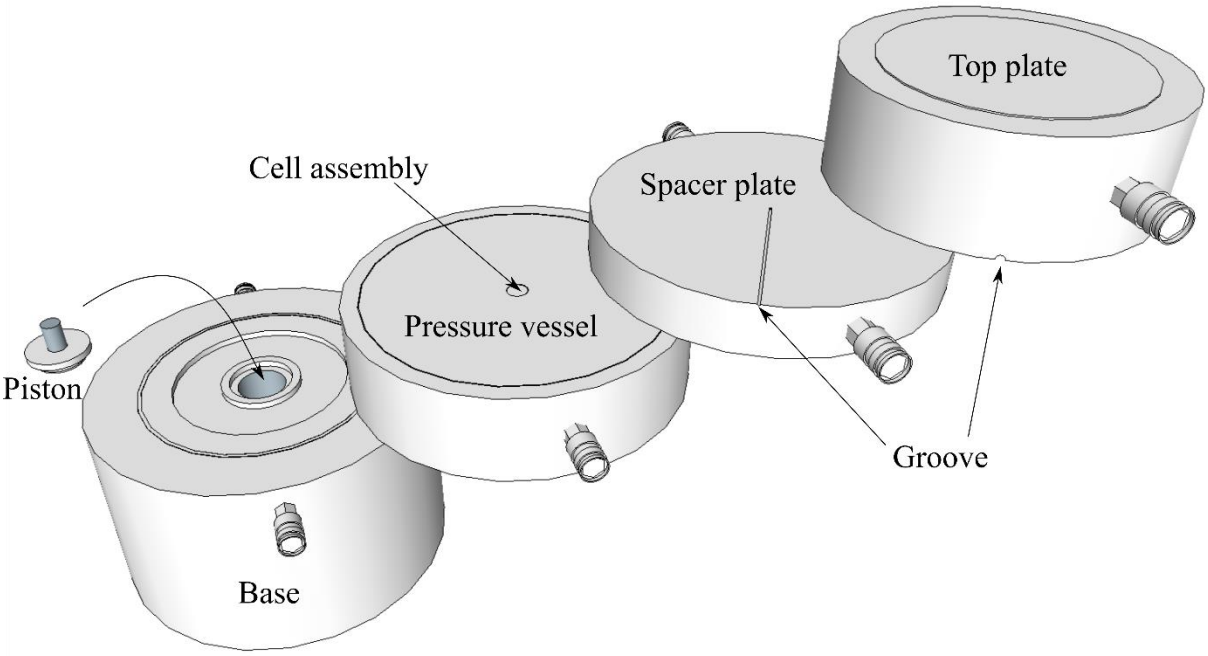

Figure 3-4: The mounting of the different pieces of the piston-cylinder assembly. First, the small piston is placed on the base, and then the pressure vessel is put on top of it. The spacer plate is placed above the pressure vessel, and holds the thermocouple. Finally, the top plate is put on top of the apparatus, with both grooves superposed to let the wires of the thermocouple come out.

3.3.5.2 Inserting the thermocouple

Thermocouples are used to precisely monitor the temperature of the experiment. A thermocouple is composed of two wires made of different metals joined at one end, called the hot junction, where the temperature is measured. The other ends of the wires are linked to a voltmeter and is called the cold junction. The voltmeter measures a current induced by the difference of temperature at both junctions, named the Seebeck effect. This weak current, measured in mV, can be interpreted and used to calculate the temperature if the metals of the wires are known. In experimental petrology, the thermocouples used are usually made of Pt and Rh (type R, S and B) or W and Re (type C, G and D). The choice of the type of thermocouple depends on its characteristics, mainly the range of temperatures measured, the resistance to heat or oxidation, and its price.

For experimental purposes, the wires are inserted in a stiff sheath made of alumina (Al_2O_3) or mullite ($Al_6Si_2O_{13}$). The sheath has 4 holes, so that the wires are inserted in two neighboring holes, and the hot junction is made at the other end by crossing the wires on top of another and inserting each wire end in its respective opposite hole (to make a “cross”). Because the inner walls of the sheath are fragile, the wires should be inserted slowly and with care; a break in one of the walls could make the wires touch in the middle of the sheath, so that temperature readings would be incorrect. The stability of the connection at the hot junction should be tested with a voltmeter before inserting the thermocouple inside the assembly.

Inserting the thermocouple inside the assembly can be one of the trickiest parts of piston-cylinder experiments. Because of the brittleness of the sheath, it should be inserted after the spacer plate is put, and not before; indeed, while it is easier to insert it before, the risk of breaking the sheath by placing the spacer plate on top is too high, and not worth it. The sheath should be inserted (with the cross first) inside the spacer plate, then through the steel plug, and pushed carefully all the way down the assembly, till the wafer is reached and it is not possible to push anymore. The main problem with this method is the alignment between the hole of the spacer plate and the rest of the cell assembly. Moreover, the spacer plate has to be at least partially screwed to the upper electrode to avoid any movement of the plate after the thermocouple is inserted. There are different methods to solve this problem, but one of the most effective is to align the plate with the assembly by using a metal rod of the exact diameter of the sheath. Once they are aligned, the spacer plate can be screwed (with the metal rod still inside) to the upper electrode. After that, the rod can be taken out and replaced by the thermocouple. The wires coming out of the spacer plate can be placed inside the groove using a few pieces of tape and, if not done already, attached to the voltmeter (the cold junction).

3.3.5.3 Finalizing the preparation for the experiment

Once the thermocouple is inserted, the top plate can be laid on the spacer plate, with the groove of the former placed above the groove of the latter. Finally, a sheet of mylar can be put on top of the top plate, to electrically isolate the apparatus and the press, and make sure the current exits through the electrodes.

The apparatus now needs to be put under pressure. To do so, the bleeder valve and the fine valve of the upper piston need to be closed and opened, respectively, and the user can start to pump manually. The press is equipped with two gear for pumping, so that it is easier to pump once the pressure increases. The user can feel the difference once the piston hit the top plate. The required upper piston pressure depends on the desired pressure for the experiment (Table 3-2). A pressure too low is dangerous, as it means that the upper piston pressure could be overcome by the lower piston pressure, which could cause the apparatus to explode. On the other hand, increasing the upper pressure higher than required unnecessarily wears the apparatus. It is in anyway better to have a pressure too high than too low. After reaching the upper piston pressure, the fine valve can be closed. In the piston-cylinder of Liège, friction is estimated to reduce the nominal pressure of 9.3% (see Condamine et al., 2022, Table 3-2).

Table 3-2: This table shows the upper ram pressure needed to compensate the lower ram, as well as the nominal pressure applied to the sample, both uncorrected (Nominal pressure) and corrected for friction.

Lower ram (bar)	Upper ram (bar)	Nominal pressure (GPa)	Corrected pressure (GPa)
5	500	0.05	0.05
10	500	0.1	0.09
20	500	0.19	0.17
30	500	0.29	0.26
40	500	0.39	0.35
50	500	0.48	0.44
70	500	0.68	0.62
90	500	0.87	0.79
120	500	1.16	1.05
140	500	1.36	1.23
180	500	1.74	1.58
230	575	2.23	2.02
280	700	2.71	2.46
360	900	3.49	3.17

Once the apparatus is under pressure, the water pipes can be plugged, with the water input connected with the top plate, water pipes connected to the subsequent lower parts, and finally plugging the water output to the last available water port on the base. Each connection should be carefully checked, as it possible that a pipe is not perfectly plugged, which could result in a water leak once the water pump starts. In case of water leak, heating should not be switch on as long as the apparatus and the press are not dry. The pump can be started, and the user can check by touching the water pipes that the water is indeed running. This step is crucial, as an uncooled experiment is very dangerous for the apparatus, the press and the users; the temperature of the whole apparatus, and even part of the press can increase up to a few hundred degrees, with a risk of serious burns to people or even of starting a fire if flammable material is on the press. Moreover, heating of the press, and the oil, can increase the upper and lower pressure to dangerous values, which could break the apparatus. After making sure that the water is running through the apparatus, lower piston compression can start. As for the upper piston, the bleeder valve has to be closed, and the fine valve opened. The user can pump the lower piston up to 80% of the target value.

3.3.5.4 Programming a run

The Voggenreiter software can be opened, and a new program can be designed. In the program window, we can set the different steps necessary for our experiments. All our experiments consisted of a first

heating ramp up to 865°C at 100°C/min, a dwell at temperature for 5 min, and subsequent heating up to the desired temperature at a rate of 50°C/min. The program was then ordered to stay at the same temperature, until we manually quenched the experiments. It is possible to do more complex programs, with controlled decrease of temperature, to perform crystallization experiments, for example. The rate of heating is also controlled by the PDI parameters, so that the measured temperature stays close to the setpoint. Incorrect PDI value can lead to slow heating where temperature strongly lags behind the setpoint, or to overshoot the setpoint and overcompensate the increase or decrease of the electrical current passing through the sample. In Liège, we use the following values: 1000 (proportional band, in %), 4 (integral time, in second) and 0 (differential time, in second).

3.3.5.5 Heating the experiment

Once the program is established, it can then be uploaded to the controller. The mode "automatic" should be selected, and the inhibiter should be disabled. The switch on the heater tool cabinet should be on "on". Checking if the water is still running and if the thermocouples are still functioning after putting the experiment under pressure is always good habits. After clicking on "start run", the current starts flowing after ~30 seconds, and a clear electrical buzz can be heard. After the resistance increases and is stabilized, temperature should increase and try to catch up with the target. Lower piston pressure should be carefully monitored and constantly adjusted, as heating decreases the pressure. It is also important to never touch the electrodes at the back of the apparatus during heating.

Once the dwell temperature is reached, the user can slowly (over the duration of the dwell) increase pressure up to the target. After the dwell, the temperature will continue to increase up to the target. Once reached, it is important to stay close to the apparatus to check that the parameters of the experiment are constant, especially the pressure, which usually slightly decreases during the first tens of minutes after reaching the target temperature. Some problems can be observed during that time: slow increase of the lower piston pressure with time, erratic temperature measurements, drop of the resistance value… If all the parameters are somewhat constant after 30 minutes, the experiment can be considered stable and left alone without supervision. It is always a good idea to check on an experiment before leaving the lab if it is planned to run overnight.

3.3.5.6 The quench and the retrieve of the sample

In experimental petrology, a good quench is, after a good equilibrium, the most important quality of a sample. It has to be fast and homogeneous. That means, there should not be crystallization of phases that were not present at target temperature during the rapid cooling, nor should there be textural differences between the outer and the inner part of the sample, caused by heterogeneous cooling. The quench is often accompanied with cracks in the sample, as rapid cooling of the experiment brutally decreases the pressure in the sample.

To quench, the user can simply click on “immediate quench” on the Voggenreiter software. The current stops, and cracks can be heard as the temperature rapidly decreases. Once the temperature is low enough, the water pump can be shut down, and the water contained in the pipe must be evacuated. Failure to do so will result in important water leak during decompression. To purge the water inside the apparatus, the user needs to replace the inner flow pipe with the compressed air pipe, and the outer flow pipe with the pipe without a plug. This pipe can be put outside through the window or in the sink. By slowly opening the valve to let compressed air enter the pipe system, the water is pushed outside and the apparatus is clear of water. Once there is no water left in the apparatus, all the pipes can be unplugged, and the decompression can start. Both fine valves need to be closed at this point. After opening the bleeder valve of both the upper and the lower piston, the user can slowly open the fine valves of first the lower piston, and then the upper piston once the pressure of the lower piston fell back to 0.

After both pistons are back in their initial position (i.e. the pressure is 0 for both), top plate can be taken out and the wires of the thermocouple cut as close to the sheath as possible. The height of the sheath that sticks out of the spacer plate should be noted before taking it out. Taking the spacer plate out should more or less destroy the thermocouple, but there could still be a bit coming out of the cell in the pressure vessel. The remains of the thermocouple sticking out should be cut using pliers. The pressure vessel can be moved to the small Enerpac press, and placed on top of the orange steel cylinder. A protective glass needs to be put between the user and the pressure vessel. The thin steel piston should be installed, and used to push the cell out of the pressure vessel. It is crucial that the piston is perfectly centered with the cell to avoid any damage to the tungsten carbide core. The pressure must be increased slowly, and the cell should start moving down. Higher pressure experiments require higher pressure to get the cell out of the pressure vessel. A loud popping noise might be heard. Once the cell is out, it is important to measure and write its length (without the graphite cylinder at the bottom and the steel plug at the top). A careful peeling of the cell is necessary to retrieve to capsule, especially if the latter is in graphite (Figure 3-5).

Figure 3-5: A $BaCO_3$ cell with the steel plug wrapped in pyrophyllite at the bottom after an experiment. $BaCO_3$ is very brittle, and so careful peeling is necessary to reach the capsule in the center without breaking it.

To help break open the cell, a small hammer can be used on the extremities of the cell (furthest from the position of graphite). Once the capsule is retrieved, the different parts need to be sorted for recycling: there are jars for steel plugs, thermocouple wires, and barium carbonate with lead sheets. In any case, barium carbonate and lead sheets should never be thrown into the bin for health and environmental safety. Thermocouple are valuable, and all bits should be recycled. The workplan, the different plates, the small piston and the Enerpac have to be cleaned after each experiment.

3.4 Evacuated silica tube experiments

3.4.1 The vacuum line

The vacuum line is an apparatus used to pump the air out (i.e. evacuate) of (silica) tubes. It is composed of a horizontal main glass tube connected to an electrical air pump. Multiple glass tubes, smaller in diameter, are perpendicularly joined to the main line, with an opening at their bottom. At the junction between each glass tubes and the main one there is a screw, that can be used to open and close air passage between them (Figure 3-6).

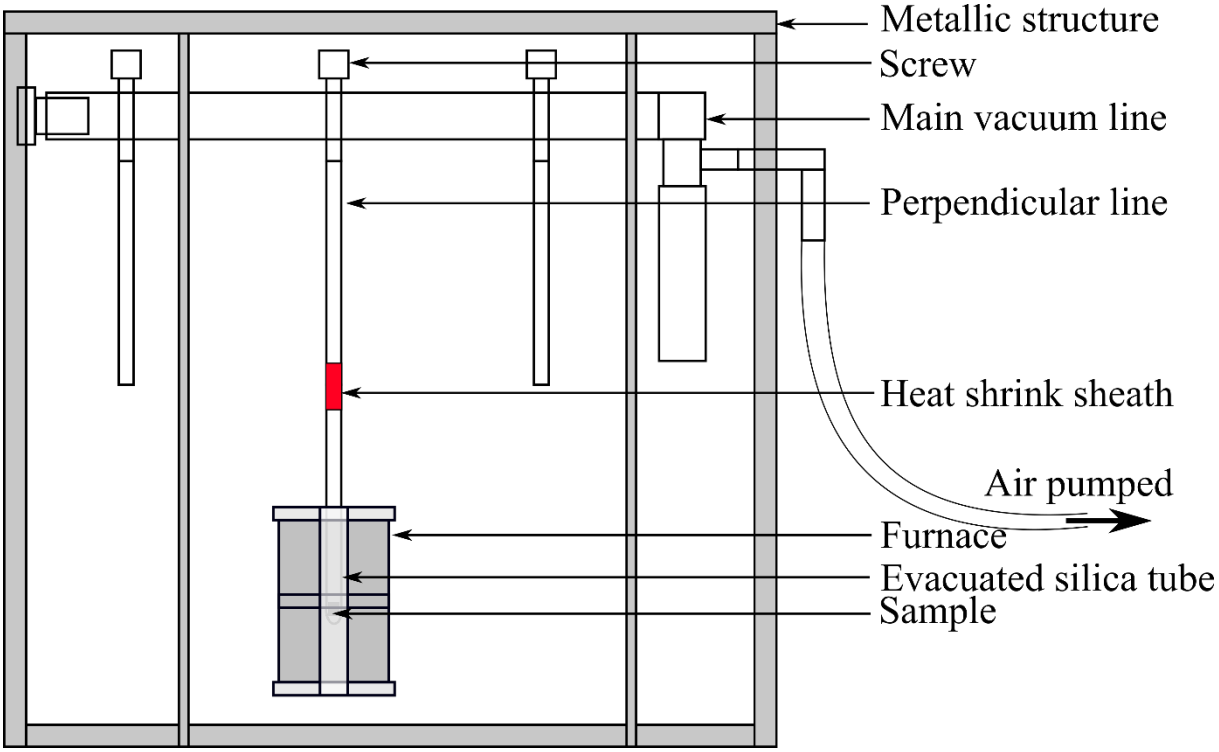

Figure 3-6: Schematic of the vacuum line in Liège. The metallic structure holds the main vacuum line, from which are joined perpendicular lines. The main line is linked to an air pump (on the right, not represented).

3.4.2 Evacuated silica tube experiments

Evacuated silica tube experiments have been carried out to study geological settings for over 50 years now, starting with the production of samples to understand the moon's geology (e.g. Walker et al., 1976). In this method, the sample is usually contained in a capsule, which in this work was a 12 × 5 mm graphite cylinder, with a 10 mm deep hole drilled in its center to pour the powder. The capsule is placed at the bottom of a silica tube of 10 to 20 cm of height and 1 cm of width which is open at the top and closed at the bottom. The tube is linked to a vacuum line using heat shrink sheath, where an air pump creates a vacuum (1 to 0.01 mbar) inside the tube. To get rid of undesirable volatiles such as H_2O, the tube is placed inside a small furnace (~120°C) while the pump is running. After some time (depending on the pressure reached inside the line, or on how long the tube has been evacuated while heated) the silicate tube is sealed using a blowtorch (oxy-acetylene for fastest results) slightly below the sheath to maximize

the volume of sealed tube. Once the tube is sealed, it can be kept safely for days without any risk of oxidation/hydration of the sample (Figure 3-7).

Figure 3-7: Closed evacuated silica tube with at its bottom the graphite crucible containing the sample.

To perform the experiment itself, the tube must be placed inside an oven upright (usually in an alumina crucible). During the high temperature experiment, the sealed tube will keep the volatile released by the sample (such as Na, K, S, Cl…) and an equilibrium between the sample and the atmosphere of the tube will form. Depending on the temperature, the experiments shouldn't stay too long inside the oven, as the system is not completely closed and some exchange still happen through the silica tube (such as some oxygen going through). It is difficult to estimate the pressure inside the tubes, but as some tubes swell during experiments, it is safe to assume that it can reach several bars. The glass, if too thin, or if submitted to some constrains (high temperature for a long time, contamination of the glass by spilled sample powder, reaction between the glass and some volatile, such as Na…) could shatter and end the quasi-closed system, and make this whole setting useless. The use of thick glass (~2mm) is thus recommended. In the laboratory of the University of Liège, the rate of success is very high (>90%) thanks to the quality of the tubes. To quench, the tubes can be taken out of the oven while at target temperature and cool by contact with the air, or by contact with water for a much quicker quench. The experimentalist should be advised to wear the recommended protection in this endeavor, as sudden breaking of the glass can occur during the quench, with bits of hot glass flying everywhere. The sample can be retrieved from the capsule after breaking the glass, but it can also be kept safely inside its atmosphere for future study. Shattering the glass should be done in a ventilated spot, as toxic gas (such

as CO, if using a graphite capsule) could be contained within the sealed tube. The sample should appear as a glassy marble if it was molten enough (Figure 3-8). Gas bubbles can be observed in the retrieved sample, if a lot of volatile were present in the starting material (Figure 3-8, left).

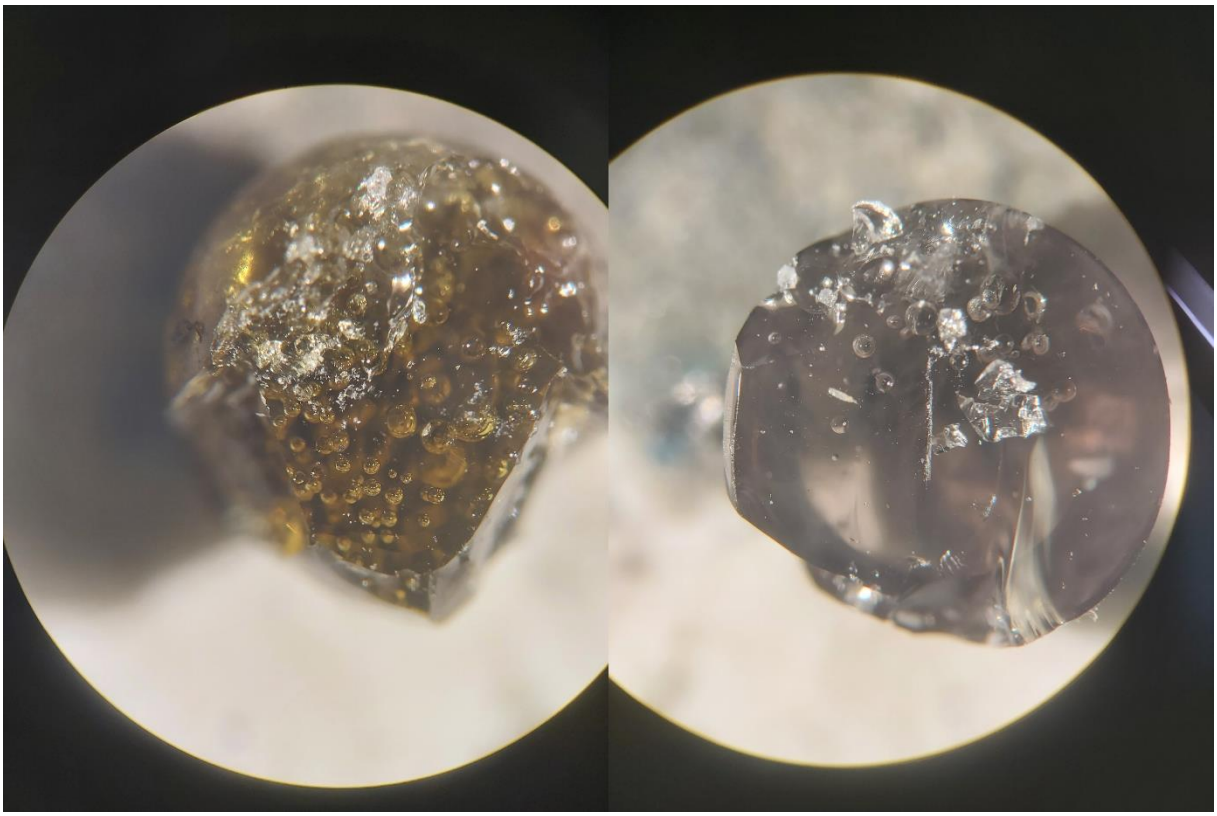

Figure 3-8: Spheres seen under binoculars. In the sample on the left, the sphere is full of bubbles and has a reddish hue, which I interpret as the presence of CaS as the dominant sulfide in solution in the silicate melt, in agreement with the work of Anzures et al. (2020). The sphere on the right is devoid of sulfur, and is transparent. Bubbles are visible in both samples, but are much more present in the left one, which was equilibrated under a S-rich atmosphere.

The color of the glass, observed simply with binocular, can give insights on some of its components. For example, in our experiments, glasses containing 1-2 wt% S present reddish coloration, which is probably due to the Na_2S bonds dominating S speciation at these conditions (Figure 3-8, left; Anzures et al., 2020).

3.4.3 Some additional information

One of the key aspects of this method is that the atmosphere is in equilibrium with the sample. In a gas-mixing furnace, while it is possible to control oxygen fugacity using a mix of reducing agent (CO-CO_2, H_2-H_2S), it is impossible to keep the volatile contained in the sample. In evacuated silica tube, the oxygen fugacity can be buffered (in graphite capsule, fO_2 is buffered at C-CO) and volatiles can be kept, leading to an equilibrium between their presence in the melt and in the atmosphere. This retention of volatiles in the tube can be used in so called "double capsules" settings, where two samples in the same tube can be equilibrated under the same atmosphere. This can be used to exchange volatile between two melts;

for example, we equilibrated two basaltic powders, one containing sulfur (as CaS) but no iron and the other one containing no sulfur but some iron (Fe^0), which led to the incorporation of sulfur in the second one (with formation of FeS) while the first one remained Fe-free (as Fe does not enter the gas phase and cannot "travel" to other samples). In Renggli et al. (2022), they used evacuated silica tubes to study the reactions of volatiles on the surface of solids, to simulate the S-rich atmosphere-silicate surface interactions that could have happened in the early history of Mercury.

Another interesting feature of this apparatus is the possibility of shaping the samples. Indeed, while most experiment setups in vacuum line yield spherical glasses, it is possible to constrain the shape of the final product. In Pommier et al. (2023), we produced glass cylinders of a predetermined width by using custom cylinder capsules. Thanks to this system, we were able to load these glass cylinders inside the multi-anvil assembly in order to run high-pressure experiments on pre-equilibrated glasses (see Appendix B: Experimental investigation of the bonding of sulfur in highly reduced silicate glasses and melts).

3.4.4 Limitations

While the vacuum line method has a wide range of applications and is easy to use, there are still some limitations that are important to keep in mind. Firstly, the method is limited to temperature up to ~1450 °C; above this temperature, the silica tube starts to melt. Secondly, without a complex system involving the breaking of the tube inside a vacuum chamber to measure its internal pressure with a barometer, it is impossible to precisely know the pressure inside the tube after an experiment. This in turn makes fO_2 calculation difficult, as pressure is going to drastically change the fO_2 of buffers (such as C-CO for example) at low values. Thirdly, while a lot of information could be acquired if we were able to measure the composition of the gas phase (speciation of volatile species, oxidation of the components…), we haven't found a way to perform this yet. The best we could do is to detect CO using a gas detector when breaking the tube, or use our smell to detect the presence of H_2S, recognizable by its strong odor of rotten egg.

3.5 The multi-anvil

In his review on the history of this apparatus, Liebermann (2011) defined it as "a high-pressure apparatus with more than one axis of loading and four or more anvils compressing the sample". The invention of the multi-anvil is attributed to Hall (1958), which created a tetrahedral-anvil apparatus capable of reaching 10 GPa and 3000 °C. Over the years, it saw further improvements, that increased the maximum pressure exerted on the sample. Notably, Naoto Kawai developed an octahedral-anvil apparatus, capable of exceeding 10 GPa of pressure (Kawai and Endo, 1970), later improved and simplified by David Walker in the nineties, which led to its spread in many laboratories around the world. During this thesis,

I used the multi-anvil of the department of Geology of the Vrije Universiteit Amsterdam to produce phase equilibria experiments on composition EC001, at 6 GPa and 1700 °C. At the University of California San Diego, I used a multi-anvil coupled with an electrical impedance spectrometer to measure the in-situ electrical conductivity of EC powders, while at Carnegie Institution for Science the experiments were done on both powders and glasses of NVP compositions (see Appendix B: Experimental investigation of the bonding of sulfur in highly reduced silicate glasses and melts).

3.6 The internally heated pressure vessel (IHPV)

According to Holloway (1971), the invention of the IHPV can be traced back to Percy Bridgman, who developed the concept in his book from 1949 (Bridgman, 1949). Basically, the apparatus is composed of a gas-filled vessel that contains one or more samples. Each sample is contained in Pt capsules, and the Ar-pressured vessel controls the internal pressure on the samples, while a resistance heats it. The apparatus can reach pressures up to 1 GPa. Since the work of Roux and Lefèvre (1992) and Holloway et al. (1992), fast-quench became possible in these apparatuses, and thus the possibility of rapidly quenching high temperature samples became possible. The experiments presented here were performed with the IHPV of the University of Hanover, Germany. Details on IHPVs can be found in Halloway (1971) and Berndt et al. (2002).

3.7 Analytical methods

3.7.1 Sample preparation

To analyze the samples, they need to be put in epoxy. For piston-cylinder and IHPVs experiments, we cut the capsule in half using a diamond saw, and pour epoxy resin on each half. In multi-anvil experiments, the octahedral assembly is put entirely in epoxy, and we cut it almost in half horizontally using either a diamond saw or a cutting wire to get as close as possible to the capsule. Finally, for evacuated silica tube experiments, we pour epoxy on the entire glass sphere until it is completely covered. If the sample is stuck in the graphite capsule, we carefully cut it to free the sphere. Once the epoxy is solid, we polish the sample using SiC pads and diamond powder. For sulfide-rich samples, we tried to avoid using lubricants, for fear of dissolving these easily oxidable phases.

3.7.2 The SEM and the EDS

Scanning electron microscopes (SEM) are capable of imaging samples down to a few nanometers. By bombarding a sample with a beam of electrons, the atoms react and reemit various signals, such as secondary electrons (SE), back-scattered electrons (BSE), and X-rays. Detectors, by analyzing the SE and/or the BSE can produce images of the sample. Because BSE depend on the density of the emitting

elements, the imaging produced by this technique are very useful for our analyses, as we can see the difference in density of the phases. Moreover, SEM are sometimes coupled with detectors capable of performing Energy Dispersive X-ray Spectroscopy (EDS), by using the aforementioned X-rays emitted by the sample. This semi-quantitative method is very useful to quickly identify the different phases for more complex assemblage. As we have in our sample some exotic phases (Fe-free sulfides and Fe-free metals such as Si-Cr -P), EDS was systematically used in this work.

All samples were analyzed by SEM to determine the phases and describe the textures. We used the FEI Quanta 600 of the University of Aachen in Germany, which can perform SE and BSE imaging, and produce EDS spectra as well.

3.7.3 The microprobe

Electron microprobe, or electron probe microanalyzer (EPMA) are devices commonly used in geosciences to analyze the chemical composition of precise points in a sample. EPMAs work relatively the same as SEMs, but they can use Wavelength Dispersive X-ray Spectroscopy (WDS) to acquire precise chemical composition. While EDS is easier to use and shorter than WDS, only the latter can give accurate quantitative compositions. WDS requires the use of standards, so that choosing the right standards for a sample is critical to accurate measurements.

Typically, samples that were deemed interesting after analyzes with the SEM were analyzed with the EPMA. We used the JEOL JXA-8530F electron probe micro-analyzer (EPMA) of the University of Münster in Germany. The standards used for our experiments were jadeite (Na), olivine (Mg), disthene (Al), hypersthene (Si), pentlandite (Ni), apatite (P), sanidine (K), diopside (Ca), pyrite (S), rutile (Ti), Cr2O3 (Cr), rhodonite (Mn), and fayalite (Fe) for silicates, and olivine (Mg), apatite (P), diopside (Ca), pyrite (S), and Si, Ti, Cr, Fe, Mn, and Ni metal standards for metals and sulfides due to the reduced nature of our samples.

3.7.4 The LA-ICPMS

The last instruments used to measure the chemical composition of the samples was the laser ablation inductively coupled plasma mass spectrometry (LA-ICPMS). This destructive method ablates the point of measure with a powerful laser, vaporizing its content, which are then sucked in the ICP part of the device. There, the content is ionized (i.e., transformed into a plasma) by inductive heating generated by an electromagnetic coil. The plasma is then sent to the mass spectrometer, so that the relative concentration of elements can be measured.

We performed LA-ICPMS measurements on ~20 samples to produce silicate-sulfide and silicate-metal partitioning data for over 30 minor and trace elements. We use the Photon Machines (Analyte G2) 193nm ArF excimer laser (the LA-ICP) coupled to a ThermoFisher ElementXR sector field mass spectrometer (MS) from the University of Münster in Germany. We used the NIST 612 and the BHVO-

2G reference materials for silicate glass and for sulfide/metal analyzes, respectively. For data treatment, we use the GLITTER software. Internal standards used were Ca and Fe for silicate glass and sulfide/metal respectively. While previous studies used NIST 612 for sulfides and metals (e.g., Steenstra et al., 2020a, b), we found that using the Fe-rich basalt BHVO-2G gave better results for sulfides and metals (that are rich in Fe).

3.8 Experimental results

3.8.1 Piston-cylinder

The dimensions of the capsule are 3 × 3.6 mm (3.8 × 3.6 mm with the lid), so that after being cut in half and put in epoxy, the sample forms a rectangle that on average in our 1GPa experiments is 4 × 2.5 mm. All our experiments were made in graphite capsules, except for two exclusive tests made with enstatite capsules. The B-series was performed by Prof. Olivier Namur and synthetized at the University of Hanover in a piston-cylinder following the similar procedure as exposed above. The B-series was analyzed (both EPMA and LA-ICPMS) in this work. The list of experiments carried out in piston cylinder can be found in Table 3-3.

Table 3-3: List of experiments carried out in piston-cylinder and the conditions of their synthesis. Sil. Melt = silicate melt.

Name	Composition	Capsule	Si^{met}/Si^{tot}	Doping	T (°C)	P (GPa)	Duration (min)	Phases:		
A019	EC001	Graphite	20	CaS	1600	1.31	60	Sil. Melt		
A020	EC001	Graphite	20	CaS	1500	1.31	120	Sil. Melt	Metal	
A021	EC001	Graphite	20	CaS	1400	1.31	120	Sil. Melt	Metal	
A022	EC001	Graphite	20	FeS + CaS	1600	1.31	60	Sil. Melt	Metal	
A023	EC001	Graphite	20	FeS + CaS	1500	1.31	120	Sil. Melt	Metal	
A024	EC001	Graphite	20	FeS + CaS	1400	1.31	120	Sil. Melt	Metal	(Ca,Mg,Fe)S
A025	EC001	Graphite	20	CaS	1500	1.31	120	Sil. Melt	Metal	
A026	EC001	Graphite	10	FeS + CaS	1500	1.31	120	Sil. Melt		FeS
A027	EC001	Graphite	20	FeS	1500	1.31	120	Sil. Melt		FeS
A028	EC002	Graphite	20		1500	1.31	120	Sil. Melt	Metal	
A029	EC002	Graphite	20		1400	1.31	240	Sil. Melt	Metal	MgS
A030	EC002	Graphite	20		1500	1.31	1680	Sil. Melt	Metal	MgS
A031	EC002	Graphite	20		1650	1.35	120	Sil. Melt	Metal	
A032	EC002	Graphite	20		1700	1.41	120	Sil. Melt	Metal	
A033	EC003	Graphite	20		1500	1.31	120	Sil. Melt		
A034	EC003	Graphite	20		1500	3.19	120	Sil. Melt		MgS+SiS
A035	EC003	Graphite	20	FeS	1500	1.31	60	Sil. Melt	Metal	FeS
A037	EC003	Graphite	20		1600	1.31	30	Sil. Melt		
A038	EC001	Graphite	20	FeS	1600	1.31	45	Sil. Melt		FeS
A039	EC001	Graphite	20	FeS	1600	2	45	Sil. Melt		FeS
A040	EC001	Graphite	20	FeS	1700	1.31	45	Sil. Melt		FeS
A041	EC001	Graphite	20	FeS	1700	2	45	Sil. Melt		FeS
A042	EC001	Graphite	50	FeS	1600	1.31	45	Sil. Melt	Metal	
A043	EC001	Graphite	10	FeS	1600	1.31	45	Sil. Melt		FeS
A044	EC001	Graphite	10	FeS	1600	3.19	45	Sil. Melt		FeS
A049	EC004	Forsterite	20	FeS	1700	1.31	15	Sil. Melt		

Name	Composition	Capsule	Si^{met}/Si^{tot}	Doping	T (°C)	P (GPa)	Duration (min)	Phases:		
B873	EC001	Graphite + Pt	0	Fe	1700	3	240	Sil. Melt	Metal	
B875	EC001	Graphite + Pt	10	Fe	1700	3	240	Sil. Melt	Metal	
B877	EC001	Graphite + Pt	50	Fe	1700	3	240	Sil. Melt	Metal	
B879	EC001	Graphite + Pt	50	FeS	1700	3	240	Sil. Melt		FeS
B880	EC001	Graphite + Pt	20	Fe	1700	3	240	Sil. Melt	Metal	

3.8.2 Evacuated silica tubes

Two kind of samples were produced in this work. Most samples produced were spherical glasses (Figure 3-9, left), but a series of experiments (VT42 to VT44 and VT46 to VT56) were cylindrically shaped (Figure 3-9, right; Table 3-4). The first 22 samples produced were tests to setup the vacuum line, and are not included in Table 3-4.

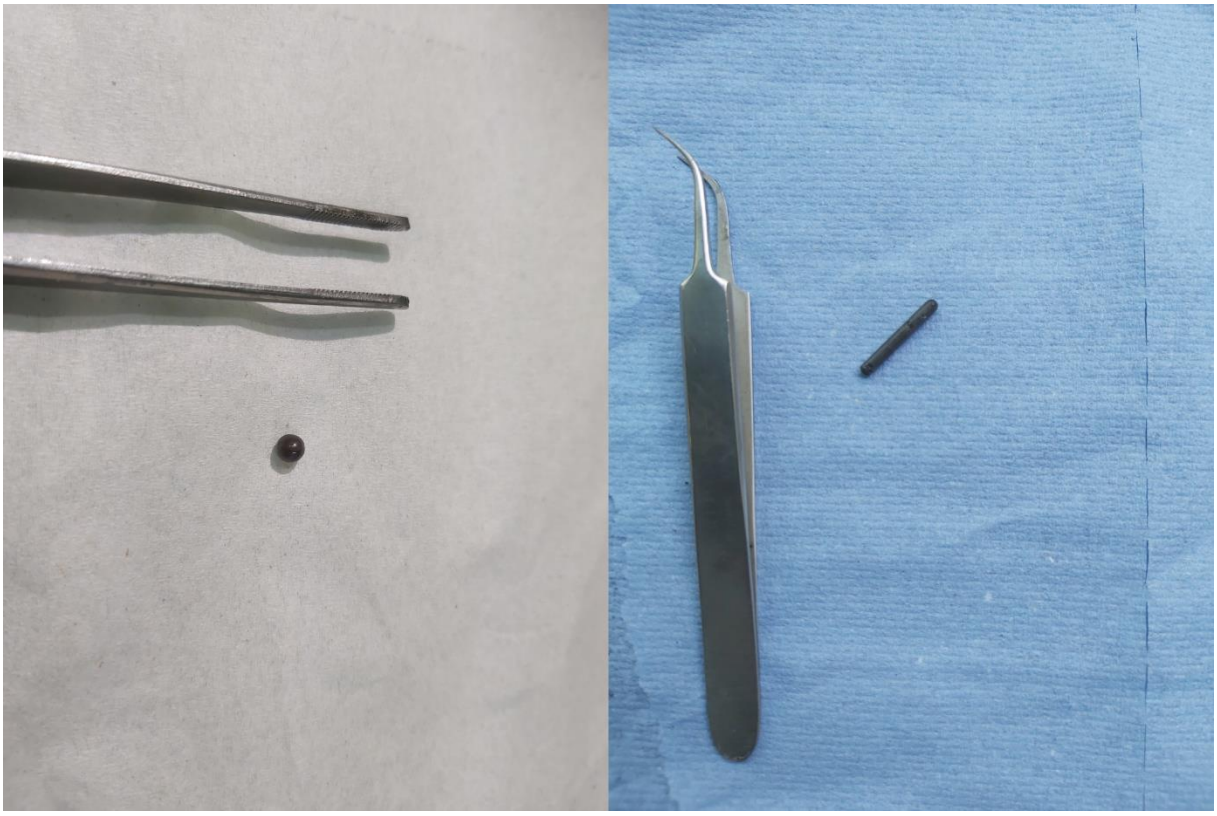

Figure 3-9: Retrieved products of quenched silicate glass from evacuated silica tube experiments. Left: glassy marble. Right: glass cylinder to be used in electrical impedance measurement experiments (see Appendix B: Experimental investigation of the bonding of sulfur in highly reduced silicate glasses and melts).

Table 3-4: List of experiments carried out in the vacuum line and the conditions of their synthesis. There is no "pressure" column as it is not possible to know the pressure in these experiments. Suffix B means "bottom" and T "top" for experiments where two capsules where placed in the same silica tube. Sil. melt = silicate melt.

Name	Composition	Capsule	Si^{met}/Si^{tot}	Doping	T (°C)	Duration (hour)	Phases:		
VT023	NVP	Long Graphite	10	CaS	1400	2	Sil.melt		
VT024	NVP	Long Graphite	0	CaS	1400	2	Sil.melt		
VT025	NVP	Graphite	0	CaS	1300	2	Sil.melt		
VT026	NVP	Graphite	0	CaS	1400	1	Sil.melt		
VT027	NVP	Graphite	0	CaS	1350	1.5	Sil.melt		
VT028	NVP	Graphite	0	FeS	1300	2	Sil.melt		FeS
VT029	NVP	Graphite	0	FeS	1400	1	Sil.melt		FeS
VT030	NVP	Graphite	0	CaS	1300	2.5	Sil.melt		CaS
VT032	NVP	Graphite	0		1300	1.5	Sil.melt		
VT033	NVP	Graphite	0		1350	1	Sil.melt		
VT034	NVP	Graphite	0	Si	1350	1	Sil.melt	Metal	
VT035	NVP	Graphite	0		1350	1	Sil.melt	Metal	
VT036 B	NVP	Graphite	0		1350	1	Sil.melt		
VT036 T	Si metal	Graphite			1350	1			
VT037	NVP	Graphite	5		1350	1	Sil.melt	Metal	
VT038	NVP	Graphite	0	CaS + Fe	1350	1	Sil.melt	Metal	FeS
VT039 B	NVP	Graphite	0	CaS	1350	1	Sil.melt		CaS
VT039 T	NVP	Graphite	0	Fe	1350	1	Sil.melt	Metal	FeS
VT040	NVP	Graphite	0	CaS + Fe	1350	1	Sil.melt	Metal	CaS
VT041B	NVP	Graphite	0	S	1300	1	Sil.melt		
VT041T	NVP (CaSiO3)	Graphite	0	Fe	1300	1	Sil.melt		FeS
VT042	NVP (CaSiO3)	Long Graphite	0	Fe	1350	1	Sil.melt		
VT043	NVP (CaSiO3)	Long Graphite	0	Fe	1350	1	Sil.melt		
VT044	NVP	Long Graphite	0	Fe	1350	1	Sil.melt	Metal	
VT045B	NVP	Graphite	0		1350	1	Sil.melt		

Name	Composition	Capsule	Si^{met}/Si^{tot}	Doping	T (°C)	Duration (hour)	Phases:	
VT045T	Si metal	Graphite	0		1350	1	Sil.melt	
VT046	NVP	Long Graphite	0	CaS + Fe	1350	1	Sil.melt	FeS
VT047	NVP	Long Graphite	0	CaS	1350	1	Sil.melt	
VT048	NVP	Long Graphite	0	CaS	1300	1.5	Sil.melt	
VT051	NVP (CaSiO3)	Long Graphite	0		1300	1.5	Sil.melt	
VT052	NVP	Long Graphite	0	CaS	1350	1	Sil.melt	CaS
VT053	NVP (CaSiO3)	Long Graphite	0		1300	1.5	Sil.melt	
VT054	NVP	Long Graphite	0	CaS	1300	1.5	Sil.melt	
VT055	NVP	Long Graphite	0	CaS	1400	0.75	Sil.melt	
VT056	NVP (CaSiO3)	Long Graphite	0		1350	1	Sil.melt	
VT066	NVP (CaSiO3)	Graphite	0		1400	1	Sil.melt	
VT067B	CaS	Graphite	0		1400	1	Sil.melt	
VT067T	NVP (CaSiO3)	Graphite	0		1400	1	Sil.melt	
VT070	NVP (CaSiO3)	Graphite	0		1350	2	Sil.melt	
VT071	NVP (CaSiO3)	Graphite	0	CaS	1350	2	Sil.melt	
VT087	NVP (CaSiO3)	Graphite	0		1350	1.5	Sil.melt	
VT088	NVP (CaSiO3)	Graphite	0	CaS	1350	1.5	Sil.melt	
VT088J	NVP (CaSiO3)	Graphite	0	CaS	1350	3	Sil.melt	

3.8.3 Multi-anvil

The retrieved octahedral assembly is first put entirely in epoxy. It is cut in half but with a slight horizontal offset to avoid cutting through the sample. The goal is to almost expose the sample at the surface so that polishing is easier and faster. Two kind of experiments were made in multi-anvil. The first series was made at the Vrije Universiteit Amsterdam in the Netherlands, and consisted in simple phase equilibria experiments (A45 to A48). The BB and BBC series were made at the University of California San Diego and the Carnegie Institution for Science, respectively, with a multi-anvil coupled with an electrical impedance spectrometer (Table 3-5). The BBC series was used in Pommier et al., (2023) (see Appendix B: Experimental investigation of the bonding of sulfur in highly reduced silicate glasses and melts).

Table 3-5: List of experiments carried out in multi-anvil and the conditions of their synthesis. The BB and BBC series were not phase equilibria experiments, and so the temperature corresponds to the highest reached during the experiments, and does not corresponds to the temperature of equilibrium. In fact, because we measure the electrical impedance as temperature increase, the equilibrium is ever changing. BB and BBC experiments typically lasted a few hours, up to 12 for the longest. Finally, BBC experiments were performed on pre-equilibrated samples, found in Table 3-4.

Name	Composition	Capsule	Si^{met}/Si^{tot}	Doping	T (°C)	P (GPa)	Duration (min)	Phases		
A045	EC001	Graphite	50	FeS	1700	6	45	Silicate melt	Metal	FeS
A046	EC001	Graphite	50	FeS + S	1700	6	45	Silicate melt	Metal	FeS
A047	EC001	Graphite	20	FeS	1700	6	45	Silicate melt		FeS
A048	EC001	Graphite	20	FeS + S	1700	6	45	Silicate melt	Metal	FeS
BB259	EC004	Alumina + Fe	40	FeS	1400	2				
BB261	EC004	Alumina + Fe	40	FeS	1400	2				
BB268	EC002	Alumina + Fe	38		1300	2				
BB270	EC004	Alumina + Fe	20	CaS	1200	1				
BB271	EC004	Alumina + Fe	20	CaS	1350	2				
BB273	EC004	Alumina + Fe	20		1300	2				
BB274	EC002	Alumina + Fe	38		1400	2				
BB275	EC002	Alumina + Fe	38		20	2				
BB276	EC002	Alumina + Fe	38		1600	2				
BB277	EC004	Alumina + Fe	20		1600	2				
BBC008	VT051	MgO + Fe	/	/	500	2				
BBC009	VT047	MgO + Fe	/	/	650	2				
BBC010	VT056	Alumina + Fe	/	/	1400	2				
BBC012	VT055	MgO + Fe	/	/	670	2				
BBC013	VT053	MgO + Fe	/	/	750	2				

Name	Composition	Capsule	Si^{met}/Si^{tot}	Doping	T (°C)	P (GPa)	Duration (min)	Phases
BBC014	VT054	MgO + Fe	/	/	700	2		
BBC015	VT047	Alumina + Fe	/	/	1350	2		
BBC016	VT048	MgO + Fe	/	/	600	2		
BCC017	VT052	Alumina + Fe	/	/	1375	2		
BBC018	VT055	Alumina + Fe	/	/	1325	2		
BBC019	VT056	Alumina + Fe	/	/	1300	2		

3.8.4 Internal heated pressured vessel (IHPV)

The Y series has been done by Prof. Olivier Namur at the University of Hanover. Capsules were cut in half, put in epoxy and polished. The Y-series was analyzed (both EPMA and LA-ICPMS) in this thesis.

Table 3-6: List of experiments carried out in IHPV and the conditions of their synthesis.

Name	Composition	Capsule	Si^{met}/Si^{tot}	Doping	T (°C)	P (GPA)	Duration (min)	Phases:		
Y037-2	EC001	Pt	0	FeS	1600	0.1	300	Sil. Melt	Metal	FeS
Y056-1	EC001	Pt	20	FeS + Fe	1520	0.1	300	Sil. Melt	Metal	FeS
Y056-2	EC001	Pt	50	FeS + Fe	1520	0.1	300	Sil. Melt	Metal	(Fe,Cr,Mg)S
Y058-2	EC001	Pt	50	S	1520	0.1	300	Sil. Melt	Metal	MgS
Y083-2	EC001	Pt	10	FeS + Fe	1520	0.1	300	Sil. Melt	Metal	FeS
Y085-1	EC001	Pt	50	FeS + Fe	1520	0.1	300	Sil. Melt	Metal	
Y087-2	EC001	Pt	50	S	1520	0.1	300	Sil. Melt	Metal	MgS

Chapter 4: Internal differentiation and volatile budget of Mercury inferred from the partitioning of heat-producing elements at highly reduced conditions

Hadrien Pirotte [a*], Camille Cartier [b], Olivier Namur [c],

Anne Pommier [d], Yishen Zhang[c], Jasper Berndt[e], Stephan Klemme[e], Bernard Charlier [a]

[a] Department of Geology, University of Liège, 4000 Sart Tilman, Belgium

[b] Centre de Recherches Pétrographiques et Géochimiques, Université de Lorraine, 54501 Vandœuvre-lès-Nancy, France

[c] Department of Earth and Environmental Sciences, KU Leuven, Leuven, 3001, Belgium

[d] Carnegie Institution for Science, Earth and Planets Laboratory, Washington, DC 20015, USA

[e]Institut für Mineralogie, Westfälische Wilhelms-Universität Münster, Münster, 48149, Germany

[*]Corresponding author. Email: hadrien.pirotte@uliege.be

Manuscript published in *Icarus*

Abstract

Understanding the behavior of elements under highly reduced conditions is fundamental to explain the differentiation, crust formation, and volatile budget of Mercury. Here we report experiments on a synthetic composition representative of the bulk silicate Mercury (BSM), at pressure up to 3 GPa, temperature up to 1720 °C, and under highly reduced conditions (~IW − 8 to ~IW − 1, with IW the iron-wüstite oxygen fugacity buffer). We determined partition coefficients for > 30 minor and trace elements between silicate melt, metal melt (Fe-Si), sulfide melt (FeS), and MgS solid sulfides. Based on these results and published literature, we modeled the behavior of heat-producing elements (HPE: U, Th, and K) during Mercury's early differentiation and mantle partial melting and estimated their concentrations in the mantle and crust. We found that U, K and especially Th are principally concentrated in the BSM and did not partition into the core because they are not siderophile elements. Uranium is chalcophile under highly reduced conditions, and so our model suggests that an FeS layer at the core-mantle boundary formed during Mercury's primordial differentiation would likely have incorporated large amounts of U, significantly increasing the Th/U ratio of the BSM. However, this is inconsistent with the chondritic or slightly sub-chondritic Th/U ratios of Mercury's lavas. In addition, the likely presence of mantle sulfides, such as MgS, would have also fractionated U and Th, increasing the mantle Th/U. It is possible to have an FeS layer if Mercury formed under less reduced conditions, or if the building blocks of Mercury had Th/U ratios close to the lower end of chondritic data. If, as suggested by our model, no FeS layer formed during differentiation, it means that the majority of HPE are concentrated in Mercury's thin silicate part. Based on the compatibility of U, Th and K, we also show that surface K/Th and K/U ratios are respectively 2–4 times and 3–6 times lower than expected for initial K/Th and K/U ratios similar to enstatite chondrites, implying that the planet suffered an important volatile loss via mechanisms that remain undetermined.

4.1 Introduction

The partitioning of major and trace elements between silicate, sulfide, and metallic melts strongly depends on the prevailing thermodynamic conditions, particularly oxygen fugacity (fO_2; e.g., Kilburn and Wood, 1997; McCoy et al., 1999; Kiseeva and Wood, 2013, 2015; Wood and Kiseeva, 2015; Namur et al., 2016a; Vander Kaaden and McCubbin, 2016; Wohlers and Wood, 2017; Cartier and Wood, 2019; Steenstra et al., 2020a, 2020b). Investigating the geochemical behavior of elements at various fO_2 conditions is therefore particularly important for understanding the origin and evolution of planets that span a wide range of redox conditions. In particular, Mercury experienced the most reduced conditions among the terrestrial planets of our solar system, with fO_2 expected to be between IW − 7 and IW − 3 (i.e., 7 to 3 log units below the fO_2 of the iron-wüstite equilibrium; McCubbin et al., 2012; Zolotov et al., 2013; Namur et al., 2016a). These peculiar reducing conditions affect elemental partitioning, which itself impacts Mercury's core composition via the incorporation of light elements into liquid iron, such as Si (Chabot et al., 2014; Boujibar et al., 2019; Vander Kaaden et al., 2020; Knibbe et al., 2021).

Mercury's density is similar to Earth (~5.43 vs. 5.514 g cm^{-1}), even though the former is much smaller than the latter, with a radius of ~2400 km and ~6400 km respectively. On Earth, materials are more compressed in its center (increasing their density) than on Mercury, which means that for Mercury to have a similar density, the planet must have a large metallic core (Ash et al., 1971; Howard et al., 1974; Anderson et al., 1987; Margot et al., 2018). The present-day core is considered to be partially molten (Margot et al., 2007), with a total core radius of ~2000 km (Hauck et al., 2013; Rivoldini and Van Hoolst, 2013) and a solid inner core radius of 0–1600 km (Knibbe and van Westrenen, 2015, 2018; Genova et al., 2019; Knibbe et al., 2021; Goossens et al., 2022). At the pressure of Mercury's core-mantle boundary (CMB, ~5 GPa; Margot et al., 2018; Steinbrügge et al., 2021) a miscibility gap exists in the Fe-Si-S system (Malavergne et al., 2007; Morard and Katsura, 2010); an FeS-rich melt segregates from the coexisting Fe-Si-rich melt at sulfide saturation. Under Mercury's reduced fO_2 conditions, the FeS liquid incorporates a wide array of elements that would otherwise behave as lithophile or siderophile under more oxidized conditions, as on present Earth (Wohlers and Wood, 2015, 2017; Boujibar et al., 2019; Cartier and Wood, 2019; Steenstra et al., 2020a; Wilbur et al., 2022). Therefore, if sulfide saturation occurred during the primordial differentiation of Mercury, its core should be compositionally layered in terms of major and trace elements, including light elements and heat-producing elements. Under highly reduced conditions, sulfur should also be highly soluble in silicate melts (Namur et al., 2016a), consistent with the high sulfur contents of Mercurian lavas (0.5–3.5 wt%; Peplowski et al., 2015; Weider et al., 2015; Namur et al., 2016a). Therefore, Mercury's silicate mantle most likely contains abundant sulfides, probably of the oldhamite (CaS)–niningerite (MgS) series (Namur et al., 2016b; Boukaré et al., 2019; Anzures et al., 2020), which are commonly observed in enstatite chondrites (Crozaz and Lundberg, 1995; Lehner et al., 2013) and are enriched in various trace elements, notably

rare-earth elements and actinides (Hammouda et al. 2022) that otherwise behave as lithophile (Ingrao et al., 2019).

Malavergne et al. (2010) first proposed that a solid FeS layer could be stable at the CMB and estimated that it should be < 15 km thick if Mercury formed from S-poor Benccubinite chondrites or 100–220 km thick if accreted from S-rich enstatite chondrites. The presence of an FeS layer up to 200 km thick was also proposed based on initial estimates of Mercury's normalized polar moment of inertia using *MESSENGER* gravity measurements (Smith et al., 2012). However, petrological modeling based on sulfur solubility in silicate melt and the Ti contents of Mercury lavas suggests that if an FeS layer exists at the CBM, it must be thinner than 90 km (Namur et al., 2016a; Cartier et al., 2020).

High-spatial resolution measurements by the X-Ray Spectrometer (XRS) onboard *MESSENGER*, which was able to detect fluorescent X-ray emissions from up to ~10 µm of depth (Nittler et al., 2011), were combined in order to map the distributions of Si-normalized major elements (Al, Fe, Mg, Ca, S; Nittler et al., 2018a) and some minor elements, such as Ti (Cartier et al., 2020) and Cr (Nittler et al., 2018b), on the surface of Mercury; lower and upper bounds on Mn concentrations have also been provided (Nittler et al., 2018a). Additional chemical data for O, Na, Cl, K, Th, and U of the surface (up to 100 µm of depth) were acquired at lower spatial resolution by the Gamma-Ray Spectrometer (Peplowski et al., 2011, 2012, 2014; Evans et al., 2012, 2015; McCubbin et al., 2017). New compositional information is expected from the BepiColombo mission. In particular, BepiColombo will measure the concentrations of elements such as P and Ni, as well as heat-producing elements U, Th, and K at higher spatial resolution than *MESSENGER*, using the Mercury Imaging X-ray Spectrometer (MIXS) and the Mercury Gamma ray and Neutron Spectrometer (MGNS) (Bunce et al., 2020; Rothery et al., 2020). These elements are important tracers for investigating the volatile budgets and differentiation histories of terrestrial planets (e.g., McLennan, 2003). In the case of Mercury, it has been suggested that U and K may strongly partition into liquid FeS but not liquid Fe-Si (Wohlers and Wood, 2015, 2017, Boujibar et al., 2019). However, even though Boujibar et al. (2019) recently produced data for U, Th and K partitioning relevant to Mercury's geological context, with a focus on metal/silicate melt partitioning data, data are still scarce at low fO_2 to address key questions regarding the thermochemical evolution of Mercury's interior (Tosi et al., 2013; Boujibar et al., 2019; Boukaré et al., 2019; Peterson et al., 2021).

Here, we report high-pressure and high-temperature experiments on a composition representative of the bulk silicate Mercury (BSM, i.e., the mantle and crust), which we equilibrated with sulfide and metallic melts. We report partitioning data for major, minor, and trace elements between the three melts, and we also present the first data on partitioning between solid MgS and silicate melt. We particularly focus on presenting U, Th and K partition coefficients between FeS and the silicate melt, which complements the data set produced by previous studies, notably Boujibar et al (2019). These

results are used to discuss the distribution of the heat-producing elements (U, Th and K) between Mercury's metallic core, the potential FeS layer at the CMB, and the BSM. We found that the surface Th/U can be used to better constrain the thermodynamic conditions for the formation of an FeS layer. We also discuss the importance of mantle sulfides, such as MgS, for the potential fractionation of U, Th, and K, and their importance for calculating the global volatile budget of Mercury. Our study indicates that it is not possible to reconcile the measured K/Th and K/U surface ratios with a chondritic bulk-composition of Mercury, and the planet must have lost an important fraction of its K.

4.2 Experimental and analytical methods

4.2.1 Starting compositions

Mercury's building blocks are often assumed to be compositionally similar to enstatite chondrites (Malavergne et al., 2010, 2014; Zolotov et al., 2013, Cartier and Wood, 2019), and so we synthesized a powder representative of the average silicate portion of enstatite chondrites (Table 4-1, Wiik, 1956; Lodders and Fegley, 1998; Berthet et al., 2009). Sample synthesis consisted of four steps. (1) High-purity oxides/silicates/phosphate (SiO_2, TiO_2, Al_2O_3, Cr_2O_3, MnO, MgO, $CaSiO_3$, Na_2SiO_3, $K_2Si_4O_9$, $AlPO_4$) were mixed with ethanol in an agate mortar. (2) The powder was then doped with 1000 ppm of U and Th and 500 ppm of other trace elements (Sc, V, Co, Ni, Cu, Zn, Ga, Ge, Rb, Sr, Y, Zr, Nb, Mo, Ce, Nd, Sm, Eu, Gd, Yb, Hf, Ta, and W) using premixed standard solutions. Powders were then dried in an oven at 450 °C overnight. (3) Different amounts of S, FeS, ± CaS were added to the powders to reach sulfide saturation in the silicate melt. In some experiments, only Fe was added to study metal/silicate melt partitioning data in the absence of sulfur. (4) To reduce the oxygen fugacity of the experiments, Si metal was added to the powder. The Si/SiO_2 ratio was balanced accordingly to keep the total Si content of enstatite chondrites. In this way, the total silicon content of the starting material was the same in all experiments but the Si/SiO_2 ratio changed, leading to various fO_2 conditions between experiments (Namur et al., 2016a, 2016b; Anzures et al., 2020). The final powders were dried in an oven at 120 °C and stored in a desiccator until use.

Table 4-1: Composition of the starting material (in wt%) compared to S-free silicate composition of enstatite chondrites (EH) in the literature.

	This study	Indarch[a]	Indarch[b]	EH[c]
SiO_2	61.26	61.26	67.1	60.83
TiO_2	0.1	0.1	0.05	0.11
Al_2O_3	2.76	2.52	2.18	2.65
Cr_2O_3	0.82	0.82	0.09	0.83
MnO	0.43	0.43	0.26	0.46
MgO	31.37	30.37	27.68	30.48
CaO	1.65	1.65	1.47	2.04
Na_2O	1.55	1.75	1.05	1.57
K_2O	0.19	0.19	0.11	0.17
P_2O_5	0.9	0.9	-	0.84
Total	101.03	100	100	100

a: Wiik (1956), b: Berthet et al. (2009), c: Lodders and Fegley (1998)

4.2.2 Experimental methods

Experiments were conducted using a piston-cylinder apparatus and an internally heated pressure vessel (IHPV). Experimental conditions are listed in Table 4-2. The first set of piston-cylinder experiments (series A) was performed at 1–2 GPa at the University of Liège (Belgium) following the method described in Condamine et al. (2022). We used 0.5" barium carbonate cells with graphite capsules to maintain intrinsically reduced conditions. Samples were initially pressurized at room temperature to around 0.75 GPa, then heated to 865 °C at a rate of 100 °C/min and held at that temperature for 5 min. During the dwell period, pressure was increased to the target pressure before the sample was heated to the target temperature at a rate of 50 °C/min. The experimental temperature was monitored using a Type-D (W_3-Re_{97}/W_{25}-Re_{75}) thermocouple. Due to the location of the thermocouple tip ~ 1 mm above the sample, we estimate that the sample was ~20 °C hotter than the temperature measured by the thermocouple, and we reported the corrected temperature in Table 4-2. The duration of the highest temperature piston-cylinder experiment (1720 °C) was 45 min, and experiments at lower temperatures had durations of 120 min. The experiments were quenched by shutting off the electrical current to the heater. The second set of piston-cylinder experiments (series B) was performed at 3 GPa at the Bayerisches Geoinstitut (BGI, University of Bayreuth) following a procedure similar to that of the University of Liège. In BGI, we however used a talc-Pyrex pressure cell. For these experiments, an outer platinum capsule was used to minimize sulfur and alkali losses.

Table 4-2: Experimental conditions and oxygen fugacity calculated for each experiment. Met = metal, Qtz = quartz, Si = silicon metal. All experiments contain a silicate melt.

Run #	T (°C)	P (GPa)	Duration (min)	Source of S*	Phases in quenched silicate melts samples	fO_2[a]	fO_2[b]	fO_2[c]
A022	1620	1.31	60	FeS + Cas	Met	-4.9	-6	
A023	1520	1.31	120	FeS + Cas	Met	-5	-6.4	
A025	1520	1.31	120	CaS	Met	-5.6	-6.8	
A026	1520	1.31	120	FeS + Cas	FeS			-6.5
A027	1520	1.31	120	FeS	FeS, Qtz, Si			-4.7
A038	1620	1.31	45	FeS	FeS, Qtz			-4.7
A039	1620	2	45	FeS	FeS, Qtz, Si			-4.7
A040	1720	1.31	45	FeS	FeS			-4.4
A041	1720	2	45	FeS	FeS, Qtz			-4.5
A042	1620	1.31	45	FeS	Met	-5.5	-6.7	
A043	1620	1.31	45	FeS	FeS			-2.7
B873	1700	3	240	/	Met	-1.9	-1.4	
B875	1700	3	240	/	Met	-4.2	-3.6	
B877	1700	3	240	/	Met	-5	-7	
B879	1700	3	240	FeS	Met + FeS	-4.4	-5.8	-6.7
B880	1700	3	240	/	Met	-5.2	-5.4	
Y037-2	1600	0.1	300	FeS	FeS			-4
Y056-1	1520	0.1	300	FeS	Met + FeS	-4.9	-4	-5.3
Y083-2	1520	0.1	300	FeS	Met + FeS	-4.7	-5.2	-6.4
Y087-2	1520	0.1	300	S	MgS			-8.5

**The source of sulfur added in the powder; a: calculated using the Fe-FeO equilibrium; b: calculated using the Si-SiO2 equilibrium; c: using the equation from Namur et al. (2016a)*

IHPV experiments (series Y) were performed at 0.1 GPa at the University of Hanover (Germany). Details about the apparatus are available in Berndt et al. (2002) and details about the experimental protocol in Namur et al. (2016a). The powder was loaded into a graphite capsule enclosed in a platinum jacket and placed in the hotspot of the furnace using a 0.1 mm Pt wire. Before heating, the pressure was increased to 0.1 GPa using pure argon as the pressure medium. Two Type-S (Pt/Pt_{90}-Rh_{10}) thermocouples were inserted along the sample to control the heating at the top and bottom of the cell, and two additional Type-S thermocouples were used to monitor the sample temperature. IHPV experiments were conducted at 1520 °C for 300 min, except for experiment Y037-2, which was performed at 1600 °C (Table 4-2). Experiments were quenched by applying a current to the Pt wire, causing the sample to fall onto a copper plate at ~20 °C at the bottom of the sample holder. Quench rate is expected to be ~100 ˚C/s down to the glass transition temperature.

4.2.3 Analytical techniques

Quenched samples were cut in half, mounted in epoxy, and polished for textural and chemical analyses. Samples were dry-polished using SiC pads and diamond powder to avoid sulfide dissolution in the presence of water or other lubricants. Phase determination and description of experimental textures were conducted with a scanning electron microscopy (SEM; FEI Quanta 600, operating at 5 kV accelerating voltage) at the University of Aachen (Germany). Major and minor element concentrations were quantified using a JEOL JXA-8530F electron probe micro-analyzer (EPMA) at the University of Münster (Germany) with a 15 kV accelerating voltage and a 10 nA beam current. On-peak and background analysis times were 15 (10 for Na and K) and 5 s, respectively, for silicate melts and 20 (peak) and 10 (background) s for metals and sulfides. We calibrated Kα X-ray lines with jadeite (Na), olivine (Mg), disthene (Al), hypersthene (Si), pentlandite (Ni), apatite (P), sanidine (K), diopside (Ca), pyrite (S), rutile (Ti), Cr_2O_3 (Cr), rhodonite (Mn), and fayalite (Fe) for silicates, and olivine (Mg), apatite (P), diopside (Ca), pyrite (S), and Si, Ti, Cr, Fe, Mn, and Ni metal standards for metals and sulfides.

Trace element concentrations were analyzed by laser ablation inductively coupled plasma mass spectrometry (LA-ICP-MS) at the University of Münster (Germany) using a Photon Machines (Analyte G2) 193 nm ArF excimer laser (ca. 5 J/cm^2 laser fluence, 10 Hz repetition rate) coupled to a ThermoFisher ElementXR sector field mass spectrometer (MS). The laser spot size was adapted to the size of the phase being analyzed; typical spot diameters were 30–60 µm for silicate glass, 20–60 µm for metals and iron-rich sulfides, and 10–20 µm for MgS. Analytical positions were carefully chosen based on SEM images of the samples to avoid contamination by adjacent phases, and we monitored for contamination by metal inclusions (mainly from small Fe-rich blobs in the silicate glass, see Results) based on the signals (counts per second) of key elements (Si and Fe) in the acquired spectra. Ablated material was transported in a He carrier gas to plasma of the MS. Low-resolution (^{23}Na, ^{27}Al, ^{29}Si, ^{43}Ca, ^{45}Sc, ^{47}Ti, ^{51}V, ^{53}Cr, ^{55}Mn, ^{56}Fe, ^{59}Co, ^{60}Ni, ^{63}Cu, ^{66}Zn, ^{69}Ga, ^{73}Ge, ^{85}Rb, ^{88}Sr, ^{89}Y, ^{90}Zr, ^{93}Nb, ^{95}Mo, ^{137}Ba, ^{140}Ce, ^{146}Nd, ^{147}Sm, ^{153}Eu, ^{157}Gd, ^{172}Yb, ^{178}Hf, ^{181}Ta, ^{182}W, ^{232}Th, ^{238}U) and high-resolution analyses (^{24}Mg, ^{29}Si, ^{31}P, ^{39}K, ^{43}Ca, ^{47}Ti, ^{51}Cr, ^{53}Mn, ^{56}Fe, ^{60}Ni) were performed on each sample. The material was ablated and its composition measured for 40 s after the background was measured for 20 s. We used a washout of 10 s between successive measurements. We did not use a pre-raster of the surface but no obvious surface contamination was observed during the first second of analyses.

Raw trace element data were processed using the GLITTER software (Van Achterbergh et al., 2001; Griffin et al., 2008). Calcium concentrations determined by EPMA were used as an internal standard for silicate glass analyses, whereas those of iron were used for sulfide and metallic melt analyses. We used the NIST 612 reference material for silicates, and BHVO-2G basalt for sulfides and metals; using this Fe-rich basalt produced data more consistent with the microprobe data than using NIST 612 for FeS and Fe-Si.

4.2.4 Oxygen fugacity estimates

The oxygen fugacity (fO_2) of the samples can be estimated from the FeO content of the silicate melt and the Fe content of the metallic melt following the thermodynamic equilibrium between iron and wüstite:

$$Fe^{Met} + \frac{1}{2}O_2 = FeO^{Sil} \quad (1)$$

where the superscripts 'Met' and 'Sil' indicate metallic and silicate melts, respectively. However, under reducing conditions, the silicate melt FeO content is too low (Table 4-3) to be accurately measured, leading to large errors when estimating fO_2 (Cartier et al., 2014b; Namur et al., 2016a). We therefore used the equilibrium reaction (Cartier et al., 2014b):

$$Si^{Met} + O_2 = SiO_2^{Sil} \quad (2)$$

Oxygen fugacity was calculated by considering the effects of temperature and pressure, and is expressed as the difference relative to the IW buffer (in bar). We consider ideality in our calculations. All details on the calculation methods, including the calculation of ΔIW at high-pressure, are available in Namur et al. (2016a). We estimate that errors on fO_2 calculations are ~0.5 log units (Namur et al., 2016a).

Some of the sulfide-saturated experiments did not contain a metal phase, and we could not use silicate-metal equilibrium to calculate fO_2. For those experiments, we used the following empirical equation linking the S content in the silicate melt to fO_2 (Namur et al., 2016a):

$$\ln[S]_{SCSS} = a + b \times \frac{1}{T} + c \times \frac{P}{T} + d \times \log fO_2 + \sum e_i \frac{X_i}{X_{SiO_2}} \quad (3)$$

where $[S]_{SCSS}$ is the sulfur content at sulfide saturation (SCSS, wt%) in the silicate melt, T is temperature (K), P is pressure (bar), fO_2 is oxygen fugacity (bar), a, b, c, d and e_i are regression coefficients, and X_i is the mole fraction of oxide i in the melt, recalculated on a sulfur-free basis (Namur et al., 2016a). We estimate that errors using this method are ~1 log unit. We also used this equation to calculate fO_2 for some sulfide-saturated experiments from the literature with anomalously high Si contents (>20 wt%) in the metal phase and low $[S]_{SCSS}$ (<2 wt%). Comparison between fO_2 calculation methods can be found in the supplementary materials. Oxygen fugacity estimates for our experiments range from IW − 8.5 to IW − 1.4. The most reduced experiment contains solid MgS (Table 4-2).

4.3 Results

4.3.1 Attainment of equilibrium

The attainment of equilibrium in our experiments is supported by several observations. First, the duration of our experiments is similar to that of previous experiments performed on similar compositions (e.g., Wholers and Wood, 2017; Boujibar et al., 2019; Steenstra et al., 2020a, 2020b) and well above the duration needed to attain equilibrium, as estimated by Thibault and Walter (1995) and Corgne et al. (2008). Second, optical observations and the measured chemical compositions reveal a homogeneous silicate melt phase in all samples. We explained the presence of Si blobs surrounded by SiO_2 in two of our experiments (A027 and A039) by the shielding of Si by stable SiO_2 phase, leading to uncomplete Si oxidation. Third, our partition coefficient data are in good agreement with previous studies where thermodynamic equilibrium was reached (e.g., Cartier et al., 2014a; Wohlers and Wood 2015, 2017; Ingrao et al., 2019; Steenstra et al., 2020a, 2020b).

4.3.2 Phase assemblages and textural analyses

Some samples (B879, Y056-1, Y083-2) contain three equilibrated melts (silicate melt quenched to glass, metallic melt, and sulfide melt), but most experiments contain either equilibrated FeS and silicate melts without Fe-Si metal or equilibrated Fe-Si and silicate melts without FeS (Table 4-2). Backscattered electron images of selected samples are presented in Figure 4-1. Large FeS globules (>100 µm in diameter) are circular and usually host small Fe-Si globules (Figure 4-1c) which result from the miscibility gap in the Fe-S-Si system at the pressure and temperature conditions of our experiments (Malavergne et al., 2007; Morard and Katsura, 2010). Fe-Si metal globules, when present, are mostly spherical and can exceed 100 µm in diameter (Figure 4-1b, c). Regardless of whether or not experiments contain large metal globules, some small (<10 µm diameter) Fe droplets and (Fe,Ca,Mg)S blobs are observed in the FeS phase, both probably forming by exsolution during the quench (Figure 4-1c). In the Fe-free IHPV experiment (Table 4-2: Y087-2; Figure 4-1d), the only sulfide phase is pure MgS, which occurred as 30–40 µm in width blobs with smooth and irregular contours. MgS was likely a solid phase, because the experiment was performed well below (1520 °C) their very high melting temperature (~2200 °C, Jantzen et al., 2017). In several experiments, the silicate glass contains micro-globules (<1 µm) of metal comparable to those described in previous studies (Figure 4-1a: Boujibar et al., 2014; Malavergne et al., 2014). These inclusions are thought to be formed during quench (Boujibar et al., 2014). Quartz grains are sometimes present in the quenched samples, they are most commonly circular and, in some experiments (A027 and A039), they locally enclosed silicon metal, suggesting incomplete Si oxygenation due to SiO_2 shielding, as explained in section 4.3.1.

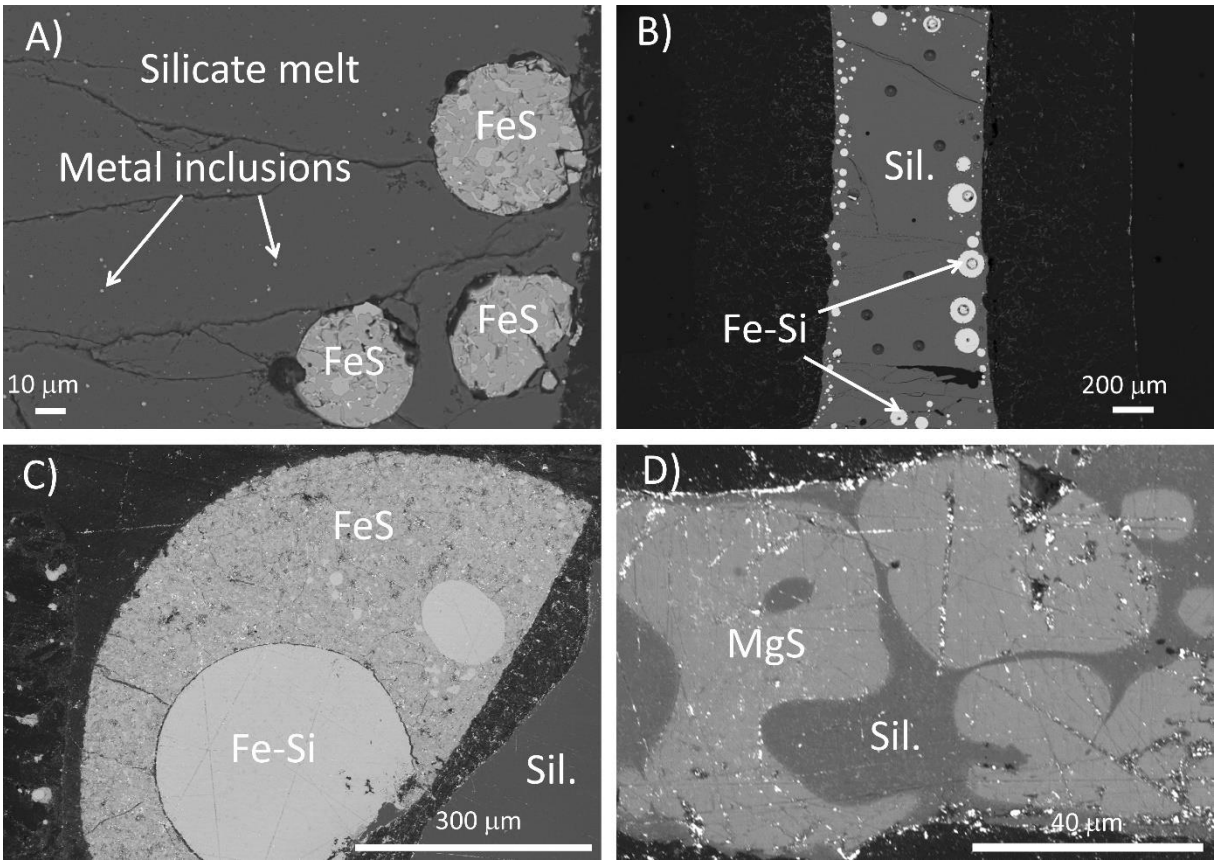

Figure 4-1: Back-scattered electron images of selected quenched samples. (a) Metal inclusions in the silicate glass and Fe inclusions in FeS (experiment A040). (b) Large (≥50 μm) globules of Fe–Si in FeS-free experiment A042. We were able to perform large laser points on those. (c) Fe–Si globules surrounded by FeS due to their immiscibility (experiment Y083–2). Smaller Fe–Si globules are also present in the FeS. They were avoided during analyses for both EPMA and LA-ICPMS. (d) MgS sulfide crystals in an Fe-free IHPV experiment (experiment Y087–2).

4.3.3 Major and minor element compositions

In most experiments, the composition of the silicate melt is relatively similar to that of the starting material (Table 4-3). The SiO_2 content of the glass varies from 55 to 70 wt% but is typically around 60 wt%. The MgO content varies from 20 to 30 wt% and the Al_2O_3 content is around 2 wt%. CaO content in the glass is between ~1 and ~2 wt%, except in the CaS-doped experiments (A022, A023, A025 and A026) in which CaO content reaches values from ~11 to ~14 wt%. The highest S content in the quenched glass in all experiments is about 15 wt%, but most samples contain <10 wt% S. Variable S contents are mostly responsible for the observed variations in the other elemental contents. Glass FeO contents are generally low (<1 wt%), except for experiment B873 (>10 wt%). Glasses in all experiments have similar alkali contents of ~1.5 wt% Na_2O and ~0.2 wt% K_2O.

*Table 4-3: Chemical composition of the silicate glass (in wt%). The totals above 100% are due to excess calculated oxygen. The first line shows the composition of the starting material (Start. mat.). Fe and S were added in different proportion in the starting material for each experiment (see Table 4-1). *CaS doped experiments.*

Run #	SiO_2	TiO_2	Al_2O_3	Cr_2O_3	MnO	MgO	CaO	FeO	Na_2O	K_2O	P_2O_5	S	Total
Start. Comp	61.26	0.10	2.76	0.82	0.43	31.37	1.65	0.00	1.55	0.19	0.90	0.00	101.03
A022*	57.68	0.01	2.20	0.16	0.29	19.23	11.49	0.28	0.87	0.17	0.01	8.28	100.66
1σ	0.60	0.01	0.04	0.04	0.03	0.42	0.38	0.09	0.05	0.02	0.02	0.30	0.37
A023*	56.55	0.01	3.15	0.17	0.30	18.74	11.89	0.27	1.05	0.14	0.01	8.41	100.70
1σ	0.31	0.01	0.22	0.03	0.03	0.26	0.22	0.04	0.04	0.02	0.01	0.16	0.21
A025*	58.21	0.01	2.27	0.07	0.26	19.22	12.45	0.12	0.68	0.19	0.01	5.80	99.29
1σ	0.28	0.01	0.04	0.03	0.03	0.87	0.41	0.05	0.05	0.02	0.02	0.15	1.26
A026*	53.52	0.01	2.15	0.05	0.13	22.14	13.84	0.32	1.08	0.16	0.40	5.40	99.20
1σ	0.20	0.01	0.05	0.01	0.03	0.13	0.22	0.07	0.04	0.03	0.05	0.08	0.23
A027	63.31	0.07	3.19	0.05	0.12	27.34	1.78	0.55	1.63	0.26	0.01	1.96	100.27
1σ	1.37	0.01	0.21	0.02	0.02	1.43	0.22	0.05	0.13	0.03	0.01	0.20	0.43
A038	70.72	0.02	4.35	0.02	0.07	19.11	1.14	0.26	1.26	0.17	0.01	2.46	99.63
1σ	1.08	0.01	1.08	0.02	0.02	1.51	0.07	0.07	0.17	0.02	0.01	0.14	0.33
A039	61.10	0.03	3.04	0.02	0.09	28.75	1.72	0.52	2.28	0.33	0.00	3.09	100.97
1σ	1.68	0.01	0.17	0.01	0.01	1.63	0.12	0.07	0.38	0.06	0.00	0.13	0.29
A040	73.08	0.02	2.05	0.02	0.10	19.00	1.12	0.28	1.19	0.18	0.01	2.76	99.86
1σ	0.72	0.01	0.03	0.02	0.03	0.57	0.17	0.12	0.20	0.02	0.01	0.07	0.77
A041	68.71	0.02	2.37	0.05	0.13	21.70	1.26	0.46	1.65	0.19	0.00	3.22	99.78
1σ	0.61	0.01	0.04	0.02	0.03	0.47	0.06	0.15	0.31	0.02	0.01	0.07	0.53
A042	59.67	0.11	3.05	0.13	0.47	26.62	1.54	0.13	1.64	0.25	0.00	9.75	103.41
1σ	0.51	0.01	0.04	0.03	0.09	0.32	0.19	0.18	0.10	0.01	0.01	0.34	0.45
A043	69.19	0.08	2.08	0.08	0.16	20.95	1.18	1.14	1.22	0.17	0.27	0.82	97.36
1σ	0.41	0.01	0.03	0.02	0.02	0.21	0.04	0.10	0.03	0.01	0.05	0.05	0.39
B873	55.97	0.13	2.35	0.65	0.38	24.40	1.42	10.57	1.23	0.19	0.16	0.00	97.45
1σ	0.29	0.02	0.09	0.03	0.02	0.51	0.06	0.13	0.10	0.02	0.03	0.00	0.39

Run #	SiO_2	TiO_2	Al_2O_3	Cr_2O_3	MnO	MgO	CaO	FeO	Na_2O	K_2O	P_2O_5	S	Total
B875	64.43	0.17	3.16	0.27	0.45	25.49	1.95	0.71	1.84	0.27	0.01	0.00	98.76
1σ	0.24	0.01	0.08	0.03	0.03	0.49	0.09	0.03	0.10	0.03	0.02	0.01	0.21
B877	53.60	0.07	3.65	0.01	0.07	37.53	2.15	0.18	1.72	0.24	0.02	0.00	99.26
1σ	0.80	0.01	0.33	0.01	0.03	1.77	0.33	0.09	0.33	0.04	0.02	0.01	0.30
B879	54.53	0.02	3.74	0.06	0.24	30.80	1.65	0.58	1.95	0.23	0.01	12.50	106.32
1σ	0.38	0.01	0.16	0.03	0.04	0.66	0.24	0.24	0.13	0.02	0.01	0.30	0.47
B880	63.58	0.15	3.39	0.09	0.37	26.75	2.13	0.18	1.85	0.28	0.01	0.00	98.80
1σ	0.39	0.02	0.11	0.02	0.04	0.73	0.12	0.05	0.26	0.03	0.02	0.01	0.51
Y037-2	63.00	0.10	2.56	0.07	0.12	27.30	1.53	1.08	1.49	0.22	0.02	1.55	99.05
1σ	0.79	0.01	0.05	0.02	0.02	0.40	0.04	0.11	0.04	0.01	0.02	0.04	1.28
Y056-1	61.61	0.06	2.66	0.03	0.11	28.58	1.62	0.35	1.55	0.22	0.02	2.68	99.51
1σ	0.24	0.02	0.04	0.02	0.02	0.11	0.02	0.13	0.06	0.01	0.02	0.05	0.27
Y083-2	60.37	0.06	2.70	0.07	0.15	29.16	1.63	0.40	1.56	0.21	0.00	4.88	101.19
1σ	0.30	0.01	0.04	0.03	0.02	0.22	0.04	0.10	0.04	0.02	0.01	0.10	0.30
Y087-2	52.62	0.13	2.75	0.47	0.37	31.30	1.80	0.03	1.70	0.22	0.03	15.66	107.08
1σ	2.58	0.03	0.14	0.14	0.11	1.75	0.23	0.02	0.08	0.03	0.03	1.25	0.76

Metallic phases are dominated by an iron-silicon alloy containing 1–25 wt% Si (Table 4-4). Chromium and nickel are minor components (up to 2 wt% for Cr and around ~0.2 wt% for Ni). Phosphorous is also a minor component in the metallic phases (≤ 2.4 wt%). At the investigated pressures of our experiments (≤3 GPa), there is a miscibility gap in the Fe-Si-S system and almost no S is present in the metal (<1 wt%). The S content in the silicate melt is positively correlated with the silicon content in the metal (Figure 4-2), consistent with previous works showing that both Si and S are controlled by fO_2 (e.g., Cartier et al., 2014b; Cartier and Wood 2019).

Table 4-4: Major and minor elements composition of metals (in wt%). Low totals are explained by the incorporation of minor/trace elements not measured using the electron microprobe, and notably carbon.

Run #	Si	Ti	Cr	Mn	Ca	Ni	Fe	P	S	Total
A022	13.81	0.01	2.33	0.02	0.02	0.30	77.84	2.11	0.04	96.49
1σ	0.32	0.01	0.08	0.01	0.02	0.02	0.35	0.16	0.02	0.32
A023	12.83	0.03	2.25	0.03	0.04	0.31	78.41	1.93	0.13	95.95
1σ	0.44	0.07	0.18	0.03	0.04	0.04	2.64	0.39	0.33	2.15
A025	16.78	0.02	2.31	0.23	0.02	0.19	75.25	1.81	0.01	96.62
1σ	0.24	0.02	0.11	0.03	0.02	0.05	0.38	0.17	0.01	0.36
A042	21.28	0.07	1.87	0.16	0.00	0.12	73.27	1.11	0.00	97.88
1σ	0.26	0.01	0.07	0.02	0.00	0.02	0.38	0.07	0.00	0.31
B873	0.01	0.00	0.17	0.00	0.01	0.10	89.09	2.42	0.03	91.83
1σ	0.01	0.00	0.05	0.01	0.01	0.03	0.47	0.44	0.01	0.42
B875	1.22	0.01	2.06	0.08	0.00	0.11	87.41	1.50	0.04	92.44
1σ	0.18	0.01	0.04	0.04	0.01	0.05	0.35	0.17	0.03	0.28
B877	26.31	0.24	2.35	1.28	0.01	0.13	67.54	1.09	0.00	98.95
1σ	1.07	0.03	0.22	0.07	0.01	0.02	1.12	0.22	0.00	0.57
B879	14.95	0.00	0.03	0.00	0.00	0.13	82.90	0.91	0.31	99.25
1σ	0.95	0.01	0.01	0.00	0.01	0.03	0.84	0.08	0.08	0.30
B880	10.60	0.04	2.39	0.41	0.00	0.15	80.48	1.25	0.01	95.34
1σ	0.36	0.01	0.07	0.02	0.00	0.03	1.12	0.08	0.01	1.16
Y056-1	0.85	0.01	0.09	0.02	0.00	0.21	90.60	1.98	0.92	94.69
1σ	0.47	0.01	0.10	0.05	0.01	0.07	3.19	1.00	1.78	1.79
Y083-2	5.27	0.01	0.24	0.02	0.01	0.16	89.05	1.89	0.49	97.14
1σ	1.72	0.01	0.09	0.02	0.01	0.05	2.07	0.65	0.30	0.57

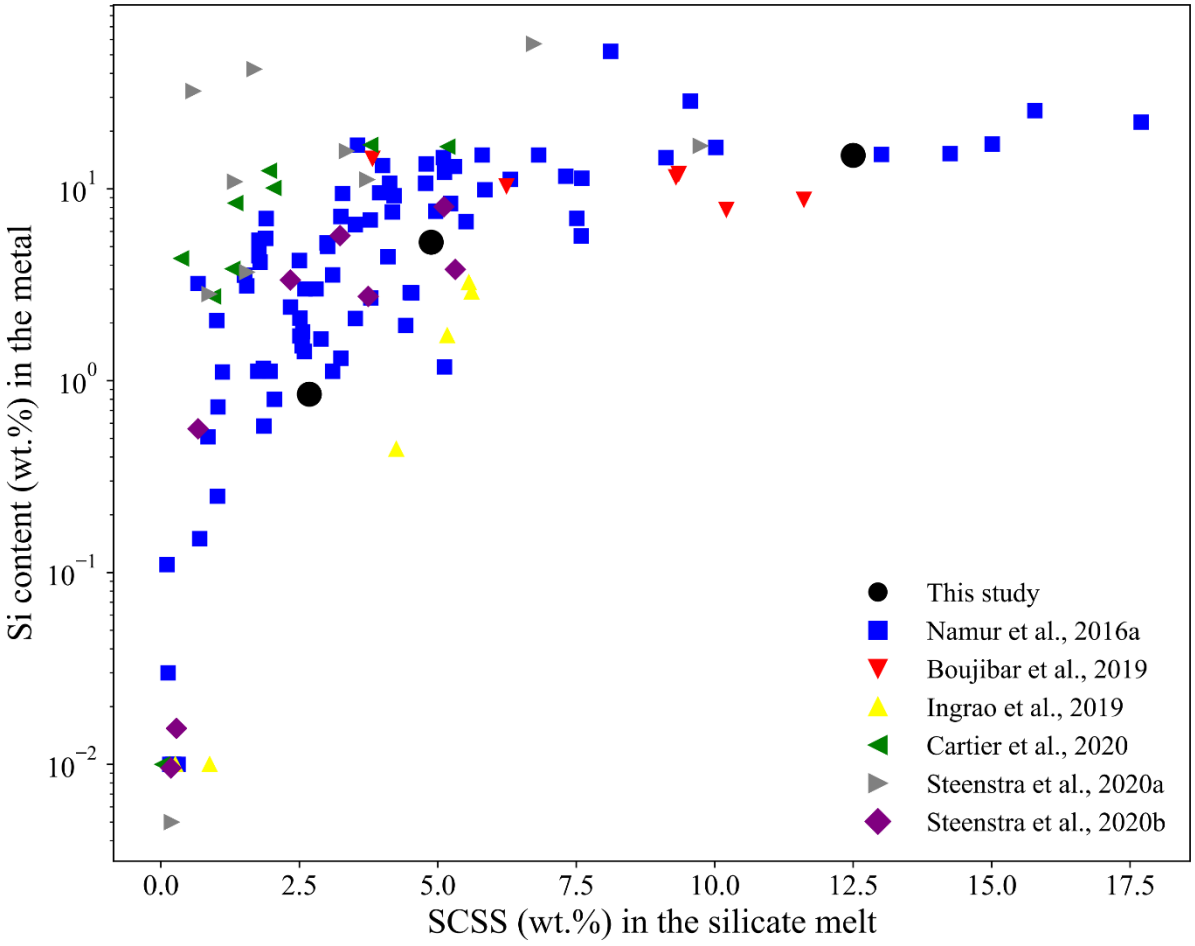

Figure 4-2: Si content in metal phases vs. sulfur content at sulfide saturation (SCSS) in the silicate melt. The SCSS corresponds to the maximum solubility of sulfur in a silicate melt at saturation. These two measures are positively correlated because they are linked by the oxygen fugacity.

Sulfide melt compositions are mostly composed of Fe and S, with up to 5 wt% Cr and Mn substituting for Fe (Table 4-5). The S contents of FeS phases are constant at around 37 wt%, corresponding to stoichiometric FeS. This indicates that there is no oxygen (i.e. another -2 anion) in the FeS globules. FeS globules are quenched liquids because all experiments were performed significantly above the FeS liquidus at the investigated pressures (e.g., Chen et al., 2008). Pure solid MgS is only observed in the iron-free experiment Y087-2, quenched at 0.1 GPa and 1520 °C (Table 4-5).

Table 4-5: Major and minor elements composition of sulfides (in wt%).

Run #	Si	Ti	Cr	Mn	Mg	Ca	Ni	Fe	S	Total
A026	0.01	0.16	4.17	0.99	0.12	0.03	0.10	54.81	37.14	97.58
1σ	0.00	0.02	0.15	0.04	0.02	0.02	0.02	0.22	0.13	0.39
A027	0.04	0.31	2.78	1.12	0.10	0.01	0.01	57.01	36.99	98.38
1σ	0.01	0.04	0.37	0.08	0.01	0.01	0.02	0.36	0.08	0.15
A038	0.01	0.30	2.31	0.81	0.15	0.01	0.03	57.96	36.61	98.20
1σ	0.01	0.13	0.49	0.13	0.04	0.01	0.01	0.77	0.27	0.32
A039	0.09	0.18	1.44	0.83	0.15	0.01	0.03	58.67	36.23	97.66
1σ	0.15	0.07	0.41	0.05	0.06	0.01	0.02	0.84	0.24	0.59
A040	0.01	0.24	1.73	0.76	0.16	0.02	0.03	58.87	36.16	97.99
1σ	0.00	0.07	0.30	0.05	0.03	0.02	0.01	0.58	0.58	0.49
A041	0.02	0.39	2.56	0.91	0.14	0.00	0.02	57.32	36.50	97.88
1σ	0.01	0.13	0.29	0.10	0.03	0.00	0.02	0.61	0.39	0.59
A043	0.01	0.03	1.63	0.62	0.01	0.00	0.03	59.26	36.41	98.04
1σ	0.01	0.02	0.25	0.05	0.01	0.00	0.02	0.42	0.13	0.33
B879	0.04	0.35	2.68	0.47	0.18	0.01	0.01	57.70	37.29	98.74
1σ	0.04	0.20	0.69	0.10	0.05	0.01	0.01	1.16	0.34	0.44
Y037-2	0.00	0.09	2.06	0.87	0.28	0.01	0.04	58.96	37.26	99.57
1σ	0.00	0.02	0.25	0.02	0.04	0.01	0.02	0.45	0.06	0.29
Y056-1	0.01	0.18	1.69	0.75	0.13	0.02	0.02	59.13	37.08	99.01
1σ	0.01	0.12	0.67	0.10	0.03	0.02	0.01	0.83	0.27	0.37
Y083-2	0.01	0.64	3.86	0.93	0.22	0.01	0.02	56.57	37.34	99.61
1σ	0.01	0.30	0.75	0.04	0.02	0.01	0.01	1.29	0.09	0.23
Y087-2	0.02	0.41	3.81	4.46	35.19	0.85	0.02	0.29	54.17	99.23
1σ	0.01	0.03	0.66	0.42	0.83	0.03	0.01	0.02	0.31	0.11

4.3.4 Trace element partitioning between sulfides (FeS and MgS) and the silicate melt

The partition coefficient *D* of an element *M* between phases *A* (FeS sulfide; or MgS sulfide) and *B* (silicate melt) is defined as:

$$D_M^{A/B} = C_M^A / C_M^B \quad (4)$$

where C_M^A and C_M^B are the concentrations of element *M* in phases *A* and *B* (in wt%), respectively. Our results show that most transition metals (V, Cr, Mn, Co, Ni, Cu, Nb, Mo, Ta, W) present a strong affinity for FeS (Figure 4-3). Except for Ti, which mainly partitions into FeS at ≤IW−4, group 3 and 4 transition metals (Sc, Y, Zr, Hf) remain strongly lithophile. Zn, Ga, and Ge also strongly partition into FeS (Figure 4-3). Lanthanides are strongly lithophile even under very reduced conditions, except for Eu, which has a stronger affinity for FeS (Figure 4-3). In contrast, Eu partitions less into MgS than the other lanthanides (Figure 4-3, $D^{MgS/silicate\ melt} \sim 0.1$ for Eu, while it increases from 0.25 for Ce to 1.75 for Yb). Alkali metals and alkaline earth metals are also mostly lithophile (Figure 4-3). Actinides (U and Th) are both lithophile, although U partitions more strongly into FeS and MgS than Th.

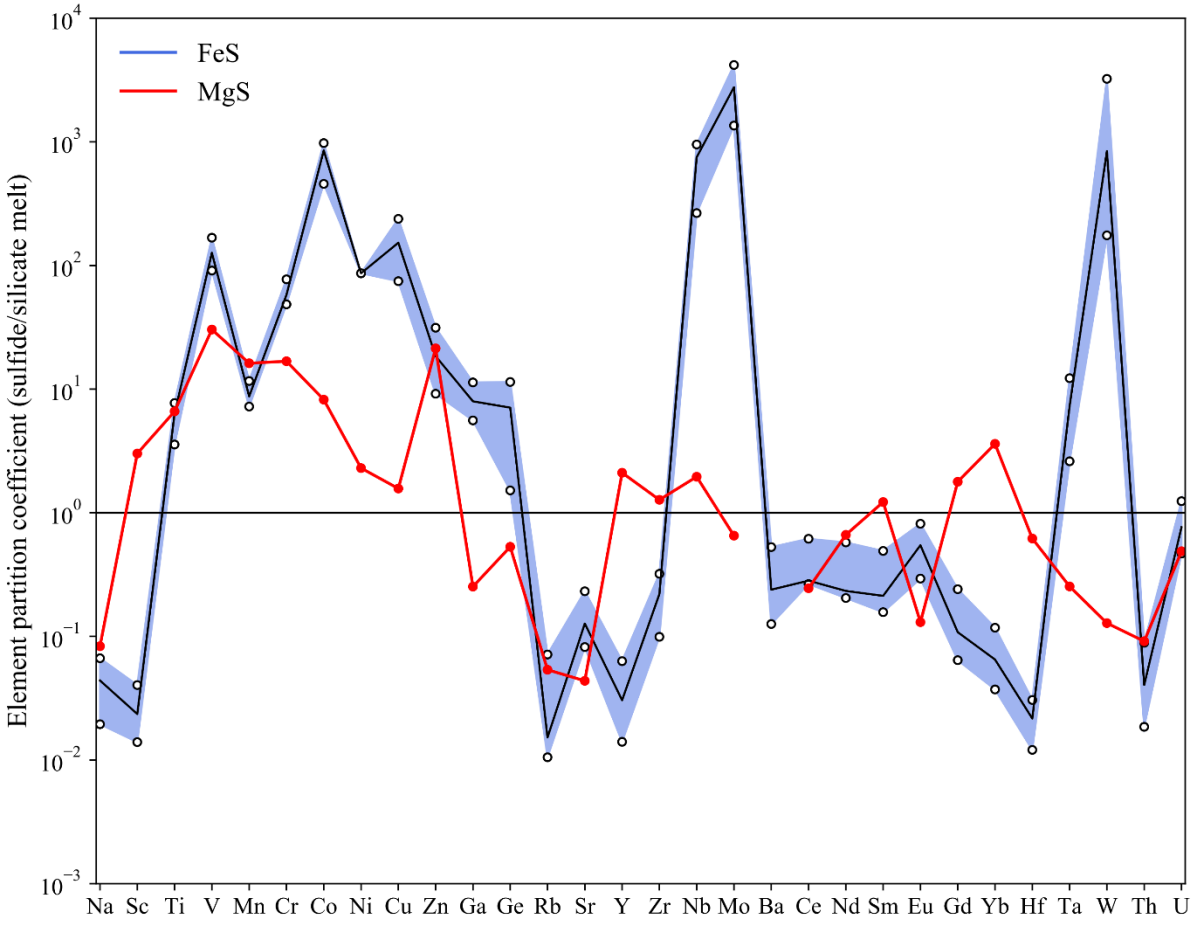

Figure 4-3: Elemental sulfide/silicate partition coefficients. Elements are sorted by increasing atomic number. The blue line shows the median values of FeS/silicate melt partition coefficients from experiments between IW - 6 and IW - 4. The blue shaded area indicates the ±95% confidence interval for each element. The red line shows the data from MgS/silicate partitioning. There is no confidence interval as only one experiment contained MgS. The black horizontal line marks D = 1, i.e., the element partitions equally between the silicate melt and sulfides.

We investigated trace element partitioning between MgS and the silicate melt in a single experiment. We observe significant differences between the partitioning behavior of trace elements in MgS and in FeS. Although the observed differences are probably mainly related to the phase composition (MgS *vs*. FeS), they also result from the physical state of the phase (solid for MgS *vs*. liquid for FeS) and the experimental fO_2. Indeed, the only experiment containing MgS was at ~IW − 8.5, significantly more reduced than experiments containing FeS (IW − 2.7 to IW − 6.7). Nonetheless, our results tentatively show that $D^{MgS/silicate} > D^{FeS/silicate}$ for Sc, Ti, Y, Zr, and Hf (with $D^{MgS/silicate} > 1$ for those elements, except for Hf), whereas $D^{MgS/silicate} < D^{FeS/silicate}$ for all other transition metals as well as Zn, Ga, and Ge. MgS also incorporates less U ($D_U^{MgS/silicate} \approx 0.5$) and Th ($D_{Th}^{MgS/silicate} \approx 0.1$) than FeS. In FeS, lanthanides are characterized by a decrease in $D^{FeS/silicate}$ with increasing atomic weight (Figure 4-3), whereas they behave oppositely in MgS (this study), CaS (Ingrao et al., 2019), and (Ca,Mg)S (Dickinson et al., 1990). We also observed a positive Eu anomaly in FeS and CaS (Ingrao et al., 2019), but none in MgS (this study) or (Ca,Mg)S, as previously observed by Dickinson et al. (1990).

4.3.5 Metal/silicate trace element partitioning

Under the reduced conditions of our experiments, most transition metals (V, Cr, Co, Ni, Cu, Nb, Mo, W) have always a strong affinity for metals (Figure 4-4), while Mn and Ta have their $D^{metal/silicate} > 1$ only at low fO_2. However, transition metals from groups 3 and 4 (Sc, Y, Zr, Hf) are lithophile, except for Ti, whose $D^{metal/silicate} > 1$ at lower fO_2 (Figure 4-4 and Figure 4-5). Zn, Ga, and Ge are incorporated into metals, lanthanides are strongly lithophile ($D^{metal/silicate} < 0.1$), and actinides (U and Th) are also strongly lithophile, with $D_U^{metal/silicate} < 0.05$ and $D_{Th}^{metal/silicate} < 0.01$ (Figure 4-4).

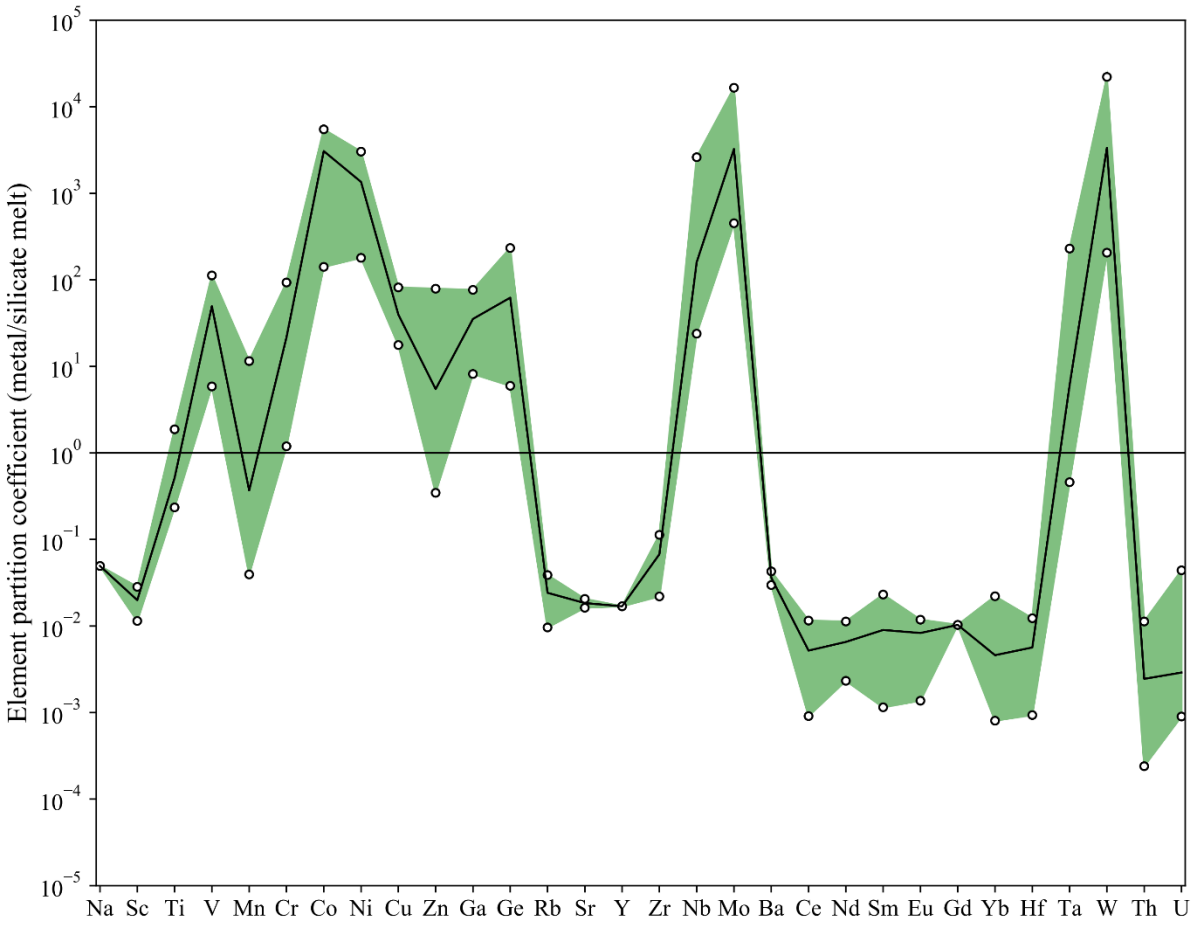

Figure 4-4: Element metal/silicate partition coefficients. Elements are sorted by increasing atomic number. The black line shows the median values of metal/silicate melt partition coefficients from experiments between IW - 7 and IW - 1. The green shaded area represents the ±95% confidence interval for each element. The horizontal line shows D = 1, i.e., the element partitions equally between the silicate melt and the metal.

4.4 Discussion

4.4.1 The effect of fO_2 on elemental partitioning

In order to apply our results to Mercury's primordial evolution, we focus here on the elements that were measured by *MESSENGER* (Ti, Cr, Mn, K, Th, U) or are likely to be measured by BepiColombo (e.g., Ni; Benkhoff et al., 2010). D values for all the other measured elements are however provided in the supplementary material.

As oxygen fugacity decreases, many elements become less lithophile and increasingly chalcophile and/or siderophile (Wohlers and Wood, 2015, 2017; Wood and Kiseeva, 2015; Vander Kaaden and McCubbin, 2016; Namur et al., 2016a; Ingrao et al., 2019; Boujibar et al., 2019; Cartier et al., 2020; Steenstra et al., 2020a, 2020b). As illustrated in Figure 4-3 and Figure 4-4, most transition metals are chalcophile/siderophile under Mercurian conditions, and their partitioning behavior strongly depends on fO_2. All experiments from the literature had their fO_2 recalculated following the method described above (section 4.2.4). Ti starts being majorly incorporated into FeS at around IW − 4 and below, whereas Cr, Mn, and Ni are always strongly incorporated into sulfides under such conditions (Figure 4-5). Mn is 5 to 10 times less incorporated into FeS than Cr, and Ni has the most affinity with FeS of these four elements (Figure 4-5). These elements also become highly incorporated into metals under reducing conditions, with Cr and Ni having the most affinity, followed by Mn and Ti.

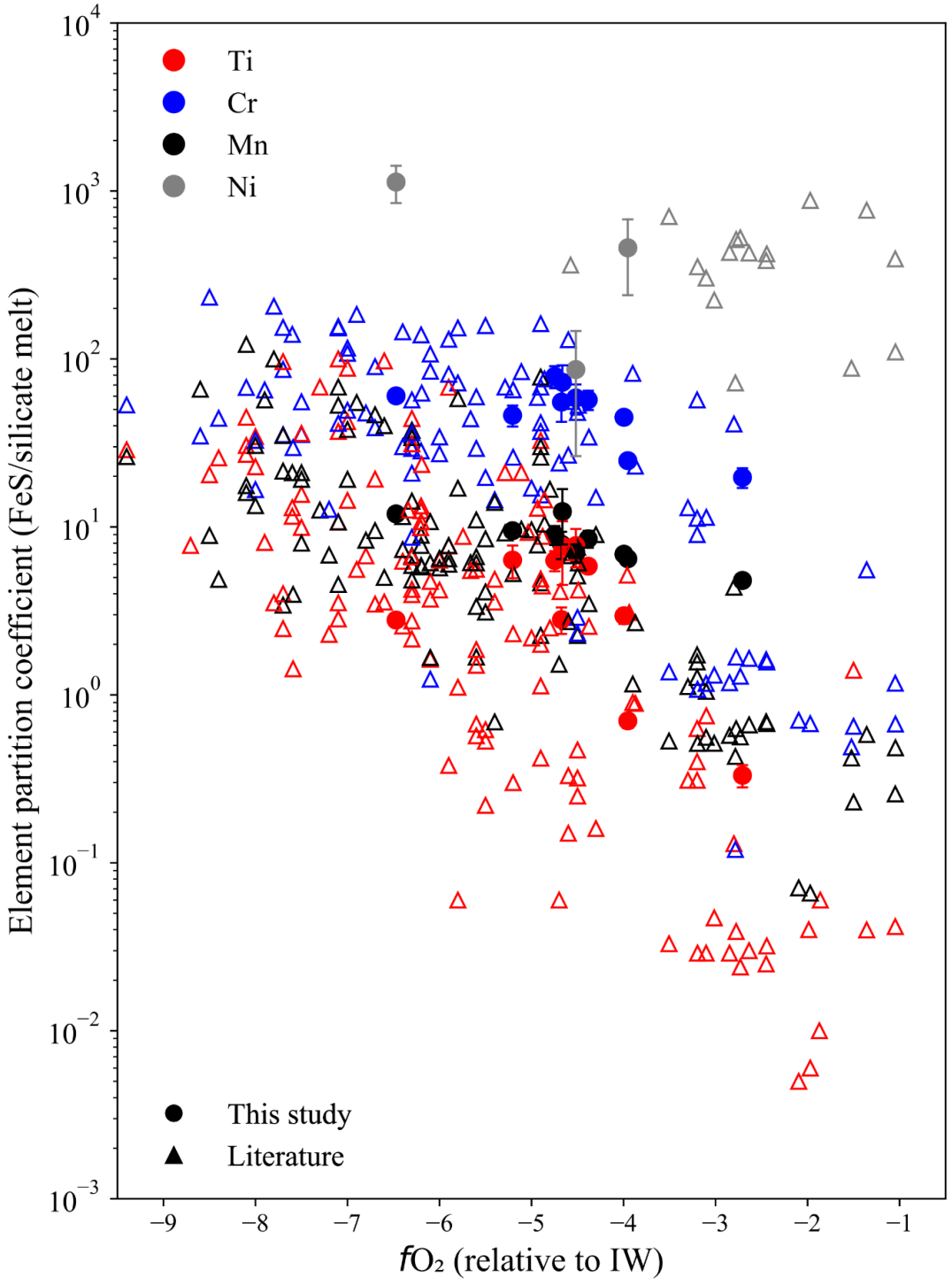

Figure 4-5: FeS/silicate melt partition coefficients for Ti, Cr, Mn, and Ni as a function of oxygen fugacity. Element affinities for FeS exponentially increase with decreasing oxygen fugacity. Error bars are shown for partition coefficients from this study. Literature data are from Namur et al. (2016a), Cartier et al. (2020), Steenstra et al. (2020a, 2020b).

Our data show that U and Th become less lithophile as oxygen fugacity decreases (Figure 4-6, left panel), with values of $D_U^{FeS/silicate}$ ranging from ~10^{-2} to 1 and of $D_{Th}^{FeS/silicate}$ from ~10^{-3} to 10^{-1} for IW-2 to IW-6. Th remains lithophile at all fO_2 values investigated here, and is ~20 times less chalcophile than U. These partitioning data are in good agreement with the literature (e.g., Wohlers and Wood, 2015,

2017; Boujibar et al., 2019, Steenstra et al., 2020b). There is no clear trend for U and Th partitioning between metal and silicate with the fO_2 (Figure 4-6, right panel). U and Th partition only slightly into the Fe-Si metal, even under very reducing conditions, with $D_U^{metal/silicate}$ < ~0.1, with the exception of one value from Malavergne et al., 2007, and $D_{Th}^{metal/silicate}$ < ~0.01. Based on our results and previous data (Chabot and Drake, 1999; Corgne et al., 2007; Mills et al., 2007; Bouhifd et al., 2007, 2013; Steenstra et al., 2018; Boujibar et al., 2019), $D_K^{FeS/silicate}$ has a fairly constant partition coefficient value over the entire range of oxygen fugacity considered, with a median value of ~0.06 and a standard deviation of ~0.13 when excluding the data from Chabot and Drake (1999), which show anomalous high partition coefficients for K (Figure 4-6, left panel). For metal-silicate partitioning, K shows an increasing siderophile behavior as oxygen fugacity decreases (Figure 4-6, right panel).

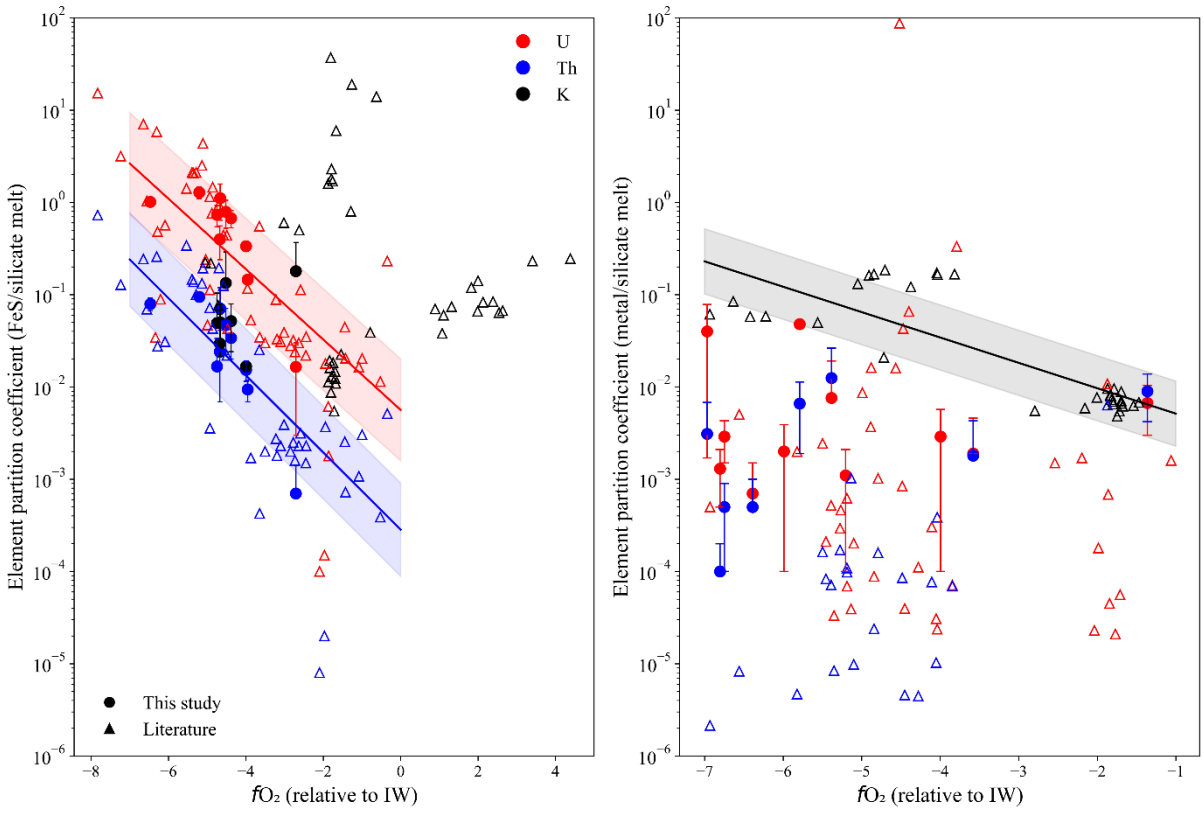

Figure 4-6: Left panel: FeS/silicate melt partition coefficients for U, Th, and K as a function of oxygen fugacity. U and Th become increasingly chalcophile with decreasing oxygen fugacity but D_U/D_{Th} stays constant at ~20. Right panel: Metal/silicate melt partition coefficients for U, Th, and K as a function of oxygen fugacity. No clear trend can be seen between partition coefficients and fO_2 for U and Th. K seems to be more siderophile with decreasing oxygen fugacity. Error bars are shown for partition coefficients from this study. Regression lines for $D_U^{FeS/silicate}$, $D_{Th}^{FeS/silicate}$ and $D_K^{metal/silicate}$ were calculated from Eq. (5) in the following section (4.4.2, Parameterization of U, Th, and K partition coefficients). The colored areas are the 1 s interval of confidence. Literature data for the left panel are from: Chabot and Drake (1999), Bouhifd et al. (2007), Corgne et al. (2007), Malavergne et al. (2007), Mills et al. (2007), Cartier (2014), Wohlers and Wood (2015), Wohlers and Wood (2017), Boujibar et al. (2019) and Steenstra et al. (2020b). Literature data for the right panel are from Bouhifd et al. (2007), Corgne et al. (2007), Malavergne et al. (2007), Bouhifd et al. (2013), Cartier (2014), Wohlers and Wood (2017), Boujibar et al. (2019).

4.4.2 Parameterization of U, Th, and K partition coefficients

Given the relative abundance of partitioning data for U and Th at low fO_2 conditions, we parameterized FeS/silicate melt partitioning using a least squares regression. The partition coefficients can be modeled as a function of fO_2 using the following equation

$$\ln(D_X) = a + b \times \log(fO_2) \quad (5)$$

The regression coefficients and their uncertainties are reported in Table 4-6. Temperature was found not to be a significant parameter for the regression. To parameterize the behavior of U and Th between FeS and silicate melt, we selected samples with $D_U^{FeS/silicate} > 0.001$ and $D_{Th}^{FeS/silicate} > 0.0001$ because considering smaller values provided unsatisfactory parameterization, especially for U. This observation may be due to the difficulty to measure such low U concentrations and/or to a change in the partitioning behavior of U at higher fO_2.

Based on a dataset of 53 measurements, we find a very strong correlation ($R^2 = 0.942$) between $D_U^{FeS/silicate}$ and $D_{Th}^{FeS/silicate}$:

$$\ln(D_U^{FeS/silicate}) = 2.7320 + 0.9763\ln(D_{Th}^{FeS/silicate}) \quad (6)$$

This regression allows the modeling of the evolution of the Th/U ratio during Mercury's differentiation, even if the absolute concentrations of U and Th in different reservoirs might be imprecise due to the uncertainties of Equation (5) ($R^2 < 0.7$; Table 4-6). No parameterization was obtained for $D_K^{FeS/silicate}$ with fO_2. As seen in Section 4.4.1 (Figure 4-6, left panel), $D_K^{FeS/silicate}$ is somewhat constant at around ~0.06 for any fO_2 considered in this study or the literature.

Table 4-6: Coefficients of regression for Equations (5), (6) and (7). R^2 is the coefficient of determination, F is the score of a F-test for a significant linear regression between the response variable and the predictor variables, and n is the number of observations.

Equation (5)	a	b	R^2	F	n
$D_U^{FeS/Silicate\ melt}$	-5.1788	-0.8785	0.620	92.98	59
Standard error	0.403	0.091			
$D_{Th}^{FeS/Silicate\ melt}$	-8.167	-0.9629	0.685	106.7	51
Standard error	0.41	0.093			
$D_K^{Metal/Silicate\ melt}$	-5.9038	-0.6332	0.672	63.59	33
Standard error	0.294	0.079			
Equation (6)	a	b	R^2	F	n
$D_U^{FeS/Silicate\ melt}$	2.732	0.9763	0.942	827.3	53
Standard error	0.174	0.034			
Equation (7)	a	b	R^2	F	n
$D_{Th}^{Metal/Silicate\ melt}$	-3.278	0.6568	0.523	23.04	23
Standard error	1.03	0.137			

We observe no clear correlation between $D_U^{metal/silicate}$ or $D_{Th}^{metal/silicate}$ and fO_2 (Figure 4-6, right panel). $D_U^{metal/silicate}$ seems correlated with pressure, but the available data are insufficient to obtain a statistically meaningful regression. Similarly, it was not possible to obtain a satisfying parameterization for $D_{Th}^{metal/silicate}$. As observed with $D_U^{FeS/silicate}$ and $D_{Th}^{FeS/silicate}$, there is a correlation between $D_U^{metal/silicate}$ and $D_{Th}^{metal/silicate}$. Although the error is large, we can nonetheless express the relation as:

$$\ln\left(D_{\mathrm{Th}}^{\mathrm{metal/silicate}}\right) = -3.2780 + 0.6568\ln(D_{\mathrm{U}}^{\mathrm{metal/silicate}}) \qquad (7)$$

with $R^2 = 0.523$ (Table 4-6) with 23 data points, restricted to $D_{Th}^{metal/silicate} > 10^{-5}$. It was possible to parameterize $D_K^{metal/silicate}$ with oxygen fugacity using Equation (5), with a R^2 of 0.672 using 33 samples. Standard errors are listed in Table 4-6.

4.4.3 Distribution of U and Th in Mercury and existence of an FeS layer

We developed a model to estimate the concentrations of heat-producing elements U and Th in the BSM for different plausible core and FeS layer formation scenarios (Figure 4-7). In this model, we calculated the mass of each geochemical reservoir (metallic core, FeS layer, BSM) using their respective fixed densities and sizes (Hauck et al., 2013). We consider a fixed silicate layer thickness of 440 km and a maximum core radius of 2000 km, which decreases with increasing the thickness of the FeS layer from 0 to 100 km.

Two scenarios were considered for the differentiation of Mercury. In Scenario 1 (Figure 4-7, left panel), Mercury is initially saturated in sulfide during primordial differentiation and FeS droplets form and sink in the magma ocean. Because they are less dense than Fe-Si metal, the FeS droplets aggregate to form an FeS layer at the core-mantle boundary in equilibrium with the magma ocean (Malavergne et al., 2014). In Scenario 2 (Figure 4-7, right panel), Mercury is not initially saturated in sulfide, and the formation of an FeS layer (if present) results from the crystallization of the S-bearing Fe-Si core; the formation of an Fe-Si solid core results in increasing the S content of the outer residual liquid core, which exsolve FeS droplets when it exceeds the solubility of S at the pressure conditions of the CMB (Morard and Katsura, 2010; Charlier and Namur, 2019). This occurs after complete solidification of the magma ocean so that the FeS layer and the silicate portion do not equilibrate.

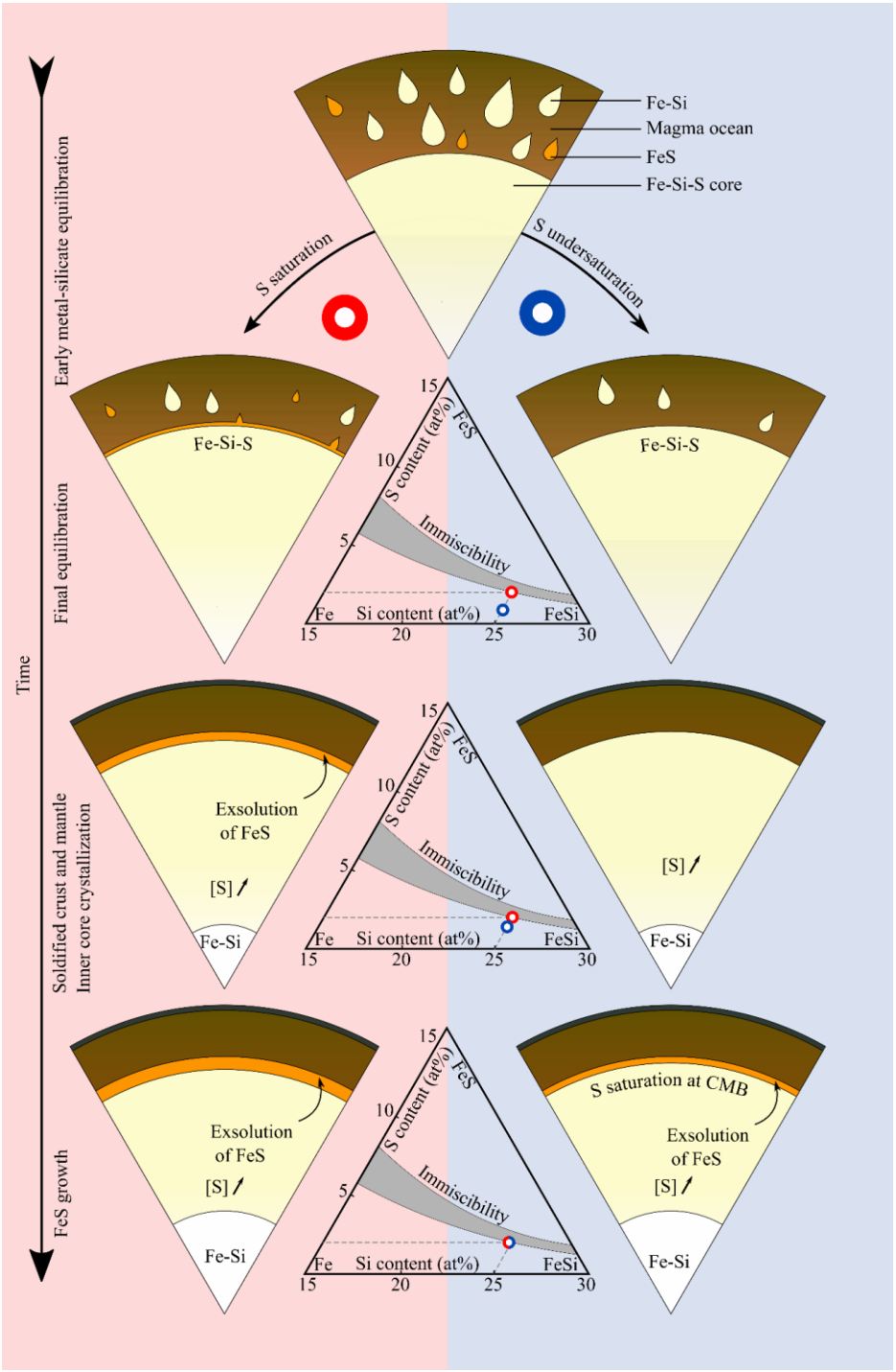

Figure 4-7: Scenarios for the evolution of Mercury's interior during planetary cooling. Left panel, red background: the sulfide saturation scenario. Here, the excess of S in the mantle during differentiation results in the early formation of an FeS layer at the CMB. In this scenario, the formation of an Fe–Si inner core is possible, and also leads to the exsolution of FeS, further contributing to the formation of an FeS layer. The Fe-Si-S phase diagrams (modified after Morard and Katsura, 2010) shown in the middle indicate the hypothetical initial compositions of the liquid core for both scenarios (blue and red points corresponding to the two scenarios). Right panel, blue background: formation scenario of Mercury in case the BSM was undersaturated in S. Because sulfide is not initially saturated in the magma ocean, there is no early formation of an FeS layer. The crystallization of the Fe–Si inner core leads to the exsolution of FeS because the enrichment of S in the outer core drives the metal composition into the immiscibility field of the Fe-Si-S system. Based on Namur et al. (2016a), we considered the case where 2 at.% S was present in the metallic core.

In both scenarios, we calculated the distribution of U and Th in the different reservoirs. The FeS/silicate partition coefficients for U and Th are calculated using Equation (5). Oxygen fugacity was varied from IW − 7 to IW − 3. This redox range is relevant to the estimated fO_2 during differentiation (McCubbin et al., 2012) and corresponds to the range in the experiments used to parameterize the partition coefficients. Because it was not possible to precisely parameterize $D_U^{metal/silicate}$ and $D_{Th}^{metal/silicate}$ as a function of fO_2, we considered two end-member cases for metal-silicate partition coefficients, consisting in some of the highest and the lowest values of $D_U^{metal/silicate}$ found in our experiments and the literature between IW − 7 and IW − 3. $D_{Th}^{metal/silicate}$ was then calculated using Equation (7). The first case corresponds to a high incorporation of U and Th in the core ($D_U^{metal/silicate}$ = 0.01 and $D_{Th}^{metal/silicate}$ = 0.0018), and the second case to a low incorporation of these elements in the core ($D_U^{metal/silicate}$ = 0.0001 and $D_{Th}^{metal/silicate}$ = 0.00009).

To model an initially sulfide-saturated Mercury (Scenario 1;Figure 4-7, left panel), we considered that the three geochemical reservoirs (BSM, FeS layer, and core) were in equilibrium during Mercury's primordial differentiation. U, and to a lesser extent, Th can be slightly incorporated into the core. This incorporation slightly fractionates U and Th, so that the bulk silicate Th/U slightly increases. The fractionation is negligible in the case where $D_U^{metal/silicate}$ is low (< 0.001). While Th is mostly lithophile, U is strongly incorporated into FeS at low fO_2 conditions (<IW − 5), with $D_U^{FeS/silicate} \sim 1$ at IW − 6. Under the least reduced conditions, however, U mainly dominantly stays in the BSM along with Th. It means that although almost no fractionation occurs between these elements above IW − 5, they are increasingly fractionated under increasingly reducing conditions if an FeS layer is present. As the thickness of the FeS layer increases, this fractionation becomes larger because FeS incorporates large amounts of U and lower amounts of Th, as observed in Boujibar et al. (2019). Therefore, the amount of U in the BSM, and thus, its Th/U ratio, depend on the thickness of the hypothetical FeS layer and the oxygen fugacity during differentiation.

In contrast, if Mercury was not initially sulfide-saturated, the FeS layer formed via the exsolution of FeS from the liquid core because of crystallization of Fe-Si solids (Miozzi et al., 2022; Edmund et al., 2022; Scenario 2; Figure 4-7, right panel). In this case, most of U and Th remain in the BSM during early differentiation, and only a small amount of U is incorporated into the core. If the inner core crystallized to exsolve FeS, it is probable that this process occurred after the solidification of the BSM (i.e., after mantle/crust differentiation) and the FeS layer would only be in equilibrium with the liquid core, i.e., it would not reequilibrate with the solidified mantle. Formation of the FeS layer would thus deplete the core in U and Th because these elements have a stronger affinity for FeS than for metal under reducing conditions. Ultimately, in this scenario, the planet should have a silicate Th/U ratio similar to the chondritic ratio, and heat-producing elements should be concentrated in the BSM. This exsolution of FeS from the liquid core could also happen in the first scenario, which would increase the

size of the FeS layer and change its composition, but would ultimately not change the composition of the already solidified silicate part (Scenario 1;Figure 4-7, left panel).

The calculated Th/U ratios of the two scenarios can be compared with Th and U measurements at the surface of Mercury by *MESSENGER*. We assume that U and Th were not fractionated during partial melting of the mantle and formation of the crust. This assumption is reasonable because, on Earth, these elements are highly incompatible and do not fractionate during partial melting (Wipperfurth et al., 2018). However, because the BSM likely hosts sulfides such as CaS or MgS, this assumption may not be fully correct, as discussed below (section 4.4.4). Chemical data from *MESSENGER* provided surface Th/U ratios of 2.5 ± 0.9, so that the upper limit for surface Th/U is 3.4 for 1σ. If Mercury initially had the same Th/U ratio as the average EH chondritic ratio (3.3, Javoy and Kaminski, 2014), the fractionation of U and Th during the formation of even a thin (<20 km) FeS layer under reducing conditions during the primordial differentiation of the planet (Scenario 1;Figure 4-7, left panel) would increase the BSM Th/U ratio above the upper limit of 3.4 (Figure 4-8), unless the planet formed at fO_2 conditons above IW−4 (Figure 4-8). If incorporation of U and Th in the core is low (dashed lines), it is possible to form a thicker FeS layer (up to 80 km) at high fO_2 (<IW - 4), but we do not observe significant changes between high and low incorporation of U and Th into the core for more reducing conditions, meaning that it is the formation of an FeS layer that dominates U-Th fractionation at these fO_2.

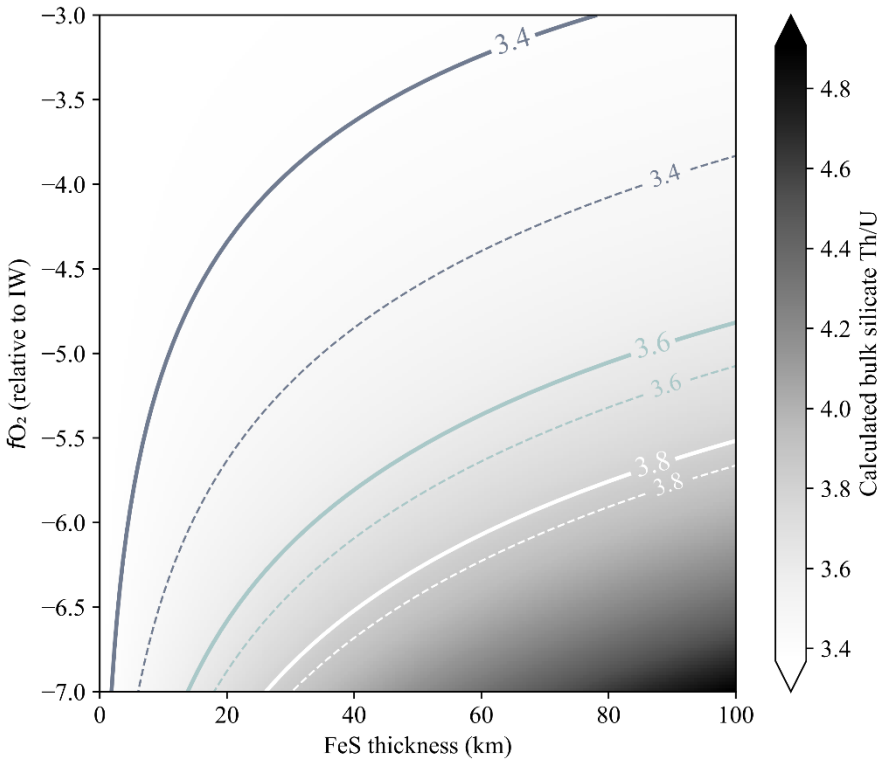

Figure 4-8: The calculated Th/U ratio of the BSM as a function of the FeS layer thickness and oxygen fugacity during primordial differentiation. The mesh and the thick lines were calculated with high incorporation of U and Th in the core, and the dashed lines were calculated with low incorporation of U and Th in the core. The initial Th/U ratio in this model is taken

as 3.3, the average in EH chondrites. MESSENGER measured surface Th/U ratios of 2.5 ± 0.9; therefore, any value above 3.4 is unlikely.

To reconcile the observed Th/U ratios with the existence of a thick FeS layer, the bulk planet could have an initial Th/U ratio lower than 3.3. Indeed, enstatite chondrites have Th/U values as low as ~2.7 and up to >4 (Javoy and Kaminski, 2014 and references therein). However, only a few meteorites exhibit low Th/U, and there are still large uncertainties between different studies; for exemple, Barrat et al. (2014) found a ratio of 3.84 in Indarch, while Dauphas and Pourmand (2011) and Morgan and Lovering (1968) found a value of 2.9 and 2.66 respectively. Therefore, we calculated the maximum FeS layer thickness that would lead to a surface Th/U ratio < 3.4 for a range of bulk Th/U ratios of 2.86 - 3.45 (Figure 4-9).

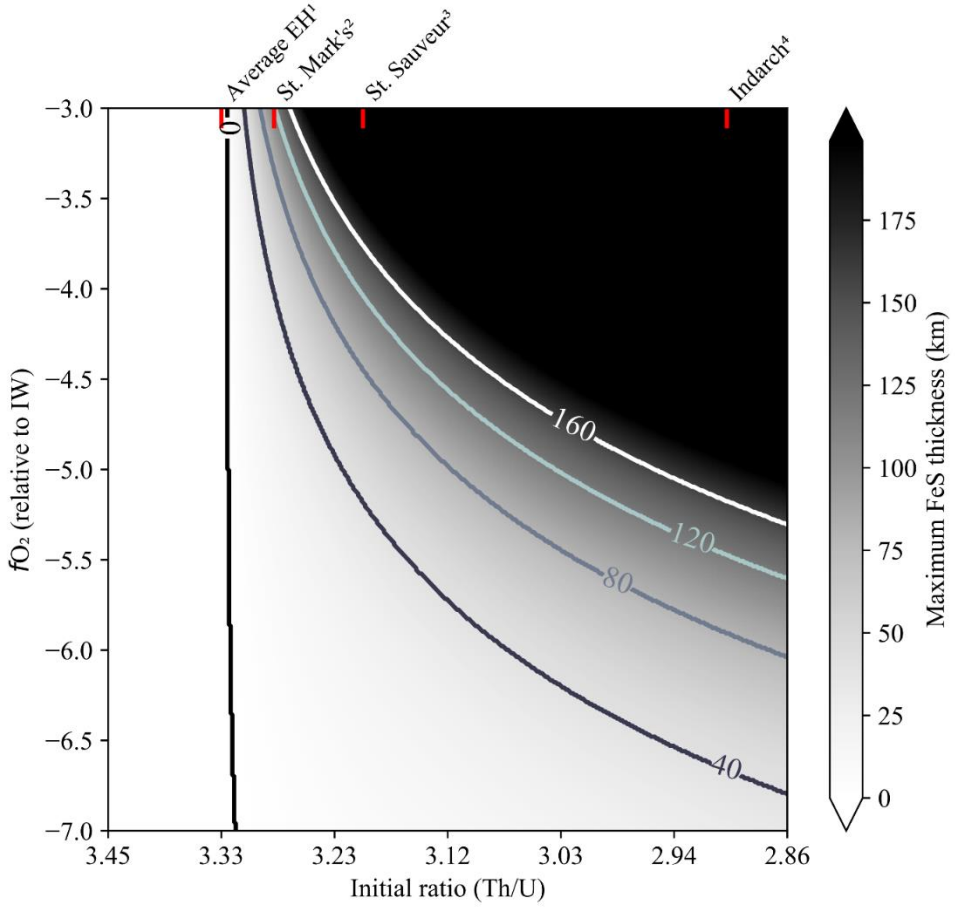

Figure 4-9: Maximum thickness of an FeS layer formed in equilibrium with the core and the BSM as a function of oxygen fugacity and the initial Th/U ratio. The mesh and the lines were calculated with high incorporation of U and Th in the core. The low incorporation model slightly offsets all the lines to the left, but its effect is not significant. The maximum FeS layer thickness represents the point where the remaining silicate Th/U ratio is equal to the upper value measured at the surface (~3.4), so that it is impossible to have a thicker FeS layer without increasing the Th/U ratio above 3.4. The black part in the upper right part of the plot represents thicknesses >200 km. The Th/U ratios of some enstatite chondrites (EH), as well as their global average value, are shown at the top. 1: Wasson and Kallemeyn (1988); 2: Barrat et al. (2014); 3,4: Dauphas and Pourmand (2011).

As shown inFigure 4-9, fO_2 conditions >IW-4 allow the existence of a thick FeS layer at any bulk initial Th/U because low fractionation at these conditions only slightly affects the resulting silicate Th/U ratio. However, at lower fO_2 (<IW-5) it is only possible to reconcile the presence of an FeS layer with lower bulk initial Th/U than the average observed in EH (3.3); if the bulk Th/U is as low as 2.9, it is possible to have an FeS layer up to 80 km thick at IW-6. As 3.4 is the upper limit of the measured ratio on the surface of Mercury (Peplowski et al., 2011), it is probable that the initial ratio was lower than the average value of 3.3 for EH meteorites. However, as a Th/U ratio below 3 is rarely observed in chondrites, it is plausible that the surface ratio of 2.5 ± 0.9 is the combined result of a low initial ratio and the absence of an FeS layer formed under reducing conditions in equilibrium with the magma ocean. Indeeed, even if the initial ratio was around ~2.7, the lowest observed in chondrites (Morgan and Lovering, 1968), the presence an FeS layer would increase the surface ratio to values close to the upper limit.

In summary, the presence of an FeS layer formed under reducing conditions in equilibrium with the silicate melt contradicts the data from *MESSENGER* (which measured a slightly sub-chondritic Th/U ratio) if the bulk Th/U was similar to the mean value found in enstatite chondrites. If the surface Th/U ratio is close to the maximum measured by MESSENGER (3.4; 2.5 ± 0.9, Peplowski et al., 2011), it is nevertheless possible to form an FeS layer if: 1) the planet formed under less reduced conditions (>IW − 4), because U partitions only slightly into FeS, which does not significantly affect the resulting silicate Th/U ratio and/or 2) the initial Th/U ratio was at the lower end of chondritic data. These outcomes indicate that, except if the initial Th/U was sub-chondritic and that Mercury formed an FeS layer under reducing conditions, almost all of Mercury's initial U and Th contents should reside in the BSM. If the planet formed under very reducing conditions without an FeS layer, there is no other reservoir to incorporate large amounts of U and Th. Alternatively, if Mercury formed under more oxidized conditions and hosts an FeS layer, then U and Th did not partition into the FeS layer.

Our model can be used to calculate the absolute concentrations of U and Th in the BSM, assuming that Mercury formed from material with chondritic concentration. Our calculations indicate that in the case of initial sulfide saturation, the U concentration in the BSM depends mainly on the thickness of the FeS layer, as well as the oxygen fugacity during formation. We considered that bulk Mercury contains 9 ppb U (the average concentration in EH chondrites; Javoy and Kaminski, 2014) and calculated the BSM U concentration to be ~35 ppb in the absence of an FeS layer (Figure 4-10, upper panel). If the layer formed in equilibrium with the BSM, the BSM U concentration is ~33 ppb at the least reducing oxygen fugacity conditions (IW − 3, 100-km thick FeS layer) to as low as ~23 ppb under the most reducing conditions (IW − 6, with a 100-km thick FeS layer) (Figure 4-10, upper panel). Th is less impacted by the formation of the FeS layer and by fO_2 conditions than U, and for an initial bulk planetary concentration of 30 ppb (Javoy and Kaminski, 2014), we calculated the BSM Th concentration

to be ~110 ppb for an FeS layer 100 km thick under the most reducing conditions or up to ~121 ppb in the absence of an FeS layer (Figure 4-10, lower panel).

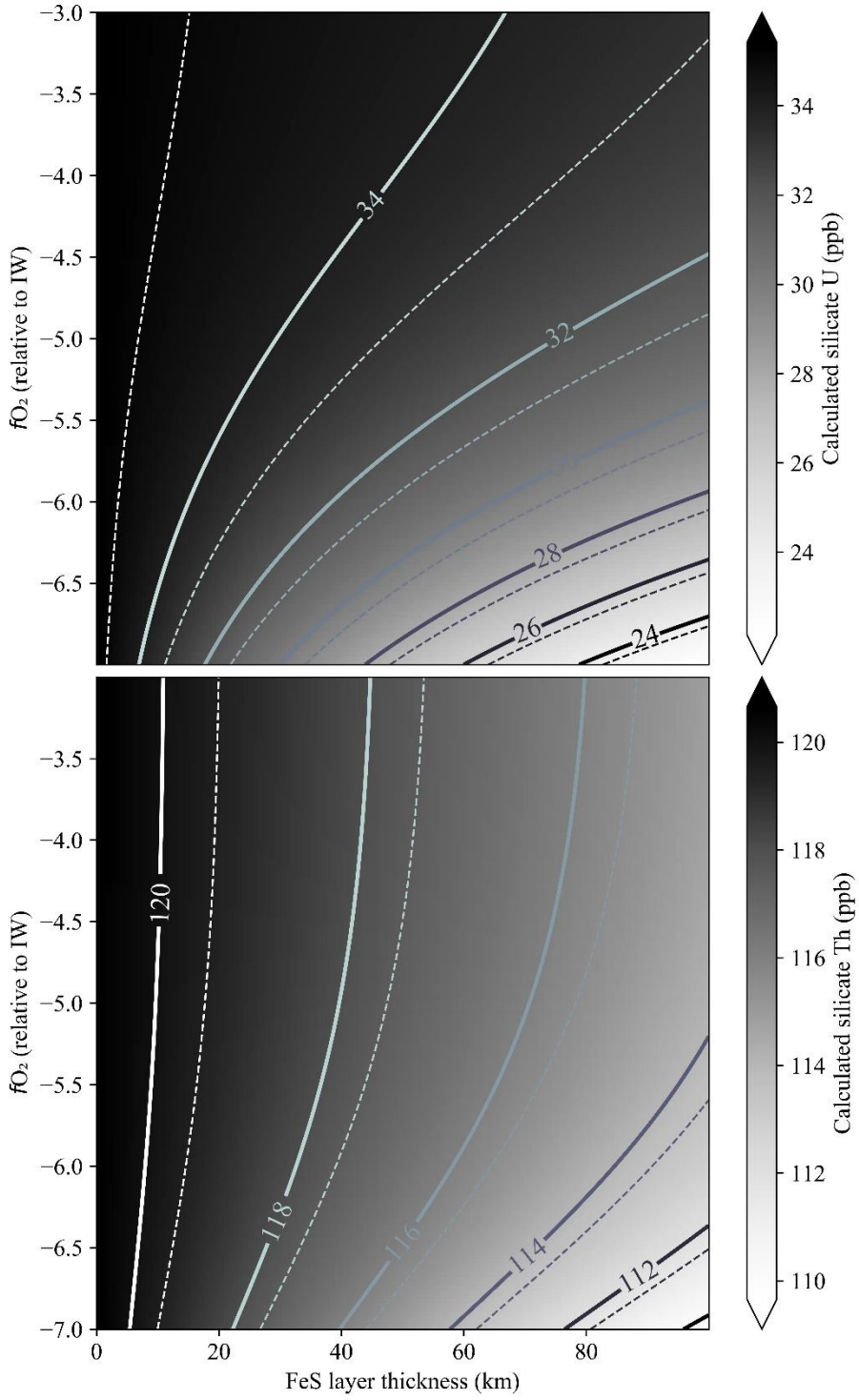

Figure 4-10: U (upper) and Th (lower) concentrations (ppb) in the BSM as a function of fO_2 and the thickness of the FeS layer (in km). The mesh and the thick lines were calculated with high incorporation of U and Th in the core, and the dashed lines were calculated with low incorporation of U and Th in the core. Thick lines and dahsed lines of the same colour have the same value. The content of U in silicate part is relatively more affected by the presence of a thick FeS layer formed at low fO_2 than Th.

4.4.4 Sulfides in the mantle and their impact on U and Th

Under reducing conditions, sulfur solubility in silicate melts increases by up to several wt% compared to Earth like fO_2 conditions (Namur et al., 2016a). Because oxygen fugacity is very low in Mercury (IW − 7 to IW − 3; McCubbin et al., 2012), Mercury's magma ocean is thought to have contained abundant sulfur, which would have formed sulfides once the magma ocean reached sulfide saturation (Boukaré et al., 2019). These sulfides may have sunk or floated depending on their relative densities and that of the silicate magma ocean (Parman et al., 2016; Boukaré et al., 2019; Mouser et al., 2021). Cooling of the magma ocean would have decreased the SCSS, which is strongly temperature dependent (Namur et al., 2016a), continuously producing sulfides. In contrast, in an initially sulfide-undersaturated magma ocean, no sulfide would have been present during the early stages of silicate magma crystallization; i.e., the sulfur content of the magma ocean was below the SCSS. As silicate cumulates crystallized, the residual silicate liquid became progressively enriched in sulfur, and the crystallization of Fe-free sulfides (such as MgS) in the magma ocean began at a depth that depends on the initial S content of the magma ocean and fO_2. At fixed bulk S content, more reducing conditions (and thus, higher S solubility) would have resulted in a shallower depth of sulfides saturation (Boukaré et al., 2019). In our model, we consider the presence of sulfides during mantle partial melting to calculate the global partition coefficient between the residual mantle and the silicate melt that ultimately formed the crust of Mercury. The details of the modeling can be found in Appendix 1.

To model the effect of sulfides in the mantle on the silicate Th/U, we use the following parameters: fO_2 = IW − 7 to IW − 3, no FeS layer, abundance of residual MgS sulfides during partial melting from 10 to 20%, and 30–60% partial melting (Namur et al., 2016a, 2016b). Initial concentrations of U and Th in the building blocks were 9 and 30 ppb, respectively (Th/U = 3.3). Our modeling results show that the presence of Fe-free sulfides in the mantle during partial melting produces melts with higher Th/U ratios because the residual mantle sulfides fractionated U and Th. However, this fractionation effect is not significant, and is even less important at higher degrees of partial melting (Figure 4-11). Our assumption that the bulk silicate Th/U ratio was equivalent to the surface ratio is thus somewhat challenged by the presence of mantle sulfides. As such, it would mean that even higher fO_2 conditions or even lower initial bulk Th/U are needed to have simultaneously mantle sulfides and an FeS layer to

have a surface Th/U below 3.4. Namur et al. (2016a), showed that the presence of these sulfides are probable in the mantle, so that it makes the presence of an FeS layer even more unlikely.

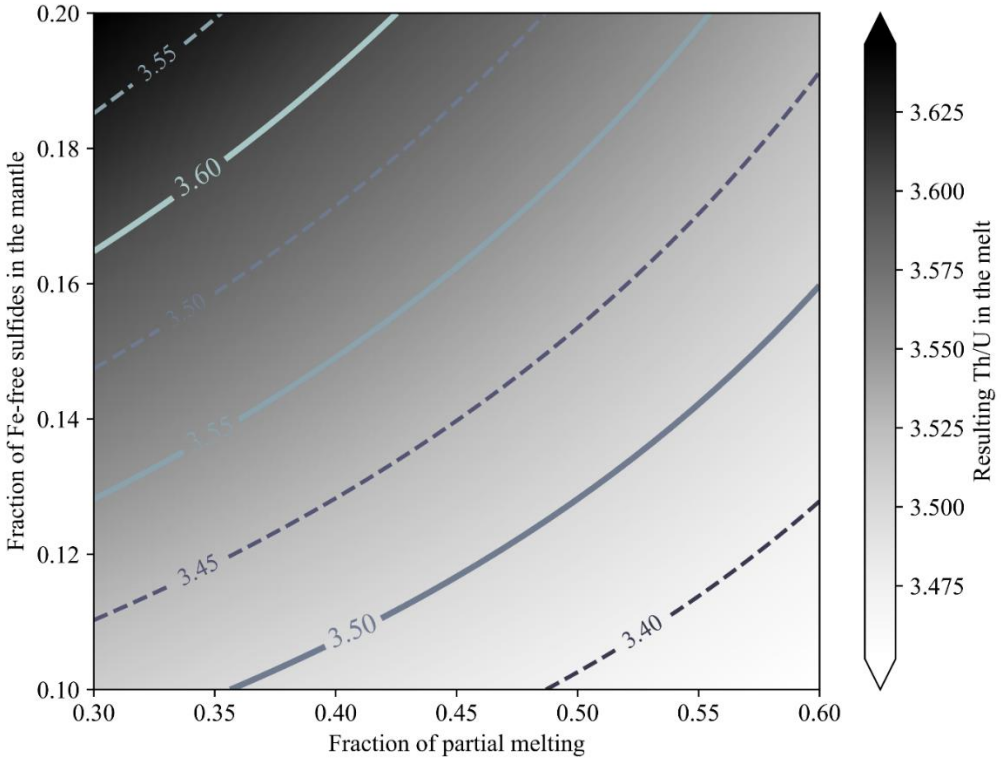

Figure 4-11: The influence of residual Fe-free sulfides in the mantle and the degree of partial melting on the surface Th/U ratio. The presence of Fe-free sulfides slightly increases the surface Th/U ratio, especially at relatively low degrees of partial melting. In this figure, fO2 during differentiation was fixed at IW - 5 (Namur et al., 2016a) to isolate the effects of sulfides in the mantle and the degree of partial melting. We also consider that no FeS layer formed. The mesh and the thick lines were calculated with high incorporation of U and Th in the core, and the dashed lines were calculated with low incorporation of U and Th in the core. Although uncertainties remain on the exact values of $D^{sulfide/silicate}$ *for U and Th in Fe-free sulfides, it seems that a fractionation of U and Th in the presence of mantle sulfides is possible.*

By varying all the parameters over possible ranges (FeS thickness, 0 - 100 km; fO_2, IW-3 – IW-7; amount of Fe-free sulfides in the mantle, 10-20 wt%; and partial melting degree, 30–60%), our models suggest that after crust formation, lavas contain ~180–400 ppb Th and ~35–115 ppb U. These concentrations match those measured at the surface by *MESSENGER*: 220 ± 60 ppb Th and 90 ± 20 ppb U (Peplowski et al., 2011), except for the lowest calculated U concentrations, which result from the presence of thick FeS layer (100 km) formed at the lowest fO_2 (IW - 7) and for lavas formed from a very high degree of partial melting (60 %). The abundance of these elements on the surface is largely affected by the degree of partial melting, as they are very incompatible. High partial melting (~60%) yields the lowest U and Th concentrations, and inversely. The presence of an FeS layer at low oxygen fugacity affects more strongly the surface concentration of U than Th, but this effect is modest compared to the effect of partial melting. The effect of mantle sulfides on the surface concentration of U and Th is

significant, but not as important as the presence of an FeS layer. Finally, the U content measured on the surface corresponds in our model to scenarios where no FeS layer formed under reducing conditions.

4.4.5 The volatile inventory of Mercury

Both U and Th are refractory elements, whereas K is moderately volatile. Because these three elements behave incompatibly and are not fractionated during partial melting, the surficial K/Th and K/U ratios are powerful tools for understanding Mercury's volatile budget (Peplowski et al., 2011). The mean K/Th value of Mercury's surface (5200 ± 1800) is similar to that of the other inner planets (Peplowski et al., 2011), a surprising discovery because Mercury was thought to be volatile-depleted due to its proximity to the Sun (Albarède, 2009; McCubbin et al., 2012). Boujibar et al. (2019) predicted that a bulk K/U ratio in agreement with models of volatile depletion with heliocentric distance (Albarède 2009), and a bulk K/Th similar to other terrestrial planets are consistent with the formation of a thick FeS layer under reducing conditions (IW-5.5). On the other hand, they also showed that higher oxygen fugacity conditions (IW-4) would lead to bulk K/Th and K/U ratios close to the ones measured on Mercury's surface regardless of the thickness of an FeS layer (Boujibar et al., 2019).

We determined the values of bulk K/Th and K/U ratios needed to match the values measured by MESSENGER. To do so, we used our differentiation model with bulk chondritic (EH) K/Th and K/U ratios of ~26,000 and ~90,000, respectively (Lodders and Fegley, 1998). In our model, we used high incorporation of U and Th into the core ($D_{Th}^{metal/silicate}$ of 0.01 and $D_{Th}^{metal/silicate}$ of 0.0018; Section 4.4.3), and we used Equation (5) to calculate $D_{K}^{metal/silicate}$. At low oxygen fugacity (IW-5.5) and without an FeS layer, we obtained after differentiation and partial melting a surface K/Th and K/U of 18,000 ± 6000 and 57,000 ± 20,000, depending on the specific compatibilities of K and Th in silicate minerals (forsterite and enstatite, see Appendix 1) and the degree of partial melting. This is respectively 2 - 4 and 3 - 6 times higher than the K/Th and K/U ratios measured on the surface of Mercury. If we calculate the surface K/Th and K/U ratios using different initial K/Th and K/U values (and fixing the initial Th/U ratio, so that only the initial K content varies), we find that only K-depleted carbonaceous chondrites can account for the observed surface ratio (Figure 4-12), contradicting hypotheses about the chemistry of Mercury's building blocks. It is more likely that, although the surface is relatively rich in volatile elements (S, K, and Na; Nittler et al., 2011; Peplowski et al., 2012, 2014), Mercury probably experienced a global loss of potassium. This volatile loss process could have been similar to the process that depleted the Earth and Mars in volatiles (i.e., early volatilization and/or a hidden reservoir of K; Humayun and Clayton, 1995; McDonough, 2016), but other potential causes remain, such as the vaporization of K from the surface by solar radiation (Dauphas et al., 2022 and references therein). Therefore, further work is needed to develop a model of Mercury's formation that can account for its sub-chondritic surface K/Th and K/U ratios and chondritic surface S content, knowing that S is more volatile than K.

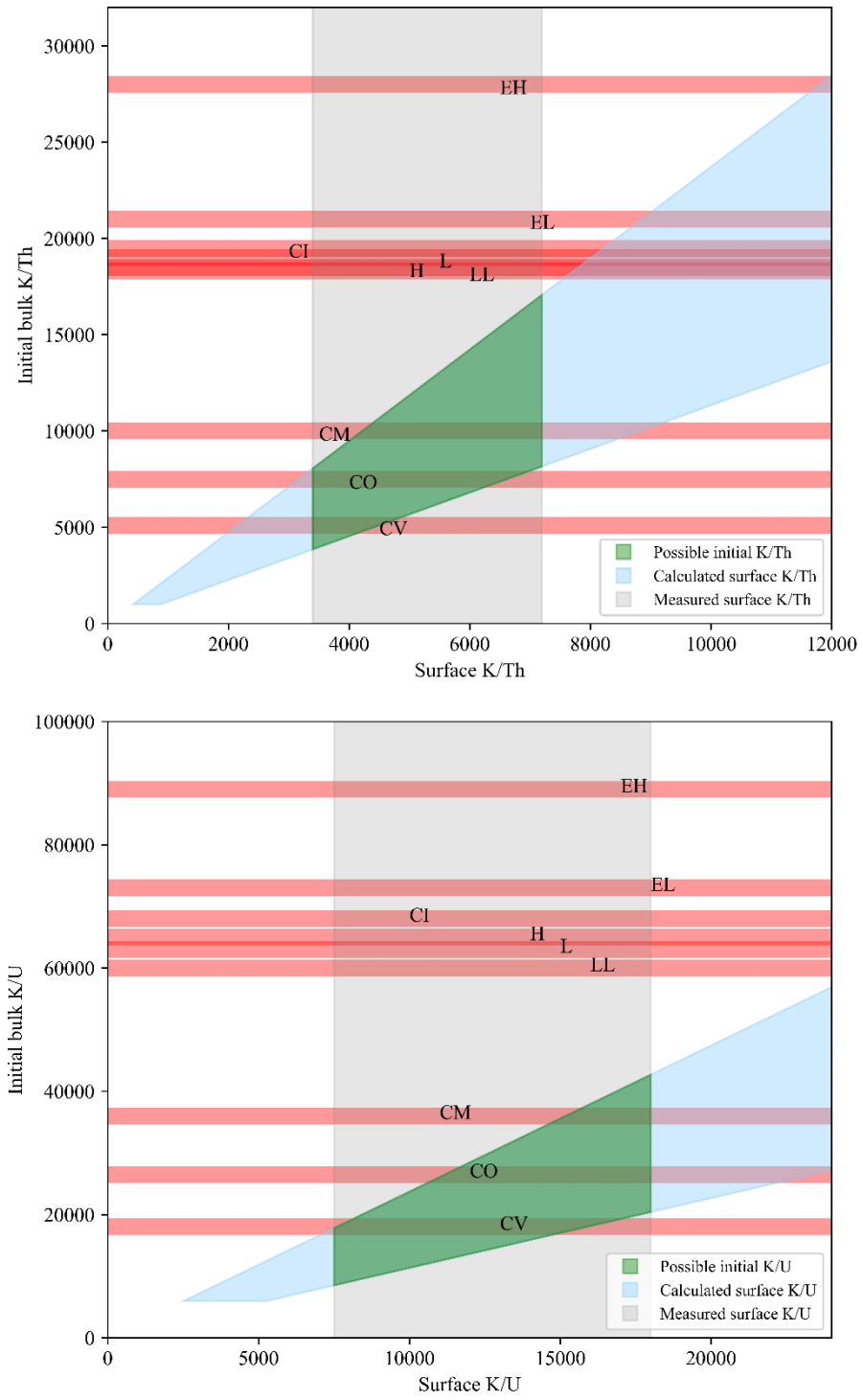

Figure 4-12: The expected range of K/Th (top) and K/U (bottom) on Mercury's surface (blue shaded area) depending on the initial bulk planet's K/Th and K/U ratios, respectively. The gray area represents MESSENGER measurements of the K/Th and K/U ratios on the surface of Mercury. Horizontal red shaded areas represent the average K/Th and K/U ratios of different chondrites. EH and EL, enstatite chondrites; H, L, LL: ordinary chondrites; CI, CM, CO, CV: carbonaceous chondrites. Data for the chondritic ratios come from Wasson and Kallemeyn (1988).

4.5 Conclusions

We performed 20 experiments on materials representative of the bulk silicate portion of Mercury under very reducing conditions (IW - 8.5 to IW - 1.4), at 0.1–3 GPa, and 1520–1720 °C. The major, minor, and trace element concentrations of the different liquids (and solids for the experiment with MgS) present in the retrieved samples were measured to establish partition coefficients for > 30 elements between silicate melt, metallic melt, sulfide melt (FeS), and MgS sulfides. We developed a mass-balance model for Mercury to evaluate the distribution of heat-producing elements (U and Th) in different reservoirs (BSM, mantle sulfides, the hypothetical FeS layer, and the core). This model was applied to two differentiation scenarios; in the first one, the FeS layer formed during differentiation from a S-saturated Mercury, while in equilibrium with both the silicate part and the core, while in the second scenario, the FeS layer formed from exsolution of an FeS-saturated core during its crystallization. We show that *MESSENGER* measurements of surface Th/U ratios preclude the existence of an FeS layer that formed under reduced conditions (< IW-4) in equilibrium with the BSM if Mercury's building blocks had mean chondritic Th/U (around 3.3). It is nonetheless possible to reconcile the presence of an FeS layer if conditions were more oxidizing during the differentiation (> IW - 4) and/or if the initial Th/U ratio of Mercury was at the lower end of chondritic data (Th/U < 3). Our results show that sulfides in the Mercurian mantle, such as MgS, should not incorporate significant amounts of U and Th, but that their presence would contribute to increase the silicate Th/U ratio at the surface. Almost all of Mercury's U and Th should be stored in the BSM, independently of the differentiation scenario considered, except in the case of the formation of an FeS layer under reducing conditions from material with sub-chondritic Th/U. Regarding Mercury's volatile inventory, measured surface K/Th and K/U ratios are respectively 2 - 4 and 3 - 6 times lower than expected if the initial bulk ratios were similar to those of enstatite chondrites. Although it remains possible that Mercury formed from K-poor materials, it is likely that Mercury lost a large portion of its K in the early history, as did Earth. Processes that could reconcile this K-loss with the high surface concentrations of other volatile elements (S, Na) remain an open question for future studies.

Acknowledgements

HP was supported by the FRIA-FNRS (Fonds pour la Formation à la Recherche dans l'Industrie et dans l'Agriculture - Fonds de la Recherche Scientifique) (grant FC 31865). ON acknowledges support from FWO through an Odysseus grant. BC is a Research Associate of the Belgian Fund for Scientific Research-FNRS. C. McCammon is thanked for her help with piston cylinder experiments at BGI. O. Namur acknowledges support from the DFG Core Facility for High-Pressure Research from the German Science Foundation for the high-pressure experiments performed at BGI. We are grateful to Rob Dennen for editing carefully the manuscript. We thank Asmaa Boujibar and an anonymous reviewer for their comments that greatly improved the manuscript. Doris Breuer is acknowledged for handling the manuscript.

Supplementary materials:

Supplementary materials containing details on experimental conditions, EPMA data, LA-ICP-MS data, and partition coefficients for every experiment are available. Another file contains a comparison between the fO_2 calculated using Namur et al. (2016a) equation and using Si-SiO_2 equilibrium.

Appendix 4A:

To evaluate the fractionation of K/Th, K/U, and Th/U ratios caused by the magmatic processes responsible for the formation of Mercury's secondary crust, we modeled the evolution of U, Th, and K concentrations during mantle partial melting. We considered that the crustal lavas formed from a high degree of partial melting (20–50 vol%) of a peridotitic mantle (Charlier et al., 2013; Namur et al., 2016b; Namur and Charlier, 2017), and calculated the abundances of K, Th, and U in these lavas using Shaw's batch melting equation (Shaw, 1970):

$$\frac{C_L^M}{C_0^M} = \frac{1}{(D+(1-D))\cdot F} \quad (1)$$

where C_L^M is the concentration of element *M* in the melt, C_0^M is the concentration of element *M* in the primordial mantle (corresponding to the BSM), *D* is the rock/melt partition coefficient of element *M*, and *F* is the melt fraction. Although this equation does not simulate the complex processes occurring in mantle plumes, we used it to evaluate the global impact of partial melting on the distributions of heat-producing elements between the mantle and the melts produced. The mantle residue in equilibrium with the lavas is composed of olivine (forsterite) and enstatite in unknown relative proportions (Namur et al., 2016b). The partitioning of K, U, and Th between these two minerals and mafic melts is not well constrained. Based on the partitioning data of Bédard (2005, 2007) and Cartier et al. (2014b), we considered that reasonable ranges of $D^{mantle/melt}$ for Equation 1 are: D_K = 0.005–0.5, D_{Th} = 0.0005–0.1, and D_U = 0.0005–0.1. Although the partitioning of these elements is not well defined, Th and U have almost identical electronic properties (Shannon, 1976) and are thus expected to behave similarly during magmatic processes. Moreover, crustal production on Earth does not fractionate U and Th (Wipperfurth et al., 2018) and there seems to be no fractionationation of Th and U in enstatites under highly reducing conditions (Cartier et al., 2014b). For these reasons, we introduced two additional constraints:$0.5 < D_{Th}/D_U < 2$ and $0.1 < D_{Th}/D_K < 10$.

Using the data on U and Th partitioning into MgS from experiment Y087-2, we obtain $D_U^{MgS/silicate} \approx 0.5$ and $D_{Th}^{MgS/silicate} \approx 0.1$ at ~IW − 8.5. Because no other experimental D_U or D_{Th} values have been determined for MgS or CaS, we used the bracketing ranges of values $D_U^{sulfide/silicate}$ = 0.1–1 and $D_{Th}^{sulfide/silicate}$ = 0.01–0.1. We also considered $D_K^{sulfde/silicate}$ = 0.01–0.1.

Chapter 5: Titanium, chromium, and manganese at the surface of Mercury as proxies for mantle mineralogy

5.1 Introduction

The MESSENGER spacecraft orbited Mercury from 2011 to 2015 and produced the first compositional data of the surface (Nittler et al., 2018a). Two main instruments were used: the Gamma-Ray Spectrometer (GRS; Goldsten et al., 2007) and the X-Ray Spectrometer (XRS; Schlemm et al., 2007). The GRS measured the gamma rays emitted from surface materials, either from natural decay of long-lived radionuclides (K, Th and U) or from the interactions of galactic cosmic-rays and stable elements (C, O, Na, Al, Si, S, Cl, Ca and Fe). The XRS measured the X-ray fluorescence derived from incident X-rays produced by the Sun, and so is dependent on the solar activity. In normal conditions, the XRS instrument was able to detect Mg, Al and Si, while rare solar flares allowed for the detection of heavier elements or less abundant Ca, Ti, Cr, Mn and Fe (e.g. Weider et al., 2014, 2015). Even though the polar orbit of the spacecraft technically permitted the mapping of the whole planet, its ellipticity implied that the northern hemisphere was mapped with higher resolution than the southern hemisphere (Nittler et al., 2020). However, as the spacecraft spent more time over the southern hemisphere, it acquired more data for Ti, Cr and Mn because of the irregular solar flares, but with lower resolutions. While initial reporting of surface data for Ti, Cr and Mn were scarce (Weider et al., 2014, 2015), recent refinement by Cartier et al. (2020) and Nittler et al. (2023) produced a large, more detailed database for surface concentration of Ti and Cr, respectively.

Surface data points toward volatile-rich compositions, especially in sulfur with up to 4 wt% S (Nittler et al., 2011), and to very reduced conditions (fO_2 between IW-2.6 to 6.3, McCubbin et al., 2012), as also deduced from the very low surficial FeO concentration (Nittler et al., 2011). The mineralogy of the mantle was derived from its surface composition. Indeed, as the surface is made of almost exclusively volcanic materials from high degree partial melting dating back to at least 3.5 Gy (Byrne et al., 2016), it should be representative of the mantle it is derived from. The mantle has been labelled as lherzolitic, dominated by forsterite and enstatite (Stockstill-Cahill et al., 2012; Charlier et al., 2013; Namur et al., 2016b; Vander Kaaden et al., 2017), with the probable presence of Fe-free sulfides (MgS and/or CaS, Namur et al., 2016b; Boukaré et al., 2019; Mouser and Dygert, 2023), that brought S to the surface during partial melting (Namur et al., 2016a).

The structure of the silicate part was determined from the data of MESSENGER (Goossens, 2022). Smith et al. (2012) calculated a silicate shell 410 ± 37 km thick, and Padovan et al. (2015) proposed a crust thickness of 35 ± 18 km. It has been suggested that the mantle of Mercury overlays an FeS matte located at the core-mantle boundary, whose thickness could reach ~200km (Malavergne et al., 2010; Smith et al., 2012; Hauck et al., 2013). Recent studies tend to decrease the upper limit of the thickness

of this FeS layer (90km, Namur et al., 2016a), or even to refute the existence of such a layer if it formed in equilibrium with the silicate part, from a S-saturated Mercury (Cartier et al., 2020; Pirotte et al., 2023).

There are still major questions regarding the mineralogy of the mantle. Notably, the proportion of olivine to pyroxene is unknown, as well as the composition and the proportion of the Fe-free sulfides, and their role during partial melting and the incorporation of various elements. In this study, we use surface compositions for titanium, chromium, and manganese as proxies to obtain information on the mineralogy of Mercury's mantle. Since Goldschmidt (1937), elements have been classified as lithophile, chalcophile, or siderophile. Lithophile elements are rock-forming, chalcophile ones bind with sulfur, and siderophile ones are incorporated in metals. However, redox conditions change the behavior of elements (e.g., McCoy et al., 1999; Wholers and Wood, 2015, 2017, Steenstra et al., 2020a). At the redox conditions expected for Mercury (IW-2.6 to -6.3, McCubbin et al., 2012), the partitioning behaviors of Ti, Cr and Mn change strongly. In particular, at low oxygen fugacity (~IW-4), all elements are incorporated into FeS, while Mn and especially Cr partitions also into metals (Cartier et al., 2020; Nittler et al., 2023; Pirotte et al., 2023). At lower fO_2 (<IW-4) even Ti is reduced and incorporated into metals (Cartier et al., 2020; Pirotte et al., 2023). Combining the use of these three elements may provide several constraints on mantle mineralogy because their behaviors are different from each other; Cr is the most siderophile of the three, and both Cr and Mn are strongly incorporated into sulfides. Ti, on the other hand, is the most lithophile of these 3 elements, being only slightly incorporated in both sulfides and metals compared to Cr and Mn. Here, starting with a bulk chondritic composition, we model the distribution of Ti, Cr, and Mn during differentiation between the core and the silicate part. As these elements also have different behavior during partial melting of the mantle, they are powerful proxies to probe mantle mineralogy that can reconcile the surface data with the expected bulk silicate Mercury composition in Ti, Cr and Mn.

5.2 Compilation of experimental data

5.2.1 The concentration of Ti, Cr and Mn at the surface of Mercury

The first measurements of Ti concentration were reported by Nittler et al. (2011), but the dataset was limited. Later, Weider et al. (2014) presented data for Ti, Cr and Mn acquired during 55 large solar flares. Concentrations of elements are given as ratios relative to Si as they are more accurate than absolute abundances (Nittler et al., 2011). Cartier et al. (2020) and Nittler et al. (2023) gave the latest and most precise concentration in Ti and Cr, respectively. The quality of the MESSENGER data for Mn is unlikely to be improved (Larry Nittler, personal communication). The available concentrations for the three elements are shown in Table 5-1.

Table 5-1: Upper: average concentration of Ti, Cr and Mn at the surface of Mercury and their associated errors. Lower: Ti/Cr and Mn/Cr ratios calculated using different datasets. a) Nittler et al., 2018a; b) Cartier et al., 2020; c) Nittler et al., 2023.

	Average[a]	Error	Average[b]	Error	Average[c]	Error
Ti/Si	0.012	0.001	0.0083	0.004	/	/
Cr/Si	0.006	0.001	/	/	0.0008	0.00024
Mn/Si	0.004	0.001	/	/	/	/
Cr/Ti[a]	0.50	0.13				
Cr/Ti[b-c]	0.10	0.06				
Mn/Ti[a]	0.33	0.11				
Mn/Ti[a-b]	0.48	0.35				
Mn/Cr[a-c]	5	2.75				

While some Ti/Si variations on the surface were observed in Cartier et al. (2020), it was not possible to construct a map of the Ti abundance. For Cr, Nittler et al. (2023) built a chemical map of the southern hemisphere, which highlights that the highest abundance of Cr (Cr/Si ~ 0.0012) are observed in the Mg-rich terranes, while the lowest ones (Cr/Si ~ 0.00036) are seen in the Al-rich Caloris Basin.

5.2.2 Parameterization of metal-silicate partition coefficients

There have been numerous studies producing partitioning data for Ti, Cr, and Mn between metal and silicate melts. We compiled and parameterized them using a least squares regression method. The following studies were used for the parameterizations: Ti: Cartier et al., 2020; Pirotte et al., 2023; Cr: Jana and Walker, 1997; Righter et al., 2010; Siebert et al., 2011; Wood et al., 2014; Boujibar et al., 2019; Pirotte et al., 2023; Mn: Righter et al., 2010; Siebert et al., 2011; Pirotte et al., 2023 (Figure 5-1).

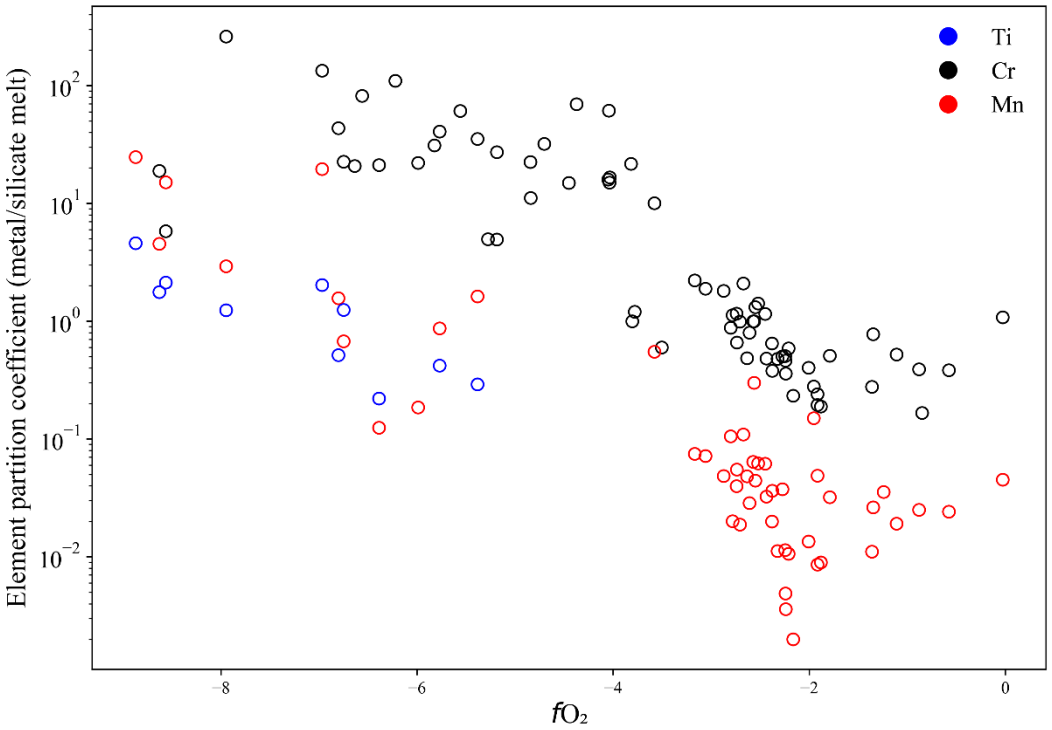

Figure 5-1: Metal/silicate melt partition coefficients of Ti, Cr and Mn as a function of fO_2. We selected only data points from metals containing less than 1 wt% S, present in samples without FeS.

The partition coefficients were expressed as:

$$\ln(D_x^{A/B}) = a + b \times \log(fO_2) \quad (1)$$

where X is the element, A and B are the two phases (A = metal and B = silicate melt), and a and b are two coefficient parameters determined empirically. Oxygen fugacity was recalculated for every experiment using the following equilibrium reaction (Cartier et al., 2014b):

$$Si^{Met} + O_2 = SiO_2^{Sil}$$

For experiments where the concentration of Si in the metal was not available, we used the following equilibrium:

$$Fe^{Met} + ½\ O_2 = FeO^{Sil}$$

Oxygen fugacity was calculated by considering the effect of temperature and pressure, relative to the difference with the iron-wüstite (IW) buffer. Details on the calculations can be found in Namur et al., (2016a).

The calculated coefficients are given in Table 5-2. We only took data points where no S was present in the metal (wt% S < 1), and in samples with no FeS. As Cr and Mn are highly chalcophile, we wanted to limit the risk of contaminating of metal-silicate partition coefficients with sulfide-silicate ones from possible FeS blobs in metals.

Table 5-2: Coefficients of regression (Eq. (1)). R^2 is the coefficient of determination, F is the score of a F-test for a significant linear regression between the response variable and the predictor variables, σ is the standard error on the calculated D, and n is the number of observations.

Eq. (1)	a	b	R^2	F	σ	n
$D_{Ti}^{metal/silicate\ melt}$	-5.426	-0.7231	0.861	37.25	0.4326	8
Standard error	0.878	0.118				
$D_{Cr}^{metal/silicate\ melt}$	-2.5499	-1.051	0.78	194.7	0.9324	57
Standard error	0.266	0.075				
$D_{Mn}^{metal/silicate\ melt}$	-4.911	-0.6397	0.411	28.57	1.054	43
Standard error	0.346	0.12				

The parameterization of Mn is rather poor, but we took the error (σ) into account in our models.

5.2.3 Ti, Cr and Mn in silicate minerals

Using experiments and modelling on surface lavas of Mercury, Namur et al. (2016b) showed that, because of the very high degrees of melting of Mercury's lava (between 20 to 50%), the residual mantle sources contain olivine and pyroxene with Mg end-member compositions (forsterite and enstatite). The partitioning of Ti, Cr and Mn in olivine and pyroxene is relatively well understood (Colson et al., 1986; Dunn, 1987; Gaeteni & Grove, 1997; Hanson & Jones, 1998; Xirouchakis et al., 2001; Papike et al., 2005; Figure 5-2), even at low fO_2 (Mikouchi et al., 1994; Cartier et al., 2014b; Namur et al., 2016b; Figure 5-2). Average values and standard deviations for partition coefficients between olivine/pyroxene and the silicate melt are given in Table 5-3.

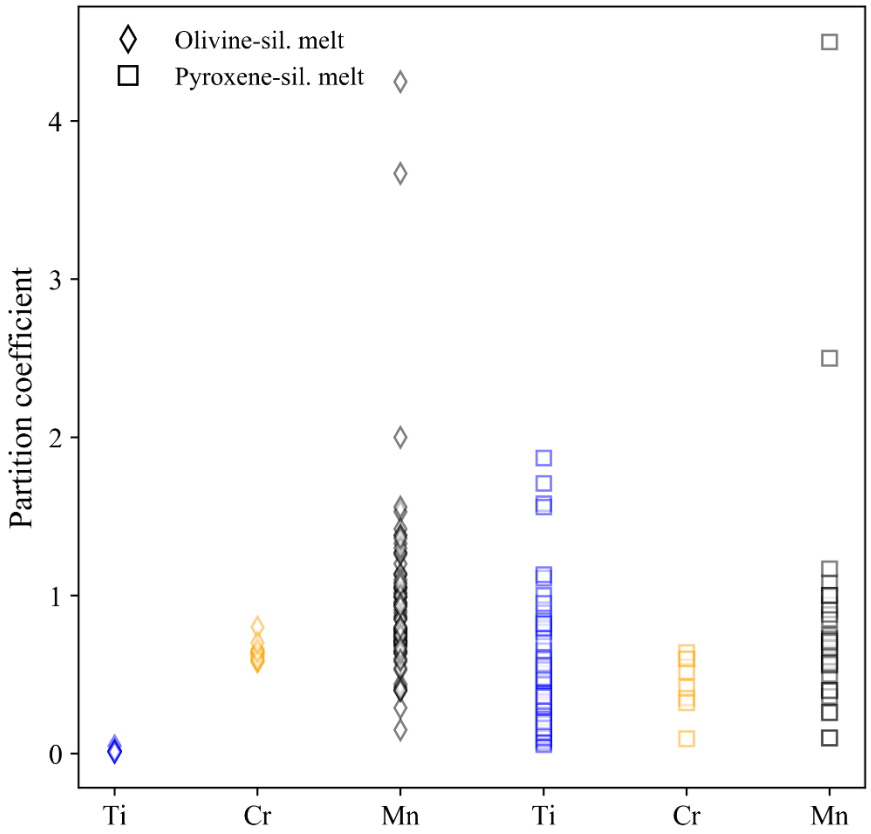

Figure 5-2: Partition coefficients from the literature. Diamond and square shaped markers represent olivine – silicate melt and pyroxene – silicate melt partition coefficients, respectively.

Table 5-3: Average partition coefficients between olivine (ol)/pyroxene (px) and the silicate melt for Ti, Cr and Mn and their respective standard deviation. An estimation of the range of oxygen fugacity of the experiments is also given.

	fO_2	$D_{Ti}^{Ol/melt}$	σ	$D_{Cr}^{Ol/melt}$	σ	$D_{Mn}^{Ol/melt}$	σ	$D_{Ti}^{Px/melt}$	σ	$D_{Cr}^{Px/melt}$	σ	$D_{Mn}^{Px/melt}$	σ
Colson et al., 1986	IW+0.5					0.961	0.160					1.083	0.045
Dunn 1987	IW+4 to IW+3	0.017	0.001			1.443	0.063	0.400	0.031			0.863	0.037
Forsythe et al., 1994	IW+4							0.511	0.350				
Mikouchi et al. (1994)	IW+5 to IW-3			~0.8	~0.2	~1	~0.2						
Gaetani et Grove 1997	IW			0.622	0.025	0.721	0.039						
Hanson & Jones, 1998	<IW-1			~0.7									
Xirouchakis et al., 2001	IW+4 to IW	0.016	0.012					0.107	0.033				
Cartier et al., 2014b	IW-1 to IW-8							0.199	0.068	0.443	0.173	0.382	0.140
Namur et al., 2016a	IW-1 to IW-8					0.947	0.828	0.557	0.469			1.017	0.891

Mikouchi et al. (1994) showed that $D_{Cr}^{olivine/silicate\ melt}$ and $D_{Mn}^{olivine/silicate\ melt}$ are constant from IW - 3 to IW + 5. Their high temperature experiments (1400 °C) show a $D_{Cr}^{olivine/silicate\ melt}$ and $D_{Mn}^{olivine/silicate\ melt}$ of ~0.6 and ~0.8, respectively, while their low temperature experiment (1225°C) show values of 0.9 and 1.2, respectively. Hanson & Jones (1998) showed $D_{Cr}^{olivine/silicate\ melt}$ ~ 0.7 at the IW buffer, with a slight increase for more reducing conditions (up to ~0.75). Of these three elements, Mn exhibits the most compatible behavior, with the average from the literature ranging $D^{olivine/melt}$ and $D^{enstatite/melt}$ from ~0.7 to ~1.4 and ~0.4 to ~1 respectively. Cr is relatively incompatible with average $D^{olivine/melt}$ and $D^{enstatite/melt}$ around ~0.6 and ~0.45 respectively. Finally, Ti is rather incompatible, with $D^{olivine/melt}$ ~0.015 and $D^{enstatite/melt}$ between ~0.1 and ~0.55.

Table 5-3 shows that the partitioning data are consistent among the literature. We decided to take the average of the available data in our model; $D_{Mn}^{olivine/melt}$ and $D_{Mn}^{enstatite/melt}$ of 1 and 0.8, respectively, $D_{Cr}^{olivine/melt}$ and $D_{Cr}^{enstatite/melt}$ of 0.7 and 0.45 respectively, and $D_{Ti}^{olivine/melt}$ and $D_{Ti}^{enstatite/melt}$ of 0.015 and 0.4 respectively.

5.2.4 Ti, Cr and Mn in sulfides

Namur et al. (2016a) estimated that there should be between 7 to 11wt% of sulfur in the magma ocean, which roughly corresponds to 14 to 22wt% of sulfides (Fe-free sulfides, such as MgS and CaS). Under reducing conditions, the three elements partition into FeS, CaS and MgS, with Mn and Ti being the most and the least chalcophile respectively. We have a lot of data for FeS/silicate melt partitioning, but data for partitioning in MgS or CaS are scarce. The partitioning data for Ti, Cr and Mn between Fe-free sulfides and the silicate melt are listed in Table 5-4.

Table 5-4: Partition coefficients of Ti, Cr and Mn between CaS/MgS and the silicate melt. The chemical analyses of VT030, VT039B, VT040 and VT052 were performed by Laurie Lldó.

Study	Experiment	Sulfide	P (GPa)	T (°C)	$D^{sulfide/silicate}$ Ti	$D^{sulfide/silicate}$ Cr	$D^{sulfide/silicate}$ Mn
Pirotte et al. (2023)	Y087-2*	MgS	0.1	1520	6.6	16.8	16.2
This work	A029	MgS	1.31	1400	32.3	11.3	133.6
This work	A030	MgS	1.31	1500	11.1	38.4	54.7
This work	VT030	CaS	0.0001	1300	0.5	13.7	24.4
This work	VT39B*	CaS	0.0001	1350	0.5	7.6	9.4
This work	VT040	CaS	0.0001	1350			43.6
This work	VT052	CaS	0.0001	1350	0.6	14.1	29.3
Ingrao et al. (2019)	1250	CaS	0.0001	1300	0.1		7.7
Ingrao et al. (2019)	1263	CaS	0.0001	1300	0.1		11.6
Ingrao et al. (2019)	1208	CaS	0.0001	1400	34.0		1.3
Ingrao et al. (2019)	1240	CaS	0.0001	1400			
Ingrao et al. (2019)	1246	CaS	0.0001	1400	0.1		4.5
Ingrao et al. (2019)	1305	CaS	0.0001	1400	0.1		12.9
Ingrao et al. (2019)	1244	CaS	0.0001	1400			5.8
Ingrao et al. (2019)	1304	CaS	0.0001	1400	0.1		21.9

** Measure performed with the LA-ICPMS*

Based on these data, we decided to take the following partitioning values for CaS and MgS: $D^{CaS/silicate\ melt}$ for Ti, Cr and Mn are 0.5, 15 and 30, respectively, and $D^{MgS/silicate\ melt}$ for Ti, Cr and Mn are 15, 25 and 50, respectively. While we observe strong variations among the data presented in Table 5-4, the most important result we want to highlight and that will impact our model is the low incorporation of Ti in oldhamite (except for one point, experiment 1208, that we consider to be an outlier). The variations of the values of the other partition coefficients do not change the conclusions of our models.

5.2.5 Ti, Cr and Mn in the building blocks

In chondrites, the concentration of Ti, Cr and Mn are fairly constant, around ~620 ± 140 for Ti, ~3300 ± 350 for Cr and ~2000 ± 410 for Mn, which is caused by their refractory nature (Ti and Cr are refractory, and Mn is only slightly volatile, Albarède, 2009). The Mn/Ti and Cr/Ti are respectively ~3.4 ± 1 and ~5.5 ± 0.9. For this work, we used the concentration reported in Lodders and Fegley (1998) for the EH (Table 5-5), thought to be potential main building block of Mercury (e.g. Cartier and Wood, 2019). It is important to note that, as explained above, it is possible to take other chondritic concentrations as starting compositions, or even a mix of them, as they have similar Ti, Cr and Mn concentrations.

Table 5-5: Concentration of Cr, Mn and Ti in chondrites (in ppm) and the calculated ratios. Ordinary: H, L and LL; Enstatite: EH and EL; Carbonaceous: CI, CM, CV and CO. a) data from Lodders and Fegley (1998) and b) data from Wasson and Kallemeyn (1988).

	H	L	LL	EH	EL	CI	CM	CV	CO
Cr[a]	3500	3690	3680	3300	3030	2650	3050	3480	3520
Cr[b]	3660	3880	3740	3150	3050	2650	3050	3600	3550
Mn[a]	2340	2590	2600	2120	1580	1940	1650	1520	1620
Mn[b]	2320	2570	2620	2200	1630	1900	1700	1450	1650
Ti[a]	630	670	680	460	550	440	550	870	730
Ti[b]	600	630	620	450	580	420	580	980	780
Mn/Ti[a]	3.71	3.87	3.82	4.61	2.87	4.41	3.00	1.75	2.22
Mn/Ti[b]	3.87	4.08	4.23	4.89	2.81	4.52	2.93	1.48	2.12
Cr/Ti[a]	5.56	5.51	5.41	7.17	5.51	6.02	5.55	4.00	4.82
Cr/Ti[b]	6.10	6.16	6.03	7.00	5.26	6.31	5.26	3.67	4.55

Using the parameterization obtained with equation (1), we calculated the distribution of Ti, Cr and Mn between the silicate part and the core.

5.3 Discussion

5.3.1 Core-silicate differentiation: concentrating Mn and depleting Cr

We developed a model to estimate the distribution of Ti, Cr and Mn between the silicate part (mantle + crust) and the core during planetary differentiation. We calculated the mass of the core and the silicate part using their mean density and volume (Hauck et al., 2013). We considered a core radius of 2000 km and a silicate layer of 440 km. The starting bulk composition of the planet in Ti, Cr and Mn were derived from their concentration in chondrites (Table 5-5). We do not consider the presence of an FeS layer formed in equilibrium with the silicate part per the recent studies (e.g., Cartier et al., 2020; Pirotte et al., 2023). The strong siderophile nature of Cr at low fO_2 highly concentrates this element in the metallic core during differentiation, as previously calculated by Nittler et al. (2023). Cr is thus strongly depleted in the bulk silicate Mercury (BSM) relative to chondritic value. Mn, on the other hand, is concentrated in the BSM, even at low oxygen fugacity (IW~5), because it is dozens of time less siderophile than Cr. Ti is roughly similarly siderophile as Mn, and thus there is not a strong fractionation between Mn and Ti during metal-silicate differentiation.

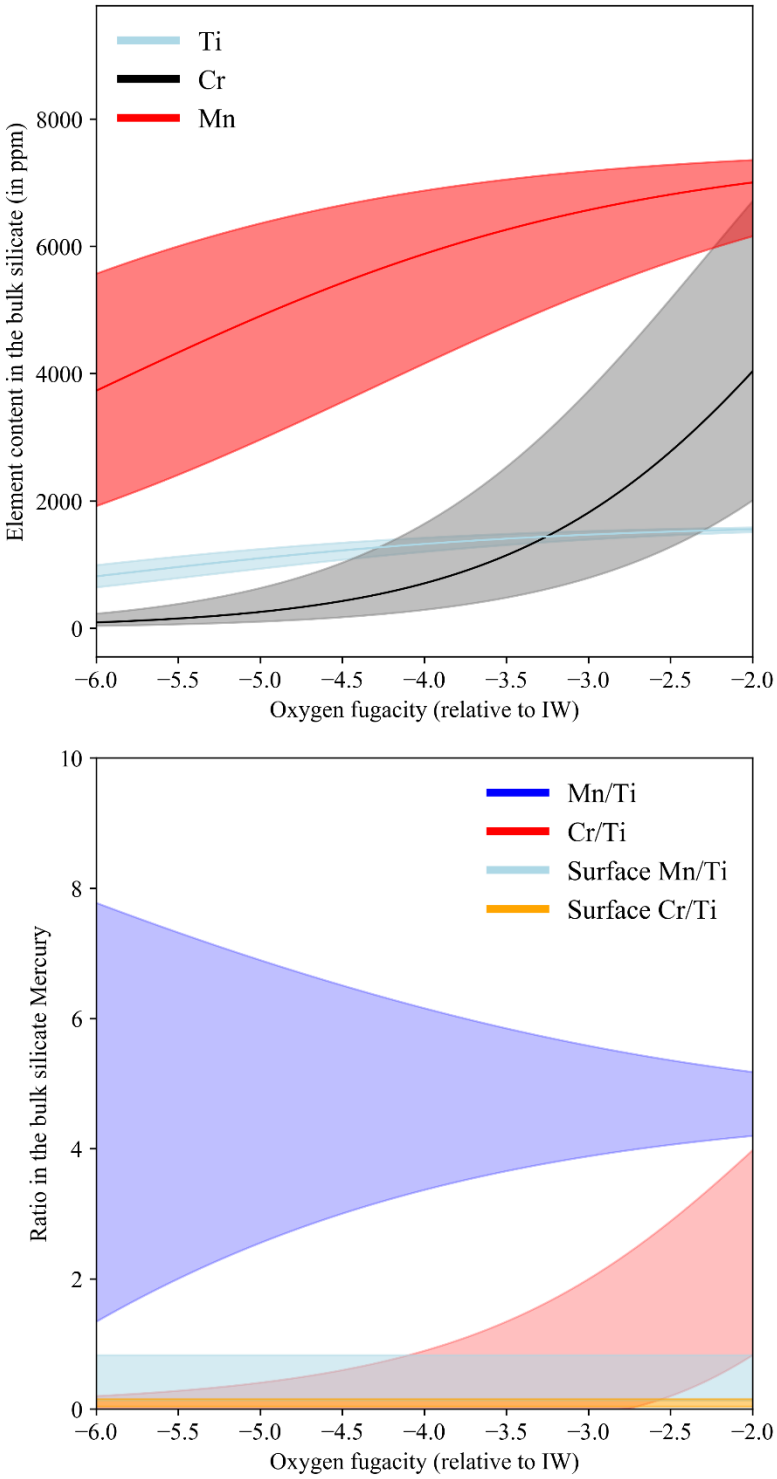

Figure 5-3: Upper: expected content (in ppm) of the three elements in the BSM. Lower: expected Cr/Ti and Mn/Ti in the BSM after differentiation as function of oxygen fugacity. For Mn/Ti, the expected ratio is too high compared to the measure one. Fractionation processes during partial melting are necessary (and expected) to reach the measured ratios of the surface lavas.

As seen in Figure 5-3, the surface content of Ti, Cr and especially Mn should not be representative of the BSM. This is not surprising, given that the three elements have different behaviors during the formation of lavas. However, while the BSM content of Ti and Cr matches reasonably the one measured

on the surface at low oxygen fugacity, the BSM content of Mn is very different from the surface. This observation requires Mn to have a very strong compatible behavior during partial melting.

5.3.2 Partial melting of the mantle

We can simulate partial melting of the mantle and test whether the lavas produced have Mn/Cr and Ti/Cr ratios similar to what is observed on the surface using Shaw's batch melting equation (Shaw, 1970):

$$\frac{C_L^M}{C_0^M} = \frac{1}{(D+(1-D))\cdot F} \quad (2)$$

where $C_L{}^M$ is the concentration of an element M in the melt, $C_O{}^M$ is the concentration of an element M in the rock (mantle), D is the global partition coefficient between the mantle and the melt, and F is the fraction of partial melting. Batch adiabatic decompression and melting is the favored hypothesis for lavas formation during a large time frame on Mercury (Namur et al., 2016a). The global partition coefficient D of an element M between the mantle and a melt is the sum of the partition coefficient $D_M{}^{C/melt}$ of each component C multiplied by their fraction x in the mantle. For this work, we decided to use the data from Nittler et al. (2018a), Cartier et al. (2020) and Nittler et al. (2023) for Mn, Ti and Cr respectively (Table 5-1); surface Cr/Ti is 0.1 ± 0.06 and Mn/Ti is 0.48 ± 0.35. By combining those with the BSM data, we can calculate global $D^{mantle/melt}$ for each element using equation (2). Varying the fO_2, changes the bulk silicate content of the three elements. F, the degree of partial melting of the mantle, varies on Mercury from 0.2 to 0.5 (Namur et al., 2016b). The surface data obtained are however not precise enough to clearly see the effect of the different terrains (and so different F) on the content of Ti and Mn; Cartier et al. (2020) did not observed changes in Ti/Al consistent with different Mg/Si, which should be expected as Mg/Si is good proxy to estimate the degrees of partial melting from which the lavas were produced. On the other hand, Nittler et al. (2023) showed that Cr/Si is correlated with the degree of partial melting. In order to keep things simple, we decided to fix the fraction of partial melting (F) to 0.4. We discuss the effect of different partial melting later in this work.

By modeling batch melting of the mantle and varying the compatibility of Ti, Cr and Mn, we can estimate the global $D^{mantle/melt}$ for each element that match surface Cr/Ti and Mn/Ti (Figure 5-4).

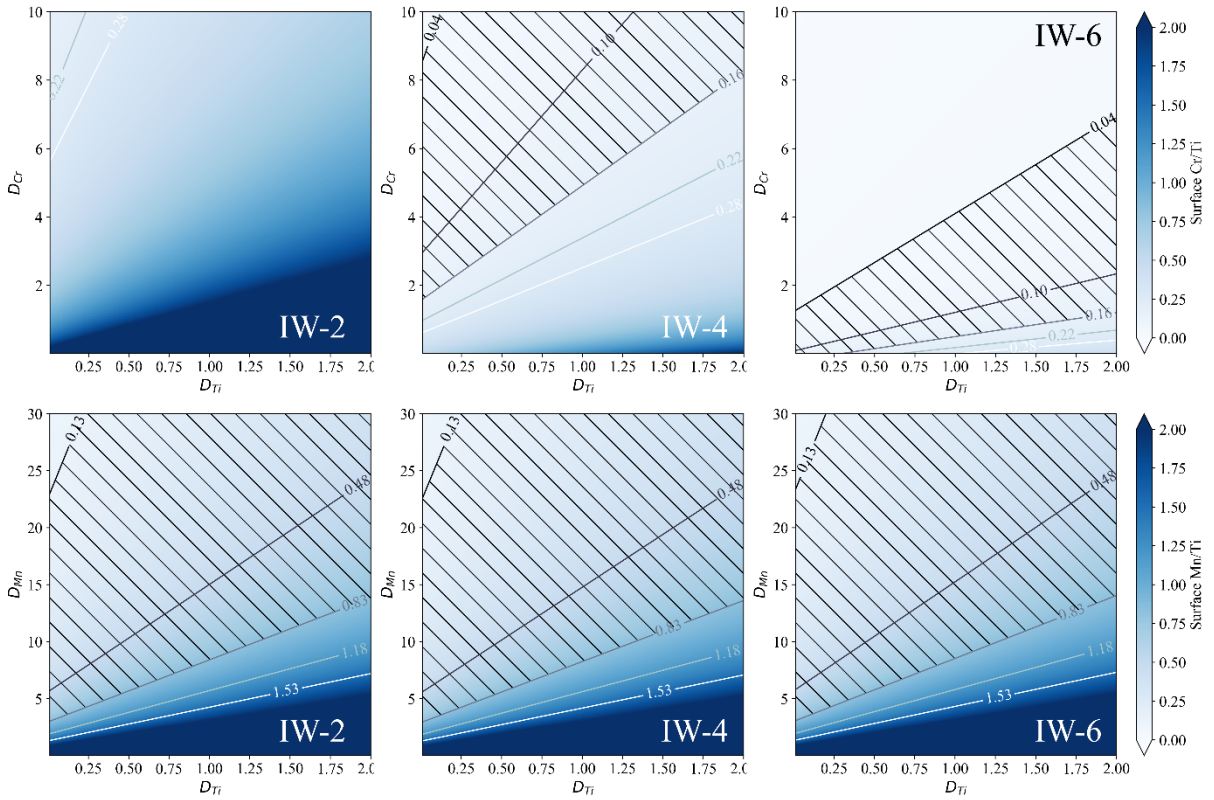

Figure 5-4: Meshgrids of surface Cr/Ti and Mn/Ti as a function of $D_{Cr}^{mantle/melt}$ and $D_{Ti}^{mantle/melt}$, and $D_{Mn}^{mantle/melt}$ and $D_{Ti}^{mantle/melt}$, respectively, for a fraction of partial melting of 0.4. The panels from left to right are made at fO_2 of IW-2, IW-4 and IW-6 respectively. The average surface Cr/Ti and Mn/Ti is 0.16 ± 0.06 and 0.48 ± 0.35 respectively, and are represented by the hatched area on the meshgrids. Each line further from the average represent additional σ. For IW-2 (upper left), the calculated surface Cr/Ti is so high that only 2σ and 3σ can be shown (no hatched area in this panel).

We can see that oxygen fugacity does not have a strong effect on the required partitioning for Ti and Mn to match surface Mn/Ti, while the depletion of Cr in the BSM with lower fO_2 changes its expected behavior from compatible to incompatible in order to concentrate it in the lavas and reach the observed Cr/Ti. While the expected behavior of Cr during mantle partial melting is dependent on the redox conditions, Mn is either compatible ($D_{Mn}^{mantle/melt} > 3$) or very compatible ($D_{Mn}^{mantle/melt} > 20$). Moreover, the recent work from Cartier et al. (2020) and Nittler et al. (2023) showed that the initial measurements of Ti/Si and Cr/Si were too high, and so we may reasonably expect that the values of Mn/Si we have are also overestimated, and may represent the upper limits, because the higher values were easier to measure by MESSENGER than lower ones. If so, the expected Mn/Ti might be even lower, requiring that Mn has an even more compatible behavior during partial melting.

5.3.3 The mineralogy of the residual mantle

In the following sections, we use global partition coefficients calculated using mantle batch melting to find the possible mineralogy that can account for the observed surface Mn/Ti and Cr/Ti. The global partition coefficient $D^{mantle/melt}$ of an element M is expressed as:

$$D_M^{mantle/melt} = \sum^{n} x_n \times D_M^{C_n/melt}$$

where x is the fraction of each component and $D_M^{C/melt}$ is the partition coefficient between a component C and the melt. Thanks to the relatively simple mineralogy of Mercury's residual mantle (Namur et al., 2016), we can simplify the global partition of each element as:

$$D_M^{mantle/melt} = x_{olivine} \times D_M^{olivine/melt} + x_{pyroxene} \times D_M^{pyroxene/melt} + x_{unknown} \times D_M^{unknown/melt}$$

where "unknown" is an unknown component, which may encompass multiple minerals. The goal here is to find values for $x_{unknown}$ and $D^{unknown/melt}$ that could explain the expected $D^{mantle/melt}$ for Ti, Cr and Mn. Because $D^{olivine/melt}$ and $D^{pyroxene/melt}$ are constrained thanks to the compiled data (Table 5-3), there is a minimum possible $D^{mantle/melt}$ below which $D_M^{unknown/melt}$ has to be negative, which is impossible. Depending on the proportion of olivine, pyroxene and unknown phase(s) (we consider that the fraction of the unknown component cannot exceed 20%, which is close to the upper limit of the fraction of sulfides in the mantle; Namur et al., 2016a), the minimum $D^{mantle/melt}$ for Ti, Cr and Mn are between ~0.07 and 0.32, 0.36 and ~0.7, and ~0.64 and 1, respectively. While the minimum $D^{mantle/melt}$ for Ti and Mn do not bring a lot of constrain, the one for Cr means that it is not as incompatible as Figure 5-4 shows for low $D_{Ti}^{mantle/melt}$.

5.3.4 Manganese: a proxy for sulfides composition of the mantle

Out of these three elements, only Mn should be clearly strongly compatible under any circumstances (Figure 5-4). Indeed, the lack of incorporation of Mn into the core suggests that it is concentrated in the BSM. However, its relatively low concentration on the surface means that it probably stays in the residual mantle during partial melting. At least one stable phase at high degree of partial melting (>20%) should contain Mn. Sulfides are probable candidates, because they are expected to be a major component of Mercury's mantle (7-11 wt% S in the mantle, Namur et al., 2016b). These sulfides should be Fe-poor (as is the whole BSM, e.g., Nittler et al., 2011; Murchie et al., 2015), and probably with an MgS and or CaS composition (e.g., Namur et al., 2016a, Boukaré et al., 2019).

We find in enstatites chondrites Fe-free cubic monosulfides, such as oldhamite (CaS), niningerite (MgS) and alabandite (MnS), that are part of a complex solid solution where the major cations Ca, Mg, and Mn can substitute (Skinner and Luce, 1971). We found experimentally that MgS can incorporate Ti, Cr and Mn (with Mn being the most compatible, Table 5-4), which confirms the measurements made on natural niningerite, which show higher Mn content than Cr content (~4 to ~12 wt% vs ~0.15 to ~1.8 wt% respectively, Keil and Snetsinger, 1967). For natural oldhamites, studies showed that Cr incorporation is very low (<0.05 wt%) while Mn is high (above 0.2 wt% and up to ~1.3 wt%, Keil, 1968; Hsu, 1998). Ti is the least incorporated element in sulfides, as observed experimentally (Table 5-4; Pirotte et al., 2023) and in meteorites (15 to 100 times less incorporated than Mn, Hsu, 1998; ~260 less incorporated

in niningerite than Mn, and not detected in oldhamite, Lehner et al., 2013). Data from Wadhwa et al. (1997) show that Mn/Cr are >1000 in sphalerite (ZnS, except in Indarch meteorites where the lowest ratio measured was ~170) and alabandite (MnS), and ~100 in niningerite. All these data show that Mn is very compatible in Fe-free sulfides, and that they could be the reason for its compatibility in Mercury's mantle.

By calculating the $D_{Mn}^{unknown/melt}$ as function of $x_{unknown}$ and $D_{Mn}^{mantle/melt}$ (Figure 5-5), we find that, logically, there needs to be a phase that incorporates increasing amount of Mn for higher $D_{Mn}^{mantle/melt}$. In the same way, if the proportion ($x_{unknown}$) of this phase in the mantle is low, then it means that it must incorporate even more Mn.

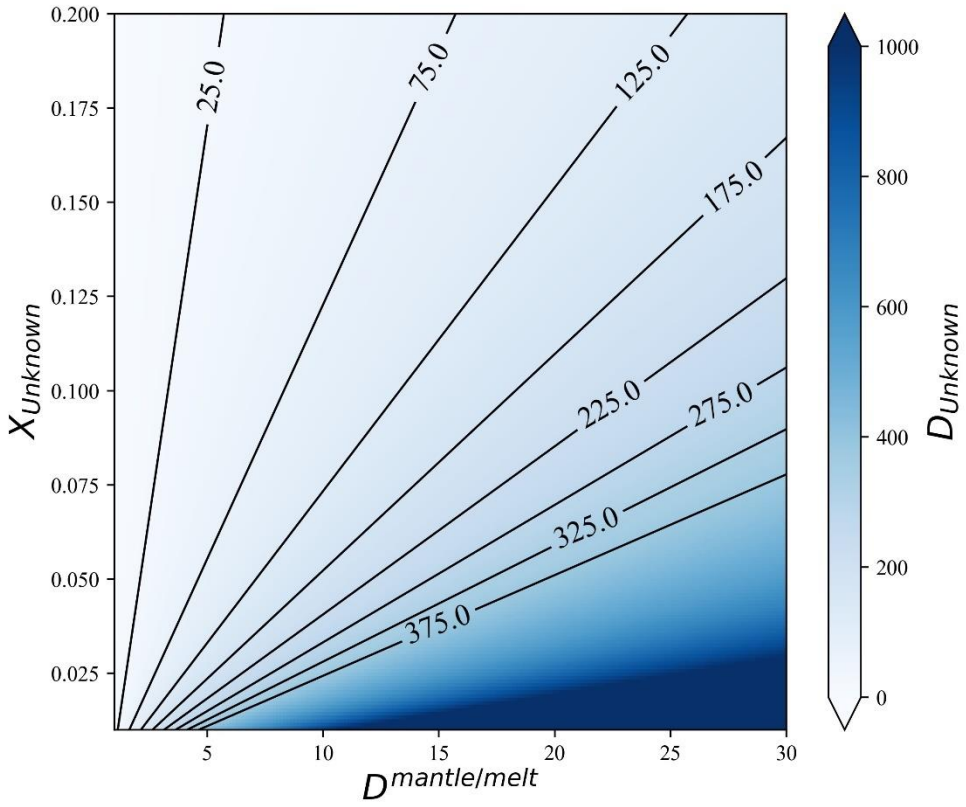

Figure 5-5: Expected partition coefficients D_{Unkown} between the mantle and the unknown phase as a function of the fraction of residual x_{Unkown} in the mantle and the global $D^{mantle/melt}$.

Interestingly, Mn is not chalcophile enough to explain its high compatibility by its incorporation in just one major phase for all the data points where $D_{Mn}^{unknown/melt}$ above ~130 (Figure 5-5), which roughly correspond to the highest $D_{Mn}^{sulfide/melt}$ experimentally measured (Table 5-4). Even though $D_{Mn}^{CaS/silicate\ melt}$ and $D_{Mn}^{MgS/silicate\ melt}$ are high (between 1 to ~40 and ~15 to ~130, respectively), their values are not as high as required from the results in Figure 5-5. An MnS (alabandite) phase in the mantle could be responsible for Mn compatibility, especially if CaS is the dominant sulfide. Indeed, stoichiometric MnS contains 63.14 wt% of Mn. If the unknown phase containing Mn is only made up of MnS, we can calculate its proportion in the mantle to satisfy the expected $D_{Mn}^{unknown/melt}$; there should be 0.63wt% and

1.1 wt% MnS in the mantle for a BSM Mn content of ~4000 (IW-6) and ~7000 (IW-2), respectively. However, because we expect MgS and/or CaS to be present, Mn should also be present in these phases, and part of it in MnS, which should make a small fraction of the sulfide inventory of Mercury's mantle.

5.3.5 Chromium: surface variations linked to melting of Cr-rich sulfides

Nittler et al. (2023) provided Cr/Si maps of Mercury's surface, and correlations are visible between the degree of partial melting and the resulting Cr/Si. The High-Mg regions have the highest Cr/Si, while the Caloris basin has the lowest. It seems that higher partial melting increases its incorporation in the melt, so that the melting of a Cr-rich phase could be responsible for this behavior. The lowest and the highest Cr/Si gave us respectively the upper and the lower limit for Cr compatibility during partial melting of the mantle. If, as it has been suggested, the mantle is rich in sulfides (e.g., Namur et al., 2016a), then they could be host candidates for Cr as it is highly chalcophile under reducing conditions. As seen in the previous section, MgS or CaS sulfides could be (at least partially) responsible for the high compatibility of Mn in the mantle, and Cr also has high affinity in both CaS and MgS (Table 5-4). Cr is relatively incompatible in both olivine and pyroxene (see section 5.2.3), and so the presence of sulfides in the mantle could be responsible for its compatibility. Other Cr-bearing minerals, such as chromite, should not be common due to the quasi absence of FeO in Mercury's silicate part.

Because the regions with the highest Mg/Si on the surface also correspond to higher S/Si and Cr/Si, an increased fraction of Cr-rich sulfides that melts with higher degree of partial melting caused by increased temperatures could explain these observed ratios, enriching the lava in both Cr and S. Data from Nittler et al. (2023) show that Cr/Ti varies from ~0.04±0.02 to ~0.14±0.07, if we consider that Ti/Si is constant on the surface, as the measurements do not show surface variation of Ti/Si (Cartier et al., 2020). A CaS dominated mantle (~20 wt% CaS) produces Cr/Ti varying from ~0.05 to ~0.13 with fraction of partial melting from 0.2 to 0.6 at IW-4.5 (Figure 5-6). This scenario roughly corresponds to what is observed on the surface, but it is important to keep in mind that we lack data on the variation of Ti/Si in the different terranes.

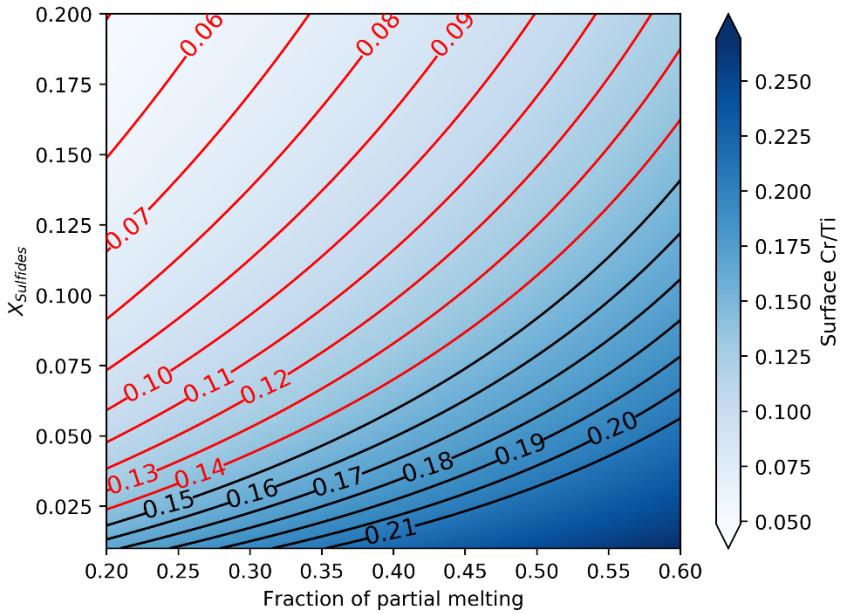

Figure 5-6: Calculated Cr/Ti of lavas as function of the fraction of partial melting and the fraction of sulfides in the mantle. The lines in red correspond to the variation of Cr/Ti on the surface from 0.04 to 0.14, while the lines in black show the variations including 1σ error. In this scenario, the mantle is dominated by pyroxene and CaS, and the primordial differentiation occurred at IW-4.5. $D_{Ti}^{CaS/silicate\ melt}$ *and* $D_{Cr}^{CaS/silicate\ melt}$ *are 0.5 and 15, respectively.*

The proportion of pyroxene to olivine is also an important factor, as well as oxygen fugacity during primordial differentiation, and these parameters are explored in section 5.3.7. In any case, the presence of CaS in the mantle is consistent with the observed Cr/Si varying with partial melting, and there are large margins to change different parameters to produce satisfying scenarios (see section 5.3.7). Other Cr-rich sulfides found in chondrites, such as daubréelite ($FeCr_2S_4$) or brezinaite (Cr_3S_4), are not expected in the mantle as they would increase the compatibility of Cr to extreme value; the presence of MgS and/or CaS already satisfies the observed Cr abundances on the surface.

5.3.6 Titanium: a tracer for the dominant mantle sulfides

Because Ti is not siderophile, its content in the BSM is not as affected by oxygen fugacity as Cr and Mn. The Ti concentration in the BSM varies from ~800 ppm at IW-6 to ~1500 ppm at IW - 2. Cartier et al. (2020) showed that the surface Ti/Al ratio of Mercury is slightly sub-chondritic (0.035±0.008, compared to ~0.058), which can be explained by the incorporation of Ti in the core during the primordial differentiation under an oxygen fugacity of ~IW - 5. The fractionation between Ti and Al by an FeS sulfide layer is thus not expected, as shown in Cartier et al. (2020). In the same way, the presence of Ti-rich sulfides should be unlikely. For now, only one titanium sulfide has been identified: wassonite (TiS), found in enstatite chondrites (Nakamura-Messenger et al., 2012). This mineral is very rare, having been only found in very low quantity in one meteoritic sample (Nakamura-Messenger et al., 2012). MgS, on the other hand, could well be present in large quantity in the mantle. However, because it seems to incorporate large amounts of Ti ($D_{Ti}^{MgS/silicate\ melt}$ between 6 and 30, see Table 5-4), a MgS dominated

residual mantle should strongly decrease the amount of Ti on the surface, and increase the resulting Cr/Ti. Moreover, the lack of variation in Ti/Si with different degrees of partial melting observed by Cartier et al. (2020) is not consistent with a phase incorporating large amount of Ti in the mantle such as MgS.

Because experimental data show that the partitioning of Ti in CaS is low (~0.5, Table 5-4), a CaS dominated mantle should be the most probable solution, assuming that the planet formed under reducing conditions. An MgS-dominated mantle does not sufficiently increase the compatibility of Cr relative to Ti, so that the resulting surface Cr/Ti is too high compared to the observed values (Figure 5-7), even at oxygen fugacity (>IW - 4).

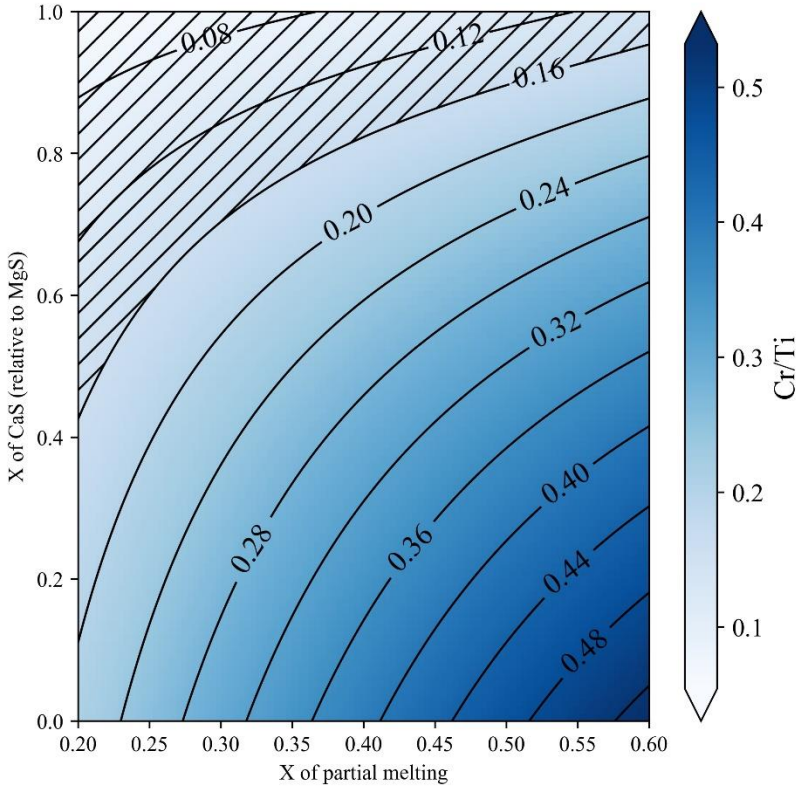

Figure 5-7: Evolution of Cr/Ti as a function of the fraction of partial melting and the fraction of CaS relative to MgS, at IW-4.5 (similar to Figure 5-6). The hatched area corresponds to the average Cr/Ti (0.1 ± 0.06). We consider 20 wt% of sulfides in the residual mantle. Higher MgS fraction increases the Cr/Ti.

5.3.7 Scenarios compatible with surface data

In this section, we explore various scenarios by changing the following parameters to study their influence on the calculated surface Mn/Ti and Cr/Ti: oxygen fugacity, the fraction of Fe-free sulfides in the residual mantle, and the relative abundances of CaS to MgS and of olivine to pyroxene.

5.3.7.1 Oxygen fugacity

The effect of oxygen fugacity is shown in Figure 5-8. The effect of different amounts of CaS in the mantle (0, 10 and 20 wt%) is also shown for comparison. As noted by Nittler et al. (2023), oxygen fugacity has a huge impact on the Cr content in the BSM, which in our simulations leads to increasingly higher Cr/Ti with higher fO_2. On the other hand, oxygen fugacity lower than IW - 6 seems unlikely, as Cr becomes too depleted in the BSM. It seems that a planet Mercury formed between IW - 6 and IW - 4 is the most probable scenario. To isolate the effect of the other parameters, we will fix the oxygen fugacity to IW - 5 for the rest of the discussion, close to the IW - 5.4 value calculated by Namur et al. (2016a).

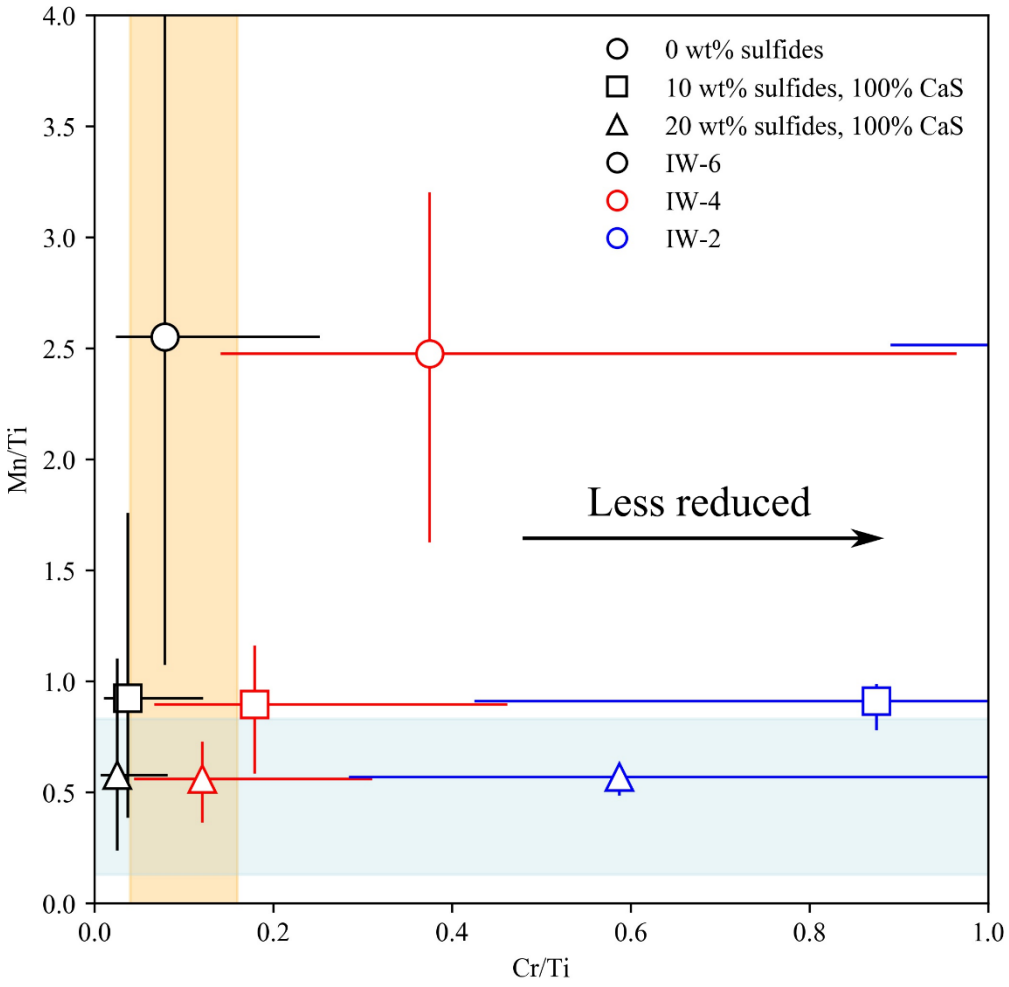

Figure 5-8: Effect of the oxygen fugacity on the calculated surface Cr/Ti and Mn/Ti. The blue and orange areas represent the measured surface Mn/Ti and Cr/Ti, respectively. The global partition coefficients at 0, 10 and 20 wt% CaS are: Ti: 0.208, 0.237, 0.266; Cr: 0.575, 2.018, 3.46; Mn: 0.9, 3.81, 6.72.

5.3.7.2 The proportion of olivine to pyroxene

While Cr and Mn have roughly similar compatibilities in olivine and pyroxene (0.45 vs 0.7 and 0.8 vs 1 for Cr and Mn respectively), Ti is very incompatible in olivine, but quite compatible in pyroxene ($D^{olivine/silicate\ melt} \sim 0.015 << D^{pyroxene/silicate\ melt} \sim 0.4$). If Mercury's mantle is dominated by olivine, then Ti should be very incompatible in the silicates, decreasing the resulting Mn/Ti compared to a pyroxene dominated residual mantle, as more Ti is incorporate in lavas (Figure 5-9). It could however increase the Ti/Si to values higher than measured on the surface. In that case, the presence of Ti-rich sulfides such as MgS in the residual mantle could balance the resulting concentration of Ti by increasing its compatibility in the mantle. As seen in Figure 5-9, although the proportion of olivine and pyroxene has a visible effect on the concentration of Ti in the melts, it is the fraction of Fe-free sulfides in the mantle that dominantly affects the resulting Mn/Ti and Cr/Ti of melts during partial melting.

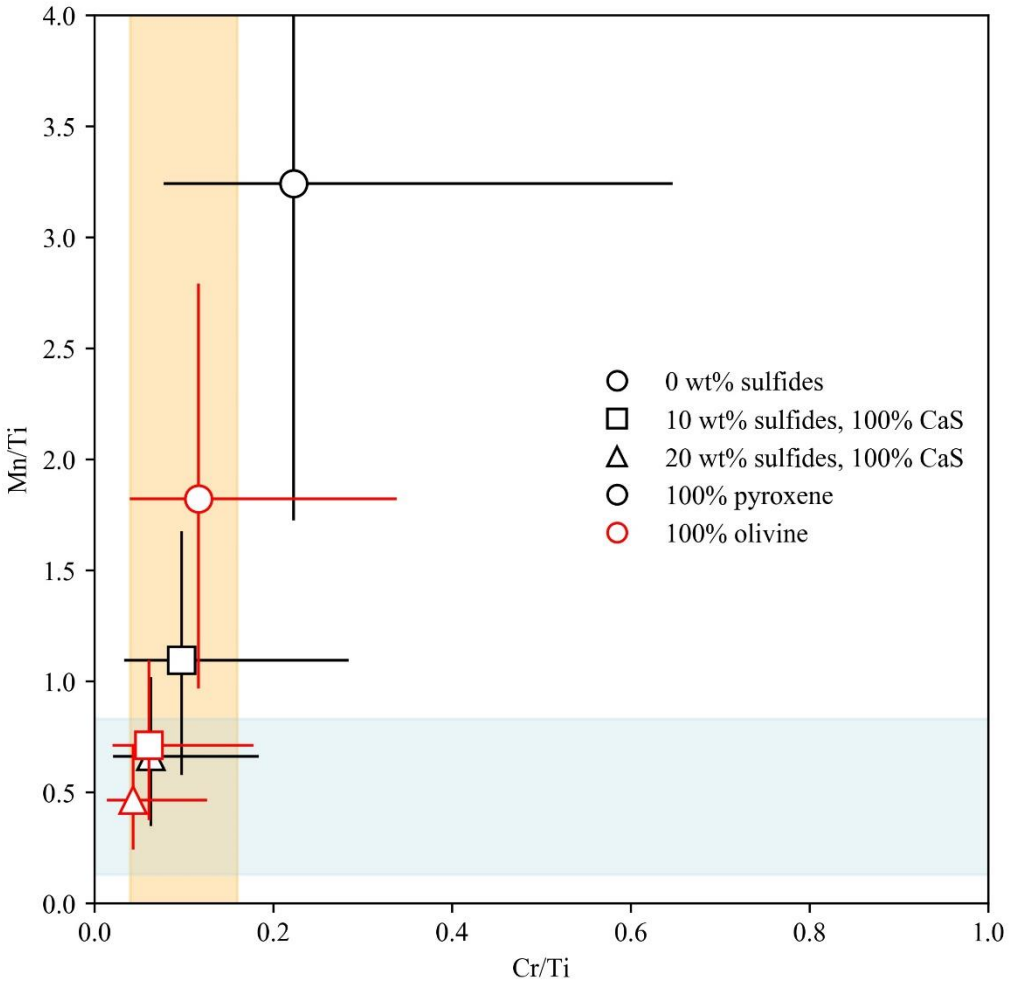

Figure 5-9: Calculated Cr/Ti and Mn/Ti depending on the composition of the silicate dominating the mantle; either pure pyroxene or pure olivine. Increasing amounts of sulfides decreases the total amount of silicates (100, 90 and 80 wt% silicates for 0, 10 and 20 wt% sulfides, respectively). The oxygen fugacity is set to IW - 5. The blue and orange areas represent the measured surface Mn/Ti and Cr/Ti, respectively. The global partition coefficients at 0, 10 and 20 wt% CaS for 100% pyroxene

are: Ti: 0.4, 0.41, 0.42; Cr: 0.45, 1.905, 3.36; Mn: 0.8, 3.72, 6.64. For 100% olivine, they are: Ti: 0.015, 0.064, 0.112; Cr: 0.7, 2.13, 3.56; Mn: 1, 3.9, 6.8.

5.3.7.3 The proportion of MgS to CaS

Although more partitioning data are needed, MgS seems to incorporate more Ti, Cr and Mn than CaS, in agreement with natural samples (see section 5.3.4). In particular, Ti seems incompatible in CaS (D ~ 0.5) but highly compatible in MgS (D ~ 15). As seen in Figure 5-10, a MgS-rich mantle increases the resulting Mn/Ti above surface values. However, because an MnS component might exist in the residual mantle of Mercury, it could decrease the Mn/Ti ratio (not shown in Figure 5-10). The problem with an MgS-rich mantle is that its incorporation of Ti should be visible on the surface, as we would observe different Ti/Si as a function of the degree of partial melting from which the lava originates from, in the same manner Nittler et al (2023) observed for Cr. While the new data from BepiColombo may produce such results, our current knowledge states that the surface Ti/Si does not strongly vary with terranes formed from different degree of partial melting (Cartier et al., 2020).

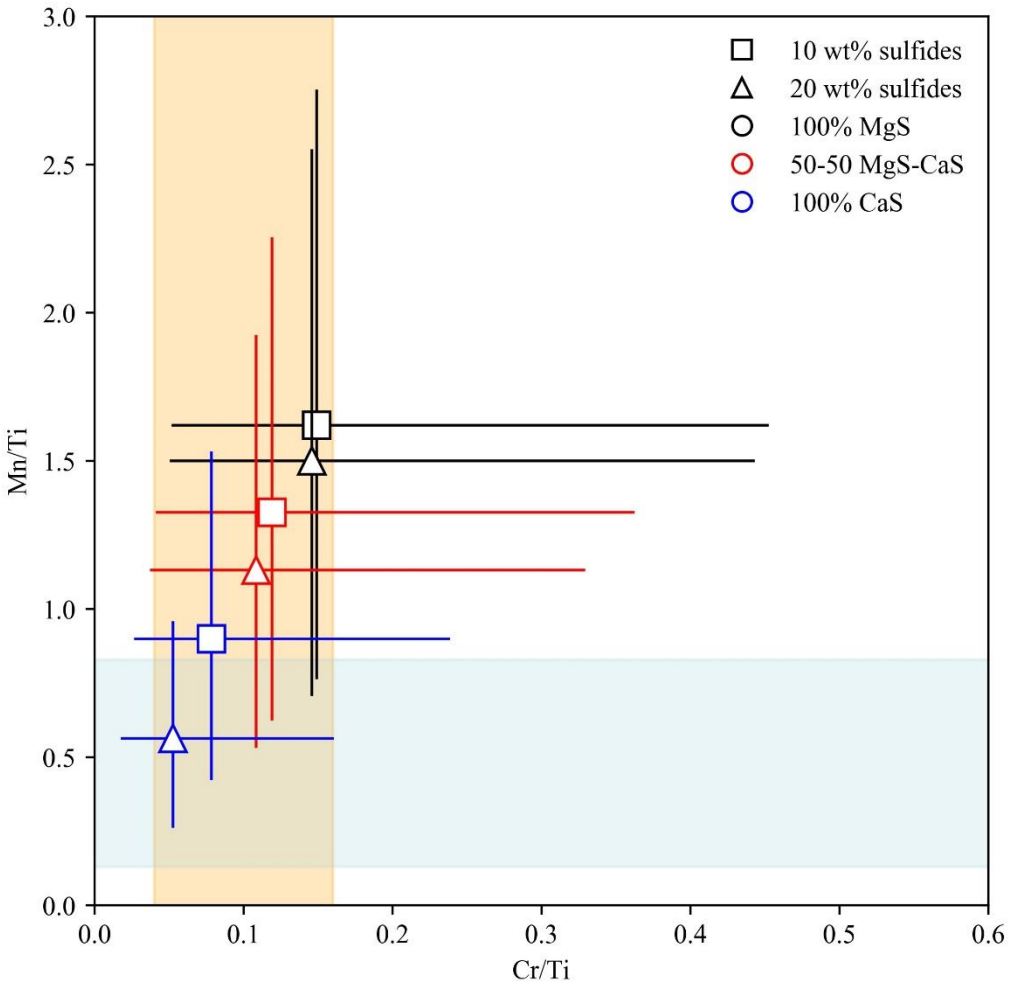

Figure 5-10: Effect of the proportion of CaS and MgS on the calculated surface Cr/Ti and Mn/Ti. The olivine to pyroxene ratio is set to 1. The oxygen fugacity is set to IW - 5. The blue and orange areas represent the measured surface Mn/Ti and Cr/Ti,

respectively. The global partition coefficients at 10 and 20 wt% CaS for 100 wt% MgS are: Ti: 1.687, 3.166; Cr: 3.018, 5.46; Mn: 5.81, 10.72. For 50 wt% MgS and 50 wt% CaS: Ti: 0.962, 1.72; Cr: 2.518, 4.46; Mn: 4.81, 8.72; 100 wt% CaS: Ti: 0.237, 0.266; Cr: 2.018, 3.46; Mn: 3.81, 6.72.

5.4 Conclusions

This chapter aims to provide some insights on Mercury's mantle mineralogy based on available surface data. The planet is ideal for this investigation; the surface is made of volcanic rocks originating from high degree of partial melting of the mantle, and so there are only two well-known silicates that should compose the residual mantle, namely olivine and pyroxene, in unknown proportion (Namur et al., 2016b).

From these simulations, it seems evident that there is at least one sulfide phase in major proportion in the mantle (between 10 - 20 wt%) which is responsible for incorporating both Cr and Mn. In particular, a CaS-rich mantle is the best candidate as it explains the simultaneous increase in Cr/Si and the lack of variation in Ti/Si with higher degree of partial melting. The presence of MnS in the residual mantle may be necessary to sufficiently decrease the surface Mn/Ti. The models do not provide definite insights on the proportion of olivine and pyroxene in the residual mantle, as it is possible the fine-tune other parameters to make it fit. If one were to compute the expected Ti/Si of an olivine dominated mantle, the results would probably exceed the value of ~0.083, measured by MESSENGER. As previously observed in Nittler et al. (2023), Cr is a powerful proxy for the oxygen fugacity of the planet, and a reduced Mercury (IW - 6 to IW - 4) seems the most probable, in agreement with previous studies (e.g., Namur et al., 2016a).

Chapter 6: Predicting element partitioning between metal and silicate melts based on the electronegativity scale

6.1 Introduction

6.1.1 The chemical behavior of elements

Emerging from both scientific and economic consideration, the chemical behavior of elements in nature has been discussed by Goldschmidt (1937). Goldschmidt (1937), inspired by the work of Washington (1920), classified elements into 5 categories; lithophile (rock-loving), siderophile (iron-loving), chalcophile (sulfur-loving), atmophile (found naturally as gases) and biophile (that are the basis of life). This classification was based on the distribution of elements in nature, and notably in meteorites, where it is common to observe three types of minerals, namely silicates, sulfides and metallic ones. Siderophile elements are thought to have massively sink in Earth's iron core, depleting the silicate part of those (Goldschmidt, 1937; Suess and Urey, 1956). The question of core-silicate differentiation and its impact on the distribution of elements is still widely studied today, with new partitioning studies being regularly published (e.g., Kilburn and Wood, 1997; McCoy et al., 1999; Malavergne et al., 2007; Boujibar et al., 2019; Steenstra et al., 2020a,b; 2022; Cartier et al., 2020; Pirotte et al., 2023). Some of these elements are found in a native state in the silicate crust, such as Au or Ni, which of course have massive economic importance.

However, the classification of Goldschmidt is only valid in a given geological/experimental setting; the behavior of elements strongly varies with intensive and extensive parameters, such as oxygen fugacity, temperature and pressure. For example, Fe^{3+} becomes Fe^{2+} when it is reduced by the presence of an electron donor (i.e., reducers). If the redox conditions are sufficiently reducing, Fe^{2+} can be reduced to Fe^{0}, which is the ground state of iron. Iron is often used as a tracer of redox conditions as it is the most abundant multi-valent elements in rocks. The following redox reactions $3Fe_2SiO_4 + O2 = 2Fe_3O_4 + 3SiO_2$ and $2Fe + O_2 = 2FeO$, respectively known as the fayalite-magnetite-quartz (FMQ, Fe^{2+} - Fe^{3+}) and iron-wustite (IW Fe^{0} – Fe^{2+}) buffers, are widely used in the geological literature to define the redox conditions of the studied environment (Frost, 1991). While some elements are commonly found in association with iron metal under Earthly redox conditions (the so called "siderophile" elements, such as Ni and Co), a growing number of elements are observed in metals as conditions become more and more reducing (e.g., Kilburn and Wood, 1997; McCoy et al., 1999; Kiseeva and Wood, 2013, 2015; Wood and Kiseeva, 2015; Namur et al., 2016a; Cartier and Wood, 2019; Steenstra et al., 2020a, 2020b). Elements normally considered lithophile such as Cr and Ti start to partition into metals at low oxygen fugacity (e.g., Cartier et al., 2020; Nittler et al., 2023). If the conditions are extremely reducing (in samples produced experimentally or in meteorites), even elements considered strongly lithophile, such

as U, can be reduced and incorporated into metal (Wohlers and Wood, 2017; Boujibar et al., 2019; Pirotte et al., 2023).

6.1.2 The concept of electronegativity

Electronegativity (E) expresses the power of an atom to attract or hold on electrons. While the concept is old, dating back to Berzelius who first introduced the term at the beginning of the 19th century, Pauling (1932) published the first scale (Jensen, 1996). Based on the empirical evidence that the energies of normal covalent bonds are additive, Pauling (1932) wrote:

$$E(AB) = ½[E(AA) + E(BB)]$$

Where E(AB), E(AA) and E(BB) are the energy of the bonds between the diatomic molecules A-B, A-A and B-B respectively. Pauling compared the theoretical and the experimental E(AB) and noticed a positive difference caused by the differences in electronegativities of the two species A and B:

$$\Delta E(AB) = E(AB)_{exp} - E(AB)$$

Where $E(AB)_{exp}$ is the experimentally measured energy of the bonds A-B. If both electronegativities of A and B are the same, the theoretical and the experimental value of E would be equal. If there is a difference in electronegativities, one atom would pull electrons closer to itself, causing a difference in bond energy with the theoretical value. The difference of electronegativities of two species A and B (χ) is given by:

$$|\chi_A - \chi_B| = (eV)^{-1/2} \times \Delta E(AB)^{1/2}$$

where eV is the value of 1 electron volt per atom, used to have a dimensionless value ($eV^{-1/2} \sim 0.208$ kcal). Because the scale is relative, the electronegativity of hydrogen was fixed originally at 2.1 (now 2.2), and the electronegativity of other elements vary relatively to H from 0.79 (Fr) to 3.98 (F) (Figure 6-1) (Cherkasov et al., 1996, and references therein).

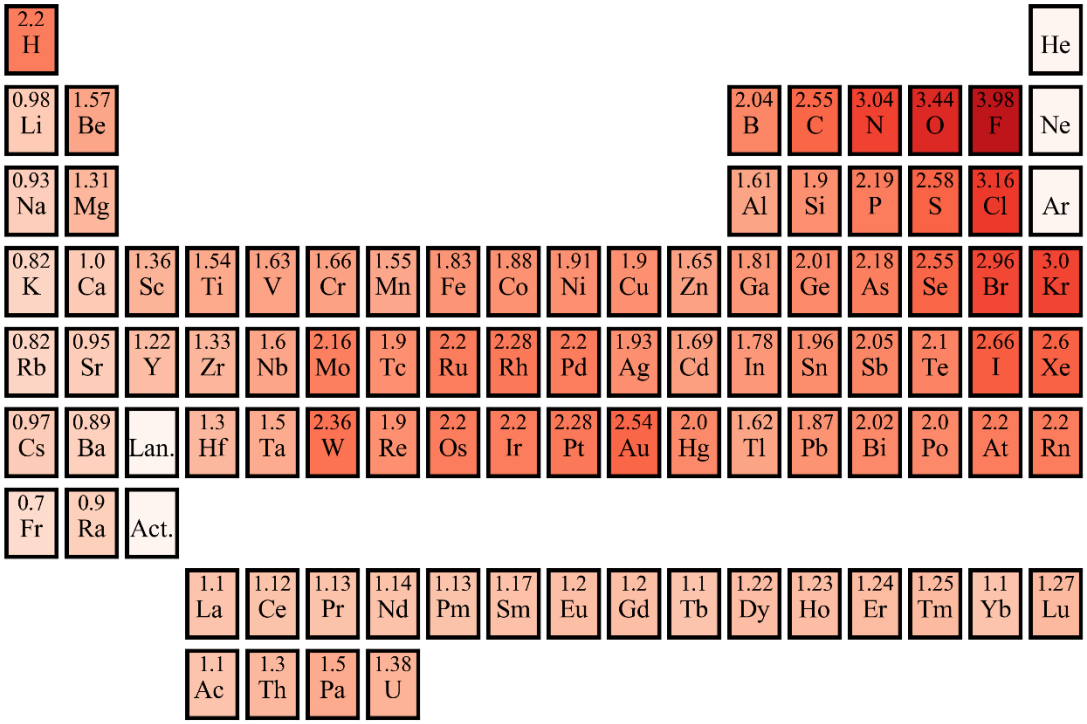

Figure 6-1: Periodic table of electronegativity using the Pauling scale. Data from Allred (1961).

The difference in electronegativity between two atoms can be used to characterize the type of bond; purely covalent if there is no difference (e.g., Cl_2), and increasingly ionic as the difference in E increases (e.g., NaCl). In this aspect, electronegativity has been used to predict the behavior of elements. Notably, oxygen anion (O^{2-}, E = 3.44) binds preferentially with elements with the lowest electronegativity, as it forms bonds dominated by an ionic component, which is stronger than covalent. It explains the affinity of low electronegative elements (such as alkaline or earth-alkaline elements) for oxygen, forming oxides and silicates, whereas lots of transition metals, which have higher E (between ~1.5 and ~2), only binds with O after these less electronegative elements are already combined with it. In the absence of remaining oxygen, they are left to bind with remaining anions such as sulfur (S^{2-}, E = 2.58) (Ringwood, 1955, and references therein). This theoretical approach is employed to explain the affinity for sulfides for high electronegative elements (Fe, Ni, Cu…) and the affinity for the metallic state (oxidation state of 0) for very high electronegative elements (Au and the PGE) (e.g., Barnes and Maier, 1999). The significant production of precise partitioning data for a wide array of elements these last ~30 years enables us to quantify the effect of electronegativity on metal/silicate partitioning.

This work presents two new methods to predict the metal-silicate partition coefficients of elements. The first method allows the prediction with a relative accuracy of partition coefficients between metals and silicate melts for a large number of elements (~1-2 σ in natural logarithm for most transition metals and metalloids), provided that the partition coefficient of at least one element is known in the studied sample.

As the high-end instruments to measure low contents of elements are not always readily available (such as LA-ICPMS) and precisely measuring some elements is particularly difficult, this method could prove useful to investigate and quantify the expected behavior of elements in many different situations. A second method to predict partition coefficients for a large number of elements when knowing only the redox conditions of a setting is provided, although its accuracy is inferior to that of the first method ($\sigma \sim 2.2$ in natural logarithm). It could provide a first approximation of the partitioning of elements in settings where direct measurements are difficult or inaccessible.

6.2 Experimental database

We compiled experimental partitioning data between metal and silicate melt from the literature for 60 elements, covering most of the periodic table, with the exception of most non-metal, halogens and noble gases (Table 6-1). In our calculations, we only include data from experiments consisting of a silicate melt in equilibrium with a metal, excluding as much as possible data containing FeS, as FeS blobs are sometime observed in metals and could lead to erroneous metal/silicate partitioning data. For elements corresponding to few data points, such as the platinoids, we included metal/silicate partitioning data from experiments containing also FeS in order to work with a larger dataset. Moreover, we selected in our dataset metal phases showing low concentration of S (< 1 wt%) to avoid incorporation of chalcophile elements in S-bearing metals.

Table 6-1: Database used in this work.

Study	Temperature (°C)	Pressure (GPa)	Data points	Elements
Hillgren et al. (1996)	2000	10	12	Co,Ni,Ga,Ge,Mo,W
Jana and Walker, 1997	1500	1	29	P,Cr,Ni,Ge,Au
Wade et Wood, 2001	1750-2300	2.5-25	45	Ti,V,Cr,Mn,Fe,Ni,Ga,Nb,Mo,Ta
Chabot and Agee., 2003	1450-2300	3-14.0	86	V,Cr,Mn
Bouhifd et al., 2007	1900	5-15.0	8	Si,K
Corgne et al., 2007	1650-2200	1-7.7	15	K
Malavergne et al., 2007	1665-2400	1.5-20	21	Si,Pb,U
Corgne et al., 2008	1850-2200	3.6-7.7	95	Si,Ti,Cr,Mn,Fe,Ni,Cu,Zn,Ga,Nb,Ta
Mann et al., 2009	1740-2100	2-6	27	Si,Mn,Ga,Ta
Rose-Weston et al., 2009	1750-2420	0.1-1.9	94	Si,Se,Te
Righter et al., 2010	1500-1900	1	155	P,V,Cr,Mn,Co,Ni,Cu,Zn,Ga,Mo,Sn,W
Siebert et al., 2011	1600-2600	0.5-18	483	Si,P,V,Cr,Mn,Co,Ni,Zn,Ga,Ge,As,Nb,Mo,Ta,W
Tuff et al., 2011	1650-1850	1.5-6.	159	Si,V,Cr,Co,Ni,Nb,Mo,W
Mann et al., 2012	2150-2500	3.5-18	57	Cr,Ru,Rh,Pd,Re,Ir,Pt
Ballhaus et al., 2013	1550-2100	1-5	106	P,Cr,Zn,Rb,Cd,In,Sn,Cs,W,Tl,Pb
Bouhifd et al., 2013	1800-2100	4-8	34	Si,Ni,Pb,U
Cartier, 2014	1640-1850	5	14	Si,Th,U
Cartier et al., 2014b	1580-1850	5	41	Si,Ti,Cr,Mn,Ni,U
Wood et al., 2014	1460-1650	1.5	85	V,Cr,Mn,Co,Cu,Zn,Ga,Ge,Nb,Mo,W
Fisher et al., 2015	2447-5427	15-100	96	V,Cr,Fe,Co,Ni,W
Clesi et al., 2016	1985-2875	0.5-2	109	Si,V,Cr,Mn,Nb,Ta
Namur et al., 2016a	1200-1750	0.0001-4	290	Si,Ti,Cr,Mn
Laurenz et al., 2016	2200	11	29	Si,Cr,Ru,Pd,Ir,Pt
Wohlers & Wood, 2017	1650	1.5	85	Si,Zr,La,Ce,Nd,Sm,Eu,Yb,Th,U
Cartier et al., 2020	1580-1850	5	79	Si,Ti,Cr,Mn,Ni
Steenstra et al., 2020a	1610	1	140	Si,V,Cr,Mn,Co,Ni,Cu,Zn,Ga,Ge,Nb,Cd,In,Sn,Sb,Te,Tl,Bi
Steenstra et al., 2020b	1510-1610	1	113	Li,Si,V,Cr,Co,Cu,Zn,Ga,Ge,As,Nb,Mo,Cd,In,Sn,Sb,Te,Cs,Ta,W,Pt,Tl,Pb,Bi,Th,U
Steenstra et al., 2020c	1610-2000	1-5	839	Si,Ti,Cr,Mn,Cu,Zn,Ga,Ge,As,Se,Mo,Cd,In,Sn,Sb,Te,W,Pt,Pb

Study	Temperature (°C)	Pressure (GPa)	Data points	Elements
Steenstra et al., 2022	1610	1	248	Mg,Al,Si,Ca,Ti,V,Cr,Mn,Fe,Co,Cu,Zn,Ga,Ge,As,Se,Zr,Nb,Mo,Pd,Ag,Cd,In,Sn,Sb,Te,Ta,W,Re,Ir,Pt,Au,Tl,Pb,Bi,Th,U
Pirotte et al., 2023	1520-1700	0.1-3	230	Na,Al,Si,Sc,Ti,V,Cr,Mn,Fe,Co,Ni,Cu,Zn,Ga,Ge,Rb,Sr,Y,Zr,Nb,Mo,Ba,Ce,Nd,Sm,Eu,Gd,Yb,Hf,Ta,W,Th,U
30 studies	1200-2875	0.0001-100	3824	60 elements

We gathered in total more than 3800 data points from 30 studies, with temperatures ranging from 1200 – 2875°C and pressure ranging from 0.0001 – 100GPa. For each experiment, oxygen fugacity was calculated using the following equilibria:

$$Fe^{Met} + ½O_2 = FeO^{Sil} \quad (1)$$

and:

$$Si^{Met} + O_2 = SiO_2^{Sil} \quad (2)$$

where Met and Sil refer to metallic and silicate melts respectively. Calculation using equation (2) was favored over equation (1), and (1) was used when Si in the metal was not measured. Indeed, FeO in the melt is sometime too low to be accurately measured, leading to erroneous fO_2 at very reducing conditions. Moreover, it is possible that Fe binds with S or Si in the silicate melt under reducing conditions, so that we overestimate the FeO content of silicate melts. Ideality was considered in our calculations. Details on the calculations can be found in Namur et al. (2016a). We estimate the error to be around ~0.5 log units (Namur et al., 2016a).

6.3 Metal/silicate partitioning and electronegativity

6.3.1 Empirical parameterization of metal/silicate partitioning

Following the definition of Pauling (1932), the elements with the highest electronegativity should be the ones that are the most easily reduced (i.e. acquiring and holding the most to electrons). While the most electronegative elements (such as fluoride, oxygen, chloride) have negative valences, most elements cannot adopt negative valences, and are at best reduced to their ground state (0). By studying the partitioning coefficient of elements (D) between silicate glasses and the associated metals measured experimentally, we observe a correlation between D of elements and their electronegativity (Figure 6-2).

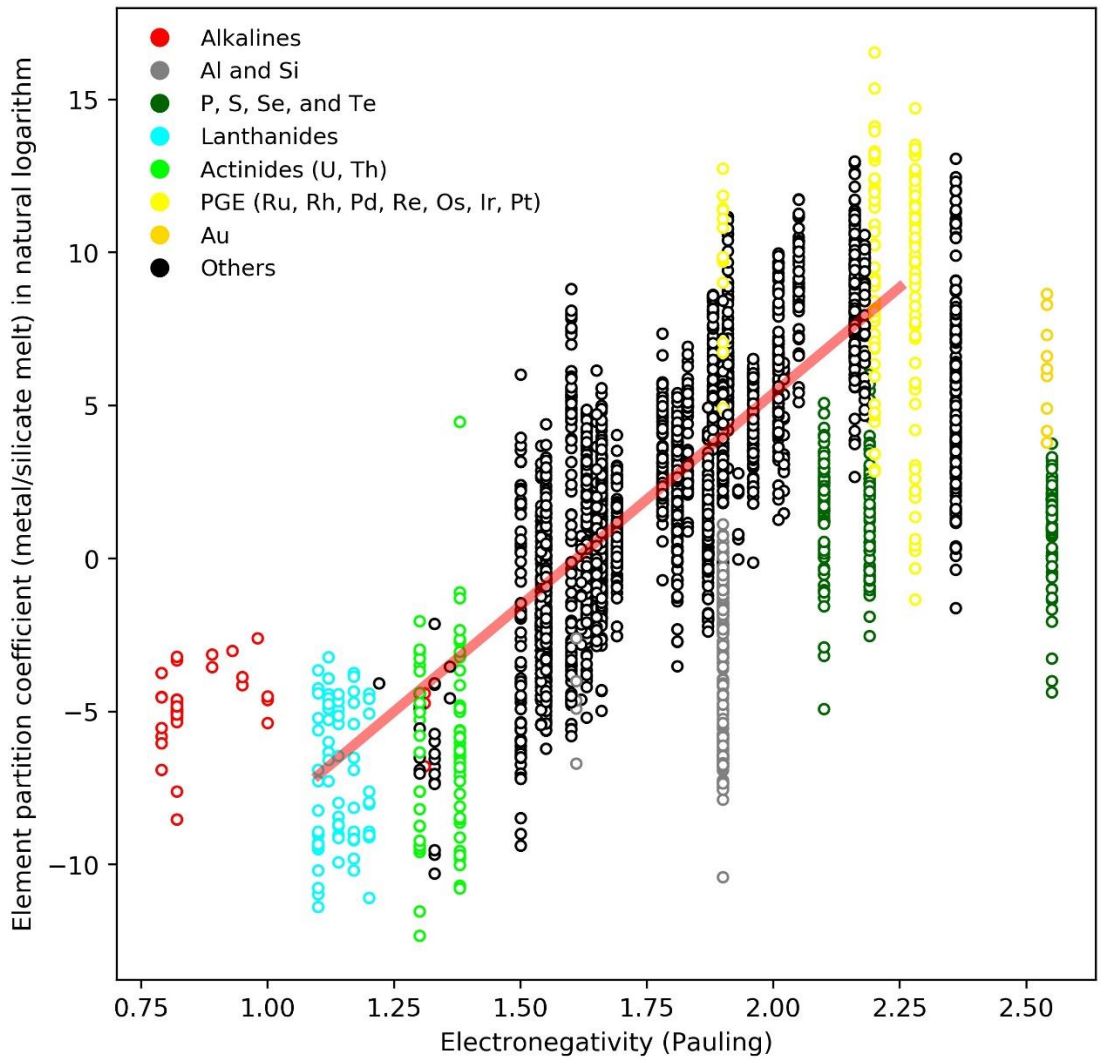

Figure 6-2: $D^{metal/silicate\ melt}$ of elements as a function of Pauling electronegativity. Most experiments compiled show exclusively silicate and metal melts. We did not consider data with experiments also containing FeS, which are common in experiments under reduced conditions, except for the platinoid group elements (PGE), for which the silicate melt was both in equilibrium with metals and FeS for some data points. Elements with the lowest and highest E show a deviation from the seemingly linear trend (in red), probably due to several factors (see section 6.3.3 for details).

As we can see in Figure 6-2, the partition coefficients of elements between E ~1 and E ~2.25 follow an upward trend (shown by the red line) with increasing electronegativity, despite the large variations of D inherent to the experimental conditions (temperature, pressure, oxygen fugacity, compositions of metal and silicate melts…). Alkaline elements with E < 1 do not follow the trend. On the other end of the spectrum, P, Se, Te and Au also strongly deviate from the observed linear trend. Finally, Si has a lower $D^{metal/silicate}$ than other elements with similar E. To quantify the effect of electronegativity on $D^{metal/silicate}$, we can calculate regressions as a function of E and some intensive and extensive parameters of the samples, such as fO_2, T, P and the composition of the silicate melt.

From these regressions, we find compositional parameters (silicate Mg/Si, Al/Si…) to be irrelevant. This is in agreement with previous studies finding that the composition of the silicate melt is not a

significant parameter for metal/silicate partitioning (e.g., Fisher et al., 2015). Moreover, the inclusion of T and P (1200°C < T < 2875°C, 0.0001 GPa < P < 100 GPa) as regression parameters does not have a significant effect on the predicted values. Only the electronegativity of the element and the oxygen fugacity of the samples are significant. We end up with the following equation to predict $D_x^{metal/silicate\ melt}$:

$$\ln D_x^{metal/silicate\ melt} = a + b \times \log(fO_2) + c \times E_x \quad (3)$$

where $\ln D_x^{metal/silicate\ melt}$ is the natural logarithm of the partition coefficient of element x, fO_2 is the oxygen fugacity, E_x is the electronegativity of element x, and a, b and c are regression coefficients equal to -31.25, -0.5266 and 17.83 respectively (Figure 6-3). For this regression, we excluded elements whose values < 1 or > 2.25, as well as Al, Si, P, and Te because they all strongly deviate from the trend in Figure 6-2 (see section 6.3.3 for more details). Such a simple regression, calculated from ~1700 data points, has a R^2 value of ~0.796. The standard deviation is ~2.2 (in natural logarithm) on the calculated D.

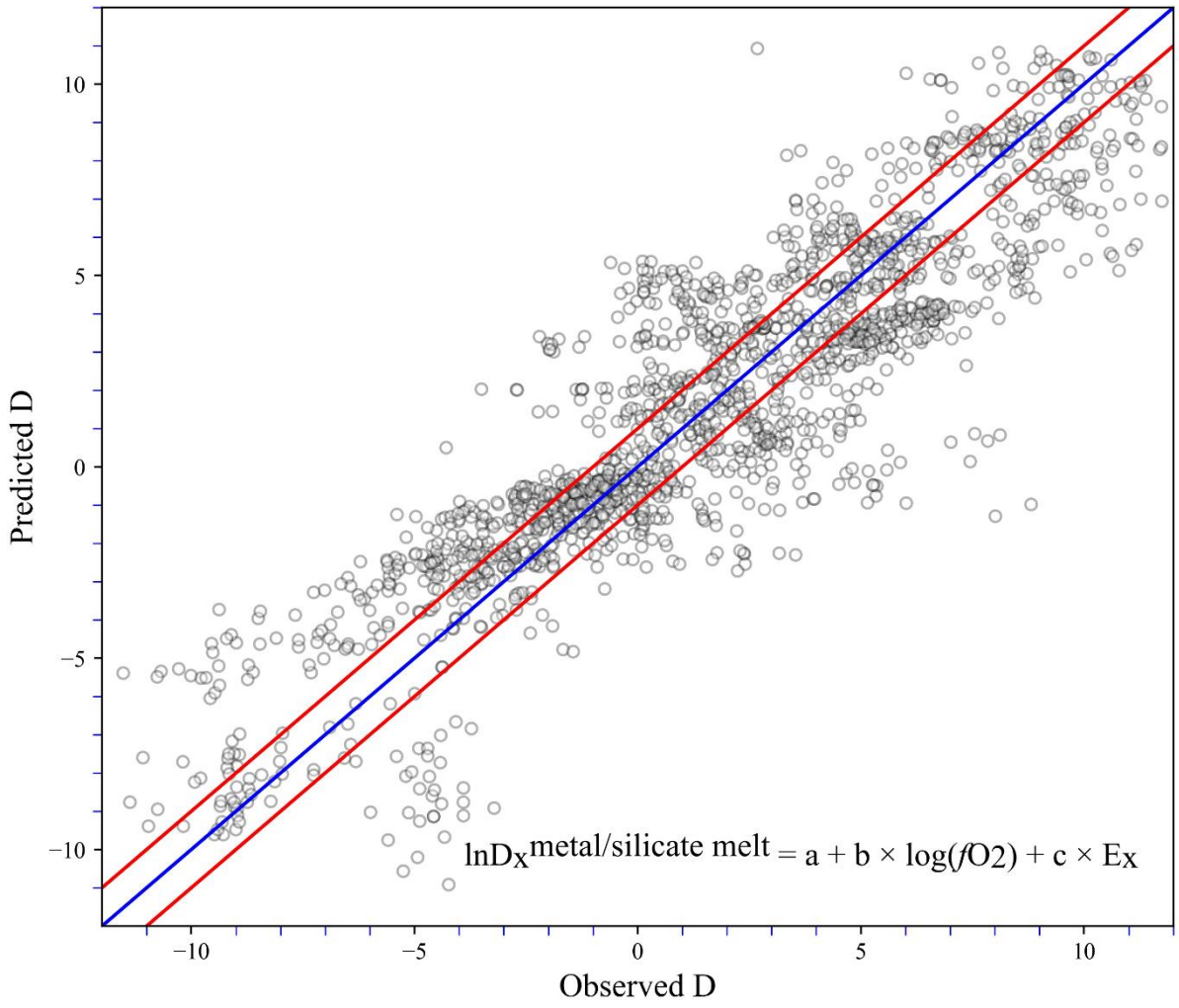

Figure 6-3: Predicted metal/silicate melt partition coefficients vs the observed values. The predicted coefficients are calculated using equation (3). The R^2 is ~0.796 and the standard deviation in natural logarithm is ~2.2, with ~1700 data points. While this very simple equation can be used to give a range of expected D in a given redox setting, it is inaccurate for precise D

prediction. The blue line represents the perfect fit between the predicted and the observed D values, and the red lines show 1 σ deviation.

It is important to keep in mind that the predicted values seen in Figure 6-3 are affected by the combined effect of errors on fO_2 calculations and analytical errors. In particular, estimating oxygen fugacity is difficult, as there are multiple calculation methods (see Cartier et al., 2014b; Namur et al., 2016a; Pirotte et al., 2023 as examples) which can give sometimes very different results.

6.3.2 The constant ratio between elements partitioning

As observed above, there is a clear correlation between electronegativity and the metal/silicate partitioning of an element. Following equation (3), we observe that temperature, pressure, and compositional parameters (such as the Mg/Si of the silicate melt) have second order effects on the metal/silicate partitioning, and that only the oxygen fugacity has a significant impact on the regression. This means that for a given redox state, the difference of partitioning between two elements should be directly linked to their difference in electronegativity. This implies that the partitioning ratio of two elements measured in a sample is theoretically constant, no matter the P, T, fO_2 and compositional factors. Figure 6-4 shows all the possible ratios of two elements for each sample in our dataset against their respective difference in electronegativity.

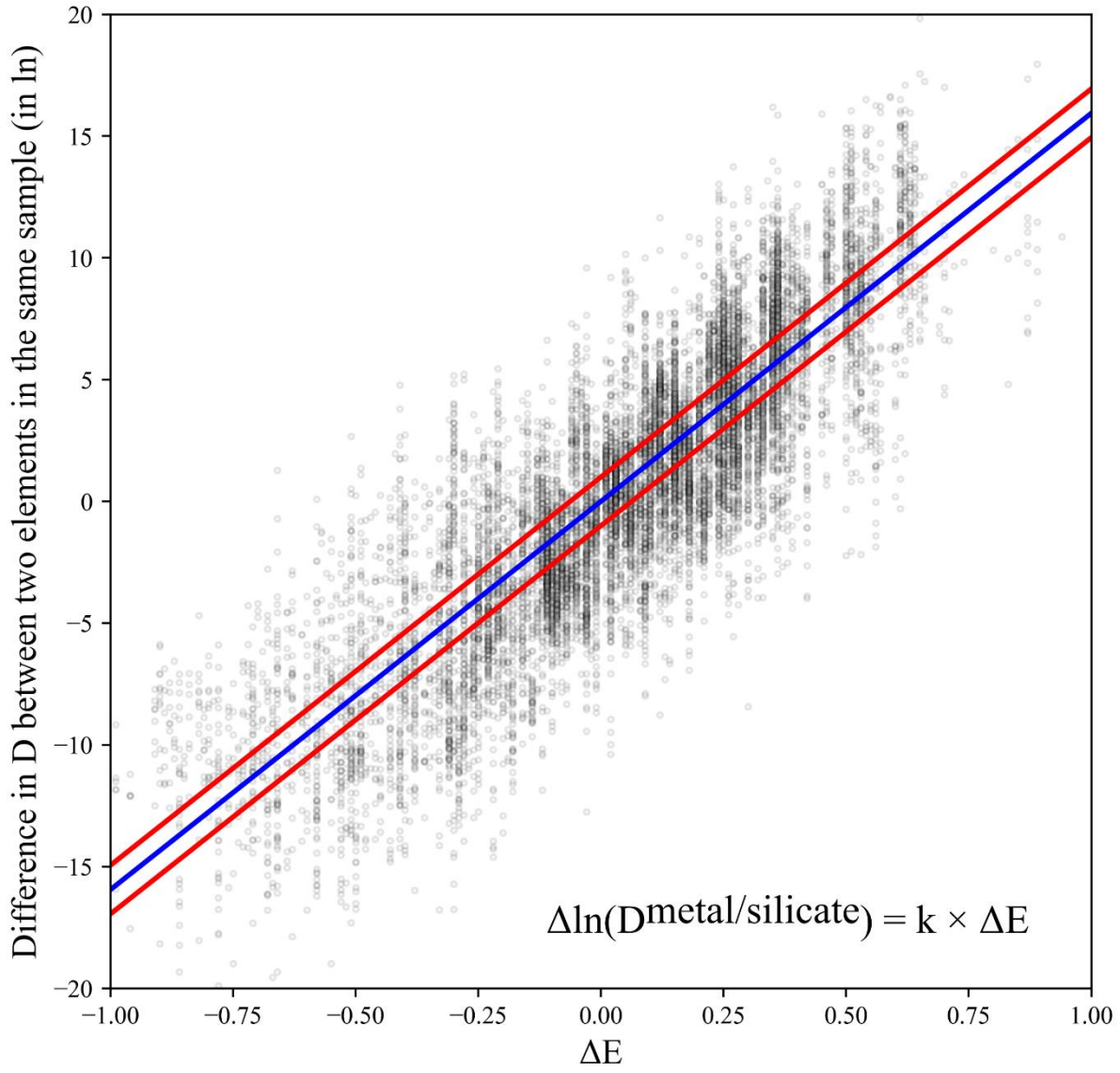

Figure 6-4: Difference of $D^{metal/silicate\ melt}$ of two elements in the same sample (in ln) as a function of their difference in electronegativity. There is a clear upwards trend, meaning that the greater their difference in E, the greater their difference in metal-silicate partitioning value. The blue line is the analytical representation of equation (4), and the red line is the 1 σ error. Only elements with 1 < E < 2.25 are considered. Si, Al, P and Te were excluded. Those elements are discussed in section 6.3.3.

We observe an upward trend, with higher differences in electronegativities linked to higher differences in metal/silicate partition coefficients. If we consider that the regression is linear, we obtain:

$$\Delta\ln(D^{metal/silicate}) = k \times \Delta E \quad (4)$$

where $\Delta\ln(D^{metal/silicate})$ is the difference between the partition coefficients (in natural logarithm) of two elements from the same sample (which mainly means the same redox conditions) and ΔE the difference of their respective electronegativities. The constant "k" is equal to 15.94, with R^2 value of ~0.73 for ~13000 tested combinations. It follows:

$$\ln(D_x^{metal/silicate}) = \ln(D_s^{metal/silicate}) + k \times E_x - k \times E_s \quad (5)$$

where $D_x^{metal/silicate}$ and $D_s^{metal/silicate}$ are the metal-silicate partition coefficients of elements x and s, taken from a same sample. This suggests that we can predict the metal-silicate partition coefficients of any element in a sample if we have the partition coefficient of at least one other element, that we can use as a standard (the s in (5) standing for "standard"). As seen in Figure 6-4, there are still large variations in the D ratios for a same ΔE. If we consider the equation (4) to be correct, then the variations can be attributed for the most part to analytical errors, especially those caused by elements that are difficult to measure, such as elements with concentrations close to the limit of detection in either the silicate melt (high E elements) or the metal phase (low E elements). These deviations are discussed in section 6.3.3.

Another way to visualize the constant ratios between metal/silicate partition coefficients is to produce the ratios of elements over another element used as a standard and calculate their respective median. We can then parameterize empirically each median $\Delta\ln(D^{metal/silicate})$ for a given standard (s) (Figure 6-5).

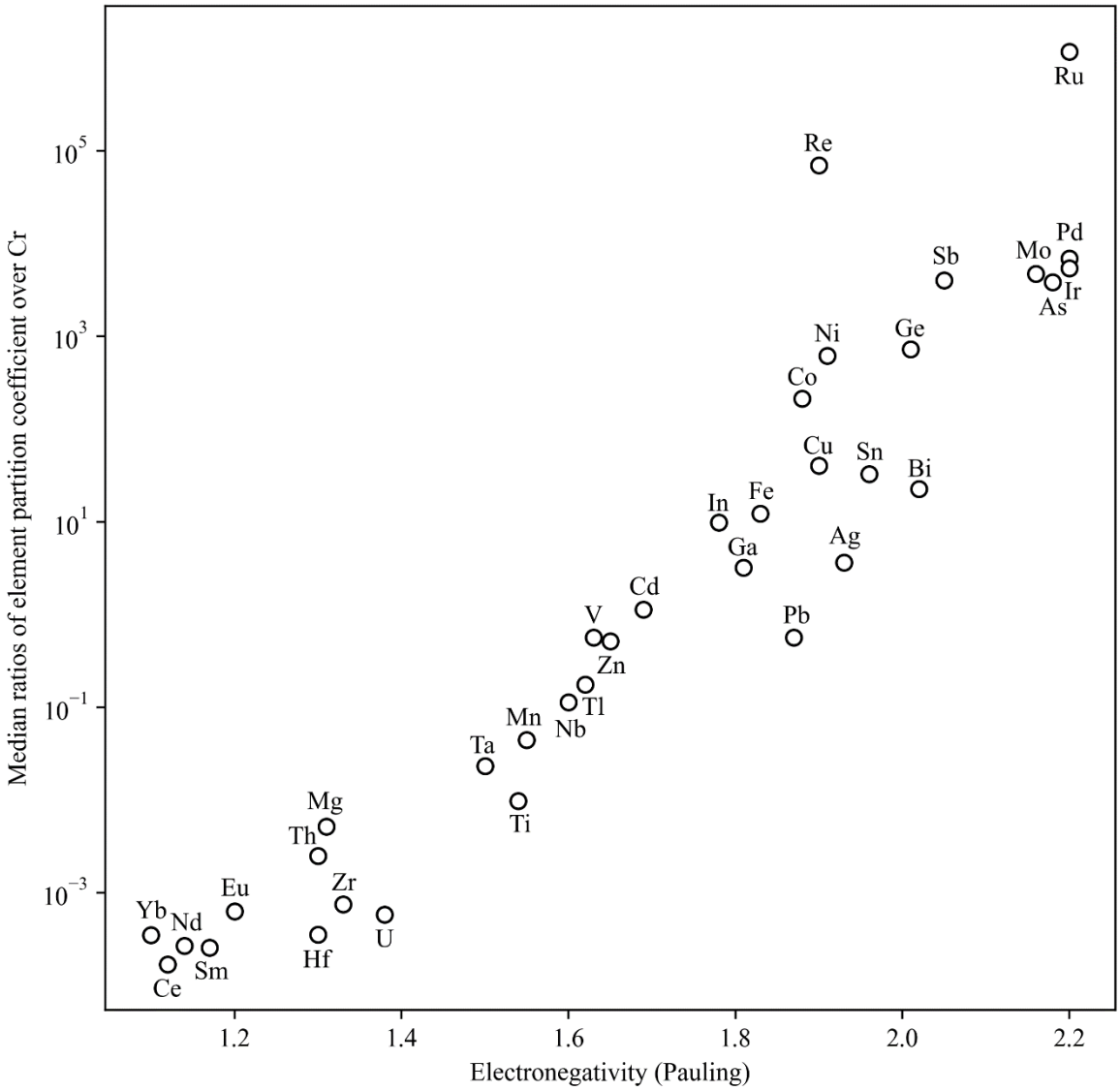

Figure 6-5: Median ratios of element partition coefficients "x" with a standard "s" (here, Cr) as function of the electronegativity of the element "x", based on 1725 data points. There is a clear trend relating the ratios to electronegativity.

As before, only elements with 1 < E < 2.25 were considered. Si, Al, P and Te were also excluded. Those are discussed in the following section.

A trend is clearly visible, and the obtained parameterizations are of the form:

$$\ln(D_x^{\text{metal/silicate melt}}) = \ln(D_s^{\text{metal/silicate melt}}) + a_s + b_s \times E_x \quad (6)$$

where x and s are the unknown and standard elements respectively, and a_s and b_s are parameters determined empirically. The formulation of this equation is very close to (5), and we find that b_s is somewhat constant for most standards, with a value around ~16 (Table 6-2), close to the value of k in equation (4) and (5). This value of k is also similar to parameter c in equation (3). Parameter "k" can be consistently interpreted as the difference between partition coefficients of two elements (in natural logarithm) whose difference in electronegativity is 1. Parameter a_s is roughly equal to the term $-k \times E_s$ in equation (5). These results tend to show that, barred the analytical errors on the measurements, the ratio of the metal/silicate melt partition coefficient of two elements is constant and its value is linked to their difference in electronegativity. If so, it would mean that the measurement of one element in the silicate melt and the metal phase of a sample can be sufficient to use it as a standard and predict, or at least estimate, the partitioning of other elements. We can calculate parameters a_s and b_s for each element to use as standards (Table 6-2).

Table 6-2: Empirically determined parameters a_s and b_s for some elements to use as standards for equation (6). Nb. of elements indicates the number of different elements the standard was calibrated with. Commonly measured elements (such as Cr) have larger nb. of elements than rarer elements (such as Cd for example). SE is the standard error of the predicted $D_x^{\text{metal/silicate melt}}$ value obtained by using this element as a standard (in natural logarithm). We strongly recommend the use of Cr and Mn, which were parameterized with the most representative dataset.

Element	E	Nb. Of element	Data points	a_s	error	b_s	error	R^2	SE
Ti	1.54	34	808	-23.1362	1.721	16.3219	0.997	0.893	1.9157
V	1.63	35	980	-29.3942	1.811	17.4503	1.058	0.892	2.1023
Cr	1.66	36	1725	-29.4446	1.78	17.5986	1.031	0.896	2.1166
Mn	1.55	35	1544	-23.2962	1.51	15.6624	0.881	0.906	1.7471
Fe	1.83	35	464	-28.1169	1.672	14.6872	0.98	0.872	1.9420
Co	1.88	35	903	-29.9067	1.582	14.4866	0.928	0.881	1.8346
Ni	1.91	17	746	-37.6252	2.59	18.3894	1.451	0.915	1.3447
Cu	1.9	34	1068	-25.7956	1.849	13.7196	1.078	0.835	2.0648
Zn	1.65	35	1053	-25.8608	1.5	15.7259	0.876	0.907	1.7417
Ga	1.81	34	1179	-28.1434	1.529	15.987	0.89	0.91	1.7351
Ge	2.01	35	885	-26.2132	1.91	12.6554	1.124	0.794	2.2010
As	2.18	29	609	-31.5004	2.787	14.4385	1.563	0.76	2.1650
Nb	1.6	35	740	-32.8155	2.397	19.4518	1.4	0.854	2.7800
Mo	2.16	35	1076	-28.9421	1.966	1.8978	1.16	0.789	2.2342
Cd	1.69	28	489	-27.4815	2.369	15.8582	1.318	0.848	1.8921

Element	E	Nb. Of element	Data points	a_s	error	b_s	error	R^2	SE
In	1.78	28	741	-28.2037	2.524	15.1596	1.407	0.817	2.0229
Sn	1.96	29	787	-31.3036	2.399	16.2856	1.339	0.846	1.9170
Sb	2.05	26	399	-30.3454	2.871	13.6704	1.582	0.757	1.9783
Hf	1.3	20	125	-16.4261	2.338	14.2761	1.473	0.839	2.0349
Ta	1.5	34	621	-29.9497	2.181	19.057	1.264	0.877	2.4563
Pb	2.33	28	792	-25.1846	2.352	15.3362	1.3	0.843	1.7780
Bi	2.02	28	174	-26.554	2.296	13.9283	1.286	0.819	1.8207
Th	1.3	35	364	-10.2629	1.858	9.4839	1.093	0.695	2.2085
U	1.38	36	398	-13.1154	1.99	11.3205	1.168	0.734	2.3917

The values predicted by equations (5) and (6) can be compared with the observed values for experiments in the literature. As seen in Figure 6-6, there are visible correlations between the calculated and observed D for a large number of elements (Figure 6-6A, B, C and D), even though there are some strong deviation for some data points (Figure 6-6E and F). Figure 6-6 shows partition coefficients calculated from equation (6) against observed values, using Cr as a standard. It may be of course beneficial to calculate multiple values by using several standards, and take the median of the predicted values, in order to increase the accuracy of the D calculated. The predicted values were calculated for our whole dataset, including samples containing both metals and FeS. While it may increase the errors by increasing the risk of having metal-silicate partition coefficients contaminated with FeS-silicate ones, it allows testing the equations with a larger amount of data.

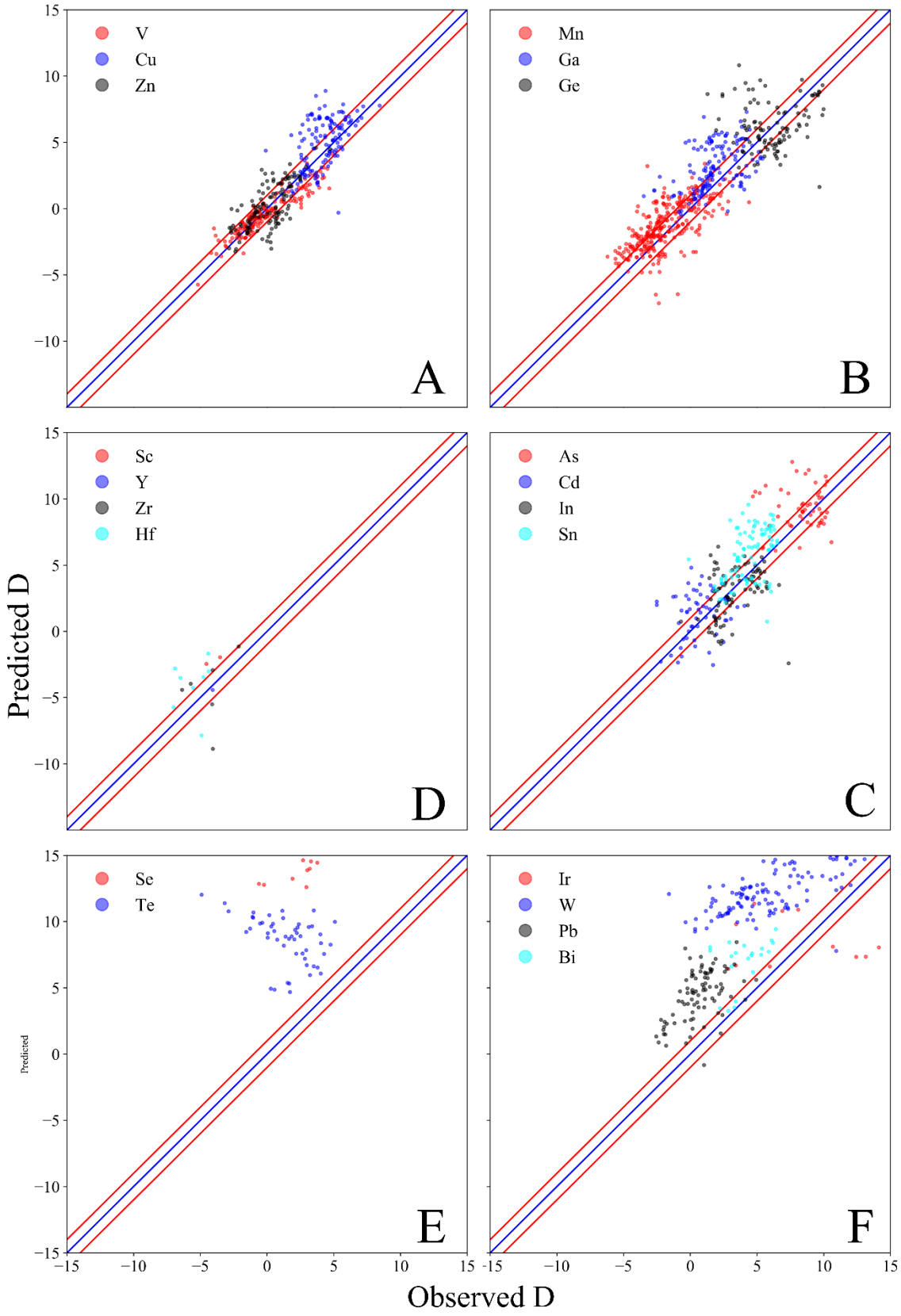

Figure 6-6: Predicted metal/silicate melt partition coefficients obtained by equation (6) as a function of the observed partition coefficients (in natural logarithm). Cr was used as the standard in equation (6). The blue line shows the perfect correlation between the observed and the predicted values, and the red lines show 1σ deviation. The large error of panel E and F are explained below.

6.3.3 Assessment of model quality

The deviations of the predicted values from the observed ones can be classified into four different groups:

- The most widespread type of errors we observe are probably due to a mix of analytical errors and imperfect parameterization of the equations. The elements considered show a correct calculated range of D for their electronegativity, but there are some deviations (1 or 2σ for the most of them) from the observed value (Figure 6-6A, B, C, and D).
- Another type of deviation is due to inaccurate calculation of partition coefficients for elements either strongly siderophile or lithophile; their concentration in the silicate melt (or in the metal in the case of lithophile element) is so low and in the metal (and silicate melt, respectively) so high, that a slight error on the measured value as tremendous effects on the partition coefficient (Figure 6-6F). For example, molybdenum in the silicate melt is often close to the limit of detection of mass spectrometers in reduced experiments, with concentrations below 1 ppm, while in metal it can reach a few 1000s. An error of 0.1 ppm on a measured value of 0.2 in the silicate melt gives a range of D from ~3000 to 10000 for a metal concentration of 1000, which is almost an order of magnitude. This hypothesis is supported by the fact that these large errors happen for elements with electronegativity values either very high (>2) or very low (<1) (Figure 6-6F). For the strong lithophile elements, the equation tends to underestimate the D value. We think that, in addition to the inaccuracy of measurement hypothesis and the actual lack of data, there may also be dissolution of a few anions in the metal at high temperature. For example, O^{2-} dissolves in metals (Rubie et al., 2004; Wood et al., 2006; Huand et al., 2011), which would bind to lithophile elements and increase their amount in the metal, so that only a small amount of these elements is actually reduced and the rest is bond to dissolved oxygen in the metal. The same should be true for chalcophile elements if S is present in the metal.
- For elements with a very high electronegativity, they can form metal nuggets in the silicate melt, which could lead to underestimate their content in metals. It was especially observed for Au (e.g., Steenstra et al., 2022), which is one of the elements that deviates the most from the predictions. Also, it is possible that the strong siderophile elements reach their maximum reduction, and that equation (5) or (6) overestimate D values; the kinetics of redox reactions could place an upper bound to the maximum reduction of an element in a sample (i.e., there is a minimum number of atoms that are still oxidized and cannot be reduced).
- Finally, Se and Te should have very high D because their E is very high (2.55 and 2.1, respectively) but their partitioning is actually multiple orders of magnitude lower (Figure 6-6E). One explanation is that these elements can have negative valence (-2) so that, under reduced conditions, their lowest reduction state is not 0 but -2. It means that only a portion of these elements is reduced to 0 and enters the metal phase, while the rest is -2 and mainly stays in the silicate melt.

To illustrate the quality of equation (6) for each element, we constructed a periodic table which shows the standard deviation of the predicted $D^{metal/silicate\ melt}$ values from the observed $D^{metal/silicate\ melt}$ for each element, using Cr as the standard (Figure 6-7).

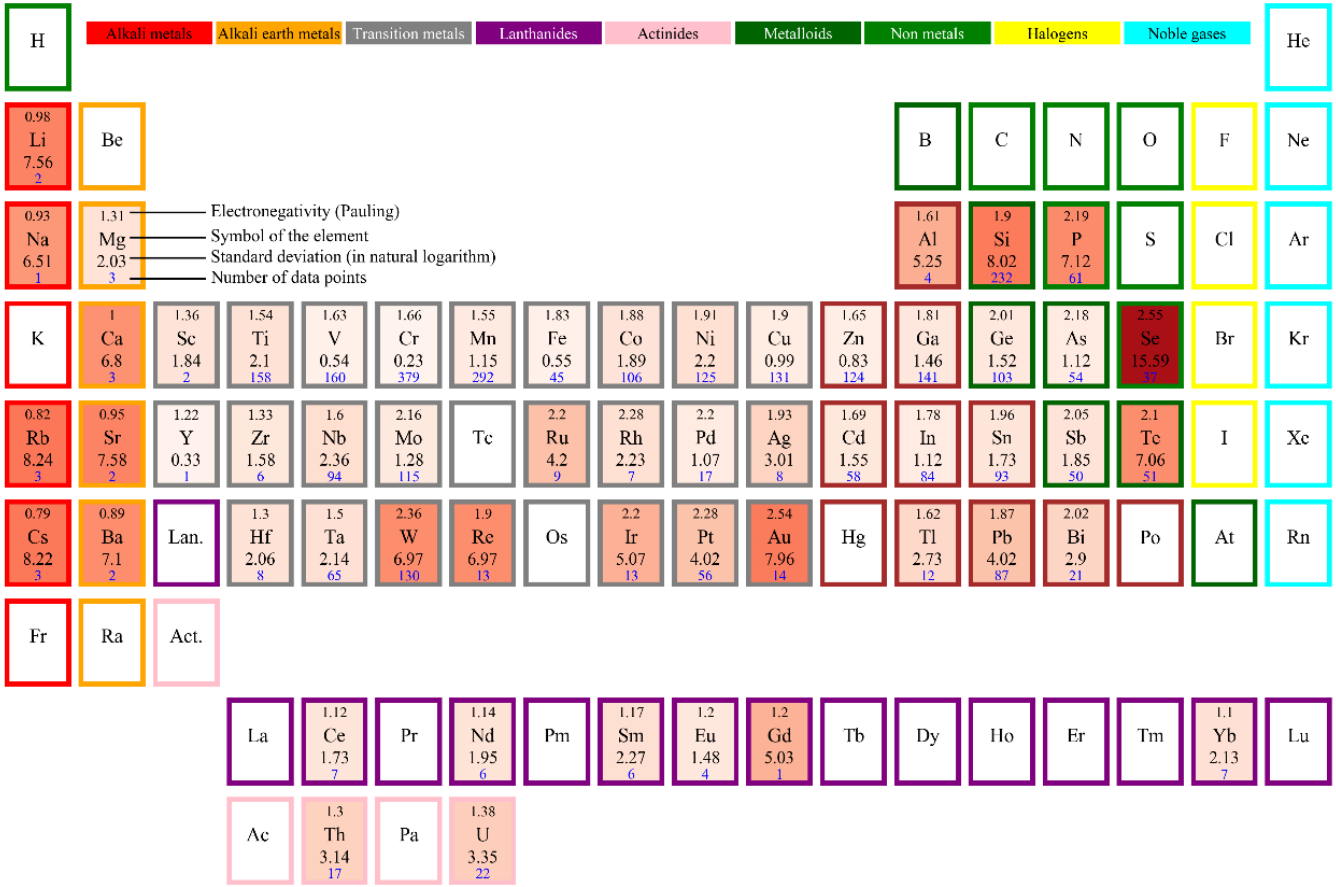

Figure 6-7: Periodic table showing the median standard deviation (in natural logarithm) between the predicted and observed $D^{metal/silicate\ melt}$ using equation (6) with Cr as standard. While most transition metals show good agreement, alkali and alkali earth metals show strong deviation, as well as most elements with very high E. Se and Te are also not in agreement with the result from equation (6). We only considered partitioning data of alkali and alkali earth metals measured by LA-ICPMS, as EPMA measurements of these elements are unreliable in metals. The same was applied to Al.

As we can see, the equation works relatively well for transition metals of the 4th and 5th row. Very high electronegative elements show strong deviations (W, Re, Ir, Pt and especially, Au) where the predicted $D^{metal/silicate\ melt}$ value is higher than what is observed. Alkaline metals also show very important deviation due to their very low electronegativity, partly due to a lack of data for those elements. A surprising result is that the D values of Si cannot be predicted; they are largely overestimated. Maybe the role of Si as the main network former makes it difficult for this element to be reduced as much as we would expect from its high electronegativity. The same can be said for Al, which should have a siderophile behavior equivalent to V. Although P is known to be siderophile under reducing conditions, it is not as siderophile as we would predict, maybe due to its non-metallic nature.

6.4 Conclusions

We compiled metal-silicate partition coefficients for 60 elements from 30 different studies, which cover a range of temperature from 1200 to 2875°C and pressure of 0.0001 to 100 GPa. We showed that, as expected from the its definition, electronegativity is a first order factor of the siderophilic nature of elements. While this has been known for a long time, the last ~30 years of production of partitioning data from experiments enabled us to quantify this effect, and produce a simple predictive model that can estimate the partition coefficients of an element based solely on its electronegativity and the oxygen fugacity of its environment. Moreover, we showed that elements in a sample (i.e., sharing the same intensive and extensive parameters) have constant partitioning ratios, which are related by their difference in electronegativity. Based on this observation, we created a simple equation between the ratio of the partition coefficient of two elements and the difference in their electronegativities, linked by a constant "k". The prediction is satisfactory for a large number of elements (mainly the transition metals and some metalloids). However, there are large variations between the expected and the observed $D^{metal/silicate\ melt}$ for several elements. Further work is needed to understand these variations fully. We suggest that diving deeper into the electronic properties of elements could improve the prediction of metal-silicate partitioning. In particular, it is possible that the number of electrons in valence in the silicate melt plays a role in predicting $D^{metal/silicate}$, in addition to electronegativity: indeed, Ti deviates relatively strongly from its predicted behavior compared to element with similar electronegativity such as Mn.

This work is a first attempt to quantify the link between electronegativity and the metal-silicate partitioning of elements. While these results are promising, there is a need for a comprehensive, accurate dataset for metal-silicate partitioning for all elements, especially for strong lithophile ones. We recognize the difficulty to produce such data, as metals incorporate only very low amounts of these elements, so that their accurate measurements would require very reducing conditions. S-free

experiments should also be favored to determine solely the effect of the siderophile behavior of elements.

Appendix 6A:

While in this work we overwhelmingly used partition coefficients between silicate melts and Fe-rich metals, we note that the equations (5) and (6) also work for other types of metals. For example, in sample Y087-2 (Pirotte et al., 2023), we have a silicate melt equilibrated with a Si-Cr metal, devoid of Fe. I hypothesize that these equations in fact predict global reduced/oxidized partition coefficients. As we considered FeS-free experiments in this study, the only oxidized phase is the silicate melt, while the only reduced one is the metal. In FeS-bearing experiments, the predicted $D^{reduced/oxidized}$ should deviate from the observed $D^{metal/silicate\ melt}$, as some oxidized (or more correctly, not reduced) atoms are stored in FeS. However, because the fraction of FeS to silicate melt is usually small, the deviations are not easily seen. For very chalcophile elements, the effect should be noticeable (and may actually be responsible for the deviations observed in Figure 6-6, as we included there FeS-bearing experiments). Further work on this subject should focus on calculating the total concentration of an element as oxidized, using the pondered average of the element in the silicate melt and the FeS. This method could theoretically also be applied in geological, crystallized setting, as long as a group of elements in valence 0 is easily identifiable (e.g., a nuggets of metal). It would need careful counting of the proportion of each phase to determine a global $D^{reduced/oxidized}$.

It is possible to construct a new redox scale, using electronegativity, that I chose to call E1. It represents the electronegativity of a virtual element whose $D^{reduced/oxidized}$ would be 1 in the studied system (where elements that have E higher to E1 have $D^{reduced/oxidized}$ above 1 and elements that have E lower to E1 below 1). It can be calculated using equation (5):

$$\ln(D_1^{metal/silicate}) = \ln(D_s^{metal/silicate}) + k \times E_1 - k \times E_s$$

where $D_1^{metal/silicate} = 1$ and s is an element chosen as a standard in the sample. We obtain:

$$E_1 = E_s - \ln(D_s^{metal/silicate})/k \quad (7)$$

The advantage of such a method is that it only measures the redox state of a geological or experimental setting, independently of temperature, pressure, or other parameters. In Figure 6-8, we can see a comparison between the E1 scale and oxygen fugacity values. The correlation is clearly visible, as well as the known effect of temperature on the increased incorporation of elements in metals.

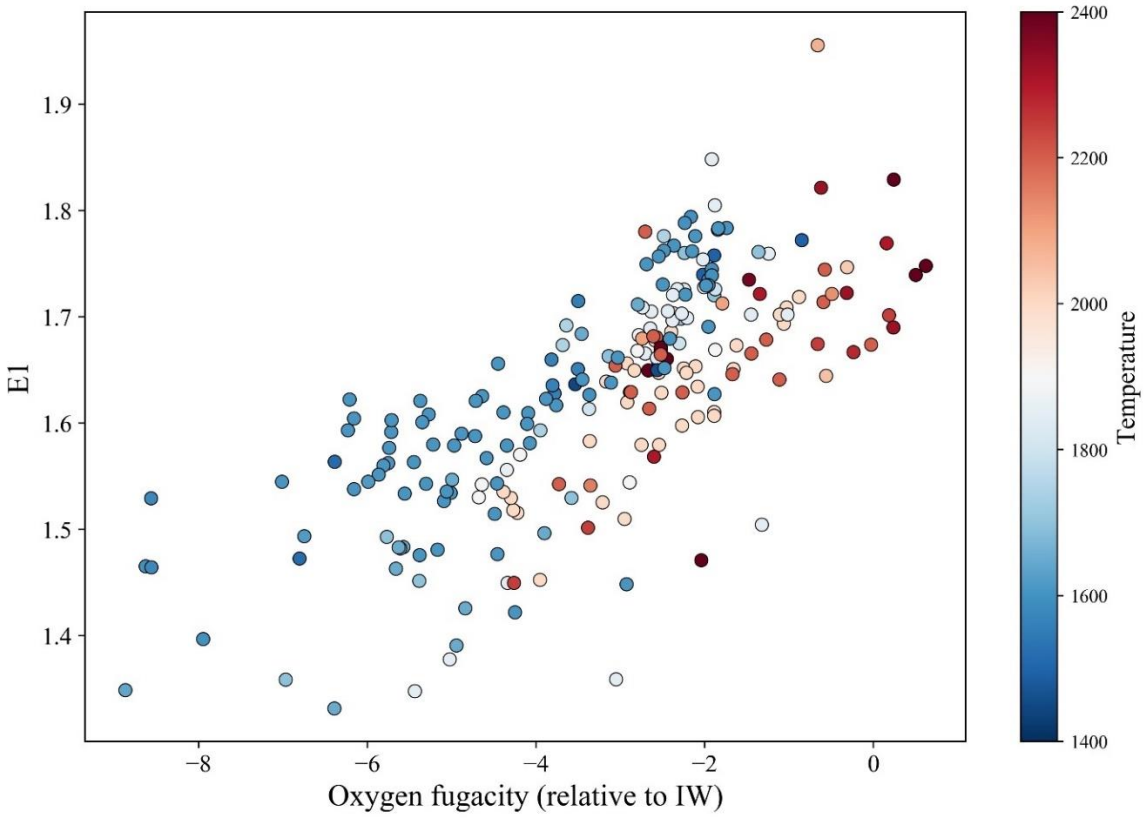

Figure 6-8: Comparison of two redox scale for the compiled experiments. The E1 redox scale correlates with the calculated oxygen fugacity. We can see the effect of temperature, which increases the partitioning of elements in metal (and so, their reduction) for a given oxygen fugacity value. The E1 values were calculated from the median values of equation (7) using several standards (V, Cr, Mn, Fe, Cu, Zn, As).

The proposed E1 scale could prove useful to compare the redox state of samples from very different/unknown P-T conditions. Naturally, this is a new, early concept, and more developments are needed to evaluate the real usefulness of this scale.

General conclusions

This thesis emphasizes the importance of understanding elemental behavior to improve our knowledge and constraints on planetary formation, structures, and geology. Of course, the behavior of elements is the focus of this study but is also of prime importance for other subjects, such as mining and metallurgy. Experimental petrology is the best way to acquire significant, accurate, and precise partitioning data. This method has been extensively applied in this thesis to produce the information we needed to better understand Mercury.

We carried out more than a hundred experiments under various pressure (0.0001 – 6GPa) and temperature (1300 – 1700°C) under reducing conditions (~IW-1 – ~IW-8) using three different types of apparatuses, namely a piston-cylinder, two multi-anvils, and a vacuum line. Moreover, we carefully analyzed by EPMA and LA-ICPMS experiments done previously in both piston-cylinder and IHPV. From the analyzes of these samples, we produced hundreds of partition coefficients between metals (Fe, Fe-Si, Si-Cr-Mn…), sulfides (FeS, CaS, MgS…), and their coexisting silicate melts for over 30 elements. Combining our data with the literature, we applied this knowledge to constrain different aspects of Mercury's geology.

Using the partition coefficients of heat-producing elements (HPE: U, Th and K) between metals/sulfides and the silicate melt, we modelled the distribution of these elements during the primordial differentiation of Mercury, when the core, the silicate part, and a hypothetical FeS layer were in equilibrium. As seen in previous studies, U, Th and K are not siderophile, but U become chalcophile at low oxygen fugacity. We showed that, under reducing conditions, U and Th are increasingly fractionated by the presence of an increasingly thick FeS layer. It turns out that, if the bulk Mercury Th/U is chondritic, then an FeS layer cannot have formed in equilibrium with the silicate melt, as it would have resulted in a fractionation of the silicate Th/U, a feature we do not observe in MESSENGER data. In addition, it seems that mantle Fe-free sulfides, thought to form a significant fraction of the mantle mineralogy, would also further fractionate Th and U. The most probable solution is that Mercury formed from materials showing Th/U close to the lowest values of the chondritic inventory, and that no FeS layer formed during primordial differentiation. This result imply that the silicate part hosts most HPE, which has important effect on the mantle's heat budget, and that the planet was not saturated in sulfur, as it would otherwise have formed an FeS layer. Finally, we show that Mercury surface K/Th and K/U ratios are several times lower than what we would expect from chondritic K content. This means that Mercury lost some K during its formation and/or geological processes. One particular possibility is the loss of K from space weathering.

Using the partition coefficients of Ti, Cr and Mn between the metal and the silicate melt, we studied the evolution of their concentration in the silicate part after core-silicate differentiation. We showed that Cr, being highly siderophile, is greatly depleted in the silicate part at lower oxygen fugacity, while Ti, and

especially Mn, are strongly concentrated in the silicate part. By comparing the measured Cr/Ti and Mn/Ti in Mercury's lavas, we modeled the expected behavior of each elements during partial melting of the mantle. Because Mercury's lavas were the products of high-degree partial melting of the mantle (20 - 50%), the residual rocks must be composed of olivines, pyroxenes, and Fe-free sulfides (CaS and/or MgS). Because we know from previous works the partitioning of these elements between olivines and pyroxenes, we could focus on calculating which phase(s) could be responsible for their expected compatibilities. We showed that Mn should be strongly compatible during partial melting, so that only a large proportion of Fe-free sulfides could explain it, with possibly the presence of alabandite (MnS) in the mantle as an accessory phase to increase its compatibility to the required values. We explain the surficial variations of Cr/Si with degree of partial melting observed by Nittler et al. (2023) by the presence of Fe-free sulfides in the mantle, which incorporates large amount of Cr, so that high degree of partial melting releases Cr in the melt. On the other hand, the lack of variation of Ti/Si observed by Cartier et al. (2020) is used to discriminate which sulfides (CaS or MgS) should dominate the mantle. Ti is very compatible in MgS, but not in CaS. This difference in behavior makes CaS the best candidate for the main sulfides in Mercury's mantle. Finally, by varying different parameters of our models, we show that the most probable scenarios for Mercury's mineralogy is of a planet that differentiated between IW - 4 and IW - 6, with a mantle rich in CaS. While each element has a distinct behavior in olivines and pyroxenes, we were not able to constrain their respective proportion in the mantle, other than stating that an olivine dominated mantle would strongly decrease the compatibility of Ti during partial melting, so that it would be concentrated on the surface, perhaps to values higher than what was measured.

Finally, the extensive production of metal/silicate partition coefficients these last ~30 years enabled us to revisit quantitatively the link between the electronegativity (E) of an element and its siderophile behavior. As such, we compiled almost 4000 data points from 30 studies on 60 elements, spanning pressures from 0.0001 to 100 GPa and temperatures from 1200 to 2875 °C. We showed that the value of the metal/silicate partition coefficient of an element can be estimated from its electronegativity and the oxygen fugacity of the sample. Moreover, we showed that, in any sample, the ratio of the partition coefficient of two elements seems constant and is proportional to the difference of electronegativity of the two elements, linked by a constant "k". For partition coefficients values in natural logarithm, the constant "k" is equal to ~16, so that a difference of electronegativity of 0.1 results in an increased metal/silicate partitioning of ~1.6. This relationship can be used to predict somewhat accurately the values of partition coefficients for a large number of elements, provided that the partition coefficient of at least one element is known in the sample. This is useful to calculate the partitioning of elements that were not measured by the lack of access to the appropriate equipment, or for those that are too difficult to measure. There are however strong deviations from this law for low electronegative elements (such as the alkaline and the rare-earth alkaline), the very electronegative elements (those with E>~2.25) and

the elements that can adopt negative valences, such as Se and Te. We were able to explain these deviations in most cases, expect for Si and Al, which are several orders of magnitude less siderophile than expected from there electronegativity. We propose that their role as network former in the silicate melt decreases their “effective” electronegativity.

Glossary

Aerobraking: a space maneuver aimed at slowing down a spacecraft passing near a planet with an atmosphere by using the drag caused by the latter. This maneuver is used to conserve fuel.

Bow shock: see Magnetosphere.

Chemical sputtering: release of atoms and molecules from the surface by chemical reactions that results from the action of solar wind or magnetospheric ions. The interaction of these ions with the material leads to chemical reactions where the product is only loosely bound to the surface, leading to its desorption (Jacob and Roth, 2007; Killen et al., 2018).

Desorption: the process from which an adsorbed molecule is released from its surface. An adsorbed molecule is a molecule which is bound to a surface, but does not penetrate it.

Exosphere: the term was coined by Spitzer (1952) to express the height of an atmosphere at which collisions cease to be important, and Chamberlain (1963) developed a model with the analytical tools to describe it. It is a region of very low material density, where collisions between atoms or molecules are very rare (we can even describe the environment as "uncollisional"), and occur mainly in the region below (i.e., the atmosphere -on Earth- or the surface -on Mercury-). It is characterized by a column density of constituents below 10^{14} cm^{-2}, where particles follow ballistic trajectories. A surface-bound exosphere, as observed on Mercury or the Moon, works radically different than an exosphere above an atmosphere, as it is in direct contact with the surface and not a denser atmosphere underneath.

Fly-by: a space maneuver that consists in a spacecraft passing by a body, without getting into its orbit. Reducing the speed of a spacecraft to get into a stable orbit around a planetary body consumes a lot of energy, and so fly-bys are used to visit them without expending too much fuel. It can also be used to perform gravity assists.

Graben: typical feature characteristic of extensive tectonics. On Mercury, they are probably formed by thermal contraction of a volcanic plain, which leads to extensional stresses (Blair et al., 2013).

Gravity assist: a type of fly-by where the spacecraft use the gravity of the encountered object (usually a planet) to change its path, or to gain or reduce its speed relative to the body the object orbits around. For example, Mariner 10 used a gravity assist at Venus to decrease its velocity in relation with the Sun, in order to get an encounter with Mercury by crossing its orbit.

Gravity well: a concept to represent the region of space that is affected by the gravitational field of a body. The more massive the body is, the deeper (and larger) the well is. The Sun, with its enormous mass compared to other bodies of the solar system, has a huge gravity well. Object in its orbit that want to fall in or climb out of its gravity well, such as a spacecraft going from the orbit of Earth to the orbit of Mercury, situated deeper inside the gravity well, have to spend large amount energy.

High-relief ridge: broadly symmetric landforms in cross section that, akin to lobate scarp, transect impact craters, and are thus interpreted as contractional features (Watters and Nimmo, 2010). They can exceed 1km in height (Watters and Schultz, 2010).

Impact vaporization: objects (meteoroids or comets) impacting the surface ejects material at high temperature. While large impacts reveal deeper geological layers and expose fresh material to the surface, micrometeoroids contribute to the daily production of ejecta, melt and vapor (Killen et al., 2018).

Ionosphere: the term was invented by R.A. Watson-Watt in 1926 (Gardiner, 1969) to describe the part of an atmosphere composed of electrons and partially ionized particles (Rishbeth, 1988).

Ion-sputtering: extraction of a surficial particles by the impact of high energy ions, such as protons coming from the solar wind (Killen et al., 2018).

Jeans escape: particles in exosphere, in opposition to particles in denser regions of atmospheres, follow ballistic paths and (almost) never collide with other particles. This means that particles with enough energy can overcome the gravitational forces of a body and leave (Jeans, 1925). This phenomenon is present on every body of the solar system, and is used to explain why some are with an atmosphere, and if certain atmospheric components are stable or if they should escape. Jeans escape is influenced by the mass of the component, the escape velocity of the body, and the heating of the upper part of the atmosphere by the Sun. Figure G1 show which chemical species is stable as a function of escape velocity and temperature of the exobase (base of the exosphere) of the body.

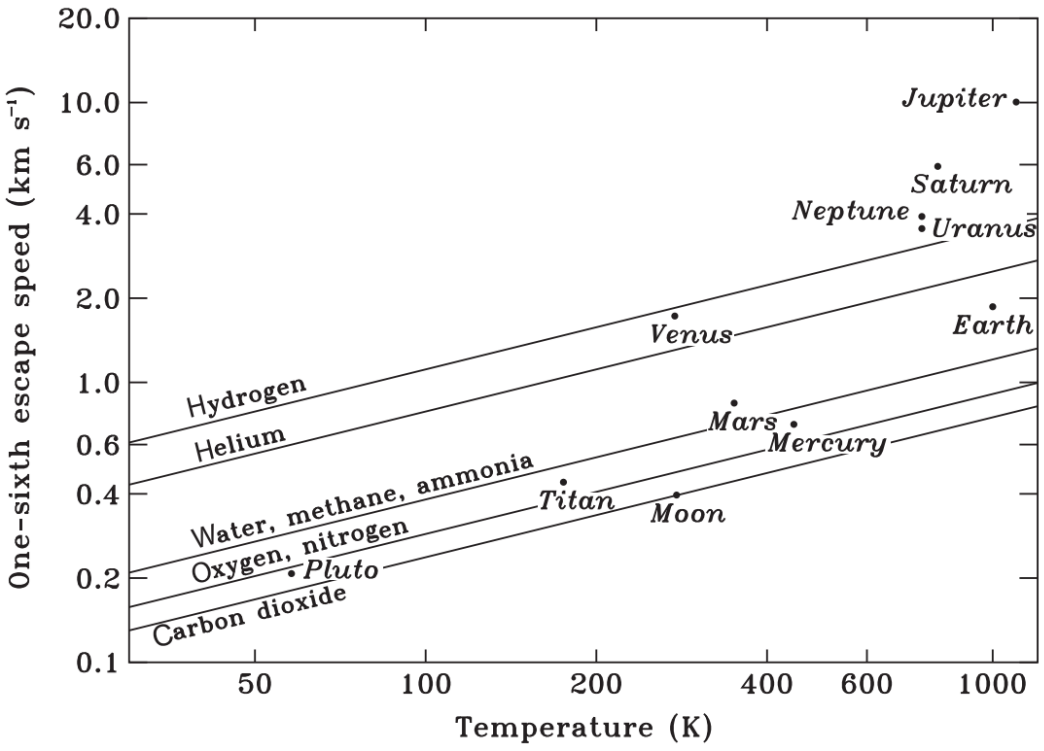

Figure G1: Stable chemical species in an atmosphere as a function of the escape velocity of the body and the temperature of its exobase. High temperatures excite the particles, which increases their chance to escape, while high escape velocity keep them gravitationally bound to the body (from Catling and Kasting, 2017).

Lobate scarp: landforms generally asymmetric in cross section, with a steep slope at the front and a gentle slope at the back (Figure G2). Their length can reach hundreds of km, and they show a lobate outline, a bit like a bow (Strom et al., 1975). Because they transect impact craters, they are interpreted as surface-breaking thrust fault, a sign of the planet's contraction (Watters and Nimmo, 2010).

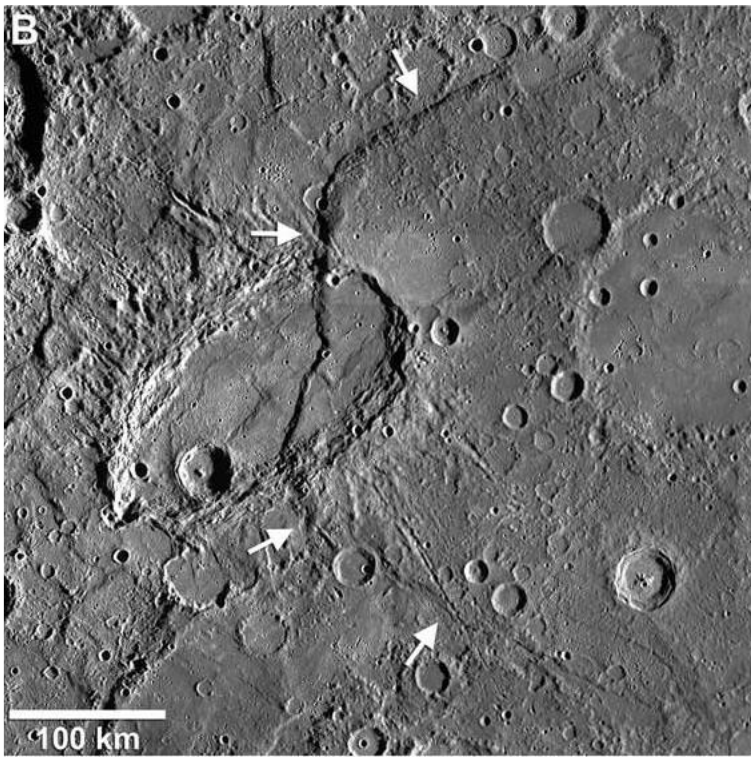

Figure G2: Example of a lobate scarp (named Beagles Rupes) crosscutting the Sveinsdottir crater (Watters et al., 2015).

Magnetic field: Most bodies of the solar system show significant magnetic fields. Other, such as a Venus or Mars, have very weak ones. Magnetic fields give us crucial information on planetary interior from afar (i.e., orbit or flybys), which are, for some bodies, one of the only ways to gather insights on their internal structure. The origins of these magnetic fields are varied; while most current magnetic fields are caused by dynamo effects in the core, some are remnant of past dynamos, such as Mars and the Moon, other are induced by the complex interactions of external field (e.g., the moons of Jupiter), and some, like Venus, arises from the interactions between the ionosphere and the solar wind (Luhmann and Cravens, 1991; Stevenson, 2010). Dynamos, the most common sources for intrinsic magnetic fields (i.e., which comes from within the planet), are thought to be created by the motion of an electrically conducting fluid. In terrestrial planets, the fluids are made of liquid metallic iron, mixed with other light elements, such as sulfur (Stevenson, 2010; Schubert and Soderlund, 2011).

Magnetopause: see Magnetosphere.

Magnetosphere: space is permeated with the solar wind, which consists of ionized particles coming from the Sun (H^+ and He^{2+}), forming a magnetized plasma. The electromagnetic interactions with the magnetic field of a planet creates a cavity in the solar wind, which is called the magnetosphere (Parks, 2003; Blanc et al., 2005) (Figure G3). Every planet of our solar system has an intrinsic magnetosphere, with the exception of Venus and Mars that do not have intrinsic magnetic field. Planetary bodies act as obstacles to the flow of the solar wind. The obstacle can be the surface itself, if no atmosphere is present,

the atmosphere or the ionosphere (as on Venus and Mars), or the magnetic field itself (Parks, 2003; Blanc et al., 2005).

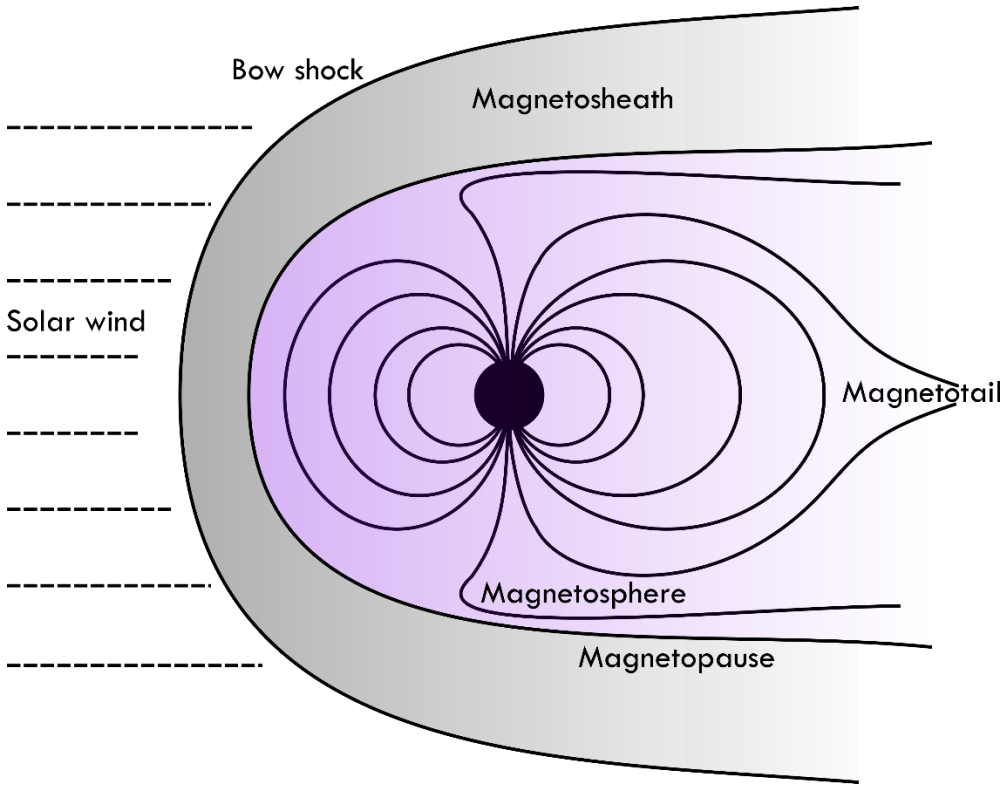

Figure G3: Schematic of a magnetosphere and its component. The planet is represented by a black circle in the center. The magnetic lines are represented by the black lines coming from the planet. The magnetosphere region is delimited by the magnetopause. The magnetopause is enveloped by a magnetosheath, itself delimited by the bow shock line, where the solar wind collides with. The magnetosphere is compressed in the dayside of the planet, and extended on its nightside.

The external limit of the magnetosphere is the magnetopause, where there is a balance between the pressure from the solar wind and the magnetic field. The shape of the magnetosphere is asymmetrical: the magnetopause's extension is the lowest on the dayside at noon, expends slightly at dusk and dawn, and expands further on the nightside. On the nightside (the antisunward direction), it forms the geomagnetic tail ("magnetotail"). A shock wave, called a bow shock, forms in front of the planet's magnetosphere. It is separated from the magnetopause by another region, named the magnetosheath (Parks, 2003; Blanc et al., 2005) (Figure G3).

Magnetotail: see Magnetosphere.

One-plate planet: see Stagnant lid.

Permanently shaded regions (PSR): on some planetary bodies, there are locations never illuminated by the Sun over geological times, typically in polar craters. On airless bodies, such as Mercury, we observe accumulation of frozen volatile as the temperature in PSR is very low; indeed, the only source of heat comes from the residual interior heat of the planet, and so ice is stable. PSR were observed on both

Mercury and the Moon, thanks to their almost vertical inclination (Lawrence, 2017, and references therein).

Photoionization: the absorption of high energy radiation from the Sun by neutral particles can lead to the formation of an ion. These ions are then trapped by the magnetic field of Mercury and, following certain lines of the magnetic field (those are "open"), can escape the exosphere (Ip, 1987; Cheng et al., 1987; Potter et al., 2002; Jasinski et al., 2021).

Photon-simulated desorption (PSD): ejection of ions, atoms or molecules from a surface caused by photon-induced electronic excitation of repulsive electronic states (Stockbauer, 1984; Killen et al., 2018). It is an important process for the volatile elements, such as Na and K. The vapor produced by PSD is of higher temperature than thermal evaporation (or desorption), but lower than impact vaporization (Killen et al., 2018).

Photophoresis: an illuminated particle has a warm side and a cold side. As gas molecules impact its surface, they are rejected with a higher force on the warm side than on the cold, which, in accordance to the action-reaction principle, give the particle a net momentum away from the source of light (here, the Sun). The force of ejection is inversely dependent on thermal conductivity, so that thermally conductive particles are less affected than low thermally conductive ones (e.g., Wurm et al., 2013).

Radiation pressure: the particles in Mercury's exosphere are submitted to constant solar radiation. The solar photon, all coming with the same incidence, are absorbed by the particle, and almost instantly reemitted isotropically. Photons have no mass, but they carry momentum; they accelerate the particles encountered by an impulse equal to the difference in momentum between the incident and the reemitted photons. This process pushes neutral species (meaning those that are not subjected to Mercury's magnetic field) anti-sunward. This forms a tail behind Mercury, whose composition is studied to infer the composition of Mercury's exosphere (Ip, 1986; Killen et al., 2018).

Solar wind: see Magnetosphere.

Stagnant-lid: Mercury, the Moon and Mars are stagnant-lid bodies, which means that they possess a single non-fragmented lithosphere, as opposed to Earth, where the lithosphere is divided into tectonic plates. As such, their crust does not experience recycling as on Earth. A review on the different tectonic modes, and how planets can switch from one to another, can be found in Lenardic (2018).

Thermal evaporation: thermal evaporation (or desorption) is the effect of removing atoms from surface materials by heat. It depends on the surface temperature and is function of the binding energy of atoms to the surface (Leblanc and Johnson, 2003; Killen et al., 2018).

Uncompressed density: the density without the compressing effect of pressure caused by gravity. While Earth's density is superior to Mercury's one because the former is more massive than the latter, its uncompressed density is lower, due to Mercury's richness in dense material, such as iron.

Wrinkle ridge: ubiquitous tectonic features found on all terrestrial planets and the Moon. They consist of a low sinuous ridge, associated with volcanic plains, and are characterized as anticlines formed by thrust faulting and folding (Watters and Schultz, 2010; Schleicher et al., 2019).

References

Aharonson, O., Zuber, M.T., Solomon, S.C., 2004. Crustal remanence in an internally magnetized non-uniform shell: a possible source for Mercury's magnetic field? Earth and Planetary Science Letters 218, 261–268. https://doi.org/10.1016/S0012-821X(03)00682-4

Albarède, F., 2009. Volatile accretion history of the terrestrial planets and dynamic implications. Nature 461, 1227–1233. https://doi.org/10.1038/nature08477

Alexander, C.M.O., Boss, A.P., Carlson, R.W., 2001. The Early Evolution of the Inner Solar System: A Meteoritic Perspective. Science 293, 64–68. https://doi.org/10.1126/science.1052872

Allred, A.L., 1961. Electronegativity values from thermochemical data. Journal of Inorganic and Nuclear Chemistry 17, 215–221. https://doi.org/10.1016/0022-1902(61)80142-5

Amelin, Y., Krot, A.N., Hutcheon, I.D., Ulyanov, A.A., 2002. Lead Isotopic Ages of Chondrules and Calcium-Aluminum-Rich Inclusions. Science 297, 1678–1683. https://doi.org/10.1126/science.1073950

Anderson, B.J., Acuña, M.H., Korth, H., Slavin, J.A., Uno, H., Johnson, C.L., Purucker, M.E., Solomon, S.C., Raines, J.M., Zurbuchen, T.H., Gloeckler, G., McNutt, R.L., 2010. The Magnetic Field of Mercury. Space Science Reviews 152, 307–339. https://doi.org/10.1007/s11214-009-9544-3

Anderson, B.J., Johnson, C.L., Korth, H., Purucker, M.E., Winslow, R.M., Slavin, J.A., Solomon, S.C., McNutt, R.L., Raines, J.M., Zurbuchen, T.H., 2011. The Global Magnetic Field of Mercury from MESSENGER Orbital Observations. Science 333, 1859–1862. https://doi.org/10.1126/science.1211001

Anderson, B.J., Johnson, C.L., Korth, H., Winslow, R.M., Borovsky, J.E., Purucker, M.E., Slavin, J.A., Solomon, S.C., Zuber, M.T., McNutt, R.L., 2012. Low-degree structure in Mercury's planetary magnetic field. Journal of Geophysical Research. 117, 2012JE004159. https://doi.org/10.1029/2012JE004159

Anderson, D.L., 1981. Hotspots, Basalts, and the Evolution of the Mantle. Science 213, 82–89. https://doi.org/10.1126/science.213.4503.82

Anderson, J.D., Colombo, G., Esposito, P.B., Lau, E.L., Trager, G.B., 1987. The mass, gravity field, and ephemeris of Mercury. Icarus 71, 337–349. https://doi.org/10.1016/0019-1035(87)90033-9

Anzures, B.A., Parman, S.W., Milliken, R.E., Namur, O., Cartier, C., Wang, S., 2020. Effect of sulfur speciation on chemical and physical properties of very reduced mercurian melts. Geochimica et Cosmochimica Acta 286, 1–18. https://doi.org/10.1016/j.gca.2020.07.024

Ash, M.E., Shapiro, I.I., Smith, W.B., 1971. The System of Planetary Masses. Science 174, 551–556. https://doi.org/10.1126/science.174.4009.551

Asphaug, E., Reufer, A., 2014. Mercury and other iron-rich planetary bodies as relics of inefficient accretion. Nature Geoscience 7, 564–568. https://doi.org/10.1038/ngeo2189

Ballhaus, C., Laurenz, V., Münker, C., Fonseca, R.O.C., Albarède, F., Rohrbach, A., Lagos, M., Schmidt, M.W., Jochum, K.-P., Stoll, B., Weis, U., Helmy, H.M., 2013. The U/Pb ratio of the Earth's mantle—A signature of late volatile addition. Earth and Planetary Science Letters 362, 237–245. https://doi.org/10.1016/j.epsl.2012.11.049

Banks, M.E., Xiao, Z., Watters, T.R., Strom, R.G., Braden, S.E., Chapman, C.R., Solomon, S.C., Klimczak, C., Byrne, P.K., 2015. Duration of activity on lobate-scarp thrust faults on Mercury. Journal of Geophysical Research: Planets 120, 1751–1762. https://doi.org/10.1002/2015JE004828

Banks, M.E., Xiao, Z., Braden, S.E., Barlow, N.G., Chapman, C.R., Fassett, C.I., Marchi, S.S., 2017. Revised constraints on absolute age limits for Mercury's Kuiperian and Mansurian stratigraphic systems. Journal of Geophysical Research: Planets 122, 1010–1020. https://doi.org/10.1002/2016JE005254

Banks, P.M., Johnson, H.E., Axford, W.I., 1970. The atmosphere of Mercury. Comments on Astrophysics and Space Physics 2, 214.

Barlow, N.G., Ferguson, S.N., Horstman, R.M., Maine, A., 2017. Comparison of central pit craters on Mars, Mercury, Ganymede, and the Saturnian satellites. Meteoritics & Planetary Science 52, 1371–1387. https://doi.org/10.1111/maps.12857

Barnes, S.J., Maier, W.D., 1999. The fractionation of Ni, Cu and the noble metals in silicate and sulphide liquids. Short Course Notes-Geological Association of Canada 13, 69–106.

Barrat, J.A., Zanda, B., Jambon, A., Bollinger, C., 2014. The lithophile trace elements in enstatite chondrites. Geochimica et Cosmochimica Acta 128, 71–94. https://doi.org/10.1016/j.gca.2013.11.042

Baumjohann, W., Matsuoka, A., Narita, Y., Magnes, W., Heyner, D., Glassmeier, K.-H., Nakamura, R., Fischer, D., Plaschke, F., Volwerk, M., Zhang, T.L., Auster, H.-U., Richter, I., Balogh, A., Carr, C.M., Dougherty, M., Horbury, T.S., Tsunakawa, H., Matsushima, M., Shinohara, M., Shibuya, H., Nakagawa, T., Hoshino, M., Tanaka, Y., Anderson, B.J., Russell, C.T., Motschmann, U., Takahashi, F., Fujimoto, A., 2020. The BepiColombo–Mio Magnetometer en Route to Mercury. Space Science Reviews 216, 125. https://doi.org/10.1007/s11214-020-00754-y

Bédard, J.H., 2005. Partitioning coefficients between olivine and silicate melts. Lithos 83, 394–419. https://doi.org/10.1016/j.lithos.2005.03.011

Bédard, J.H., 2007. Trace element partitioning coefficients between silicate melts and orthopyroxene: Parameterizations of D variations. Chemical Geology 244, 263–303. https://doi.org/10.1016/j.chemgeo.2007.06.019

Belton, M.J.S., Hunten, D.M., McElroy, M.B., 1967. A Search for an Atmosphere on Mercury. Astrophysical Journal 150, 1111. https://doi.org/10.1086/149408

Benkhoff, J., Van Casteren, J., Hayakawa, H., Fujimoto, M., Laakso, H., Novara, M., Ferri, P., Middleton, H.R., Ziethe, R., 2010. BepiColombo—Comprehensive exploration of Mercury: Mission overview and science goals. Planetary and Space Science 58, 2–20. https://doi.org/10.1016/j.pss.2009.09.020

Benz, W., Slattery, W.L., Cameron, A.G.W., 1988. Collisional stripping of Mercury's mantle. Icarus 74, 516–528. https://doi.org/10.1016/0019-1035(88)90118-2

Berndt, J., Liebske, C., Holtz, F., Freise, M., Nowak, M., Ziegenbein, D., Hurkuck, W., Koepke, J., 2002. A combined rapid-quench and H_2-membrane setup for internally heated pressure vessels: Description and application for water solubility in basaltic melts. American Mineralogist 87, 1717–1726. https://doi.org/10.2138/am-2002-11-1222

Berthet, S., Malavergne, V., Righter, K., 2009. Melting of the Indarch meteorite (EH4 chondrite) at 1GPa and variable oxygen fugacity: Implications for early planetary differentiation processes. Geochimica et Cosmochimica Acta 73, 6402–6420. https://doi.org/10.1016/j.gca.2009.07.030

Biazzo, K., Bozza, V., Mancini, L., Sozzetti, A. (Eds.), 2022. Demographics of Exoplanetary Systems: Lecture Notes of the 3rd Advanced School on Exoplanetary Science, Astrophysics and Space Science Library. Springer International Publishing, Cham. https://doi.org/10.1007/978-3-030-88124-5

Bida, T.A., Killen, R.M., 2017. Observations of the minor species Al and Fe in Mercury's exosphere. Icarus 289, 227–238. https://doi.org/10.1016/j.icarus.2016.10.019

Bida, T.A., Killen, R.M., Morgan, T.H., 2000. Discovery of calcium in Mercury's atmosphere. Nature 404, 159–161. https://doi.org/10.1038/35004521

Birch, F., 1988. Elasticity and Constitution of the Earth's Interior, in: Elastic Properties and Equations of State. American Geophysical Union (AGU), pp. 31–90. https://doi.org/10.1029/SP026p0031

Blair, D.M., Freed, A.M., Byrne, P.K., Klimczak, C., Prockter, L.M., Ernst, C.M., Solomon, S.C., Melosh, H.J., Zuber, M.T., 2013. The origin of graben and ridges in Rachmaninoff, Raditladi, and Mozart basins, Mercury. Journal of Geophysical Research: Planets 118, 47–58. https://doi.org/10.1029/2012JE004198

Blanc, M., Kallenbach, R., Erkaev, N.V., 2005. Solar System Magnetospheres. Space Science Reviews 116, 227–298. https://doi.org/10.1007/s11214-005-1958-y

Blewett, D.T., Lucey, P.G., Hawke, B.R., Ling, G.G., Robinson, M.S., 1997. A Comparison of Mercurian Reflectance and Spectral Quantities with Those of the Moon. Icarus 129, 217–231. https://doi.org/10.1006/icar.1997.5785

Blewett, D.T., Robinson, M.S., Denevi, B.W., Gillis-Davis, J.J., Head, J.W., Solomon, S.C., Holsclaw, G.M., McClintock, W.E., 2009. Multispectral images of Mercury from the first MESSENGER flyby: Analysis of global and regional color trends. Earth and Planetary Science Letters 285, 272–282. https://doi.org/10.1016/j.epsl.2009.02.021

Blewett, D.T., Chabot, N.L., Denevi, B.W., Ernst, C.M., Head, J.W., Izenberg, N.R., Murchie, S.L., Solomon, S.C., Nittler, L.R., McCoy, T.J., Xiao, Z., Baker, D.M.H., Fassett, C.I., Braden, S.E., Oberst, J., Scholten, F., Preusker, F., Hurwitz, D.M., 2011. Hollows on Mercury: MESSENGER Evidence for Geologically Recent Volatile-Related Activity. Science 333, 1856–1859. https://doi.org/10.1126/science.1211681

Blewett, D.T., Vaughan, W.M., Xiao, Z., Chabot, N.L., Denevi, B.W., Ernst, C.M., Helbert, J., D'Amore, M., Maturilli, A., Head, J.W., Solomon, S.C., 2013. Mercury's hollows: Constraints on formation and composition from analysis of geological setting and spectral reflectance. Journal of Geophysical Research: Planets 118, 1013–1032. https://doi.org/10.1029/2012JE004174

Blewett, D.T., Stadermann, A.C., Susorney, H.C., Ernst, C.M., Xiao, Z., Chabot, N.L., Denevi, B.W., Murchie, S.L., McCubbin, F.M., Kinczyk, M.J., Gillis-Davis, J.J., Solomon, S.C., 2016. Analysis of MESSENGER high-resolution images of Mercury's hollows and implications for hollow formation. Journal of Geophysical Research: Planets 121, 1798–1813. https://doi.org/10.1002/2016JE005070

Borisov, A., Palme, H., Spettel, B., 1994. Solubility of palladium in silicate melts: Implications for core formation in the Earth. Geochimica et Cosmochimica Acta 58, 705–716. https://doi.org/10.1016/0016-7037(94)90500-2

Boss, A.P., 1996. Evolution of the solar nebula. III. Protoplanetary disks undergoing mass accretion. Astrophysical Journal 469, 906.

Boss, A.P., Ciesla, F.J., 2014. The Solar Nebula, in: Treatise on Geochemistry. Elsevier, 37–53. https://doi.org/10.1016/B978-0-08-095975-7.00119-4

Bouhifd, M.A., Gautron, L., Bolfan-Casanova, N., Malavergne, V., Hammouda, T., Andrault, D., Jephcoat, A.P., 2007. Potassium partitioning into molten iron alloys at high-pressure: Implications for Earth's core. Physics of the Earth and Planetary Interiors 160, 22–33. https://doi.org/10.1016/j.pepi.2006.08.005

Bouhifd, M.A., Andrault, D., Bolfan-Casanova, N., Hammouda, T., Devidal, J.L., 2013. Metal–silicate partitioning of Pb and U: Effects of metal composition and oxygen fugacity. Geochimica et Cosmochimica Acta 114, 13–28. https://doi.org/10.1016/j.gca.2013.03.034

Boujibar, A., Andrault, D., Bouhifd, M.A., Bolfan-Casanova, N., Devidal, J.-L., Trcera, N., 2014. Metal–silicate partitioning of sulphur, new experimental and thermodynamic constraints on planetary accretion. Earth and Planetary Science Letters 391, 42–54. https://doi.org/10.1016/j.epsl.2014.01.021

Boujibar, A., Habermann, M., Righter, K., Ross, D.K., Pando, K., Righter, M., Chidester, B.A., Danielson, L.R., 2019. U, Th, and K partitioning between metal, silicate, and sulfide and implications for Mercury's structure, volatile content, and radioactive heat production. American Mineralogist 104, 1221–1237. https://doi.org/10.2138/am-2019-7000

Boukaré, C.E., Parman, S.W., Parmentier, E.M., Anzures, B.A., 2019. Production and Preservation of Sulfide Layering in Mercury's Mantle. Journal of Geophysical Research: Planets 124, 3354–3372. https://doi.org/10.1029/2019JE005942

Boyd, F.R., England, J.L., 1960. The quartz-coesite transition. Journal of Geophysical Research (1896-1977) 65, 749–756. https://doi.org/10.1029/JZ065i002p00749

Brasser, R., Mojzsis, S.J., Matsumura, S., Ida, S., 2017. The cool and distant formation of Mars. Earth and Planetary Science Letters 468, 85–93. https://doi.org/10.1016/j.epsl.2017.04.005

Breuer, D., Hauck, S.A., Buske, M., Pauer, M., Spohn, T., 2007. Interior Evolution of Mercury. Space Science Reviews 132, 229–260. https://doi.org/10.1007/s11214-007-9228-9

Bridgman, P.W., 1949. The physics of high pressure, New impression with suppl. ed, International text-books of exact science. G. Bell, London.

Broadfoot, A.L., Kumar, S., Belton, M.J.S., McElroy, M.B., 1974. Mercury's atmosphere from Mariner 10: Preliminary results. Science 185, 166–169.

Broadfoot, A.L., Shemansky, D.E., Kumar, S., 1976. Mariner 10: Mercury atmosphere. Geophysical Research Letters 3, 577–580. https://doi.org/10.1029/GL003i010p00577

Brown, S.M., Elkins-Tanton, L.T., 2009. Compositions of Mercury's earliest crust from magma ocean models. Earth and Planetary Science Letters 286, 446–455. https://doi.org/10.1016/j.epsl.2009.07.010

Brunetti, M.T., Xiao, Z., Komatsu, G., Peruccacci, S., Guzzetti, F., 2015. Large rock slides in impact craters on the Moon and Mercury. Icarus 260, 289–300. https://doi.org/10.1016/j.icarus.2015.07.014

Bullen, K.E., 1952. Cores of Terrestrial Planets. Nature 170, 363–364. https://doi.org/10.1038/170363a0

Bunce, E.J., Martindale, A., Lindsay, S., Muinonen, K., Rothery, D.A., Pearson, J., McDonnell, I., Thomas, C., Thornhill, J., Tikkanen, T., Feldman, C., Huovelin, J., Korpela, S., Esko, E., Lehtolainen, A., Treis, J., Majewski, P., Hilchenbach, M., Väisänen, T., Luttinen, A., Kohout, T., Penttilä, A., Bridges, J., Joy, K.H., Alcacera-Gil, M.A., Alibert, G., Anand, M., Bannister, N., Barcelo-Garcia, C., Bicknell, C., Blake, O., Bland, P., Butcher, G., Cheney, A., Christensen, U., Crawford, T., Crawford, I.A., Dennerl, K.,

Dougherty, M., Drumm, P., Fairbend, R., Genzer, M., Grande, M., Hall, G.P., Hodnett, R., Houghton, P., Imber, S., Kallio, E., Lara, M.L., Balado Margeli, A., Mas-Hesse, M.J., Maurice, S., Milan, S., Millington-Hotze, P., Nenonen, S., Nittler, L., Okada, T., Ormö, J., Perez-Mercader, J., Poyner, R., Robert, E., Ross, D., Pajas-Sanz, M., Schyns, E., Seguy, J., Strüder, L., Vaudon, N., Viceira-Martín, J., Williams, H., Willingale, D., Yeoman, T., 2020. The BepiColombo Mercury Imaging X-Ray Spectrometer: Science Goals, Instrument Performance and Operations. Space Science Reviews 216, 126. https://doi.org/10.1007/s11214-020-00750-2

Burger, M.H., Killen, R.M., McClintock, W.E., Vervack, R.J., Merkel, A.W., Sprague, A.L., Sarantos, M., 2012. Modeling MESSENGER observations of calcium in Mercury's exosphere. Journal of Geophysical Research 117, 2012JE004158. https://doi.org/10.1029/2012JE004158

Burger, M.H., Killen, R.M., McClintock, W.E., Merkel, A.W., Vervack, R.J., Cassidy, T.A., Sarantos, M., 2014. Seasonal variations in Mercury's dayside calcium exosphere. Icarus 238, 51–58. https://doi.org/10.1016/j.icarus.2014.04.049

Butler, B.J., Muhleman, D.O., Slade, M.A., 1993. Mercury: full-disk radar images and the detection and stability of ice at the North Pole. Journal of Geophysical Research: Planets 98, 15003–15023. https://doi.org/10.1029/93JE01581

Byrne, P.K., Klimczak, C., Celâl Şengör, A.M., Solomon, S.C., Watters, T.R., Hauck, Ii, S.A., 2014. Mercury's global contraction much greater than earlier estimates. Nature Geoscience 7, 301–307. https://doi.org/10.1038/ngeo2097

Byrne, P.K., Ostrach, L.R., Fassett, C.I., Chapman, C.R., Denevi, B.W., Evans, A.J., Klimczak, C., Banks, M.E., Head, J.W., Solomon, S.C., 2016. Widespread effusive volcanism on Mercury likely ended by about 3.5 Ga. Geophysical Research Letters 43, 7408–7416. https://doi.org/10.1002/2016GL069412

Byrne, P.K., Whitten, J.L., Klimczak, C., McCubbin, F.M., Ostrach, L.R., 2018. The Volcanic Character of Mercury, in: Anderson, B.J., Nittler, L.R., Solomon, S.C. (Eds.), Mercury: The View after MESSENGER, Cambridge Planetary Science. Cambridge University Press, Cambridge, 287–323. https://doi.org/10.1017/9781316650684.012

Cameron, A.G.W., 1985. The partial volatilization of Mercury. Icarus 64, 285–294. https://doi.org/10.1016/0019-1035(85)90091-0

Camichel, H., Dollfus, A., 1968. La rotation et la cartographie de la planete Mercure. Icarus 8, 216–226. https://doi.org/10.1016/0019-1035(68)90075-4

Carmichael, I.S.E., 1991. The redox states of basic and silicic magmas: a reflection of their source regions? Contributions to Mineralogy and Petrology 106, 129–141. https://doi.org/10.1007/BF00306429

Cartier, C., 2014. Comportement des terres rares (REE) et des éléments fortement chargés (HSFE) pendant la différenciation précoce de la Terre sous faible fugacité d'oxygène (These de doctorat). Clermont-Ferrand 2.

Cartier, C., Wood, B.J., 2019. The Role of Reducing Conditions in Building Mercury. Elements 15, 39–45. https://doi.org/10.2138/gselements.15.1.39

Cartier, C., Hammouda, T., Boyet, M., Bouhifd, M.A., Devidal, J.-L., 2014a. Redox control of the fractionation of niobium and tantalum during planetary accretion and core formation. Nature Geoscience 7, 573–576. https://doi.org/10.1038/ngeo2195

Cartier, C., Hammouda, T., Doucelance, R., Boyet, M., Devidal, J.-L., Moine, B., 2014b. Experimental study of trace element partitioning between enstatite and melt in enstatite chondrites at low oxygen fugacities and 5GPa. Geochimica et Cosmochimica Acta 130, 167–187. https://doi.org/10.1016/j.gca.2014.01.002

Cartier, C., Namur, O., Nittler, L.R., Weider, S.Z., Crapster-Pregont, E., Vorburger, A., Frank, E.A., Charlier, B., 2020. No FeS layer in Mercury? Evidence from Ti/Al measured by MESSENGER. Earth and Planetary Science Letters 534, 116108. https://doi.org/10.1016/j.epsl.2020.116108

Cartier, C., Llado, L., Pirotte, H., Tissandier, L., Namur, O., Collinet, M., Wang, S-J., Charlier, B., in rev. Partitioning of Ni and Co between metal and silicate melts: expanding the oxy-barometer to reducing conditions.

Catling, D.C., Kasting, J.F., 2017. Atmospheric Evolution on Inhabited and Lifeless Worlds, 1st ed. Cambridge University Press. https://doi.org/10.1017/9781139020558

Chabot, N.L., Drake, M.J., 1999. Potassium solubility in metal: the effects of composition at 15 kbar and 1900°C on partitioning between iron alloys and silicate melts. Earth and Planetary Science Letters.

Chabot, N.L., Agee, C.B., 2003. Core formation in the Earth and Moon: new experimental constraints from V, Cr, and Mn. Geochimica et Cosmochimica Acta 67, 2077–2091. https://doi.org/10.1016/S0016-7037(02)01272-3

Chabot, N.L., Ernst, C.M., Denevi, B.W., Nair, H., Deutsch, A.N., Blewett, D.T., Murchie, S.L., Neumann, G.A., Mazarico, E., Paige, D.A., Harmon, J.K., Head, J.W., Solomon, S.C., 2014a. Images of surface volatiles in Mercury's polar craters acquired by the MESSENGER spacecraft. Geology 42, 1051–1054. https://doi.org/10.1130/G35916.1

Chabot, N.L., Wollack, E.A., Klima, R.L., Minitti, M.E., 2014b. Experimental constraints on Mercury's core composition. Earth and Planetary Science Letters 390, 199–208. https://doi.org/10.1016/j.epsl.2014.01.004

Chabot, N.L., Ernst, C.M., Paige, D.A., Nair, H., Denevi, B.W., Blewett, D.T., Murchie, S.L., Deutsch, A.N., Head, J.W., Solomon, S.C., 2016. Imaging Mercury's polar deposits during MESSENGER's low-altitude campaign. Geophysical Research Letters 43, 9461–9468. https://doi.org/10.1002/2016GL070403

Chabot, N.L., Shread, E.E., Harmon, J.K., 2018. Investigating Mercury's South Polar Deposits: Arecibo Radar Observations and High-Resolution Determination of Illumination Conditions. Journal of Geophysical Research: Planets 123, 666–681. https://doi.org/10.1002/2017JE005500

Chamberlain, J.W., 1963. Planetary coronae and atmospheric evaporation. Planetary and Space Science 11, 901–960. https://doi.org/10.1016/0032-0633(63)90122-3

Charlier, B., Namur, O., 2019. The Origin and Differentiation of Planet Mercury. Elements 15, 9–14. https://doi.org/10.2138/gselements.15.1.9

Charlier, B., Grove, T.L., Zuber, M.T., 2013. Phase equilibria of ultramafic compositions on Mercury and the origin of the compositional dichotomy. Earth and Planetary Science Letters 363, 50–60. https://doi.org/10.1016/j.epsl.2012.12.021

Chaufray, J.-Y., Leblanc, F., Werner, A.I.E., Modolo, R., Aizawa, S., 2022. Seasonal variations of Mg and Ca in the exosphere of Mercury. Icarus 384, 115081. https://doi.org/10.1016/j.icarus.2022.115081

Chen, B., Li, J., Hauck, S.A., 2008. Non-ideal liquidus curve in the Fe-S system and Mercury's snowing core. Geophysical Research Letters 35, 2008GL033311. https://doi.org/10.1029/2008GL033311

Cheng, A.F., Johnson, R.E., Krimigis, S.M., Lanzerotti, L.J., 1987. Magnetosphere, exosphere, and surface of mercury. Icarus 71, 430–440. https://doi.org/10.1016/0019-1035(87)90038-8

Cherkasov, A.R., Galkin, V.I., Zueva, E.M., Cherkasov, R.A., 1998. The concept of electronegativity. The current state of the problem. Russian Chemical Reviews 67, 375–392. https://doi.org/10.1070/RC1998v067n05ABEH000383

Clarke, F.W., 1889. The relative abundance of the chemical elements. Philosophical society of Washington Bulletin 11, 131–142.

Clarke, F.W., 1911. The Data of Geochemistry. ISGS Bulletin 491.

Clement, M.S., Raymond, S.N., Chambers, J.E., 2021. Mercury as the Relic of Earth and Venus Outward Migration. The Astrophysical Journal Letters 923, L16. https://doi.org/10.3847/2041-8213/ac3e6d

Clesi, V., Bouhifd, M.A., Bolfan-Casanova, N., Manthilake, G., Fabbrizio, A., Andrault, D., 2016. Effect of H2O on metal–silicate partitioning of Ni, Co, V, Cr, Mn and Fe: Implications for the oxidation state of the Earth and Mars. Geochimica et Cosmochimica Acta 192, 97–121. https://doi.org/10.1016/j.gca.2016.07.029

Colson, R.O., McKay, G.A., Taylor, L.A., 1988. Temperature and composition dependencies of trace element partitioning: Olivine/melt and low-Ca pyroxene/melt. Geochimica et Cosmochimica Acta 52, 539–553. https://doi.org/10.1016/0016-7037(88)90109-3

Condamine, P., Tournier, S., Charlier, B., Médard, E., Triantafyllou, A., Dalou, C., Tissandier, L., Lequin, D., Cartier, C., Füri, E., Burnard, P.G., Demouchy, S., Marrocchi, Y., 2022. Influence of intensive parameters and assemblies on friction evolution during piston-cylinder experiments. American Mineralogist 107, 1575–1581. https://doi.org/10.2138/am-2022-7958

Corgne, A., Keshav, S., Fei, Y., McDonough, W.F., 2007. How much potassium is in the Earth's core? New insights from partitioning experiments. Earth and Planetary Science Letters 256, 567–576. https://doi.org/10.1016/j.epsl.2007.02.012

Corgne, A., Keshav, S., Wood, B.J., McDonough, W.F., Fei, Y., 2008. Metal–silicate partitioning and constraints on core composition and oxygen fugacity during Earth accretion. Geochimica et Cosmochimica Acta 72, 574–589. https://doi.org/10.1016/j.gca.2007.10.006

Cremonese, G., Sprague, A., Warell, J., Thomas, N., Ksamfomality, L., 2007. The Surface of Mercury as Seen by Mariner 10. Space Science Reviews 132, 291–306. https://doi.org/10.1007/s11214-007-9231-1

Crozaz, G., Lundberg, L.L., 1995. The origin of oldhamite in unequilibrated enstatite chondrites. Geochimica et Cosmochimica Acta 59, 3817–3831. https://doi.org/10.1016/0016-7037(95)00268-5

Dantowitz, R.F., Teare, S.W., Kozubal, M.J., 2000. Ground-based High-Resolution Imaging of Mercury. Astronomical Journal 119, 2455. https://doi.org/10.1086/301328

Dauphas, N., 2017. The isotopic nature of the Earth's accreting material through time. Nature 541, 521–524. https://doi.org/10.1038/nature20830

Dauphas, N., Pourmand, A., 2011. Hf–W–Th evidence for rapid growth of Mars and its status as a planetary embryo. Nature 473, 489–492. https://doi.org/10.1038/nature10077

Dauphas, N., Nie, N.X., Blanchard, M., Zhang, Z.J., Zeng, H., Hu, J.Y., Meheut, M., Visscher, C., Canup, R., Hopp, T., 2022. The Extent, Nature, and Origin of K and Rb Depletions and Isotopic Fractionations in Earth, the Moon, and Other Planetary Bodies. Planetary Science Journal 3, 29. https://doi.org/10.3847/PSJ/ac2e09

Denevi, B.W., Ernst, C.M., Meyer, H.M., Robinson, M.S., Murchie, S.L., Whitten, J.L., Head, J.W., Watters, T.R., Solomon, S.C., Ostrach, L.R., Chapman, C.R., Byrne, P.K., Klimczak, C., Peplowski, P.N., 2013. The distribution and origin of smooth plains on Mercury. Journal of Geophysical Research: Planets 118, 891–907. https://doi.org/10.1002/jgre.20075

Denevi, B.W., Robinson, M.S., Solomon, S.C., Murchie, S.L., Blewett, D.T., Domingue, D.L., McCoy, T.J., Ernst, C.M., Head, J.W., Watters, T.R., Chabot, N.L., 2009. The Evolution of Mercury's Crust: A Global Perspective from MESSENGER. Science 324, 613–618. https://doi.org/10.1126/science.1172226

Denevi, B.W., Ernst, C.M., Prockter, L.M., Robinson, M.S., 2018. The Geologic History of Mercury, in: Anderson, B.J., Nittler, L.R., Solomon, S.C. (Eds.), Mercury: The View after MESSENGER, Cambridge Planetary Science. Cambridge University Press, Cambridge, 144–175. https://doi.org/10.1017/9781316650684.007

Dollfus, A., 1961. Visual and photographic studies of planets at the Pic du Midi. Planets and Satellites 534.

Dollfus, A., 1963. Mesure du diametre de Mercure lors de son passage devant le Soleil le 7 Novembre 1960: Resultats des observations collectives demandees par l'Union Astronomique Internationale. Icarus 2, 219–225. https://doi.org/10.1016/0019-1035(63)90017-4

Domingue, D.L., D'Amore, M., Ferrari, S., Helbert, J., Izenberg, N.R., 2019. Analysis of the MESSENGER MASCS photometric targets part II: Photometric variability between geomorphological units. Icarus 319, 140–246. https://doi.org/10.1016/j.icarus.2018.07.018

Doressoundiram, A., Leblanc, F., Foellmi, C., Erard, S., 2009. Metallic species in Mercury's exosphere: EMMI/New technology telescope observations. Astronomical Journal 137, 3859. https://doi.org/10.1088/0004-6256/137/4/3859

Dumberry, M., 2011. The free librations of Mercury and the size of its inner core. Geophysical Research Letters 38. https://doi.org/10.1029/2011GL048277

Dumberry, M., Rivoldini, A., Van Hoolst, T., Yseboodt, M., 2013. The role of Mercury's core density structure on its longitudinal librations. Icarus 225, 62–74. https://doi.org/10.1016/j.icarus.2013.03.001

Dunn, T., 1987. Partitioning of Hf, Lu, Ti, and Mn between olivine, clinopyroxene and basaltic liquid. Contributions to Mineralogy and Petrology 96, 476–484. https://doi.org/10.1007/BF01166692

Easton, A. j., 1985. E-Chondrites: Significance of the Partition of Elements Between 'Silicate' and 'Sulphide.' Meteoritics 20, 89–101. https://doi.org/10.1111/j.1945-5100.1985.tb00849.x

Ebel, D.S., Alexander, C.M.O., 2011. Equilibrium condensation from chondritic porous IDP enriched vapor: Implications for Mercury and enstatite chondrite origins. Planetary and Space Science 59, 1888–1894. https://doi.org/10.1016/j.pss.2011.07.017

Edmund, E., Morard, G., Baron, M.A., Rivoldini, A., Yokoo, S., Boccato, S., Hirose, K., Pakhomova, A., Antonangeli, D., 2022. The Fe-FeSi phase diagram at Mercury's core conditions. Nature Communication 13, 387. https://doi.org/10.1038/s41467-022-27991-9

Elkins-Tanton, L.T., 2008. Linked magma ocean solidification and atmospheric growth for Earth and Mars. Earth and Planetary Science Letters 271, 181–191. https://doi.org/10.1016/j.epsl.2008.03.062

Elkins-Tanton, L.T., 2012. Magma Oceans in the Inner Solar System. Annual Review of Earth and Planetary Sciences 40, 113–139. https://doi.org/10.1146/annurev-earth-042711-105503

Elkins-Tanton, L.T., Burgess, S., Yin, Q.-Z., 2011. The lunar magma ocean: Reconciling the solidification process with lunar petrology and geochronology. Earth and Planetary Science Letters 304, 326–336. https://doi.org/10.1016/j.epsl.2011.02.004

Ernst, C.M., Chabot, N.L., Klima, R.L., Kubota, S., Rogers, G., Byrne, P.K., Hauck, S.A., Vander Kaaden, K.E., Vervack, R.J., Besse, S., Blewett, D.T., Denevi, B.W., Goossens, S., Indyk, S.J., Izenberg, N.R., Johnson, C.L., Jozwiak, L.M., Korth, H., McNutt, R.L., Murchie, S.L., Peplowski, P.N., Raines, J.M., Rampe, E.B., Thompson, M.S., Weider, S.Z., 2022. Science Goals and Mission Concept for a Landed Investigation of Mercury. Planetary Science Journal 3, 68. https://doi.org/10.3847/PSJ/ac1c0f

Eugster, H.P., 1957. Heterogeneous Reactions Involving Oxidation and Reduction at High Pressures and Temperatures. The Journal of Chemical Physics 26, 1760–1761. https://doi.org/10.1063/1.1743626

Eugster, H.P., 1977. Compositions and Thermodynamics of Metamorphic Solutions, in: Fraser, D.G. (Ed.), Thermodynamics in Geology. Springer Netherlands, Dordrecht, 183–202. https://doi.org/10.1007/978-94-010-1252-2_10

Eugster, H.P., Wones, D.R., 1962. Stability Relations of the Ferruginous Biotite, Annite. Journal of Petrology 3, 82–125. https://doi.org/10.1093/petrology/3.1.82

Evans, L.G., Peplowski, P.N., Rhodes, E.A., Lawrence, D.J., McCoy, T.J., Nittler, L.R., Solomon, S.C., Sprague, A.L., Stockstill-Cahill, K.R., Starr, R.D., Weider, S.Z., Boynton, W.V., Hamara, D.K., Goldsten, J.O., 2012. Major-element abundances on the surface of Mercury: Results from the MESSENGER Gamma-Ray Spectrometer. Journal of Geophysical Research: Planets 117. https://doi.org/10.1029/2012JE004178

Evans, L.G., Peplowski, P.N., McCubbin, F.M., McCoy, T.J., Nittler, L.R., Zolotov, M.Yu., Ebel, D.S., Lawrence, D.J., Starr, R.D., Weider, S.Z., Solomon, S.C., 2015. Chlorine on the surface of Mercury: MESSENGER gamma-ray measurements and implications for the planet's formation and evolution. Icarus 257, 417–427. https://doi.org/10.1016/j.icarus.2015.04.039

Fegley, B., Cameron, A.G.W., 1987. A vaporization model for iron/silicate fractionation in the Mercury protoplanet. Earth and Planetary Science Letters 82, 207–222. https://doi.org/10.1016/0012-821X(87)90196-8

Ferrari, S., Massironi, M., Marchi, S., Byrne, P.K., Klimczak, C., Martellato, E., Cremonese, G., 2015. Age relationships of the Rembrandt basin and Enterprise Rupes, Mercury. Geological Society, London, Special Publications 401, 159–172. https://doi.org/10.1144/SP401.20

Field, G., 1964. The Atmosphere of Mercury, in: The Origin and Evolution of Atmospheres and Oceans. Presented at the The Origin and Evolution of Atmospheres and Oceans, p. 269.

Fischer, R.A., Nakajima, Y., Campbell, A.J., Frost, D.J., Harries, D., Langenhorst, F., Miyajima, N., Pollok, K., Rubie, D.C., 2015. High pressure metal–silicate partitioning of Ni, Co, V, Cr, Si, and O. Geochimica et Cosmochimica Acta 167, 177–194. https://doi.org/10.1016/j.gca.2015.06.026

Fischer-Gödde, M., Kleine, T., 2017. Ruthenium isotopic evidence for an inner Solar System origin of the late veneer. Nature 541, 525–527. https://doi.org/10.1038/nature21045

Fricker, P.E., Reynolds, R.T., Summers, A.L., Cassen, P.M., 1976. Does Mercury have a molten core? Nature 259, 293–294. https://doi.org/10.1038/259293a0

Frost, B.R., 1991. Introduction to oxygen fugacity and its petrologic importance. Reviews in Mineralogy and Geochemistry 25, 1–9.

Fyfe, W.S., 1951. Isomorphism and bond type. American Mineralogist 36, 538–542.

Gaetani, G.A., Grove, T.L., 1997. Partitioning of moderately siderophile elements among olivine, silicate melt, and sulfide melt: Constraints on core formation in the Earth and Mars. Geochimica et Cosmochimica Acta 61, 1829–1846. https://doi.org/10.1016/S0016-7037(97)00033-1

Gannoun, A., Boyet, M., El Goresy, A., Devouard, B., 2011. REE and actinide microdistribution in Sahara 97072 and ALHA77295 EH3 chondrites: A combined cosmochemical and petrologic investigation. Geochimica et Cosmochimica Acta 75, 3269–3289. https://doi.org/10.1016/j.gca.2011.03.017

Genova, A., Goossens, S., Mazarico, E., Lemoine, F.G., Neumann, G.A., Kuang, W., Sabaka, T.J., Hauck, S.A., Smith, D.E., Solomon, S.C., Zuber, M.T., 2019. Geodetic Evidence That Mercury Has A Solid Inner Core. Geophysical Research Letters 46, 3625–3633. https://doi.org/10.1029/2018GL081135

Gardiner, G.W., 1969. Origin of the Term Ionosphere. Nature 224, 1096–1096. https://doi.org/10.1038/2241096a0

Gessmann, C.K., Rubie, D.C., McCammon, C.A., 1999. Oxygen fugacity dependence of Ni, Co, Mn, Cr, V, and Si partitioning between liquid metal and magnesiowüstite at 9–18 GPa and 2200°C. Geochimica et Cosmochimica Acta 63, 1853–1863. https://doi.org/10.1016/S0016-7037(99)00059-9

Gessmann, C.K., Wood, B.J., Rubie, D.C., Kilburn, M.R., 2001. Solubility of silicon in liquid metal at high pressure: implications for the composition of the Earth's core. Earth and Planetary Science Letters 184, 367–376. https://doi.org/10.1016/S0012-821X(00)00325-3

Giacomini, L., Massironi, M., Galluzzi, V., Ferrari, S., Palumbo, P., 2020. Dating long thrust systems on Mercury: New clues on the thermal evolution of the planet. Geoscience Frontiers 11, 855–870. https://doi.org/10.1016/j.gsf.2019.09.005

Gibson, D.T., 1949. The terrestrial distribution of the elements. Quarterly Reviews, Chemical Society 3, 263. https://doi.org/10.1039/qr9490300263

Gladman, B., Coffey, J., 2009. Mercurian impact ejecta: Meteorites and mantle. Meteoritics & Planetary Science 44, 285–291. https://doi.org/10.1111/j.1945-5100.2009.tb00734.x

Glassmeier, K., Auster, H., Motschmann, U., 2007a. A feedback dynamo generating Mercury's magnetic field. Geophysical Research Letters 34, 2007GL031662. https://doi.org/10.1029/2007GL031662

Glassmeier, K.-H., Grosser, J., Auster, U., Constantinescu, D., Narita, Y., Stellmach, S., 2007b. Electromagnetic Induction Effects and Dynamo Action in the Hermean System. Space Science Reviews 132, 511–527. https://doi.org/10.1007/s11214-007-9244-9

Goldschmidt, V.M., 1923. Geochemische Verteilungsgesetze der Elemente, Norsk videnskaps-akademi i Oslo. Skrifter. I. Mathematisk- naturvidenskabelig klasse. In Kommission bei J. Dybwad, I kommission hos J. Dybwad, Kristiania : Oslo.

Goldschmidt, V.M., 1937. The principles of distribution of chemical elements in minerals and rocks. The seventh Hugo Müller Lecture, delivered before the Chemical Society on March 17th, 1937. Journal of the Chemical Society 0, 655–673. https://doi.org/10.1039/JR9370000655

Goldsten, J.O., Rhodes, E.A., Boynton, W.V., Feldman, W.C., Lawrence, D.J., Trombka, J.I., Smith, D.M., Evans, L.G., White, J., Madden, N.W., Berg, P.C., Murphy, G.A., Gurnee, R.S., Strohbehn, K., Williams, B.D., Schaefer, E.D., Monaco, C.A., Cork, C.P., Eckels, J.D., Miller, W.O., Burks, M.T., Hagler, L.B., DeTeresa, S.J., Witte, M.C., 2007. The MESSENGER Gamma-Ray and Neutron Spectrometer, in: Domingue, D.L., Russell, C.T. (Eds.), The Messenger Mission to Mercury. Springer, New York, NY, 339–391. https://doi.org/10.1007/978-0-387-77214-1_10

Goossens, S., Renaud, J.P., Henning, W.G., Mazarico, E., Bertone, S., Genova, A., 2022. Evaluation of Recent Measurements of Mercury's Moments of Inertia and Tides Using a Comprehensive Markov Chain Monte Carlo Method. Planetary Science Journal 3, 37. https://doi.org/10.3847/PSJ/ac4bb8

Griffin, W.L., Powell, W.J., Pearson, N.J., O'Reilly, S.Y., 2008. GLITTER: data reduction software for laser ablation ICP-MS, in: Laser Ablation ICP-MS in the Earth Sciences: Current Practices and Outstanding Issues, Short Course Series. 308–311.

Grosser, J., Glassmeier, K.-H., Stadelmann, A., 2004. Induced magnetic field effects at planet Mercury. Planetary and Space Science 52, 1251–1260. https://doi.org/10.1016/j.pss.2004.08.005

Grott, M., Breuer, D., Laneuville, M., 2011. Thermo-chemical evolution and global contraction of mercury. Earth and Planetary Science Letters 307, 135–146. https://doi.org/10.1016/j.epsl.2011.04.040

Guerrero, J.M., Lowman, J.P., Tackley, P.J., 2021. Did the cessation of convection in Mercury's mantle allow for a dynamo supporting increase in heat loss from its core? Earth and Planetary Science Letters 571, 117108. https://doi.org/10.1016/j.epsl.2021.117108

Haggerty, S.E., 1978. The redox state of planetary basalts. Geophysical Research Letters 5, 443–446. https://doi.org/10.1029/GL005i006p00443

Hall, H.T., 1958. Some High-Pressure, High-Temperature Apparatus Design Considerations: Equipment for Use at 100 000 Atmospheres and 3000°C. Review of Scientific Instruments 29, 267–275. https://doi.org/10.1063/1.1716172

Hammouda, T., Boyet, M., Frossard, P., Cartier, C., 2022. The message of oldhamites from enstatite chondrites. Progress in Earth and Planetary Science 9, 13. https://doi.org/10.1186/s40645-022-00471-w

Hanson, B., Jones, J.H., 1998. The systematics of Cr3+ and Cr2+ partitioning between olivine and liquid in the presence of spinel. American Mineralogist 83, 669–684. https://doi.org/10.2138/am-1998-7-801

Harder, H., Schubert, G., 2001. Sulfur in Mercury's Core? Icarus 151, 118–122. https://doi.org/10.1006/icar.2001.6586

Harkins, W.D., 1917. The evolution of the elements and the stability of comlex atoms. I. A new periodic system which shows a relation between the abundance of the elements and the structure of the nuclei of atoms. Journal of the American Chemical Society 39, 856–879. https://doi.org/10.1021/ja02250a002

Harmon, J.K., Slade, M.A., 1992. Radar Mapping of Mercury: Full-Disk Images and Polar Anomalies. Science 258, 640–643. https://doi.org/10.1126/science.258.5082.640

Harmon, J.K., Campbell, D.B., Bindschadler, D.L., Head, J.W., Shapiro, I.I., 1986. Radar altimetry of Mercury: A Preliminary analysis. Journal of Geophysical Research 91, 385–401. https://doi.org/10.1029/JB091iB01p00385

Harmon, J.K., Slade, M.A., Rice, M.S., 2011. Radar imagery of Mercury's putative polar ice: 1999–2005 Arecibo results. Icarus 211, 37–50. https://doi.org/10.1016/j.icarus.2010.08.007

Hauck, S.A., Johnson, C.L., 2019. Mercury: Inside the Iron Planet. Elements 15, 21–26. https://doi.org/10.2138/gselements.15.1.21

Hauck, S.A., Dombard, A.J., Phillips, R.J., Solomon, S.C., 2004. Internal and tectonic evolution of Mercury. Earth and Planetary Science Letters 222, 713–728. https://doi.org/10.1016/j.epsl.2004.03.037

Hauck, S.A., Eng, D.A., Tahu, G.J., 2010. Mercury Lander Mission Concept Study. NASA Solar System Exploration.

Hauck, S.A., Margot, J., Solomon, S.C., Phillips, R.J., Johnson, C.L., Lemoine, F.G., Mazarico, E., McCoy, T.J., Padovan, S., Peale, S.J., Perry, M.E., Smith, D.E., Zuber, M.T., 2013. The curious case of Mercury's internal structure. Journal of Geophysical Research: Planets 118, 1204–1220. https://doi.org/10.1002/jgre.20091

Head, J.W., 1974. Stratigraphy of the descartes region (Apollo 16): implications for the origin of samples. The Moon 11, 77–99. https://doi.org/10.1007/BF01877795

Head, J.W., Chapman, C.R., Domingue, D.L., Hawkins, S.E., McClintock, W.E., Murchie, S.L., Prockter, L.M., Robinson, M.S., Strom, R.G., Watters, T.R., 2007. The Geology of Mercury: The View Prior to the MESSENGER Mission. Space Science Reviews 131, 41–84. https://doi.org/10.1007/s11214-007-9263-6

Head, J.W., Murchie, S.L., Prockter, L.M., Robinson, M.S., Solomon, S.C., Strom, R.G., Chapman, C.R., Watters, T.R., McClintock, W.E., Blewett, D.T., Gillis-Davis, J.J., 2008. Volcanism on Mercury: Evidence from the First MESSENGER Flyby. Science 321, 69–72. https://doi.org/10.1126/science.1159256

Head, J.W., Murchie, S.L., Prockter, L.M., Solomon, S.C., Chapman, C.R., Strom, R.G., Watters, T.R., Blewett, D.T., Gillis-Davis, J.J., Fassett, C.I., Dickson, J.L., Morgan, G.A., Kerber, L., 2009. Volcanism on Mercury: Evidence from the first MESSENGER flyby for extrusive and explosive activity and the volcanic origin of plains. Earth and Planetary Science Letters, MESSENGER's First Flyby of Mercury 285, 227–242. https://doi.org/10.1016/j.epsl.2009.03.007

Head, J.W., Chapman, C.R., Strom, R.G., Fassett, C.I., Denevi, B.W., Blewett, D.T., Ernst, C.M., Watters, T.R., Solomon, S.C., Murchie, S.L., Prockter, L.M., Chabot, N.L., Gillis-Davis, J.J., Whitten, J.L., Goudge, T.A., Baker, D.M.H., Hurwitz, D.M., Ostrach, L.R., Xiao, Z., Merline, W.J., Kerber, L., Dickson, J.L., Oberst, J., Byrne, P.K., Klimczak, C., Nittler, L.R., 2011. Flood Volcanism in the Northern High Latitudes of Mercury Revealed by MESSENGER. Science 333, 1853–1856. https://doi.org/10.1126/science.1211997

Helbert, J., Maturilli, A., D'Amore, M., 2013. Visible and near-infrared reflectance spectra of thermally processed synthetic sulfides as a potential analog for the hollow forming materials on Mercury. Earth and Planetary Science Letters 369–370, 233–238. https://doi.org/10.1016/j.epsl.2013.03.045

Heyner, D., Wicht, J., Gómez-Pérez, N., Schmitt, D., Auster, H.-U., Glassmeier, K.-H., 2011. Evidence from Numerical Experiments for a Feedback Dynamo Generating Mercury's Magnetic Field. Science 334, 1690–1693. https://doi.org/10.1126/science.1207290

Heyner, D., Auster, H.-U., Fornaçon, K.-H., Carr, C., Richter, I., Mieth, J.Z.D., Kolhey, P., Exner, W., Motschmann, U., Baumjohann, W., Matsuoka, A., Magnes, W., Berghofer, G., Fischer, D., Plaschke, F., Nakamura, R., Narita, Y., Delva, M., Volwerk, M., Balogh, A., Dougherty, M., Horbury, T., Langlais, B., Mandea, M., Masters, A., Oliveira, J.S., Sánchez-Cano, B., Slavin, J.A., Vennerstrøm, S., Vogt, J., Wicht, J., Glassmeier, K.-H., 2021. The BepiColombo Planetary Magnetometer MPO-MAG: What Can We Learn from the Hermean Magnetic Field? Space Science Reviews 217, 52. https://doi.org/10.1007/s11214-021-00822-x

Hillgren, V.J., 1991. Partitioning behavior of NI, CO, MO, and W between basaltic liquid and Ni-rich metal: Implications for the origin of the moon and lunar core formation. Geophysical Research Letters 18, 2077–2080. https://doi.org/10.1029/91GL02534

Hillgren, V.J., Drake, M.J., Rubie, D.C., 1996. High pressure and high temperature metal-silicate partitioning of siderophile elements: The importance of silicate liquid composition. Geochimica et Cosmochimica Acta 60, 2257–2263. https://doi.org/10.1016/0016-7037(96)00079-8

Holloway, J.R., 1971. Internally Heated Pressure Vessels, in: Ulmer, G.C. (Ed.), Research Techniques for High Pressure and High Temperature. Springer, Berlin, Heidelberg, 217–258. https://doi.org/10.1007/978-3-642-88097-1_8

Holloway, J.R., Pan, V., Gudmundsson, G., 1992. High-pressure fluid-absent melting experiments in the presence of graphite: oxygen fugacity, ferric/ferrous ratio and dissolved CO2. European Journal of Mineralogy 4, 105–114.

Holzheid, A., Borisov, A., Palme, H., 1994. The effect of oxygen fugacity and temperature on solubilities of nickel, cobalt, and molybdenum in silicate melts. Geochimica et Cosmochimica Acta 58, 1975–1981. https://doi.org/10.1016/0016-7037(94)90429-4

Hood, L.L., Schubert, G., 1979. Inhibition of solar wind impingement on mercury by planetary induction currents. Journal of Geophysical Research 84, 2641–2647. https://doi.org/10.1029/JA084iA06p02641

Hood, L.L., Oliveira, J.S., Galluzzi, V., Rothery, D.A., 2018. Investigating Sources of Mercury's Crustal Magnetic Field: Further Mapping of MESSENGER Magnetometer Data. Journal of Geophysical Research: Planets 123, 2647–2666. https://doi.org/10.1029/2018JE005683

Howard, H.T., Tyler, G.L., Esposito, P.B., Anderson, J.D., Reasenberg, R.D., Shapiro, I.I., Fjeldbo, G., Kliore, A.J., Levy, G.S., Brunn, D.L., Dickinson, R., Edelson, R.E., Martin, W.L., Postal, R.B., Seidel, B., Sesplaukis, T.T., Shirley, D.L., Stelzried, C.T., Sweetnam, D.N., Wood, G.E., Zygielbaum, A.I., 1974a. Mercury: Results on Mass, Radius, Ionosphere, and Atmosphere from Mariner 10 Dual-Frequency Radio Signals. Science 185, 179–180. https://doi.org/10.1126/science.185.4146.179

Howard, H.T., Tyler, G.L., Fjeldbo, G., Kliore, A.J., Levy, G.S., Brunn, D.L., Dickinson, R., Edelson, R.E., Martin, W.L., Postal, R.B., Seidel, B., Sesplaukis, T.T., Shirley, D.L., Stelzried, C.T., Sweetnam, D.N., Zygielbaum, A.I., Esposito, P.B., Anderson, J.D., Shapiro, I.I., Reasenberg, R.D., 1974b. Venus: Mass, Gravity Field, Atmosphere, and Ionosphere as Measured by the Mariner 10 Dual-Frequency Radio System. Science 183, 1297–1301. https://doi.org/10.1126/science.183.4131.1297

Hsu, W., 1998. Geochemical and petrographic studies of oldhamite, diopside, and roedderite in enstatite meteorites. Meteoritics & Planetary Science 33, 291–301. https://doi.org/10.1111/j.1945-5100.1998.tb01633.x

Huang, H., Fei, Y., Cai, L., Jing, F., Hu, X., Xie, H., Zhang, L., Gong, Z., 2011. Evidence for an oxygen-depleted liquid outer core of the Earth. Nature 479, 513–516. https://doi.org/10.1038/nature10621

Hubbard, A., 2014. Explaining Mercury's density through magnetic erosion. Icarus 241, 329–335. https://doi.org/10.1016/j.icarus.2014.06.032

Humayun, M., Clayton, R.N., 1995. Potassium isotope cosmochemistry: Genetic implications of volatile element depletion. Geochimica et Cosmochimica Acta 59, 2131–2148. https://doi.org/10.1016/0016-7037(95)00132-8

Iacovino, K., McCubbin, F.M., Vander Kaaden, K.E., Clark, J., Wittmann, A., Jakubek, R.S., Moore, G.M., Fries, M.D., Archer, D., Boyce, J.W., 2023. Carbon as a key driver of super-reduced explosive volcanism on Mercury: Evidence from graphite-melt smelting experiments. Earth and Planetary Science Letters 602, 117908. https://doi.org/10.1016/j.epsl.2022.117908

Ingrao, N.J., Hammouda, T., Boyet, M., Gaborieau, M., Moine, B.N., Vlastelic, I., Bouhifd, M.A., Devidal, J.-L., Mathon, O., Testemale, D., Hazemann, J.-L., Proux, O., 2019. Rare earth element partitioning between sulphides and melt: Evidence for Yb2+ and Sm2+ in EH chondrites. Geochimica et Cosmochimica Acta 265, 182–197. https://doi.org/10.1016/j.gca.2019.08.036

Ip, W.-H., 1986. The sodium exosphere and magnetosphere of Mercury. Geophysical Research Letters 13, 423–426. https://doi.org/10.1029/GL013i005p00423

Ip, W.-H., 1987. Dynamics of electrons and heavy ions in Mercury's magnetosphere. Icarus 71, 441–447. https://doi.org/10.1016/0019-1035(87)90039-X

Jacob, W., Roth, J., 2007. Chemical Sputtering, in: Sputtering by Particle Bombardment. 329–400. https://doi.org/10.1007/978-3-540-44502-9_6

Jana, D., Walker, D., 1997. The influence of sulfur on partitioning of siderophile elements. Geochimica et Cosmochimica Acta 61, 5255–5277. https://doi.org/10.1016/S0016-7037(97)00307-4

Jantzen, T., Hack, K., Yazhenskikh, E., Müller, M., 2017. Evaluation of thermodynamic data and phase equilibria in the system Ca–Cr–Cu–Fe–Mg–Mn–S part I: Binary and quasi-binary subsystems. Calphad 56, 270–285. https://doi.org/10.1016/j.calphad.2016.04.011

Jasinski, J.M., Cassidy, T.A., Raines, J.M., Milillo, A., Regoli, L.H., Dewey, R., Slavin, J.A., Mangano, V., Murphy, N., 2021. Photoionization Loss of Mercury's Sodium Exosphere: Seasonal Observations by MESSENGER and the THEMIS Telescope. Geophysical Research Letters 48, e2021GL092980. https://doi.org/10.1029/2021GL092980

Javoy, M., 1995. The integral enstatite chondrite model of the Earth. Geophysical Research Letters 22, 2219–2222. https://doi.org/10.1029/95GL02015

Javoy, M., Kaminski, E., 2014. Earth's Uranium and Thorium content and geoneutrinos fluxes based on enstatite chondrites. Earth and Planetary Science Letters 407, 1–8. https://doi.org/10.1016/j.epsl.2014.09.028

Javoy, M., Kaminski, E., Guyot, F., Andrault, D., Sanloup, C., Moreira, M., Labrosse, S., Jambon, A., Agrinier, P., Davaille, A., Jaupart, C., 2010. The chemical composition of the Earth: Enstatite chondrite models. Earth and Planetary Science Letters 293, 259–268. https://doi.org/10.1016/j.epsl.2010.02.033

Jeans, J., 1925. The dynamical theory of gases, 4th ed. ed. Cambridge University Press, Cambridge.

Jeffreys, H., 1937. The Density Distributions in the inner Planets. Geophysical Supplements to the Monthly Notices of the Royal Astronomical Society 4, 62–71. https://doi.org/10.1111/j.1365-246X.1937.tb00410.x

Jensen, W.B., 1996. Electronegativity from Avogadro to Pauling: Part 1: Origins of the Electronegativity Journal of Chemical Education 73, 11. https://doi.org/10.1021/ed073p11

Jia, X., Slavin, J.A., Poh, G., DiBraccio, G.A., Toth, G., Chen, Y., Raines, J.M., Gombosi, T.I., 2019. MESSENGER Observations and Global Simulations of Highly Compressed Magnetosphere Events at Mercury. Journal of Geophysical Research: Space Physics 124, 229–247. https://doi.org/10.1029/2018JA026166

Johansen, A., Lambrechts, M., 2017. Forming Planets via Pebble Accretion. Annual Review of Earth and Planetary Sciences 45, 359–387. https://doi.org/10.1146/annurev-earth-063016-020226

Johansen, A., Oishi, J.S., Low, M.-M.M., Klahr, H., Henning, T., Youdin, A., 2007. Rapid planetesimal formation in turbulent circumstellar disks. Nature 448, 1022–1025. https://doi.org/10.1038/nature06086

Johnson, C.L., Phillips, R.J., Purucker, M.E., Anderson, B.J., Byrne, P.K., Denevi, B.W., Feinberg, J.M., Hauck, S.A., Head, J.W., Korth, H., James, P.B., Mazarico, E., Neumann, G.A., Philpott, L.C., Siegler, M.A., Tsyganenko, N.A., Solomon, S.C., 2015. Low-altitude magnetic field measurements by

MESSENGER reveal Mercury's ancient crustal field. Science 348, 892–895. https://doi.org/10.1126/science.aaa8720

Johnson, C.L., Philpott, L.C., Anderson, B.J., Korth, H., Hauck, S.A., Heyner, D., Phillips, R.J., Winslow, R.M., Solomon, S.C., 2016. MESSENGER observations of induced magnetic fields in Mercury's core. Geophysical Research Letters 43, 2436–2444. https://doi.org/10.1002/2015GL067370

Jozwiak, L.M., Head, J.W., Wilson, L., 2018. Explosive volcanism on Mercury: Analysis of vent and deposit morphology and modes of eruption. Icarus 302, 191–212. https://doi.org/10.1016/j.icarus.2017.11.011

Kawai, N., Endo, S., 1970. The Generation of Ultrahigh Hydrostatic Pressures by a Split Sphere Apparatus. Review of Scientific Instruments 41, 1178–1181. https://doi.org/10.1063/1.1684753

Keil, K., 1968. Mineralogical and chemical relationships among enstatite chondrites. Journal of Geophysical Research 73, 6945–6976. https://doi.org/10.1029/JB073i022p06945

Keil, K., 2007. Occurrence and origin of keilite, (Fe>0.5,Mg<0.5)S, in enstatite chondrite impact-melt rocks and impact-melt breccias. Geochemistry 67, 37–54. https://doi.org/10.1016/j.chemer.2006.05.002

Keil, K., Andersen, C.A., 1965. Electron microprobe study of the Jajh deh Kot Lalu enstatite chondrite. Geochimica et Cosmochimica Acta 29, 621–632. https://doi.org/10.1016/0016-7037(65)90059-1

Keil, K., Snetsinger, K.G., 1967. Niningerite: A New Meteoritic Sulfide. Science 155, 451–453. https://doi.org/10.1126/science.155.3761.451

Kerber, L., Head, J.W., Blewett, D.T., Solomon, S.C., Wilson, L., Murchie, S.L., Robinson, M.S., Denevi, B.W., Domingue, D.L., 2011. The global distribution of pyroclastic deposits on Mercury: The view from MESSENGER flybys 1–3. Planetary and Space Science 59, 1895–1909. https://doi.org/10.1016/j.pss.2011.03.020

Kilburn, M.R., Wood, B.J., 1997. Metal–silicate partitioning and the incompatibility of S and Si during core formation. Earth and Planetary Science Letters 152, 139–148. https://doi.org/10.1016/S0012-821X(97)00125-8

Killen, R.M., Hahn, J.M., 2015. Impact vaporization as a possible source of Mercury's calcium exosphere. Icarus 250, 230–237. https://doi.org/10.1016/j.icarus.2014.11.035

Killen, R.M., Potter, A.E., Morgan, T.H., 1990. Spatial distribution of sodium vapor in the atmosphere of Mercury. Icarus 85, 145–167. https://doi.org/10.1016/0019-1035(90)90108-L

Killen, R.M., Burger, M.H., Vervack, R.J., Cassidy, T.A., 2018. Understanding Mercury's Exosphere: Models Derived from MESSENGER Observations. https://doi.org/10.1017/9781316650684.016

Kiseeva, E.S., Wood, B.J., 2013. A simple model for chalcophile element partitioning between sulphide and silicate liquids with geochemical applications. Earth and Planetary Science Letters 383, 68–81. https://doi.org/10.1016/j.epsl.2013.09.034

Kiseeva, E.S., Wood, B.J., 2015. The effects of composition and temperature on chalcophile and lithophile element partitioning into magmatic sulphides. Earth and Planetary Science Letters 424, 280–294. https://doi.org/10.1016/j.epsl.2015.05.012

Knibbe, J.S., Van Westrenen, W., 2015. The interior configuration of planet Mercury constrained by moment of inertia and planetary contraction: The interior configuration of Mercury. Journal of Geophysical Research: Planets 120, 1904–1923. https://doi.org/10.1002/2015JE004908

Knibbe, J.S., Van Westrenen, W., 2018. The thermal evolution of Mercury's Fe–Si core. Earth and Planetary Science Letters 482, 147–159. https://doi.org/10.1016/j.epsl.2017.11.006

Knibbe, J.S., Luginbühl, S.M., Stoevelaar, R., Van Der Plas, W., Van Harlingen, D.M., Rai, N., Steenstra, E.S., Van De Geer, R., Van Westrenen, W., 2018. Calibration of a multi-anvil high-pressure apparatus to simulate planetary interior conditions. EPJ Techniques and Instrumentation 5, 5. https://doi.org/10.1140/epjti/s40485-018-0047-z

Knibbe, J.S., Rivoldini, A., Luginbuhl, S.M., Namur, O., Charlier, B., Mezouar, M., Sifre, D., Berndt, J., Kono, Y., Neuville, D.R., Van Westrenen, W., Van Hoolst, T., 2021. Mercury's Interior Structure Constrained by Density and P-Wave Velocity Measurements of Liquid Fe-Si-C Alloys. Journal of Geophysical Research: Planets 126, e2020JE006651. https://doi.org/10.1029/2020JE006651

Kuiper, G.P., 1956a. The Formation of the Planets, Part I. Journal of the Royal Astronomical Society of Canada 50, 57.

Kuiper, G.P., 1956b. The Formation of the Planets, Part II. Journal of the Royal Astronomical Society of Canada 50, 105.

Kuiper, G.P., 1956c. The Formation of the Planets, Part III. Journal of the Royal Astronomical Society of Canada 50, 158.

Laurenz, V., Rubie, D.C., Frost, D.J., Vogel, A.K., 2016. The importance of sulfur for the behavior of highly-siderophile elements during Earth's differentiation. Geochimica et Cosmochimica Acta 194, 123–138. https://doi.org/10.1016/j.gca.2016.08.012

Lawrence, D.J., 2017. A tale of two poles: Toward understanding the presence, distribution, and origin of volatiles at the polar regions of the Moon and Mercury. Journal of Geophysical Research: Planets 122, 21–52. https://doi.org/10.1002/2016JE005167

Lawrence, D.J., Feldman, W.C., Goldsten, J.O., Maurice, S., Peplowski, P.N., Anderson, B.J., Bazell, D., McNutt, R.L., Nittler, L.R., Prettyman, T.H., Rodgers, D.J., Solomon, S.C., Weider, S.Z., 2013. Evidence for Water Ice Near Mercury's North Pole from MESSENGER Neutron Spectrometer Measurements. Science 339, 292–296. https://doi.org/10.1126/science.1229953

Le Bas, M.J., 2000. IUGS Reclassification of the High-Mg and Picritic Volcanic Rocks. Journal of Petrology 41, 1467–1470. https://doi.org/10.1093/petrology/41.10.1467

Leblanc, F., Johnson, R.E., 2003. Mercury's sodium exosphere. Icarus 164, 261–281. https://doi.org/10.1016/S0019-1035(03)00147-7

Leblanc, F., Doressoundiram, A., Schneider, N., Massetti, S., Wedlund, M., López Ariste, A., Barbieri, C., Mangano, V., Cremonese, G., 2009. Short-term variations of Mercury's Na exosphere observed with very high spectral resolution. Geophysical Research Letters 36, 2009GL038089. https://doi.org/10.1029/2009GL038089

Lehner, S.W., Petaev, M.I., Zolotov, M.Yu., Buseck, P.R., 2013. Formation of niningerite by silicate sulfidation in EH3 enstatite chondrites. Geochimica et Cosmochimica Acta 101, 34–56. https://doi.org/10.1016/j.gca.2012.10.003

Lenardic, A., 2018. The diversity of tectonic modes and thoughts about transitions between them. Philosophical Transactions of the Royal Society A. 376, 20170416. https://doi.org/10.1098/rsta.2017.0416

Lewis, J.S., 1972. Metal/silicate fractionation in the solar system. Earth and Planetary Science Letters 15, 286–290. https://doi.org/10.1016/0012-821X(72)90174-4

Liebermann, R.C., 2011. Multi-anvil, high pressure apparatus: a half-century of development and progress. High Pressure Research 31, 493–532. https://doi.org/10.1080/08957959.2011.618698

Lodders, K., Fegley, B., 1993. Lanthanide and actinide chemistry at highCO/ ratios in the solar nebula. Earth and Planetary Science Letters 117, 125–145. https://doi.org/10.1016/0012-821X(93)90122-P

Lodders, K., Fegley, B., 1998. The planetary scientist's companion. Oxford University Press, New York.

Lodders, K., Amari, S., 2005. Presolar grains from meteorites: Remnants from the early times of the solar system. Geochemistry 65, 93–166. https://doi.org/10.1016/j.chemer.2005.01.001

Lodders, K., Palme, H., Gail, H.-P., 2009. Abundances of the Elements in the Solar System. Landolt Börnstein 4B, 712. https://doi.org/10.1007/978-3-540-88055-4_34

Lü, J., Sun, Y., Nafi Toksöz, M., Zheng, Y., Zuber, M.T., 2011. Seismic effects of the Caloris basin impact, Mercury. Planetary and Space Science 59, 1981–1991. https://doi.org/10.1016/j.pss.2011.07.013

Lucchetti, A., Pajola, M., Galluzzi, V., Giacomini, L., Carli, C., Cremonese, G., Marzo, G.A., Ferrari, S., Massironi, M., Palumbo, P., 2018. Mercury Hollows as Remnants of Original Bedrock Materials and Devolatilization Processes: A Spectral Clustering and Geomorphological Analysis. Journal of Geophysical Research: Planets 123, 2365–2379. https://doi.org/10.1029/2018JE005722

Luhmann, J.G., Cravens, T.E., 1991. Magnetic fields in the ionosphere of Venus. Space Science Reviews 55, 201–274. https://doi.org/10.1007/BF00177138

Lyttleton, R.A., 1969. On the internal structures of mercury and venus. Astrophysics and Space Science 5, 18–35. https://doi.org/10.1007/BF00653933

MacDonald, G.J.F., 1963. The internal constitutions of the inner planets and the moon. Space Science Reviews 2, 473–557. https://doi.org/10.1007/BF00172383

Malavergne, V., Siebert, J., Guyot, F., Gautron, L., Combes, R., Hammouda, T., Borensztajn, S., Frost, D., Martinez, I., 2004. Si in the core? New high-pressure and high-temperature experimental data. Geochimica et Cosmochimica Acta 68, 4201–4211. https://doi.org/10.1016/j.gca.2004.04.013

Malavergne, V., Tarrida, M., Combes, R., Bureau, H., Jones, J., Schwandt, C., 2007. New high-pressure and high-temperature metal/silicate partitioning of U and Pb: Implications for the cores of the Earth and Mars. Geochimica et Cosmochimica Acta 71, 2637–2655. https://doi.org/10.1016/j.gca.2007.03.011

Malavergne, V., Toplis, M.J., Berthet, S., Jones, J., 2010. Highly reducing conditions during core formation on Mercury: Implications for internal structure and the origin of a magnetic field. Icarus 206, 199–209. https://doi.org/10.1016/j.icarus.2009.09.001

Malavergne, V., Cordier, P., Righter, K., Brunet, F., Zanda, B., Addad, A., Smith, T., Bureau, H., Surblé, S., Raepsaet, C., Charon, E., Hewins, R.H., 2014. How Mercury can be the most reduced terrestrial planet and still store iron in its mantle. Earth and Planetary Science Letters 394, 186–197. https://doi.org/10.1016/j.epsl.2014.03.028

Mangano, V., Massetti, S., Milillo, A., Mura, A., Orsini, S., Leblanc, F., 2013. Dynamical evolution of sodium anisotropies in the exosphere of Mercury. Planetary and Space Science 82–83, 1–10. https://doi.org/10.1016/j.pss.2013.03.002

Mann, U., Frost, D.J., Rubie, D.C., 2009. Evidence for high-pressure core-mantle differentiation from the metal–silicate partitioning of lithophile and weakly-siderophile elements. Geochimica et Cosmochimica Acta 73, 7360–7386. https://doi.org/10.1016/j.gca.2009.08.006

Mann, U., Frost, D.J., Rubie, D.C., Becker, H., Audétat, A., 2012. Partitioning of Ru, Rh, Pd, Re, Ir and Pt between liquid metal and silicate at high pressures and high temperatures - Implications for the origin of highly siderophile element concentrations in the Earth's mantle. Geochimica et Cosmochimica Acta 84, 593–613. https://doi.org/10.1016/j.gca.2012.01.026

Marchi, S., Chapman, C.R., Fassett, C.I., Head, J.W., Bottke, W.F., Strom, R.G., 2013. Global resurfacing of Mercury 4.0–4.1 billion years ago by heavy bombardment and volcanism. Nature 499, 59–61. https://doi.org/10.1038/nature12280

Margot, J.L., Peale, S.J., Jurgens, R.F., Slade, M.A., Holin, I.V., 2007. Large Longitude Libration of Mercury Reveals a Molten Core. Science 316, 710–714. https://doi.org/10.1126/science.1140514

Margot, J.-L., Hauck, S.A., Mazarico, E., Padovan, S., Peale, S.J., 2018. Mercury's Internal Structure, in: Solomon, S.C., Nittler, L.R., Anderson, B.J. (Eds.), Mercury. Cambridge University Press, 85–113. https://doi.org/10.1017/9781316650684.005

Mason, B., 1966. The enstatite chondrites. Geochimica et Cosmochimica Acta 30, 23–39. https://doi.org/10.1016/0016-7037(66)90089-5

Maurice, M., Tosi, N., Samuel, H., Plesa, A., Hüttig, C., Breuer, D., 2017. Onset of solid-state mantle convection and mixing during magma ocean solidification. Journal of Geophysical research: Planets 122, 577–598. https://doi.org/10.1002/2016JE005250

McCammon, C.A., 2005. Mantle oxidation state and oxygen fugacity: Constraints on mantle chemistry, structure, and dynamics, in: Van Der Hilst, R.D., Bass, J.D., Matas, J., Trampert, J. (Eds.), Geophysical Monograph Series. American Geophysical Union, Washington, D. C., 219–240. https://doi.org/10.1029/160GM14

McClintock, W.E., Vervack, R.J., Bradley, E.T., Killen, R.M., Mouawad, N., Sprague, A.L., Burger, M.H., Solomon, S.C., Izenberg, N.R., 2009. MESSENGER Observations of Mercury's Exosphere: Detection of Magnesium and Distribution of Constituents. Science 324, 610–613. https://doi.org/10.1126/science.1172525

McClintock, W.E., Cassidy, T.A., Merkel, A.W., Killen, R.M., Burger, M.H., Vervack, R.J., 2018. Observations of Mercury's Exosphere: Composition and Structure, in: Solomon, S.C., Nittler, L.R., Anderson, B.J. (Eds.), Mercury. Cambridge University Press, 371–406. https://doi.org/10.1017/9781316650684.015

McCoy, T.J., Dickinson, T.L., Lofgren, G.E., 1999. Partial melting of the Indarch (EH4) meteorite: A textural, chemical, and phase relations view of melting and melt migration. Meteoritics & Planetary Science 34, 735–746. https://doi.org/10.1111/j.1945-5100.1999.tb01386.x

McCubbin, F.M., Riner, M.A., Vander Kaaden, K.E., Burkemper, L.K., 2012. Is Mercury a volatile-rich planet? Geophysical Research Letters 39, 2012GL051711. https://doi.org/10.1029/2012GL051711

McCubbin, F.M., Vander Kaaden, K.E., Peplowski, P.N., Bell, A.S., Nittler, L.R., Boyce, J.W., Evans, L.G., Keller, L.P., Elardo, S.M., McCoy, T.J., 2017. A Low O/Si Ratio on the Surface of Mercury: Evidence

for Silicon Smelting? Journal of Geophysical research: Planets 122, 2053–2076. https://doi.org/10.1002/2017JE005367

McDonough, W.F., 2016. The Composition of the Lower Mantle and Core, in: Terasaki, H., Fischer, R.A. (Eds.), Geophysical Monograph Series. Wiley, 143–159. https://doi.org/10.1002/9781118992487.ch12

Mclennan, S.M., 2003. Large-ion lithophile element fractionation during the early differentiation of Mars and the composition of the martian primitive mantle. Meteoritics & Planetary Science 38, 895–904. https://doi.org/10.1111/j.1945-5100.2003.tb00286.x

Mendillo, M., Warell, J., Limaye, S.S., Baumgardner, J., Sprague, A., Wilson, J.K., 2001. Imaging the surface of Mercury using ground-based telescopes. Planetary and Space Science 49, 1501–1505. https://doi.org/10.1016/S0032-0633(01)00088-5

Merkel, A.W., Cassidy, T.A., Vervack, R.J., McClintock, W.E., Sarantos, M., Burger, M.H., Killen, R.M., 2017. Seasonal variations of Mercury's magnesium dayside exosphere from MESSENGER observations. Icarus 281, 46–54. https://doi.org/10.1016/j.icarus.2016.08.032

Michel, N.C., Hauck, S.A., Solomon, S.C., Phillips, R.J., Roberts, J.H., Zuber, M.T., 2013. Thermal evolution of Mercury as constrained by MESSENGER observations. Journal of Geophysical research: Planets 118, 1033–1044. https://doi.org/10.1002/jgre.20049

Mikouchi, T., McKay, G., Le, L., 1994. Cr, MN and CA Distributions for Olivine in Angritic Systems: Constraints on the Origins of Cr-rich and Ca-poor Core Olivine in Angrite LEW87051 907. Abstracts of the 25th Lunar and Planetary Science Conference.

Milillo, A., Wurz, P., Orsini, S., Delcourt, D., Kallio, E., Killen, R.M., Lammer, H., Massetti, S., Mura, A., Barabash, S., Cremonese, G., Daglis, I.A., De Angelis, E., Di Lellis, A.M., Livi, S., Mangano, V., Torkar, K., 2005. Surface-Exosphere-Magnetosphere System Of Mercury. Space Science Reviews 117, 397–443. https://doi.org/10.1007/s11214-005-3593-z

Mills, N.M., Agee, C.B., Draper, D.S., 2007. Metal–silicate partitioning of cesium: Implications for core formation. Geochimica et Cosmochimica Acta 71, 4066–4081. https://doi.org/10.1016/j.gca.2007.05.024

Minear, J.W., Fletcher, C.R., 1978. Crystallization of a lunar magma ocean. Lunar and Planetary Science Conference Proceedings 1, 263–283.

Miozzi, F., Morard, G., Antonangeli, D., Baron, M.A., Pakhomova, A., Clark, A.N., Mezouar, M., Fiquet, G., 2022. The Fe-Si-C system at extreme P-T conditions: A possible core crystallization pathway for reduced planets. Geochimica et Cosmochimica Acta 322, 129–142. https://doi.org/10.1016/j.gca.2022.01.013

Morard, G., Katsura, T., 2010. Pressure–temperature cartography of Fe–S–Si immiscible system. Geochimica et Cosmochimica Acta 74, 3659–3667. https://doi.org/10.1016/j.gca.2010.03.025

Morbidelli, A., Bitsch, B., Crida, A., Gounelle, M., Guillot, T., Jacobson, S., Johansen, A., Lambrechts, M., Lega, E., 2016. Fossilized condensation lines in the Solar System protoplanetary disk. Icarus 267, 368–376. https://doi.org/10.1016/j.icarus.2015.11.027

Morgan, J.W., Lovering, J.F., 1968. Uranium and thorium abundances in chondritic meteorites. Talanta 15, 1079–1095. https://doi.org/10.1016/0039-9140(68)80031-1

Morlok, A., Renggli, C., Charlier, B., Namur, O., Klemme, S., Reitze, M.P., Weber, I., Stojic, A.N., Bauch, K.E., Hiesinger, H., Helbert, J., 2023. A mid-infrared study of synthetic glass and crystal mixtures analog to the geochemical terranes on mercury. Icarus 396, 115498. https://doi.org/10.1016/j.icarus.2023.115498

Morrison, D., 1976. IAU nomenclature for topographic features on Mercury. Icarus 28, 605–606. https://doi.org/10.1016/0019-1035(76)90134-2

Mouser, M.D., Dygert, N., 2023. On the Potential for Cumulate Mantle Overturn in Mercury. Journal of Geophysical Research: Planets 128, e2023JE007739. https://doi.org/10.1029/2023JE007739

Mouser, M.D., Dygert, N., Anzures, B.A., Grambling, N.L., Hrubiak, R., Kono, Y., Shen, G., Parman, S.W., 2021. Experimental Investigation of Mercury's Magma Ocean Viscosity: Implications for the Formation of Mercury's Cumulate Mantle, Its Subsequent Dynamic Evolution, and Crustal Petrogenesis. Journal of Geophysical Research: Planets 126, e2021JE006946. https://doi.org/10.1029/2021JE006946

Murchie, S.L., Klima, R.L., Denevi, B.W., Ernst, C.M., Keller, M.R., Domingue, D.L., Blewett, D.T., Chabot, N.L., Hash, C.D., Malaret, E., Izenberg, N.R., Vilas, F., Nittler, L.R., Gillis-Davis, J.J., Head, J.W., Solomon, S.C., 2015. Orbital multispectral mapping of Mercury with the MESSENGER Mercury Dual Imaging System: Evidence for the origins of plains units and low-reflectance material. Icarus 254, 287–305. https://doi.org/10.1016/j.icarus.2015.03.027

Murchie, S.L., Klima, R.L., Izenberg, N.R., Domingue, D.L., Blewett, D.T., Helbert, J., 2018. Spectral Reflectance Constraints on the Composition and Evolution of Mercury's Surface, in: Anderson, B.J., Nittler, L.R., Solomon, S.C. (Eds.), Mercury: The View after MESSENGER, Cambridge Planetary Science. Cambridge University Press, Cambridge, 191–216. https://doi.org/10.1017/9781316650684.009

Murchie, S.L., Izenberg, N.R., Klima, R.L., 2019. Spectral Analyses of Mercury, in: Bishop, J.L., Bell Iii, J.F., Moersch, J.E. (Eds.), Remote Compositional Analysis. Cambridge University Press, 351–367. https://doi.org/10.1017/9781316888872.019

Murray, B.C., Belton, M.J.S., Danielson, G.E., Davies, M.E., Gault, D., Hapke, B., O'Leary, B., Strom, R.G., Suomi, V., Trask, N., 1974a. Mariner 10 Pictures of Mercury: First Results. Science 184, 459–461. https://doi.org/10.1126/science.184.4135.459

Murray, B.C., Belton, M.J.S., Danielson, G.E., Davies, M.E., Gault, D.E., Hapke, B., O'Leary, B., Strom, R.G., Suomi, V., Trask, N., 1974b. Mercury's Surface: Preliminary Description and Interpretation from Mariner 10 Pictures. Science 185, 169–179. https://doi.org/10.1126/science.185.4146.169

Murray, B.C., Strom, R.G., Trask, N.J., Gault, D.E., 1975. Surface history of Mercury: Implications for terrestrial planets. Journal of Geophysical Research 80, 2508–2514. https://doi.org/10.1029/JB080i017p02508

Murray, J.B., Dollfus, A., Smith, B., 1972. Cartography of the surface markings of Mercury. Icarus 17, 576–584. https://doi.org/10.1016/0019-1035(72)90023-1

Nakamura-Messenger, K., Clemett, S.J., Rubin, A.E., Choi, B.-G., Zhang, S., Rahman, Z., Oikawa, K., Keller, L.P., 2012. Wassonite: A new titanium monosulfide mineral in the Yamato 691 enstatite chondrite. American Mineralogist 97, 807–815. https://doi.org/10.2138/am.2012.3946

Namur, O., Charlier, B., 2017. Silicate mineralogy at the surface of Mercury. Nature Geoscience 10, 9–13. https://doi.org/10.1038/ngeo2860

Namur, O., Charlier, B., Holtz, F., Cartier, C., McCammon, C., 2016a. Sulfur solubility in reduced mafic silicate melts: Implications for the speciation and distribution of sulfur on Mercury. Earth and Planetary Science Letters 448, 102–114. https://doi.org/10.1016/j.epsl.2016.05.024

Namur, O., Collinet, M., Charlier, B., Grove, T.L., Holtz, F., McCammon, C., 2016b. Melting processes and mantle sources of lavas on Mercury. Earth and Planetary Science Letters 439, 117–128. https://doi.org/10.1016/j.epsl.2016.01.030

Ness, N.F., Whang, Y.C., 1971. Solar wind interaction with Mercury. Journal of Geophysical Research 76, 3136–3143. https://doi.org/10.1029/JA076i013p03136

Ness, N.F., Behannon, K.W., Lepping, R.P., Whang, Y.C., Schatten, K.H., 1974. Magnetic Field Observations near Mercury: Preliminary Results from Mariner 10. Science 185, 151–160. https://doi.org/10.1126/science.185.4146.151

Ness, N.F., Behannon, K.W., Lepping, R.P., Whang, Y.C., 1975. The magnetic field of Mercury, 1. Journal of Geophysical Research 80, 2708–2716. https://doi.org/10.1029/JA080i019p02708

Nimmo, F., 2002. Constraining the crustal thickness on Mercury from viscous topographic relaxation. Geophysical Research Letters 29, 7-1-7–4. https://doi.org/10.1029/2001GL013883

Nisbet, E., Walker, D., 1982. Komatiites and the structure of the Archaean mantle. Earth and Planetary Science Letters 60, 105–113. https://doi.org/10.1016/0012-821X(82)90025-5

Nittler, L.R., Starr, R.D., Weider, S.Z., McCoy, T.J., Boynton, W.V., Ebel, D.S., Ernst, C.M., Evans, L.G., Goldsten, J.O., Hamara, D.K., Lawrence, D.J., McNutt, R.L., Schlemm, C.E., Solomon, S.C., Sprague, A.L., 2011. The Major-Element Composition of Mercury's Surface from MESSENGER X-ray Spectrometry. Science 333, 1847–1850. https://doi.org/10.1126/science.1211567

Nittler, L. R., Chabot, N.L., Grove, T.L., Peplowski, P.N., 2018a. The Chemical Composition of Mercury, in: Solomon, S.C., Nittler, L.R., Anderson, B.J. (Eds.), Mercury. Cambridge University Press, 30–51. https://doi.org/10.1017/9781316650684.003

Nittler, L. R., Boujibar, A., Crapster-Pregont, E., Frank, E.A., McCoy, T.J., McCubbin, F.M., Starr, R.D., Vander Kaaden, K.E., Vorburger, A., Weider, S.Z., 2018b. Heterogeneous Distribution of Chromium on Mercury 2047, 6095.

Nittler, L.R., Weider, S.Z., 2019. The Surface Composition of Mercury. Elements 15, 33–38. https://doi.org/10.2138/gselements.15.1.33

Nittler, L.R., Frank, E.A., Weider, S.Z., Crapster-Pregont, E., Vorburger, A., Starr, R.D., Solomon, S.C., 2020. Global major-element maps of Mercury from four years of MESSENGER X-Ray Spectrometer observations. Icarus 345, 113716. https://doi.org/10.1016/j.icarus.2020.113716

Nittler, L.R., Boujibar, A., Crapster-Pregont, E., Frank, E.A., McCoy, T.J., McCubbin, F.M., Starr, R.D., Vorburger, A., Weider, S.Z., 2023. Chromium on Mercury: New Results From the MESSENGER X-Ray Spectrometer and Implications for the Innermost Planet's Geochemical Evolution. Journal of Geophysical Research: Planets 128, e2022JE007691. https://doi.org/10.1029/2022JE007691

Oberbeck, V.R., Quaide, W.L., Arvidson, R.E., Aggarwal, H.R., 1977. Comparative studies of lunar, Martian, and Mercurian craters and plains. Journal of Geophysical Research 82, 1681–1698. https://doi.org/10.1029/JB082i011p01681

Oddo, G., 1914. Die Molekularstruktur der radioaktiven Atome. Zeitschrift für anorganische Chemie 87, 253–268. https://doi.org/10.1002/zaac.19140870118

Okada, A., Keil, K., 1982. Caswellsilverite, $NaCrS_2$: a new mineral in the Norton County enstatite achondrite. American Mineralogist 67, 132–136.

Oliveira, J.S., Hood, L.L., Langlais, B., 2019. Constraining the Early History of Mercury and Its Core Dynamo by Studying the Crustal Magnetic Field. Journal of Geophysical Research: Planets 124, 2382–2396. https://doi.org/10.1029/2019JE005938

O'Neill, H.St.C., Dingwell, D.B., Borisov, A., Spettel, B., Palme, H., 1995. Experimental petrochemistry of some highly siderophile elements at high temperatures, and some implications for core formation and the mantle's early history. Chemical Geology 120, 255–273. https://doi.org/10.1016/0009-2541(94)00141-T

Padovan, S., Wieczorek, M.A., Margot, J., Tosi, N., Solomon, S.C., 2015. Thickness of the crust of Mercury from geoid-to-topography ratios. Geophysical Research Letters 42, 1029–1038. https://doi.org/10.1002/2014GL062487

Paige, D.A., Wood, S.E., Vasavada, A.R., 1992. The Thermal Stability of Water Ice at the Poles of Mercury. Science 258, 643–646. https://doi.org/10.1126/science.258.5082.643

Paige, D.A., Siegler, M.A., Harmon, J.K., Neumann, G.A., Mazarico, E.M., Smith, D.E., Zuber, M.T., Harju, E., Delitsky, M.L., Solomon, S.C., 2013. Thermal Stability of Volatiles in the North Polar Region of Mercury. Science 339, 300–303. https://doi.org/10.1126/science.1231106

Palme, H., Lodders, K., Jones, A., 2014. Solar System Abundances of the Elements, in: Treatise on Geochemistry. Elsevier, 15–36. https://doi.org/10.1016/B978-0-08-095975-7.00118-2

Papike, J.J., 2005. Comparative planetary mineralogy: Valence state partitioning of Cr, Fe, Ti, and V among crystallographic sites in olivine, pyroxene, and spinel from planetary basalts. American Mineralogist 90, 277–290. https://doi.org/10.2138/am.2005.1779

Parks, G.K., 2015. Magnetosphere, in: Encyclopedia of Atmospheric Sciences. Elsevier, 309–315. https://doi.org/10.1016/B978-0-12-382225-3.00211-5

Parman, S.W., Parmentier, E.M., Wang, S., 2016. Crystallization of Mercury's Sulfur-Rich Magma Ocean 2990.

Pauling, L., 1932. The nature of the chemical bond. IV. The energy of single bonds and the relative electronegativity of atoms. Journal of the American Chemical Society 54, 3570–3582. https://doi.org/10.1021/ja01348a011

Peale, S.J., 1976. Orbital Resonances in the Solar System. Annual Review of Astronomy and Astrophysics 14, 215–246. https://doi.org/10.1146/annurev.aa.14.090176.001243

Peplowski, P.N., Stockstill-Cahill, K., 2019. Analytical Identification and Characterization of the Major Geochemical Terranes of Mercury's Northern Hemisphere. Journal of Geophysical Research: Planets 124, 2414–2429. https://doi.org/10.1029/2019JE005997

Peplowski, P.N., Evans, L.G., Hauck, S.A., McCoy, T.J., Boynton, W.V., Gillis-Davis, J.J., Ebel, D.S., Goldsten, J.O., Hamara, D.K., Lawrence, D.J., McNutt, R.L., Nittler, L.R., Solomon, S.C., Rhodes, E.A., Sprague, A.L., Starr, R.D., Stockstill-Cahill, K.R., 2011. Radioactive Elements on Mercury's

Surface from MESSENGER: Implications for the Planet's Formation and Evolution. Science 333, 1850–1852. https://doi.org/10.1126/science.1211576

Peplowski, P.N., Lawrence, D.J., Rhodes, E.A., Sprague, A.L., McCoy, T.J., Denevi, B.W., Evans, L.G., Head, J.W., Nittler, L.R., Solomon, S.C., Stockstill-Cahill, K.R., Weider, S.Z., 2012. Variations in the abundances of potassium and thorium on the surface of Mercury: Results from the MESSENGER Gamma-Ray Spectrometer. Journal of Geophysical Research 117, 2012JE004141. https://doi.org/10.1029/2012JE004141

Peplowski, P.N., Evans, L.G., Stockstill-Cahill, K.R., Lawrence, D.J., Goldsten, J.O., McCoy, T.J., Nittler, L.R., Solomon, S.C., Sprague, A.L., Starr, R.D., Weider, S.Z., 2014. Enhanced sodium abundance in Mercury's north polar region revealed by the MESSENGER Gamma-Ray Spectrometer. Icarus 228, 86–95. https://doi.org/10.1016/j.icarus.2013.09.007

Peplowski, P.N., Lawrence, D.J., Feldman, W.C., Goldsten, J.O., Bazell, D., Evans, L.G., Head, J.W., Nittler, L.R., Solomon, S.C., Weider, S.Z., 2015. Geochemical terranes of Mercury's northern hemisphere as revealed by MESSENGER neutron measurements. Icarus 253, 346–363. https://doi.org/10.1016/j.icarus.2015.02.002

Peplowski, P.N., Klima, R.L., Lawrence, D.J., Ernst, C.M., Denevi, B.W., Frank, E.A., Goldsten, J.O., Murchie, S.L., Nittler, L.R., Solomon, S.C., 2016. Remote sensing evidence for an ancient carbon-bearing crust on Mercury. Nature Geoscience 9, 273–276. https://doi.org/10.1038/ngeo2669

Peterson, G.A., Johnson, C.L., Jellinek, A.M., 2021. Thermal evolution of Mercury with a volcanic heat-pipe flux: Reconciling early volcanism, tectonism, and magnetism. Science Advances 7, eabh2482. https://doi.org/10.1126/sciadv.abh2482

Pettengill, G.H., Dyce, R.B., 1965. A Radar Determination of the Rotation of the Planet Mercury. Nature 206, 1240–1240. https://doi.org/10.1038/2061240a0

Pfleger, M., Lichtenegger, H.I.M., Wurz, P., Lammer, H., Kallio, E., Alho, M., Mura, A., McKenna-Lawlor, S., Martín-Fernández, J.A., 2015. 3D-modeling of Mercury's solar wind sputtered surface-exosphere environment. Planetary and Space Science, Solar wind interaction with the terrestrial planets 115, 90–101. https://doi.org/10.1016/j.pss.2015.04.016

Pirotte, H., Cartier, C., Namur, O., Pommier, A., Zhang, Y., Berndt, J., Klemme, S., Charlier, B., 2023. Internal differentiation and volatile budget of Mercury inferred from the partitioning of heat-producing elements at highly reduced conditions. Icarus 405, 115699. https://doi.org/10.1016/j.icarus.2023.115699

Poirier, J.-P., 1994. Light elements in the Earth's outer core: A critical review. Physics of the Earth and Planetary Interiors 85, 319–337. https://doi.org/10.1016/0031-9201(94)90120-1

Pommier, A., Leinenweber, K., Tran, T., 2019. Mercury's thermal evolution controlled by an insulating liquid outermost core? Earth and Planetary Science Letters 517, 125–134. https://doi.org/10.1016/j.epsl.2019.04.022

Pommier, A., Leinenweber, K., Pirotte, H., Yu, T., Wang, Y., 2021. In situ electrical resistivity and viscosity measurements of iron alloys under pressure using synchrotron X-ray radiography. High Pressure Research 41, 1–13. https://doi.org/10.1080/08957959.2020.1865343

Pommier, A., Tauber, M.J., Pirotte, H., Cody, G.D., Steele, A., Bullock, E.S., Charlier, B., Mysen, B.O., 2023. Experimental investigation of the bonding of sulfur in highly reduced silicate glasses and melts. Geochimica et Cosmochimica Acta. https://doi.org/10.1016/j.gca.2023.10.027

Potter, A.E., Morgan, T.H., 1985. Discovery of Sodium in the Atmosphere of Mercury. Science 229, 651–653. https://doi.org/10.1126/science.229.4714.651

Potter, A.E., Morgan, T.H., 1986. Potassium in the atmosphere of Mercury. Icarus 67, 336–340. https://doi.org/10.1016/0019-1035(86)90113-2

Potter, A.E., Morgan, T.H., 1990. Evidence for Magnetospheric Effects on the Sodium Atmosphere of Mercury. Science 248, 835–838. https://doi.org/10.1126/science.248.4957.835

Potter, A.E., Anderson, C.M., Killen, R.M., Morgan, T.H., 2002. Ratio of sodium to potassium in the Mercury exosphere. Journal of Geophysical Research: Planets 107, 7-1-7–8. https://doi.org/10.1029/2000JE001493

Prockter, L.M., Ernst, C.M., Denevi, B.W., Chapman, C.R., Head, J.W., Fassett, C.I., Merline, W.J., Solomon, S.C., Watters, T.R., Strom, R.G., Cremonese, G., Marchi, S., Massironi, M., 2010. Evidence for Young Volcanism on Mercury from the Third MESSENGER Flyby. Science 329, 668–671. https://doi.org/10.1126/science.1188186

Rabe, E., 1950. Derivation of fundamental astronomical constants from the observations of Eros during 1926-1945. The Astronomical Journal 55, 112. https://doi.org/10.1086/106364

Ramberg, H., 1952. Chemical Bonds and Distribution of Cations in Silicates. The Journal of Geology 60, 331–355. https://doi.org/10.1086/625982

Ramsey, W.H., 1948. On the Constitution of the Terrestrial Planets. Geophysical Supplements to the Monthly Notices of the Royal Astronomical Society 108, 406–413. https://doi.org/10.1111/j.1365-246X.1949.tb02951.x

Ramsey, W.H., 1949. On the Nature of the Earth's Core. Geophysical Supplements to the Monthly Notices of the Royal Astronomical Society 5, 409–426. https://doi.org/10.1111/j.1365-246X.1949.tb02956.x

Ramsey, W.H., 1950. On the Compressibility of the Earth. Geophysical Journal International 6, 42–49. https://doi.org/10.1111/j.1365-246X.1950.tb02972.x

Rayleigh, Lord, 1916. LIX. *On convection currents in a horizontal layer of fluid, when the higher temperature is on the under side*. The London, Edinburgh, and Dublin Philosophical Magazine and Journal of Science 32, 529–546. https://doi.org/10.1080/14786441608635602

Raymond, S.N., Morbidelli, A., 2014. The Grand Tack model: a critical review. Proceedings of the International Astronomical Union 9, 194–203. https://doi.org/10.1017/S1743921314008254

Redmond, H.L., King, S.D., 2007. Does mantle convection currently exist on Mercury? Physics of the Earth and Planetary Interiors 164, 221–231. https://doi.org/10.1016/j.pepi.2007.07.004

Renggli, C.J., Klemme, S., Morlok, A., Berndt, J., Weber, I., Hiesinger, H., King, P.L., 2022. Sulfides and hollows formed on Mercury's surface by reactions with reducing S-rich gases. Earth and Planetary Science Letters 593, 117647. https://doi.org/10.1016/j.epsl.2022.117647

Righter, K., 2003. Metal-Silicate Partitioning of Siderophile Elements and Core Formation in the Early Earth. Annual Review of Earth and Planetary Sciences 31, 135–174. https://doi.org/10.1146/annurev.earth.31.100901.145451

Righter, K., Pando, K.M., Danielson, L., Lee, C.-T., 2010. Partitioning of Mo, P and other siderophile elements (Cu, Ga, Sn, Ni, Co, Cr, Mn, V, and W) between metal and silicate melt as a function of temperature and silicate melt composition. Earth and Planetary Science Letters 291, 1–9. https://doi.org/10.1016/j.epsl.2009.12.018

Righter, K., Sutton, S., Danielson, L., Pando, K., Schmidt, G., Yang, H., Berthet, S., Newville, M., Choi, Y., Downs, R.T., Malavergne, V., 2011. The effect of fO2 on the partitioning and valence of V and Cr in garnet/melt pairs and the relation to terrestrial mantle V and Cr content. American Mineralogist 96, 1278–1290. https://doi.org/10.2138/am.2011.3690

Riner, M.A., Lucey, P.G., Desch, S.J., McCubbin, F.M., 2009. Nature of opaque components on Mercury: Insights into a Mercurian magma ocean. Geophysical Research Letters 36. https://doi.org/10.1029/2008GL036128

Ringwood, A.E., 1955. The principles governing trace element distribution during magmatic crystallization Part I: The influence of electronegativity. Geochimica et Cosmochimica Acta 7, 189–202. https://doi.org/10.1016/0016-7037(55)90029-6

Ringwood, A.E., 1966. Chemical evolution of the terrestrial planets. Geochimica et Cosmochimica Acta 30, 41–104. https://doi.org/10.1016/0016-7037(66)90090-1

Rishbeth, H., 1988. Basic physics of the ionosphere: a tutorial review. Journal of the Institution of Electronic and Radio Engineers 58, S207–S223. https://doi.org/10.1049/jiere.1988.0060

Rivoldini, A., Van Hoolst, T., 2013. The interior structure of Mercury constrained by the low-degree gravity field and the rotation of Mercury. Earth and Planetary Science Letters 377–378, 62–72. https://doi.org/10.1016/j.epsl.2013.07.021

Rivoldini, A., Van Hoolst, T., Verhoeven, O., 2009. The interior structure of Mercury and its core sulfur content. Icarus 201, 12–30. https://doi.org/10.1016/j.icarus.2008.12.020

Roberts, J.H., Barnouin, O.S., 2012. The effect of the Caloris impact on the mantle dynamics and volcanism of Mercury. Journal of Geophysical Research 117, 2011JE003876. https://doi.org/10.1029/2011JE003876

Robinson, M.S., Lucey, P.G., 1997. Recalibrated Mariner 10 Color Mosaics: Implications for Mercurian Volcanism. Science 275, 197–200. https://doi.org/10.1126/science.275.5297.197

Rodriguez, J.A.P., Leonard, G.J., Kargel, J.S., Domingue, D., Berman, D.C., Banks, M., Zarroca, M., Linares, R., Marchi, S., Baker, V.R., Webster, K.D., Sykes, M., 2020. The Chaotic Terrains of Mercury Reveal a History of Planetary Volatile Retention and Loss in the Innermost Solar System. Scientific Reports 10, 4737. https://doi.org/10.1038/s41598-020-59885-5

Rose-Weston, L., Brenan, J.M., Fei, Y., Secco, R.A., Frost, D.J., 2009. Effect of pressure, temperature, and oxygen fugacity on the metal-silicate partitioning of Te, Se, and S: Implications for earth differentiation. Geochimica et Cosmochimica Acta 73, 4598–4615. https://doi.org/10.1016/j.gca.2009.04.028

Rothery, D.A., Thomas, R.J., Kerber, L., 2014. Prolonged eruptive history of a compound volcano on Mercury: Volcanic and tectonic implications. Earth and Planetary Science Letters 385, 59–67. https://doi.org/10.1016/j.epsl.2013.10.023

Rothery, D.A., Massironi, M., Alemanno, G., Barraud, O., Besse, S., Bott, N., Brunetto, R., Bunce, E., Byrne, P., Capaccioni, F., Capria, M.T., Carli, C., Charlier, B., Cornet, T., Cremonese, G., D'Amore, M., De Sanctis, M.C., Doressoundiram, A., Ferranti, L., Filacchione, G., Galluzzi, V., Giacomini, L., Grande, M., Guzzetta, L.G., Helbert, J., Heyner, D., Hiesinger, H., Hussmann, H., Hyodo, R., Kohout, T., Kozyrev, A., Litvak, M., Lucchetti, A., Malakhov, A., Malliband, C., Mancinelli, P., Martikainen, J., Martindale, A., Maturilli, A., Milillo, A., Mitrofanov, I., Mokrousov, M., Morlok, A., Muinonen, K., Namur, O., Owens, A., Nittler, L.R., Oliveira, J.S., Palumbo, P., Pajola, M., Pegg, D.L., Penttilä, A., Politi, R., Quarati, F., Re, C., Sanin, A., Schulz, R., Stangarone, C., Stojic, A., Tretiyakov, V., Väisänen, T., Varatharajan, I., Weber, I., Wright, J., Wurz, P., Zambon, F., 2020. Rationale for BepiColombo Studies of Mercury's Surface and Composition. Space Science Reviews 216, 66. https://doi.org/10.1007/s11214-020-00694-7

Roux, J., Lefèvre, A., 1992. A fast-quench device for internally heated pressure vessels. European Journal of Mineralogy 4, 279–282. https://doi.org/10.1127/ejm/4/2/0279

Rubie, D.C., Gessmann, C.K., Frost, D.J., 2004. Partitioning of oxygen during core formation on the Earth and Mars. Nature 429, 58–61. https://doi.org/10.1038/nature02473

Rubie, D.C., Jacobson, S.A., Morbidelli, A., O'Brien, D.P., Young, E.D., De Vries, J., Nimmo, F., Palme, H., Frost, D.J., 2015. Accretion and differentiation of the terrestrial planets with implications for the compositions of early-formed Solar System bodies and accretion of water. Icarus 248, 89–108. https://doi.org/10.1016/j.icarus.2014.10.015

Safronov, V.S., 1969. Эволюция допланетного облака и образование Земли и планет (Evolution of the Proto-Planetary Cloud and Formation of the Earth and Planets), Nauka. ed, 1969. Moscow.

Sanloup, C., Jambon, A., Gillet, P., 1999. A simple chondritic model of Mars. Physics of the Earth and Planetary Interiors 112, 43–54. https://doi.org/10.1016/S0031-9201(98)00175-7

Schleicher, L.S., Watters, T.R., Martin, A.J., Banks, M.E., 2019. Wrinkle ridges on Mercury and the Moon within and outside of mascons. Icarus 331, 226–237. https://doi.org/10.1016/j.icarus.2019.04.013

Schlemm, C.E., Starr, R.D., Ho, G.C., Bechtold, K.E., Hamilton, S.A., Boldt, J.D., Boynton, W.V., Bradley, W., Fraeman, M.E., Gold, R.E., Goldsten, J.O., Hayes, J.R., Jaskulek, S.E., Rossano, E., Rumpf, R.A., Schaefer, E.D., Strohbehn, K., Shelton, R.G., Thompson, R.E., Trombka, J.I., Williams, B.D., 2007. The X-Ray Spectrometer on the MESSENGER Spacecraft. Space Science Reviews 131, 393–415. https://doi.org/10.1007/s11214-007-9248-5

Schmidt, O.Yu., 1957. Четыре лекции о теории происхождения Земли (Four lectures on the theory of the origin of the Earth), AN SSSR. ed. Moscow.

Schramm, L.S., Brownlee, D.E., Wheelock, M.M., 1989. Major element composition of stratospheric micrometeorites. Meteoritics 24, 99–112. https://doi.org/10.1111/j.1945-5100.1989.tb00950.x

Schubert, G., Soderlund, K.M., 2011. Planetary magnetic fields: Observations and models. Physics of the Earth and Planetary Interiors 187, 92–108. https://doi.org/10.1016/j.pepi.2011.05.013

Schubert, G., Ross, M.N., Stevenson, D.J., Spohn, T., 1988. Mercury's thermal history and the generation of its magnetic field., Mercury, University of Arizona Press.

Schultz, P.H., Gault, D.E., 1975. Seismic effects from major basin formations on the moon and mercury. The Moon 12, 159–177. https://doi.org/10.1007/BF00577875

Shannon, R.D., 1976. Revised effective ionic radii and systematic studies of interatomic distances in halides and chalcogenides. Acta Crystallographica Section A 32, 751–767. https://doi.org/10.1107/S0567739476001551

Shaw, D.M., 1953. The Camouflage Principle and Trace-Element Distribution in Magmatic Minerals. The Journal of Geology 61, 142–151. https://doi.org/10.1086/626062

Shaw, D.M., 1970. Trace element fractionation during anatexis. Geochimica et Cosmochimica Acta 34, 237–243. https://doi.org/10.1016/0016-7037(70)90009-8

Siebert, J., Corgne, A., Ryerson, F.J., 2011. Systematics of metal–silicate partitioning for many siderophile elements applied to Earth's core formation. Geochimica et Cosmochimica Acta 75, 1451–1489. https://doi.org/10.1016/j.gca.2010.12.013

Siegfried, R.W., Solomon, S.C., 1974. Mercury: Internal structure and thermal evolution. Icarus 23, 192–205. https://doi.org/10.1016/0019-1035(74)90005-0

Skinner, B.J., Luce, F.D., 1971. Solid Solutions of the Type (Ca,Mg,Mn,Fe)S and their use as Geothermometers for the Enstatite Chondrites. American Mineralogist 56, 1269–1296.

Slade, M.A., Butler, B.J., Muhleman, D.O., 1992. Mercury Radar Imaging: Evidence for Polar Ice. Science 258, 635–640. https://doi.org/10.1126/science.258.5082.635

Slavin, J.A., DiBraccio, G.A., Gershman, D.J., Imber, S.M., Poh, G.K., Raines, J.M., Zurbuchen, T.H., Jia, X., Baker, D.N., Glassmeier, K.-H., Livi, S.A., Boardsen, S.A., Cassidy, T.A., Sarantos, M., Sundberg, T., Masters, A., Johnson, C.L., Winslow, R.M., Anderson, B.J., Korth, H., McNutt Jr., R.L., Solomon, S.C., 2014. MESSENGER observations of Mercury's dayside magnetosphere under extreme solar wind conditions. Journal of Geophysical Research: Space Physics 119, 8087–8116. https://doi.org/10.1002/2014JA020319

Smart, W.M., 1951. The Origin of the Earth. Cambridge University Press.

Smith, D.E., Zuber, M.T., Phillips, R.J., Solomon, S.C., Hauck, S.A., Lemoine, F.G., Mazarico, E., Neumann, G.A., Peale, S.J., Margot, J.-L., Johnson, C.L., Torrence, M.H., Perry, M.E., Rowlands, D.D., Goossens, S., Head, J.W., Taylor, A.H., 2012. Gravity Field and Internal Structure of Mercury from MESSENGER. Science 336, 214–217. https://doi.org/10.1126/science.1218809

Smith, J.V., 1977. Mineralogy of the Planets: A Voyage in Space and Time. Philosophical Transactions of the Royal Society of London. Series A, Mathematical and Physical Sciences 286, 433–437.

Smith, J.V., 1982. Heterogeneous Growth of Meteorites and Planets, Especially the Earth and Moon. The Journal of Geology 90, 1–48. https://doi.org/10.1086/628650

Solomatov, V., 2007. Magma Oceans and Primordial Mantle Differentiation, Evolution of the Earth. https://doi.org/10.1016/B978-044452748-6.00141-3

Solomon, S.C., 1976. Some aspects of core formation in Mercury. Icarus 28, 509–521. https://doi.org/10.1016/0019-1035(76)90124-X

Solomon, S.C., 1978. On volcanism and thermal tectonics on one-plate planets. Geophysical Research Letters 5, 461–464. https://doi.org/10.1029/GL005i006p00461

Solomon, S.C., Longhi, J., 1977. Magma oceanography: 1. Thermal evolution. Lunar and Planetary Science Conference Proceedings 1, 583–599.

Solomon, S.C., Byrne, P.K., 2019. The Exploration of Mercury by Spacecraft. Elements 15, 15–20. https://doi.org/10.2138/gselements.15.1.15

Solomon, S.C., McNutt, R.L., Watters, T.R., Lawrence, D.J., Feldman, W.C., Head, J.W., Krimigis, S.M., Murchie, S.L., Phillips, R.J., Slavin, J.A., Zuber, M.T., 2008. Return to Mercury: A Global Perspective on MESSENGER's First Mercury Flyby. Science 321, 59–62. https://doi.org/10.1126/science.1159706

Solomon, S.C., McNutt, R.L., Gold, R.E., Acuña, M.H., Baker, D.N., Boynton, W.V., Chapman, C.R., Cheng, A.F., Gloeckler, G., Head III, J.W., Krimigis, S.M., McClintock, W.E., Murchie, S.L., Peale, S.J., Phillips, R.J., Robinson, M.S., Slavin, J.A., Smith, D.E., Strom, R.G., Trombka, J.I., Zuber, M.T., 2001. The MESSENGER mission to Mercury: scientific objectives and implementation. Planetary and Space Science, Returns to Mercury 49, 1445–1465. https://doi.org/10.1016/S0032-0633(01)00085-X

Spinrad, H., Field, G.B., Hodge, P.W., 1965. Spectroscopic Observations of Mercury. The Astrophysical Journal 141, 1155. https://doi.org/10.1086/148205

Spitzer, L.Jr., 1952. The terrestrial atmosphere above 300km, in: The Atmospheres of the Earth and Planets. University of Chicago Press, Chicago, 211–247.

Sprague, A.L., Hunten, D.M., Lodders, K., 1995. Sulfur at Mercury, Elemental at the Poles and Sulfides in the Regolith. Icarus 118, 211–215. https://doi.org/10.1006/icar.1995.1186

Srnka, L.J., 1976. Magnetic dipole moment of a spherical shell with TRM acquired in a field of internal origin. Physics of the Earth and Planetary Interiors 11, 184–190. https://doi.org/10.1016/0031-9201(76)90062-5

Steenstra, E.S., Agmon, N., Berndt, J., Klemme, S., Matveev, S., van Westrenen, W., 2018. Depletion of potassium and sodium in mantles of Mars, Moon and Vesta by core formation. Scientific Reports 8, 7053. https://doi.org/10.1038/s41598-018-25505-6

Steenstra, E.S., Trautner, V.T., Berndt, J., Klemme, S., Van Westrenen, W., 2020a. Trace element partitioning between sulfide-, metal- and silicate melts at highly reduced conditions: Insights into the distribution of volatile elements during core formation in reduced bodies. Icarus 335, 113408. https://doi.org/10.1016/j.icarus.2019.113408

Steenstra, E.S., Kelderman, E., Berndt, J., Klemme, S., Bullock, E.S., Van Westrenen, W., 2020b. Highly reduced accretion of the Earth by large impactors? Evidence from elemental partitioning between sulfide

liquids and silicate melts at highly reduced conditions. Geochimica et Cosmochimica Acta 286, 248–268. https://doi.org/10.1016/j.gca.2020.07.002

Steenstra, E.S., Seegers, A.X., Putter, R., Berndt, J., Klemme, S., Matveev, S., Bullock, E.S., Van Westrenen, W., 2020c. Metal-silicate partitioning systematics of siderophile elements at reducing conditions: A new experimental database. Icarus 335, 113391. https://doi.org/10.1016/j.icarus.2019.113391

Steenstra, E.S., Berndt, J., Rohrbach, A., Bullock, E.S., Van Westrenen, W., Klemme, S., Walter, M.J., 2022. Partitioning of Ru, Pd, Ag, Re, Pt, Ir and Au between sulfide-, metal- and silicate liquid at highly reduced conditions: Implications for terrestrial accretion and aubrite parent body evolution. Geochimica et Cosmochimica Acta 336, 15–32. https://doi.org/10.1016/j.gca.2022.08.021

Steinbrügge, G., Padovan, S., Hussmann, H., Steinke, T., Stark, A., Oberst, J., 2018. Viscoelastic Tides of Mercury and the Determination of its Inner Core Size. Journal of Geophysical Research: Planets 123, 2760–2772. https://doi.org/10.1029/2018JE005569

Steinbrügge, G., Dumberry, M., Rivoldini, A., Schubert, G., Cao, H., Schroeder, D.M., Soderlund, K.M., 2021. Challenges on Mercury's Interior Structure Posed by the New Measurements of its Obliquity and Tides. Geophysical Research Letters 48, e2020GL089895. https://doi.org/10.1029/2020GL089895

Stephenson, A., 1976. Crustal remanence and the magnetic moment of Mercury. Earth and Planetary Science Letters 28, 454–458. https://doi.org/10.1016/0012-821X(76)90206-5

Stevenson, D.J., 2010. Planetary Magnetic Fields: Achievements and Prospects. Space Science Reviews 152, 651–664. https://doi.org/10.1007/s11214-009-9572-z

Stevenson, D.J., Spohn, T., Schubert, G., 1983. Magnetism and thermal evolution of the terrestrial planets. Icarus 54, 466–489. https://doi.org/10.1016/0019-1035(83)90241-5

Stewart, S.T., Lock, S.J., Petaev, M.I., Jacobsen, S.B., Sarid, G., Leinhardt, Z.M., Mukhopadhyay, S., Humayun, M., 2016. Mercury Impact Origin Hypothesis Survives the Volatile Crisis: Implications for Terrestrial Planet Formation 2954.

Stockbauer, R., 1984. Instrumentation for photon stimulated desorption. Nuclear Instruments and Methods in Physics Research 222, 284–290. https://doi.org/10.1016/0167-5087(84)90546-5

Stockstill-Cahill, K.R., McCoy, T.J., Nittler, L.R., Weider, S.Z., Hauck, S.A., 2012. Magnesium-rich crustal compositions on Mercury: Implications for magmatism from petrologic modeling. Journal of Geophysical Research 117, 2012JE004140. https://doi.org/10.1029/2012JE004140

Strom, R.G., 1979. Mercury: A post-Mariner 10 assessment. Space Science Reviews 24, 3–70. https://doi.org/10.1007/BF00221842

Strom, R.G., Trask, N.J., Guest, J.E., 1975. Tectonism and volcanism on Mercury. Journal of Geophysical Research 80, 2478–2507. https://doi.org/10.1029/JB080i017p02478

Suess, H.E., Urey, H.C., 1956. Abundances of the Elements. Reviews of Modern Physics 28, 53–74. https://doi.org/10.1103/RevModPhys.28.53

Sutton, S.R., Goodrich, C.A., Wirick, S., 2017. Titanium, vanadium and chromium valences in silicates of ungrouped achondrite NWA 7325 and ureilite Y-791538 record highly-reduced origins. Geochimica et Cosmochimica Acta 204, 313–330. https://doi.org/10.1016/j.gca.2017.01.036

Taylor, G.J., Norman, M.D., 1992. Evidence for Magma Oceans on Asteroids, the Moon, and Earth 58.

Taylor, G.J., Scott, E.R.D., 2003. 1.18 - Mercury, in: Holland, H.D., Turekian, K.K. (Eds.), Treatise on Geochemistry. Pergamon, Oxford, pp. 477–485. https://doi.org/10.1016/B0-08-043751-6/01071-9

Taylor, S.R., McLennan, S.M., 2009. Planetary crusts: their composition, origin and evolution, Cambridge planetary science. Cambridge university press, Cambridge.

Thibault, Y., Walter, M.J., 1995. The influence of pressure and temperature on the metal-silicate partition coefficients of nickel and cobalt in a model C1 chondrite and implications for metal segregation in a deep magma ocean. Geochimica et Cosmochimica Acta 59, 991–1002. https://doi.org/10.1016/0016-7037(95)00017-8

Thomas, G.E., 1974. Mercury: Does Its Atmosphere Contain Water? Science 183, 1197–1198. https://doi.org/10.1126/science.183.4130.1197

Thomas, K.L., Blanford, G.E., Keller, L.P., Klöck, W., McKay, D.S., 1993. Carbon abundance and silicate mineralogy of anhydrous interplanetary dust particles. Geochimica et Cosmochimica Acta 57, 1551–1566. https://doi.org/10.1016/0016-7037(93)90012-L

Thomas, R.J., Rothery, D.A., Conway, S.J., Anand, M., 2014a. Long-lived explosive volcanism on Mercury. Geophysical Research Letters 41, 6084–6092. https://doi.org/10.1002/2014GL061224

Thomas, R.J., Rothery, D.A., Conway, S.J., Anand, M., 2014b. Hollows on Mercury: Materials and mechanisms involved in their formation. Icarus 229, 221–235. https://doi.org/10.1016/j.icarus.2013.11.018

Tosi, N., Padovan, S., 2021. Mercury, Moon, Mars: Surface Expressions of Mantle Convection and Interior Evolution of Stagnant-Lid Bodies, in: Marquardt, H., Ballmer, M., Cottaar, S., Konter, J. (Eds.), Geophysical Monograph Series. Wiley, pp. 455–489. https://doi.org/10.1002/9781119528609.ch17

Tosi, N., Grott, M., Plesa, A. -C., Breuer, D., 2013. Thermochemical evolution of Mercury's interior. Journal of Geophysical Research: Planets 118, 2474–2487. https://doi.org/10.1002/jgre.20168

Tranell, G., Ostrovski, O., Jahanshahi, S., 2002. The equilibrium partitioning of titanium between Ti3+ and Ti4+ valency states in CaO-SiO2-TiO x slags. Metallurgical and Materials Transactions B 33, 61–67. https://doi.org/10.1007/s11663-002-0086-2

Trask, N.J., Guest, J.E., 1975. Preliminary geologic terrain map of Mercury. Journal of Geophysical Research (1896-1977) 80, 2461–2477. https://doi.org/10.1029/JB080i017p02461

Tuff, J., Wood, B.J., Wade, J., 2011. The effect of Si on metal–silicate partitioning of siderophile elements and implications for the conditions of core formation. Geochimica et Cosmochimica Acta 75, 673–690. https://doi.org/10.1016/j.gca.2010.10.027

Urey, H.C., 1951. The origin and development of the earth and other terrestrial planets. Geochimica et Cosmochimica Acta 1, 209–277. https://doi.org/10.1016/0016-7037(51)90001-4

Urey, H.C., 1952. On the Early Chemical History of the Earth and the Origin of Life. Proceedings of the National Academy of Sciences 38, 351–363. https://doi.org/10.1073/pnas.38.4.351

Urey, H.C., Craig, H., 1953. The composition of the stone meteorites and the origin of the meteorites. Geochimica et Cosmochimica Acta 4, 36–82. https://doi.org/10.1016/0016-7037(53)90064-7

van Achterbergh, E., Ryan, C., Jackson, S., Griffin, W., 2001. Data reduction software for LA-ICP-MS., in: Short Course Handbook. pp. 239–243.

Van Hoolst, T., Rivoldini, A., Baland, R.-M., Yseboodt, M., 2012. The effect of tides and an inner core on the forced longitudinal libration of Mercury. Earth and Planetary Science Letters 333–334, 83–90. https://doi.org/10.1016/j.epsl.2012.04.014

Vander Kaaden, K.E., McCubbin, F.M., 2015. Exotic crust formation on Mercury: Consequences of a shallow, FeO-poor mantle. Journal of Geophysical Research: Planets 120, 195–209. https://doi.org/10.1002/2014JE004733

Vander Kaaden, K.E., McCubbin, F.M., 2016. The origin of boninites on Mercury: An experimental study of the northern volcanic plains lavas. Geochimica et Cosmochimica Acta 173, 246–263. https://doi.org/10.1016/j.gca.2015.10.016

Vander Kaaden, K., M. McCubbin, F., R. Nittler, L., N. Peplowski, P., Z. Weider, S., A. Frank, E., J. McCoy, T., 2017. Geochemistry, mineralogy, and petrology of boninitic and komatiitic rocks on the mercurian surface: Insights into the mercurian mantle. Icarus 285, 155–168. https://doi.org/10.1016/j.icarus.2016.11.041

Vander Kaaden, K.E., McCubbin, F.M., Byrne, P.K., Chabot, N.L., Ernst, C.M., Johnson, C.L., Thompson, M.S., 2019. Revolutionizing Our Understanding of the Solar System via Sample Return from Mercury. Space Science Reviews 215, 49. https://doi.org/10.1007/s11214-019-0614-x

Vander Kaaden, K.E., McCubbin, F.M., Turner, A.A., Ross, D.K., 2020. Constraints on the Abundances of Carbon and Silicon in Mercury's Core From Experiments in the Fe-Si-C System. Journal of Geophysical Research: Planets 125, e2019JE006239. https://doi.org/10.1029/2019JE006239

Varatharajan, I., Maturilli, A., Helbert, J., Alemanno, G., Hiesinger, H., 2019. Spectral behavior of sulfides in simulated daytime surface conditions of Mercury: Supporting past (MESSENGER) and future missions (BepiColombo). Earth and Planetary Science Letters 520, 127–140. https://doi.org/10.1016/j.epsl.2019.05.020

Veasey, M., Dumberry, M., 2011. The influence of Mercury's inner core on its physical libration. Icarus 214, 265–274. https://doi.org/10.1016/j.icarus.2011.04.025

Vervack, R.J., Killen, R.M., McClintock, W.E., Merkel, A.W., Burger, M.H., Cassidy, T.A., Sarantos, M., 2016. New discoveries from MESSENGER and insights into Mercury's exosphere. Geophysical Research Letters 43. https://doi.org/10.1002/2016GL071284

Vilas, F., Chapman, C.R., Matthews, M.S., 1988. Mercury. University of Arizona Press.

Vilas, F., Domingue, D.L., Helbert, J., D'Amore, M., Maturilli, A., Klima, R.L., Stockstill-Cahill, K.R., Murchie, S.L., Izenberg, N.R., Blewett, D.T., Vaughan, W.M., Head, J.W., 2016. Mineralogical indicators of Mercury's hollows composition in MESSENGER color observations. Geophysical Research Letters 43, 1450–1456. https://doi.org/10.1002/2015GL067515

Wade, J., Wood, B.J., 2001. The Earth's 'missing' niobium may be in the core. Nature 409, 75–78. https://doi.org/10.1038/35051064

Wadhwa, M., 2008. Redox Conditions on Small Bodies, the Moon and Mars. Reviews in Mineralogy and Geochemistry 68, 493–510. https://doi.org/10.2138/rmg.2008.68.17

Wadhwa, M., Zinner, E.K., Crozaz, G., 1997. Manganese-chromium systematics in sulfides of unequilibrated enstatite chondrites. Meteoritics & Planetary Science 32, 281–292. https://doi.org/10.1111/j.1945-5100.1997.tb01266.x

Walker, D., Longhi, J., Hays, J.F., 1975. Differentiation of a very thick magma body and implications for the source region of mare basalts. Lunar and Planetary Science Conference Proceedings 1, 1103–1120.

Walker, D., Kirkpatrick, R.J., Longhi, J., Hays, J.F., 1976. Crystallization history of lunar picritic basalt sample 12002: Phase-equilibria and cooling-rate studies. GSA Bulletin 87, 646–656. https://doi.org/10.1130/0016-7606(1976)87<646:CHOLPB>2.0.CO;2

Walker, J.C.G., 1961. The Thermal Budget of the Planet Mercury. Astrophysical Journal 133, 274. https://doi.org/10.1086/147023

Wänke, H., Dreibus, G., 1988. Chemical composition and accretion history of terrestrial planets. Philosophical Transactions of the Royal Society of London. Series A, Mathematical and Physical Sciences 325, 545–557. https://doi.org/10.1098/rsta.1988.0067

Warren, P.H., 1985. The Magma Ocean Concept and Lunar Evolution. Annual Review of Earth and Planetary Sciences 13, 201–240. https://doi.org/10.1146/annurev.ea.13.050185.001221

Washington, H.S., 1920. The chemistry of the earth's crust. Journal of the Franklin Institute 190, 757–815. https://doi.org/10.1016/S0016-0032(20)90061-3

Wasson, J.T., Kallemeyn, G.W., 1988. Compositions of chondrites. Philosophical Transactions of the Royal Society of London. Series A, Mathematical and Physical Sciences 325, 535–544. https://doi.org/10.1098/rsta.1988.0066

Watters, T.R., 2021. A case for limited global contraction of Mercury. Communications Earth & Environment 2, 9. https://doi.org/10.1038/s43247-020-00076-5

Watters, T.R., Nimmo, F., 2010. The tectonics of Mercury, in: Schultz, R.A., Watters, T.R. (Eds.), Planetary Tectonics, Cambridge Planetary Science. Cambridge University Press, Cambridge, pp. 15–80. https://doi.org/10.1017/CBO9780511691645.003

Watters, T.R., Schultz, R.A., 2010. Planetary tectonics: introduction, in: Schultz, R.A., Watters, T.R. (Eds.), Planetary Tectonics, Cambridge Planetary Science. Cambridge University Press, Cambridge, pp. 1–14. https://doi.org/10.1017/CBO9780511691645.002

Watters, T.R., Robinson, M.S., Cook, A.C., 1998. Topography of lobate scarps on Mercury: New constraints on the planet's contraction. Geology 26, 991. https://doi.org/10.1130/0091-7613(1998)026<0991:TOLSOM>2.3.CO;2

Watters, T.R., Solomon, S.C., Robinson, M.S., Head, J.W., André, S.L., Hauck, S.A., Murchie, S.L., 2009. The tectonics of Mercury: The view after MESSENGER's first flyby. Earth and Planetary Science Letters 285, 283–296. https://doi.org/10.1016/j.epsl.2009.01.025

Watters, T.R., Selvans, M.M., Banks, M.E., Hauck, S.A., Becker, K.J., Robinson, M.S., 2015. Distribution of large-scale contractional tectonic landforms on Mercury: Implications for the origin of global stresses. Geophysical Research Letters 42, 3755–3763. https://doi.org/10.1002/2015GL063570

Watters, T.R., Daud, K., Banks, M.E., Selvans, M.M., Chapman, C.R., Ernst, C.M., 2016. Recent tectonic activity on Mercury revealed by small thrust fault scarps. Nature Geoscience 9, 743–747. https://doi.org/10.1038/ngeo2814

Weidenschilling, S.J., 1978. Iron/silicate fractionation and the origin of Mercury. Icarus 35, 99–111. https://doi.org/10.1016/0019-1035(78)90064-7

Weider, S.Z., Nittler, L.R., Starr, R.D., McCoy, T.J., Stockstill-Cahill, K.R., Byrne, P.K., Denevi, B.W., Head, J.W., Solomon, S.C., 2012. Chemical heterogeneity on Mercury's surface revealed by the MESSENGER X-Ray Spectrometer. Journal of Geophysical Research 117, 2012JE004153. https://doi.org/10.1029/2012JE004153

Weider, S.Z., Nittler, L.R., Starr, R.D., McCoy, T.J., Solomon, S.C., 2014. Variations in the abundance of iron on Mercury's surface from MESSENGER X-Ray Spectrometer observations. Icarus 235, 170–186. https://doi.org/10.1016/j.icarus.2014.03.002

Weider, S.Z., Nittler, L.R., Starr, R.D., Crapster-Pregont, E.J., Peplowski, P.N., Denevi, B.W., Head, J.W., Byrne, P.K., Hauck, S.A., Ebel, D.S., Solomon, S.C., 2015. Evidence for geochemical terranes on Mercury: Global mapping of major elements with MESSENGER's X-Ray Spectrometer. Earth and Planetary Science Letters 416, 109–120. https://doi.org/10.1016/j.epsl.2015.01.023

Weider, S.Z., Nittler, L.R., Murchie, S.L., Peplowski, P.N., McCoy, T.J., Kerber, L., Klimczak, C., Ernst, C.M., Goudge, T.A., Starr, R.D., Izenberg, N.R., Klima, R.L., Solomon, S.C., 2016. Evidence from MESSENGER for sulfur- and carbon-driven explosive volcanism on Mercury. Geophysical Research Letters 43, 3653–3661. https://doi.org/10.1002/2016GL068325

Weisberg, M.K., Prinz, M., Clayton, R.N., Mayeda, T.K., Sugiura, N., Zashu, S., Ebihara, M., 2001. A new metal-rich chondrite grouplet. Meteoritics & Planetary Science 36, 401–418. https://doi.org/10.1111/j.1945-5100.2001.tb01882.x

Whipple, F.L., 1941. Earth, Moon and Planets, 3rd Printing (1945). ed. Blakiston, Philadelphia.

Whitten, J.L., Head, J.W., Denevi, B.W., Solomon, S.C., 2014. Intercrater plains on Mercury: Insights into unit definition, characterization, and origin from MESSENGER datasets. Icarus 241, 97–113. https://doi.org/10.1016/j.icarus.2014.06.013

Wiik, H.B., 1956. The chemical composition of some stony meteorites. Geochimica et Cosmochimica Acta 9, 279–289. https://doi.org/10.1016/0016-7037(56)90028-X

Wilbur, Z.E., Udry, A., McCubbin, F.M., Vander Kaaden, K.E., DeFelice, C., Ziegler, K., Ross, D.K., McCoy, T.J., Gross, J., Barnes, J.J., Dygert, N., Zeigler, R.A., Turrin, B.D., McCoy, C., 2022. The effects of highly reduced magmatism revealed through aubrites. Meteoritics & Planetary Science 57, 1387–1420. https://doi.org/10.1111/maps.13823

Wipperfurth, S.A., Guo, M., Šrámek, O., McDonough, W.F., 2018. Earth's chondritic Th/U: Negligible fractionation during accretion, core formation, and crust–mantle differentiation. Earth and Planetary Science Letters 498, 196–202. https://doi.org/10.1016/j.epsl.2018.06.029

Wood, B.J., Kiseeva, E.S., 2015. Trace element partitioning into sulfide: How lithophile elements become chalcophile and vice versa. American Mineralogist 100, 2371–2379. https://doi.org/10.2138/am-2015-5358CCBYNCND

Wohlers, A., Wood, B.J., 2015. A Mercury-like component of early Earth yields uranium in the core and high mantle 142Nd. Nature 520, 337–340. https://doi.org/10.1038/nature14350

Wohlers, A., Wood, B.J., 2017. Uranium, thorium and REE partitioning into sulfide liquids: Implications for reduced S-rich bodies. Geochimica et Cosmochimica Acta 205, 226–244. https://doi.org/10.1016/j.gca.2017.01.050

Wood, J.A., Dickey, J.S., Jr., Marvin, U.B., Powell, B.N., 1970. Lunar anorthosites and a geophysical model of the moon. Geochimica et Cosmochimica Acta Supplement 1, 965.

Wood, J.A., 1975. Lunar petrogenesis in a well-stirred magma ocean. Lunar and Planetary Science Conference Proceedings 1, 1087–1102.

Wood, B.J., Walter, M.J., Wade, J., 2006. Accretion of the Earth and segregation of its core. Nature 441, 825–833. https://doi.org/10.1038/nature04763

Wood, B.J., Kiseeva, E.S., Mirolo, F.J., 2014. Accretion and core formation: The effects of sulfur on metal–silicate partition coefficients. Geochimica et Cosmochimica Acta 145, 248–267. https://doi.org/10.1016/j.gca.2014.09.002

Wright, J., Rothery, D.A., Balme, M.R., Conway, S.J., 2018. Constructional Volcanic Edifices on Mercury: Candidates and Hypotheses of Formation. Journal of Geophysical Research Planets 123, 952–971. https://doi.org/10.1002/2017JE005450

Wurm, G., Trieloff, M., Rauer, H., 2013. Photophoretic separation of metals and silicates: the formation of Mercury-like planets and metal depletion in chondrites. Astrophysical Journal 769, 78. https://doi.org/10.1088/0004-637X/769/1/78

Xiao, Z., Komatsu, G., 2013. Impact craters with ejecta flows and central pits on Mercury. Planetary and Space Science 82–83, 62–78. https://doi.org/10.1016/j.pss.2013.03.015

Xirouchakis, D., Hirschmann, M.M., Simpson, J.A., 2001. The effect of titanium on the silica content and on mineral-liquid partitioning of mantle-equilibrated melts. Geochimica et Cosmochimica Acta 65, 2201–2217. https://doi.org/10.1016/S0016-7037(00)00549-4

Zhang, N., Parmentier, E.M., Liang, Y., 2013. Effects of lunar cumulate mantle overturn and megaregolith on the expansion and contraction history of the Moon. Geophysical Research Letters 40, 5019–5023. https://doi.org/10.1002/grl.50988

Zhang, Y., Zhang, N., Tian, M., 2022. Internal dynamics of magma ocean and its linkage to atmospheres. Acta Geochimica 41, 568–591. https://doi.org/10.1007/s11631-021-00514-x

Zharkova, A.Yu., Kreslavsky, M.A., Head, J.W., Kokhanov, A.A., 2020. Regolith textures on Mercury: Comparison with the Moon. Icarus 351, 113945. https://doi.org/10.1016/j.icarus.2020.113945

Zolotov, M.Yu., Sprague, A.L., Hauck, S.A., Nittler, L.R., Solomon, S.C., Weider, S.Z., 2013. The redox state, FeO content, and origin of sulfur-rich magmas on Mercury. Journal of Geophysical Research: Planets 118, 138–146. https://doi.org/10.1029/2012JE004274

Appendix A: In situ electrical resistivity and viscosity measurements of iron alloys under pressure using synchrotron X-ray radiography

During my stay in the United States at the University of California San Diego (24th of September 2019 – 26th of February 2020), I joined Dr. Anne Pommier to the Advanced Photon Source (APS) synchrotron in Chicago to use a new experimental setup that combines joint measurements of electrical conductivity and viscosity, as well as X-ray diffraction. My contribution to this study was to help with the preparation and loading of the assemblies, as well as performing the experiments together with Dr. Pommier. The samples were placed in a multi anvil linked to an electrical impedance spectrometer, using an assembly with four wires. The sample was centered so that the beam could go through it to perform X-ray diffraction. The falling-sphere viscosity measurements were performed by placing a tungsten marble on top of the powder, which falls through once the latter melts. Using X-ray images of the sample during the falling of the microsphere, we calculated its velocity during its fall, from which the viscosity of the sample is obtained. The work performed there resulted in an article published in High Pressure Research journal.

Taylor & Francis
Taylor & Francis Group

High Pressure Research
An International Journal

ISSN: (Print) (Online) Journal homepage: https://www.tandfonline.com/loi/ghpr20

In situ electrical resistivity and viscosity measurements of iron alloys under pressure using synchrotron X-ray radiography

A. Pommier, K. Leinenweber, H. Pirotte, T. Yu & Y. Wang

To cite this article: A. Pommier, K. Leinenweber, H. Pirotte, T. Yu & Y. Wang (2021) In situ electrical resistivity and viscosity measurements of iron alloys under pressure using synchrotron X-ray radiography, High Pressure Research, 41:1, 1-13, DOI: 10.1080/08957959.2020.1865343

To link to this article: https://doi.org/10.1080/08957959.2020.1865343

HIGH PRESSURE RESEARCH
2021, VOL. 41, NO. 1, 1–13
https://doi.org/10.1080/08957959.2020.1865343

Taylor & Francis
Taylor & Francis Group

In situ electrical resistivity and viscosity measurements of iron alloys under pressure using synchrotron X-ray radiography

A. Pommier[a], K. Leinenweber[b], H. Pirotte[a,c], T. Yu [d] and Y. Wang[d]

[a]Scripps Institution of Oceanography, UC San Diego, La Jolla, CA, USA; [b]Eyring Materials Center, ASU, Tempe, AZ, USA; [c]Department of Geology, University of Liege, Sart Tilman, Belgium; [d]Center for Advanced Radiation Sources, The University of Chicago, Chicago, IL, USA

ABSTRACT

We have developed a new type of experimental setup utilizing a multi-anvil large volume press and designed for simultaneous measurements of structure-sensitive thermophysical properties (diffraction, electrical resistivity, viscosity). This multi-probe capability was tested on iron alloys at 2 GPa and up to 1750 K. Phase transitions as detected by X-ray diffraction patterns are clearly associated with changes in the electrical response of the samples. In Fe-S liquids, viscosity measurements in the molten state indicate an increase in viscosity with increasing the amount of alloying agent. A correlation between electrical resistivity and viscosity from our data and previous works is observed. This multi-probe measurement capability improves the detection of solid-state transformations and solid-melt transitions, relates structural and electrical properties of geomaterials, and allows constraining the mobility of melts using viscosity data. This new setup advances research about melt distribution and mobility at conditions relevant to planetary interiors.

ARTICLE HISTORY
Received 14 August 2020
Accepted 14 December 2020

KEYWORDS
Multi-anvil; impedance spectroscopy; viscosity; X-ray; iron alloys

Introduction

The investigation of transport properties (such as electrical resistivity, viscosity, and density) of metallic alloys under pressure and temperature is fundamental to understand different high-pressure research problems. In condensed matter physics, studying the viscosity and electrical resistivity in liquid metals across a liquid/liquid structural transition can elucidate the transport properties of the condensed state and improve knowledge of atomic bonds [*e.g.* 1]. Electrical resistivity measurements also helped discover the presence of an average band gap for some metals and contributed to develop a theory of transport properties for liquid metals by probing electron-ion interactions [2]. In Earth and planetary science, the transport properties of iron alloys are needed to understand their mobility at depth and their role in planetary dynamics. In particular, iron sulfides are major carriers of metals in the mantle and may be responsible for some geophysical signals in cratons [3]. Iron sulfides' mobility inside a terrestrial planet or moon has also

CONTACT A. Pommier pommier@ucsd.edu Scripps Institution of Oceanography, UC San Diego, La Jolla, CA 92093, USA

Supplemental data for this article can be accessed https://doi.org/10.1080/08957959.2020.1865343

contributed to shape its structure and dynamics during planetary cooling, from the time of metal-silicate differentiation leading to a metallic core formation and present-day mantle convection.

Among thermally activated transport properties, electrical resistivity (or its inverse, conductivity) and viscosity are fundamental properties in material sciences and planetary sciences. Because it is sensitive to temperature, composition, inter-connectivity changes and phase transformations, the electrical response of geomaterials provides information about their chemistry and structure [*e.g.* 4]. Being measured both in the field (by electromagnetism) and in the laboratory (by impedance spectroscopy technique), electrical resistivity is key to improving our knowledge of the thermal and petrologic structure of the crust and upper mantle [5]. Viscosity is necessary to understand melt mobility at depth and thus, places constraints on convection, mixing processes, and melt migration in the mantle as it depends strongly on temperature and chemistry [*e.g.* 6,7]. Therefore, the combination of electrical and viscosity measurements has the potential to interpret electrical anomalies detected at depth in terms of melt mobility, and hence, to provide information on both mantle structure and dynamics.

A major challenge with the investigation of transport properties is to combine them, ideally by measuring the different properties as part of the same experiment in order to circumvent issues related to discrepancies in temperature, pressure, or redox environment between separate experiments. The use of the same cell assembly and experimental conditions minimizes uncertainties on data interpretation. Another advantage with simultaneous measurements is that it facilitates the prediction of viscosity at temperatures where falling-sphere measurements are not tractable, using the electrical-viscosity relationship. Indeed, electrical measurements can be conducted at low and high temperatures (*e.g.* in both solid and liquid states) whereas viscosity measurements using the falling-sphere technique require the entire sample to be in the liquid state. Developing a laboratory-based model of electrical conductivity and viscosity of melts could ultimately help estimate viscosity using electrical data at temperature lower than the liquidus temperature (near the melting temperature), where the sample is partially molten and partially solid.

Previous investigations of iron sulfides pointed out that electrical resistivity is highly sensitive to temperature and phase transitions, in particular, the α–γ (or bcc-fcc) transformation of iron [8–10]. Partial melting is detected, though it is less visible at high pressure (>∼5 GPa) than at low pressure [9]. Coupling *in situ* electrical and synchrotron X-ray radiography measurements improves the ability to identify electrical changes in terms of solid–solid and solid-melt transitions in metals and alloys, as previously observed for Fe-S alloys [11] and bismuth [12]. Experimental viscosity studies investigated experimentally the effect of temperature, pressure, and chemistry of these alloys at ambient pressure [13–14] and up to 6.9 GPa, using the synchrotron-based falling-sphere technique [15–20]. In particular, studies of the Fe-S system have led to contrasting conclusions regarding the dependence of viscosity to the amount of S [15,20], motivating further work. Only very few attempts were made to combine electrical and viscosity measurements, and they were not conducted at temperature and pressure conditions relevant to planetary interiors. In metal alloys, both physical properties were measured at 1 atm and up to 850 K on different Sn alloys in order to probe the effect of metal admixtures on the physical properties of liquid Sn [21]. At 1 atm and up to 1100 K, both techniques

as well as additional XRD measurements at ambient temperature were used jointly to study the effect of Co on the structure of Sn-Cu alloys [22]. The correlation between electrical and viscosity properties was also explored experimentally in silicates, in particular in borosilicate glasses and melts at 1atm [23,24].

We present a setup that allows the synchrotron-based measurement of structure-sensitive thermophysical properties (diffraction, electrical resistivity, viscosity) under pressure and temperature. To demonstrate the feasibility of this technique, experimental data were collected on iron alloys at 2 GPa. This new setup can be used more generally to study the temperature- and pressure-dependence of transport and structural properties of any thermoelectric materials. Our multi-probe approach has a strong potential to advance multidisciplinary research in mineral physics with applications to Earth and planetary sciences and to promote technical discussions among the high-pressure community.

Materials and methods

The experimental setup was developed at Beamline 13-ID-D of GSECARS of the Advanced Photon Source, Argonne National Laboratory and is presented in Figure 1. Three types of data can be collected: structural data, electrical resistivity and viscosity. The assembly, placed in the 1000-ton Large Volume Press (LVP), is connected to a Solartron 1260A impedance-meter in order to acquire *in situ* complex impedance signals by performing a scan

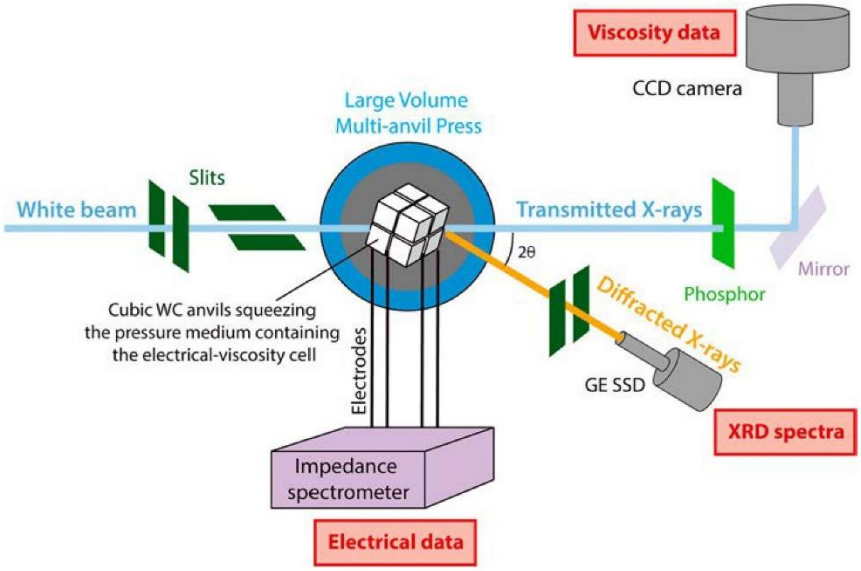

Figure 1. Beamline configuration for diffraction measurements (XRD spectra), electrical measurements (using the impedance spectrometer), and falling sphere viscosity measurements (using the CCD camera) in the 1000-ton Large Volume Press at 13-ID-D. In the X-ray radiography mode, the slits are moved out of the X-ray path and the transmitted X-ray produces a visible image, which is recorded by the CCD camera. In the diffraction mode, the beam size of incident X-ray is reduced by the slits to 100 × 100 μm and the diffracted X-ray is collected on the GE solid-state detector (SSD).

Table 1. Composition of the starting materials.

	Starting compositions					
System	O (wt.%)	S (wt.%)	Ni (wt.%)	O (at.%)	S (at.%)	Ni (at.%)
Fe-S	–	5.0	–	–	8.4	–
Fe-S	–	20.0	–	–	30.3	–
Fe-S-O	0.5	5.0	–	1.7	8.3	–
Fe-Ni	–	–	5.0	–	–	4.8

in frequency [9,25]. Structural data of the sample during the high-pressure, high-temperature experiments are obtained using an energy dispersive X-ray diffraction (EDXD) setup, at a 2-θ angle of 6.1° (+/- 0.003). As part of falling-sphere viscosity experiments, the sample is imaged and recorded using the radiographic imaging system that consists of a fluorescent screen, optical mirrors, and a CCD camera. Imaging and diffraction modes are switched back and forth by moving the front beam collimating slit in or out of the beam path, respectively for diffraction or imaging.

Our setup was tested on four compositions: Fe-5wt.%S-0.5wt.%O (labeled $FeS_5O_{0.5}$) (XRD and electrical), Fe-5wt.%Ni ($FeNi_5$) (XRD, electrical and viscosity), Fe-5wt.%S (FeS_5) (XRD and viscosity), and Fe-20wt.%S (FeS_{20}) (XRD, electrical and viscosity). The detailed compositions are listed in Table 1 and the conditions of the experiments are shown in Table 2. The starting materials were homogeneous powder mixtures of high-purity (> 99%) Fe, Ni, FeS, and FeO powders (Alfa Aesar) prepared in the Planetary and Experimental Petrology Laboratory at UC San Diego and were stored in a sealed container placed in a vacuum oven at 383 K until use.

Experiments were conducted in the large volume multi-anvil press (LVP) at 2 GPa using tungsten carbide cubes with a corner-truncation edge length of 8 mm and MgO octahedral pressure media with an edge length of 14 mm. The cell assembly is presented in Figure 2. This assembly was adapted from our previous 14/8 COMPRES electrical assembly [25] to allow X-ray access to the sample. In this assembly, the starting powder was packed firmly into an alumina sleeve and a WC microsphere (90–120 μm in diameter) was inserted in some runs in the upper part of the sample for viscosity measurements. Both the powder and Fe electrode disks are held together in a three-alumina ring system (Figure 2). The rhenium furnace contains two windows that are aligned along the X-ray path, in order to reduce X-ray absorption by the surrounding parts, as well as four notches for the four electrode wires. The four wires are placed in two 4-bore MgO tubes and correspond to two Type-C thermocouples as well as serving as electrodes. Assemblies were pressurized at ambient temperature and then heated, with pressure estimated at high temperature using XRD measurements in the iron electrodes using the EOS

Table 2. Experimental conditions.

			Measurements		
Material	*P* (GPa)	*T* range (K)	Diffraction	Electrical	Viscosity
FeS_5	2	773–1648	x		x
FeS_{20}	2	773–1723	x	x	x
$FeS_5O_{0.5}$	2	726–1499	x	x	
$FeNi_5$	2	798–1733	x	x	x

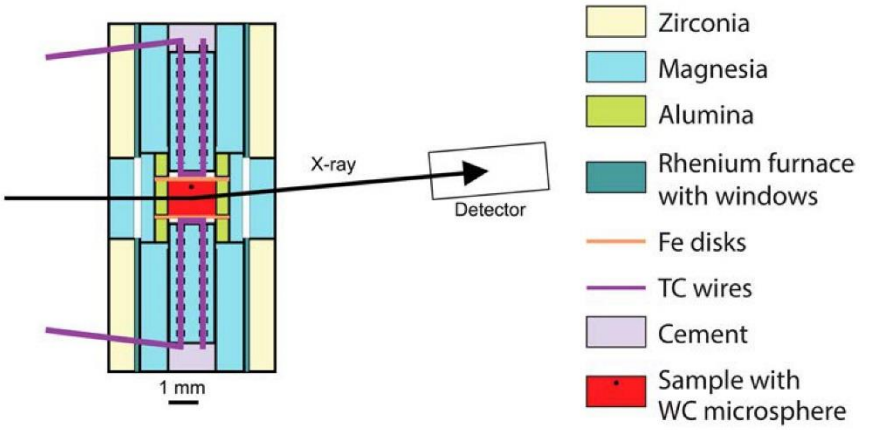

Figure 2. Modified 14/8 electrical COMPRES cell assembly using a rhenium heater with windows. This cell is available through COMPRES.

of hcp Fe. Thermocouple (temperature reading) and electrode (electrical response) modes were switched back and forth during electrical measurements.

All experiments were quenched by shutting off the power to the heating system. *In situ* electrical measurements were performed under quasi-hydrostatic conditions in the multi-anvil press during heating and cooling cycles using the four-electrode method [9]. The excellent heating reproducibility of cell assemblies is presented in the Supplementary Material. The electrode system consists of four wires, two wires for voltage drop measurement and two wires for current measurement. The sample resistance was obtained from the measured (bulk) resistance value by removing the contribution from the iron disks and the alumina ring [25]. The electrical resistance R of the sample and the geometric factor G are used to calculate the electrical resistivity defined as $\rho = R \times G$ with $G = A/l$, where A is the area of one electrode and l is the thickness of the sample. With this cell, relative errors on values of ρ correspond to a few % over the entire temperature range [25] (Supplementary Material).

In situ falling-sphere measurements were conducted at high temperature, when the sample is fully molten. We used WC probing microspheres because of the large density contrast relative to the molten sample density that minimizes errors due to uncertainty in the density of the sample. We also tested corundum microspheres but they are not visible with the white beam at the facility. For viscosity measurements, temperature was increased very rapidly (~283–290 K/s) above 1000 K to minimize (1) sphere-sample interactions and (2) motion of the sphere before the sample is fully molten. The sample was brought too rapidly to the fully molten state for electrical measurements to be collected, and electrical data were thus acquired during heating at low temperature, after the viscosity measurements, and during cooling. The settling velocity of the falling microsphere was determined using digital recordings of experiments that were converted to images for computer analysis [26]. The falling distance of the sphere was calibrated using the known diameter of the marker sphere. Liquid viscosity (η) was computed using a modified form of Stokes' law, with a correction for the wall and end effects (see Supplementary Material for details).

Results and discussion

Joint structural-electrical measurements

The comparison between XRD data and electrical resistivity measurements of the samples is illustrated in Figures 3 and 4. Electrical resistivity was calculated from impedance measurements using Eq.1. For each experiment, images of the sample collected during heating suggest that, at the target pressure of 2 GPa, no detectable change occurs in the sample thickness, due to the 3-alumina ring design that helps maintain the sample geometry under pressure and temperature conditions. As a result, the same sample length value can be used to calculate the geometric factor G (and hence, electrical resistivity) over the entire temperature range without any correction. Reproducibility of the results is demonstrated in Figure 3 with (1) the repeat of XRD analyses on two different experiments at the same conditions, and (2) with the excellent agreement between electrical data during heating and cooling cycles at low temperature.

Electrical resistivity is sensitive to the α–γ phase transformation in iron (Figures 3 and 4b), the onset of melting (Figures 3 and 4), and the incorporation of compounds (*e.g.* FeO, Figure 3) into the solid solution as temperature is increased. Electrical resistivity increases significantly with increasing temperature until the martensitic α–γ transition, which is clearly identified and is located around 1000 K (±50 K). The resistivity values are in very good agreement with previous electrical works on Fe and Fe-S materials at comparable pressure [*e.g.* 8,9,25]. Figure 3 shows that melting, the disappearance of α iron and of FeO each correspond to a slight but detectable decrease in resistivity during heating of the Fe-S-O sample (Figure 3), confirming that the electrical tool is a very sensitive probe of the structural changes.

The electrical response of the samples allows monitoring the evolution of the material structure as a function of temperature. Below the melting temperature, electrical changes indicate that the samples correspond to several coexisting phases (Fe, FeS, FeO, and/or Ni) that are incorporated progressively into the solid solution as temperature increases. There is significant Fe-S-O alloying as shown in the diffraction patterns prior to melting, where iron sulfide phases appear rapidly at temperatures well before melting (the peaks of sulfide phases disappear above 1000K). The FeO peaks also decrease in intensity with increasing T but do not completely disappear until melting occurs. This indicates that sulfur is fully dissolved in the solid Fe while oxygen is partly dissolved and becomes fully dissolved in the melt. It is an indirect evidence of solubility because we do not observe large enough changes in the Fe lattice parameter to detect the presence of sulfur or oxygen directly by Fe lattice parameter. Above $T_{melting}$, the samples have become a single phase, as supported by the flat background of the XRD spectra (Figures 3 and 4). The temperature-dependence of electrical resistivity during heating and cooling is different; in particular, a significant decrease in resistivity is observed during cooling of the molten alloys and resistivity at $T<T_{melting}$ is lower during cooling than during heating (Figure 4). As previously proposed for Fe-B alloys [26], it is possible that heating to a temperature well above $T_{melting}$ induces in the alloy an irreversible transformation to the state of true solution, and during subsequent cooling, the melt keeps the state of dissolution of heterogeneities at the microscale it had reached during the heating cycle. Additionally, the diffraction from the solid phases is not observed during the cooling cycle, which could

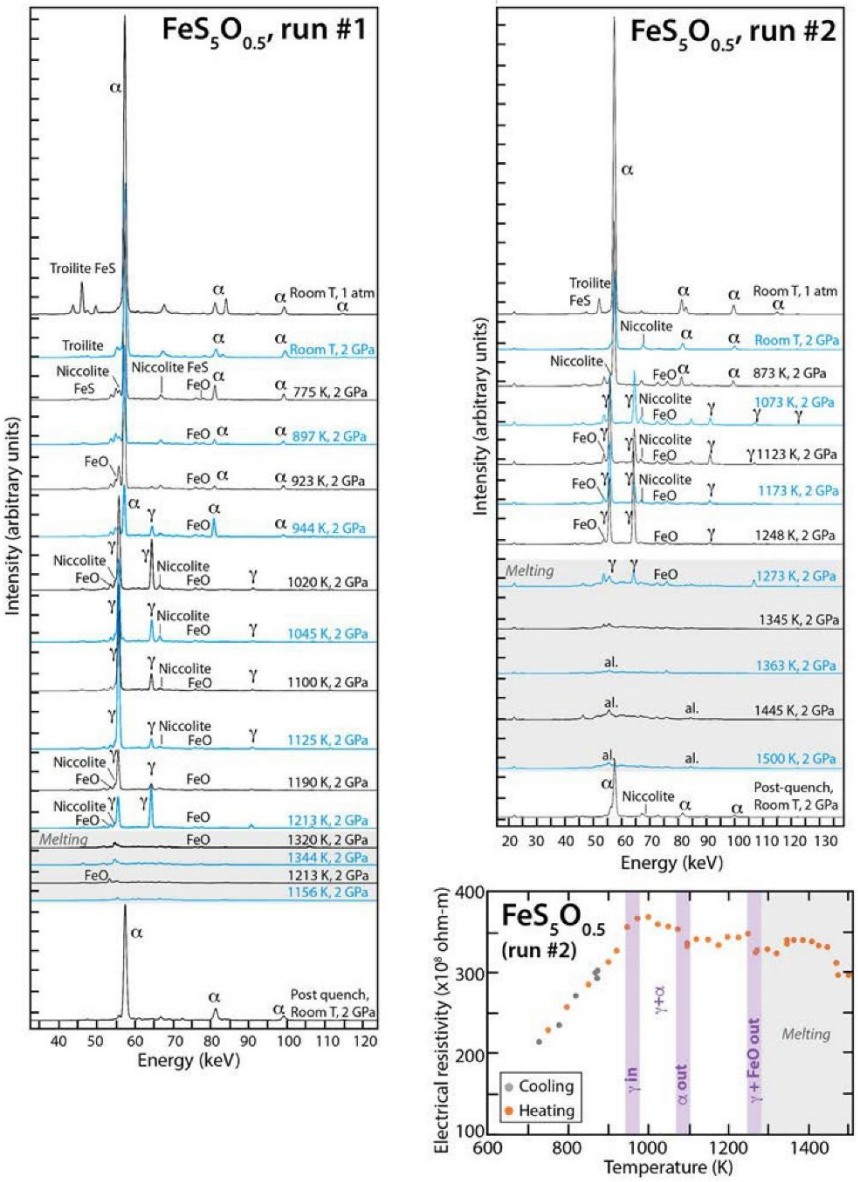

Figure 3. XRD and electrical data for the Fe-S-O sample. Reproducibility of the data was checked by reproducing the experiment for XRD analyses and by collecting electrical data at low temperature (before the bcc-fcc transition) during cooling and heating cycles. The terms niccolite and troilite refer to different FeS crystallographies. The pressure is listed as the last pressure observed before melting. The color code of the spectra (blue and black) is to help with clarity.

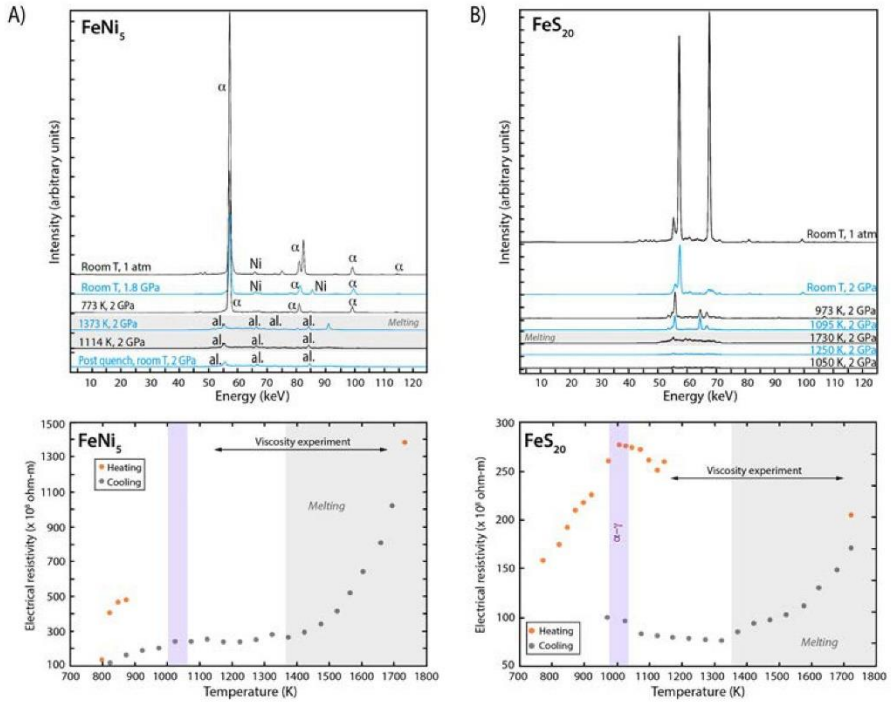

Figure 4. XRD and electrical data for the $FeNi_5$ and FeS_{20} samples. Data were not collected during heating at high temperature (arrows in bottom plots) due to very rapid heating as part of viscosity measurements. The pressure is listed as the last pressure observed before melting. The color code of the spectra (blue and black) is to help with clarity.

be indicative of textural changes (granularity) as is commonly observed with *in situ* X-ray diffraction experiments once the sample has melted and re-crystallized with large grain sizes. It is interesting that iron diffraction peaks re-appear after rapid quench to room temperature, which indicates the re-growth of small crystals possibly during the reversion to the α-iron phase. However, as previously pointed out, what is happening during the subsequent cooling cycle is not yet fully understood [26]. A difference between heating and cooling rates could also influence the electrical response. The dissolution of the WC microsphere at high temperature is unlikely to influence sample resistivity because its volume and its mass is insignificant compared to those of the sample, representing about 0.025% of the volume occupied by the sample, and only ~0.066 wt% of its mass.

Coupling with viscometry experiments

Examples of falling sphere sequences are shown in Figure 5. Despite the short fall distance due to the rapid melting of the microsphere in the metallic liquid and the limited available number of frames, time-distance relationships of falling spheres were determined, and regions of constant fall velocity were identified and used to estimate terminal velocities (Supplementary Material). For the three investigated compositions in the Fe-Ni and Fe-S

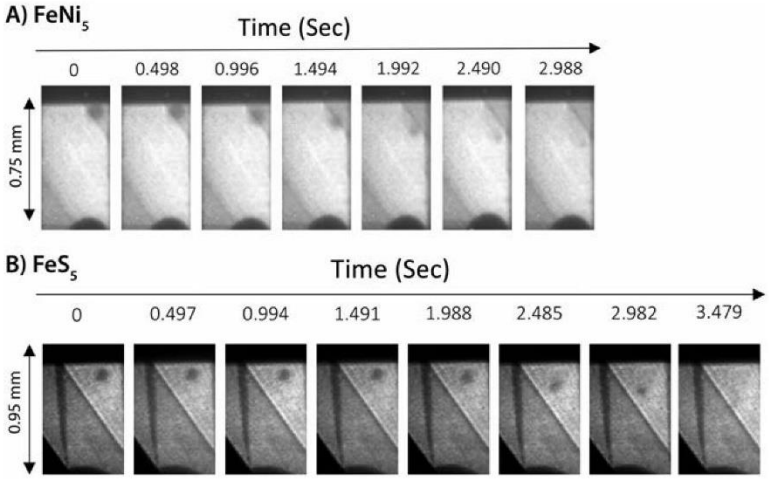

Figure 5. X-ray radiograph images of two samples (A) $FeNi_5$, and (B) FeS_5 during falling-sphere experiments. Dissolution of the sphere occurs after a few seconds. The sequences allow estimating the velocity of the falling sphere. Temperature was 1748 K in (A) and in 1648 K in (B).

systems, velocities vary from 87 to 117 microns/s (Table 2). These velocity values (ν) were then implemented in Eq. 2 to calculate viscosity (Supplementary Material). Viscosity data are plotted in Figure 6. The temperature of the sphere fall for each experiment is either 1648, 1723, or 1748 K and is indicated on Figure 6. The temperature increase during the sphere fall was 5°C or less, and the temperatures on Figure 6 indicate the average temperature of the sphere fall. At the time of the fall, the samples were either fully or almost fully molten, because (1) the sphere trajectory was straight and unaffected by the presence of solids, and (2) the rapid dissolution of the sphere is consistent with a molten sample.

Viscosity values at 2 GPa range from $6.1.10^{-4}$–$1.3.10^{-3}$ Pa-s for the three molten samples (Table 2). Although these estimates likely present a significant uncertainty due to the error on terminal velocity estimates, they are in good agreement with previous works at comparable pressure (2 GPa ±0.5), in particular with the viscosity estimate from [18] collected at 1.7 GPa on an intermediate Fe-S composition (Fe-14S), and the FeS viscosity estimate at 2.2 GPa from [20]. Additionally, our estimates agree well with the Fe-S estimate from a computational study [27] calculated at 1573 K and a moderately higher pressure than in our experiments (5 GPa). We observe that melt viscosity increases only very slightly with increasing the amount of alloying agent (in our case, S or Ni), though pure iron is not fitting the viscosity-composition trend as well as the other compositions in the Fe-FeS system (Figure 6). This small dependence of viscosity to alloy chemistry is consistent with the observations formulated by [15] for Fe-S alloys at comparable pressure (1.5–2.5 GPa) and temperature (1563–1820 K) conditions. At the atomic level, this result is consistent with the absence of a significant variation of liquid structure and polymerization through the clustering of S atoms as a function of temperature and pressure, which would have inhibited diffusion [20]. Note that the clustering of atoms is specific to the nature of the alloying agents, and therefore can be different in other iron alloys [*e.g.* 28]. The variations in pure iron viscosity data from previous studies might originate from differences in the techniques used,

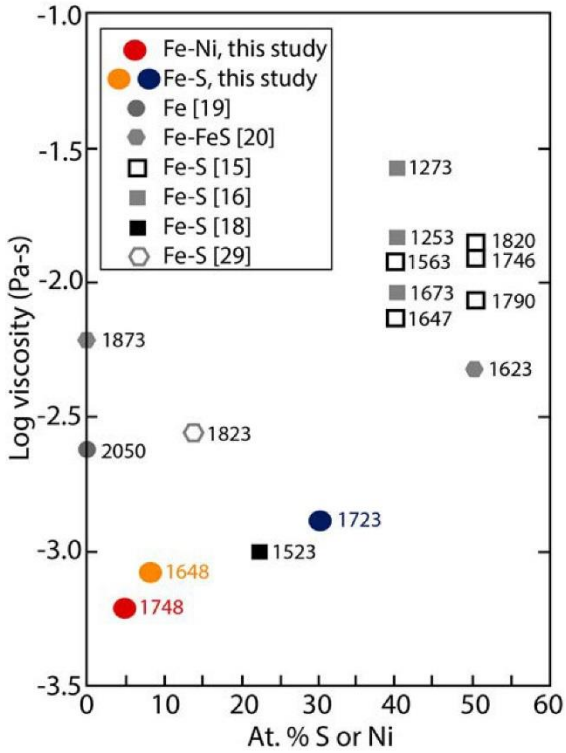

Figure 6. Viscosity as a function of alloy chemistry for our experiments and previous works in the Fe-S system.

the experimental protocol, and temperature differences [20], and addressing this issue is beyond the scope of the present study.

Comparison between electrical resistivity and viscosity for Fe-S liquids normalized to the average temperature of the fall is shown in Figure 7 for the Fe-S system. Resistivity and viscosity values for the different compositions are from our experiments and from previous works (Figure 6) at comparable conditions [9,15–20,29,30]. We observe that at first approximation, both transport properties normalized to temperature present a linear correlation for the considered dataset. For a defined temperature, this observation suggests that (1) adding sulfur increases both viscosity and resistivity, and (2) the higher the resistivity (or the lower the conductivity) of the sulfide melt, the higher its viscosity, and therefore, the lower its mobility at depth. This correlation between the two physical properties as a function of melt chemistry likely reflects the complex interplay between the self-diffusion of Fe and S species (that control viscosity) and the mean free path of electrons (that is proportional to the electrical conductivity). The structure of the liquid alloys being affected by the presence and the amount of alloying agent, it is likely to explain the observed correlation between transport properties. Actually, previous works have pointed out the relationship between the structure factor (S(q)) of metallic melts and electrical resistivity [2] and viscosity [31]. Further work is required to develop a

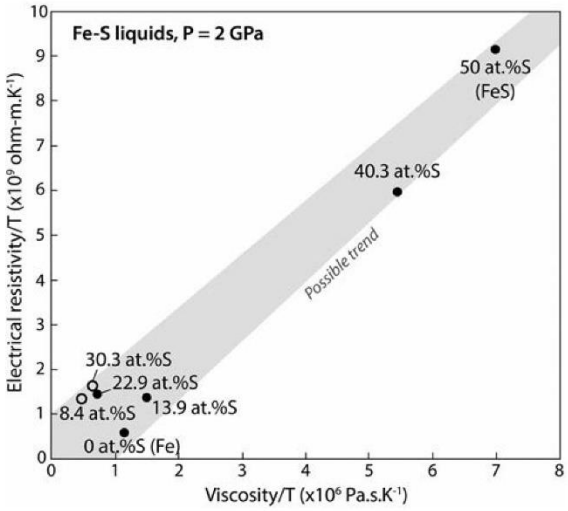

Figure 7. Electrical resistivity vs. viscosity normalized to temperature for the Fe-S system. The composition and values for resistivity and viscosity come from this study (open circles) and previous works (filled circles). See text for details. The gray area only represents a guide for the eyes.

theoretical framework to understand the effect of the structure on the resistivity and viscosity of molten iron alloys under pressure. These necessary data are crucial for linking rheology to other melt properties and structure, and ultimately needed for developing a joint electrical-viscosity model of molten alloys from the solidus to above the liquidus, and to depths (pressures) relevant to planetary interiors.

Conclusions

Three thermophysical properties (diffraction, electrical resistivity, viscosity) were successfully and simultaneously measured under pressure and temperature at Beamline 13-ID-D of the APS synchrotron facility. We have demonstrated the feasibility of this technique by collecting experimental data on iron alloys at 2 GPa and up to 1748 K. Our setup, that is made available to the community, offers a new avenue to investigate and combine the transport properties of geomaterials in the solid and liquid states, with potential for significant impact in the mineral physics and experimental geophysics community. Our experimental approach allows interpreting variations in the bulk electrical response in terms of structural changes in the sample. The effect of chemistry (amount of alloying agents) on both resistivity and viscosity is also measured. At high temperature, comparison between electrical and viscosity data in the Fe-S system suggests a linear correlation that needs to be explored extensively in order to develop joint electrical-viscosity models of metallic melts.

Acknowledgments

This study, including the purchase of the impedance spectrometer, was funded by NSF-CAREER grant EAR 1750746 awarded to AP. AP and KL also acknowledge financial support from an NSF-

COMPRES IV EOID subaward. Use of the COMPRES Cell Assembly Project was also supported by COMPRES under NSF Cooperative Agreement EAR 1661511. We thank Pin-Cheng Chen for technical assistance with some experiments. AP is grateful to Charles Lesher for the opportunity to learn the falling-sphere viscometry technique and to Jonathan Souders for his help with the development of the APS electrical-temperature switch box. This work was performed at GeoSoilEnviroCARS (The University of Chicago, Sector 13), Advanced Photon Source (APS), Argonne National Laboratory. GeoSoilEnviroCARS is supported by the National Science Foundation – Earth Sciences (EAR – 1634415) and Department of Energy- GeoSciences (DE-FG02-94ER14466). This research used resources of the Advanced Photon Source, a U.S. Department of Energy (DOE) Office of Science User Facility operated for the DOE Office of Science by Argonne National Laboratory under Contract No. DE-AC02-06CH11357. We thank two anonymous reviewers for their thoughtful comments and Stefan Klotz for his editorial work.

Disclosure statement

No potential conflict of interest was reported by the author(s).

Funding

This work was supported by NSF EAR [grant number 1634415,1661511,1750746]; Department of Energy- GeoSciences [grant number DE-FG02-94ER14466].

ORCID

T. Yu http://orcid.org/0000-0001-8283-2780

References

[1] Wang M, Geng H, Li Z, et al. Viscosity, resistivity, and structural changes of $Bi_{60}Ga_{40}$ alloy melt with liquid-liquid phase separation. Rev Adv Mater Sci. 2013;33:311–315.
[2] Ziman JM. A theory of the electrical properties of liquid metals. I: the monovalent metals. Phil Mag. 1961;6(68):1013–1034. DOI:10.1080/14786436108243361
[3] Helffrich G, Kendall JM, Hammond JOS, et al. Sulfide melts and long-term low seismic wavespeeds in lithospheric and asthenospheric mantle. Geophys Res Lett. 2011;38:L11301. DOI:10.1029/2011GL047126
[4] Tyburczy JA, Fisler DK. Electrical properties of minerals and melts. mineral physics and crystallography: a handbook of physical constants. AGU Reference Shelf. 1995;2:185–208.
[5] Pommier A, Evans RL. Constraints on fluids in subduction zones from electromagnetic data. Geosphere. 2017;13(4). DOI:10.1130/GES01473.1
[6] Tinker D, Lesher CE, Baxter GM, et al. High-pressure viscometry of polymerized silicate melts and limitations of the eyring equation. Am Min. 2004;89:1701–1708.
[7] Karki BB, Stixrude L. First-principles study of enhancement of transport properties of silica melt by water. Phys Rev Lett. 2010;104:215901.
[8] Deng L, Seagle C, Fei Y, et al. High pressure and temperature electrical resistivity of iron and implications for planetary cores. Geophys Res Lett. 2013;40:33–37.
[9] Pommier A. Influence of sulfur on the electrical resistivity of a crystallizing core in small terrestrial bodies. Earth Planet Sci Lett. 2018;496:37–46.
[10] Silber RE, Secco RA, Yong W, et al. Electrical resistivity of liquid Fe to 12 GPa: implications for heat flow in cores of terrestrial bodies. Sci Reports. 2018;8(1):10758–10759.
[11] Manthilake G, Chantel J, Monteux J, et al. Thermal conductivity of FeS and its implications for mercury's long-sustaining magnetic field. J Geophys Res: Planets. 2019;124(23). DOI:10.1029/2019JE005979

[12] Baker J, Kumar R, Velisavljevic N, et al. In situ x-ray diffraction, electrical resistivity and thermal measurements using a Paris- Edinburgh cell at HPCAT 16BM-B beamline. J Phys: Conf Series. 2014;500:142003.
[13] Vostryakov AA, Vatolin NA, Yesin OA. Viscosity and electrical resistivity of molten alloys of iron with phosphorus and sulphur. Fiz Metal Metalloed. 1964;18(3):167–169.
[14] Barmin LN, Estin OA, Dobrovinskii IE. Application of theory of regular solutions to isotherms of viscosity and molar volume in binary sulphide melts. Russ J Phys Chem USSR. 1970;44:1450–1453.
[15] Dobson DP, Crichton WA, Vocadlo L, et al. In situ measurement of viscosity of liquids in the Fe–FeS system at high pressures and temperatures. Am Mineral. 2000;85:1838–1842.
[16] Terasaki H, Kato T, Urakawa S, et al. The effect of temperature, pressure, and sulfur content on viscosity of the Fe–FeS melt. Earth Planet Sci Lett. 2001;190:93–101.
[17] Urakawa S, Terasaki H, Funakoshi K, et al. Radiographic study on the viscosity of the Fe–FeS melts at the pressure of 5 to 7 GPa. Am Mineral. 2001;86:578–582.
[18] Secco RA, Rutter MD, Balog SP, et al. Viscosity and density of Fe–S liquids at high pressures. J Phys: Condens Matter. 2002;14:11325.
[19] Rutter MD, Secco RA, Liu H, et al. Viscosity of liquid Fe at high pressure. Phys Rev B. 2002;66:060102.
[20] Kono Y, Kenney-Benson C, Shibazaki Y, et al. High-pressure viscosity of liquid Fe and FeS revisited by falling sphere viscometry using ultrafast X-ray imaging. Phys Earth Planet Int. 2015;241:57–64.
[21] Plevachuk Y, Sklyarchuk V, Hoyer W, et al. Electrical conductivity, thermoelectric power and viscosity of liquid Sn-based alloys. J Mater Sci. 2006;41:4632.
[22] Yakymovych A, Sklyarchuk V, Plevachuk Y, et al. Viscosity and electrical conductivity of the liquid Sn-3.8Ag-0.7Cu alloy with minor Co admixtures. JMEPEG. 2016;25:4437.
[23] Grandjean A, Malki M, Simonnet C, et al. Correlation between electrical conductivity, viscosity, and structure in borosilicate glass-forming melts. Phys Rev B. 2007;75:054112.
[24] Ehrt D, Keding R. Electrical conductivity and viscosity of borosilicate glasses and melts. Phys Chem Glasses: Eur J Glass Sci Technol. 2009;B50:165–171.
[25] Pommier A, Leinenweber K, Tran T. Mercury's thermal evolution controlled by an insulating liquid outermost core? Earth Planet Sci Lett. 2019;517:125–134.
[26] Sidorov VE, Calvo-Dahlborg M, Dahlborg U, et al. Physical properties of some iron based alloys in liquid and amorphous states. J Mat Sci. 2000;35:2255–2262.
[27] Vocadlo L, Alfè D, Price GD, et al. First principles calculations on the diffusivity and viscosity of liquid Fe–S at experimentally accessible conditions. Phys Earth Planet Sci. 2000;120:145–152.
[28] Wang J, Chen B, Williams Q, et al. Short- and intermediate-range structure and dynamics of Fe-Ni-C liquid under compression. Front Earth Sci. 2019;7:258. DOI:10.3389/feart.2019.00258
[29] Rutter MD, Secco RA, Uchida T, et al. Towards evaluating the viscosity of the Earth's outer core: An experimental high pressure study of liquid Fe-S (8.5 wt.% S). Geophys Res Lett. 2002;29 (8):1217.
[30] Secco RA, Schloessin HH. The electrical resistivity of solid and liquid Fe at pressures up to 7 GPa. J Geophys Res. 1989;94(B5):5887.
[31] Shen G, Prakapenka VB, Rivers ML, et al. Structure of liquid iron at pressures up to 58 GPa. Phys Rev Lett. 2004;92(18). DOI:10.1103/PhysRevLett.92.185701

Appendix B: Experimental investigation of the bonding of sulfur in highly reduced silicate glasses and melts

During a first stay at the University of California San Diego (24th of September 2019 – 26th of February 2020) and a second stay at the Carnegie Institution for Science (December 2021), I performed multi-anvil experiments on S-bearing reduced silicates in collaboration with Dr. Anne Pommier. Experiments were conducted using a cell assembly that incorporates 4 thermocouple wires, each pair touching an Fe-disk placed on top and on the bottom of the capsule containing the sample. With this setup, it is possible to apply a current through the sample thanks to the two pairs of thermocouples placed on the top and on the bottom electrodes (Figure B1). When no current is applied, the thermocouples monitor the temperature of the sample. The assembly was developed by Pommier and Leinenweber (2018).

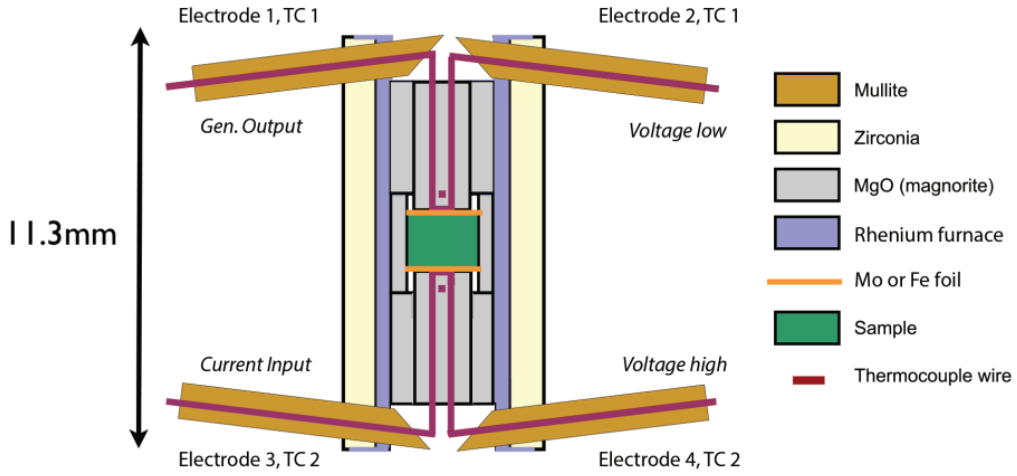

Figure B1: Electrical assembly used at San Diego and Washington D.C. (modified from Pommier and Leinenweber, 2018).

The first objective was to measure the electrical impedance of S-rich and S-poor powders to quantify the effect of S on the electrical conductivity of silicate melts. Because the powder samples are very refractory, the time to reach equilibrium was very long and never reached. The experiments were performed at low temperature (<800°C) to avoid melting before they reach equilibrium. The results were difficult to exploit, and it was decided to redo the experiments using a different method. Thanks to this preliminary inquiry, we understood how to perform these experiments successfully, and we opted to perform electrical measurements on pre-equilibrated glasses. To this end, I carried out phase equilibria experiments on NVP powders in an evacuated silica tube (see Chapter 3:). This method allowed to shape the glass products by using long cylindric graphite capsule whose width fits the sample sleeve in the multi anvil cell assembly (Figure B2). Electrical experiments on glasses were performed with Dr. Pommier at the Carnegie Institution for Science (Washington, DC).

Figure B2: Glass cylinder fitting perfectly inside the alumina ring of the multi-anvil assembly.

The results are published in Geochimica and Cosmochimica Acta (Pommier et al., 2023). The corrected-proof version of this paper is presented below. My contribution to this paper was to make the starting materials and to perform most of the electrical experiments.

ARTICLE IN PRESS

Geochimica et Cosmochimica Acta xxx (xxxx) xxx

Contents lists available at ScienceDirect

Geochimica et Cosmochimica Acta

journal homepage: www.elsevier.com/locate/gca

Experimental investigation of the bonding of sulfur in highly reduced silicate glasses and melts

A. Pommier [a,*], M.J. Tauber [a,b], H. Pirotte [a,c], G.D. Cody [a], A. Steele [a], E.S. Bullock [a], B. Charlier [c], B.O. Mysen [a]

[a] Carnegie Institution for Science, Earth and Planets Laboratory, Washington, DC 20015, USA
[b] University of California San Diego, Department of Chemistry and Biochemistry, La Jolla, CA 92093, USA
[c] University of Liège, Department of Geology, Sart Tilman, Belgium

ARTICLE INFO

Associate editor: Sung Keun Lee

Keywords:
Mercury
Silicate glasses
Silicate melts
Sulfur
Impedance spectroscopy
NMR spectroscopy
Raman spectroscopy

ABSTRACT

Elucidating the role of sulfur on the structure of silicate glasses and melts at elevated pressures and temperatures is important for understanding transport properties, such as electrical conductivity and viscosity, of magma oceans and mantle-derived melts. These properties are fundamental for modeling the evolution of terrestrial planets and moons. Despite several investigations of sulfur speciation in glasses, questions remain regarding the effect of S on complex glasses at highly reducing conditions relevant to Mercury. Glasses were synthetized with compositions representative of the Northern Volcanic Plains of Mercury and containing quantities of S up to 5 wt %. Multiple spectroscopic methods and microprobe analyses were employed to probe the glasses, including *in situ* impedance spectroscopy at 2- and 4-GPa pressures and temperatures up to 1740 K using a multi-anvil press, ^{29}Si NMR spectroscopy, and Raman spectroscopy. Electrical activation energies (Ea) in the glassy state range from 0.56 to 1.10 eV, in agreement with sodium as the main charge carrier. The electrical measurements indicate that sulfide improves Na^+ transport and may overcome a known impeding effect of the divalent cation Ca^{2+}. The glass transition temperature lies between 700 and 750 K, and for temperatures up to 970 K Ea decreases (0.35–0.68 eV) and the conductivities of the samples converge (~5–8 × 10^{-3} S/m). At T_{quench}, the melt fraction is 50–70% and melt conductivity varies from 0.7 to 2.2 S/m, with the sample containing 5 wt% S the most conductive among the set. ^{29}Si NMR spectra reveal that a high fraction of S bonds with Si in these complex glasses, a characteristic that has not been recognized previously. Raman spectra and maps reveal regions rich in Ca–S or Mg–S bonds. The evidence of sulfide interactions with both Si and Ca/Mg suggest that alkaline earth sulfides can be considered weak network modifiers in these glasses, under highly reduced conditions.

1. Introduction

Sulfur is a major volatile component in terrestrial magmas. The presence of sulfur can influence the structure of silicate melts and glasses (e.g., O'Neill and Mavrogenes, 2002; Fleet et al., 2005; Tsujimura et al., 2004; Klimm and Botcharnikov, 2010) affecting transport properties such as diffusivity (Lierenfeld et al., 2018), thermal conductivity (Lonergan et al., 2020), and viscosity (Mouser et al., 2021). Understanding the effect of sulfur on these properties at the temperatures, pressures, and redox conditions relevant to planetary interiors is an important part of modeling the composition and dynamics of terrestrial planets and moons. High S concentrations (up to 4 wt%), together with low FeO content (≤2–3 wt%) were measured at the surface of Mercury during the MESSENGER mission by using gamma-ray, X-ray, and ultraviolet – near-infrared reflection spectroscopy (Nittler et al., 2011, 2018; Zolotov et al., 2013; Evans et al., 2012; Izenberg et al., 2014; Weider et al., 2015; Peplowski et al., 2015; McCoy et al., 2018). These data are consistent with a highly reducing environment (<IW-3, with IW the iron-wüstite oxygen fugacity buffer; McCubbin et al., 2012; Zolotov et al., 2013; Namur et al., 2016a). These conditions are thought to have affected planetary differentiation and magmatic processes (e.g., Malavergne et al., 2010; Charlier and Namur, 2019; Renggli et al., 2022). However, the effect of highly reduced S-rich magmas on the dynamics that shaped the planet remains largely unknown.

In natural silicate glasses and melts, sulfur can exist in a wide range of oxidation states, from S^{2-} to S^{6+} (e.g., Carroll and Rutherford, 1988;

* Corresponding author.
E-mail address: apommier@carnegiescience.edu (A. Pommier).

https://doi.org/10.1016/j.gca.2023.10.027
Received 5 July 2023; Accepted 24 October 2023
Available online 4 November 2023

Please cite this article as: A. Pommier et al., *Geochimica et Cosmochimica Acta*, https://doi.org/10.1016/j.gca.2023.10.027

Wilke et al., 2011; O'Neill and Mavrogenes, 2002). At an oxygen fugacity (fO_2) above that of the nickel-nickel oxide oxygen buffer, S^{6+} in the form of sulfate (SO_4^{2-}) is dominant, whereas at very low fO_2 values relevant to Mercury magmas, sulfide (S^{2-}) is the predominant sulfur species (e.g., Jugo et al., 2010). The following equilibrium characterizes the displacement of oxide for sulfide in a melt (Fincham and Richardson, 1954; Baker and Moretti, 2011):

$$\frac{1}{2}S_2^{gas} + O^{2-,melt} = \frac{1}{2}O_2^{gas} + S^{2-,melt} \quad (1)$$

For fO_2 values significantly below the IW buffer, the maximum concentration of S^{2-} in a silicate melt (sulfide saturation) increases as oxygen fugacity decreases (e.g., O'Neill and Mavrogenes, 2002; Namur et al., 2016a). Therefore, the remarkably low fO_2 conditions in Mercury have been invoked to explain the substantial solubility of sulfide in its lavas (Nittler et al., 2011; Namur et al., 2016a). Sulfide has an affinity for divalent cations (Ca^{2+}, Mg^{2+}, Fe^{2+}), forming complexes in various glasses (O'Neill and Mavrogenes, 2002; Fleet et al., 2005; Namur et al., 2016a; Anzures et al., 2020). Additional processes which may induce the formation of Ca or Mg sulfides at the surface of Mercury have been suggested, such as gas–solid interactions during volcanic and impact processes (Renggli et al., 2022). SiS_2 is another compound that can form during volcanic degassing at the surface of this planet (Iacovino et al., 2023).

Our current understanding of the effect of S on the structure of silicate glasses and melts has benefitted significantly from industry-related research on simple binary or ternary systems. As reviewed elsewhere (Wilke et al., 2011), various spectroscopic techniques have been used to investigate the speciation and bonding of sulfur in alkali silicate glasses, including Raman scattering (Asahi et al., 1999; Tsujimura et al., 2004; Klimm and Botcharnikov, 2010; Klimm et al., 2012; Namur et al., 2016a; Watson and Martin, 2017; Lonergan et al., 2020), nuclear magnetic resonance (NMR) (Tsujimura et al., 2004; Watson and Martin, 2017), X-ray photoelectron spectroscopy (Asahi et al., 1999), and X-ray absorption near-edge structure (XANES) spectroscopy (Fleet et al., 2005; Klimm et al., 2012; Anzures et al., 2020). Generally, simple glass compositions were targeted in these studies, and further investigations are needed to elucidate the role of S in complex (natural) glasses and under highly reducing conditions relevant to Mercury.

Among the spectroscopic techniques commonly used to study complex S-bearing glasses and melts, ^{29}Si NMR spectroscopy is outstanding for identifying the various nearest neighbors of Si and for providing essential information about glass polymerization. The speciation of silicon is of particular interest, with the extent of polymerization commonly denoted by the parameter Q^n, where Q refers to a tetrahedrally-bonded Si species and an integer n (1–4) quantifies the number of bridging oxygen atoms (e.g., Stebbins, 1987; Engelhardt and Michel, 1987; Maekawa et al., 1991). Raman spectroscopy is another powerful probe of silicate glasses, including those bearing S (Wilke et al., 2011). This technique has been used to probe sulfide compositions in natural samples (Avril et al., 2013), and identify S complexes with Mg^{2+} and Ca^{2+} in the structure of highly reduced silicate melts (Namur et al., 2016a).

Knowledge of the transport properties (such as viscosity and electrical conductivity) of such glasses and melts at conditions relevant to Mercury is limited. Results from viscosity experiments on highly reduced S-bearing andesitic glasses up to 6.2 GPa and 2000° C revealed a decrease in viscosity with the addition of S (Mouser et al., 2021). The mechanism for the decrease is uncertain, however, the generally weaker interaction of S^{2-} relative to O^{2-} with cations such as $Si^{2+,4+}$ and Ca^{2+} could influence viscosity. Additionally, low viscosity values at low fO_2 can perhaps be explained by the decreased valence of Si and Ti, thereby decreasing polymerization (Mouser et al., 2021). Impedance spectroscopy is sensitive to the short- and long-range motion of charged species and yields insights that are complementary to those from other spectroscopic techniques and viscosity experiments. For example, a study of S-bearing Li silicate glasses (Tatsumisago et al., 2000) benefitted from electrical measurements, combined with ^{29}Si NMR spectroscopy and XPS. However, the previous electrical studies of S-bearing, alkali silicate glasses (e.g., Ravaine, 1980 and references therein; Hayashi et al., 1998; Tatsumisago et al., 2000; Minami et al., 2000) were restricted to simple systems and oxysulfides at 1 atm. To elucidate planetary interiors, measurements of electrical and other transport properties of complex, sulfide-bearing silicate glasses are needed at high pressures and temperatures.

In this study, we investigate the role of sulfur in highly reduced complex silicate glasses and melts. Several spectroscopic techniques are applied to probe the electrical properties (impedance spectroscopy) and molecular structure (^{29}Si NMR spectroscopy and Raman spectroscopy) of these glasses. Electron microprobe analyses complement the characterization of the samples. The different insights gained from each technique combine to elucidate the bonding of sulfur in highly reduced silicate glasses.

2. Experimental and analytical techniques

2.1. Sample preparation

The starting glasses were synthesized from powders representative of the compositions from the low-Mg Northern Volcanic Plains (termed NVP) in the Borealis Planitia region on Mercury (Weider et al., 2015; Namur and Charlier, 2017; Vander Kaaden et al., 2017). Magmas from this location are rich in Mg, alkali metals, and S, but are depleted in Al, Ca and Fe compared with Earth basalts (e.g., Peplowski et al., 2014, 2015). High-purity oxides (TiO_2, Al_2O_3, Cr_2O_3, MnO, MgO, $CaSiO_3$, Na_2SiO_3, $K_2Si_4O_9$, $AlPO_4$) were mixed with ethanol in an agate mortar. Different amounts of S, in the form of CaS, were added to the powders (Table 1). Iron was added as Fe to two batches. The powders were dried in an oven at 393 K and stored in a desiccator until use.

Starting glasses were obtained by loading the powders into graphite capsules and melting with a multi-step process. The capsule was first placed in a silica tube under vacuum and heated at 393 K for about 15 h. The tube containing the sample was then sealed while still under vacuum using an oxy-acetylene torch, and placed in a box oven at 1573 to 1673 K for 0.75–1.5 h (Table 1). The pressure is estimated to be slightly above 1 bar based on slight inflation of some silica tubes. The redox conditions of the sample are expected to be close to the C-CO redox buffer at the oven temperature. Therefore, at the 1573–1673 K temperatures and ~1 bar pressure of the syntheses, the fO_2 values were approximately six log units lower than those of the iron-wüstite buffer ($\Delta IW \approx -6$) (Herd, 2008 using Eugster and Wones, 1962 and Darken and Gurry, 1945). Samples were quenched by dropping the silica tubes inside a water-filled beaker. The quenching rate is estimated to be >200–300 K/s. Upon opening the silica tubes, representative samples showed evidence of CO and H_2S gases. Glass cylinders were retrieved by removing the graphite capsule, and have a diameter of 1.5 mm and length of ~1–2 cm.

Table 1
Starting materials and conditions of glass synthesis experiments (P = 1 atm).

Glass sample	Added materials (wt.%)		Experimental conditions[a]	
	CaS	Fe	Temperature (K)	Duration (hr)
VT42	0	10	1623	1.0
VT53	0	0	1573	1.5
VT56	0	0	1623	1.0
VT46	7	10	1623	1.0
VT47	7	0	1623	1.0
VT48	7	0	1573	1.0
VT54	12	0	1573	1.5
VT55	15	0	1673	0.75
VT52	30	0	1623	1.0

[a] Graphite capsules for all annealing.

The synthesized S-bearing glasses were reddish brown in color. Optical microscopic examinations do not reveal the presence of crystals. Scarce metal-rich micro-droplets are observed in a few samples. Bubbles are present in some glasses; in this case, the glass cylinder was pulverized for electrical experiments to avoid artifacts in the measurement of bulk electrical properties. Nine starting compositions were synthesized, with S content varying from 0 to 4.8 wt%. Because the starting glasses were synthesized in graphite capsules, fine graphite particles are observed on the surface of most glass cylinders.

Starting glasses and samples retrieved after electrical experiments under pressure and temperature were analyzed using the electron microprobe to characterize the phases, composition, and texture. Analyses were performed with a JEOL 8530F field-emission electron microprobe, with an acceleration voltage of 15 kV and a sample current of 20 nA. Integration times were 20 s on peak and 10 s on background, except for Na and P, that were analyzed with 50% shorter times. The beam was slightly defocused (~5 μm). The following standards were used: basaltic glass (for measuring Na, Mg, Ti, Ca, Al, Si, Fe), ilmenite (Mn), orthoclase (K), pyrite (S), and apatite (P). In addition to spot analyses on the silicate and sulfide phases, energy dispersive spectroscopy (EDS) and wavelength dispersive spectroscopy (WDS) were used to obtain chemical maps of selected samples. High-resolution WDS maps used a 1-μm diameter beam and a 20-ms dwell time. Each spectroscopic technique used to study the glasses (Table 2) is described in the following subsections.

2.2. Impedance spectroscopy measurements under pressure and temperature

Electrical experiments were carried out at 2 GPa (except for one experiment performed at 4 GPa) under quasi-hydrostatic conditions in a 1,100-ton Walker-type Rockland multi-anvil press. Experimental conditions are listed in Table 2. Pressure was applied using eight tungsten carbide cubes with corner-truncated edge length of 8 mm and MgO octahedral pressure media with an edge length of 14 mm. All MgO parts were fired at ≥1273 K and stored in a desiccator until use. Two types of electrical cell assembly were used, depending on the temperature range of the electrical measurements (Appendix B, Fig. S1). For experiments quenched at a temperature slightly above the glass transition of the sample (low-T experiments), the cell assembly was composed of three MgO sleeves, with the middle one containing the sample, and of two high-purity Fe disks (Pommier and Leinenweber, 2018). The sample used for these low-T experiments was a glass cylinder with the same diameter as the synthesized glasses (1.5 mm). For experiments quenched at a temperature for which the sample was partially molten (high-T experiments), the electrical cell assembly consisted of three MgO sleeves, with the middle one comprised of three alumina rings separated from each other by two high-purity Fe disks (Saxena et al., 2021). The starting material used for these high-T experiments was glass powder. The middle alumina ring contained the sample, and the design prevented molten material from escaping the cell. With either assembly, the sample was heated by applying a current to the surrounding Re foil, and temperature was monitored using one of two Type-C thermocouples ($W_{95}Re_5$-$W_{74}Re_{26}$). Each thermocouple contacted one of two Fe-metal disks that were electrodes for impedance measurements.

The cell assembly was initially compressed to the target pressure at room temperature, and the temperature was then increased in 25 K increments. Impedance data were collected during heating. Fig. S2 (Appendix B) shows the temperature–time and the temperature-power paths for all experiments. The pressure remained within (±) 2% of the target value throughout the heating cycle. All experiments were quenched by turning off the power to the heater at a temperature below the melting point of the Fe electrodes (~1850 K; e.g., Buono and Walker, 2011). After decompression, the electrical cell was mounted in an epoxy resin, sliced longitudinally, and polished to expose the surface of the sample for chemical and textural microprobe analyses.

Electrical measurements consisted of 4-electrode impedance spectroscopy (Ametek 1260 Solartron Impedance/Gain-Phase Analyzer). To measure the complex impedance, a potential with DC component 1 V and AC amplitude ≤ 1 V was applied from 1 MHz to ~1 Hz. The sample response was not sensitive to variation in AC amplitude between 200 mV and 1 V. The complex impedance Z is composed of a real part Z' and an imaginary part Z''. The Z' value determined at relatively low frequency, either as a local minimum in the complex impedance plane, otherwise as an intersection or extrapolated intersection with the real axis, is considered the bulk electrical resistance (R). The sample resistance R_{sample} is obtained from R after removing very minor contributions from the alumina ring (electrically in parallel with the sample in the high-T assembly; Fig. S1) and the two electrode disks (electrically in series with the sample). Reproducibility was checked by (1) making multiple measurements during an experiment at defined temperature, and (2) duplicating electrical experiments for glass VT55 at overlapping temperature ranges using a different electrical cell (BBC12 and BBC18 experiments, Table 2).

The electrical conductivity σ of the sample at each temperature is calculated from R_{sample}:

$$\sigma = \frac{1}{R_{sample} \times G} \quad (2)$$

In Eq. (2), the geometric factor G is the ratio (electrode disk area, πr^2) / (sample thickness, l). The error in each conductivity value is typically a few percent (Appendix B, Supplementary material).

2.3. ^{29}Si NMR spectroscopy

^{29}Si NMR spectra were acquired on starting glasses VT53, VT48, VT52, and VT54 using a solid-state NMR spectrometer (Chemagnetics Infinity). The resonant frequency of ^{29}Si is 59 MHz in the 7-tesla static field. The synthesized glasses were crushed into a powder and loaded into a 5-mm diameter rotor. Spectra were acquired with a 1.3-μs pulse width, corresponding to a 30° nutation angle. The iron content in those samples analyzed by NMR spectroscopy (≤0.02 wt% Fe_2O_3) is below the

Table 2
Summary of the different measurements performed on starting glasses.

Glass	Impedance spectroscopy				EMPA	NMR spectroscopy	Raman spectroscopy
	Experiment	Starting material	Pressure (GPa)	T range (K)			
VT42 (S free)	BBC21	Powder	2	1473–1673	SG and QM*	–	SG
VT46	BBC22	Powder	2	1578–1738	SG and QM	–	QM
VT47	BBC15	Powder	2	1388–1619	SG and QM	–	–
VT48	BBC16	Cylinder	2	573–874	SG and QM	SG	QM
VT52	BBC17	Powder	2	623–1657	SG and QM	SG	SG and QM
VT53 (S free)	BBC13	Cylinder	2	598–1031	SG and QM	SG	–
VT54	BBC14	Cylinder	2	523–973	SG and QM	SG	–
VT55	BBC12, BBC18	Cylinder, powder	2, 2	475–944, 673–1593	SG and QM	–	SG and QM
VT56 (S free)	BBC10, BBC19	Powder, powder	2, 4	593–1669, 625–1585	SG and QM	–	SG

* SG: analyses on starting glass; QM: analyses on quenched material from electrical experiment.

levels previously reported to cause significant shortening of T1 relaxation times (Maekawa et al., 1991; Ackerson et al., 2020). However, the presence of paramagnetic Mn^{2+} (0.04–0.32 wt% MnO) is comparable to quantities known to decrease T1 significantly (Scholz and Thomas, 1995) thereby allowing a short (2-s) recycle delay without saturation. The magic-angle spinning (MAS) frequency ($\omega_r/2\pi$) was 8 kHz. The number of acquisitions was 40,000 × 4. The chemical shifts were referenced to the ^{29}Si frequency of tetramethylsilane (TMS) defined as 0 ppm. NMR spectra were not acquired for the quenched samples from electrical experiments, because the amount of material in the multi-anvil cell assembly was insufficient.

2.4. Raman spectroscopy

Raman spectra were collected on selected starting glasses and quenched samples from electrical experiments (Table 2). Methods used in this study are similar to those outlined in Steele et al. (2007, 2012). Two scanning near-field optical microscope systems (WITec Alpha) were

Table 3
Summary of electron microprobe analyses (in wt.%) of starting glasses and quenched samples after electrical experiments.

Silicate analyses		Na_2O	MgO	TiO_2	CaO	Al_2O_3	SiO_2	FeO	MnO	K_2O	S	P_2O_5	Total
VT42	*Starting glass*												
	average (9)*	5.09	10.7	0.39	5.59	14.3	64.2	0.62	0.32	0.18	0.00	0.01	101.4
	std dev.	*0.08*	*0.3*	*0.06*	*0.13*	*0.3*	*0.7*	*0.23*	*0.04*	*0.01*	*0.00*	*0.01*	
	BBC21, 2 GPa, 1673 K												
	average (58)	5.05	10.3	0.38	5.40	14.2	65.1	1.23	0.29	0.19	0.00	–	102.2
	std dev.	*0.30*	*0.5*	*0.02*	*0.20*	*0.5*	*1.0*	*0.21*	*0.03*	*0.03*	*0.00*	–	
VT46	*Starting glass*												
	average (6)	5.22	10.6	0.35	5.76	14.7	62.4	1.29	0.20	0.36	0.12	0.04	101.0
	std dev.	*0.29*	*0.3*	*0.03*	*0.28*	*0.3*	*0.9*	*0.47*	*0.04*	*0.02*	*0.02*	*0.05*	
	BBC22, 2 GPa, 1738 K												
	average (68)	4.99	9.16	0.36	5.40	15.0	64.1	1.27	0.19	0.40	0.15	–	101.1
	std dev.	*0.47*	*1.64*	*0.02*	*0.18*	*0.6*	*0.9*	*0.34*	*0.02*	*0.05*	*0.05*	–	
VT47	*Starting glass*												
	average (9)	4.27	11.4	0.41	5.92	14.8	62.4	0.02	0.27	0.32	1.19	0.17	101.1
	std dev.	*0.33*	*0.9*	*0.08*	*0.29*	*0.6*	*0.6*	*0.02*	*0.13*	*0.04*	*0.74*	*0.10*	
	BBC15, 2 GPa, 1619 K												
	average (30)	5.00	9.40	0.32	5.30	14.1	63.8	0.07	0.21	0.41	2.11	0.19	101.0
	std dev.	*0.52*	*1.83*	*0.07*	*0.47*	*1.2*	*1.0*	*0.04*	*0.06*	*0.08*	*0.40*	*0.06*	
VT48	*Starting glass*												
	average (6)	5.05	10.2	0.32	5.45	14.4	63.6	0.01	0.13	0.37	1.71	0.21	101.5
	std dev.	*0.16*	*0.3*	*0.06*	*0.31*	*0.6*	*1.0*	*0.02*	*0.02*	*0.01*	*0.07*	*0.04*	
	BBC16, 2 GPa, 874 K												
	average (29)	4.99	10.4	0.36	5.39	14.3	64.3	0.01	0.16	0.37	1.77	0.22	102.2
	std dev.	*0.16*	*0.8*	*0.04*	*0.40*	*0.6*	*1.5*	*0.01*	*0.04*	*0.03*	*0.10*	*0.04*	
VT52	*Starting glass*												
	average (6)	4.57	8.61	0.28	13.1	12.8	59.2	0.02	0.04	0.33	3.82	0.07	102.9
	std dev.	*0.27*	*0.36*	*0.04*	*0.9*	*0.2*	*0.7*	*0.01*	*0.02*	*0.04*	*0.72*	*0.06*	
	BBC17, 2 GPa, 1657 K												
	average (25)	4.45	8.41	0.22	15.1	12.2	57.0	0.05	0.04	0.35	5.62	0.07	103.6
	std dev.	*0.15*	*0.82*	*0.03*	*0.3*	*0.2*	*0.4*	*0.05*	*0.02*	*0.06*	*0.93*	*0.05*	
VT53	*Starting glass*												
	average (15)	6.30	10.1	0.38	6.30	15.5	61.8	0.01	0.32	0.16	0.00	0.15	101.1
	std dev.	*0.08*	*0.1*	*0.02*	*0.09*	*0.1*	*0.4*	*0.01*	*0.03*	*0.01*	*0.00*	*0.02*	
	BBC13, 2 GPa, 1031 K												
	average (6)	5.84	9.48	0.41	5.62	14.8	64.6	0.14	0.33	0.18	0.01	–	101.4
	std dev.	*0.09*	*0.49*	*0.04*	*0.38*	*0.6*	*1.5*	*0.16*	*0.02*	*0.01*	*0.00*	–	
VT54	*Starting glass*												
	average (7)	4.46	9.59	0.34	8.49	13.6	61.7	0.02	0.08	0.34	4.20	0.19	103.0
	std dev.	*0.22*	*0.35*	*0.07*	*0.31*	*0.4*	*0.8*	*0.02*	*0.01*	*0.02*	*0.28*	*0.05*	
	BBC14, 2 GPa, 973 K												
	average (7)	4.95	8.79	0.33	7.35	11.0	62.4	0.01	0.06	0.36	4.11	–	99.3
	std dev.	*0.10*	*0.48*	*0.02*	*0.49*	*0.3*	*1.9*	*0.02*	*0.02*	*0.03*	*0.18*	–	
VT55	*Starting glass*												
	average (8)	5.31	10.1	0.31	10.4	14.7	55.9	0.00	0.18	0.37	4.79	0.11	102.2
	std dev.	*0.13*	*0.1*	*0.02*	*0.3*	*0.3*	*0.2*	*0.00*	*0.04*	*0.01*	*0.33*	*0.05*	
	BBC12, 2 GPa, 944 K												
	average (50)	5.14	10.2	0.34	9.93	14.6	57.9	0.02	0.21	0.37	4.54	0.14	103.4
	std dev.	*0.10*	*0.2*	*0.02*	*0.15*	*0.2*	*0.4*	*0.02*	*0.03*	*0.02*	*0.23*	*0.13*	
	BBC18, 2 GPa, 1593 K												
	average (29)	5.05	10.3	0.29	10.5	14.7	57.4	0.04	0.17	0.42	4.61	0.12	103.5
	std dev.	*0.34*	*0.7*	*0.05*	*0.3*	*0.2*	*0.5*	*0.02*	*0.10*	*0.08*	*0.73*	*0.07*	
VT56	*Starting glass*												
	average (17)	6.00	11.7	0.38	6.28	15.2	61.4	0.02	0.32	0.17	0.00	0.12	101.6
	std dev.	*0.06*	*0.1*	*0.02*	*0.08*	*0.4*	*0.5*	*0.02*	*0.03*	*0.01*	*0.00*	*0.02*	
	BBC19, 1 GPa, 1585 K												
	average (25)	5.51	9.86	0.41	5.37	14.0	64.8	0.04	0.31	0.17	0.00	–	100.5
	std dev.	*0.31*	*0.60*	*0.04*	*0.32*	*0.8*	*1.7*	*0.02*	*0.03*	*0.05*	*0.00*	–	

Sulfide analyses		Fe	S	Si	Mg	Ca	Mn	Total
VT46	*BBC22, 2 GPa, 1738 K*							
	average (5)*	68.7	27.9	0.08	0.01	0.03	0.08	96.8
	std dev.	*2.71*	*2.14*	*0.03*	*0.01*	*0.04*	*0.05*	

* Number of analyses. Each analysis was performed using a 5-μm defocused beam.

employed, both with confocal Raman spectroscopic imaging capability. The excitation wavelength was 532 nm. The power at the sample was 0.3 to 1 mW. Spectra were collected without analysis of polarization. The excitation laser was focused either at the surface of the sample, or several µm below it. The entrance to a 50-µm optical fiber served as the confocal aperture. The scattered light was dispersed with a 600-groove/mm grating, and Raman spectra in the 200–3600 cm^{-1} range were acquired with an integration time of 1 to 6 s per pixel. Imaged areas were typically (20–50 µm) × (20–50 µm), and the spatial resolution was 1 µm. Raw spectra were first processed using WITec software (Project Plus version 5.2) to remove any signals from cosmic rays, or to subtract a broad emission background (when present) using the shape function (curve diameter 50 cm^{-1}). Principal component analysis (PCA) was also performed on the full set of Raman spectra within selected imaged areas, using the WITec software.

3. Results and discussion

3.1. Chemical composition

The chemical composition of the synthesized glasses is summarized in Table 3. The S concentration can be categorized in three groups: samples with 0.0–0.1 wt% S (VT42, VT53, VT56, VT46); those with 1–2 wt% S (VT47, VT48) and those with 3.8–4.8 wt% S (VT52, VT54, VT55). The fact that ~5 wt% S was the maximum amount, even upon addition of 12–30 wt% CaS, is consistent with sulfur solubility at an fO_2 of −6 relative to IW and the temperatures of the syntheses (see Fig. 3 of Namur et al., 2016a and Fig. 2 of Anzures et al., 2020). Samples with added iron (VT42, VT46) were analyzed to have 0.6 or 1.3 wt% FeO. The amounts of Ti and K are small (<0.5 wt% TiO_2 or K_2O) for all samples. Likewise, the concentrations of Mn are small (0.04–0.32 wt% MnO) but even these quantities likely affect the NMR spectroscopy, as mentioned above.

Relative molar quantities of the constituents are fundamentally important and can be summarized as follows. The sulfide-free (VT42, 53, 56) and low-S (VT46, 47, 48) glasses have a combined average mol.% composition of 5 Na_2O, 16 MgO, 6 CaO, and 9 Al_2O_3, 63 SiO_2. The average mol.% composition of S-rich (VT54, 55, 52) glasses, assuming all cations as oxides and excluding S from the analysis, is 5 Na_2O, 14 MgO, 12 CaO, 8 Al_2O_3, and 61 SiO_2. These glasses contain 12 to 16 mol.% S relative to Si, which replaces O. Alkaline earth metals Mg^{2+} and Ca^{2+} are the dominant cations (other than Si^{4+}) in the glasses; combined, they are on average 35 mol.% of Si for the samples with low or no S, and 43 mol.% of Si for the S-rich samples. Na^+ is the only alkali cation with significant quantity (16 mol.% relative to Si). Network former Al_2O_3 is ~14 mol.% of SiO_2.

Back-scattered electron (BSE) images of selected samples from electrical experiments are shown in Fig. 1. The sample diameter remained identical during the experiment, but because Fe disks deformed slightly during compression (Fig. 1**A**), the sample thickness considered in Eq. (2) is an average value. Crystals are visible in the samples quenched at high temperature (high-T cell assembly) (Fig. 1**B**) and indicate a partially molten state at the quenching temperature. The olivine crystals observed in the retrieved samples are small and characterized by euhedral shapes with well-developed faces, and are thought to have formed prior to quenching (crystals grown during the quench would have skeletal shapes). A partially crystallized state after quenching also agrees with previous phase-equilibria experiments that indicate a liquidus temperature of ~1673 K for the S-bearing NVP composition at 1 GPa (Namur et al., 2016b). From analysis of the BSE images (ImageJ software; see Fig. S3 (Appendix B) for example), the melt fraction in samples for the high-T experiments is estimated to be ~0.5–0.7, with the lowest values for the S-free glasses. In contrast, samples quenched at low temperature (cells with an MgO sample sleeve) preserved a clean glass texture (Fig. 1**C**). Only two samples have iron sulfides (BBC21 and BBC22), as illustrated in Fig. 1**D** for BBC22. These samples contain the highest Fe content (reported as 1.2 and 1.3 wt% FeO in Table 3). In addition to Fe and S, these sulfides also contain some silicon and trace amounts of phosphorus. WDS maps for this sample (Fig. S4**A**, Appendix B) show that Fe is not in the silicate phase, or it is below the detection limit of the electron microprobe analyses.

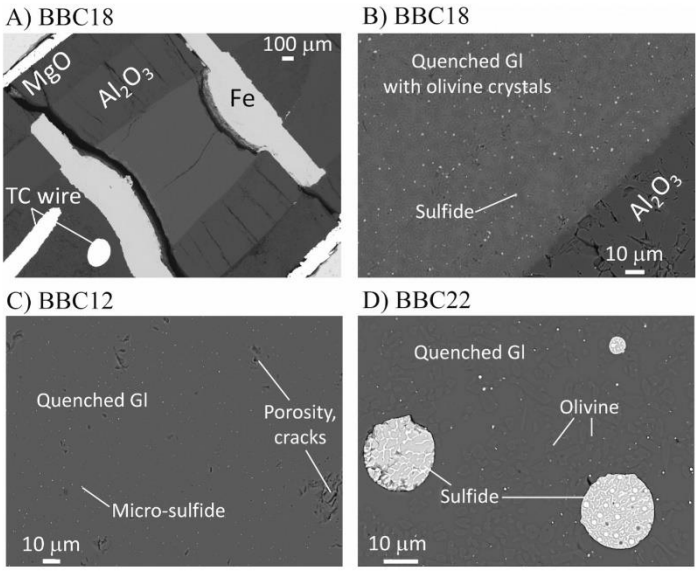

Fig. 1. Back-scattered electron (BSE) images of selected quenched samples from electrical experiments: A) and B) BBC18 (glass VT55 quenched at 1593 K showing the presence of olivine crystals), C) BBC12 (glass VT55 quenched at 944 K), and D) BBC22 (glass VT46 quenched at 1738 K).

The bulk composition of quenched samples after electrical experiments is in good agreement with that of the starting glasses (Table 3). Most importantly, sulfur was maintained in the samples even at high temperature. The contamination of the samples by the middle sleeve (MgO ring for the low-T experiments, alumina ring for the high-T experiments) is insignificant, with an Mg-rich or Al-rich thin spinel layer limited to a few μm in thickness located at the MgO-sample or alumina-sample interface, respectively (Fig. 2). This layer is formed by the diffusion of Mg or Al into the sample at elevated temperature. One exception is sample BBC22 (using Fe-bearing glass VT46), where a few distinct crystals are observed at the alumina-sample interface (Fig. S4**b**, Appendix B). Chemical analyses suggest that this S-free silicate phase is rich in Al, Mg, Ca, Na and Fe (Table 3), consistent with an augite (porricin, or grünblende). Iron from the electrodes incorporates in the sample, but only over a restricted range (up to ~50 μm from the interfaces) (Fig. 2). The chemical interactions between the electrode disks or the sample sleeve and the sample have a negligible effect on the bulk electrical measurements because of the limited thickness of the contaminated regions.

Significant compositional variation is observed in the starting glasses and remains in the quenched samples. The example of BBC16, quenched at 874 K, is shown in Fig. 3. For traverses across the sample diameter, the variation in content (wt.%) is: S, from 1.2 to 2.7; Na_2O, from 4 to 5.4; MgO, from 7.5 to 12; CaO, from 3.2 to 6.4; and SiO_2, from 58 to 68. WDS maps of samples also reveal some spatial variation in chemical content (Fig. 3). For samples quenched at high temperatures such as BBC18 (Fig. 2) there is similarly significant variation in chemical content across the sample, e.g., S, 2 to 6 wt%; MgO, 8 to 13 wt%. Spatial heterogeneity is common in alkaline silicate glasses but is typically minimized if alumina is present, as in our glasses. The specific causes for the heterogeneity within the glasses of the present study are not yet known. We note that the impedance and NMR measurements probe the samples as a whole, and the impact of spatial heterogeneity was not analyzed.

3.2. Impedance spectroscopy

Examples of impedance spectra for different samples at selected temperatures are presented in Fig. 4. The electrical resistance is determined from the low frequency portion (right side) of a relevant arc in the complex impedance plane, as described above. At low temperature, one impedance arc is observed for all samples as is typical of semiconductors (Fig. 4**a** and 4**b**). At high temperature (>1373 K), the sample resistance is derived from the second impedance arc at lower frequency (e.g., see arrows marking Z' positions in Fig. 4**c**). For all samples, resistance decreases with increasing temperature.

The electrical conductivity during heating of all glass samples is presented in Fig. 5. For each composition, conductivity increases non-linearly by more than four log units over the T range under consideration. In both the glassy and partially molten states, the S-rich samples are generally most conductive though there are exceptions. Given the addition of sulfide as CaS, S-rich samples also have relatively high Ca content. Some divalent cations, including Ca^{2+}, are known to impede alkali transport in silicate glasses and melts (e.g., Doremus, 1994; Shelby, 2020). It is likely that the S-rich samples would have greater conductivity if the Ca^{2+} content were the same as in the samples without S.

At temperatures below 700–750 K, the conductivity of most samples tracks reasonably well with the Arrhenius equation,

$$\sigma = \sigma_0 \times exp\left(\frac{-\Delta H}{RT}\right) \quad (3)$$

with σ_0 the pre-exponential term and ΔH the activation energy. Previous studies of alkali silicate glasses showed that the approach developed for ionic crystals can be applied to explain the physical significance of σ_0 and ΔH (Souquet and Perera, 1990; Caillot et al., 1994; Souquet et al., 1998). The formation of charge carriers in silicate glasses is similar to the formation of a Frenkel defect, and the thermally activated diffusion of charge carriers involves interstitial jumps (e.g., Souquet and Perera, 1990). In our glasses, ΔH ranges from 0.56 to 1.10 eV. The highest ΔH values are observed for S-free samples (VT42, VT56; Table 4), except for VT53 (0.63 eV). The lowest values of ΔH (0.54, 0.55 eV for samples VT54, VT55 respectively) are found with samples containing 4–5 wt% S. Although the results show a tendency for sulfide to decrease ΔH, several factors prevent us from claiming a systematic correlation for these glasses: (1) sulfide content is limited to <5%, an amount that constrains the extent of change in conductivity, (2) variation of other elements (particularly Ca^{2+}) can influence conductivity, and (3) there is a possible interference from carbon (see below). Despite these complications, a variety of synthetic systems have demonstrated that glasses with sulfide can greatly improve transport of alkali cations relative to those with oxide, for example a 10× greater conductivity at 100 °C, and significantly lower activation energy, for Na_2S-SiS_2 versus Na_2O-SiO_2 (Ribes et al., 1979); 100× greater conductivity and much lower activation energy for $0.6Li_2S{\cdot}0.4\ SiS_2$ versus $60\%(0.6Li_2S{\cdot}0.4\ SiS_2) + 40\%(Li_4SiO_4)$

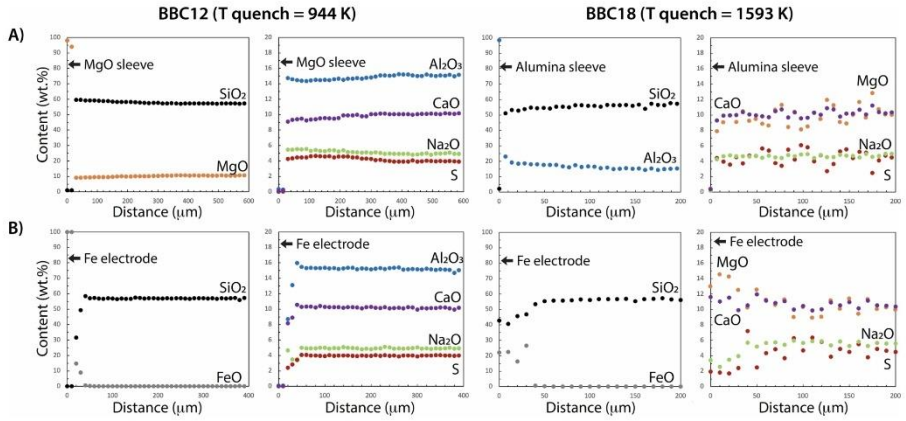

Fig. 2. Electron microprobe traverses for samples BBC12 and BBC18 (VT55 glass). A) Sample sleeve-sample traverses, with the sample sleeve being either MgO (BBC12) or Al_2O_3 (BBC18). B) Fe electrode-sample traverses.

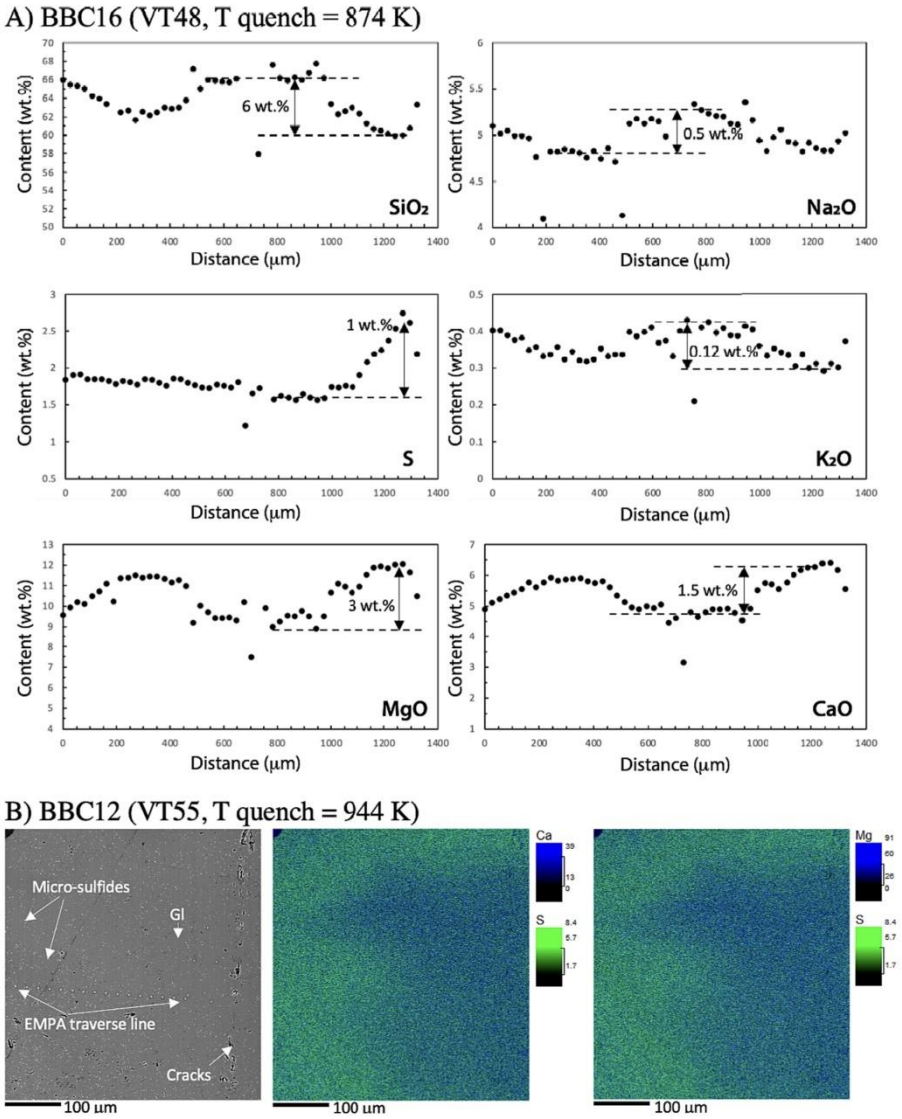

Fig. 3. Chemical variations across selected quenched samples. A) EMPA traverses across sample BBC16 (glass VT48) quenched at 874 K. B) Back-scattered electron (BSE) image and wavelength dispersive X-ray spectroscopy (WDS) maps of S, Ca, and Mg across sample BBC12 (glass VT55). The color scale bars reflect the number of counts for each element considered.

(Hirai et al., 1995; Minami et al, 2000); 100× greater conductivity of lithium sulfide + SiS_2 versus the oxide counterparts (Pradel and Ribes, 2014); and similar comparisons (Martin, 2016). The glasses in the present work generally contain much less sulfide and are prepared in a more reducing environment than these examples, nevertheless the tendency for sulfide to enhance conductivity and lower activation energy appears to be consistent with prior studies. The trend can be readily explained in terms of weaker coulombic interactions between sulfide and alkali ions relative to oxide and alkali ions, because sulfide has a larger ionic radius. Coulombic interactions are weakened further in sulfide-bearing samples because the larger relative dielectric permittivity, a consequence of the greater polarizability of S^{2-} versus O^{2-} (Martin, 2016).

Comparisons with previous electrical studies of natural silicate glasses below the glass transition temperature are limited because the effect of sulfide has not been explored, and the conditions of prior studies involving sulfur tend to be significantly less reducing than in the present study. Dry and hydrous complex silicate glasses in oxidizing environments show slightly lower conductivities than our samples

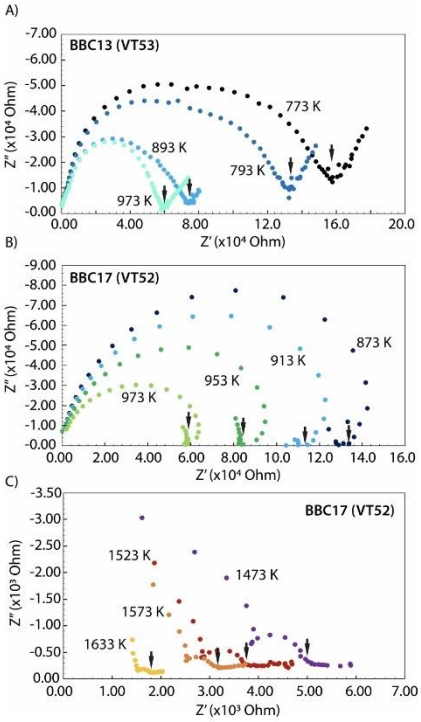

Fig. 4. Impedance spectra at selected temperatures for experiments A) BBC13 (S-free glass VT53), and B and C) BBC17 (S-bearing glass VT52). For both experiments, pressure is 2 GPa.

(Fig. 5**A**), but the activation energies of dry and hydrated tephritic, andesitic, or rhyolitic glasses range from 0.63 to 1.35 eV at pressures ≤ 3 GPa, with hydrogen decreasing ΔH (Gaillard, 2004; Pommier et al., 2008; Laumonier et al., 2015), similar to ΔH values in the present study.

The ΔH values found in the present work agree with the activation energies for Na tracer diffusion in silicate glasses and melts (e.g., Jambon, 1982; Henderson et al., 1985; Behrens, 1994; Lesher, 2010). The agreement is consistent with alkali ions (Na^+) being the major charge carriers, as is prevalent for silicate glasses (e.g., Terai, 1968; Shelby, 2020; Doremus, 1994). In contrast, the mobility of divalent cations (e.g., Ca^{2+}) in silicate glasses is much lower, and characterized by an activation energy ≥ 2.0 eV (Behrens, 1994; Natrup et al., 2005). The individual contribution of each charged species to bulk conductivity can be estimated using the tracer diffusion coefficient of each element (Appendix A). Estimates of the different ionic contributions to charge transport in our glasses emphasize the preponderant role of sodium cations that are almost entirely (>96%) responsible for bulk conductivity, while all other potential charge carriers have limited or negligible contributions. One possible exception is the S-rich glass VT55, for which sulfide could contribute up to 15% if S were not bonded to Si, a scenario that is not supported by the present work (see below).

The glass transition temperature (Tg) occurs at ~650–750 K for all samples, based on a small change in slope in Fig. 5 (e.g., Caillot et al., 1994). Tg corresponds to the temperature at which the electrical conductivity switches from an Arrhenius law (low T data) to a modified one. No clear effect of S on Tg is observed, though the highest Tg values tend to correspond to those of S-free glasses (VT53 and VT56). The non-Arrhenian temperature dependence of conductivity at $T > Tg$ and until crystallization starts at ~973 K characterizes most samples. As previously observed (e.g., Souquet et al., 1998; Souquet, 2021), the departure from an Arrhenian behavior can be explained by local deformations of macromolecular chains, affecting the transfer of charges. In this model, the low-T activated mechanism remains significant above Tg, and an additional cooperative displacement mechanism becomes active as well (Caillot et al., 1994; Souquet et al., 1998). The following equation reflects both processes above Tg:

$$\sigma = A \times exp\left(\frac{-B_1}{R(T-T_2)} - \frac{B_2}{RT}\right) \quad (4)$$

Our conductivity values are fitted satisfactorily with Eq. (4), and optimized values of B_1, B_2, and T_2 are listed in Table 4. The energy term B_1 is very low ($\leq$0.02 eV) compared to B_2 (0.07–0.34 eV). Comparison of the first and second exponential terms over the relevant temperature range indicates that the Arrhenian term is generally dominant. Over this T range, the conductivities of all samples are comparable, with the exception of BBC14 (VT54) (Fig. 5). This sample is significantly more conductive than the others, especially VT55, which has comparable S, alkali, and alkaline earth content (Table 3). The high conductivity of VT54 is likely an artefact caused by small amounts of graphite from the capsule, which were visible on the surface of the starting glass cylinder.

The onset of crystallization starts at ~973 K for all samples. It is very difficult to isolate the melt and crystal conductivity values based on bulk measurements once crystals have formed (Pommier et al., 2008). Therefore, the temperature was raised quickly (on the order of a few minutes) to reach higher temperatures (≥1373 K) where the melt phase is interconnected and dominates bulk conductivity. Above 1373 K, conductivities range from 5×10^{-2} to > 1 S/m and increase steeply with temperature. This behavior is consistent with a connected melt and a melt fraction that increases significantly with temperature. Based on melt fraction estimates using BSE images of quenched samples (e.g., Fig. S3), the melt conductivity at T_{quench} can be estimated. Assuming an interconnected melt phase and assuming a forsterite composition for the solid phase (Namur and Charlier, 2017), the Hashin-Shtrikman upper bound, derived from the effective medium theory, can be applied (e.g., Hashin and Shtrikman, 1962; Glover, 2015)

$$\sigma_{bulk} = \sigma_m \left(1 - \frac{3(1-X_m)(\sigma_m - \sigma_{fo})}{3\sigma_m - X_m(\sigma_m - \sigma_{fo})}\right) \quad (5)$$

with σ_{bulk} the bulk (measured) conductivity, X_m the melt fraction (0.5–0.7 at the time of quenching; see section 3.1), σ_m the melt conductivity, and σ_{fo} the conductivity of the forsterite crystals. The conductivity of forsterite comes from the study by ten Grotenhuis et al. (2005) for olivine aggregates with a 1.1 μm grain size, which is comparable to the grain size observed in our quenched samples (Fig. S3). Eq. (5) yields melt conductivities ranging from 0.7 to 2.2 S/m at T_{quench}, with S-free melt VT42 (BBC21) being least conductive and VT55 melt (BBC18) being most conductive. These values suggest that increasing S from 0 to ~5 wt% increases melt conductivity by a factor of 3. For a S content < 5 wt%, no clear effect on conductivity is observed.

We note that increasing pressure from 2 to 4 GPa has a relatively minor effect on bulk conductivity (see S-free glass VT56; Fig. 5). At 500 °C the conductivity of VT56 decreases from 3.3 to 2.1 S/m. This pressure effect is consistent with sodium cation hopping (e.g., Ryan and Smedley, 1984; Gaillard, 2004; Pommier et al., 2008; Ni et al., 2011a). Comparison with previous electrical studies of hydrous melts at comparable pressure and temperature conditions (Gaillard, 2004; Pommier et al., 2008; Ni et al., 2011b; Laumonier et al., 2015) shows that H-bearing melts are more conductive than the S-bearing melts in the present study (Fig. 5). The composition of the glasses from these previous studies is listed in Table S1.

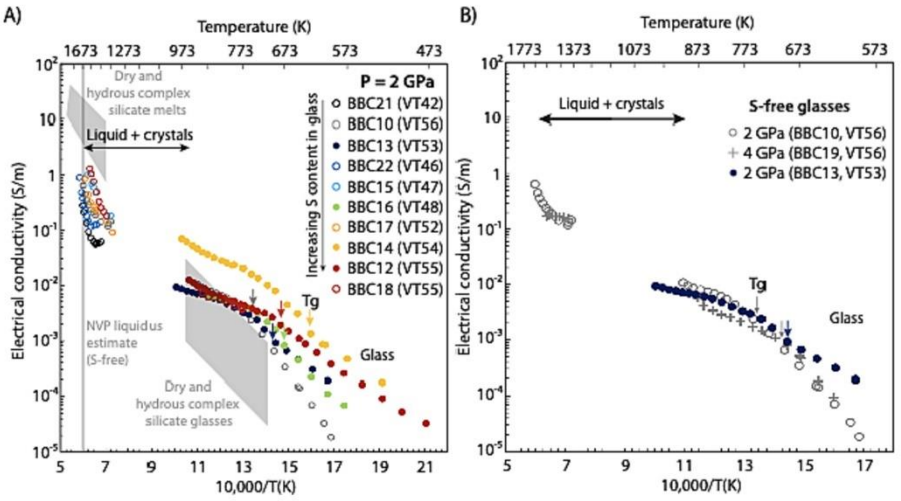

Fig. 5. Electrical conductivity for all experiments as a function of inverse temperature. A) Experiments at a pressure of 2 GPa. Vertical black arrows indicate a change in slope that corresponds to the glass transition (Tg), and the vertical grey line indicates the liquidus estimate of the S-free NVP composition at 1 GPa (after Namur and Charlier, 2017). Open circles: starting glass powders, filled circles: starting glass cylinders. Grey areas indicate electrical conductivity ranges from previous studies on dry and hydrous complex silicate glasses and melts (Gaillard, 2004; Pommier et al., 2008; Ni et al., 2011; Laumonier et al., 2015). B) Conductivity of S-free glasses VT56 and VT53, and effect of pressure on conductivity for S-free glass sample VT56, at 2 (grey circles) and 4 GPa (grey crosses).

Table 4
Summary of electrical experiments and activation energies for DC conductivity. (NA: not applicable; Tg: glass transition temperature; Tc: crystallization temperature). See Eqs. (3) and (4) for definition of other paramaters.

Run	Composition	S content (wt. %)*	P (GPa)	T_{quench} (K)	T < Tg			T > Tg and T < Tc				
					T range (K)	Ln (σ_0) (S/m)	ΔH (eV)	T range (K)	Ln (A) (S/m)	B_1 (eV)	B_2 (eV)	T_2 (K)
BBC21	VT42	0	2	1673	NA	NA	NA	NA	NA	NA	NA	NA
BBC13	VT53	0	2	1031	598–718	3.78	0.63	718–973	−3.24	0.02	0.07	575
BBC10	VT56	0	2	1669	593–750	11.0	1.10	750–884	−0.50	0.002	0.31	720
BBC19	VT56	0	4	1585	625–672	9.92	1.01	672–858	0.04	0.000	0.41	674
BBC22	VT46	0.1	2	1738	NA	NA	NA	NA	NA	NA	NA	NA
BBC15	VT47	1.2	2	1619	NA	NA	NA	NA	NA	NA	NA	NA
BBC16	VT48	1.7	2	874	573–694	8.06	0.88	694–874	−2.25	0.002	0.20	666
BBC17	VT52	3.8	2	1657	623–700	6.05	0.74	700–874	−3.10	0.004	0.10	669
BBC14	VT54	4.2	2	973	523–626	3.32	0.54	626–973	0.46	0.015	0.26	558
BBC12	VT55	4.8	2	944	475–667	2.95	0.55	667–944	−0.22	0.000	0.34	656
BBC18	VT55	4.8	2	1593	NA	NA	NA	673–893	−0.25	0.004	0.34	648

* From EMPA analyses onstarting glasses.

3.3. ^{29}Si NMR spectroscopy

The NMR spectra of starting glasses VT53 (S-free), VT48, 52, and 54 (S-bearing) are presented in Fig. 6. Starting glasses with added iron were not considered, because excessive quantities of paramagnetic Fe^{2+} cause severe peak broadening and strong spinning side bands (SSB) (Engelhardt and Michel, 1987 and references therein). Two components characterize the spectra of all samples. The major band with maximum located at −93.7 to −97.3 ppm can be attributed largely to a mixture of Q^3 and Q^4 species with shifts influenced by partial aluminum substitution (Engelhardt and Michel 1987), in agreement with previous studies of silicate glasses, with or without sulfur (e.g., Maekawa et al., 1991; Minami et al., 2000; Tsujimura et al., 2004). The small sharp peak at −62 ppm is attributed to very small amounts of crystalline olivine (e.g., Kanzaki and Xue, 2016). Forsterite olivine is the first liquidus phase in the NVP composition at low pressure (Namur and Charlier, 2017) and submicron-sized crystals likely formed during quenching of the glass, explaining why they were not visible in the BSE images. The small integral of this band relative to the rest of the ^{29}Si NMR spectrum indicates that such nanocrystals of olivine are present in very small amounts (<0.1 Si %).

Paramagnetic Mn^{2+} cations present in the samples analyzed by NMR reduce T1 spin–lattice relaxation times (Scholz and Thomas, 1995), and can also increase the ^{29}Si linewidth (Engelhardt and Michel, 1987). The quantity of Mn in the S-free glass VT53 (0.32 wt% MnO) is higher than in the other samples (0.04–0.13 wt%), and the additional amount may cause the pedestal for the main band (Fig. 6).

In typical S-free silicate glasses, as illustrated in Fig. S5 with a calcium-alumino-silicate (CAS) glass, the primary ^{29}Si band is typically symmetric with no peak shoulders, whereas in our glasses this symmetry is affected by the presence of an obvious broad shoulder on the high frequency side of the main band spanning a range from −35 to −70 ppm (Fig. 6). Sample VT52 exhibits the highest ^{29}Si intensity at ~−58 ppm. A shoulder at this frequency is inconsistent with silicon oxide Q^n species

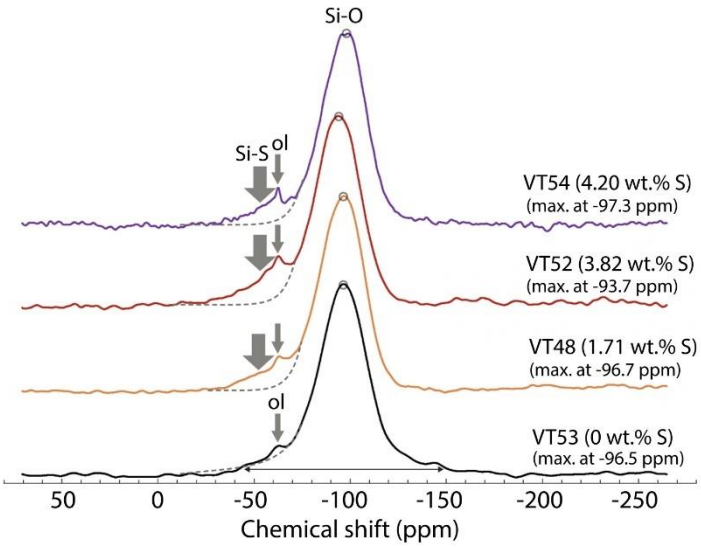

Fig. 6. ^{29}Si NMR results for starting glasses VT48, 52, 53 and 54. The grey circles indicate the maximum of the main peak (exact values are listed to the right). The dashed lines on the left side of the main peak are a mirror image of the right side of the same peak, highlighting the effects of Si–S bonds and quenched olivine crystals. The horizontal double arrow indicates the pedestal for glass VT53, possibly caused by relatively high Mn content.

for these compositions (Engelhardt and Michel, 1987). As has been previously observed for Na_2S-SiO_2 and Li_2S-SiS_2-Li_4SiO_4 oxysulfide glasses at ambient pressure (e.g., Asahi et al., 1999; Tatsumisago et al., 1996; Minami et al., 2000), Si–S bonds shift the ^{29}Si frequencies to higher values than for Si bonded only to oxygen. Specifically, a band centered at −50 to −60 ppm has been assigned to the chemical species $(SiO_3S)^{4-}$ (Hayashi et al., 2000). Spectral decomposition with Gaussian components (Fig. S6) reveals that the area of the shoulder in the case of VT52 is 14 ± 2% of the total silicon species. The composition of the same glass based on microprobe analysis indicates a S/Si atomic ratio of 12.1%, which is within the error limit of the value based on NMR spectroscopy. This agreement is consistent with (1) all, or nearly all, sulfide bonded to Si, and (2) few or no sulfide atoms bridging between two Si atoms. NMR results for VT48 bolster this analysis. For this sample, the S/Si percentage from EMPA is 5.0 mol.% and in the NMR spectrum the shoulder assigned to $(SiO_3S)^{4-}$ is ~50% the intensity of that observed for VT52 (Fig. 6). Sample VT54 is not in good agreement with the other sulfide-containing samples, because the area of the shoulder is smallest of the three, despite having the highest S/Si percentage (12.8 mol.%) from EMPA. The sample has less Ca than VT52, and less Mg than VT48, so the disagreement cannot be simply explained by proposing that alkaline metals disrupt bonding of sulfide to Si. Further study is needed to fully understand the area ratios in the NMR spectra.

The chemical shift at the maximum of the Si–O band reflects the mean degree of polymerization of the glass and can be compared with the amount of sulfide and alkaline metal content in the samples. In general, decreased polymerization of the sample (i.e., decrease in quantity of bridging oxygen atoms) causes the resonant frequency of ^{29}Si to increase, thereby causing the chemical shift to become less negative. Sample VT53 has no added S, and the maximum position of the $^{29}SiO_4$ band is at −96.5 ppm. Sample VT48 has minimal S (1.71 wt%) and the position of the band is unchanged (−96.7 ppm) within error of the fitting. Sample VT52 (3.82 wt% S) has a significantly less negative peak position (−93.7 ppm) which could suggest that the increased Si–S bonds are associated with decreased polymerization. However, an alternative explanation for the small shifts must be considered, because the addition of sulfide also causes a significant increase in the amount of Ca^{2+}, an established network modifier. The mol.% values of the two alkaline metals Mg^{2+} and Ca^{2+}, relative to SiO_2, are: VT53 (35%), VT48 (33%) and VT52 (46%). Therefore, the less negative value for δ at the band maximum is consistent with the greater alkaline metal content in sample VT52. Sample VT54, which has the most sulfide of the samples probed by NMR, has the most negative chemical shift (−97.3 ppm) but given significant broadening of the band (~30 ppm, full-width at half-maximum, FWHM) as well as slight asymmetry in the band shape, the <1 ppm difference in chemical shift relative to the sulfide-free sample VT53 (−96.5 ppm) is within error of the analysis. The alkaline metal content in VT54 (38 at.% of SiO_2) is nearly the same as for VT53, which reinforces the suggestion that the chemical shift of the main band can be rationalized in terms of network depolymerization arising from alkaline earth cations, without invoking a correlation to sulfide content.

3.4. Raman spectroscopy

Unpolarized Raman spectra of selected starting glasses and samples quenched after electrical experiments are shown over the 200–1250 cm^{-1} frequency range in Figs. 7 and 8. All glasses are luminescent, which is likely caused by the presence of transition metals (particularly Mn) and/or defects in the glass structure (e.g., Gaft et al., 2015). The Raman spectrum of starting glass VT55 containing approximately 5 wt% S is shown in Fig. 7 and compared with previous studies. The glass response is dominated by two broad bands with peak positions 550 and 1100 cm^{-1}. These bands reflect the silicate glass structure (e.g., McMillan and Piriou, 1983; Mysen and Frantz, 1992, 1994; Neuville and Mysen, 1996), particularly alkaline earth-bearing alumina silicate glasses (Merzbacher and White, 1991) that are most relevant to the present study. The low-frequency Raman band near 550 cm^{-1} has been assigned to the deformation vibration of Si–O–Si coupled with bending vibrations of tetrahedral O–Si–O (McMillan and Piriou, 1983). The high-frequency band near 1100 cm^{-1} is attributed to the symmetric Si–O stretching vibration of Q^3 species (e.g., Brawer and White, 1975, 1977; Moulton et al., 2021).

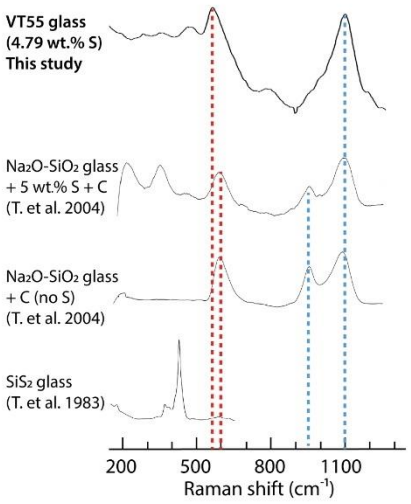

Fig. 7. Raman spectrum of a sulfide-rich silicate glass (VT55) acquired with 532-nm excitation. The spectrum is a spatial average and does not include PCA. Representative spectra from Tsujimura et al. (2004) and Tenhover et al. (1983) are also shown, with dashed vertical lines to aid comparison. See text for details.

Compared with S-free glasses, the most notable changes occur in the low-frequency region (<500 cm^{-1}), where several Raman bands with varying intensity are observed. Raman bands assigned to Si–S stretching modes in SiS_2 glasses have been measured near 430 and 370 cm^{-1} (Tenhover et al., 1983). Using density-functional theory (DFT), Devi et al. (2013) computed peak positions for SiS_2 and other Si–S glasses in the 200–600 cm^{-1} spectral window. Given extensive overlap of experimental and computed band positions assigned to various Si–S modes, with ones spanning the range 225–470 cm^{-1} which have been reported for MgS (niningerite) or mixed Mg/CaS samples (Avril et al., 2013), specific assignments to MgS, CaS, or Si–S are difficult. Nevertheless, based on the principal component spectra presented in Fig. 8, there is remarkable overlap between sample VT55/BBC18 and oldhamite from Avril et al. (2013), suggesting that clusters of CaS may be present in this sample. The decomposed spectra of VT52 show a prominent band at 330 cm^{-1} (starting glass) or 250 cm^{-1} (after electrical run BBC17). These features do not match spectra of niningerite or oldhamite. Possibly the peak positions reflect unique chemical structures (and vibrational modes) that are specific to our samples, e.g., Ca–S–Si, or Mg–S–Si. Interestingly, the amplitude of the principal component associated with sulfide-cation vibrations shows a high degree of spatial variation (see images in Fig. S7), perhaps providing additional support for spatial heterogeneity of sulfide distribution in the quenched sample. At this point, the preceding proposals are speculative, and it would also be premature to claim that our Raman spectra provide support for Si–S bonds in the quenched samples and starting materials. Prior Raman spectra of glasses acquired for a slightly reduced ($\Delta IW \sim +2.5$) S-bearing KSi_4O_9 glass (Klimm and Botcharnikov, 2010) or for more reduced ($\Delta IW < -1.5$) (Mg,Ca,Fe)S-bearing silicate melts (Namur et al., 2016a) found no indication of Si–S bonds. In addition, we see no evidence for Na-S bonds, which can be explained by the weak interactions between sodium and sulfide, and by the absence of Na_2S species at our highly reduced conditions (Anzures et al., 2020).

Forsterite was not observed in any of our Raman spectra, as evidenced by the absence of peaks in the 820–980 cm^{-1} range (e.g., Chopelas, 1991; McKeown et al., 2010). The NMR spectra showed that this phase is present in very small amounts in the bulk starting glasses (Section 3.3). Most likely, the sharp olivine doublet is missing in our Raman spectra because of the low concentration, or the spatial regions that were probed did not have this minor component in them.

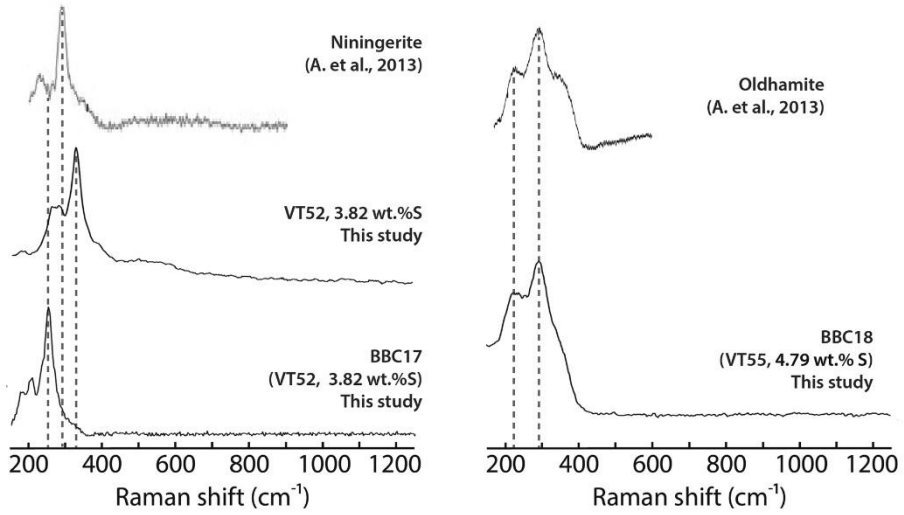

Fig. 8. Principal component spectra that highlight vibrational bands of sulfide bonded to alkaline-earth metals or silicon (–S–Ca, –S–Mg, –S–Si–O moieties). The samples are sulfide-rich glasses VT52 (before and after electrical experiment BBC17 performed at high pressure and temperature) and VT55. The spectrum of VT52 starting glass (middle left) is the same as Component 1 illustrated in Fig. S7. Spectra of Ca-rich and Mg-rich sulfides selected from Avril et al. (2013) are also shown for comparison.

3.5. Structure of highly reduced S-bearing alkali silicate glasses from a multi-spectroscopic approach

The complementary results from different spectroscopic techniques used in our study provide a multifaceted view of the role of sulfur on the structure and transport properties of highly reduced S-bearing glasses. Impedance spectroscopy highlights the mobility of charge carriers both in the glassy and partially molten states; ^{29}Si NMR spectroscopy provides direct insight regarding the interactions between S and the silica network; and Raman spectroscopy reveals interactions between S and alkaline earth elements.

The NMR results show that significant amounts of sulfur enter the silica framework by bonding with silicon, possibly even quantitative for two of the samples (VT48 and 52). Most or all of the S bound to Si is non-bridging, i.e., it can also interact with network modifier cations. Raman spectroscopy reveals alkaline earth-sulfides bonds, although the amount cannot be quantified. In general, alkaline earth elements are known to be strongly network modifying cations (e.g., Mysen and Richet, 2005), depolymerizing the structure of silicate glasses via the following scheme, where the equilibrium is strongly shifted to the right in the case of CaO:

$$\text{Si-O-Si} + \text{CaO} = \text{Si-O-Ca-O-Si} \quad (6)$$

For glasses of the present work, alkaline earth sulfides (CaS complexes) can modify the network in an analogous way:

$$\text{Si-O-Si} + \text{CaS} = \text{Si-O-Ca-S-Si} \quad (7)$$

Given that the bond energy (BE) of silicon oxide is considerably larger than that of silicon sulfide (e.g., BE_{SiO} of SiO_2 is 622 kJ/mol, and BE_{SiS} of SiS_2 is 533 kJ/mol; Holleman and Wiberg, 1995) it is reasonable to conclude that CaS is not as strong network modifier as CaO, i.e., the equilibrium reaction Eq. (7) is not as strongly driven to the right as in Eq. (6). In the case of Ca^{2+} added as a sulfide, our results from NMR and Raman spectroscopy indicate that CaS and Si–O–Ca–S–Si moieties coexist in the glasses, when prepared under highly reduced conditions. Regions rich with Ca–S or Mg–S bonds in the glass are also compatible with the chemical variations observed using WDS analyses. The heterogeneity in the spatial distribution of sulfide species can be seen as analogous to the micro-segregation of network modifiers that has been described in S-free alkaline-earth silicate glasses, where network former-rich regions coexist with network modifier-rich regions (Greaves, 1985; Ingram, 1987; Greaves and Ngai, 1995).

Although not directly probing the structure of glasses, electrical conductivity depends strongly on structural aspects (Martin, 2016) and provides information at the atomic scale about sulfide - cation interactions. Our electrical measurements show that samples with the highest S content (VT54 and VT55) can have conductivities ~3 times more than those without S. The larger ionic radius of S relative to O atoms imply weaker coulombic interactions with Na^+, therefore the mobility of Na^+ and bulk conductivity are enhanced in the presence of S (Ingram, 1987; Martin, 2016). Two arguments can explain why conductivity of our glasses is not uniformly correlated with S content: (1) the S content ranges from 0 to 5 wt%, which might not be sufficient to affect conductivity significantly (but this range was chosen for its relevance to Mercury lavas); (2) the S-rich glasses also have relatively high Ca content, causing competitive effects on conductivity because alkaline earth elements are known to impede the transport of Na^+ in aluminosilicate glasses (e.g., Shelby, 2020; Doremus, 1994). This argument is consistent with molecular dynamics and NMR studies (e.g., Cormack and Cao, 1996; Lee and Stebbins, 2003). The fact that the sample with the highest S content is ~3 times more conductive than the S-free glass suggests that the effect of sulfur may be quite strong, i.e., sufficient to overcome the effect of calcium on electrical conductivity.

3.6. Implication for Mercury

Quantifying Mercury's electrical conductivity-depth profile is a specific science objective of the ESA-JAXA BepiColombo mission because electrical conductivity can be used to describe the present-day thermal state and inform about planetary cooling (Genova et al., 2021). The transport properties of highly reduced S-rich silicate melts are required to understand and model the cooling history and dynamics of a young Mercury, when it hosted a magma ocean. Our samples are representative compositions from the Borealis Planitia region, and their electrical conductivity suggests that Mercury silicate melts are electrically less conductive than oxidized melts (Fig. 5**A**). Applied to the planet's early history, these observations imply that the expected low fO_2 conditions of the magma ocean enhanced its electrically insulating characteristic. Numerical convection models predict extremely high conductivity values for a convecting magma ocean to generate and sustain a dynamo (e.g., $>10^3$ S/m; Scheinberg et al., 2018). Given the low conductivity of Mercury's silicate melt, the magma ocean would have to be mostly composed of metal or to contain a large amount of graphite to reach conductivities $> 10^3$ S/m and generate a magnetic field. Present-day observations show that a dynamo is generated in the large metallic core. Whether an electrically insulating silicate shell influenced the internally generated magnetic field in the core remains to be investigated at the conditions of Mercury.

Our electrical results will help determine the relationship between conductivity and viscosity for S-bearing natural melts, which is useful to understand melt mobility at depth. Developing a laboratory-based model of electrical conductivity and viscosity of melts allows prediction of viscosity at low temperature (at the end of magma ocean crystallization) using electrical data (Pommier et al., 2013). Furthermore, probing melts with other spectroscopic methods (NMR and Raman spectroscopy) yields atomic insights that may overcome the challenge that viscosity and conductivity depend differently on composition, bonding, and other material properties. Laboratory experiments on reduced (IW-5) silicate melts showed that viscosity tends to decrease with increasing S content (Mouser et al., 2021), which would be consistent with depolymerization by S. A low-viscosity magma ocean would enhance convection, facilitating heat transport from the core. As a result, core cooling would be accelerated, affecting the magnetic field. Further experimental and theoretical studies of the electrical, thermal, and viscosity properties of a reduced magma ocean are needed to understand and model planetary differentiation and cooling.

4. Conclusions

We have synthesized highly reduced ($\Delta IW = -6$) sulfur-bearing silicate melts at temperatures of 1573–1673 K, and a pressure of ~1 bar. At these redox conditions, sulfur is present as S^{2-} (sulfide), and we have investigated its effect on the glass structure using different techniques: impedance spectroscopy at elevated pressure and temperature, electron microscopy, ^{29}Si NMR spectroscopy, and Raman spectroscopy.

Conductivity is a sensitive probe of ionic transport in glasses. Our results show that conductivity is significantly increased by S content, even in the small amounts representative of Mercury (<~5 wt%). ^{29}Si NMR spectroscopy supports the presence of Si–S bonds and for some samples, band areas suggest that nearly all S is bonded to Si. Regions rich with Ca–S or Mg–S bonds in the glass are identified using Raman spectroscopy to probe starting glasses and quenched materials from electrical experiments. Calcium sulfide appears to act as a network modifier, but one with a weaker effect than CaO.

Our study as well as the previous viscosity study of highly reduced S-rich silicate glasses and melts (Mouser et al., 2021) reveal the complex behavior of S on transport properties. Further work under pressure and temperature is needed to develop laboratory-based models of these properties that can then be applied to magma oceans and mantle-derived melts. Such models shed light on the evolution of Mercury

during differentiation and will contribute to the interpretation of data expected from the ESA-JAXA Bepi-Colombo mission.

Declaration of Competing Interest

The authors declare that they have no known competing financial interests or personal relationships that could have appeared to influence the work reported in this paper.

Acknowledgments

AP thanks Olivier Namur, Mike Walter, and Dionysis Foustoukos for fruitful discussions, Carnegie-EPL librarians Shaun Hardy and M.A. O'Donnell for their assistance, and the Carnegie-EPL Facilities team for their invaluable support. Use of the COMPRES Cell Assembly Project was supported by COMPRES under NSF Cooperative Agreement EAR-1661511. AP acknowledges financial support from NSF-CAREER award EAR-1750746 and the Carnegie endowment. BC is a Research Associate of the Belgian Fund for Scientific Research-FNRS. The NMR spectroscopy was performed at the W.M. Keck Solid State NMR facility (at EPL) that received support from the W. M. Keck Foundation, the NSF, and Carnegie Science. The authors thank editor S. K. Lee, R. F. Cooper, Y. Li, and an anonymous reviewer for helpful comments.

Data Availability

The experimental data used in the figures are available through Dryad at: https://doi.org/10.6076/D1TP4S.

Appendix A. Determination of the contribution of different monovalent cations to the bulk conductivity of glasses

Conductivity in our silicate glasses is ionic. Electronic conductivity due to iron is negligible because our glasses are either Fe-free or contain very small amounts of iron and Si^0 (Table 3). Conductivity by electrons was also found negligible in sulfide glasses (Na_2S-SiS_2 and K_2S-SiS_2) (Ravaine, 1980). The contribution of each element i to the bulk conductivity can be estimated using the Nernst-Einstein equation (e.g., Terai, 1968; Souquet and Perera, 1990; Gaillard, 2004; Pommier et al., 2008):

$$\sigma_i = \frac{x_i \times q^2 \times D_i}{k_B \times T \times H_r} \quad \text{(A1)}$$

with σ_{bulk} the bulk conductivity, σ_i the conductivity of charge carrier i, x_i the number of charge carriers per unit volume, q its charge, D_i the tracer diffusion coefficient of i, k_B the Boltzmann constant, T the temperature, and H_r the Haven ratio. In silicate glasses with high Na^+ contents, H_r ranges from 0.44 to 0.55 (Souquet, 2021). Here we assume an intermediate value of 0.50.

Alkali (Na^+ and K^+), major alkaline earth (Ca^{2+} and Mg^{2+}), and sulfide are considered possible charge carriers in the glasses of the present study. For each possible charge carrier, diffusion coefficients are from tracer diffusion studies: Terai (1968) and Jambon (1982) for Na^+, Jambon and Carron (1976) for K^+, Behrens (1994) and Natrup et al. (2005) for Ca^{2+} (the same D values were used for Mg^{2+}), and Lierenfeld et al. (2018) for S^{2-}. At a defined temperature, the conductivity of each element (σ_i) is calculated using Eq. (A1) and the individual contributions are obtained by comparison with the measured conductivity.

Although the presence of Si^{2+} has been invoked in reduced glasses (Cooper et al., 2010), the tracer diffusion coefficient of silicon is extremely low ($\sim 3.10^{-22}$ m^2/s at 1073 K in an aluminosilicate glass; Lepke et al., 2013). Similarly, aluminum has very low D values ($<10^{-22}$ m^2/s below Tg; Lepke et al., 2013). As a result, we did not consider Si and Al as plausible charge carriers in our glasses. Oxygen is part of the silica network and is not expected to contribute to the transfer of charges. However, if O^{2-} were diffusing in the glasses, its contribution would be insignificant because its D value ($\sim 10^{-20}$ m^2/s at 873 K; after Lepke et al., 2013) is several orders of magnitude lower than that of alkali, alkaline earth and sulfur (respectively $\sim 10^{-12}$, $\sim 10^{-17}$, and 2.10^{-13} m^2/s at 873 K).

As an example, at 873 K, the contribution of sodium cations to bulk conductivity ranges from 96.5 to 99.9% depending on the experiment considered, and sulfur anions represent the second major contributor with 0–3.5%. One exception is experiment BBC12 (VT55 glass), with estimated contributions of Na^+ and S^{2-} of 85.5% and 15%, respectively. The estimate for the contribution of sulfur is an upper limit because most sulfur enters the silica framework (Section 3.3) and thus does not contribute to charge transport. The contributions of network modifiers potassium, calcium, and magnesium cations amount to less than 1%, in agreement with previous studies on dry and hydrous silicate glasses (e.g., Gaillard, 2004; Pommier et al., 2008).

Appendix B. Supplementary material

The supplementary material includes: method for estimating conductivity error; drawings of electrical cell assemblies; time-temperature paths and power-temperature curves for electrical experiments; an example of image analysis using software ImageJ; back-scattered electron (BSE) images and wavelength dispersive spectroscopy (WDS) maps of quenched sample BBC22; the ^{29}Si NMR spectrum of a CAS glass; Raman spectra and images for starting glass VT52. Supplementary material to this article can be found online at https://doi.org/10.1016/j.gca.2023.10.027.

References

Ackerson, M.R., Cody, G.C., Mysen, B.O., 2020. ^{29}Si solid state NMR and Ti K-edge XAFS pre-edge spectroscopy reveal complex behavior of Ti in silicate melts. Prog. Earth Planet. Sci. 7, 14.

Anzures, B.A., Parman, S.W., Milliken, R.E., Namur, O., Cartier, C., Wang, S., 2020. Effect of sulfur speciation on chemical and physical properties of very reduced mercurian melts. Geochim. Cosmochim. Acta 286, 1–18.

Asahi, T., Miura, Y., Nanba, T., Yamashita, H., 1999. Chemical bonding state of sulfur in oxysulfide glasses. Korean J. Ceramics 5, 178–182.

Avril, C., Malavergne, V., Caracas, R., Zanda, B., Reynard, B., Charon, E., Bobocioiu, E., Brunet, F., Borensztajn, S., Pont, S., Tarrida, M., Guyot, F., 2013. Raman spectroscopic properties and Raman identification of CaS-MgS-MnS-FeS-Cr_2FeS_4 sulfides in meteorites and reduced sulfur-rich systems. Meteorit. Planet. Sci. 48, 1415–1426.

Baker, D., Moretti, R., 2011. Modeling the solubility of sulfur in magmas: A 50-year old geochemical challenge. Rev. Mineral. Geochem. 73, 167–213.

Behrens, H., 1994. Na and Ca tracer diffusion in plagioclase glasses and supercooled melts. Chem. Geol. 96, 267–275.

Brawer, S.A., White, W.B., 1975. Raman spectroscopic investigation of the structure of silicate glasses (I). The binary alklai silicates. J. Chem. Phys. 63, 2421–2432.

Brawer, S.A., White, W.B., 1977. Raman spectroscopic investigation of the structure of silicate glasses (II). Soda-alkaline earth-alumina ternary and quaternary glasses. J. Non-Cr. Sol. 23, 261–278.

Buono, A.S., Walker, D., 2011. The Fe-rich liquidus in the Fe–FeS system from 1 bar to 10 GPa. Geochim. Cosmochim. Acta 75, 2072–2087.

Caillot, E., Duclot, M.J., Souquet, J. L., et al., 1994. A unified model for ionic transport in alkali disilicates below and above the glass transition. Phys. Chem. Glasses 35, 22–27.
Carroll, M.R., Rutherford, M.J., 1988. Sulfur speciation in hydrous experimental glasses of varying oxidation states: Results from measured wavelength shifts of sulfur X-rays. Am. Min. 73, 845–849.
Charlier, B., Namur, O., 2019. The origin and differentiation of planet Mercury. Elements 15, 9–14.
Chopelas, A., 1991. Single crystal Raman spectra of forsterite, fayalite, and monticellite. Am. Mineral. 76, 1101–1109.
Cooper, R.F., Everman, R.L.A., Hustoft, J.W., Shim, S.-H.-D., 2010. Mechanism and kinetics of reduction of a FeO-Fe_2O_3-CaO-MgO aluminosilicate melt in a high-CO-activity environment. Am. Mineral. 95, 810–824.
Cormack, A.N., Cao, Y., 1996. Molecular dynamics simulation of silicate glasses. Mol. Eng. 6, 183–227.
Darken, L.S., Gurry, R.W., 1945. The system iron oxygen I. the wüstite field and related equilibria. J. Am. Chem. Soc. 67, 1398–1412.
Devi, V.R., Zabidi, N.A., Shrivastava, K.N., 2013. Interpretation of the Raman spectra of the glassy states of Si_xS_{1-x} and Si_xSe_{1-x}. Mat. Chem. Phys. 141, 651–656.
Doremus, R.H., 1994. Glass Science, 2nd edition, 352 pp., ISBN: 978-0-471-89174-1.
Engelhardt, G., Michel, D., 1987. High-resolution sild-state NMR of silicates and zeolites. 485 pp., John Wiley & Sons. ISBN-10: 0471915971.
Engster, H.P., Wones, D.R., 1962. Stability relations of the ferruginous biotite, annite. J. Petrol. 3, 82–125.
Evans, L.G., et al., 2012. Major element abundances on the surface of Mercury: Results from the MESSENGER Gamma Ray Spectrometer. J. Geophys. Res. 117, E00L07.
Fincham, C.J.B., Richardson, F.D., 1954. The behavior of sulphur in silicate and aluminate melts. Proc. R. Soc. Lond. A 223, 40–62.
Fleet, M.E., Liu, X., Harmer, S.L., King, P.L., 2005. Sulfur K-edge XANES spectroscopy: Chemical state and content of sulfur in silicate glasses. Can. Mineral. 43, 1605–1618.
Gaft, M., Reisfeld, R., Panczer, G., 2015. Modern Luminescence Spectroscopy of Minerals and Materials, Springer, 625 pp.
Gaillard, F., 2004. Laboratory measurements of electrical conductivity of hydrous and dry silicic melts under pressure. Earth Planet. Sci. Lett. 218 (1–2), 215–228.
Genova, A., et al., 2021. Geodesy, Geophysics and Fundamental Physics Investigations of the BepiColombo Mission. Space Sci. Rev. 217, 31.
Glover, P.W.J., 2015. Geophysical Properties of the Near Surface Earth: Electrical Properties, second ed. Treatise on Geophysics, pp. 89–137.
Greaves, G.N., 1985. EXAFS and the structure of glass. J. Non-Cr. Sol. 71 (1–3), 203–217.
Greaves, G.N., Ngai, K.L., 1995. Relating the atomic structure of alumino-silicate glasses to their ionic transport properties. J. Non Cr. Sol. 192–193, 405–410.
Hashin, Z., Shtrikmann, S., 1962. A variational approach to the theory of the effective magnetic permeability of multiphase materials. J. Appl. Phys. 33, 3125–3131.
Hayashi, A., Araki, R., Komiya, R., Tadanaga, K., Tatsumisago, M., Minami, T., 1998. Thermal and electrical properties of rapidly quenched Li_2S-SiS_2-Li_2O-P_2O_5 oxysulfide glasses. Solid State Ionics 113–115, 7338–7738.
Hayashi, A., Tatsumisago, M., Minami, T., 2000. Crystallization process of lithium oxysulfide glasses. J. Non-Cr. Sol. 276, 27–34.
Henderson, P., Nolan, J., Cunningham, G.C., Lowry, R.K., 1985. Structural control and mechanisms of diffusion in natural silicate melts. Contrib. Mineral. Petrol. 89 (2–3), 263–272.
Herd, C.D.K., 2008. Basalts as probes of planetary interior redox state. Rev. Mineral. Geochem. 68, 527–553.
Hirai, K., Tatsumisago, M., Minami, T., 1995. Thermal and electrical properties of rapidly quenched glasses in the systems Li_2S-SiS_2-Li_xMO_y (Li_xMO_y = Li_4SiO_4, Li_2SO_4). Solid State Ionics 78, 269–273.
Holleman, A.F., Wiberg, E., 1995. Inorganic Chemistry, de Gruyter, 1884 pp., ISBN 0-12-352651-5.
Iacovino, K., McCubbin, F.M., Vander Kaaden, K.E., Clark, J., Wittmann, A., Jakubek, R. S., Moore, G.M., Fries, M.D., Archer, D., Boyce, J.W., 2023. Carbon as a key driver of super-reduced explosive volcanism on Mercury: Evidence from graphite-melt smelting experiments. Earth Planet. Sci. Lett. 602, 117908.
Ingram, M.D., 1987. Ionic conductivity in glass. Phys. Chem. Glasses 28 (6), 215–268.
Izenberg, N.R., Klima, R.L., Murchie, S.L., Blewett, D.T., Holsclaw, G.M., McClintock, W. E., Malaret, E., Mauceri, C., Vilas, F., Sprague, A.L., Helbert, J., Domingue, D.L., Head III, J.W., Goudge, T.A., Solomon, S.C., Hibbitts, C.A., Dyar, M.D., 2014. The low-iron, reduced surface of Mercury as seen in spectral reflectance by MESSENGER. Icarus 228, 364–374.
Jambon, A., 1982. Tracer diffusion in granitic melts: Experimental results for Na, K, Rb, Cs, Ca, Sr, Ba, Ce, Eu, to 1300 °C and a model of calculation. J. Geophys. Res. 87 (B13), 10797–10810.
Jambon, A., Carron, J. P., 1976. Diffusion of Na, K, Rb, and Cs in glasses of albite and orthoclase composition. Geochim. Cosmochim. Acta 40, 897–903.
Kanzaki, M., Xue, X., 2016. Cation distribution in Mg Zn olivine solid solution: a Si 29 MAS NMR and first-principles calculation study. J. Mineral. Petrol. Sci. 111 (4), 292–296.
Klimm, K., Botcharnikov, R.E., 2010. The determination of sulfate and sulfide species in hydrous silicate glasses using Raman spectroscopy. Am. Mineral. 95, 1574–1579.
Klimm, K., Kohn, S.C., O'Dell, L.D., Botcharnikov, R.E., Smith, M.E., 2012. The dissolution mechanism of sulphur in hydrous silicate melts. I: Assessment of analytical techniques in determining the sulphur speciation in iron free to iron poor glasses. Chem. Geol. 322–323, 237–249.
Laumonier, M., Gaillard, F., Sifre, D., 2015. The effect of pressure and water concentration on the electrical conductivity of dacitic melts: Implication for magnetotelluric imaging in subduction areas. Chem. Geol. 418, 66–76.
Lee, S.K., Stebbins, J.F., 2003. Nature of Cation Mixing and Ordering in Na-Ca Silicate Glasses and Melts. J. Phys. Chem. B 2003 (107), 3141–3148.
Lepke, et al., 2013. Oxygen-18, aluminium-26 and silicon-30 self diffusion in aluminosilicate glasses. Phys. Chem. Glasses: Eur. J. Glass Sci. Technol. B 54 (1), 15–19.
Lesher, C.E., 2010. Self-diffusion in silicate melts: theory, observations and applicatiobs to magnatic systems. Rev. Mineral. Geochem. 72, 269–309.
Lierenfeld, M.B., Zajacz, Z., Bachmann, O., Ulmer, P., 2018. Sulfur diffusion in dacitic melt at various oxidation states: Implications for volcanic degassing. Geochim. Cosmochim. Acta 226, 50–68.
Lonergan, J.M., Lonergan, C., Silverstein, J., Cholsaipant, P., McCloy, J., 2020. Thermal properties of sodium borosilicate glasses as a function of sulfur content. J. Am. Ceram. Soc. 103 (6), 3610–3619.
Maekawa, H., Maekawa, T., Kawamura, K., Yokokawa, T., 1991. The structural groups of alkali silicate glasses determined from ^{29}Si MAS-NMR. J. Non-Cryst. Solids 127, 53–64.
Malavergne, V., Toplis, M.J., Berthet, S., Jones, J., 2010. Highly reducing conditions during core formation on Mercury: implications for internal structure and the origin of a magnetic field. Icarus 206, 199–209.
Martin, S.W., 2016. Glass and glass-ceramic sulfide and oxy-sulfide solid electrolytes. Chapter 14 in Handbook of Solid State Batteries 2nd Edition edited by Dudney, N.J., West, W.C., Nanda, J. World Scientific.
McCoy, T.J., Peplowski, P.N., McCubbin, F.M., Weider, S.Z., Solomon, S.C., Nittler, L.R., Anderson, B.J., 2018. The geochemical and mineralogical diversity of Mercury. In: Mercury, the View After MESSENGER. Cambridge University Press, pp. 176–190.
McCubbin, F.M., Riner, M.A., Vander Kaaden, K.E., Burkemper, L.K., 2012. Is Mercury a volatile-rich planet? Geophys. Res. Lett. 39.
McKeown, D.A., Bell, M.I., Caracas, R., 2010. Theoretical determination of the Raman spectra of single-crystal forsterite (Mg_2SiO_4). Am. Mineral. 95, 980–986.
McMillan, P., Piriou, B., 1983. Raman spectroscopic studies of silicate and related glass structure - a review. Bull. Mineral. 106, 57–75.
Merzbacher, C.I., White, W.B., 1991. The structure of alkaline earth aluminosilicate glasses as determined by vibrational spectroscopy. J. Non-Cr. Sol. 130, 18–34.
Minami, T., Hayashi, T., Tatsumisago, M., 2000. Preparation and characterization of lithium ion-conducting oxysulfide glasses. Solid State Ionics 136–137, 1015–1023.
Moulton, B.J.A., Silva, L.D., Doerenkamp, C., Lozano, H., Zanotto, E.D., Eckert, H., Pizani, P.S., 2021. Speciation and polymerization in a barium silicate glass: Evidence from ^{29}Si NMR and Raman spectroscopies. Chem. Geol. 586, 120611.
Mouser, M.D., Dygert, N., Anzures, B.A., Gramblin, N.L., Hrubiak, R., Kono, Y., et al., 2021. Experimental investigation of Mercury's magma ocean viscosity: Implications for the formation of Mercury's cumulate mantle, its subsequent dynamic evolution, and crustal petrogenesis. J. Geophys. Res.: Planets 126.
Mysen, M.O., Richet, P., 2005. Silicate Glasses and Melts, Properties and Structure, 544 pp., Elsevier, Amsterdam, Netherlands.
Mysen, B.O., Frantz, J.D., 1992. Raman spectroscopy of silicate melts at magmatic temperatures: Na_2O-SiO_2, K_2O-SiO_2 and Li_2O-SiO_2 binary compositions in the temperature range 25–1475°C. Chem. Geol. 96, 321–332.
Mysen, B.O., Frantz, J.D., 1994. Silicate melts at magmatic temperatures: in-situ structure determination to 1651 °C and effect of temperature and bulk composition on the mixing behavior of structural units. Contrib. Mineral. Petrol. 117, 1–14.
Namur, O., Charlier, B., 2017. Silicate mineralogy at the surface of Mercury. Nat. Geosci. 10, 9–13.
Namur, O., Charlier, B., Holtz, F., Cartier, C., McCammon, C., 2016a. Sulfur solubility in reduced mafic silicate melts: implications for the speciation and distribution of sulfur on Mercury. Earth Planet. Sci. Lett. 448, 102–114.
Namur, O., Collinet, M., Charlier, B., Grove, T.L., Holtz, F., McCammon, C., 2016b. Melting processes and mantle sources of lavas on Mercury. Earth Planet. Sci. Lett. 439, 117–128.
Natrup, F.V., Bracht, H., Murugavel, S., Roling, B., 2005. Cation diffusion and ionic conductivity in soda-lime silicate glasses. Phys. Chem. Chem. Phys. 7, 2279–2286.
Neuville, D.R., Mysen, B.O., 1996. Role of aluminium in the silicate network: In situ, high-temperature study of glasses and melts on the join SiO_2-$NaAlO_2$. Geochim. Cosmochim. Acta 60 (10), 1727–1737.
Ni, H., Keppler, H., Manthilake, G., Katsura, T., 2011a. Electrical conductivity of dry and hydrous $NaAlSi_3O_8$ glasses and liquids at high pressures. Contrib. Mineral. Petrol. 162, 501–513.
Ni, H., Keppler, H., Behrens, H., 2011b. Electrical conductivity of hydrous basaltic melts: implications for partial melting in the upper mantle. Contrib. Mineral. Petrol. 162, 637–650.
Nittler, L.R., Starr, R.D., Weider, S.Z., McCoy, T.J., Boynton, W.V., Ebel, D.S., Ernst, C.M., Evans, L.G., Goldsten, J.O., Hamara, D.K., Lawrence, D.J., McNutt, R.L., Schlemm, C. E., Solomon, S.C., Sprague, A.L., 2011. The major-element composition of Mercury's surface from MESSENGER X-ray spectrometry. Science 333, 1847–1850.
Nittler, L.R., Chabot, N.L., Grove, T.L., Peplowski, P.N., 2018. The chemical composition of Mercury. In: Solomon, S.C., Nittler, L.R., Anderson, B.J. (Eds.), Mercury: The View after MESSENGER, vol. 3. Cambridge University Press.
O'Neill, H.St.C., Mavrogenes, J.A., 2002. The sulfide capacity and the sulfur content at sulfide saturation of silicate melts at 1400°C and 1 bar. J. Petrol. 43, 1049–1087.
O'Neill, H.St.C., Mavrogenes, J.A., 2022. The sulfate capacities of silicate melts. Geochim. Cosmochim. Acta 334, 368–382.
Peplowski, P.N., Evans, L.G., Stockstill-Cahill, K.R., Lawrence, D.J., Goldsten, J.O., McCoy, T.J., et al., 2014. Enhanced sodium abundance in Mercury's north polar region revealed by the MESSENGER Gamma-Ray Spectrometer. Icarus 228, 86–95.
Peplowski, P.N., Lawrence, D.J., Feldman, W.C., Goldsten, J.O., Bazell, D., Evans, L.G., Head, J.W., Nittler, L.R., Solomon, S.C., Weider, S.Z., 2015. Geochemical terranes of

Mercury's northern hemisphere as revealed by MESSENGER neutron measurements. Icarus 253, 346–363.
Pommier, A., Gaillard, F., Pichavant, M., Scaillet, B., 2008. Laboratory measurements of electrical conductivities of hydrous and dry Mount Vesuvius melts under pressure. J. Geophys. Res. 113, B05205.
Pommier, A., Evans, R.L., Key, K., Tyburczy, J.A., Mackwell, S., Elsenbeck, J., 2013. Prediction of silicate melt viscosity from electrical conductivity: A model and its geophysical implications. Geophys. Geosyst. Geochem. 14.
Pommier, A., Leinenweber, K., 2018. Electrical cell assembly for reproducible conductivity experiments in the multi-anvil. Am. Mineral. 103, 1298–1305.
Pradel, A., Ribes, M., 2014. Ionic conductivity of chalcogenide glasses. In: Adam, J.-L., Zhang, X. (Eds.), Chapter 7 in Chalcogenide Glasses - Preparation, Properties and Applications. Woodhead Publishing, pp. 16–208.
Ravaine, D., 1980. Glasses as solid electrolytes. J. Non-Cryst. Solids 38–39, 353–358.
Renggli, C.J., Klemme, S., Morlok, A., Berndt, J., Weber, I., Hiesinder, H., King, P.L., 2022. Sulfides and hollows formed on Mercury's surface by reactions with reducing S-rich gases. Earth Planet. Sci. Lett. 593, 117647.
Ribes, M., Ravaine, D., Souquet, J.L., Maurin, M., 1979. Synthèse, structure et conduction ionique de nouveaux verres à base de sulfures. Rev. Chim. Min. 16, 339–348.
Ryan, M.J., Smedley, S.I., 1984. The effect of pressure on fast ion conductivity in glasses. J. Non-Cryst. Sol. 65, 29–37.
Saxena, S., Pommier, A., Tauber, M.J., 2021. Iron sulfides and anomalous electrical resistivity in cratonic environments. J. Geophys. Res.: Solid Earth 126.
Scheinberg, A.L., Soderlund, K.M., Elkins-Tanton, L., 2018. A basal magma ocean dynamo to explain the early lunar magnetic field. Earth Planet. Sci. Lett. 492, 144–151.
Scholz, K., Thomas, B., 1995. Measurements of spin-lattice relaxation times, T_1, in Na_2O-MgO-SiO_2 glasses doped with MnO. Sol. State Nucl. Magn. Res. 4, 309–311.
Shelby, J.E., 2020. Introduction to Glass Science and Technology, 3rd ed., Royal Society of Chemistry, 326 pp.
Souquet, J.L., Perera, W.G., 1990. Thermodynamics applied to ionic transport in glasses. Solid State Ionics 40–41, 595–604.
Souquet, J.L., Duclot, M., Levy, M., 1998. Ionic transport mechanisms in oxide based glasses in the supercooled and glassy states. Solid State Ionics 105, 237–242.
Souquet, J.-L., 2021. Ionic and electronic transport, Chapter 4.2, pp. 453–463. In: Encyclopedia of Glass Science, Technology, History, and Culture, Volume I, First Edition, Ed: Pascal Richet, The American Ceramic Society. John Wiley & Sons, Inc.
Stebbins, J.F., 1987. Identification of multiple structural species in silicate glasses by ^{29}Si NMR. Nature 330, 465–467.
Steele, A., Fries, M.D., Amundsen, H.E.F., Mysen, B.O., Fogel, M.L., Schweizer, M., Boctor, N.Z., 2007. Comprehensive imaging and Raman spectroscopy of carbonate globules from Martian meteorite ALH 84001 and a terrestrial analogue from Svalbard. Meteor. Planet. Sci. 42 (9), 1549–1566.
Steele, A., McCubbin, F.M., Fries, M.D., et al., 2012. A reduced organic carbon component in martian basalts. Science 337 (6091), 212–215.
Tatsumisago, T., Hirai, K., Hirata, T., Takahashi, M., Minami, T., 1996. Structure and properties of lithium ion conducting oxysulfide glasses prepared by rapid quenching. Solid State Ionics 86–88, 487–490.
Tatsumisago, M., Yamashita, H., Hayashi, A., Morimoto, H., Minami, T., 2000. Preparation and structure of amorphous solid electrolytes based on lithium sulfide. J. Non-Cryst. Solids 274, 30–38.
ten Grotenhuis, S.M., Drury, M.R., Spiers, C.J., Peach, C.J., 2005. Melt distribution in olivine rocks based on electrical conductivity measurement. J. Geophys. Res. 110, B12201.
Tenhover, M., Hazle, M.A., Grasselli, R.K., 1983. Atomic structure of SiS_2 and $SiSe_2$ glasses. Phys. Rev. Lett. 51, 404–406.
Terai, R., 1968. Self-diffusion of sodium ions and electrical conductivity in sodium aluminosilicate glasses. J. Ceram. Assoc. Jpn. 76, 189–197.
Tsujimura, T., Xue, X., Kanzaki, M., Walter, M.J., 2004. Sulfur speciation and network structural changes in sodium silicate glasses: Constraints from NMR and Raman spectroscopy. Geochim. Cosmochim. Acta 68 (24), 5081–5101.
Vander Kaaden, K.E., McCubbin, F.M., Nittler, L.R., Peplowski, P.N., Weider, S.Z., Frank, E.A., McCoy, T.J., 2017. Geochemistry, mineralogy, and petrology of boninitic and komatiitic rocks on the mercurian surface: Insights into the mercurian mantle. Icarus 285, 155–168.
Watson, D.E., Martin, S.W., 2017. Short range order characterization of the Na2S + SiS2 glass system using Raman, infrared and 29Si magic angle spinning nuclear magnetic resonance spectroscopies. J. Non-Cryst. Solids 471, 39–50.
Weider, S.Z., Nittler, L.R., Starr, R.D., Crasper-Pregont, E.J., Peplowski, P.N., Denevi, B. W., et al., 2015. Evidence of geochemical terranes on Mercury: the first global mapping of major elements on the surface of the innermost planet. Earth Planet. Sci. Lett. 416, 109–120.
Wilke, M., Klimm, K., Kohn, S.C., 2011. Spectroscopic studies on sulfur speciation in synthetic and natural glasses. Rev. Mineral. Geochem. 73, 41–78.
Zolotov, M.Y., Sprague, A.L., Hauck, S.A., Nittler, L.R., Solomon, S.C., Weider, S.Z., 2013. The redox state, FeO content, and origin of sulfur-rich magmas on Mercury. J. Geophys. Res. Planets 118, 138–146.

Appendix C: Partitioning of Ni and Co between metal and silicate melts: expanding the oxy-barometer to reducing conditions

Partitioning of Ni and Co between metal and silicate melts: expanding the oxy-barometer to reducing conditions

Camille Cartier[1*], Laurie Lladó[1,2], Hadrien Pirotte[2], Laurent Tissandier[1], Olivier Namur[3], Max Collinet[4], Shui-Jiong Wang[5] and Bernard Charlier[2]

* camille.cartier@univ-lorraine.fr
1- Université de Lorraine, CNRS, CRPG, F-54000 Nancy, France
2- Department of Geology, University of Liège, 4000 Sart Tilman, Belgium
3- Department of Earth and Environmental Sciences, KU Leuven, 3001 Heverlee, Belgium
4- Institute of Planetary Research, German Aerospace Center (DLR), 12489 Berlin, Germany
5- State Key Laboratory of Geological Processes and Mineral Resources, China University of Geosciences (Beijing), Beijing 100083, China

Abstract

Moderately siderophile elements (MSE) are potential tracers of the thermodynamic conditions prevailing during core formation because their metal/silicate partition coefficients ($D^{met/sil}$) vary as a function of P, T, and oxygen fugacity (fO_2). Those properties result in the production of planetary mantles with unique MSE depletion signatures. Among the MSE, Ni and Co are reliable magma ocean barometers because their $D^{met/sil}$ are strongly correlated to pressure, decreasing over almost 3 orders of magnitude between 1 bar and 100 GPa. Current pressure-dependent expressions of $D^{met/sil}$ were calibrated on experiments performed under relatively oxidizing conditions, mostly with fO_2 slightly below the IW (Fe-FeO) buffer relevant for the Earth and Mars mantles. However, planets and asteroids formed at a wide range of redox conditions going from the most reduced Mercury (fO_2 ~ IW-5.5) to the most oxidized angrite parent body (IW-1.5 $\leqslant fO_2 \leqslant$ IW+1). In this study we performed and analyzed 38 metal – silicate experiments over a wide range of pressures (1 bar to 26 GPa) and oxygen fugacities (IW-6.4 to IW-1.9) to expand the literature Ni and Co $D^{met/sil}$ database to reducing conditions. We then parameterize 251 Ni and 194 Co $D^{met/sil}$ as a function of T (1573 K to 5700 K), P (1 bar to 100 GPa) and fO_2 (IW-6.4 to IW+0.2). We model the evolution of Ni and Co $D^{met/sil}$ along the liquidus of a chondritic mantle at various P and fO_2 and apply this modelling tool to investigate thermodynamic conditions for various planetary bodies magma ocean. We show that the P and fO_2 obtained for Earth, Mars, Moon and Vesta are consistent with previous studies using similar methods, and P are strongly correlated to planetary sizes. Application of our parametrization to other achondrites Ni-Co data suggest a wide variety of core formation conditions, from the asteroid-sized and oxidized angrite parent body, to the planet-sized and highly reduced aubrite parent body.

Keywords

Magma ocean – planetary differentiation – moderately siderophile elements – core formation – achondrites

1. Introduction

The distribution of elements between the core and the mantle of planets and differentiated asteroids was primarily established by high pressure, high temperature metal–silicate partitioning during core segregation in a magma ocean context (Rubie et al., 2003; Righter, 2015). Moderately siderophile elements (MSE) serve as valuable indicators of the thermodynamic conditions that existed during core formation. This is due to their metal/silicate partition coefficients ($D^{met/sil}$), which vary based on pressure (P), temperature (T), and oxygen fugacity (fO_2). As a result, planetary mantles exhibit distinct depletion patterns of MSE, providing insights into their formation processes. Hence, much efforts have been dedicated to understanding the composition of the bulk silicate Earth and Mars, and constraining the differentiation of these planets was done by investigating metal–silicate reactions between liquid metal and liquid silicates at high P–T (Righter and Drake, 1996; Wade and Wood, 2005; Rubie et al., 2011; Fischer et al., 2015). Among the MSE, nickel (Ni) and cobalt (Co) are excellent and reliable magma ocean barometers because their $D^{met/sil}$ are strongly correlated to pressure, decreasing over almost 3 orders of magnitude between 1 bar and 100 GPa (Righter, 2011; Fischer et al., 2015). Using parameterized Ni and Co $D^{met/sil}$, previous studies found metal-silicate equilibrium pressures in the range of 30-60 GPa for Earth (Li and Agee, 2001; Wade and Wood, 2005; Bouhifd and Jephcoat, 2011; Siebert et al., 2012; Fischer et al., 2015) and 7-17 GPa for Mars (Righter et al., 1998; Righter and Chabot, 2011; Brennan et al., 2020). These pressures, recording metal-silicate equilibrium at mantellic liquidus temperatures, are lower (in the range of 0.25 - 0.95 %) than the pressures at the actual core-mantle boundaries (CMB) as estimated from geophysical measurements (CMB: 136 GPa for Earth, Dehant et al., 2022, and 18-21 GPa for Mars, Rivoldini et al., 2011; Stähler et al., 2021). Whereas the depth of magma oceans may differ significantly from the depth suggested by the apparent equilibration pressures due to fractionation and mixing processes (Rubie et al., 2003), the relatively low pressures compared to the CMB pressures indicate that planetary embryos were not fully molten during the last stages of their accretion (Rubie et al., 2003, 2011; Righter, 2015; Brennan et al., 2020).

Current pressure-dependent expressions of $D^{met/sil}$ were calibrated on experiments performed under relatively oxidizing conditions (Wade and Wood, 2005; Bouhifd and Jephcoat, 2011; Fischer et al., 2015; Righter, 2015), mostly with oxygen fugacities (fO_2) slightly below the IW (Fe-FeO) buffer, corresponding to the redox conditions of the terrestrial and Martian mantle (Righter et al., 2020). Recent experiments conducted at very low fO_2 suggest that Ni and Co $D^{met/sil}$ values are also strongly dependent on fO_2 (Steenstra et al., 2020a, b). However, the Steenstra et al. experiments were conducted at a single pressure (1 GPa). The behavior of Ni and Co at reducing and high pressure conditions remains therefore unknown. Planet and asteroids formed at a wide range of redox conditions going from the most reduced Mercury (fO_2 ~ IW-5.5, Namur et al., 2016; Cartier and

Wood, 2019) to the most oxidized angrite parent body (IW-1.5 $\leqslant fO_2 \leqslant$ IW+1, (Righter et al., 2016; Tissot et al., 2022)). A new parameterization of $D^{met/sil}$ for Co and Ni under reducing conditions and at a range of pressures is thus critically needed.

In this study we performed 38 metal – silicate experiments over a wide range of pressures (1 bar to 26 GPa) and oxygen fugacities (IW-6.4 to IW-1.9) to expand the Ni and Co $D^{met/sil}$ database to reducing conditions. Among the 38 experiments, 25 are published here for the first time while the other 13 have already been used in Cartier et al., 2014a, b and Bouhifd et al., 2015. In order to construct a tool that is fully applicable to most planetary conditions, we compile our new data with the experimental partitioning database of Fischer et al., (2015), to which we added recent studies conducted under highly reducing conditions (see 3.2. Ni and Co metal/silicate partition coefficients). We then parameterize Ni and Co $D^{met/sil}$ as a function of T, P and fO_2 following a formalism identical to that of Fischer et al., 2015. Our new model allows predicting confidently the evolution of Ni and Co $D^{met/sil}$ between 1 bar and 80 GPa, IW to IW-7, and 1550 K to 4450 K. We finally apply our tool to investigate various planetary bodies magma ocean thermodynamic conditions, including Earth, Mars, the Moon and various achondrite parent bodies.

2. Material and methods

Metal-silicate experiments were performed with various starting chondritic compositions using multi-anvil apparatus (MA), piston-cylinder (PC), internally heated pressure vessel (HIPV) and evacuated silica tubes (EST) in various institutes (Table 1). Some of the 5 GPa and 26 GPa experiments have been published in previous studies (Cartier et al., 2014a, b; Bouhifd et al., 2015), but most of them are published for the first time. Details on each method and experiment series are given below.

[Insert Table 1]

2.1.Multi-anvil experiments

Experiments were performed at 5 GPa and 26 GPa with multi-anvil presses at the Laboratoire Magmas et Volcans (LMV), Clermont-Ferrand, France. The starting compositions consisted in a natural enstatite chondrite (Hvittis, EL6, composition given by (Rubin, 1983), Table S1) powder, except the experiment 1198 for which a natural tholeiitic basalt powder was used, to which were added various amounts of Si metal (0 – 50 wt%) to reduce the instrinsic fO_2 (Table S2). Experiments

at 26 GPa were performed using a 1500 T multi-anvil press, and the 5 GPa experiments were performed using a 1000 T press. Pressure calibrations were similar to those described previously for the 1000 T press by (Hammouda, 2003) and for the 1500 T press by (Boujibar et al., 2014). The pressure assembly consisted of Cr-doped MgO octahedron of 18 or 14 or 10mm edge length for 5 GPa experiments and of 10mm edge length for 26 GPa experiments, compressed between pyrophyllite gaskets by 32 mm tungsten carbide anvils with truncation edge lengths of 11, 8 and 4 mm, respectively. The sample were contained in graphite capsules that transformed to diamond in 26 GPa experiments, except experiment #1188 that was run in a MgO capsule. The assembled octahedra were dried in an oven at 500 K overnight before each experiment. The samples were first compressed to the desired pressure at room temperature, with an uncertainty of ~0.5 GPa, and then heated to the target temperature and kept isothermal for durations of 20 min to 4h (Table 1). These durations are sufficient to achieve equilibrium between silicate and metallic liquids in these pressure-temperature conditions (Li and Agee, 2001; Bouhifd and Jephcoat, 2011). A $LaCrO_3$ heater insulated by ZrO_2 sleeves provided high temperatures. Temperature was monitored using $W_5Re_{95}/W_{26}Re_{74}$ type C thermocouples, with no correction for pressure effect on the electromotive force (e.m.f.), which yields an uncertainty of ± 100K. In case thermocouple was lost, temperature was determined using power/temperature relation determined in previous experiments. Samples were quenched at a rate of approximately 800 K/s own to the glass transition temperature by shutting off the power.

2.2. Piston-cylinder experiments

Experiments at 1.3, 2 and 3 GPa were performed with a piston-cylinder (PC). The starting material was a synthetic powder representative of the silicate portion of enstatite chondrites (Lodders and Fegley, 1998; Berthet et al., 2009) made off of high purity oxides (TiO_2, Al_2O_3, Cr_2O_3, MnO, MgO, $CaSiO_3$, Na_2SiO_3, $K_2Si_{14}O_9$, $AlPO_4$) to which different amounts of Fe and/or Si and/or FeS and/or CaS were added (Table S3, S4), resulting in low intrinsic fO_2s (Table 1). The powder was doped with 500 ppm Ni and 500 ppm Co. The 1.3 and 2 GPa experiments were conducted at the University of Liège (Belgium). The cells were made of barium carbonate, and the samples were contained in graphite capsules. The cells were pressurized at room temperature up to 0.75 GPa, and heated to 865°C. The pressure was then increased to the target pressure after a 5 minutes dwell. After final pressure was reached, heating resumed up to target temperature (1500 – 1700°C). We used D-type thermocouples (W_3-Re/W-Re_{25}) to monitor temperature. The difference between the measured temperature and the sample temperature was estimated to be around 20°C. The sample were left at target temperature for 45 minutes to 3 hours, depending on the temperature (Table 1). Quenching was done by shutting off the electrical current. The 3 GPa experiments were performed at the

Bayerisches Geoinstitut (BGI, University of Bayreuth) using a talc-Pyrex pressure cell, and a graphite capsule with an outer platinum capsule. The protocol was similar than the one used in Liège, with a target temperature of 1700°C.

2.3. Internally heated pressure vessel experiments

Experiments at 0.1 GPa were performed using internally heated pressure vessels (IHPV) at the University of Hannover (Germany) with the same starting powders as for PC experiments (section 2.2, Table S5). The apparatus and the protocol used is detailed in Berndt et al., (2002) and Namur et al. (2016) respectively. We used graphite capsule surrounded by a platinum jacket. Thin (0.1mm) Pt wire was used to place the sample in the hotspot of the furnace. Pressure was increased to 0.1 GPa using argon as the pressure medium before heating. Two S-type ($Pt/Pt\text{-}Rh_{10}$) thermocouples were used to control the heating at the top and bottom of the cell. Two other S-type thermocouples were used to monitor the sample temperature. The experiments were run for 3h between 1520 and 1600°C (Table 1). The quenching was done by applying a current to the Pt wire, which caused the sample to fall onto a water-cooled copper plate at room temperature at the bottom of the sample holder.

2.4. Evacuated silica tubes experiments

Evacuated silica tube (EST) experiments were performed at Centre de Recherches Pétrographiques et Géochimiques (CRPG), Nancy, France. The starting compositions consisted in two natural chondrite powders, the carbonaceous chondrite NWA 11345 (CM2) and the ordinary chondrite Tamdakht (H5). The bulk chemical composition of these powders were measured at SARM (CRPG, Nancy) for major and trace elements using the procedure involving alkali fusion, ICP-MS and LC-ICP-MS described by (Carignan et al., 2001) (Table S6). The experimental charge was composed of a sealed silica tube of 1.5 to 3 cm^3 and a graphite crucible containing the chondritic powder. Before the experiments, the silica tubes, sealed on one side, were evacuated under vacuum at a pressure of 10^{-2} mbar at 120°C during 24h. After sealing the other side of the tubes, the silica tubes were introduced in a muffle furnace at target temperature (1300 – 1400°C). Experiment duration was between 5 and 48 hours, depending to the temperature. During experiment, the oxygen carried by the sample reacted with the carbon of the capsule to produce carbon monoxide gas, theoretically buffering the fO_2 at C-CO, i.e. fO_2 = IW-5.8 at 1300°C to fO_2 = IW-6.4 at 1400°C (fO_2 calculated with NIST-JANAF thermodynamic tables, see Supplementary Materials for details). The experiments were quenched by taking the tube out of the furnace.

2.5. Imaging with SEM and major and minor element analyses with EPMA

After quench, all experiments were mounted in epoxy and polished for chemical analyses. Back-scattered electron (BSE) images and energy-dispersive X-ray spectroscopy (EDS) chemical maps were acquired with the scanning electron microscope (SEM) at CRPG Nancy. Major and minor elements contents in the metal and silicate phases of 26 GPa, 5 GPa, and EST experiments were analyzed with a CAMECA SX100 electron microprobe at Laboratoire Magma et Volcans (LMV), Clermont-Ferrand, France, using an accelerating voltage of 15 kV (Table 2). Silicate glasses were measured using a 4 nA beam current, whereas 15 nA were applied for metal and sulfides. The beam was defocused to 5–20 µm. Oxygen concentrations of most glasses were measured with the electron microprobe using a PC1 crystal with counting time of 15 s on peak. Otherwise, when not measured, oxygen was estimated according to oxide stoichiometry. The standards were natural minerals and synthetic oxides for silicates (Si, Ca: wollastonite; Mg: Forsterite; Al: Al_2O_3; Fe: Fayalite; Na: Albite; K: Orthoclase; Ti, Mn: $MnTiO_3$; Cr: Cr_2O_3; Ni: NiO), pyrite for sulfur, pure metals (Fe, Mn, Si, Ni, Cr) for metallic alloys, and andradite ($Ca_3Fe_2Si_3O_{12}$) for oxygen. The PC and IHPV experiments were imaged with a SEM at the University of Aachen (Germany). We used the JEOL JXA-8530F electron probe micro-analyzer of the University of Münster (Germany) to measure major and minor elements with a 15kV accelerating voltage and a 10nA beam current. On-peak and background analysis times were 15 (10 for Na, Ni and K) and 5 respectively for the silicate glass, and 20 and 10 seconds for metals and sulfides respectively. The standards were all minerals (expect for Cr) for silicate melt measurements (Na: Jadeite; Mg: Olivine; Al: Disthene; Si: Hypersthene; Ni: Pentlandite; P: Apatite; K: Sanidine; Ca: Diospide; S: Pyrite; Ti: Rutile; Cr: Cr_2O_3; Mn: Rhodonite; Fe: Fayalite). For metals and sulfides, we used standards from minerals and metals (Mg: Olivine; P: Apatite; Ca: Diopside; S: Pyrite; Si; Ti; Cr; Fe; Mn; Ni).

2.6. Ni and Co analyzes with LA ICP-MS

Ni and Co concentrations in silicate melts, metals and sulfides when present were determined by laser ablation induced coupled plasma-mass spectrometry (LA ICP-MS). For the 5 GPa experiments and EST experiments we used an Agilent 7500-cs ICP-MS coupled with a Resonetics M-50 laser at LMV Clermont-Ferrand. The laser was operated at 193 nm wavelength with 6 mJ energy, and 2 Hz pulse frequency. Laser spot size was 15–50 µm for silicate melts, 15–50 for metals and 6 – 33 µm for sulfides. Ablation duration was usually about 80 s and was done in a pure He atmosphere. The analyte was carried to the ICP torch by a gas mixture wherein N_2 + Ar were added to He. We used the following gas flows: He, 750 ml/min; N_2, 4 ml/min; Ar nebulizer gas, 0.88 l/min; Ar cool gas, 15 l/min; Ar auxiliary gas, 1 L/min. Plasma power was 1350 W. For the 26 GPa, the PC and the IHPV experiments, we used an ICP-QQQ 3900 Agilent induced coupled plasma-mass

spectrometer (ICP-MS) coupled with a Teledyne 193 nm Cetac laser with a HelEx II cell at the Department of Earth and Environmental Sciences, KU Leuven. The laser was operated at 193 nm wavelength with 6 mJ energy, and 2 Hz pulse frequency. Laser spot size was 20 – 60 µm for silicate melts, metals and sulfides. Ablation duration was usually about 80s and was done in a pure He atmosphere. The analyte was carried to the ICP torch by a gas mixture wherein Ar was added to He. We used the following gas flows: He, 600 ml/min; Ar nebulizer gas, 1.39 l/min; Ar cool gas, 15 l/min; Ar auxiliary gas, 1 L/min. Plasma power was 1550 W. NIST 610 glass standard (values from (Gagnon et al., 2008) was used for signal calibration, using Si concentrations for silicate melts and Fe concentrations for metal and sulfides. NIST 612 and BCR glasses were used as checks for accuracy. Our measurements are in good agreement with (Gagnon et al., 2008) values, the deviation being always less than 20%. Detection limits (as determined from counting statistic on the samples) were ≥ 0.5 ppm.

2.7. Oxygen fugacity calculation

Sample intrinsic fO_2 values were determined using the composition of co-existing metallic alloy and silicate melt. fO_2 in log units relative to the iron-wüstite (IW) buffer is defined as:

[1] $$\Delta IW = 2\log_{10}\frac{a_{FeO}^{sil}}{a_{Fe}^{met}}$$

Where a_{FeO}^{sil} is the activity of FeO in the silicate melt and a_{Fe}^{met} is the activity of Fe in the metal. a_{FeO}^{sil} and a_{Fe}^{met} were approximated here as their mole fractions, whatever the conditions. Hence, the calculated fO_2s range from IW-1.9 to IW-6.4. Incorporating activities for Fe and FeO that differ from unity based on a thermodynamic model (Holzheid et al., 1997; Wade and Wood, 2005) results in a calculated fO_2 that is higher by ~ 0.5 log units, in agreement with previous studies. However this method was not applied since activity coefficients of FeO are not known in highly reduced systems nor high pressures (Righter and Ghiorso, 2012). The EST experiments were theoretically buffered at C-CO at 1300°C, 1350°C and 1400°C, which fO_2 is IW-5.8, IW-6.1 and IW-6.4 respectively (fO_2 calculated with NIST-JANAF thermodynamic tables, SM). The fO_2s determined with eq. [1] in these experiments lie between IW-5.3 and IW-5.6 (Table 1). We therefore consider an error of +/- 1 log unit on the fO_2s values calculated with eq. 1. Despite the significant error on absolute fO_2 values, calculating fO_2s s with the same method for all experiments permits to built an internally consistent database and allows to investigating the influence of fO_2s on element partitioning, as well as to investigating the fO_2s of planetary materials. Hence, in the following, we recalculate the fO_2 of all the compiled experiments using the same method.

3. Results

3.1. Compositions of the experiments

Each experiment contains at least a silicate melt and a metal phase, but most of them contain additional phases (sulfide, enstatite, forsterite, quartz, coesite, stishovite, majorite, bridgmanite) depending on the starting composition and the P, T conditions (Table 1). Typical samples obtained at various pressures are presented in Fig. 1.

[Insert Fig. 1]

All experiments contain a single or few metal beads surrounded by silicate melt (Fig. 1). When present, sulfide coats the metal beads (Fig. 1b,c). Silicate crystals display euhedral textures. Together with the homogeneity of chemical composition of the various phases through a sample, these textures attest attainment of chemical equilibrium. All silicate melts were quenched to glass except in the 26 GPa experiments in which dendritic crystals formed (Fig. 1a).

[Insert Table 2]

Silicate melts are roughly chondritic in composition, with NBO/T ranging from 0.7 to 2.5 and FeO content ranging from 0.03 to 12.9 wt%, corresponding to fO_2 going from IW-6.4 to IW-1.9 (Table 1, 2). They contain 0 – 12.5 wt% sulfur, strongly depending on their temperature and fO_2 (i.e. the more reduced and hot they are, the more sulfur they contain, Namur et al., 2016, Fig. 2). Metallic melts are dominated by Fe, alloyed with 0 – 42.6 wt% Si, also strongly depending on temperature and fO_2 (Kilburn and Wood, 1997, Fig. 2). Due to a large miscibility gap in Fe–S–Si systems at P $\leq$ 5 GPa (Morard and Katsura, 2010), most experiments conducted in this pressure range contained enough S to make two alloys, the 'metallic melt' described before and an FeS-dominated melt that we will call 'sulfide' in the following (Fig. 1b). Hence, experiments performed at P $\leq$ 5 GPa have metals with 0.01 to 5.75 wt% S, with the highest S contents corresponding to the most oxidizing experiments that contain negligible Si in the metal (Fig. 2). At 26 GPa, there is no immiscibility in the Fe-Si-S system (Morard and Katsura, 2010). Our experiments at 26 GPa therefore contain a single metallic phase dominated by Fe and containing 0.01 – 23.07 wt% Si and 6.65 – 36.02 wt% S, the composition strongly depending on temperature and fO_2 (Fig. 2). Few 26 GPa experiments

were contaminated by La and Cr coming from the $LaCrO_3$ furnace diffusing at high P-T conditions (Table 2), hence some metals contain a high amount of Cr (up to 27.04 wt% Cr in the metal phase of sample #143), and some silicate melts contain high La concentrations (up to 4.28 wt% La in the silicate melt of sample #143). The contaminated experiments are however fully equilibrated and show similar results for Ni and Co partitioning than non-contaminated experiments conducted under similar conditions. The sulfides, present in most ≤ 5 GPa experiments, are dominated by an FeS component, except for the most reduced experiments which contain up to 22.4 wt% Mg, 14.3 wt% Cr, 5.9 wt% Mn, 2.7 wt% Ca and 2.0 wt% Ti as these elements abundances are strongly anticorrelated to fO_2 (Fig. S1).

[Insert Fig. 2]

3.2. Ni and Co metal/silicate partition coefficients

Using our experiments we calculated Ni and Co metal/silicate partition coefficients as D(Ni) = (Ni wt% metal)/(Ni wt% silicate melt) and D(Co) = (Co wt% metal)/(Co wt% silicate melt). We compilated this data with literature data (Thibault and Walters, 1995; Hillgren et al., 1996; Jana and Walker, 1997; Righter et al., 1997, 2010; Gaetani and Grove, 1997; Gessmann and Rubie, 1998; Wade and Wood, 2001, 2005; Bouhifd and Jephcoat, 2003, 2011; Asahara et al., 2004; Chabot et al., 2005; Kegler, 2008; Corgne et al., 2008; Mann et al., 2009; Wood et al., 2009; Siebert et al., 2011, 2012, 2013; Bouhifd et al., 2013; Cartier et al., 2014a, b; Righter, 2015; Fischer et al., 2015; Steenstra et al., 2020b, a) to build a database of 315 experiments corresponding to 251 D(Ni) and 194 D(Co), and covering a wide range of pressure (1 bar ≤ P ≤ 100 GPa), oxygen fugacity (IW-6.4 ≤ log fO_2 ≤ IW+0.2) and temperature (1573 K ≤ T ≤ 5700 K) (Fig. 3, Table S7), and for which fO_2 and Ni and Co partition coefficients were calculated with the same method as for our experiments.

[Insert Fig. 3]

3.3. Ni and Co metal/silicate partition coefficients parameterization

As previously observed, D(Ni) and D(Co) are strongly correlated to oxygen fugacity (fO_2), pressure (P) and temperature (T) (Fig. 3). In agreement with (Fischer et al., 2015) but contrary to (Righter,

2015) we find that D(Ni) and D(Co) are not significantly affected by silicate melt and metal compositions. We explored the influence of silicate melt composition using NBO/T (NBO: number of non-bridging oxygens, T: tetrahedrally coordinated network former cations (Mysen, 1983); NBO/T expressing the degree of polymerization in silicate melts, Table 1, Table S7) but found no statistically significant correlation (pValue = 0.2 for Ni and pValue = 0.05 for Co), in agreement with the results of (Fischer et al., 2015). We also investigated the influence of metal composition and in particular the role of S which in our database ranges from X = 0 to X = 0.52 (Table 1). Contrary to (Righter, 2015), we found the correlation between the partition coefficients and XS to be statistically not significant (pValue = 0.2 for Ni and pValue = 0.2 for Co). We therefore parameterized the experimental D(Ni) and D(Co) as a function of pressure, temperature and oxygen fugacity following similar formalism as (Fischer et al., 2015) using equation [1].

[1] $\ln(D) = a + b*IW + c*1/T + d*P/T$

The fitting parameters are given in Table 3. The fits are good with R^2 values of 0.875 for Ni and 0.864 for Co (Fig. S2). D(Ni) is found to be more strongly dependent on pressure and temperature than D(Co), and D(Ni) and D(Co) are found to have a similar fO_2 dependence (Table 3), all as previously reported by Righter (2015) and Fischer et al. (2015).

[Insert Table 3]

Our results are very similar to those of (Fischer et al., 2015) for Ni and Co concerning the effect of pressure; Righter (2015) found a more pronounced P effect on D(Ni) (Fig. 4). We find a fO_2 weaker effect on D(Ni) than that of Fischer et al. (2015), but slightly more pronounced than that of Righter (2015). Similarly we find a fO_2 effect on D(Co) slightly less important than that of Fischer et al. (2015), but more pronounced than that of Righter (2015).

[Insert Fig. 4]

3.4. Ni and Co sulfide/silicate partition coefficients

Using our sulfide saturated experiments we calculated Ni and Co sulfide/silicate partition coefficients as D(Ni) = (Ni wt% sulfide/(Ni wt% silicate melt) and D(Co) = (Co wt% sulfide)/(Co wt% silicate melt) (Table 2). Together with the experiments of (Steenstra et al., 2020b), our results

show that Ni and Co sulfide/silicate partition coefficients follow the same P, T and fO_2 dependency as the metal/silicate partition coefficients, but D values are roughly 10 and 5 times lower for Ni and Co respectively (Fig. S3).

4. Discussion

4.1. Modeling Ni and Co $D^{met/sil}$ along the liquidus of a chondritic mantle

Using our parameterization, we model Ni and Co $D^{met/sil}$ along the liquidus of a chondritic mantle (Herzberg and Zhang, 1996; Andrault et al., 2011) (Fig. S4) at various P and fO_2, covering the range of 1 bar – 80 GPa and IW – IW-7. The fO_2 and P dependency of D(Ni) and D(Co) displayed by experimental data is very well reproduced by our model (Fig. S5). We then plot these models in a D(Ni) vs D(Co) space for the P and fO_2 ranges mentioned above (Fig. 5). By making the hypothesis that in planetary bodies, metal-silicate equilibrium takes place in magma oceans at liquidus temperatures, plotting bulk core / bulk silicate Ni and Co partition coefficients in this P-fO_2 space gives insights into the pressure and redox conditions at which the body differentiated. Fortunately, as developed in the following section, the hypothesis of liquidus temperatures during core/mantle differentiation has very limited impact on the pressures and fO_2s retrieved by our model. Finally, as our model integrates S-bearing systems, any terrestrial body can be investigated, including those that are likely to have a sulfide component in their core, in addition to the metallic component (e.g. Mercury, (Cartier et al., 2020; Pirotte et al., 2023)) because their differentiation occurred at low pressure enough for Fe(Si) and FeS melts to be immiscible (Morard and Katsura, 2010). Indeed, the formation of such a sulfide phase during core formation would have negligible effect on the primitive mantle Ni and Co contents compared to the metal phase, because Ni and Co sulfide/silicate partition coefficients are, in every P-fO_2 conditions covered by our model, 5-10 times lower than metal/silicate partition coefficients (see 3.4).

[Insert Fig. 5]

4.2. Application to Earth, Mars, the Moon and Vesta

Earth and Mars (SNC meteorites parent body) have very well constrained bulk silicate and well constrained bulk core compositions (Dreibus and Wänke, 1980; McDonough and Sun, 1995;

Lodders and Fegley, 1998; Taylor, 2013; Palme and O'Neill, 2014). The Moon (lunar meteorites parent body) and Vesta (HED meteorites parent body) have much less constrained compositions, but a variety of models exist for their silicate portion and core (Dreibus and Wänke, 1980; Delano, 1986; Steenstra, 2016). Table 4 presents selected values of Ni and Co contents of the bulk silicates and the bulk cores of these four terrestrial bodies, and corresponding calculated bulk core / bulk silicate Ni and Co partition coefficients.

[Insert Table 4]

The bulk silicate Earth, Mars, Moon, and Vesta have been estimated in previous studies (Table 4) following a cosmochemical formalism that we develop here, and will apply to achondrite parent bodies in the following section. Fig. 6 shows a compilation of bulk rock Ni and Co analyses of rocks and meteorites originating from Earth, Mars, the Moon and Vesta, plotted as a function of Mg/Al, and compared with the bulk silicate values selected in Table 4. Planetary differentiation is the result of early and long-term processes: the formation of a metal core during a magma ocean stage, the crystallization of the silicate portion able to generate a primitive crust, and later melting of the mantle producing a secondary crust. All the rocks making up the silicate fraction of a planet, from the most primitive mantle rocks to the most evolved crustal rocks, are therefore linked to their parent reservoir (i.e. the bulk silicate planet), by a combination of crystallization, melting, mechanical sorting and mixing processes (Palme and O'Neill, 2014). The composition of terrestrial igneous, mantellic and crustal rocks (GEOROC database), when plotted as a function of Mg/Al, reveal continuous trends whose shape indicates, for each element, what are the main phases controlling its fractionation during magmatic processes (Palme and O'Neill, 2014) (Fig. 5). Making the assumption that the bulk silicate Earth has refractory lithophile elements (RLE) in chondritic ratios (e.g. a Mg/Al ratio of 8-13 (Lodders and Fegley, 1998; Palme and O'Neill, 2014), the intersection of the trends with the chondritic RLE range gives the composition of the bulk silicate Earth (Fig. 5) (McDonough and Sun, 1995; Palme and O'Neill, 2014). Using a similar approach, the bulk silicate compositions of any other terrestrial body for which we have enough data can theoretically be calculated. Silicate rocks from Mars, as sampled by SNC meteorites (MetBase database) and surface rocks (Yen et al., 2006), the Moon, as sampled by surface rocks and regolith (Lunar Sample Compendium database, (Lodders and Fegley, 1998) and lunar meteorites (MetBase database), and Vesta, as sampled by HED meteorites (MetBase database), align along continuous trends (although the data is particularly scattered for Vesta, and Moon Ni, due to regolith contamination by late accretion of chondritic material (Wang et al., 2023)) for their bulk Ni and Co contents (Fig. 5). The

intersection between these trends and a chondritic Mg/Al therefore matches their bulk silicate compositions (Fig. 5). Each of these bulk silicate Ni and Co are strongly subchondritic indicating siderophile element depletion during core formation, as both element are not volatile, so not affected by devolatilization processes (Lodders, 2003). This method will therefore be used to estimate the Ni and Co contents of the silicate portion of less constrained planetary bodies in the following section.

[Insert Fig. 6]

We then plot planetary D(Ni) and D(Co) for Earth, Mars, the Moon and Vesta (Table 4) in the modeled P-fO_2 space to investigate these objects magma ocean thermodynamic conditions (Fig. 5). Ni and Co partitioning between the cores and bulk silicate planets indicates IW-2.1 and 46 GPa for the Earth, IW-1.3 and 6 GPa for Mars, IW-1.2 and 1 GPa for the Moon, and IW- 2.2 and <1 bar for Vesta (Table 5). We tested the influence of the assumption of liquidus temperature on the results. We hence calculate two adiabats, one hotter than liquidus (+160° at 1 bar, +249° at 80 GPa) and one colder than liquidus, corresponding to the 50% melting curve (-160° at 1 bar, -249° at 80 GPa) (Fig. S4), which we input in our model to compare with the results obtained using the liquidus (Fig. S6). The maximum difference between the three models is 2 GPa for pressure and 0.1 log unit for fO_2, extremely much lower than the error bar induced by the uncertainties of planetary D(Ni) and D(Co) (Fig. S6, Table S8). We therefore conclude that modeling D(Ni) and D(Co) along a peridotitic/chondritic liquidus is adequate, even if the planetary bodies had a hotter or cooler adiabat than the Earth or Mars.

[Insert Table 5]

The results for Earth and Mars are in excellent agreement with both the fO_2 and pressure conditions estimated for core formation in these planets using MSE (including Ni and Co) abundances in their silicate portion (Righter and Drake, 1997; Wade and Wood, 2005; Wood et al., 2009; Righter and Chabot, 2011; Rubie et al., 2011; Mandler and Elkins-Tanton, 2013; Fischer et al., 2015; Righter, 2015), as well as fO_2 estimations based on independent methods (e.g. XANES (Righter et al., 2016)). Concerning the Moon, (Righter and Drake, 1996) estimated a pressure of 3.5 GPa and (Steenstra et al., 2016) recently estimated a pressure of 4-5 GPa, also based on MSE abundances in the lunar mantle. Our results indicate a lower pressure, but are identical to those of (Righter and

Drake, 1996) and (Steenstra et al., 2016), within the error bars. The fO_2 we find for the Moon matches the fO_2 found in these studies and fO_2 measured in lunar rocks (Righter et al., 2016). Finally, (Righter and Drake, 1996) estimated a pressure ≤ 1 bar and a fO_2 of IW-2.2 for Vesta, the HED parent body; our results are identical. The Ni-Co P obtained for Earth corresponds to 34% of its CMB pressure (135 GPa). Similarly, Ni-Co P obtained for Mars is 24% of its CMB (24 GPa). Surprisingly, because the Moon did not form as Earth and Mars by accretion of chondritic-like material, the Ni-Co P obtained for it is 20% of the CMB (4.5 GPa, (Briaud et al., 2023) very similar to the Moon and Mars. Finally, the Ni-Co P of Vesta (< 1 bar) is significantly lower than the CMB pressure estimated for Vesta (1000-2000 bars, (Lenhart and Secco, 2022)). This is equivalent to a correlation between Ni-Co pressures and parent body sizes, as shown in Fig. 7. Plotting Vesta and Moon with Earth and Mars data produce an excellent polynomial curve, attesting of the robustness of the method. This gives us the opportunity to unravel the thermodynamic conditions of any other terrestrial bodies, on condition of being able to estimate bulk bodies Ni and Co partition coefficients. Alternatively, our model can be used in any object containing silicate melt and metal at equilibrium, such as chondrules (van Kooten et al., 2022) or individual achondrites (Ray et al., 2019), by measuring in-situ Ni and Co partition coefficients.

[Insert Fig. 7]

4.3.Application to other achondrite parent bodies

Angrites, aubrites, the paired ungrouped achondrites NWA 7325, NWA 8486 and NWA 8409, the paired ungrouped achondrites NWA 011 and NWA 2976, and the ungrouped achondrite Erg Chech 002 form five groups of achondrites, each deriving from one or multiple parent bodies which properties, in particular the size, are controversial or unknown (Yamaguchi et al., 2002, 2021; Isa et al., 2008; Irving et al., 2013; Mittlefehldt, 2014; Barrat et al., 2015, 2021; Weber et al., 2015; Frossard et al., 2019; Nicklas et al., 2022). The five achondrite families are considered to be of asteroidal origin, some of them having shown to share spectral properties with specific asteroid families (Mittlefehldt, 2014; DeMeo et al., 2022). However, even if the parenthood is proven, like it is the case for aubrites with E-type asteroids (Gaffey et al., 1992; Fornasier et al., 2008), this does not say much about the size of the original parent body as most of asteroids are rubble piles, reassembled pieces of precursor parent bodies (Delbo et al., 2017). All these meteorites are unambiguously differentiated achondrites, i.e. crystallized from a melt in the silicate portion of their

parent body after core formation (Mittlefehldt, 2014). Homogeneous oxygen isotopic compositions of ($\Delta^{17}O$) of angrites on one side and of aubrites on the other, indicate that the angrite parent body (APB) and the aubrite parent body (AuPB) underwent large scale melting, possibly corresponding to a magma ocean stage (Greenwood et al., 2005). Furthermore, setting aside samples that show clear evidence of chondritic contamination (due to late accretion and/or exogeneous contamination in the regolith (Wang et al., 2023)), all these achondrites are depleted in siderophile and chalchophile elements compared to chondrites and these depletions are homogeneous for each parent body, even if the data is more scatter for aubrites, as discussed in the following (Fig. 8). Efficient core formation in the parent bodies of angrites, aubrites and NWA 7325/8486/8409 is further supported by several arguments, such as the Ni isotopic composition of these meteorites (Wang et al., 2023) and the presence of melt inclusions in their minerals (Mittlefehldt, 2014). Moreover, the siderophile element depletions in these achondrites are mostly correlated to the degree of siderophility/chalcophility of each element, indicating that the parent bodies experienced core formation via metal/silicate or sulfide/silicate equilibrium (Lodders et al., 1993; Mittlefehldt, 2014; Goodrich et al., 2017). This theoretically allows us to use the Ni and Co subchondritic contents to model the achondrite parent bodies core/mantle partition coefficients and probe the P – fO_2 conditions of their differentiation, whether total or partial, on condition that core formation was complete and that no relict chondritic metal/sulfide was left over in the primitive mantles.

[Insert Fig. 8]

In achondrites, most of Ni and Co budgets is carried by metal and/or sulfide phases, present, in average, in trace amounts in angrites, NWA 7325/ 8486/8709, NWA 011/2976, Erg Chech 002, and account for 0.2 vol.% of the aubrites on average (Keil, 2010; Mittlefehldt, 2014; Goodrich et al., 2017). In the angrite and aubrite families, some sample have wt% abundances of metal phases, producing outliers anomalously enriched in Ni and Co (Fig. 8). Most of these samples contain identified exogeneous particles, chondritic material or more rarely iron meteorite components (Keil, 2012; Ray et al., 2018; Zhu et al., 2022)). In a similar way, some metal-rich aubrite samples have been proposed to contain metal particles originating from the core of the AuPB, mixed with the silicate during its catastrophic disruption (Van Acken et al., 2012). Except those outliers, each of these five achondrite families display rather homogeneous Ni and Co contents despite important scatter for aubrites (Fig. 8). This scatter might be related to late addition contamination that would artificially increase the Ni and Co contents of some samples (Wang et al., 2023). In a similar way,

505 some samples could contain relict metal trapped in the silicate portion of the parent body during
506 magma ocean crystallization, as it has been proposed (but nevertheless debated (Cartier et al.,
507 2022)) for the origin of metal in aubrites (Casanova et al., 1993). Such processes would randomly
508 affect samples and artificially increase the average bulk Ni and Co contents. However, the effect of
509 this contamination is order of magnitude below the depletions of the achondrites in Ni and Co
510 compared to chondrites. Here, we therefore make the hypothesis that excluding the Ni-Co-rich
511 outliers, and as for lunar, SNC and HED meteorites which also contain trace metal/sulfides (Dreibus
512 and Wänke, 1980; Paquet et al., 2021; Wang et al., 2023), those Ni and Co abundances are
513 representative of the bulk silicate portion (Fig. 5, 8). This implies that the origin of the metal and/or
514 sulfide phases is mostly magmatic, i.e. they formed by exsolution processes from magmas and/or
515 subsolidus processes, as proposed for sulfides and/or metal in aubrites, SNC meteorites and angrites
516 (Mccoy, 1998; Fogel, 2005; Jambon et al., 2011; Paquet et al., 2021). In this scheme, the significant
517 scatter of aubrite data could simply result from heterogeneous sampling of various lithologies,
518 containing various amounts of magmatic metal/sulfides, by the achondrites. This argument is
519 consistent with the fact that aubrites are coarse-grained almost monomineralic lithologies, making
520 the sampling for bulk analyses random (Keil, 2010). In this scenario, the median Ni and Co contents
521 of bulk achondrites would be representative of the bulk silicate (Fig. 8).

522

523 [Insert Table 6]

524

525 In order to apply our model, we therefore relied on the hypothesis described above to estimate the
526 bulk silicate achondrite parent bodies. As in the five achondrite families Ni and Co abundances are
527 not correlated with Mg/Al (meaning Ni and Co are not significantly fractionated during magmatic
528 processes, (Fig. 8, (Palme and O'Neill, 2014)), we use the median contents (excluding the outliers)
529 and median absolute deviation to define the bulk silicate compositions and associate error (Table 6,
530 Fig. 8). We then estimate the APB, AuPB, NWA 7325/ 8486/8409 PB, NWA 011/2976 PB and Erg
531 Chech 002 PB Ni and Co core contents by mass balance (Table 6). We chose a bulk composition
532 of CV (1.32 wt.% Ni, 640 ppm Co) for the APB, of EH (1.84 wt.% Ni, 870 ppm Co) for the AuPB
533 and the NWA 7325/ 8486/8409 PB, of CR (1.38 wt.% Ni, 644 ppm Co) for the NWA 011/2976 PB,
534 and of LL (1.06 wt.% Ni, 480 ppm Co) for the Erg Chech 002 PB, as these chondrites are supposed
535 to be similar to the primitive building blocks of the five achondrite parent bodies respectively
536 (Lodders et al., 1993; Yamaguchi et al., 2002; Jambon et al., 2011; Barrat et al., 2015, 2021;
537 Goodrich et al., 2017; Steenstra et al., 2017; Nicklas et al., 2022; Tissot et al., 2022). When then
538 hypothesize that the cores are in the range of 20 to 35 wt.% of the bulk planet, to bracket the cases

539 of Earth (core ~ 33 wt.%), Mars (core ~ 24 wt.%) and Vesta (core ~ 22 wt.%, (Dreibus et al., 1997)).
540 This unconstrained hypothesis produces large error bars. We finally calculate the bulk core / bulk
541 silicate partitions coefficients, with associated errors (Table 6), that we plot on the P – fO_2 model
542 grid (Fig. 9). The P and fO_2 results for each achondrite parent body are shown in Table 7, and
543 discussed in the following.

544

545 [Insert Fig. 9]

546

547 The model (Fig. 9) indicates < 1 bar / IW-1.4 for the APB, 28 GPa / IW-4.9 for the AuPB, < 1 bar
548 / IW-1.7 for the Erg Chech 002 PB, <1 bar / IW-2.1 for the NWA 7325/8486/8409 PB, and 4 GPa
549 / IW-1.4 for the NWA 011/2976 PB (Table 7). As temperature during core formation on achondrite
550 parent bodies is not well constrained, we also ran our model using the two additional adiabats hotter
551 and colder than liquidus used in the previous section (Fig. S4). The resulting fO_2 and P are very
552 similar than doing the model with liquidus temperature, and identical within the error bars (Fig. S7).
553 The error bars on the P and fO_2 retrieved from modeling are very large (Fig. 9, Table 7), but
554 nevertheless allow us to discuss some implications of these results.

555

556 [Insert Table 7]

557

558 The intrinsic fO_2 of a bulk planetary body is difficult to assess, particularly for large and
559 geologically active planets such as Earth, because mineral transformation at high pressures and
560 volatile recycling in the mantle produce rocks with a variety of fO_2. Nevertheless, the bulk silicate
561 FeO, established during metal/silicate differentiation, is a proxy of the bulk planet fO_2, itself
562 inherited from the planet primordial building blocks and the physico-chemical processes affecting
563 this primitive matter during the magma ocean stage (Righter et al., 2020). Hence, we find a
564 correlation between the mean silicate FeO content of achondrites and the Ni-Co fO_2 obtained with
565 our model, within error bars (Fig. 10). The logarithmic form of the correlation has a thermodynamic
566 meaning since $\Delta IW \propto \log_{10}(a_{FeO}^{sil})$ (eq. 1). Moreover, the Ni-Co fO_2 obtained for the achondrite
567 parent bodies are consistent with the fO_2 ranges of individual achondrites obtained with independent
568 methods, such as XANES (Righter et al., 2016) and experimental petrology: IW-1.5 to IW+1 for
569 angrites (Tissot et al., 2022), IW-7 to IW-5 for aubrites (Fogel, 2005; Keil, 2010), ~ IW-1.4 for Erg

570 Chech 002 (Nicklas et al., 2022), ~IW-2.9 to for NWA 7325/8486/8409 (Goodrich et al., 2017;
571 Sutton et al., 2017), and ~ IW-1.4 for NWA 011/2976 (Ma et al., 2022).
572 .
573
574 [Insert Fig. 10]
575
576 The empirical correlation obtained between Ni-Co P and radius of Earth, Mars, Moon and Vesta
577 (Fig. 7) is used to estimate a size for the APB, AuPB, NWA 7325/8486/8409 PB, NWA 011/2976
578 PB and Erg Chech 002 PB, based on Ni-Co results (Table 7). Given the very large errors associated
579 to these results (Fig. 11), and the underlying assumptions, parent body size estimates have to be
580 taken with a grain of salt. Hence, the following discussion should serve as a starting point to
581 investigate achondrite parent bodies properties with our method, in future dedicated studies. There
582 have been a number of attempts to estimate the APB size; conflicting arguments lead to a size range
583 going from to <100 km to > 340 km in radius (Keil, 2012; Sarafian et al., 2017; Tissot et al., 2022).
584 Our model suggest that the APB was asteroid-sized, with a radius < 263 km; considering error bars,
585 the APB could however be as large as 3713 km in radius (Table 7). In the same way, our Ni-Co
586 pressures are consistent with the Erg Chech 002 and NWA 7325/8486/8409 parent bodies to have
587 been asteroid-sized, with a radius < 263 km, and with a possible maximum radius of 263 km and
588 2970 km respectively (Fig. 11, Table 7). These results are in agreement with (Sturtz et al., 2022)
589 who constrained the Erg Chech 002 parent body size to 70-130 km in radius, and with (Sarafian et
590 al., 2017; Frossard et al., 2019) who suggested that the NWA 7325/8486/8409 parent body was a
591 planetesimal large enough (> 100 km in radius) to form and retain a basaltic crust. The Ni-Co
592 pressure obtained for the NWA 011/2976 is 4 GPa, consistent with a parent body of 2970 km in
593 radius (Fig. 11, Table 7). This appears in contradiction with (Yamaguchi et al., 2002; Floss et al.,
594 2005) who find likely that the NWA 011/2976 PB was a planetesimal. However, within the very
595 large error bars, our Ni-Co results are consistent with a parent body of < 263 km to 4320 km. Finally,
596 our Ni-Co results give a different case for the aubrite parent body. Indeed, the pressure of 28 GPa
597 suggest a parent body of 5469 km in radius, and considering the error bars gives a possible radius
598 range of 3713 to > 7557 km. Either this parent body is one of the current planets, either it has been
599 destroyed after the formation of the aubrite lithologies. Many arguments supports the fact that E-
600 type asteroids, mostly located in the Hungaria region of the main belt, are the immediate source of
601 aubrites (Ćuk et al., 2014). Recently, (Cartier et al., 2022) proposed that these asteroids are relicts
602 of the silicate portion of a large proto-Mercury, pulverized by a giant impact. Our results, with an
603 AuPB with intermediate size between Mars and Earth, are consistent with this scenario.

604

605 ## 5. Conclusions

606 This study expands our knowledge of Ni and Co as tracers for the thermodynamic conditions
607 prevailing during core formation in planetary bodies. The metal/silicate partition coefficients of Ni
608 and Co show strong correlations with P and fO_2, making them reliable barometers and
609 oxybarometers for magma ocean processes. While previous calibrations were based on experiments
610 conducted under moderately reducing conditions similar to Earth and Mars, this research fills a gap
611 by incorporating numerous metal-silicate experiments conducted over a range of pressure (1 bar to
612 26 GPa) under highly reducing conditions (down to IW-6.4) to the Ni and Co Dmet/sil database.
613 The resulting parameterization accurately predicts the evolution of Dmet/sil for Ni and Co across a
614 broad range of conditions, encompassing pressures from 1 bar to 80 GPa, oxygen fugacities
615 spanning IW to IW-7, and temperatures from 1550 K to 4450 K. Using this parameterization, we
616 modeled Ni and Co Dmet/sil along the liquidus of a chondritic mantle at different P and fO_2, leading
617 to the creation of a D(Co) vs D(Ni) grid. We then apply this tool to investigate various planetary
618 bodies magma ocean thermodynamic conditions using core/primitive mantle Ni and Co partition
619 coefficients. The P and fO_2 obtained for Earth, Mars, Moon and Vesta are in agreement with
620 previous studies applying similar methods, and strongly correlate to these planetary sizes,
621 supporting the reliability of the method. The tool is finally applied to investigate the angrite, aubrite,
622 NWA 7325/8486/8409, NWA 011/2976 and Erg Chech 002 parent bodies. Despide the large errors
623 associated to the results, the P and fO_2 obtained for these five achondrite families suggest a wide
624 variety of core formation conditions, from the asteroid-sized and oxidized angrite parent body, to
625 the planet-sized and highly reduced aubrite parent body. Overall, this comprehensive study provides
626 a model and a method that could easily be applied for furthur investigations of achondrite parent
627 body properties, or to investigate individual objects (achondrites, chondrules…) using in-situ Ni
628 and Co partition coefficients.

629

630

631 ## 6. Aknowledgements

632 The IHPV and piston-cylinder experiments support from the von Humboldt Foundation and
633 from a Marie Curie Intra-European Fellowship (SULFURON-MERCURY – 327046). The
634 evacuated silica tube experiments received funding from the French PNP program (INSU-
635 CNRS). The multi-anvil experiments received funding from the European Research Council

under the European Community's Seventh Framework Program (FP7/2007-2013 Grant Agreement 209035) and from the French PNP program (INSU-CNRS). The multianvil apparatus of Laboratoire Magmas et Volcans is financially supported by the Centre National de la Recherche Scientifique (Instrument National de l'INSU). C. Cartier thanks R. Fischer, K. Righter, and D. van Acken for discussions.

7. Appendix A. Supplementary Material

Supplementary Materials consist in a PDF file containing supplementary Tables S1 to S8, except the sup. Table S7 provided as a separate .xls file, and supplementary Figures S1 to S7.

8. Data availability

Figures and tables are available through https://data.mendeley.com/datasets/rz9htpr2rh/draft?a=6c3f181d-8476-451a-be69-86ee1a85d8da

9. References

Van Acken D., Brandon A. D. and Lapen T. J. (2012) Highly siderophile element and osmium isotope evidence for postcore formation magmatic and impact processes on the aubrite parent body. *Meteorit. Planet. Sci.* **47**, 1606–1623.

Andrault D., Bolfan-Casanova N., Nigro G. Lo, Bouhifd M. A., Garbarino G. and Mezouar M. (2011) Solidus and liquidus profiles of chondritic mantle: Implication for melting of the Earth across its history. *Earth Planet. Sci. Lett.* **304**, 251–259.

Asahara Y., Kubo T. and Kondo T. (2004) Phase relations of a carbonaceous chondrite at lower mantle conditions. *Phys. Earth Planet. Inter.* **143**, 421–432.

Barrat J. A., Chaussidon M., Yamaguchi A., Beck P., Villeneuve J., Byrne D. J., Broadley M. W. and Marty B. (2021) A 4,565-My-old andesite from an extinct chondritic protoplanet. *Proc. Natl. Acad. Sci. U. S. A.* **118**, 1–7.

Barrat J., Greenwood R. C., Verchovsky A., Gillet P., Bollinger C., Langlade J., Liorzou C., Franchi I. A., Barrat J., Greenwood R. C., Verchovsky A., Gillet P. and Bollinger C. (2015) Crustal

668 differentiation in the early solar system : clues from the unique achondrite Northwest Africa 7325
669 To cite this version : Crustal differentiation in the early solar system : clues from the unique
670 achondrite Northwest Africa 7325 (NWA 7325). **7325**.

671 Berndt J., Liebske C., Holtz F., Freise M., Nowak M., Ziegenbein D., Hurkuck W. and Koepke J.
672 (2002) A combined rapid-quench and H2-membrane setup for internally heated pressure vessels:
673 Description and application for water solubility in basaltic melts. *Am. Mineral.* **87**, 1717–1726.

674 Berthet S., Malavergne V. and Righter K. (2009) Melting of the Indarch meteorite (EH4 chondrite) at
675 1 GPa and variable oxygen fugacity: Implications for early planetary differentiation processes.
676 *Geochim. Cosmochim. Acta* **73**, 6402–6420.

677 Bouhifd M. A., Andrault D., Bolfan-Casanova N., Hammouda T. and Devidal J. L. (2013) Metal-
678 silicate partitioning of Pb and U: Effects of metal composition and oxygen fugacity. *Geochim.*
679 *Cosmochim. Acta* **114**, 13–28.

680 Bouhifd M. A., Boyet M., Cartier C., Hammouda T., Bolfan-Casanova N., Devidal J. L. and Andrault
681 D. (2015) Superchondritic Sm/Nd ratio of the Earth: Impact of Earth's core formation. *Earth*
682 *Planet. Sci. Lett.* **413**, 158–166.

683 Bouhifd M. A. and Jephcoat A. P. (2011) Convergence of Ni and Co metal-silicate partition
684 coefficients in the deep magma-ocean and coupled silicon-oxygen solubility in iron melts at high
685 pressures. *Earth Planet. Sci. Lett.* **307**, 341–348.

686 Bouhifd M. A. and Jephcoat A. P. (2003) The effect of pressure on partitioning of Ni and Co between
687 silicate and iron-rich metal liquids: a diamond-anvil cell study. *Earth Planet. Sci. Lett.* **209**, 245–
688 255.

689 Boujibar A., Andrault D., Bouhifd M. A., Bolfan-Casanova N., Devidal J.-L. L. and Trcera N. (2014)
690 Metal-silicate partitioning of sulphur, new experimental and thermodynamic constraints on
691 planetary accretion. *Earth Planet. Sci. Lett.* **391**, 42–54.

692 Brennan M. C., Fischer R. A. and Irving J. C. E. (2020) Core formation and geophysical properties of
693 Mars. *Earth Planet. Sci. Lett.* **530**, 115923.

694 Briaud A., Ganino C., Fienga A., Mémin A. and Rambaux N. (2023) The lunar solid inner core and
695 the mantle overturn. *Nature* **617**.

696 Carignan J., Hild P., Mevelle G., Morel J. and Yeghicheyan D. (2001) Routine analyses of trace
697 elements in geological samples using flow injection and low pressure on-line liquid
698 chromatography coupled to ICP-MS: A study of geochemical reference materials BR, DR-N,
699 UB-N, AN-G and GH. *Geostand. Newsl.* **25**, 187–198.

700 Cartier C., Charlier B., Boyet M., Spalding C. and Namur O. (2022) A large Proto-Mercury as the
701 Aubrite Parent Body. In *53rd Lunar and Planetary Science Conference*

702 Cartier C., Hammouda T., Boyet M., Bouhifd M. A. and Devidal J. L. (2014a) Redox control of the
703 fractionation of niobium and tantalum during planetary accretion and core formation. *Nat.*
704 *Geosci.* **7**, 573–576.

705 Cartier C., Hammouda T., Doucelance R., Boyet M., Devidal J. L. and Moine B. (2014b)
706 Experimental study of trace element partitioning between enstatite and melt in enstatite
707 chondrites at low oxygen fugacities and 5GPa. *Geochim. Cosmochim. Acta* **130**, 167–187.

708 Cartier C., Namur O., Nittler L. R., Weider S. Z., Crapster-Pregont E., Vorburger A., Franck E. A. and
709 Charlier B. (2020) No FeS layer in Mercury? Evidence from Ti/Al measured by MESSENGER.
710 *Earth Planet. Sci. Lett.* **534**, 116108.

711 Cartier C. and Wood B. J. (2019) The role of reducing conditions in building Mercury. *Elements* **15**,
712 39–45.

713 Casanova I., Keil K. and Newsom H. E. (1993) Composition of metal in aubrites: Constraints on core
714 formation. *Geochim. Cosmochim. Acta* **57**, 675–682.

715 Chabot N. L., Draper D. S. and Agee C. B. (2005) Conditions of core formation in the Earth :
716 Constraints from Nickel and Cobalt partitioning. *Geochim. Cosmochim. Acta* **69**, 2141–2151.

717 Corgne A., Keshav S., Wood B. J., McDonough W. F. and Fei Y. (2008) Metal-silicate partitioning
718 and constraints on core composition and oxygen fugacity during Earth accretion. *Geochim.*
719 *Cosmochim. Acta* **72**, 574–589.

720 Ćuk M., Gladman B. J. and Nesvorný D. (2014) Hungaria asteroid family as the source of aubrite
721 meteorites. *Icarus* **239**, 154–159.

722 Dehant V., Campuzano S. A., De Santis A. and van Westrenen W. (2022) Structure, Materials and
723 Processes in the Earth's Core and Mantle. *Surv. Geophys.* **43**, 263–302.

724 Delano J. W. (1986) Abdundances of Cobalt, Nickel, and Volatiles in the Silicate Portion of the Moon.
725 In *Origin of the Moon* pp. 232–247.

726 Delbo M., Walsh K., Bolin B., Avdellidou C. and Morbidelli A. (2017) Identification of a primordial
727 asteroid family constrains the original planetesimal population. *Science* **357**, 1026–1029.

728 DeMeo F. E., Burt B. J., Marsset M., Polishook D., Burbine T. H., Carry B., Binzel R. P., Vernazza P.,
729 Reddy V., Tang M., Thomas C. A., Rivkin A. S., Moskovitz N. A., Slivan S. M. and Bus S. J.
730 (2022) Connecting asteroids and meteorites with visible and near-infrared spectroscopy. *Icarus*
731 **380**.

732 Dreibus G., Bruckner J. and Wanke H. (1997) On the Core Mass of the Asteroid Vesta. *Meteorit.*
733 *Planet. Sci.*, A36.

734 Dreibus G. and Wänke H. (1980) The Bulk Composition of the Eucrite Parent Asteroid and its Bearing
735 on Planetary Evolution. *Zeitschrift für Naturforsch.* **35**, 204–216.

736 Fischer R. A., Nakajima Y., Campbell A. J., Frost D. J., Harries D., Langenhorst F., Miyajima N.,
737 Pollok K. and Rubie D. C. (2015) High pressure metal-silicate partitioning of Ni, Co, V, Cr, Si,
738 and O. *Geochim. Cosmochim. Acta* **167**, 177–194.

739 Floss C., Taylor L. A., Promprated P. and Rumble D. (2005) Northwest Africa 011: A "Eucritic"
740 basalt from a non-eucrite parent body. *Meteorit. Planet. Sci.* **40**, 343–360.

741 Fogel R. A. (2005) Aubrite basalt vitrophyres: The missing basaltic component and high-sulfur silicate
742 melts. *Geochim. Cosmochim. Acta* **69**, 1633–1648.

743 Fornasier S., Migliorini A., Dotto E. and Barucci M. A. (2008) Visible and near infrared spectroscopic
744 investigation of E-type asteroids, including 2867 Steins, a target of the Rosetta mission. *Icarus*
745 **196**, 119–134.

746 Frossard P., Boyet M., Bouvier A., Hammouda T. and Monteux J. (2019) Evidence for anorthositic
747 crust formed on an inner solar system planetesimal. *Geochemical Perspect. Lett.* **11**, 28–32.

748 Gaetani G. A. and Grove T. L. (1997) Partitioning of moderately siderophile elements among olivine,
749 silicate melt, and sulfide melt: Constraints on core formation in the Earth and Mars. *Geochim.*
750 *Cosmochim. Acta* **61**, 1829–1846.

751 Gaffey M. J., Reed K. L. and Kelley M. (1992) Relationship of E-Type Apollo Asteroid 3103 (1982
752 BB) to the Enstatite Achondrite Meteorites and the Hungaria Asteroids. *Icarus* **100**, 95–109.

753 Gagnon J. E., Fryer B. J., Samson I. M. and Williams-Jones A. E. (2008) Quantitative analysis of
754 silicate certified reference materials by LA-ICPMS with and without an internal standard. *J.*
755 *Anal. At. Spectrom.* **23**, 1529–1537.

756 Gessmann C. K. and Rubie D. C. (1998) The Effect of Temperature on the Partitioning of Nickel,
757 Cobalt, Manganese, Chromium, and Vanadium at 9 GPa and Constraints on Formation of the
758 Earth's Core. *Geochim. Cosmochim. Acta* **62**, 867–882.

759 Goodrich C. A., Kita N. T., Yin Q. Z., Sanborn M. E., Williams C. D., Nakashima D., Lane M. D. and
760 Boyle S. (2017) Petrogenesis and provenance of ungrouped achondrite Northwest Africa 7325
761 from petrology, trace elements, oxygen, chromium and titanium isotopes, and mid-IR
762 spectroscopy. *Geochim. Cosmochim. Acta* **203**, 381–403.

763 Greenwood R. C., Franchi I. A., Jambon A. and Buchanan P. C. (2005) Widespread magma oceans on

764 asteroidal bodies in the early Solar System. *Nature* **435**, 916–918.

765 Hammouda T. (2003) High-pressure melting of carbonated eclogite and experimental constraints on
766 carbon recycling and storage in the mantle. *Earth Planet. Sci. Lett.* **214**, 357–368.

767 Herzberg C. T. and Zhang J. (1996) Melting experiments on anhydrous peridotite KLB- 1:
768 Compositions of magmas in the upper mantle and transition zone. *J. Geophys. Res. Solid Earth*
769 **101**, 8271–8295.

770 Hillgren V. J., Drake M. J. and Rubie D. C. (1996) High pressure and high temperature metal-silicate
771 partitioning of siderophile elements: The importance of silicate liquid composition. *Geochim.*
772 *Cosmochim. Acta* **60**, 2257–2263.

773 Holzheid A., Palme H. and Chakraborty S. (1997) The activities of NiO, CoO and FeO in silicate
774 melts. *Chem. Geol.* **139**, 21–38.

775 Irving A. J., Kuehner S.M, Bunch T. E., Ziegler K., Chen G., Herd C. D. K., Conrey R. M. and Ralew
776 S. (2013) Ungrouped mafic achondrite Northwest Africa 7325: A reduced, iron-poor cumulate
777 olivine gabbor from a differentiated planetary parent body. In *44th Lunar and Planetary Science*
778 *Conference* pp. 2164–2165.

779 Isa J., Shinotsuka K., Yamaguchi A. and Ebihara M. (2008) CHEMICAL CHARACTERISTICS OF
780 NORTHWEST AFRICA 011 AND NORTHWEST AFRICA 2976. In *71st Annual Meteoritical*
781 *Society Meeting*

782 Jambon A., Barrat J., Boudouma O., Fonteilles M., Badia D., Göpel C. and Bohn M. (2011)
783 Mineralogy and petrology of the angrite Northwest Africa 1296. *Meteorit. Planet. Sci.* **40**, 631–
784 375.

785 Jana D. and Walker D. (1997) siderophile elements among metal and silicate liquids. *Earth Planet.*
786 *Sci. Lett.* **150**, 463–472.

787 Kegler (2008) New Ni and Co metal-silicate partitioning data and their relevance for an early
788 terrestrial magma ocean. *Earth Planet. Sci. Lett.* **268**, 28–40.

789 Keil K. (2012) Angrites, a small but diverse suite of ancient, silica-undersaturated volcanic-plutonic
790 mafic meteorites, and the history of their parent asteroid. *Chemie der Erde* **72**, 191–218.

791 Keil K. (2010) Enstatite achondrite meteorites (aubrites) and the histories of their asteroidal parent
792 bodies. *Chemie der Erde* **70**, 295–317.

793 Kilburn M. R. and Wood B. J. (1997) Metal – silicate partitioning and the incompatibility of S and Si
794 during core formation. *Earth Planet. Sci. Lett.* **152**, 139–148.

van Kooten E. M. M. E., Kubik E., Siebert J., Heredia B. D., Thomsen T. B. and Moynier F. (2022) Metal compositions of carbonaceous chondrites. *Geochim. Cosmochim. Acta* **321**, 52–77.

Lenhart E. M. and Secco R. A. (2022) Implications for the energy source for an early dynamo in Vesta from experiments on electrical resistivity of liquid Fe-10wt%Ni at high pressures. *Icarus* **378**, 114962.

Li J. and Agee C. B. (2001) The effect of pressure , temperature , oxygen fugacity and composition on partitioning of nickel and cobalt between liquid Fe-Ni-S alloy and liquid silicate : Implications for the Earth ' s core formation. *Geochim. Cosmochim. Acta* **65**, 1821–1832.

Lodders K. (2003) SOLAR SYSTEM ABUNDANCES AND CONDENSATION TEMPERATURES OF THE ELEMENTS. *Astrophys. J.* **591**, 1220–1247.

Lodders K. and Fegley B. (1998) *The Planetary Scientist's Companion*. Oxford University Press.

Lodders K., Palme H. and Wlotzka F. (1993) Trace elements in mineral separayes of the Pena Blanca Spring aubrite: Implications for the evolution of the aubrite parent body. *Meteorit. Planet. Sci.* **28**, 538–551.

Ma N., Neumann W., Néri A., Schwarz W. H., Ludwig T., Trieloff M., Klahr H. and Bouvier A. (2022) Early formation of primitive achondrites in an outer region of the protoplanetary disc. *Geochemical Perspect. Lett.* **23**, 33–37.

Mandler B. E. and Elkins-Tanton L. T. (2013) The origin of eucrites, diogenites, and olivine diogenites: Magma ocean crystallization and shallow magma chamber processes on Vesta. *Meteorit. Planet. Sci.* **48**, 2333–2349.

Mann U., Frost D. J. and Rubie D. C. (2009) Evidence for high-pressure core-mantle differentiation from the metal – silicate partitioning of lithophile and weakly-siderophile elements. *Geochim. Cosmochim. Acta* **73**, 7360–7386.

Mccoy T. J. (1998) A pyroxene-oldhamite clast in Bustee: igneous aubritic oldamite and a mechanism for the Ti enrichment in aubritic troilite. *Antart. Meteor. Res.* **11**, 32–48.

McDonough W. F. and Sun S. -s. (1995) The composition of the Earth. *Chem. Geol.* **120**, 223–253.

Mittlefehldt D. W. (2014) Achondrites. In *Treatise on Geochemistry: Second Edition* pp. 235–266.

Morard G. and Katsura T. (2010) Pressure – temperature cartography of Fe – S – Si immiscible system. *Geochim. Cosmochim. Acta* **74**, 3659–3667.

Mysen B. O. (1983) The structure of silicate melts. *Annu. Rev. Earth Planet. Sci.* **11**, 75–97.

Namur O., Charlier B., Holtz F., Cartier C. and Mccammon C. (2016) Sulfur solubility in reduced

826 mafic silicate melts : Implications for the speciation and distribution of sulfur on Mercury. *Earth*
827 *Planet. Sci. Lett.* **448**, 102–114.

828 Nicklas R. W., Day J. M. D., Gardner-Vandy K. G. and Udry A. (2022) Early silicic magmatism on a
829 differentiated asteroid. *Nat. Geosci.* **15**, 696–699.

830 Palme H. and O'Neill H. S. C. (2014) Cosmochemical Estimates of Mantle Composition. In *Treatise*
831 *on Geochemistry: Second Edition* pp. 1–39.

832 Paquet M., Day J. M. D., Udry A., Hattingh R., Kumler B., Rahib R. R., Tait K. T. and Neal C. R.
833 (2021) Highly siderophile elements in shergottite sulfides and the sulfur content of the martian
834 mantle. *Geochim. Cosmochim. Acta* **293**, 379–398.

835 Pirotte H., Cartier C., Namur O., Pommier A., Zhang Y., Berndt J., Klemme S. and Charlier B. (2023)
836 Internal differentiation and volatile budget of Mercury inferred from the partitioning of heat-
837 producing elements at highly reduced conditions. *Icarus* **405**, 115699.

838 Ray A. S., Wadhwa M. and Rai V. K. (2019) Iron Isotope Compositions of Large Metal Nodules From
839 the Norton County. **2019**, 49–50.

840 Ray S., Wadhwa M. and Rai V. K. (2018) the Origin of Metal Grains From Enstatite Achondrites
841 Based on Iron Isotope. In *Lunar and Planetary Science Conference* pp. 14–15.

842 Righter K. (2015) Modeling siderophile elements during core formation and accretion , and the role of
843 the deep mantle and volatiles. *Am. Mineral.* **100**, 1098–1109.

844 Righter K. (2011) Prediction of metal – silicate partition coef fi cients for siderophile elements : An
845 update and assessment of PT conditions for metal – silicate equilibrium during accretion of the
846 Earth. *Earth Planet. Sci. Lett.* **304**, 158–167.

847 Righter K. and Chabot N. L. (2011) Moderately and slightly siderophile element constraints on the
848 depth and extent of melting in early Mars. *Meteorit. Planet. Sci.* **176**, 157–176.

849 Righter K. and Drake M. J. (1997) A magma ocean on Vesta: Core formation and petrogenesis of
850 eucrites and diogenites. *Meteorit. Planet. Sci.* **944**, 929–944.

851 Righter K. and Drake M. J. (1996) Core formation in Earth's moon, Mars, and Vesta. *Icarus* **124**, 513–
852 529.

853 Righter K., Drake M. J. and Yaxley G. (1997) Prediction of siderophile element metal-silicate
854 partition coefficients to 20 GPa and 2800°C : the effects of pressure , temperature , oxygen
855 fugacity , and silicate and metallic melt compositions. *Phys. Earth Planet. Inter.* **100**, 115–134.

856 Righter K. and Ghiorso M. S. (2012) Redox systematics of a magma ocean with variable pressure-

857 temperature gradients and composition. *Proc. Natl. Acad. Sci.* **109**, 11955–11960.

858 Righter K., Herd C. D. K. and Boujibar A. (2020) Redox Processes in Early Earth Accretion and in
859 Terrestrial Bodies. *Elements* **16**, 161–166.

860 Righter K., Hervig R. L. and Kring D. A. (1998) Accretion and core formation on Mars: molybdenum
861 contents of melt inclusion glasses in three SNC meteorites. *Geochim. Cosmochim. Acta* **62**,
862 2167–2177.

863 Righter K., Pando K. M., Danielson L. and Lee C. (2010) Partitioning of Mo , P and other siderophile
864 elements (Cu , Ga , Sn , Ni , Co , Cr , Mn , V , and W) between metal and silicate melt as a
865 function of temperature and silicate melt composition. *Earth Planet. Sci. Lett.* **291**, 1–9.

866 Righter K., Sutton S. R., Danielson L., Pando K., Newville M., R K., S S. R., D L., P K. and N M.
867 (2016) Redox variations in the inner solar system with new constraints from vanadium XANES
868 in spinels. *Am. Mineral.* **101**, 1928–1942.

869 Rivoldini A., Hoolst T. Van, Verhoeven O., Mocquet A. and Dehant V. (2011) Geodesy constraints on
870 the interior structure and composition of Mars. *Icarus* **213**, 451–472.

871 Rubie D. C., Frost D. J., Mann U., Asahara Y., Nimmo F., Tsuno K., Kegler P., Holzheid A. and
872 Palme H. (2011) Heterogeneous accretion , composition and core – mantle differentiation of the
873 Earth. *Earth Planet. Sci. Lett.* **301**, 31–42.

874 Rubie D. C., Melosh H. J., Reid J. E., Liebske C. and Righter K. (2003) Mechanisms of metal-silicate
875 equilibration in the terrestrial magma ocean. *Earth Planet. Sci. Lett.* **205**, 239–255.

876 Rubin A. E. (1983) Impact Melt-Rock Clasts in the Hvittis Enstatite Chondrite Breccia: Implications
877 for a Genetic Relationship Between El Chondrites and Aubrites. *J. Geophys. Res.* **88**, 293–300.

878 Sarafian A. R., Nielsen S. G., Marschall H. R., Gaetani G. A., Hauri H., Righter K. and Sarafian E.
879 (2017) Angrite meteorites record the onset and flux of water to the inner solar system. *Geochim.*
880 *Cosmochim. Acta* **212**, 156–166.

881 Siebert J., Badro J., Antonangeli D. and Ryerson F. J. (2012) Metal – silicate partitioning of Ni and Co
882 in a deep magma ocean. *Earth Planet. Sci. Lett.* **321**–**322**, 189–197.

883 Siebert J., Badro J., Antonangeli D. and Ryerson F. J. (2013) Terrestrial Accretion Under Oxidizing
884 Conditions. *Science* **339**, 1194–1197.

885 Siebert J., Corgne A. and Ryerson F. J. (2011) Systematics of metal – silicate partitioning for many
886 siderophile elements applied to Earth ' s core formation. *Geochim. Cosmochim. Acta* **75**, 1451–
887 1489.

888 Stähler S. C., Khan A., Banerdt W. B., Lognonné P., Giardini D., Ceylan S., Drilleau M., Duran A. C.,
889 Garcia R. F., Huang Q., Kim D., Lekic V., Samuel H., Schimmel M., Schmerr N., Sollberger D.,
890 Stutzmann É., Xu Z., Antonangeli D., Charalambous C., Davis P. M., Irving J. C. E., Kawamura
891 T., Knapmeyer M., Maguire R., Marusiak A. G., Panning M. P., Perrin C., Plesa A.-C., Rivoldini
892 A., Schmelzbach C., Zenhäusern G., Beucler É., Clinton J., Dahmen N., van Driel M., Gudkova
893 T., Horleston A., Pike W. T., Plasman M. and Smrekar S. E. (2021) Seismic detection of the
894 martian core. *Science* **373**, 443–448.

895 Steenstra E. (2016) Constraints on core formation in Vesta from metal-silicate partitioning of
896 siderophile elements Constraints on core formation in Vesta from metal – silicate partitioning of
897 siderophile elements. *Geochim. Cosmochim. Acta* **177**, 48–61.

898 Steenstra E. S., Rai N., Knibbe J. S., Lin Y. H. and Westrenen W. Van (2016) New geochemical
899 models of core formation in the Moon from metal – silicate partitioning of 15 siderophile
900 elements. *Earth Planet. Sci. Lett.* **441**, 1–9.

901 Steenstra E. S., Seegers A. X., Putter R., Berndt J., Klemme S., Matveev S., Bullock E. S. and
902 Washington D. C. (2020a) Metal-silicate partitioning systematics of siderophile elements at
903 reducing conditions : A new experimental database. *Icarus* **335**, 113391.

904 Steenstra E. S., Sitabi A. B., Lin Y. H., Rai N., Knibbe J. S., Berndt J., Matveev S. and van Westrenen
905 W. (2017) The effect of melt composition on metal-silicate partitioning of siderophile elements
906 and constraints on core formation in the angrite parent body. *Geochim. Cosmochim. Acta* **212**,
907 62–83.

908 Steenstra E. S., Trautner V. T., Berndt J., Klemme S. and Westrenen W. Van (2020b) Trace element
909 partitioning between sulfide- , metal- and silicate melts at highly reduced conditions : Insights
910 into the distribution of volatile elements during core formation in reduced bodies. *Icarus* **335**,
911 113408.

912 Sturtz C., Limare A., Chaussidon M. and Kaminski É. (2022) Structure of differentiated planetesimals:
913 A chondritic fridge on top of a magma ocean. *Icarus* **385**, 115100.

914 Sutton S. R., Goodrich C. A. and Wirick S. (2017) Titanium , Vanadium and Chromium Valences in
915 Silicates of Ungrouped Achondrite NWA 7325 and Ureilite Y-791538. *Geochim. Cosmochim.*
916 *Acta* **204**, 313–330.

917 Taylor G. J. (2013) Chemie der Erde The bulk composition of Mars. *Chemie der Erde - Geochemistry*
918 **73**, 401–420.

919 Thibault Y. and Walters M. J. (1995) The influence of pressure and temperature on the metal-silicate
920 partition coefficients of nickel and cobalt in a model Cl chondrite and implications for metal

921 segregation in a deep magma ocean. *Geochim. Cosmochim. Acta* **59**.

922 Tissot F. L. H., Collinet M., Namur O. and Grove T. L. (2022) The case for the angrite parent body as
923 the archetypal first-generation planetesimal : Large , reduced and Mg-enriched. *Geochim.*
924 *Cosmochim. Acta* **338**, 278–301.

925 Wade J. and Wood B. J. (2005) Core formation and the oxidation state of the Earth. *Earth Planet. Sci.*
926 *Lett.* **236**, 78–95.

927 Wade J. and Wood B. J. (2001) The Earth 's "missing" niobium may be in the core. *Nature* **409**, 75–
928 79.

929 Wang S. J., Li S. J., Lin Y. and Sheng S. Z. (2023) Mass-dependent nickel isotopic variations in
930 achondrites and lunar rocks. *Geochim. Cosmochim. Acta* **350**, 16–27.

931 Weber I., Morlok A., Bischoff A., Hiesinger H., Ward D., Joy K. H., Crowther S. A., Jastrzebski N.
932 D., Gilmour J. D., Clay P. L., Wogelius R. A., Greenwood R. C., Franchi I. A. and Münker C.
933 (2015) Cosmochemical and spectroscopic properties of Northwest Africa 7325-A consortium
934 study. *Meteorit. Planet. Sci.* **51**, 3–30.

935 Wood B. J., Wade J. and Kilburn M. R. (2009) Core formation and the oxidation state of the Earth :
936 Additional constraints from Nb , V and Cr partitioning. *Geochim. Cosmochim. Acta* **72**, 1415–
937 1426.

938 Yamaguchi A., Barrat J., Chaussidon M., Beck P., Villeneuve J., Byrne D. J., Broadley M. W. and
939 Marty B. (2021) PETROLOGY AND GEOCHEMISTRY OF ERG CHECH 002, THE OLDEST
940 ANDESITE IN THE SOLAR SYSTEM. In *52nd Lunar and Planetary Science Conference*

941 Yamaguchi A., Clayton R. N., Mayeda T. K., Ebihara M., Oura Y., Miura Y. N., Haramura H.,
942 Misawa K., Kojima H. and Nagao K. (2002) A new source of basaltic meteorites inferred from
943 Northwest Africa 011. *Science* **296**, 334–336.

944 Yen A. S., Mittlefehldt D. W., McLennan S. M., Gellert R., Bell J. F., McSween J. Y., Ming D. W.,
945 McCoy T. J., Morris R. V., Golombek M. P., Economou T., Madsen M. B., Wdowiak T., Clark
946 B. C., Jolliff B. L., Schröder C., Brückner J., Zipfel J. and Squyres S. W. (2006) Nickel on Mars:
947 Constraints on meteoritic material at the surface. *J. Geophys. Res. Planets* **111**.

948 Zhu K., Barrat J. A., Yamaguchi A., Rouxel O., Germain Y., Langlade J. and Moynier F. (2022)
949 Nickel and Chromium Stable Isotopic Composition of Ureilites: Implications for the Earth's
950 Core Formation and Differentiation of the Ureilite Parent Body. *Geophys. Res. Lett.* **49**, 0–11.

951

952

Table 1: Experimental parameters and results. Sil. melt = silicate melt, met. = metal, sulf. = sulfide, bridg. = bridgmanite, maj. = majorite, sti. = stishovite, enst. = enstatite, forst. = forsterite, coe. = coesite, qtz = quartz. fO_2 relative to IW is calculated assuming ideal behavior of Fe and FeO, and is estimated to have error of ± 1 log unit (see 2.7).

Run	Device	P (GPa)	(K)	Duration	ΔIW	Result	X (S) Metal	NBO/T
#143	MA	26	2400	45 min	-2.4	Sil. melt, met., bridg.	0.2733	2.53
#176A	MA	26	2444	40 min	-2.4	Sil. melt, met.	0.1741	1.82
#177	MA	26	2410	35 min	-3.3	Sil. melt, met., maj., bridg., sti.	0.2245	2.02
#178	MA	26	2075	30 min	-2.8	Sil. melt, met.	0.4858	2.41
#195	MA	26	2345	20 min	-5.4	Sil. melt, met., maj., bridg., sti.	0.0892	1.82
#197	MA	26	2357	30 min	-2.1	Sil. melt, met., maj., bridg., sti.	0.3925	1.95
#198	MA	26	2360	30 min	-3.0	Sil. melt, met.	0.4739	1.80
#205	MA	26	2349	35 min	-5.6	Sil. melt, met., maj., bridg., sti.	0.1219	1.89
1083c	MA	5	1883	3h30	-5.4	Sil. melt, met., sulf., enst.	0.0049	1.08
1093b	MA	5	1953	4h	-4.9	Sil. melt, met., sulf., enst.	0.0132	0.89
1133	MA	5	1963	3h30	-4.9	Sil. melt, met., sulf., enst.	0.0157	1.31
1135	MA	5	1923	2h30	-4.9	Sil. melt, met., sulf., enst.	0.0048	1.05
1136b	MA	5	1913	2h	-4.4	Sil. melt, met., sulf., enst., coe.	0.0252	0.80
1137	MA	5	1973	3h	-1.9	Sil. melt, met., sulf., enst.	0.1008	1.65
1162	MA	5	1923	2h30	-5.3	Sil. melt, met., enst.	0.0001	1.29
1178	MA	5	1853	2h	-6.4	Sil. melt, met., enst., coe.	0.0003	1.20
1183	MA	5	1993	2h15	-2.1	Sil. melt, met., sulf., enst.	0.0549	1.72
1188	MA	5	1963	2h	-4.8	Sil. melt, met., sulf., enst.	0.0180	1.74
1198	MA	5	2073	3h	-1.9	Sil. melt, met., sulf., enst.	0.0385	1.23
1210	MA	5	2073	3h	-4.7	Sil. melt, met., sulf., enst.	0.0138	1.36
1212	MA	5	2123	3h	-4.7	Sil. melt, met., sulf., enst.	0.0214	0.99
A022	PC	1.3	1873	1h	-5.1	Sil. melt, met.	0.0007	1.36
A023	PC	1.3	1773	2h	-5.1	Sil. melt, met.	0.0020	1.34
A038	PC	1.3	1873	45 min	-4.7	Sil. melt, sulf., qtz	0.5029	0.76
A040	PC	1.3	1973	45 min	-4.7	Sil. melt, sulf	0.5030	0.79
A041	PC	2	1973	45 min	-4.3	Sil. melt, sulf., qtz	0.5064	0.97
A043	PC	1.3	1873	45 min	-3.5	Sil. melt, sulf.	0.5066	0.94
B873	PC	3	1973	3h	-2.1	Sil. melt, met.	0.0005	1.60
B879	PC	3	1973	3h	-4.6	Sil. melt, met.	0.0047	1.64
YO37-2	IHPV	0.1	1873	3h	-4.1	Sil. melt, sulf.	0.0026	1.31
YO56-1	IHPV	0.1	1793	3h	-5.1	Sil. melt, met., sulf.	0.0164	1.38
YO83-2	IHPV	0.1	1793	3h	-5.0	Sil. melt, met., sulf.	0.0082	1.44
YO43-2	IHPV	0.1	1793	3h	-4.8	Sil. melt, met., sulf.	0.0002	1.31
FM165	EST	0.0001	1673	5h	-5.5	Sil. melt, met., sulf., enst., forst.	0.0013	1.36
FM161	EST	0.0001	1573	48h	-5.6	Sil. melt, met., sulf., enst., forst.	0.0185	0.66
FM167	EST	0.0001	1623	24h	-5.5	Sil. melt, met., sulf., enst., forst.	0.0234	1.19
FM153	EST	0.0001	1623	48h	-5.4	Sil. melt, met., sulf., enst., forst.	0.0047	0.93
FM152	EST	0.0001	1623	24h	-5.3	Sil. melt, met., sulf., enst., forst.	0.0075	1.09

Fig. 1: BSE images of typical samples, a, c, c from left to right. Bridg. = bridgmantite; sil. Melt = silicate melt; maj. = majorite; sti. = stishovite; met. = metal; sulf. = sulfide; opx = enstatite; ol. = olivine.

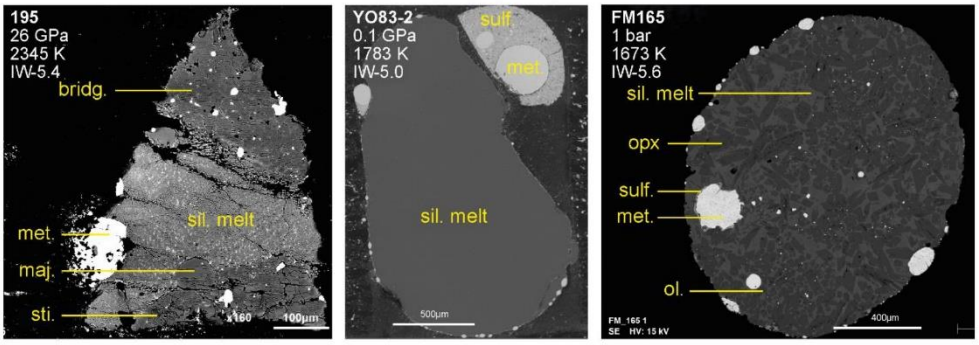

Table 2: Chemical composition of silicate melts, metal and sulfide phases in experiments and corresponding metal/silicate and sulfide/silicate partition coefficients. Major and minor elements were measured with EPMA, Ni and Co were measured by LA-ICPMS.

[Separate .xls file]

Fig. 2: Metal and silicate composition of the experiments. Circles = 26 GPa experiments; Triangles = 5 GPa and lower pressures experiments. Black symbols = sulfide-undersaturated experiments.

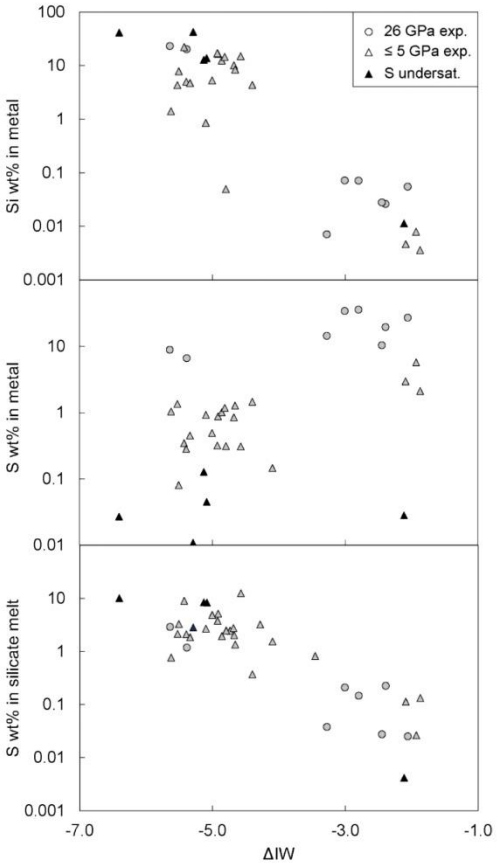

Fig. 3: Ni and Co metal/silicate partition coefficients of experiments conducted in various chemical systems at various P, T, fO_2 (Table 2, Table S7).

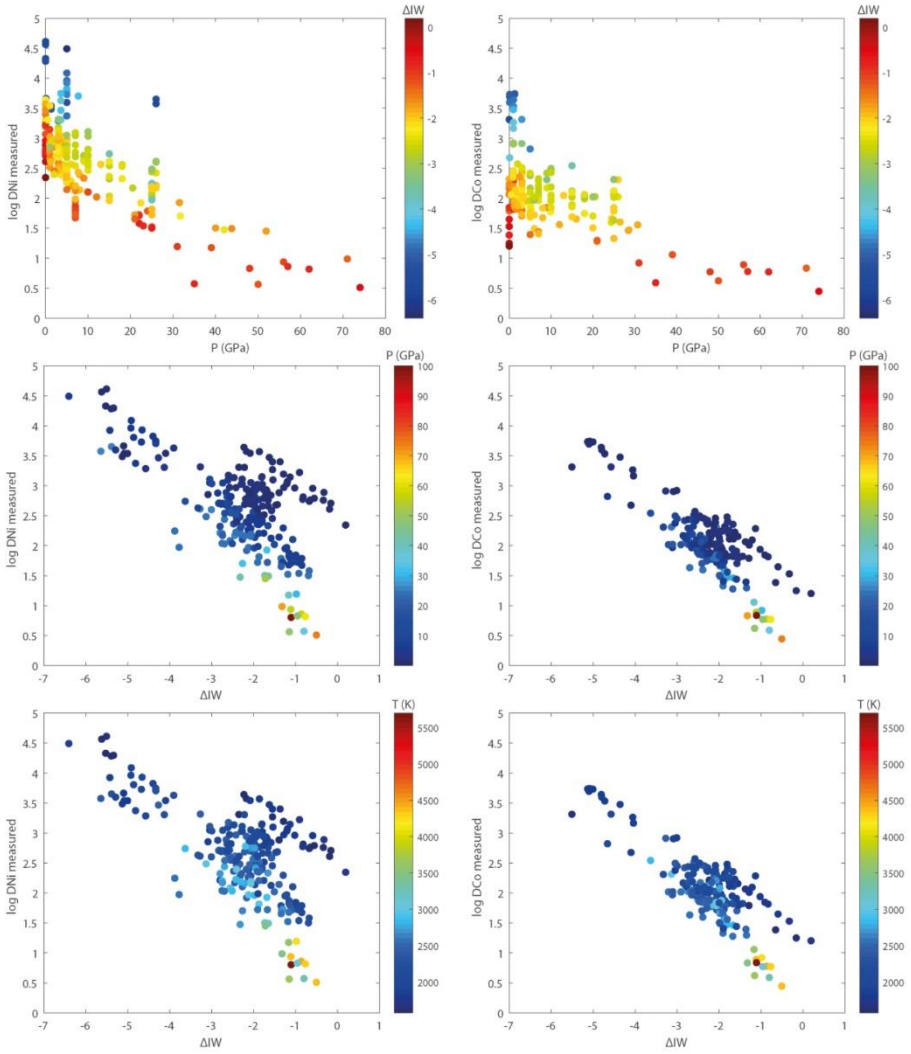

Table 3: Parameters obtained by regression of the experimental database with equation [1].

	a	b	c (1/K)	d (GPa/K)	R^2	p Value b	p Value c	p Value d
Ni	1.7363	-0.80003	6775.1	-156.2	0.875	2E-69	3E-23	7E-27
Co	1.1584	-1.0187	3573.4	-86.688	0.864	2E-65	8E-08	2E-09

Fig. 4: Comparison of the predictive models of Ni and Co metal partitioning from Righter (2015), Fischer et al. (2015), and this study. a) and b) display models ran at fixed fO_2 of IW-2.1 and chondritic liquidus temperatures (Andrault et al., 2011; Herzberg and Zhang, 1996), as a function of pressure. c) and d) display models ran at fixed pressure (15 GPa) and temperature (2472 K), as a function of fO_2. In a), b), c) and d), Righter's model was run with a sulfur- and carbon-free metal composition and a silicate NBO/T of 2.49.

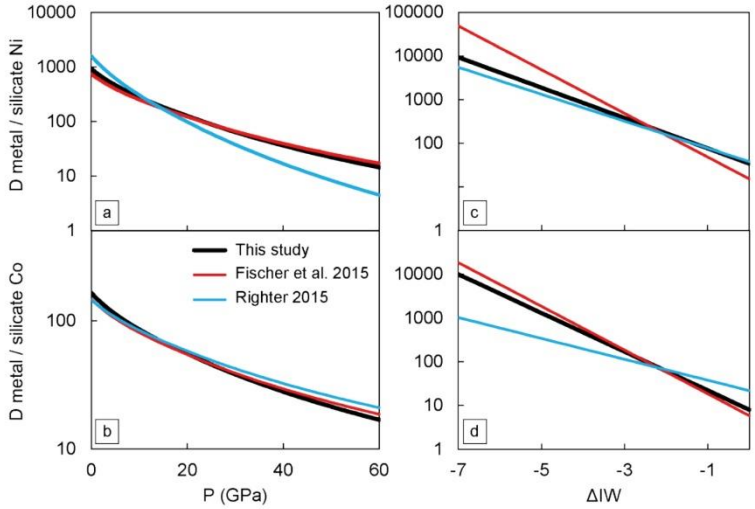

Fig. 5: Pressure (GPa) - fO_2 (ΔIW) space drawn by modelled Ni and Co Dmet/sil along the liquidus of a chondritic mantle, on which are plotted the core-mantle Ni and Co Dmet/sil calculated for the Earth, Mars, the Moon and Vesta, to retrieve the thermodynamic conditions of their core formation. The model indicates 46 GPa / IW-2.1 for the Earth, 6 GPa / IW-1.3 for Mars, 1 GPa / IW-1.2 for the Moon, and <1 bar / IW-2.2 for Vesta. The error bars intersection with the grid give maximum and minimum fO_2 and P values, giving an estimate of the error associated to the fO_2 and P values.

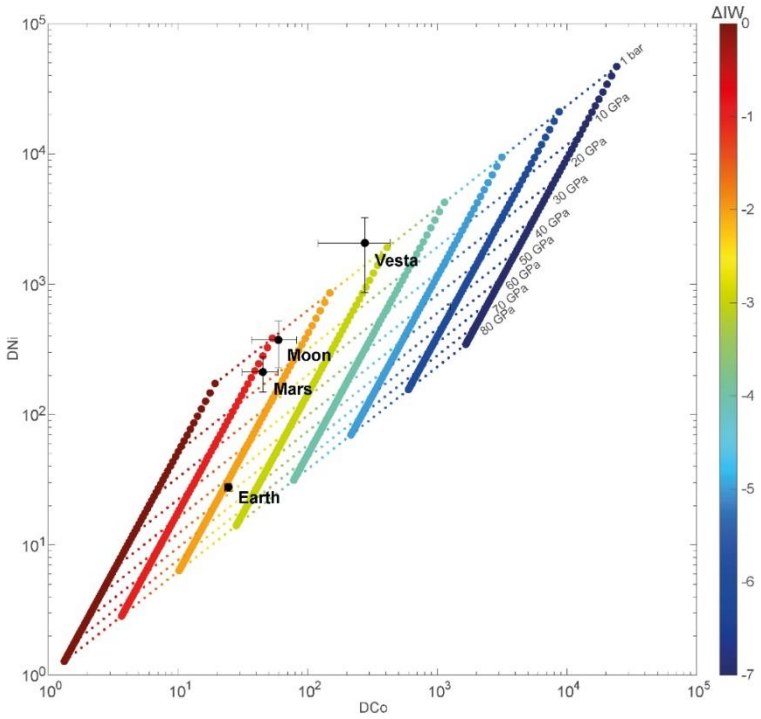

Table 4: Selected values of Ni and Co bulk silicate and bulk core weight contents for Earth, Mars, the Moon and Vesta. References are [1] (Palme and O'Neill, 2014), [2] (Mcdonough and Sun, 1995), [3] (Taylor, 2013), [4] (Righter and Drake, 1996), [5] (Delano, 1986), [6] (Steenstra, 2016) and [7] (Dreibus and Wänke, 1980).

	Bulk silicate					Bulk core					Partition coefficients			
	Reference	Ni %	σ	Co ppm	σ	Reference	Ni %	σ	Co ppm	σ	Ni	σ	Co	σ
Earth	[1]	0.186	0.009	102	5	[2]	5.2	0.3	2500	100	28	2	25	2
Mars / SNC	[3]	0.033	0.005	71	13	[4]	7.0	1.8	3200	800	212	64	45	14
Moon / Lunar met.	[5]	0.047	0.005	90	5	[6]	17.6	6.6	5355	208	374	146	60	23
Vesta / HED	[7]	0.0038	0.0015	13	5	[7]	7.9	3.1	3600	1440	2068	1170	277	157

Figure 6: Compilation of bulk rock Ni and Co data of Earth, Mars-SNC meteorites, Moon-lunar meteorites, and Vesta-HED meteorites, compared with chondrites bulk data (Lodders and Fegley, 1998), (white dots). Each element is plotted a function of Mg/Al. Earth komatiites, basalts and peridotite data are from GEOROC database. Mars rocks and soils data are from (Yen et al., 2006). Moon regolith and rock data are from the Lunar Sample Compendium database, and SNC, lunar and HED meteorites data are from the MetBase database. Earth, Mars, Moon and Vesta bulk silicate compositions (large dots) are from (Palme and O'Neill, 2014), (Taylor, 2013), (Delano, 1986) and (Dreibus and Wänke, 1980) respectively, Table 4.

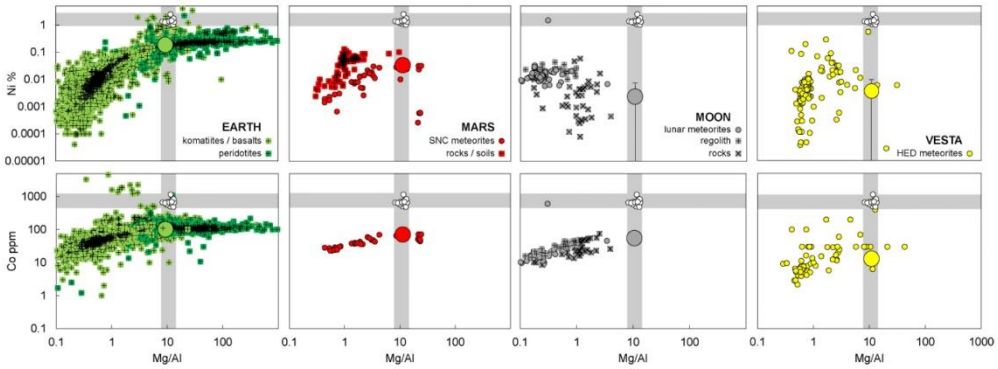

Table 5: Pressure and fO_2 results obtained by plotting planetary D(Ni) – D(Co) in the modelled P-fO_2 space (Fig. 5). Pressure and fO_2 maximum and minimum values correspond to the plot of the error bars associated with D(Ni) – D(Co); these values gives an approximate of the error on the results, e.g. the pressure obtained for Earth is 46^{+2}_{-3} GPa. Bulk silicate FeO values are from (Palme et al., 2014) (Khan et al., 2022) for Earth, Mars, Moon and Vesta respectively.

	Radius (km)	BS FeO wt%	σ	P (GPa)	P max (GPa)	P min (GPa)	fO_2 (ΔIW)	fO_2 max (ΔIW)	fO_2 min (ΔIW)
Earth	6371	8.1	1.3	46	48	43	-2.1	-2	-2.2
Mars	3390	13.7	0.5	6	12	2	-1.3	-0.6	-1.7
Moon	1737	12.4	5.0	1	8	< 0.0001	-1.2	-0.4	-1.8
Vesta	263	14.8	4.6	< 0.0001	6	< 0.0001	-2.3	-0.8	-3

Figure 7: a- Obtained Ni-Co pressures VS planetary body radius (km) and polynomial regression of the correlation.

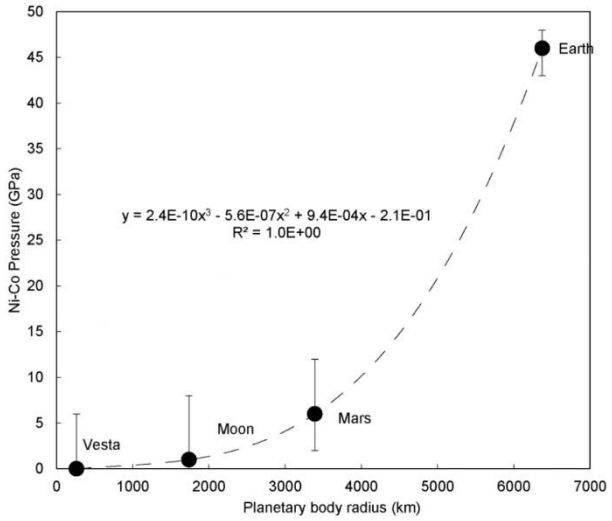

Figure 8: Compilation of bulk rock Ni and Co data of angrites, aubrites, Erg Chech 002, NWA 7325/8486/8409 and NWA 011/2976 compared with chondrites bulk data (Lodders and Fegley, 1998), (white dots). Each element is plotted a function of Mg/Al. Most achondrite data come from the MetBase database, the bulk compositions of aubrite basalt vitrophyres come from (Fogel, 2005) and (Keil et al., 2011), additional data for achondrites are from (Wang et al., 2023) and additional data for aubrites are from (Wilbur et al., 2022). The large dots correspond to our estimation of the bulk silicate achondrite parent bodies, i.e. the median values of Ni and Co data, excluding the outliers. The outliers are represented with semi-transparent figures. The error bar on the bulk silicate correspond to the median absolute deviation of these data. The Mg/Al is fixed at 11.2 (CI value, (Lodders and Fegley, 1998) for the purposes of the figure, but is not used elsewhere.

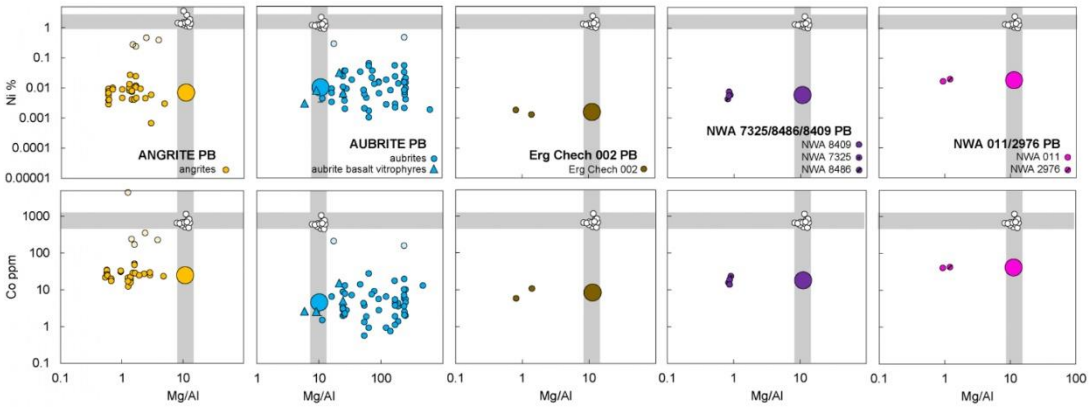

Table 6: Bulk silicate, bulk core and corresponding partition coefficients estimated for the angrite PB, the aubrite PB, the NWA 7325/ 8486/8409 PB, the NWA 011/2976 PB and the Erg Chech 002 PB.

	Bulk silicate					Bulk core					Partition coefficients			
Parent bodies	Method	Ni %	σ	Co ppm	σ	Method	Ni %	σ	Co ppm	σ	Ni	σ	Co	σ
Angrite	Med. meteor.	0.007	0.003	26.7	5.9	Mass bal. CV	5.2	2.0	2436	929	703	384	91	40
Aubrite	Med. meteor.	0.010	0.007	4.6	2.5	Mass bal. EH	7.2	2.8	3404	1311	720	560	736	490
Erg Chech 002	Med. meteor.	0.0016	0.0003	8.3	2.5	Mass bal. CI	4.2	1.6	1861	715	2633	1110	224	109
NWA 7325/8486/8409	Med. meteor.	0.0055	0.0008	17.3	2.4	Mass bal. R	7.2	2.8	3367	1292	1307	537	195	80
NWA 011/2976	Med. meteor.	0.018	0.002	41.3	1.0	Mass bal. CR	5.4	2.1	2409	913	294	116	58	22

Figure 9: Pressure (GPa) - fO_2 (ΔIW) space drawn by modelled Ni and Co Dmet/sil along the liquidus of a chondritic mantle, on which are plotted the core-mantle Ni and Co Dmet/sil calculated for the angrite PB, the aubrite PB, the NWA 7325/ 8486/8409 PB, the NWA 011/2976 PB and the Erg Chech 002 PB (Table 6) to retrieve the thermodynamic conditions of their core formation. The model indicates indicates < 1 bar / IW-1.4 for the APB, 28 GPa / IW-4.9 for the AuPB, < 1 bar / IW-1.7 for the Erg Chech 002 PB, <1 bar / IW-2.1 for the NWA 7325/8486/8409 PB, and 4 GPa / IW-1.4 for the NWA 011/2976 PB (Table 7).

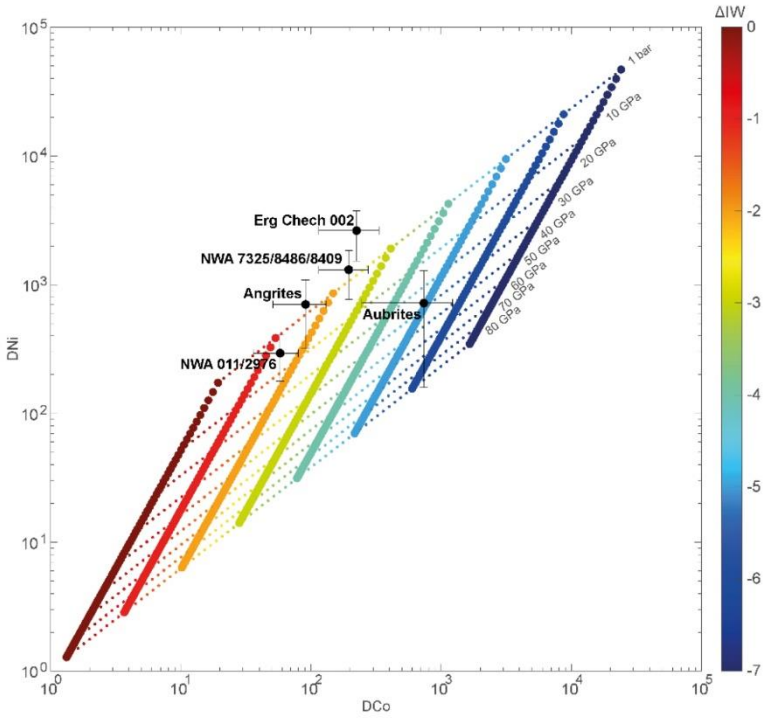

Table 7: Pressure and fO_2 results obtained by plotting achondrite parent bodies D(Ni) – D(Co) in the modelled P- fO_2 space (Fig. 9). Maximum and minimum values correspond to the plot of the error bars associated with D(Ni) – D(Co). The parent body radius is estimated using the correlation found between the Ni-Co P and radius of Earth, Mars, Moon and Vesta (Fig. 7).

Parent bodies	Estimated radius (km)	BS FeO wt%	σ	P (GPa)	P min (GPa)	P max (GPa)	fO2 (ΔIW)	fO2 min (ΔIW)	fO2 max (ΔIW)
Angrites	< 262.7	20.2	5.9	< 0.0001	< 0.0001	8	-1.4	-2.1	-0.4
Aubrites	5469	0.05	0.03	28	8	> 80	-4.9	-6.3	-3
Erg Chech 002	< 262.7	9.675	1.525	< 0.0001	< 0.0001	< 0.0001	-1.7	-2.3	-0.5
NWA 7325/8486/8409	< 262.7	0.53	0.04	< 0.0001	< 0.0001	4	-2.1	-1.7	-1.2
NWA 011/2976	2970	19.2	1.2	4	< 0.0001	13	-1.4	-1.9	-0.6

Figure 10: Ni-Co fO_2 obtained with our model VS bulk silicate FeO contents for the achondrite parent bodies (Table 7).

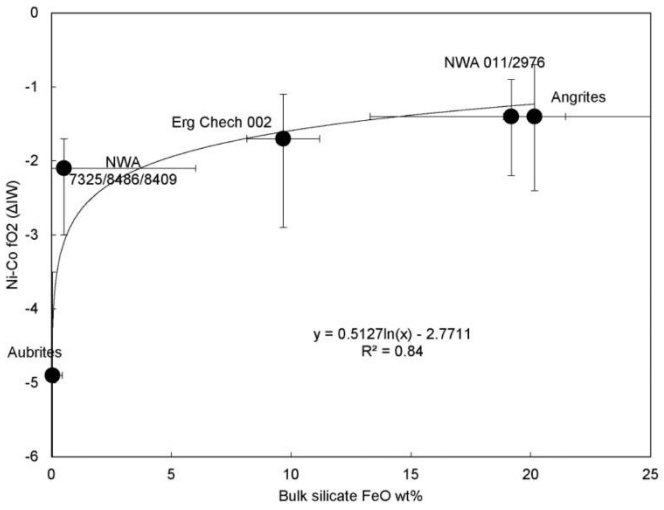

Figure 11: Obtained Ni-Co pressures VS planetary body radius (km) obtained for Earth, Mars, the Moon and Vesta and polynomial regression of the correlation. The equation has been then solved to obtain a planetary body radius for the angrite, aubrite, NWA 7325/8486/8409, NWA 011/2976 and Erg Chech 002 parent bodies using Ni-Co pressure data (Table 7).

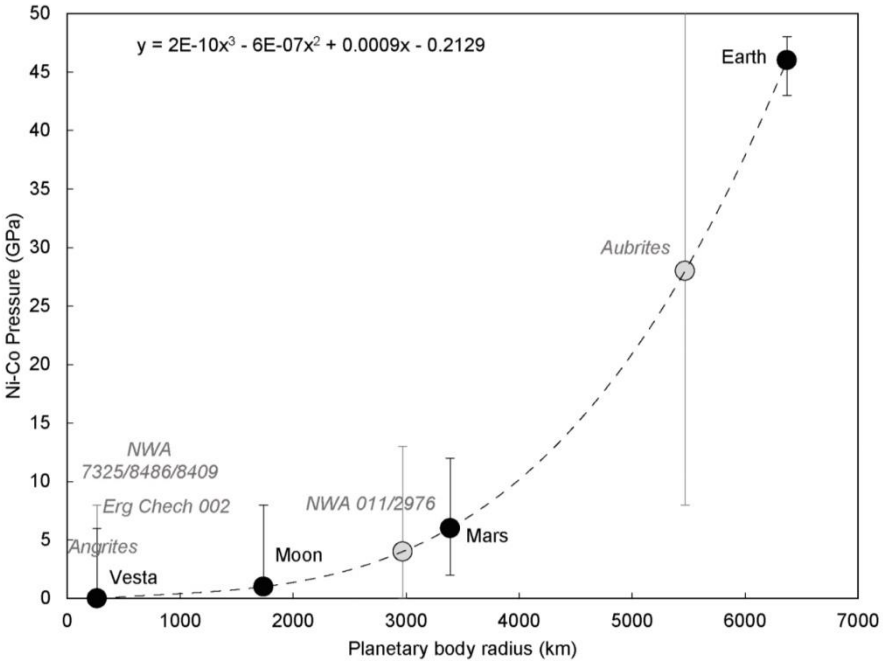
y = 2E-10x³ - 6E-07x² + 0.0009x - 0.2129
Ni-Co Pressure (GPa)
Planetary body radius (km)
0
5
10
15
20
25
30
35
40
45
50
0
1000
2000
3000
4000
5000
6000
7000
Earth
Aubrites
NWA 7325/8486/8409
Erg Chech 002
Angrites
NWA 011/2976
Mars
Moon
Vesta

Appendix D: EPMA and LA-ICPMS analyses of the samples

Here we publish the compositions measured at the EPMA (see 3.7.3) and LA-ICPMS (see 3.7.4) for all the experiments that were not already published in Pirotte et al. (2023).

Table D 1: Composition of the silicate melt from EPMA measurements.

Sample	n	SiO2	TiO2	Al2O3	Cr2O3	MnO	MgO	CaO	NiO	FeO	Na2O	K2O	P2O5	S	Total
A020	13	53.627	0.012	2.318	0.054	0.296	22.205	13.977	0.000	0.008	0.805	0.146	0.055	6.232	99.735
A021	13	54.871	0.013	2.247	0.016	0.091	21.864	13.940	0.000	0.006	0.736	0.133	0.196	5.955	100.068
A024	21	54.869	0.033	2.384	0.166	0.211	20.680	12.900	0.024	0.359	1.162	0.170	0.017	8.499	101.473
A028	5	64.980	0.011	5.150	0.023	0.012	24.874	2.888	0.030	0.005	0.786	0.124	0.140	5.084	104.107
A029	10	65.908	0.005	8.360	0.016	0.011	23.441	4.356	0.016	0.005	0.872	0.197	0.213	7.060	110.461
A030	7	61.544	0.065	6.456	0.049	0.222	27.310	3.351	0.029	0.015	0.871	0.136	0.107	7.700	107.855
A031	9	61.410	0.006	3.314	0.018	0.019	31.818	1.617	0.025	0.004	0.140	0.079	0.080	2.957	101.486
A032	7	63.076	0.037	3.087	0.025	0.075	29.906	1.649		0.010	0.767	0.106	0.167	3.449	102.354
A045	8	65.896	0.016	2.303	0.042	0.166	22.518	1.281	0.022	0.353	1.360	0.191	0.015	6.598	100.759
A047	8	51.768	0.053	1.022	0.162	0.178	40.834	0.765	0.023	2.953	0.358	0.042	0.293	0.569	99.020
A048	8	67.911	0.043	2.364	0.059	0.240	23.179	1.316	0.015	0.265	1.253	0.189	0.005	6.033	102.870
Y056-2	14	54.588	0.111	2.749	0.178	0.304	30.646	1.777	0.024	0.886	1.696	0.221	0.015	11.674	104.869
Y058-2	14	53.216	0.122	2.837	0.316	0.308	31.363	1.769		0.038	1.933	0.219	0.008	16.879	109.009
Y085-1	15	54.953	0.109	3.015	0.035	0.099	35.193	1.555	0.038	0.168	1.358	0.186	0.007	4.239	100.953

Table D 2: Standard deviations of the composition of the silicate melt from EPMA measurements.

Sample	SiO2	TiO2	Al2O3	Cr2O3	MnO	MgO	CaO	NiO	FeO	Na2O	K2O	P2O5	S	Total
A020	0.303	0.009	0.091	0.014	0.033	0.152	0.145		0.011	0.045	0.020	0.035	0.066	0.320
A021	0.346	0.014	0.064	0.017	0.021	0.287	0.098		0.011	0.047	0.024	0.034	0.069	0.340
A024	0.637	0.038	0.050	0.023	0.037	0.336	0.267	0.058	0.041	0.064	0.022	0.019	0.272	1.000
A028	0.359	0.013	1.635	0.015	0.010	4.018	1.647	0.034	0.010	0.159	0.024	0.047	1.489	0.999
A029	7.802	0.005	0.913	0.011	0.011	0.942	0.862	0.033	0.016	0.196	0.061	0.052	1.339	4.535
A030	7.629	0.020	1.022	0.033	0.125	3.445	1.019	0.038	0.016	0.122	0.032	0.032	1.133	3.773
A031	0.245	0.008	0.058	0.014	0.015	0.346	0.029	0.051	0.005	0.016	0.016	0.031	0.046	0.514
A032	0.476	0.017	0.046	0.014	0.012	0.464	0.031		0.017	0.037	0.011	0.039	0.064	0.229
A045	0.278	0.015	0.036	0.018	0.021	0.152	0.034	0.057	0.061	0.056	0.024	0.019	0.079	0.255
A047	1.099	0.014	0.239	0.020	0.028	1.240	0.367	0.031	0.498	0.183	0.029	0.068	0.264	0.377
A048	0.328	0.013	0.047	0.017	0.020	0.378	0.077	0.025	0.058	0.056	0.013	0.013	0.174	0.330
Y056-2	0.530	0.015	0.038	0.085	0.140	0.243	0.183	0.058	0.237	0.052	0.022	0.021	0.489	0.488
Y058-2	0.339	0.015	0.051	0.049	0.050	0.260	0.197		0.018	0.066	0.015	0.014	0.232	0.354
Y085-1	0.161	0.011	0.029	0.016	0.022	0.152	0.028	0.053	0.064	0.057	0.014	0.010	0.047	0.209

Table D 3: Composition of the sulfides from EPMA measurements.

Sample	n	Si	Ti	Al	Cr	Mn	Mg	Ca	Ni	Fe	Na	K	P	S	Total
A020															
A021															
A024	8	0.108	0.449		6.971	8.096	15.231	9.541	0.015	10.109			0.004	43.994	94.518
A028															
A029	13	0.301	0.089		0.126	1.179	39.444	2.961	0.007	0.007			0.004	55.772	99.888
A030	6	0.412	0.435		1.280	9.390	33.325	1.877	0.003	0.009			0.010	52.840	99.580
A031															
A032															
A045	11	0.077	0.562		2.944	0.988	0.139	0.002	0.021	56.316		0.003	0.016	36.619	97.688
A047	9	0.007	0.005		0.921	0.252	0.016	0.014	0.124	56.545		0.009	0.006	39.603	97.502
A048	4	0.183	0.479		3.757	1.274	0.120	0.013	0.027	54.637		0.007	0.027	36.138	96.662
Y056-2	2	1.034	1.400	0.000	20.145	2.490	4.550	0.557	0.014	21.650	0.000	0.000	0.007	40.790	92.638
Y058-2															
Y085-1															

Table D 4: Standard deviations of the composition of the sulfides from EPMA measurements.

Sample	Si	Ti	Al	Cr	Mn	Mg	Ca	Ni	Fe	Na	K	P	S	Total
A020														
A021														
A024	0.068	0.022		0.226	0.385	0.606	0.355	0.018	0.675			0.007	0.667	1.333
A028														
A029	0.342	0.018		0.021	0.099	0.446	0.066	0.009	0.008			0.005	0.814	0.960
A030	0.389	0.014		0.061	0.273	0.544	0.026	0.007	0.007			0.005	0.665	1.007
A031														
A032														
A045	0.107	0.128		0.401	0.081	0.036	0.003	0.021	0.944		0.004	0.013	0.412	0.397
A047	0.005	0.006		0.039	0.008	0.012	0.022	0.017	0.382		0.005	0.008	0.222	0.446
A048	0.127	0.044		0.243	0.082	0.019	0.003	0.014	0.709		0.006	0.017	0.332	0.636
Y056-2	0.786	0.220	0.000	1.135	0.220	0.690	0.025	0.009	1.620	0.000	0.000	0.005	1.720	2.988
Y058-2														
Y085-1														

Table D 5: Composition of the metals from EPMA measurements.

Sample	n	Si	Ti	Al	Cr	Mn	Mg	Ca	Ni	Fe	Na	K	P	S	Total
A020	6	1.297	1.642		40.947	3.377		0.147	2.798	3.153			19.085	0.086	72.531
A021	12	40.528	2.707		24.446	9.181		0.090	0.973	1.181			6.760	0.020	85.886
A024	14	9.832	0.005		1.361	0.027		0.065	0.279	82.432		0.001	2.032	0.043	96.077
A028	4	40.245	1.325		30.263	14.588	0.085	0.183	0.011	0.291			9.223	0.030	96.243
A029	2	51.635	1.585		36.980	9.070	0.006	0.002	0.001	0.199			1.690	0.021	101.190
A030	5	0.685	3.126		51.868	2.950	0.187	0.058	0.087	2.734			23.922	0.121	85.738
A031	1	33.030	3.460		29.990	16.990	0.044	0.016	0.013	1.440			7.640	0.026	92.649
A032	2	49.345	2.160		27.520	10.860	0.122	0.034	0.017	0.922			8.600	0.024	99.606
A045	10	15.246	0.006		0.087	0.028		0.008	0.273	79.358		0.002	1.294	0.969	97.270
A047															
A048	7	16.741	0.007		0.059	0.016	0.001	0.001	0.363	78.042		0.003	1.633	0.425	97.291
Y056-2	17	12.511	0.005		0.715	0.006	0.008	0.003	0.125	83.898			0.697	0.109	98.077
Y058-2	9	90.918	0.038		4.157	0.487		0.006	0.153	0.077			2.552	0.249	98.638
Y085-1	16	21.078	0.214		2.622	0.320	0.000	0.005	0.208	72.588			1.904	0.006	98.945

Table D 6: Standard deviations of the composition of the metals from EPMA measurements.

Sample	Si	Ti	Al	Cr	Mn	Mg	Ca	Ni	Fe	Na	K	P	S	Total
A020	0.131	0.193		1.723	0.269	0.000	0.044	0.305	0.348			1.304	0.023	2.689
A021	5.599	1.363		7.639	2.465	0.000	0.055	0.668	0.556			3.109	0.011	3.432
A024	0.526	0.009		0.175	0.017	0.000	0.041	0.028	0.390		0.004	0.367	0.017	0.520
A028	12.257	1.403		5.910	3.714	0.131	0.312	0.015	0.093			4.940	0.008	6.532
A029	1.945	0.455		0.770	0.210	0.006	0.001	0.001	0.016			0.030	0.005	0.525
A030	0.695	1.107		5.061	1.065	0.258	0.019	0.048	0.987			1.444	0.140	1.857
A031														
A032	14.775	0.330		9.410	0.460	0.118	0.007	0.016	0.043			2.600	0.014	2.171
A045	2.180	0.011		0.079	0.027		0.008	0.078	0.970		0.002	0.272	0.556	0.855
A047														
A048	0.490	0.011		0.012	0.012	0.001	0.001	0.069	0.269		0.004	0.168	0.049	0.366
Y056-2	0.673	0.008		0.102	0.009	0.009	0.006	0.025	0.812			0.251	0.075	1.001
Y058-2	4.465	0.029		1.484	0.582		0.007	0.076	0.029			1.312	0.243	1.844
Y085-1	0.692	0.043		0.138	0.032	0.002	0.006	0.050	0.631			0.463	0.007	0.646

Table D 7: Composition of the silicate melt from LA-ICPMS measurements.

	n	Na23	Al27	Si29	Ca43	Sc45	Ti47	V51	Cr53	Mn55	Fe56	Co59	Ni60	Cu63	Zn66	Ga69	Ge73	Rb85
A020	8	6471.62	12837.40	261201.48	99886.61	223.33	548.71	31.50	1019.10	2300.22	61.16	29.79	29.80	46.43	152.42	86.20	33.68	150.90
A021	7	5770.97	12461.25	260846.11	99629.32	219.19	160.72	1.93	45.89	788.55	19.16	0.91	2.35	5.81	66.21	16.56	10.90	136.53
	n	Sr88	Y89	Zr90	Nb93	Mo95	Ba137	Ce140	Nd146	Sm147	Eu153	Gd157	Yb172	Hf178	Ta181	W182	Th232	U238
A020	8	285.05	222.92	212.72	18.67	23.80	674.70	223.55	220.57	222.55	221.65	214.34	226.05	212.01	23.88	14.58	431.88	442.28
A021	7	268.94	218.29	197.98	1.15	0.93	198.22	218.61	215.44	216.88	219.54	208.41	219.00	207.41	0.74	0.62	420.23	412.71

Table D 8: Standard deviations of the composition of the silicate melt from LA-ICPMS measurements.

	n	Na23	Al27	Si29	Ca43	Sc45	Ti47	V51	Cr53	Mn55	Fe56	Co59	Ni60	Cu63	Zn66	Ga69	Ge73	Rb85
A020	8	94.57	493.42	6614.11	0.00	3.93	15.75	21.03	514.07	38.49	52.49	31.59	23.88	11.70	6.36	13.14	21.71	4.47
A021	7	77.20	82.81	1801.54	0.00	1.71	8.42	1.63	18.54	14.50	0.00	0.61	0.54	1.87	1.91	1.13	1.44	4.61
	n	Sr88	Y89	Zr90	Nb93	Mo95	Ba137	Ce140	Nd146	Sm147	Eu153	Gd157	Yb172	Hf178	Ta181	W182	Th232	U238
A020	8	4.38	4.36	4.96	15.57	21.17	159.33	3.34	2.76	4.49	2.18	3.29	3.41	6.03	13.81	12.87	11.93	9.68
A021	7	2.34	1.71	0.88	1.12	0.87	2.69	1.19	1.84	1.13	2.40	1.87	2.40	2.96	0.73	0.64	5.47	3.31

Table D 9: Composition of the metals from LA-ICPMS measurements.

	n	Na23	Al27	Si29	Ca43	Sc45	Ti47	V51	Cr53	Mn55	Fe56	Co59	Ni60	Cu63	Zn66	Ga69	Ge73	Rb85
A020	3	1864.40	2690.97	88397.88	21718.60	52.54	13713.69	19010.02	408924.92	34394.08	31527.73	19603.18	22312.48	7889.54	2196.82	6249.36	8444.52	41.69
A021	5	514.37	2252.14	552377.53	6125.11	15.57	27746.29	3777.84	136807.76	158013.85	11815.13	8307.94	10911.07	17734.28	24723.67	11515.35	4287.44	14.88
		Sr88	Y89	Zr90	Nb93	Mo95	Ba137	Ce140	Nd146	Sm147	Eu153	Gd157	Yb172	Hf178	Ta181	W182	Th232	U238
A020	3	54.80	50.99	136.94	12701.64	13117.89	120.72	44.54	40.36	44.08	43.34	45.55	46.69	48.24	9726.46	7776.31	95.31	252.56
A021	5	25.88	24.48	844.07	3054.57	1814.17	23.66	14.19	16.87	17.29	11.14	15.02	17.57	50.57	2647.41	1117.59	39.02	1274.62

Table D 10: Standard deviations of the composition of the metals from LA-ICPMS measurements.

	n	Na23	Al27	Si29	Ca43	Sc45	Ti47	V51	Cr53	Mn55	Fe56	Co59	Ni60	Cu63	Zn66	Ga69	Ge73	Rb85
A020	3	1185.15	2441.14	55707.08	16764.46	42.70	85.86	1999.98	27229.25	3987.94	0.00	2366.82	1840.11	2918.68	1060.15	5193.73	4805.31	34.33
A021	5	564.21	0.00	254247.45	5072.77	18.85	8057.15	3206.69	81189.42	56999.31	0.00	3311.23	4353.42	8307.68	13352.90	5329.54	1036.86	11.63
		Sr88	Y89	Zr90	Nb93	Mo95	Ba137	Ce140	Nd146	Sm147	Eu153	Gd157	Yb172	Hf178	Ta181	W182	Th232	U238
A020	3	46.60	46.01	48.04	829.64	1360.91	95.76	38.41	35.13	38.11	38.47	39.88	42.62	36.73	2611.26	890.43	80.93	72.82
A021	5	24.96	21.57	300.54	1389.79	1536.06	29.56	18.64	20.22	20.51	17.84	17.31	26.36	30.36	1584.23	951.24	59.56	1059.88